Group 8 & 9 Catalysts for the Dehydropolymerisation of Amine-Boranes

Mathew J. Cross

Doctor of Philosophy

University of York

Department of Chemistry

May 2025

Abstract

Chapter 1: This introductory chapter covers topics that are necessary to understand the research background upon which this thesis is built. These include fundamental amine-borane and polyaminoborane chemical properties, the origin of catalytic routes to polyaminoborane formation, the potential applications of polyaminoboranes, the mechanisms of amine-borane dehydropolymerisation and the general concept of metal ligand cooperative catalysis.

Chapter 2: In the second chapter, the activation and deactivation pathways of group 9 metal ligand cooperative amine-borane dehydropolymerisation catalysts are investigated, primarily focussing on rhodium metal-ligand cooperative aminophosphine complexes (such as Rh(^{i}Pr-PN^{H}P)H$_2$Cl) that have recently been reported by the Weller group. The slow spontaneous dissociation of amine-boranes in solution is discussed and its poisoning effect on amine-borane dehydropolymerisation catalysts, forming borohydride complexes. This is related to the as-yet unsolved problem that the substrate scope for previously reported amine-borane dehydropolymerisation catalysts is limited primarily to the parent ammonia-borane and its *N*-methyl derivative.

Chapter 3: In this chapter the structure, mechanism and speciation are investigated for amine-borane dehydropolymerisation catalysts based upon the previously reported but broadly overlooked ruthenium aminophosphine precatalyst Ru(^{i}Pr$_2$PCH$_2$CH$_2$NH$_2$)$_2$Cl$_2$. The highly unusual and reactive square-planar, d^6 and low-spin precatalyst Ru(^{i}Pr$_2$CH$_2$CH$_2$NH)$_2$ is characterised and its electronic structure discussed. Such precatalysts are shown to exhibit the highest-yet reported rate of amine-borane dehydropolymerisation, and this rapid catalysis is utilised for the synthesis of high molecular weight *N*-methyl polyaminoborane. ethyl and propyl polyaminoboranes. Parts of this chapter are published as a communication in an *Angew. Chem. Int. Ed.* article.

Chapter 4: This final discussion chapter covers the first report of selective *N*-ethyl and *N*-propyl amine-borane catalytic dehydropolymerisation, forming the *N*-ethyl and *N*-propyl polyaminoboranes utilising the ruthenium catalyst discussed in chapter 3 (Ru(^{i}Pr$_2$PCH$_2$CH$_2$NH$_2$)$_2$Cl$_2$). The possible routes of catalyst deactivation when using these amine-boranes as substrates is also discussed.

Chapter 5: Experimental data, figures, tables and methods.

Declaration

The work presented herein was carried out between September 2021 and March 2025 at the University of York, under the supervision of Prof. Andrew S. Weller. I declare that all work is my own, unless otherwise stated, and that this work has not been submitted previously for any degree at this university or any other. All sources are acknowledged as references. Work from chapter 3 of this thesis contributed toward a research publication: M. J. Cross, A. M. Sajjad, S. A. Macgregor, A. S. Weller, *Angew*. *Chem*., 2025, **64**, e202500019.

Mathew J. Cross

April 2025

Acknowledgments

First of all, I'd like to thank my supervisor *Prof Andew Weller*. You've guided me through this whole process whilst giving me freedom to explore and teaching me to really critically analyse what I do. My time in the group has introduced me to what a proper curry is, even if I only ever order an Afghani. You have been mission control, in more ways than one…

Thankyou to all the Weller group PDRA's past and present who I have worked with, you have all elevated me to be a better researcher by showing the way forward. *Laurence*: you have some strong opinions on music and strange choices in food. Our time working together was brief, but you continued to lift the mood long after you were gone. *Kris*: It's ironic that when you were first hired I was excited to have someone else to climb with, but as you joined, I promptly retired from climbing. Sorry about that. Many discussions about my haphazard meals and ropey crystal structures helped wile away those many lunches in the tearoom. I've never met anyone else who also unironically liked Sabaton. *Alex*: As the newest sacrifice to the rhodium PN^{H}P system, I wish you well. AB can be particularly gruelling, and the idiosyncrasies of each catalyst are best described the way you and Andy put it as "folklore". I can't say the fluoride depolymerisation work will be any easier, but you've got this! *Alice*: We never overlapped during our times in the group, but your work laid the foundation for my first published work. Thank you for cracking that nut for me. We seem to bump into each other at every RSC event and I look forward to many more. *Claire*: Your guidance took me from being an undisciplined undergrad and made me the chemist I am today. I'll never forget that 'short cuts cause long delays". Now I'm a postdoc myself, just a little too often I say things that you said, and which at the time made me cringe. *Matt*: Having you around throughout my entire PhD as a font of synthetic knowledge has been invaluable to me, any problem and you had the solution. I hope the old-country is treating you well and that you've gotten over your fear of Phil Collins. Thanks for helping save my face from the sulphuric acid, introducing me to Triple-J, and sorry again for operating the glovebox port with my foot that one time.

To the PhD's of the Weller group: thank you for making my time in York so fulfilling, dragging me out of my shell and making me a more well-rounded person. *James, Cameron and Olie*: Our time working together was brief, but you made an indelible

mark on the Weller spirit that was felt long after you were gone, I hope we did you proud. *Helena*: You're a force of nature, never change. From weekly mental health scores to playing bloody knuckles in Valhalla or deadlifting at York sport, we had a pretty unhinged time but that's what made it great. I didn't expect it at the time, but 'Where the Crawdads Sing' has definitely made my top 10 films. *Joe*: Where do I start, honestly. When we first met, I knew we had something special but little did I know that it would lead to a true bromance: bonding over everything from MMA and massages to scunges and eating primitive lifeforms. There are too many standout moments to count: Mt. Hatred, Crab raves, tales from the E-block toilet, rock-bottom sour sweets, 'BOC man come', the 'no-hope' jumper and being your groomsman. Together we crawled from the primordial ooze to become truly mediocre crystallographers, what an achievement. Never stop being "blasé and worse". *Chloe J (T-800)*: From the moment we became Wellers the group started slipping. I'm so glad that I joined the group at the same time as you, it made the whole process so much less daunting. Luckily you had enough personality for the both of us, so I could hide amongst my plants in the corner of the office. We both made it out the other side, but I'm more impressed that we managed to get all that red wine off your kitchen ceiling (oops). P.S Lego batman was a true masterpiece, you were right. *Chloe VB (T-1000)*: I couldn't have hoped for a better team-AB co-conspirator, you kept me grounded when I wanted to try every crazy idea and yet were critical in getting the TrAP project off the ground. Even if 'off the ground' meant only a few inches. You managed to put up with my verbalised streams of consciousness any time I had a new idea, for that I commend you. Even more impressive considering that, let's face it, for you, patience doesn't come naturally! Sorry about all the desk lunches and the shrapnel wound, you were warned to be fair. You better refer to me as AB-Wan Kenobi for all the new starters. *Jack*: Having watched you grow from a lowly MChem to a fully-fledged (and slightly jaded) PhD student has been a pleasure. You brought a level of class to the group that we'd never seen the likes of before. The time we spent together in Trieste along with Keira and Millie was a cut above what I could expect from the rest of the Weller rabble. *Rebecca*: I'm glad that Andy has finally hired someone normal. I still haven't finished reading that book. *Dom:* Another sacrifice to AB/PB, try not to let it get you down. Keep up the astrophotography!

To the MChems of the Weller group, the continual influx of fresh blood and optimism kept things from going stale, there was never a dull moment. *Kat*: Your brief jaunt in team AB was under some horrendous conditions but you survived. When we met last at Dalton I was proud to see the progress you've made, while keeping that bulletproof positive attitude. *Anna*: Thank you for helping me realise my visons for the fluoride work, you were a very capable second pair of hands. I hope your dreams of owning a horse come true. *Orry*: I never expected to bond over fossils, hopefully I can dig out the rest of that tree in St. Andrews. Now that you've started your PhD, I can live vicariously through you as a hardened f-block chemist, good luck. *Natalia*: You've gone to the SMOM dark side for now but maybe one day you'll re-join the AB light. Cheers for teaching me how to say caipirinha properly.

To my housemates over my time in York *Ollie, Talat, Ben, & Matt*: we made it in the end and have somehow all secured real adult jobs despite the odds. All those times bouldering, playing Catan/Risk and setting the world to rights over a pint were crucial. I'm still salty we lost all that money on palladium.

To my family, particularly mum and dad: your unwavering support and advice has kept me on the right track all these years. Despite your best efforts, you still haven't scared me off from a career in academia. Hopefully this ages well.

Last but not least, thank you to my beautiful and incredibly caring fiancé Keira. I'm sorry for all the weekends and evenings you've had to sit watching me just write, your care for me has really kept me going through this whole process. Your patience for all my late nights in the lab and post date-night (slightly tipsy) GPC repairs means a lot. I now have the pleasure of helping you set off on your own PhD journey, you'll be incredible. I love you lots and look forward to spending the rest of our lives together.

Abbreviations

Å	Ångström ($1x10^{-10}$ metres)
$[BAr^{F}{}_{4}]^{-}$	$[B(3,5\text{-}(CF_3)_2C_6H_3)_4]^{-}$ anion
^{t}Bu	tertiary butyl
°C	Degrees Celsius
cal	Calorie (unit of energy)
cat	Catalyst
cm^{-3}	Per centimetre cubed
COD	1,4-cyclooctadiene
COSY	Correlation Spectroscopy
Cp^{*}	1,2,3,4,5-Pentamethylcyclopentadienyl
Cy	Cyclohexyl
(d)	NMR doublet splitting
1,2-DFB	1,2-difluorobenzene
DFT	Density functional theory
dm^{-3}	Per decimetre cubed
DP	Polymer degree of polymerisation
ΔG°	Free energy change at 298 K and 1 atmosphere
ΔG‡	Free energy change of activation
$\Delta H_{diss}{}^{0}$	Standard bond dissociation enthalpy
Đ	Dispersity
e^{-}	Electron
E	Electrophile
ESI+	Electrospray ionisation (positive)

Et	Ethyl
FWHM	Full width half maximum
GPC	Gel Permeation Chromatography
g	Gram
HMBC	Heteronuclear multiple-bond coherence
HOMO	Highest occupied molecular orbital
Hz	Hertz (s^{-1})
^{i}Pr	Isopropyl (-CH(CH_3)$_2$)
^{i}Pr-PN^{H}P	HN($CH_2CH_2P^{i}Pr_2$)$_2$, MACHO type ligand
I	Nuclear spin quantum number
J	Joule (unit of energy)
^{1}J	One-bond spin-spin coupling in NMR
K	Degrees Kelvin
kcal	Kilocalorie
k_{obs}	Observed rate constant
κ	Ligand denticity
ln	Natural logarithm
LUMO	Lowest unoccupied molecular orbital
M	Molarity, moles per decimetre cubed
[M]	Generic metal centre
M^{x}	Generic metal centre where x is the oxidation state
MACHO	HN($CH_2CH_2PR_2$)$_2$
Me	Methyl
mg	Milligrams

mol	Mole(s)
mol%	Relative mole percent
M_n	Number average molecular weight
M_w	Weight average molecular weight
M_w	Molecular weight (g mol^{-1})
Myrt	Myrtanyl
m/z	Mass to charge ratio
NBD	Norbornadiene
NMR	Nuclear magnetic resonance spectroscopy
Nu	Nucleophile
OTf	Triflate ($–OSO_2CF_3$)
POCOP^{t}Bu	κ^3-2,6-bis(di-tert-butylphosphinito)benzene)
^{t}Bu-PONOP	κ^3-2,6-bis(di-tert-butylphosphinito)pyridine)
PNP	κ^3-2,6-bis(di-alkylphosphino)pyridine)
ppm	parts per million
^{n}Pr	*n*-propyl
^{i}Pr-PN^{H}P	$NH(CH_2CH_2P^iPr_2)$ ligand
R	Generic chemical group
R_1	Agreement between calculated and observed structure models
R^2	Square of the correlation coefficient
R_{int}	Agreement between equivalent observed x-ray reflections
RI	Refractive index
s	Seconds
(s)	Singlet NMR signal

S	Total electronic spin quantum number
Sec	Secondary
S_N2	Bimolecular nucleophilic substitution
SPS	Grubbs-type solvent purification system
t	Time
(t)	NMR triplet splitting
T_g	Glass transition temperature
THF	Tetrahydrofuran
TOF	Turnover frequency
VTNA	Variable-time normalized (kinetic) analysis
X	Generic electronegative atom
δ	Chemical shift (in ppm)
δ^+	Partial positive charge
δ^-	Partial negative charge
Δ	The input of thermal energy during a reaction

Contents

Abstract 2

Declaration 3

Acknowledgments 4

Abbreviations 7

1. Introduction 18

1.1 Amine-boranes and aminoboranes 18

1.2 Polyaminoboranes 23

1.2.1 Polyaminoborane characterisation methods 25

1.2.2 Substituted polyaminoboranes other than $(H_2BNHMe)_n$ and $(H_2BNH_2)_n$ 28

1.3 Polyaminoborane synthesis: mechanistic considerations 32

1.3.1 Polymerisation mechanism 32

1.3.2 Aminoborane generation mechanisms 34

1.4 Metal-ligand cooperative catalysis 41

1.5 Catalyst design for metal-ligand cooperative dehydropolymerisation 43

1.5.1 Ligand effects 43

1.5.2 Metal centre effects 44

1.6 Polyaminoborane materials applications 48

References 50

2. The dehydropolymerisation of amine-boranes with group 9 PN^HP catalysts 56

2.1 The dehydropolymerisation of amine-boranes with precatalysts [Rh(^{i}Pr-PN^HP)(NBD)][Cl] (1) and Rh(^{i}Pr-PN^HP)H_2Cl (2): background and methods 59

2.1.1 The effect of air on [Rh(^{i}Pr-PN^HP)(NBD)][Cl] (1) precatalyst activation 61

2.1.2 The effect of water on [Rh(^{i}Pr-PN^HP)(NBD)][Cl] (1) precatalyst activation 67

2.1.3 A summary of the effects of water and air on the dehydropolymerisation of *N*-methyl amine-borane with [Rh(^{i}Pr-PN^HP)(NBD)][Cl] (1) 73

2.1.4 The attempted dehydropolymerisation of *N*-alkyl amine-boranes with precatalyst [Rh(^{i}Pr-PN^HP)(NBD)][Cl] (1) 75

2.1.5 Identification of the catalyst speciation from the attempted dehydropolymerisation of $H_3B{\cdot}NH_2{}^nPr$ with precatalyst 1 80

2.1.6 The origin of BH_3 causing catalyst poisoning in amine-borane dehydropolymerisation. 86

2.1.7 The attempted dehydropolymerisation of *N*-alkyl amine-boranes with precatalyst Rh(^{i}Pr-PN^{H}P)H_2Cl (2) 89

2.1.8 The variation of reaction conditions to reduce catalyst poisoning in dehydropolymerisations with 2 95

2.1.8.1 The effect of solvent choice on the substrate conversion and catalyst poisoning for dehydropolymerisations of *N*-methyl and *N*-ethyl amine-boranes with precatalyst 2 95

2.1.8.2 The effect of added amines on the substrate conversion and catalyst poisoning for dehydropolymerisation of *N*-ethyl amine-borane with precatalyst 2 100

2.1.8.3 The effect of reaction temperature on the substrate conversion and catalyst poisoning for dehydropolymerisation of *N*-ethyl amine-borane with precatalyst 2 105

2.1.8.4 A summary of the effects of amine concentration, solvent and reaction temperature on the substrate conversion and catalyst poisoning for dehydropolymerisation of *N*-ethyl amine-borane with precatalyst 2 108

2.2 The dehydropolymerisation of amine-boranes with precatalysts Co(^{i}Pr-PN^{H}P)Cl_2 (5), Co(Cy-PN^{H}P)Cl_2 (6) and Co(Cy-PN^{H}P)H_2Cl (7) 112

2.2.1 The attempted dehydropolymerisation of $H_3B{\cdot}NH_2{}^nPr$ with Co(^{i}Pr-PN^{H}P)Cl_2 (5) & Co(Cy-PN^{H}P)Cl_2 (6) 113

2.2.2 The effect of phosphine substituent on PN^{H}P ligand donating ability and the attempted dehydropolymerisation of $H_3B{\cdot}NH_2Me$ with Rh(Cy-PN^{H}P)H_2Cl (7) . 117

2.2.3 A summary of metal centre and ligand phosphine substituent effects on the dehydropolymerisation of *N*-alkyl amine-boranes with group-9 MACHO catalysts 122

References 123

3. The dehydropolymerisation of methyl amine-borane with group 8 $H_2NCH_2CH_2P^iPr_2$ catalysts 127

3.1 The dehydropolymerisation of $H_3B{\cdot}NH_2Me$ with 8 and ^{t}BuOK 130

3.2 The activation of precatalyst 8 with 2 equivalents of ^{t}BuOK to form *P,P-trans*-$Ru(^iPr_2PCH_2CH_2NH)_2$ (9) 134

3.2.1 The proposed electronic structure of 9 137

3.2.2 Decomposition of 9 into $Ru_2H(\mu_{2,}\kappa^1\text{-}NHCH_2CH_2P^iPr_2)_2(\mu_2,\kappa^1\text{-}NCH_2CH_2P^iPr_2)(\kappa^2\text{-}^iPr_2PCH_2CH_2NH_2)$ (10) 142

3.3 Kinetic analysis of the dehydropolymerisation of $H_3B{\cdot}NH_2Me$ with 8 and ^{t}BuOK 146

3.3.1 Determination of the order in catalyst and substrate for the dehydropolymerisation of amine-boranes with in-situ generated 9 149

3.4 The dehydropolymerisation of $H_3B{\cdot}NH_2Me$ with 8 and NH_2Me 154

3.4.1 Kinetic analysis of the dehydropolymerisation of $H_3B{\cdot}NH_2Me$ with 8 and NH_2Me 159

3.5 Speciation during amine-borane dehydropolymerisation with 8 166

3.5.1 Induction period speciation during amine-borane dehydropolymerisation with 8 166

3.5.2 The identity and formation of 11 during the induction period of amine-borane dehydropolymerisation with 8 169

3.5.2.1 The dehydropolymerisation of $H_3B{\cdot}NH_2Me$ with 11 as a precatalyst. 176

3.5.3 Catalyst speciation during the active catalysis phase of amine-borane dehydropolymerisation with 8 178

3.5.4 The hydrogenation of 9 with H_2 to form a ruthenium hydride 183

3.6 The reaction of 8 with borohydride to form ruthenium hydride *P,P-cis*-$Ru(^iPr_2PCH_2CH_2NH_2)_2(\kappa^1\text{-}BH_4)H$ (13) 186

3.6.1 *P,P-cis*-$Ru(^iPr_2PCH_2CH_2NH_2)_2(\kappa^1\text{-}BH_4)H$ (13) as a precatalyst to amine-borane dehydropolymerisation 189

3.7 Possible mechanisms for the dehydropolymerisation of amine-boranes with precatalysts 8, 9 and 13 193
3.7.1 Precatalyst activation and induction period 193
3.7.2 Potential amine-borane dehydrogenation mechanisms 195
3.8 Conclusions 199
3.9 Future work 200
References 202
4. The selective catalytic synthesis of $(H_2BNHEt)_n$ and $(H_2BNH^nPr)_n$ 206
4.1 The dehydropolymerisation of $H_3B{\cdot}NH_2{}^nPr$ and $H_3B{\cdot}NH_2Et$ with 8 when activated with NH_2Me 206
4.1.1 The attempted dehydropolymerisation of $H_3B{\cdot}NH_2{}^nPr$ with 8 at low catalyst loading (0.033 mol%), with NH_2Me 207
4.1.2 The attempted dehydropolymerisation of $H_3B{\cdot}NH_2{}^nPr$ with 8 at high catalyst loading (0.33 mol%), with NH_2Me 209
4.1.3 The dehydropolymerisation of $H_3B{\cdot}NH_2Et$ and $H_3B{\cdot}NH_2{}^nPr$ with 8 at high catalyst loading (0.5 mol%), with NH_2Me 214
4.2 The NMR spectra of polyaminoboranes $(H_2BNHEt)_n$ and $(H_2BNH^nPr)_n$ 218
4.3 The future materials properties investigation of polyaminoboranes $(H_2BNHEt)_n$ and $(H_2BNH^nPr)_n$ 220
4.4 Conclusions and future work 221
References 222
5. Experimental methods 224
5.1 General experimental methods 224
5.1.1 NMR spectroscopic measurements 225
5.1.2 Gel permeation chromatography (GPC) 225
5.1.3 Mass spectrometry 225
5.1.4 Infra-red spectroscopy (IR) 226
5.1.5 UV-vis spectroscopy 226

5.2 Chapter 2 experimental methods and data 227

5.2.1 Synthesis and characterisation of Rh(*i*Pr-PN^{H}P)(κ^{1}-BH$_4$)H$_2$ (4) 228

5.2.2 Synthesis and characterisation of {*i*Pr$_2$P(=Se)CH$_2$CH$_2$}$_2$NH 233

5.2.3 Synthesis and characterisation of {Cy$_2$P(=Se)CH$_2$CH$_2$}$_2$NH 235

5.2.4 Synthesis and characterisation of {*t*Bu$_2$P(=Se)CH$_2$CH$_2$}$_2$NH 239

5.2.5 Synthesis and characterisation of Rh{κ^{3}-(Cy$_2$PCH$_2$CH$_2$)$_2$NH}H$_2$Cl (7) 243

5.2.6 The dehydropolymerisation of methyl amine-borane with Rh(*i*Pr-PN^{H}P)(NBD)][Cl] (1) under argon 248

5.2.7 The dehydropolymerisation of methyl amine-borane with Rh(*i*Pr-PN^{H}P)(NBD)][Cl] (1) in air 249

5.2.8 The attempted dehdyropolymerisation of *n*-propyl amine-borane with Rh(*i*Pr-PN^{H}P)(NBD)][Cl] (1) 250

5.2.9 The dehdyropolymerisation of methyl, ethyl and *n*-propyl amine-borane with Rh(*i*Pr-PN^{H}P)H$_2$Cl (2) 251

5.2.10 The dehdyropolymerisation of ethyl amine-borane with Rh(*i*Pr-PN^{H}P)H$_2$Cl (2), varying the solvent 252

5.2.11 The dehydropolymerisation of ethyl amine-borane with Rh(*i*Pr-PN^{H}P)H$_2$Cl (2), varying the reaction temperature 253

5.2.12 The dehydropolymerisation of ethyl amine-borane with Rh(*i*PrPN^{H}P)H$_2$Cl (2), varying the amine added 254

5.2.13 The attempted dehydropolymerisation of *n*-propyl amine-borane with Co(*i*Pr-PN^{H}P)Cl$_2$ (5) & Co(Cy-PN^{H}P)Cl$_2$ (6) 255

5.2.14 The attempted dehydropolymerisation of methyl amine-borane by Rh(PN^{H}PCy)H$_2$Cl (7) 256

5.3 Chapter 3 and 4 experimental methods and data 257

5.3.1 Synthesis and characterisation of *P,P-cis*-Ru(*i*Pr$_2$PCH$_2$CH$_2$NH$_2$)$_2$Cl$_2$ (8) 257

5.3.3 Synthesis and characterisation of *P,P-trans*-Ru(*i*Pr$_2$PCH$_2$CH$_2$NH)$_2$ (9) 260

5.3.4 Synthesis and characterisation of Ru(*i*Pr$_2$PCH$_2$CH$_2$NH)$_2$ dimer Ru$_2$H(μ$_{2,}$κ^{1}-NHCH$_2$CH$_2$P*i*Pr$_2$)$_2$(μ$_{2,}$κ^{1}-NCH$_2$CH$_2$P*i*Pr$_2$)(κ^{2}-*i*Pr$_2$PCH$_2$CH$_2$NH$_2$) (10) 264

5.3.5 Synthesis and characterisation of *P,P-cis*-Ru(^{i}Pr$_2$PCH$_2$CH$_2$NH$_2$)$_2$(OH)H (11) 273

5.3.6 Synthesis and characterisation of *P,P-cis*-Ru(^{i}Pr$_2$PCH$_2$CH$_2$NH$_2$)$_2$(κ^1-BH$_4$)H (13) 281

5.3.7 Dehydropolymerisation of methyl amine-borane with *P,P-trans*-Ru(^{i}Pr$_2$PCH$_2$CH$_2$NH)$_2$ (9) 285

5.3.8 Dehydropolymerisation of methyl amine-borane with *P,P-cis*-Ru(^{i}Pr$_2$PCH$_2$CH$_2$NH$_2$)$_2$Cl$_2$ (8) and MeNH$_2$ 288

5.3.9 dehydroplymerisation of methyl amine-borane with *P,P-cis*-Ru(^{i}Pr$_2$PCH$_2$CH$_2$NH$_2$)$_2$(OH)H (11) 290

5.3.10 Dehydropolymerisation of methyl amine-borane with *P,P-cis*-Ru(^{i}Pr$_2$PCH$_2$CH$_2$NH$_2$)$_2$(κ^1-BH$_4$)H (13) 292

5.3.11 Dehydropolymerisation of ethyl amine-borane with *P,P-cis*-Ru(^{i}Pr$_2$PCH$_2$CH$_2$NH$_2$)$_2$Cl$_2$ (8) and MeNH$_2$ 294

5.3.12 Dehydropolymerisation of *n*-propyl amine-borane with *P,P-cis*-Ru(^{i}Pr$_2$PCH$_2$CH$_2$NH$_2$)$_2$Cl$_2$ (8) and MeNH$_2$ 295

5.3.13 Dehydropolymerisation of methyl amine-borane with *P,P-cis*-Ru(^{i}Pr$_2$PCH$_2$CH$_2$NH$_2$)$_2$Cl$_2$ (8) and MeNH$_2$, recharge experiment 296

5.4 Crystallography 298

5.4.1 Additional crystallographic details 298

5.4.2 Crystallographic tables 301

5.5 Computational details 304

5.5.1 Computed geometries and spin states of *P,P-trans*-Ru(^{i}Pr$_2$PCH$_2$CH$_2$NH)$_2$ (9) 305

5.5.2 Time-Dependent Density Functional Theory (TDDFT) Calculations for *P,P-trans*-Ru(^{i}Pr$_2$PCH$_2$CH$_2$NH)$_2$ (9) 306

5.5.2 Computed Cartesian coordinates (Å) and energies (hartrees) for all species relating to *P,P-trans*-Ru(^{i}Pr$_2$PCH$_2$CH$_2$NH)$_2$ (9) 313

References 316

Chapter 1: Introduction

1. Introduction

This thesis will discuss the catalysis of amine-borane dehydropolymerisation by group 8 (**Chapter 3**) and group 9 (**Chapter 2**) catalysts. In this first chapter a general introduction into amine-borane chemistry and polyaminoborane synthesis is given before the mechanistic insights and catalyst design for the catalytic dehydropolymerisation of amine boranes are discussed. This is followed by an overall perspective on polyaminoborane applications and routes toward improved control of the polymers formed.

1.1 Amine-boranes and aminoboranes

Amine-boranes are Lewis donor-acceptor adducts consisting of an amine electron pair donor (NR_3, where R = H, alkyl, aryl), and a borane electron pair acceptor (BR_3, where R = H, alkyl, aryl) (**Figure 1**). This donation of the sp^3-hybridised lone pair from the amine nitrogen into the vacant 2p-orbital of the borane boron forms a dative B–N single bond, which brings the valence electron count of both atoms to 8 and results in a donor-acceptor complex. The resulting Lewis adduct donor-acceptor complex ($R_3B{\cdot}NR_3$) is isosteric and isoelectronic with the related alkanes ($R_3C–CR_3$): in both situations a total of 8 valence electrons are contributed by the two atoms forming each central bond, 4 + 4 (2 × C) in alkanes and 3 + 5 (B + N) in amine-boranes. In each case both atoms across the central bond are sp^3 hybridised and each form 3 additional bonds (**Figure 1**). The comparable prototypical examples of alkanes and amine-boranes are ethane and ammonia-borane ($H_3B{\cdot}NH_3$) respectively.

In contrast to the C–C bond in alkanes, the central bond (B–N) in amine-boranes is highly polarised, owing to the differing Pauling electronegativities of its constituent atoms: 2.04 for boron and 3.04 for nitrogen. [1] The greater electronegativity of nitrogen than boron means that the donated electron pair in reality remains more closely associated with the N donor atom than the B acceptor, resulting in a comparatively weak bond where only 0.2 e^- are donated from N to B. [2] This is apparent when comparing the bond lengths and dissociation energies of the B–N in ammonia-borane with the C–C in the isoelectronic and isosteric ethane. The B–N bond is significantly longer at 1.66 Å and weaker ($\Delta H_{diss}° = 130$ kJ mol^{-1}) than its C–C counterpart (1.53 Å, $\Delta H_{diss}° = 377$ kJ mol^{-1}) (**Figure 1**).[2] This low bond dissociation energy of dative B–N

bonds means they are significantly more prone to heterolytic B–N bond cleavage than C–C bonds.

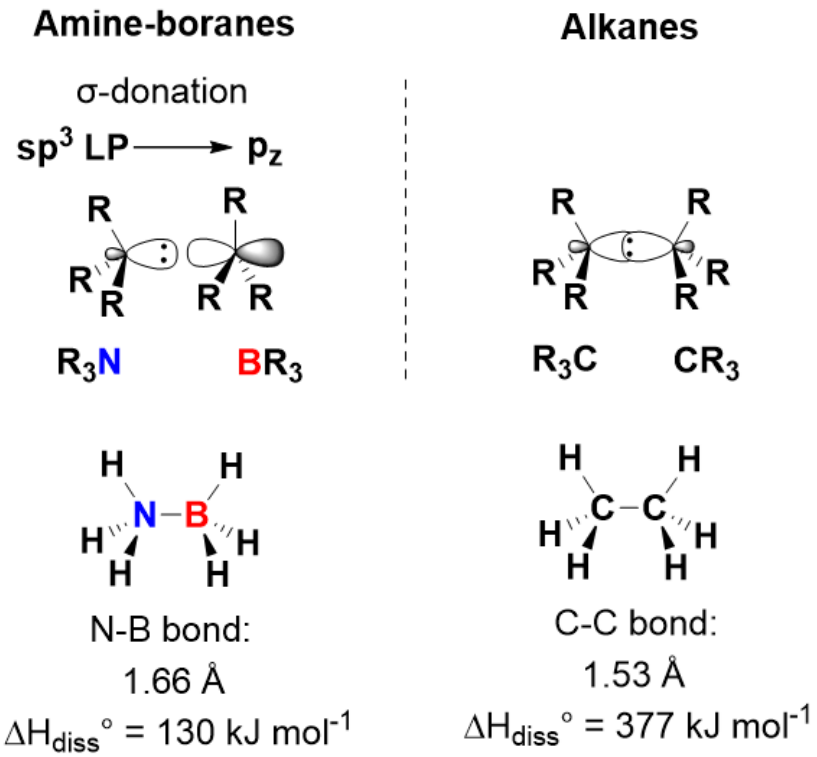

Figure 1. The comparative bonding model in amine-boranes and alkanes, relating the bond lengths and energies of the B–N vs the C–C bond in $H_3B{\cdot}NH_3$ vs ethane. [2]

The electronegativity differences and polarised B–N bond in amine-boranes lead to exaggerated polarisation of the N–H and B–H bonds respectively. As hydrogen has an electronegativity higher than that that of boron and lower than that of nitrogen (B: 2.04, H, 2.20, N: 3.04), B–H bonds are polarised with a δ^- partial charge on the hydrides and N–H bonds are polarised with a δ^+ partial charge on the protons. [1] In amine-boranes, the increased electron density at the acceptor B atom is compensated by polarisation of the B–H bonds, imparting a δ^- partial charge on the hydrides. Correspondingly the donor N atom compensates by withdrawing a larger charge density from its protons, imparting a relatively larger δ^+ partial charge on the protons than in the free amine. [3] The consequence of this is that dipolar interactions occur between N–H δ^+ and B–H δ^- moieties on amine-boranes called dihydrogen bonds.[4] Dihydrogen bonding interactions have been observed as close-contacts between N–H and B–H in the neutron-diffraction x-ray crystal structure of $H_3B{\cdot}NH_3$ (**Figure 2**).[5] These relatively strong dihydrogen bonding interactions (17 – 24 kJ mol^{-1}) mean that ammonia-borane

is a solid at room temperature, with a melting point of 124 °C, compared with the isosteric and isoelectronic ethane which has a melting point of –189 °C. [3, 4, 6, 7]

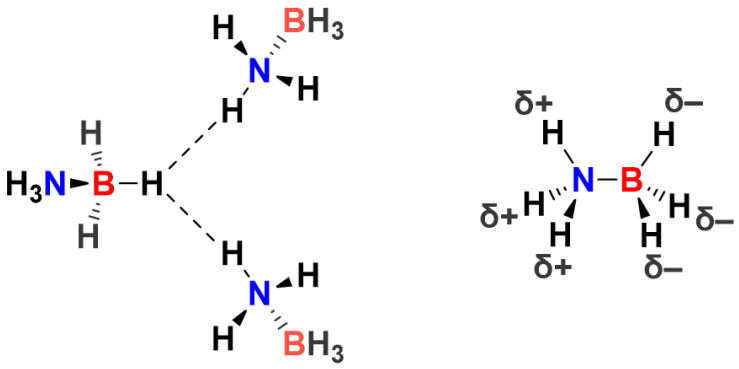

Figure 2. Left: an example of the dihydrogen bonding interactions observed in the crystal structure of ammonia-borane. [5] Right: the partial charges on ammonia-borane protons and hydrides.

The polarity of the B–N bond has a profound impact on the reactivity of amine boranes. Adjacent H δ^+ protons and H δ^- hydrides enable the facile overall loss of H_2 from across the B–N bond, making amine-boranes highly effective reducing agents. [8] Amine-boranes have been shown to act as highly selective transfer hydrogenation agents for polarised bonds such as C=O and C=N via concerted double H transfer, where complementary partial charges template the approach (**Figure 3**).[9, 10] The thermal elimination of H_2 from across the B–N bond is also facilitated, with H_2 loss from $H_3B{\cdot}NH_3$ beginning at ~ 110 °C in solution. [11] This in contrast to analogous alkanes for which dehydrogenation is highly endothermic, requiring much higher temperatures. [12]

Upon loss of H_2 amine-boranes form aminoboranes ($R_2N{=}BR_2$), that are highly unstable reactive intermediates that are isosteric and isoelectronic with alkenes. This instability is due to the presence of both the highly Lewis-acidic unhindered sp^2 BR_2 and the Lewis-basic NR_2, which undergo facile reaction between adjacent molecules that is templated by complementary partial charges (**Figure 3**).[13] Unhindered, aminoboranes rapidly cyclo-oligomerise in solution, with only bulky derivatives such as $^{i}Pr_2N{=}BH_2$ existing as monomers . [14, 15]

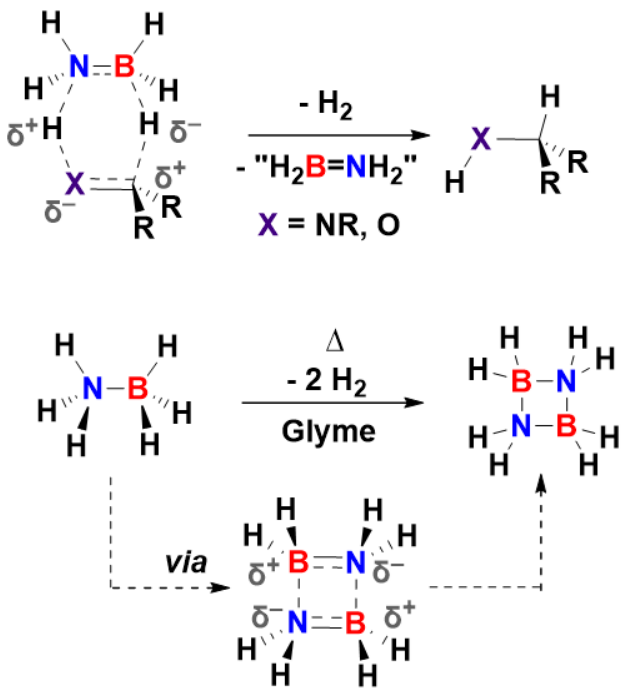

Figure 3. Top: the hydrogenation of polar double bonds by $H_3B{\cdot}NH_3$, templated by complementary dipolar interactions. [10] Bottom: The thermal decomposition of $H_3B{\cdot}NH_3$ in solution by H_2 elimination, forming an intermediate aminoborane $H_2B{=}NH_2$, which subsequently cyclo-oligomerises. Example product given as cyclodimer, experimentally multiple compounds of the empirical formula BNH_4 are formed, particularly the trimer $(H_2NBH_2)_3$ and short-chain oligomers. [11, 15, 16]

From the early 2000's, amine-boranes were of particular interest as high-density sources of H_2 for use as fuels, with 194 g of H_2 theoretically released from the complete dehydrogenation of 1 kg of $H_3B{\cdot}NH_3$. [17-20] As the thermal dehydrogenation of $H_3B{\cdot}NH_3$ requires a temperature of over 100 °C for the first equivalent of H_2 to be released and 170 °C for the second equivalent, transition metal catalysts were proposed to rapidly release H_2 from amine-boranes at ambient temperatures. [21, 22] Early examples of such catalysts are titanium Cp* complexes (such as $Ti(C_5Me_4{}^{i}Pr)_2$) and the iridium complex $Ir(POCOP^{t}{}_{Bu})H_2$ which are reported to release 1 equivalent of H_2 from $H_3B{\cdot}NH_3$ (**Figure 4**).[23, 24] Work on catalysts such as these laid the foundations for the synthesis of polyaminoboranes via the catalytic dehydropolymerisation of amine-boranes. [25, 26] The pursuit of amine-boranes as fuels has slowed due to the difficulty in regenerating (re-hydrogenating) the dehydrogenation BN products such as borazines, $(HBNR)_3$, back to amine-boranes to close the loop. To date the regeneration of spent amine-borane fuels has only been achieved under harsh conditions, requiring heating with hydrazine in liquid ammonia under high pressure. [27]

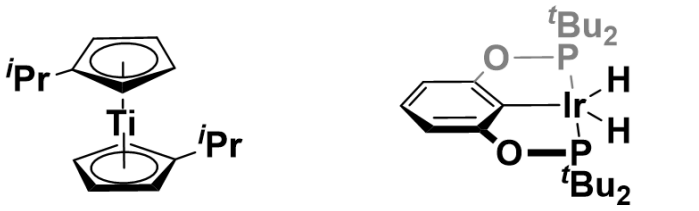

Chirik *et al* 2007 **Goldberg *et al* 2006**

Figure 4. Examples of early transition metal catalysts reported to be capable of dehydrogenating $H_3B{\cdot}NH_3$, releasing 1 equivalent of H_2. $Ti(C_5Me_4{}^{i}Pr)_2$ and $Ir(POCOP^{t}{}_{Bu})H_2$ shown. [23, 24]

1.2 Polyaminoboranes

Polyaminoboranes are boron-nitrogen based polymers that are isosteric and isoelectronic with polyolefins, consisting of aminoborane monomers (such as $H_2B{=}NHMe$) datively bonded to form an extended B–N backbone (**Figure 5**). Historically the term polyaminoborane referred to the ill-defined, highly-insoluble material of empirical formula BNH_4 formed by pyrolysis of the parent ammonia-borane $H_3B{\cdot}NH_3$ in the solid state. [28] During the pyrolysis of solid $H_3B{\cdot}NH_3$ at 120 °C, one equivalent of H_2 is lost from across the B–N bond forming the parent aminoborane $H_2B{=}NH_2$, which rapidly oligomerises. [21] Modern solid-state NMR studies of this material have shown it to be a highly branched and crosslinked polymeric material, alongside linear and cyclo-oligomeric dehydrocoupled side products (**Figure 5**).[15, 29]

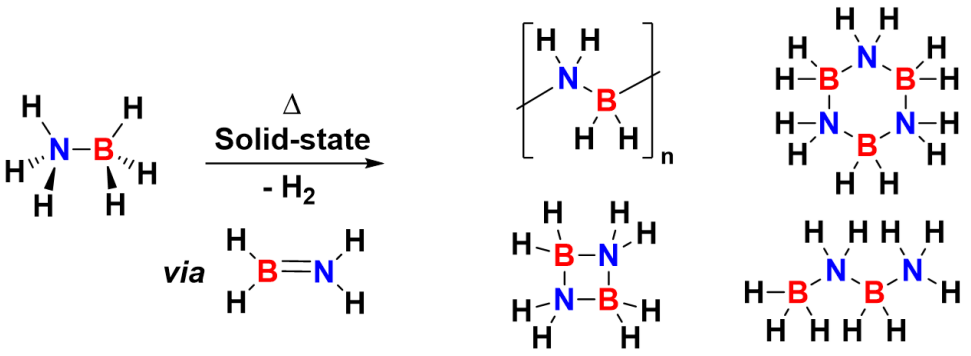

Figure 5. The solid-state pyrolysis of $H_3B{\cdot}NH_3$ at 120 °C produces a wide variety of dehydrocoupled products, of which the ill-defined non-volatile polymeric material $(H_2BNH_2)_n$ is deposited as a solid. [15, 29]

The first report of a fully characterised, high molecular weight (non-oligomeric) polyaminoborane is of poly(*N*-methylaminoborane), $(H_2BNHMe)_n$, by Manners et al. in 2008, where an iridium pincer catalyst ($Ir(POCOP^tBu)H_2$) was used to dehydropolymerise methylamine-borane ($H_3B{\cdot}NH_2Me$) (**Figure 6**).[23, 26, 30] The same catalyst had previously been shown by Goldberg et al. to dehydrogenate ammonia borane at low concentrations, whereas Manners et al. performed catalysis using 10 mol dm^{-3} of ammonia borane.[23] Investigation into the exact mechanism of operation for this catalyst is ongoing in the Weller group, and catalytic amine-borane dehydropolymerisation mechanisms will be discussed in section **1.3**. [31] The use of a catalyst for the dehydrocoupling of $H_3B{\cdot}NH_2Me$ facilitated the selective production of

linear $(H_2BNHMe)_n$, rather than the branched polymer and oligomers observed in the pyrolysis of $H_3B{\cdot}NH_3$, via the controlled production of the aminoborane intermediate ($H_2B{=}NHMe$). [32] The thermal decomposition of $H_3B{\cdot}NH_2Me$, unlike $H_3B{\cdot}NH_3$ (**Figure 5**), results primarily in the formation of the cyclic oligomer $(H_2BNHMe)_3$ as the thermodynamic product, and so the catalysed dehydrogenation allows access to the linear, kinetic product $(H_2BNHMe)_n$ (**Figure 6**). [33-35]

The Ir catalyst used by Manners et al. ($Ir(POCOP^{tBu})H_2$) is also capable of dehydropolymerising $H_3B{\cdot}NH_3$. The linear polymer formed $(H_2BNH_2)_n$, like the branched material formed from pyrolysis, is however insoluble in all common solvents hindering characterisation. [26] This is due to the high degree of dihydrogen bonding between $(H_2BNH_2)_n$ polymer chains, which is somewhat disrupted by the substitution of an N–H by a methyl group in $(H_2BNHMe)_n$. [36] Most studies of polyaminoboranes thus-far reported are of $(H_2BNHMe)_n$, partly for the reason that it is the simplest system that is readily soluble (see section **1.2.2**).

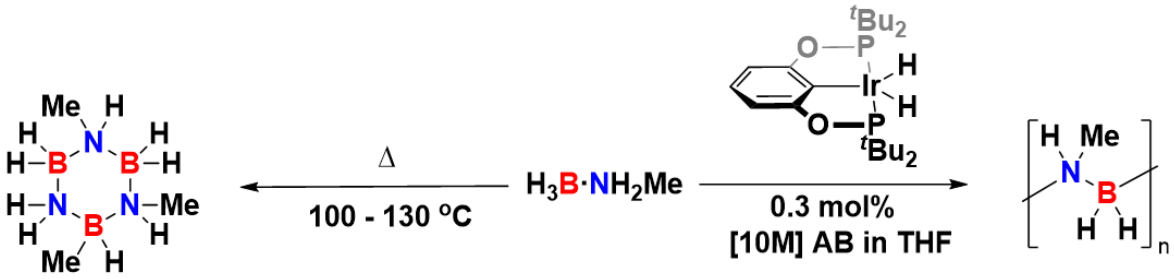

Figure 6. The thermal dehydrocoupling of $H_3B{\cdot}NH_2Me$ forming the cyclic trimer $(H_2BNHMe)_3$ and the catalysed dehydropolymerisation forming linear $(H_2BNHMe)_n$ polymer selectively. [26, 33-35]

1.2.1 Polyaminoborane characterisation methods

As previously mentioned in section **1.2**, the structural characterisation of insoluble polyaminoboranes such as $(H_2BNH_2)_n$ and highly crosslinked materials is limited to solid-state NMR. The techniques discussed here will apply primarily to soluble polymers such as $(H_2BNHMe)_n$. [37] Polyaminoboranes contain boron atoms in the main-chain backbone which consist of two isotopes: ^{11}B and ^{10}B in an approximate ratio of 4:1 respectively. Both of these isotopes are spin active (^{11}B I = – 3/2, ^{10}B I = 3) and can be observed by nuclear magnetic resonance spectroscopy (NMR), of which ^{11}B with the higher abundance and lower quadrupolar nuclear spin, is of more practical use. [38] In ^{11}B NMR spectroscopy, polyaminoboranes appear as a broad peak centred around δ – 6 ppm, which is an overlapping signal consisting of all BH_2 environments in the polymer chain, where each B atom has a slightly different chemical shift corresponding to its position in the chain (**Figure 7**).[26] Individually each ^{11}B NMR BH_2 environment would appear as a 1:2:1 triplet from ^1J coupling to the two attached I = ½ H nuclei. The BH_3 end group has also been detected by ^{11}B NMR spectroscopy for short-chain polyaminoboranes, appearing at – 18 ppm. [25] ^1H NMR spectra of polyaminoboranes show N–H protons as a broad peak at δ 2.5 – 3 ppm and B–H hydrides as a broad peak at δ 1.5 – 2 ppm (when recorded in $CDCl_3$); any pendant alkyl chains are also observed as broadened signals (**Figure 8**).[26]

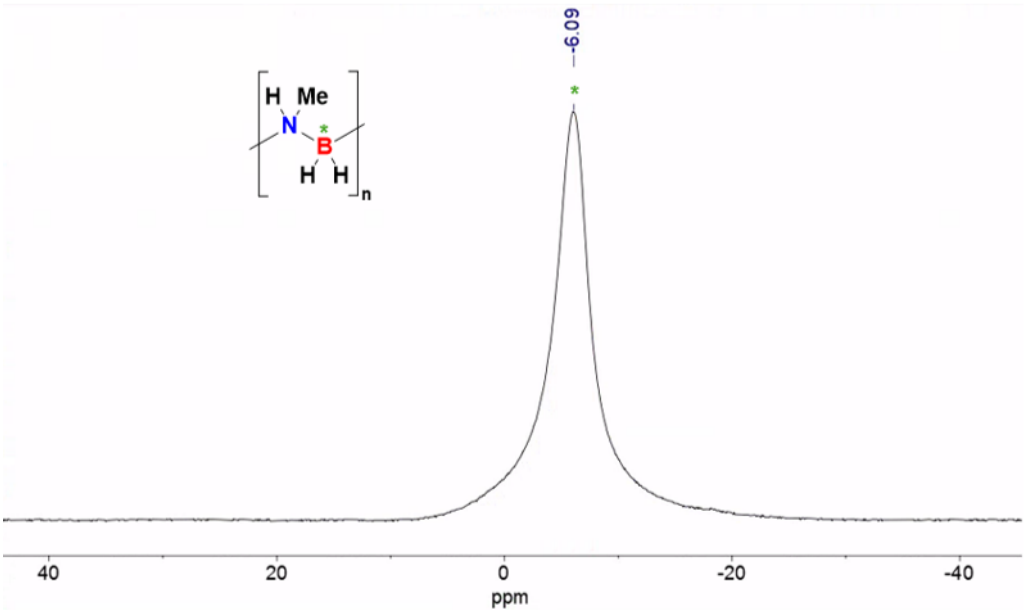

Figure 7. The ^{11}B NMR spectrum of $(H_2BNHMe)_n$ showing a broad signal corresponding to BH_2 boron environments. Recorded in chloroform-d at 298 K. Example spectrum from my own unpublished work.

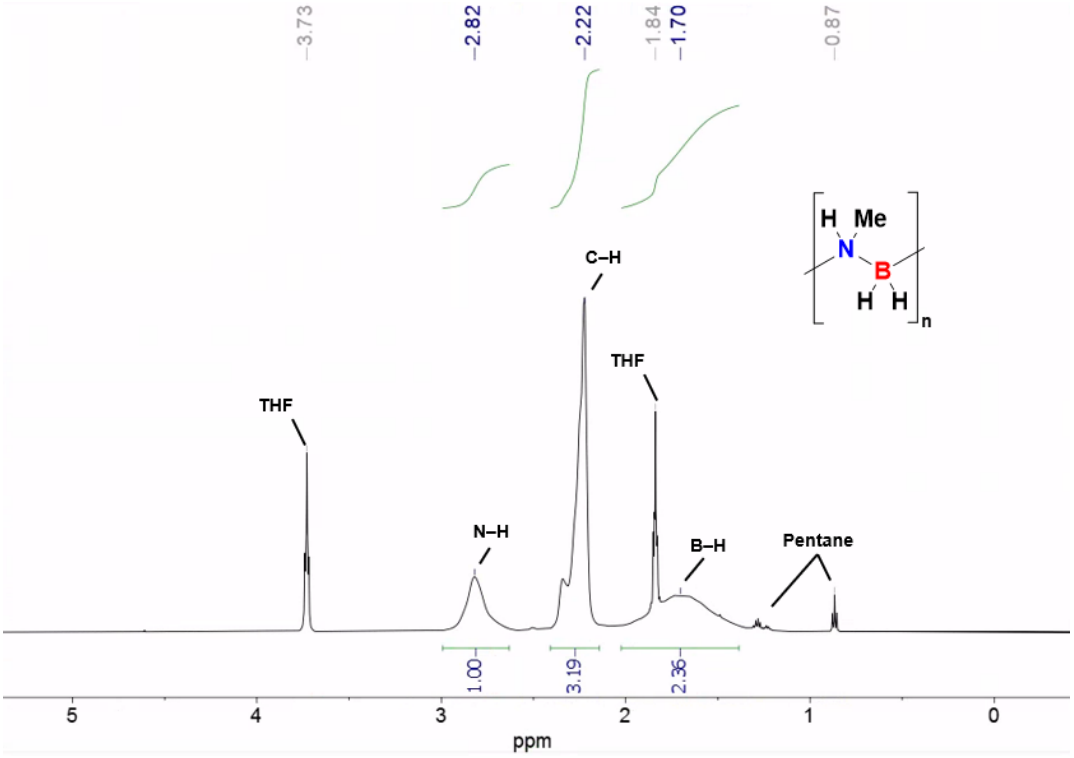

Figure 8. The ^{1}H NMR spectrum of $(H_2BNHMe)_n$ showing signals corresponding to NH, CH_3 and BH_2 ^{1}H environments at 2.82, 2.22 and 1.70 ppm respectively. Entrained solvent from synthesis (THF) and precipitation (pentane) is visible. Recorded in chloroform-d at 298 K. Example spectrum from my own unpublished work.

As with many polymers gel permeation chromatography (GPC) is an indispensable technique for the characterisation of polyaminoboranes. GPC measurements allow for the evaluation of polymer chain length and statistical metrics of the molecular weight distribution. [39] Polyaminoboranes, like most polymers, are produced as a distribution of chain lengths, described as polydisperse, and so molecular weights are given as averages. Commonly used average metrics include number average molecular weight (M_n), either side of which there are an equal number of polymer chains, and weight average molecular weight (M_w) either side of which there are an equal weight of polymer chains. [40] The breadth of the polymer molecular weight distribution is also measured, described as dispersity ($Đ$), which is calculated as $Đ = M_w/M_n$ (**Figure 9**).

The GPC average molecular weight values reported for polyaminoboranes are often obtained by refractive index (RI) detectors which are calibrated relative to polystyrene standards. This introduces a potential intrinsic error to measurement, as the hydrodynamic arrangement of polyaminoboranes is unlikely to be identical to that of polystyrene. The few reports that use direct measurement techniques of polyaminoborane M_n, such as multi-angle light scattering suggest that RI

measurements overestimate by a factor 3 – 6. [36, 41, 42] As RI detection is not a direct measurement of polymer length but rather relative, the value can be significantly affected by the instrument setup and calibration, meaning that different M_w and M_n values can be given for the same material on different machines. For this reason, the comparison of polyaminoborane molecular weights obtained by GPC with RI detection from different literature sources will not be discussed in detail beyond the classifications of 'low molecular weight' (M_n < 50,000 g mol^{-1}), 'moderate molecular weight' (100,000 g mol^{-1} > M_n > 50,000 g mol^{-1}) and 'high molecular weight' (M_n > 100,000 g mol^{-1}). GPC is however very useful for measuring relative molecular weights of polyaminoboranes when measured on the same machine under the same conditions.

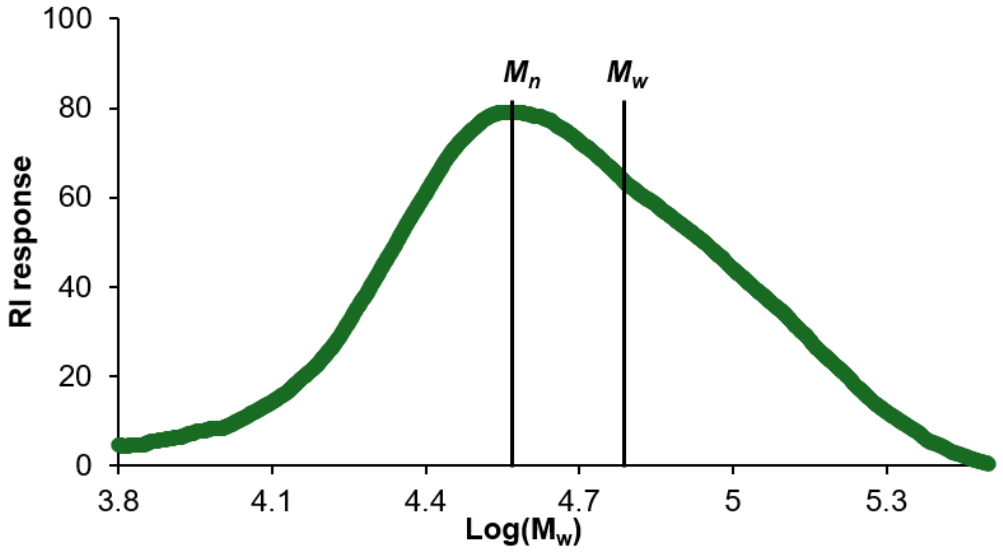

Figure 9. An example GPC trace of $(H_2BNHMe)_n$ as measured by an RI detector in THF, showing a logarithmic distribution of molecular weights (M_w) relative to polystyrene standards. Labelled with the positions of M_w and M_n. Example chromatogram from my own unpublished work

Mass spectrometric analysis of polyaminoboranes has been reported, however the molecular weights observed are significantly lower than those obtained by GPC measurement. [36] It has also been shown that the mass distributions seen by ESI+ mass spectrometry of $(H_2BNHMe)_n$ are not significantly affected by polymer molecular weight, suggesting that only the lower molecular weight and therefore lower m/z species are measurable by this technique. [41, 43] Mass spectrometry is however particularly useful when interrogating the individual aminoborane repeat units that make up the polyaminoborane, such as evidencing the copolymerisation of differently substituted monomer units. [36, 44]

1.2.2 Substituted polyaminoboranes other than $(H_2BNHMe)_n$ and $(H_2BNH_2)_n$

Polyaminoboranes can be substituted at the boron or nitrogen atoms by pendant groups. As mentioned in section **1.2**, the vast majority of research published on polyaminoboranes is of the *N*-methyl and N–H variants. This is due to the availability of the pre-monomer amine-boranes ($H_3B{\cdot}NH_2Me$ and $H_3B{\cdot}NH_3$ for $(H_2BNHMe)_n$ and $(H_2BNH_2)_n$ respectively). There have however been notable reports of other polyaminoboranes, mainly focussed on *N*-alkyl substituted derivatives.

A large number of *N*-alkyl polyaminoborane derivatives have been synthesised by stoichiometric BH_2 transfer methods (see **1.3.2**), including unbranched alkyl pendant groups of C_1 to C_6, myrtanyl, allyl and CH_2SiMe_3 (**Figure 10**).[44, 45] The synthesis of allyl substituted polyaminoborane is particularly notable as it is a rare example of a reactive pendant group that could be used for post-synthetic modification such as crosslinking. These polymers were obtained in moderate yields (60-70%), however these reactions required low temperatures for long periods of time to prevent the formation of cyclic oligomers (– 40 °C, >10 hrs). [44, 45] The polymer obtained by this non-catalytic method also has characteristically large dispersity values (*Đ* up to 10.2) and a wide range of polymer molecular weights, varying with each substituent (M_w 200,000 – 5,500,000 g mol^{-1}). [44]

A smaller variety of *N*-alkyl substituted polyaminoboranes have been synthesised by catalytic methods (**Figure 10**).[25, 26, 46] *N*-alkyl-aryl substituted polymer have also been reported, where the aryl group is at the end of an alkyl chain of $C_{1\text{-}4}$. [25, 33, 47] Catalytic syntheses of allyl and CH_2SiMe_3 substituted polymers are also reported. [46, 47] The majority of these polymers are produced by just two catalysts systems: $Ir(POCOP^tBu)H_2$ and $Ti(Cp^*)_2Me/Ti(Cp^*)_2$. The polymers are obtained in moderate yield (~50%) and highly variable selectivity, but have a much narrower dispersity and range of molecular weights than those produced by stoichiometric methods, suggesting controlled dehydropolymerisations (M_w ~ 100,000 – 200,000 g mol^{-1}, *Đ* ~ 1.5 – 2.0). [25, 26, 33, 47] These dehydropolymerisations however require high catalyst loadings (1 – 7 mol%) and suffer from low selectivity for polyaminoborane, forming also cyclic trimers, borazines and NBN side products ($(H_2BNHR)_3$, $(HBNR)_3$ and $(RHN)_2BH$ respectively).

[25, 26, 33, 46, 47] The dehydropolymerisation of hydrazine-borane ($H_3B{\cdot}NH_2NH_2$) has also been reported, resulting in a highly crosslinked and insoluble polymer. [26]

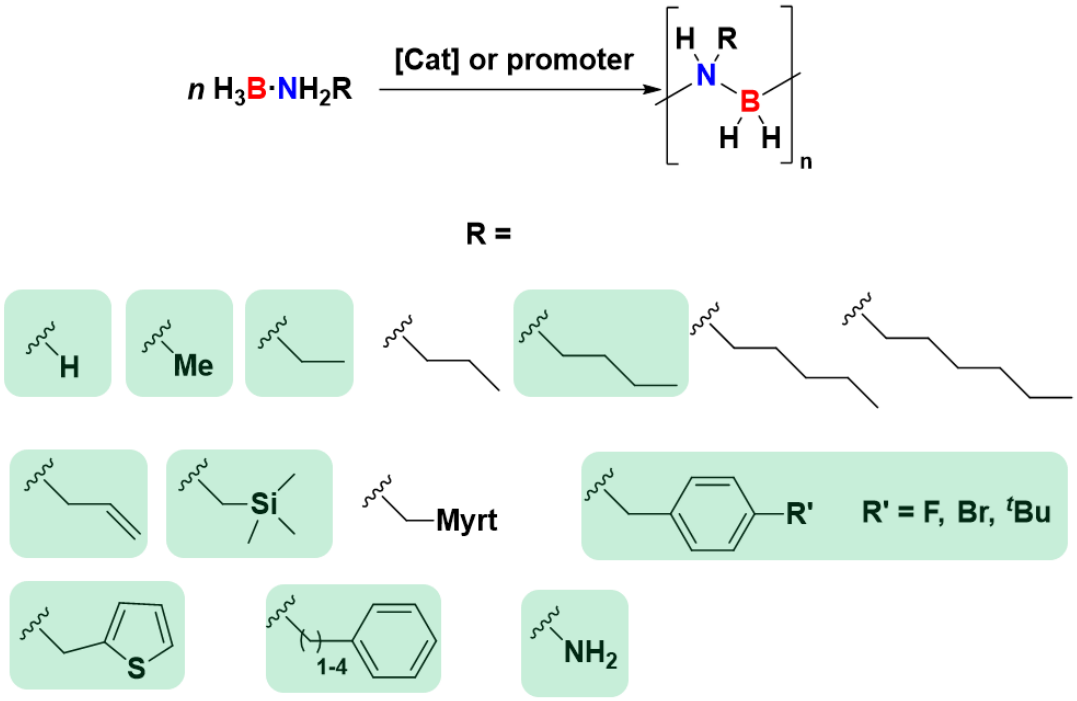

Figure 10. The reported polymerisations of *N*-substituted amine-boranes to form *N*-substituted polyaminoboranes. Amine-boranes with pendant groups highlighted in green have been synthesized catalytically, all others are only reported from stoichiometric synthesis. [25, 26, 33, 44-47]

The dehydrogenation of secondary *N*-substituted amine-boranes (e.g. $H_3B{\cdot}NHMe_2$) and bulky primary *N*-substituted amine-boranes (e.g. $H_3B{\cdot}NH_2{}^tBu$) results only in cyclic aminoborane oligomers (e.g. $(H_2B{\cdot}NMe_2)_2$) or borazines, instead of polyaminoboranes. [48-50] This is thought to be due to steric limitations of the catalysts, where bulky substrates may impede BH/NH activation during the dehydrogenation or impede subsequent aminoborane polymerisation.[33, 36, 46, 47]

Classically, it is expected that stronger inductively donating groups on a Lewis adduct donor would lead to a stronger donor-acceptor bond, e.g. larger or more *N*-alkyl substituents on an amine-borane nitrogen atom. [51, 52] For example, the B–N bond of amine boranes $H_3B{\cdot}NH_2Me$, $H_3B{\cdot}NHMe_2$ and $H_3B{\cdot}NMe_3$ strengthens with increasing number of methyl groups, observed as a shortening of the B–N bond by x-ray crystallography. [51] With larger *N*-alkyl substituents however it is clear that steric factors quickly overtake the increased N donor ability. A comparison between $H_3B{\cdot}NHMe_2$ and

$H_3B{\cdot}NH^iPr_2$ showed a significantly larger B–N distance for $H_3B{\cdot}NH^iPr_2$, suggestive of significant steric clash (1.5965(13) Å and 1.6333(6) Å respectively) and a weaker B–N bond. [53]

In the dehydropolymerisation of $H_3B{\cdot}NH_2CH_2SiMe_3$ with an iron hydride catalyst (Fe(^{i}Pr-PN^{H}P)(CO)H), at catalyst loadings lower than 2%, difficulty achieving full substrate conversion was reported, with observation that BH_3 capping of the active hydride catalyst to form a borohydride (BH_4) was observed. [46] The iron borohydride species is also an amine-borane dehydropolymerisation catalyst, albeit at lower rates and selectivity than the hydride. [46, 54] As this catalyst deactivation was not observed significantly with $H_3B{\cdot}NH_2Me$, it is possible that $H_3B{\cdot}NH_2CH_2SiMe_3$ is more prone to releasing BH_3 due to a weaker B–N bond, poisoning the active catalyst and therefore is more difficult to dehydropolymerise. [46] This may extend to other *N*-substituted amine-borane substrates and explain the sparse variety of reported *N*-substituted polyaminoboranes, this will be explored further in **Chapter 2**.

Only one account of *B*-substituted polyaminoboranes has been reported, with aromatic phenyl and para-CF_3 phenyl substituents (**Figure 11**).[55] These polymers have been prepared unselectively, forming large amounts of borazines and oligomers, and at high catalyst loadings (> 5 mol%).[55] These *B*-substituted amine-boranes and polyaminoboranes are susceptible to both the thermal redistribution of pendant groups across the B–N bond and over-dehydrogenation, leading to poor selectivity and polymer yields. [53, 55] This instability is most prominent with *B*-methyl amine-borane ($MeH_2B{\cdot}NH_3$) which decomposes slowly at 20 °C to form $Me_3B{\cdot}NH_3$, $Me_2HB{\cdot}NH_3$, $H_3B{\cdot}NH_3$ and $(HNBMe)_3$, so thus far has not been successfully dehydropolymerised, unlike it's *N*-substituted analogue. [26, 53] The observed products of catalytic dehydrocoupling are borazine $(HNBMe)_3$ and $MeB(NH_2)_2$. [53] It is suggested that the inductive electron donating effect of *B*-substituted alkyl groups leads to a less electrophilic boron and so a weaker B–N dative bond, therefore thermodynamically facilitating B–N bond cleavage and redistribution in the *B*-substituted polyaminoboranes such as $(MeHBNH_2)_n$, reducing stability. [51, 53] The more electrophilic boron in $(MeHBNH_2)_n$ (when compared to $(H_2BNHMe)_n$) is also suggested to increase the B–H hydricity, and therefore the propensity to over dehydrogenate the formed *B*-methyl polymer to *B*-methyl borazine $(HNBMe)_3$. [53]

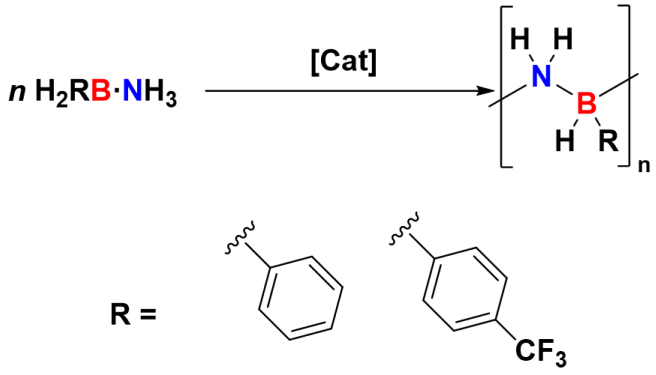

Figure 11. The reported polymerisations of *B*-substituted aryl amine-boranes to form *B*-substituted polyaminoboranes. [55]

Notably, the formation of substituted polyaminoboranes other than $(H_2BNHMe)_n$ with atom-efficient (catalytic) methods, with high selectivity and at low catalyst loading has yet to be demonstrated. For the substrate scope of dehydropolymerisation catalysts to be expanded, the mechanisms of catalysis and reasons for limited substrate scope, such as steric limitations and catalyst deactivation, need to be better understood. This will be discussed further in **Chapter 2**.

1.3 Polyaminoborane synthesis: mechanistic considerations

Since the initial report by Manners et al. in 2008 there has been considerable effort directed into understanding the process of amine-borane dehydropolymerisation to control properties of the polymer produced (i.e. selectivity and molecular weight). [26, 41] Dehydropolymerisation consists of two independent steps. First, the dehydrogenation of the amine-borane pre-monomer to form the true aminoborane monomer. Then separately the aminoborane is selectively polymerised into the linear, kinetic, product $(H_2BNHR)_n$ (**Figure 12**), rather than the cyclic thermodynamic product $(H_2BNHR)_3$.[56] This overall process is referred to as a cascade polymerisation. [57]

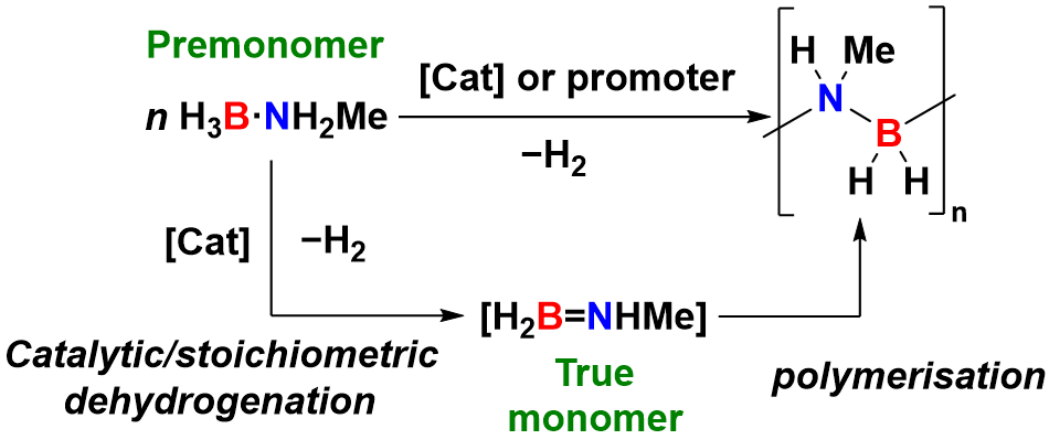

Figure 12. The two steps of amine-borane dehydropolymerisation, amine-borane dehydrogenation and subsequent aminoborane polymerisation.

1.3.1 Polymerisation mechanism

The polymerisation step in amine-borane dehydropolymerisation is the less well understood process as it is difficult to probe independently from the dehydrogenation. The aminoborane monomer produced from dehydrogenation exists only as a transient species at very low concentration, which is then immediately polymerised, meaning that the dehydrogenation step must occur concurrently with polymerisation. [32, 58] To avoid these practical difficulties, computational studies have been performed into the mechanism of chain initiation, propagation and termination. Initiation starts by the attack of a nucleophile into the B atom of an aminoborane forming a Lewis adduct (**Figure 13**).[59] The identity of this nucleophile is dependent on the method of polymerisation, and is either a solvent molecule such as THF, an amine, or a metal-hydride from the dehydropolymerisation catalyst. [34, 56, 60-62] This nucleophilic adduct then attacks from the nitrogen lone pair on the initiated adduct into a second equivalent

of aminoborane, from which the chain continues to propagate in a head-to-tail manner (**Figure 13**). [34, 56, 59, 62]

The energy barrier for polymer chain length extension when initiated by a metal hydride from a catalyst is calculated to be low at 7.8 kcal mol^{-1}, significantly lower than the energy barrier for on-metal cyclo-oligomerisation at 22.1 kcal mol^{-1}, explaining the selectivity for linear polyaminoborane. [59] Isolated metal-bound aminoborane oligomers from amine-borane dehydrogenation provide evidence for this mechanism. [63] Several suggestions have been made for the termination step of polymer chain growth based on end group analysis of polyaminoboranes by NMR spectroscopy and mass spectrometry, where both $–BH_3$ and amine capped polymers have been observed, suggesting electrophiles BH_3 and H^+ are attacked by the growing polymer chain (**Figure 13**).[46, 62] This is supported by the protonated species boronium ($H_2B(NMeH_2)_2^+$) reducing polymer molecular weight when added into catalytic dehydropolymerisations, likely acting as a chain transfer agent. [56, 62]

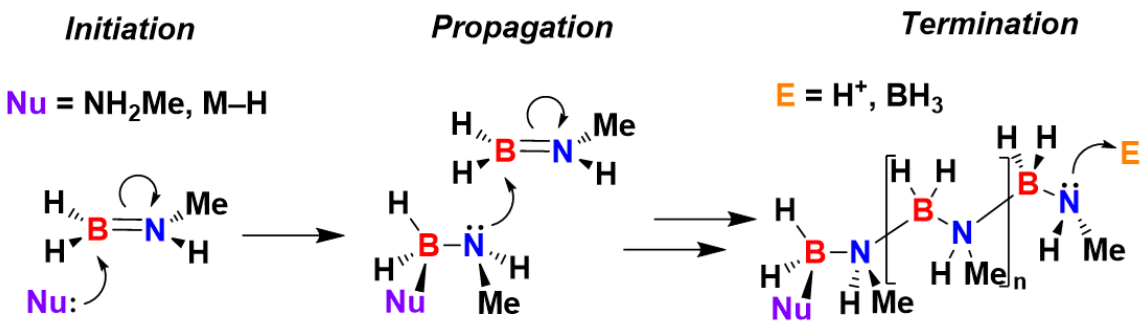

Figure 13. Mechanism for the nucleophile-initiated polymerisation where Nu can be a solvent, amine or metal-hydride catalyst. Propagation where the aminoborane-nucleophile adduct attacks into a second equivalent of aminoborane. Termination where the nucleophilic chain end attacks into an electrophile which can be H^+ or BH_3. [56]

1.3.2 Aminoborane generation mechanisms

The formation of the "true" monomer aminoboranes can be facilitated at room temperature by catalytic or stoichiometric processes. As mentioned in section **1.1**, aminoboranes can be stable toward oligomerisation if sufficiently sterically hindered. Upon reaction with primary amines, these hindered aminoboranes (e.g. $^{i}Pr_2N{=}BH_2$) can act as BH_2 transfer reagents, stoichiometrically releasing one equivalent of unhindered aminoborane and the secondary amine (**Figure 14**).[44] As mentioned in section **1.3.1**, amines can act as nucleophilic initiators for aminoborane polymerisation, and so if the reaction is performed at low temperatures to prevent oligomerisation of the primary aminoboranes, polyaminoborane can be formed. [44] This method however has limited selectivity due to side reactions such as diamine-borane formation and can also form polymer with large dispersity values ($Đ$ = 1.2 – 10.2). [44] The release of one equivalent of $^{i}PrNH_2$ per monomer unit polymerised in this process means that overall the polymerisations are poorly atom-economical.

Amine-boranes can be spontaneously dehydrogenated by the addition of a Brønsted acid (H-X where X= OTf, Cl or $B(C_6F_5)_4$), forming a boronium salt ($RH_2N{\cdot}BH_2X$) where in the case X = $B(C_6F_5)_4^-$, the anion is non-coordinating and so the BH_2 forms a solvent adduct (e.g. THF, Et_2O). [58] This boronium species can then be deprotonated by an amine base such as $^{i}Pr_2NH$ releasing an aminoborane ($RHN{=}BH_2$). [58] When R = Me the formed aminoborane polymerises, likely initiated by the amine base (**Figure 14**). This process is however unselective, producing polyaminoborane of M_n < 5000 g mol^{-1} and is also poorly atom economical.

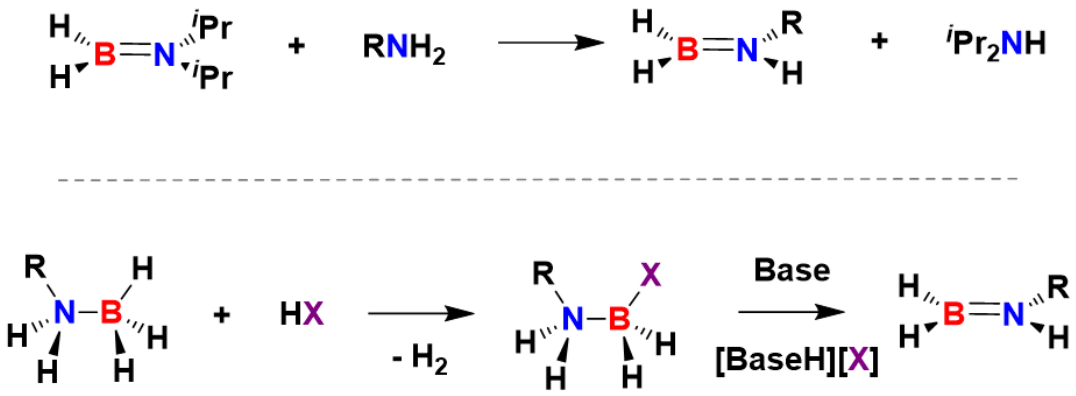

Figure 14. Top: BH_2 transfer from $^{i}Pr_2N{=}BH_2$ to a primary amine to form a primary aminoborane ($RHN{=}BH_2$). Bottom: Acid promoted exchange across an amine-borane B–N bond, followed by deprotonation to form a primary aminoborane. [44, 58]

The most reported method of aminoborane generation for polyaminoborane synthesis is the catalytic dehydrogenation of amine-borane premonomers by transition metal catalysts. These processes can be separated into four main categories based on mechanism: nanoparticle mediated; inner sphere B–H hydride abstraction; inner sphere N–H/B–H activation and metal-ligand cooperative. [41, 43] The latter 3 mechanisms invoke molecular metal-hydrides as active catalytic species. [22]

A) Nanoparticle catalysts, such as colloidal nickel used by Manners et al. are formed by the reduction of molecular transition metal species to M^0 by the amine-borane substrate. [36, 64, 65] The exact mechanism of amine-borane dehydrogenation with such species is currently unknown, however it is likely to mirror dehydrogenations of other H_2 donor substrates such as ^{i}PrOH. This would involve transfer of two hydrogen atoms from across the B–N bond to the nanoparticle surface, releasing an aminoborane, followed by subsequent elimination of H_2 (**Figure 15**).[66]

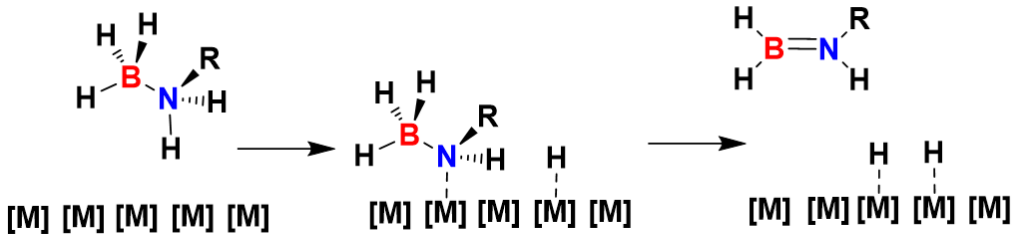

Figure 15. The proposed nanoparticle mediated dehydrogenation of amine-boranes to form aminoboranes. The aminoborane is first adsorbed to the surface of the nanoparticle, followed by N–H/B–H abstraction and aminoborane formation. Finally, the adsorbed H atoms are eliminated as H_2. [66]

B) Inner sphere B–H abstraction catalysts operate via intermediate σ-amine-borane complexes, where an equivalent of the amine-borane substrate is coordinated to the metal centre by 3-centre 2-electron bonds. [48, 62, 67, 68] This can be followed by proton abstraction from the σ-amine-borane complex N–H by a base such as an amine or adjacent metal-hydride, releasing an aminoborane. [48, 68, 69] In the case of an adjacent metal hydride acting as a base, a labile metal-dihydrogen complex is formed, such as in the [Ir(^{i}Pr-PN^{H}P)(H)$_2$(H$_2$)][BAr$^F{}_4$] precatalyst system reported by Weller et al. [62, 68, 70, 71] In the case of an amine base, the formed ammonium then re-protonates the formed metal-hydride to also form a dihydrogen complex, such as the Rh(^{t}Bu-PONOP)H precatalyst system reported by Weller et al. (**Figure 16**).[48]

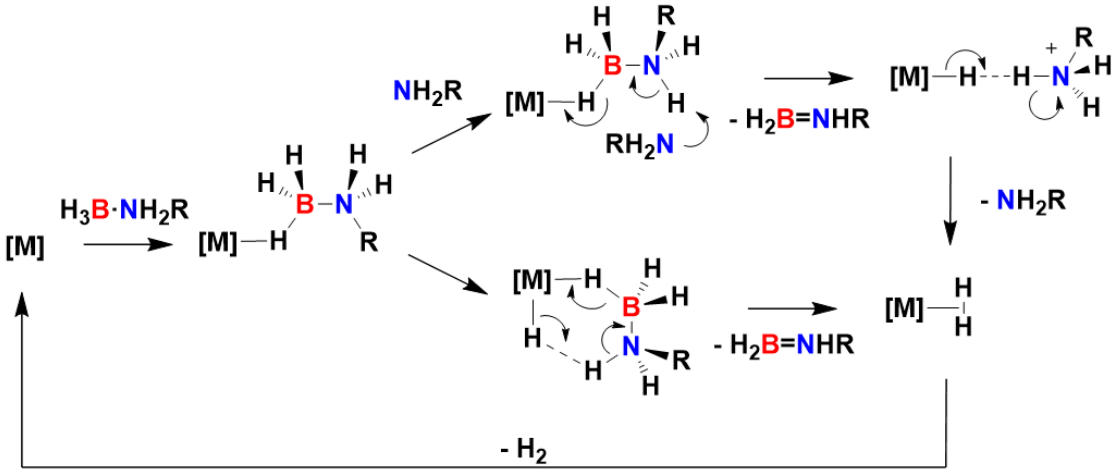

Figure 16. Proposed inner sphere B–H abstraction amine-borane dehydrogenation mechanism. Top route: amine mediated B–H transfer from a σ-amine-borane complex to the metal centre forming an aminoborane, followed by metal hydride protonation and H_2 loss. [48] Bottom: metal hydride mediated B–H transfer from a σ-amine-borane complex to the metal centre forming an aminoborane, followed by H_2 loss. [62, 68, 70, 71]

Inner-sphere B–H/N–H activation catalysts can also operate by concerted oxidative addition of H_2 from a coordinated amine-borane to the metal and simultaneous BN double bond formation (**Figure 17**). The active catalyst species is typically of a low oxidation state and low-coordinate, allowing for facile amine-borane coordination and metal centre oxidation (e.g. Ir^{I}/Ir^{III}, Co^{I}/Co^{III}). [25, 31, 72-74] Examples include the Ir(POCOP^{t}$_{Bu}$)H_2 system reported by Manners et al. for which DFT calculations suggest Ir^{I}/Ir^{III} and Ir^{III}/Ir^{V} cycles are energetically accessible (where Ir^{III}/Ir^{V} is most likely), however it should be noted that most catalyst systems for which this mechanism has been proposed also have other suggested mechanisms, such as inner sphere B–H abstraction or metal-ligand cooperativity. [72, 75, 76] It also is possible that catalysts thought to operate by a concerted oxidative addition of H_2 from simultaneous B–H/N–H activation proceed instead by sequential oxidative addition of an amine-borane B–H bond at the metal centre, followed by N–H transfer and aminoborane dissociation, then H_2 loss via reductive elimination (**Figure 17**).[77, 78] A hybrid mechanism combining aspects of that shown in **Figure 16** and **Figure 17** has been proposed by Weller et al. for amine-borane dehydropolymerisation with precatalyst Rh(^{i}Pr-Xantphos)H, where concerted B–H activation and dihydride conversion to a σ-bonded dihydrogen maintains the Rh oxidation state at (III). [70] This is followed by amine-promoted hydride transfer and ammonium protonation of a hydride to eliminate H_2. [70]

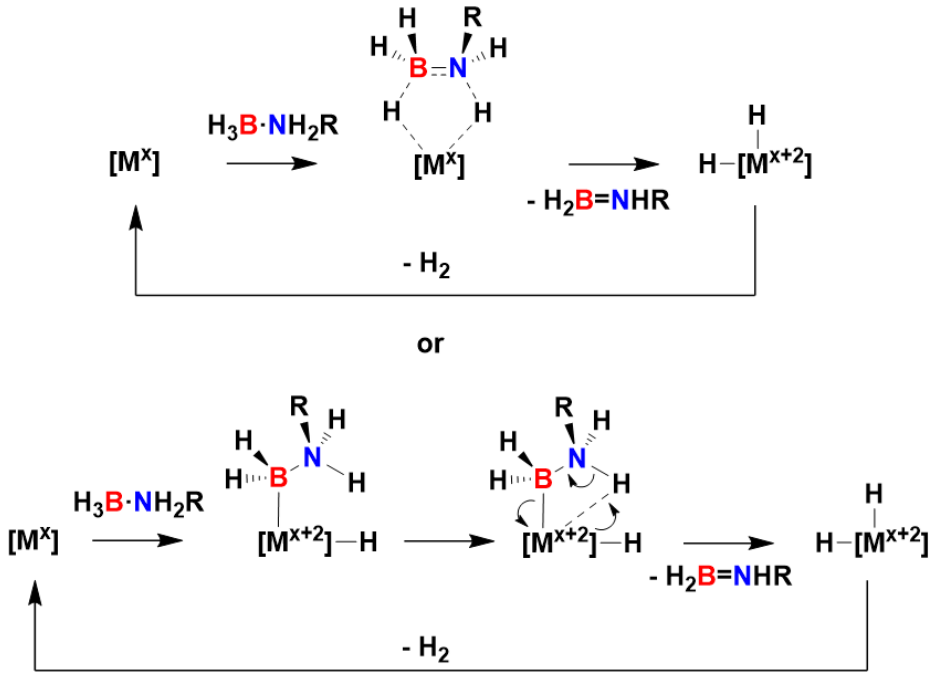

Figure 17. Proposed inner sphere B–H/N–H activation mechanisms. Top: concerted amine-borane B–H and N–H oxidative addition via a 5-membered metallacycle transition state releasing an aminoborane, followed by reductive elimination of H_2 from the metal centre. [31, 74] Bottom: stepwise amine-borane B–H oxidative addition and N–H activation releasing an aminoborane, followed by reductive elimination of H_2 from the metal centre. [77, 78]

C) Metal-ligand cooperative catalysts operate via interactions between the amine-borane substrate, catalyst metal centre and ligand. Cooperative ligands in catalysis have been studied for a wide variety of chemical transformations; relevant examples will be introduced in section **1.4**.

The first, and less common, proposed mechanism of metal-ligand cooperative amine-borane dehydrogenation applies to aromatic/dearomatised ring containing ligands. [79] Pincer ligands with aromatic/dearomatised substituents (phenyl, pyridyl etc.) can act as transient Brønsted bases, deprotonating an N–H on a bound amine-borane and facilitating B–H transfer to the metal centre. [80, 81] This is analogous to the base deprotonation a bound σ-amine borane complex N–H inducing B–H activation and hydride transfer to the catalyst metal centre as part of the inner sphere mechanism mentioned vide infra. [48, 62, 68, 70, 71] Examples where the acceptor atom is part-of and adjacent-to the aryl ring are also reported. [80, 81] This can involve aromatisation of the aryl system upon addition of an equivalent of H_2 between the metal and ligand, then dearomatized upon H_2 loss (**Figure 18**).[80] The presence of an aryl containing ligand

does not however guarantee a metal-ligand cooperative mechanism as counter examples have been reported, the prominent example being the Ir(POCOP^{t}$_{Bu}$)H$_2$ system reported by Manners et al. for which N–H and B–H activation are proposed to occur at the metal centre with a non-participating ligand. [26, 82, 83]

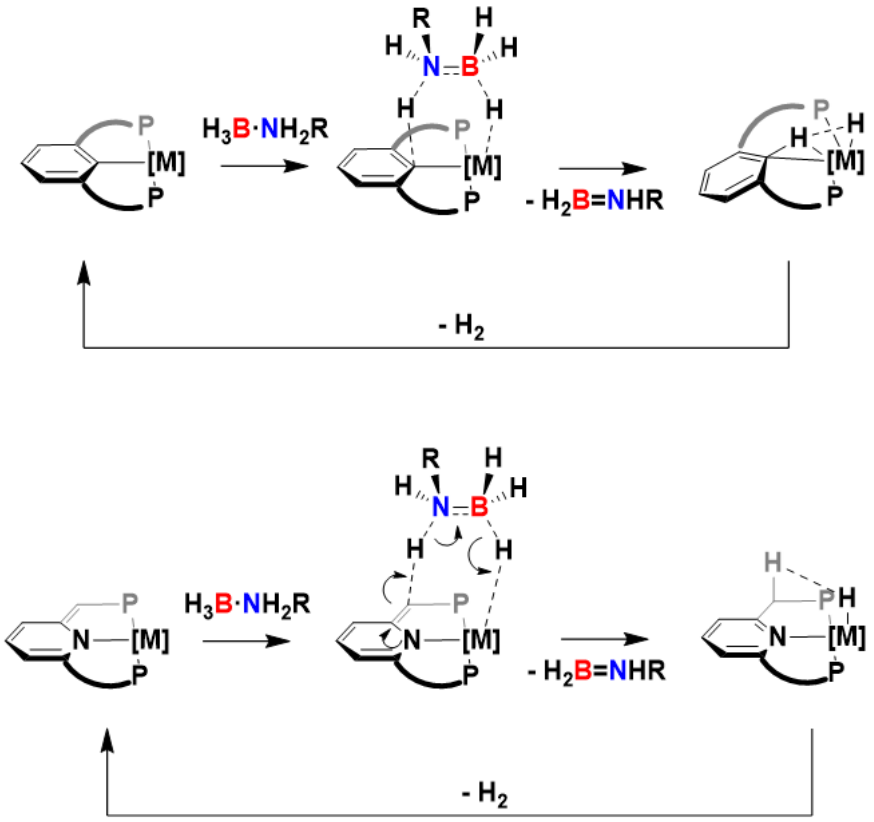

Figure 18. Proposed mechanisms for the aryl-assisted metal ligand cooperative dehydrogenation of amine boranes. Top: phenyl ring assisted B–H transfer via deprotonation of an amine-borane N–H to release an aminoborane, e.g. POCOP ligand. Bottom: assisted B–H transfer to release an aminoborane via deprotonation of an amine-borane N–H by a methine carbon on a PNP ligand, facilitated by reversible aromatisation/dearomatisation of the pyridine. The pyridine N atom changes from an L-type to an X-type donor upon reversible hydrogenation of the ligand. [80, 81]

The most studied ligand-cooperativity systems for amine-borane dehydrogenation involve a ligand N–H moiety adjacent to a metal hydride. Such catalysts typically are coordinated by bidentate or tridentate pincer ligands, such as aminophosphines, which support the geometry of the N–H and metal hydride in the syn-position. [54, 56, 72] The proposed mechanisms for such ligand cooperativity can be separated into two subtly different related routes: inner sphere amido-templated cooperative dehydrogenation and outer sphere dihydrogen bonding templated cooperative dehydrogenation. [46, 54, 56, 72, 84-87]

The inner sphere mechanism involves a metal-amido active species with a formal lone pair the ligand nitrogen and a formally vacant metal centre. The resulting partial charges across the metal-amido bond template the complementary charges on amine-boranes B–H and N–H, resulting in addition of H_2 across the M–N bond. [72, 86, 87] This occurs by deprotonation of an amine-borane N–H by the amido, followed by B–H transfer to the metal forming an amine and a metal hydride, then releasing an aminoborane (**Figure 19**). [86, 87] This is related to the role of additional amine in the inner sphere B–H abstraction mechanism mentioned vide infra, where a metal-coordinated σ-amine borane N–H is deprotonated and transfers a B–H hydride to the metal centre (**Figure 16**). [48] Also similarly to the inner sphere B–H abstraction mechanism, the amine N–H and metal hydride eliminate to re-form the metal amido bond and a sigma dihydrogen complex. [85, 87] This coordinated dihydrogen then dissociates or is displaced by another amine-borane substrate molecule (**Figure 19**).[85, 87]

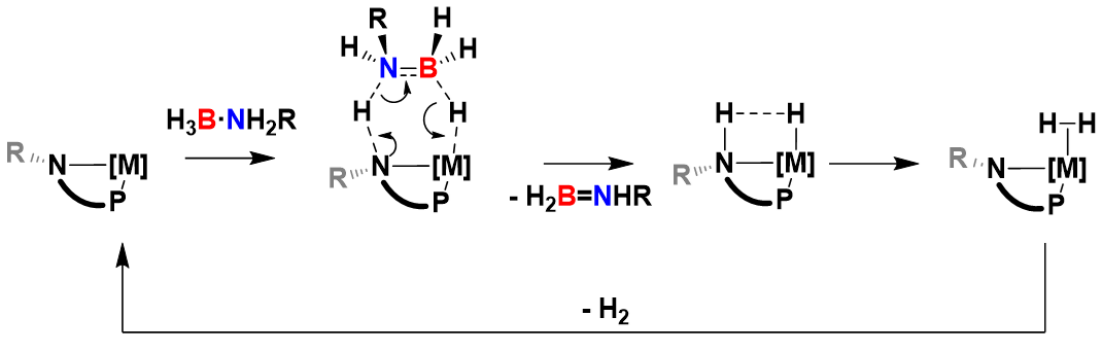

Figure 19. The inner sphere amido mediated metal ligand cooperative dehydrogenation of amine boranes. An equivalent of H_2 is transferred from across the amine-borane B–N bond to across the metal amido bond, releasing an aminoborane. The formed metal hydride deprotonates the adjacent ligand N–H, eliminating H_2 and re-forming the metal amido bond. [85-87]

In the outer sphere dihydrogen cooperative bonding mechanism, the ligand δ^+ amine proton and δ^- metal hydride template the approach of the δ^- B–H and δ^+ N–H on the amine-borane via dihydrogen bonding interactions (see section **1.1**). [54, 56] The amineborane N–H is then deprotonated by the metal hydride, forming a sigma dihydrogen complex with ligand-bound amidoborane (**Figure 20**).[54, 56] This amidoborane NH_2^- is more negatively charged than the B–H δ^- and so the fragment switches binding mode, with the NH_2^- binding to the δ^+ ligand N–H and the B–H

displacing the sigma bound dihydrogen from the metal centre (**Figure 20**).[54, 56] A variation where the amine-borane N remains bound to the ligand N–H throughout the mechanism prior to aminoborane dissociation has also been proposed. [84] The bound amidoborane then transfers a B–H to the metal centre, releasing an aminoborane and re-forming the metal hydride (**Figure 20**).[54, 56, 84] The favourability of either the inner or outer sphere metal ligand cooperative mechanisms is likely dictated by the stability of the metal hydride relative to the dihydrogen complex. If the hydride rapidly converts to the sigma dihydrogen complex, for which dissociation is facile, the inner sphere mechanism will predominate.[85] Computational study is required to deterimine which pathway is taken by a particular catalyst species.

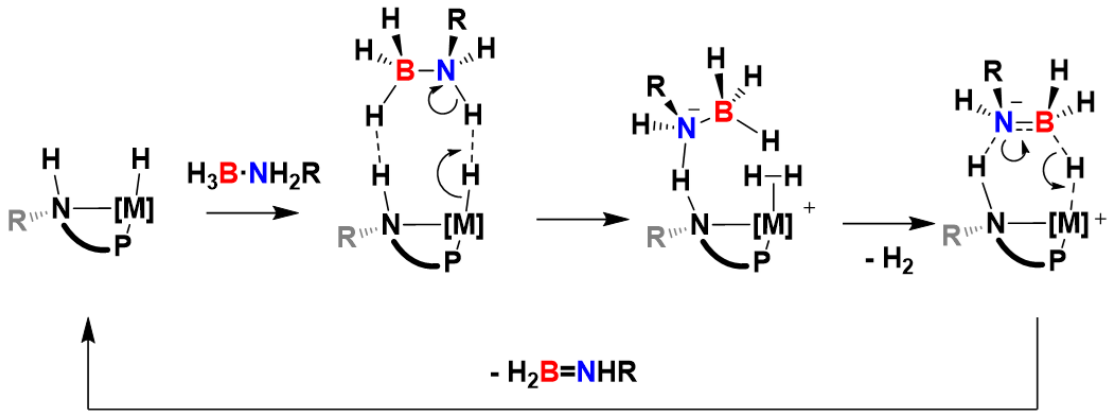

Figure 20. The outer sphere dihydrogen bond mediated metal ligand cooperative mechanism for amine-borane dehydrogenation. The metal hydride deprotonates an amine-borane N–H to form a dihydrogen complex, which is dissociates upon rearrangement of the amido fragment. An amine-borane B–H bond is then activated, re-forming the metal hydride and eliminating an aminoborane. [54, 56, 84]

1.4 Metal-ligand cooperative catalysis

Many early examples of homogeneous organometallic catalysis, where substrates are activated and transformed, involve direct reaction at the metal centre. Examples include Ziegler-Natta olefin polymerisation and Monsanto-process methanol carbonylation. [88, 89] The mechanisms of such catalysts operate via classical at-metal substrate interactions including oxidative addition, migratory insertion and reductive elimination. [90, 91]

In nature, the catalytic transformation of substrate molecules by metalloenzymes are important processes. [92] Of particular interest is the utilisation of bimetallic catalysts and metal-ligand cooperativity in enzymes to lower the activation barriers of small molecule substrates such as N_2 and H_2 activation so that heterolysis occurs readily at ambient conditions. [93, 94] Nitrogenase enzymes in certain bacteria are a critical component of the global nitrogen cycle, these often contain bimetallic MoFe active sites which lower the barrier for N_2 homolysis such that it can occur at ambient condition and be utilised biologically. [94] In hydrogenase enzymes, cysteine thiol residues form ligands to Fe or Ni metal centres facilitating the splitting of hydrogen by acting as a proximal base (**Figure 21**).[93] An analogous interaction is responsible for the catalytic activity of an asymmetric transfer hydrogenation catalyst reported by Shvo et al., where a ligand O atom facilitates the dehydrogenation of isopropanol and subsequent transfer to carbonyl substrates (**Figure 21**).[95-97]

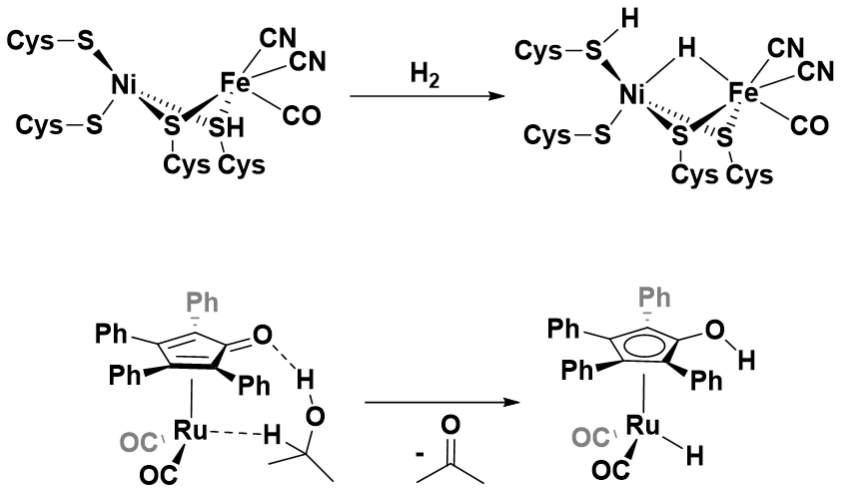

Figure 21. Top: Metal ligand cooperative activation of dihydrogen by a cysteine ligand at the active site of a FeNi hydrogenase metalloenzyme. [93] Bottom: the dehydrogenation of isopropanol with metal ligand cooperativity in Shvo's catalyst. [96, 98]

The early report by Shvo et al. of metal ligand cooperativity in hydrogenation catalysis set the stage for further advances in the field. Noyori et al. later reported the enantioselective asymmetric transfer hydrogenation of ketones with ruthenium catalysts, finding that amine ligands were favourable. [99, 100] This was further expanded on in subsequent publications where N–H containing amine based ligands were shown to vastly accelerate catalytic rate (TOF from 70 h^{-1} to 6700 h^{-1}) and an explicit metal-ligand cooperative mechanism was suggested, involving metal-amido and sigma dihydrogen complex intermediates (**Figure 22**).[101-103] The addition of H_2 across a metal-amido bond from a donor substrate such as secondary alcohols by intermolecular hydrogen bonding had been previously reported in stoichiometric reactions with group 9 complexes. [104]

Adhering to the principle of microscopic reversibility, Shvo and Noyori type metal ligand cooperative catalysts catalyse both the hydrogenation of ketones and the reverse, dehydrogenation of alcohols to give ketones and H_2. [98, 105] From this perspective it is clear that the fields of hydrogenation/transfer hydrogenation and amine borane dehydrogenation are intrinsically linked due to the similarity of the mechanisms and catalysts used; the activation of alcohols and amine boranes by dehydrogenation catalysts is mechanistically closely related. (**Figure 22**). The more recent advances in amine-borane dehydrogenation catalysts such as the use of metal ligand cooperativity and adjacent metal hydride and amine moieties are born from discoveries in hydrogenation and transfer hydrogenation in catalysis, such as those by Noyori and Shvo. Therefore, similar catalyst designs are employed for both processes. [84, 87, 106, 107]

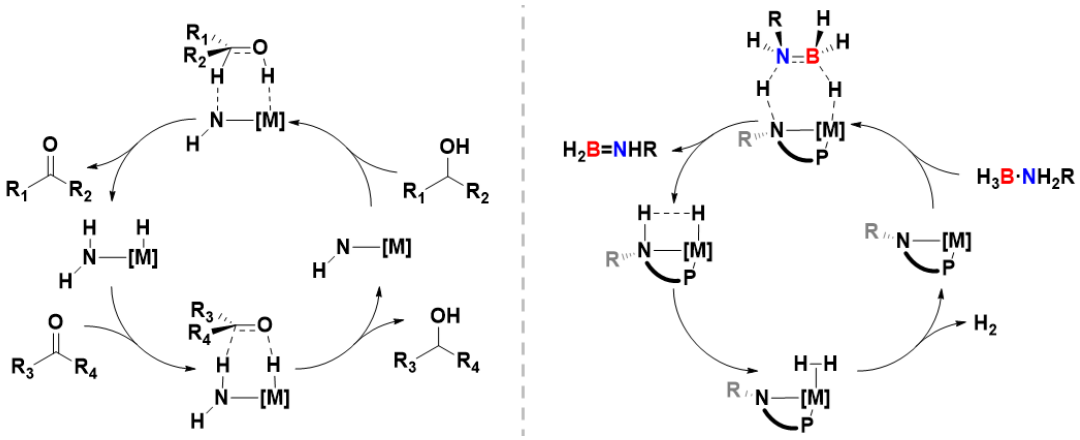

Figure 22. Left: a simplified Noyori-type transfer hydrogenation mechanism showing metal ligand cooperative dehydrogenation of an alcohol and hydrogenation of a ketone. [101-103, 105] Right: The inner-sphere amido mediated metal ligand cooperative dehydrogenation of amine boranes to form aminoboranes. [85-87]

1.5 Catalyst design for metal-ligand cooperative dehydropolymerisation

Although much work has been published on the ligand effects of transition metal homogeneous catalysts for substrate hydrogenation/dehydrogenation, the effect of the metal centre has been less thoroughly explored. This is even more true for amine-borane dehydropolymerisation catalysts due to the relative novelty of the research area. As mentioned in the previous section (**1.4**) the mechanisms for transfer hydrogenation catalysts are very similar to that of amine-borane dehydrogenation. Parallels can be drawn between metal and ligand effects on each of the two mechanisms, with the catalyst mechanisms referred to interchangeably here. Almost all recent advances in polyaminoborane synthesis involve amido metal ligand cooperative catalysts, so this will be the focus here. [46, 54, 56, 80, 84]

1.5.1 Ligand effects

For efficient activation of H_2 or other substrates such as alcohols or amine-boranes across a metal-nitrogen bond in a hydrogenation/dehydrogenation reaction, via either an inner or outer sphere metal cooperative mechanism, an adjacent metal hydride and ligand N–H are necessarily present at some point on the catalytic cycle.[108] Octahedral complexes are ideal for templating this reactivity as the H–M–N angle is constrained to ~ 90°. Multidentate amine ligands help stabilise the transition state for H_2 activation (either H_2 elimination or substrate dehydrogenation) across the M–N bond in the correct conformation and bring the H–N–M–H dihedral angle close to 0° (**Figure 23**). A commonly used ligand type for this purpose is aminophosphine MACHO pincer ligands ($HN(CH_2CH_2PR_2)_2$).[109] A strongly hydride-polarised M–H unit is also advantageous for metal ligand cooperative dehydropolymerisation catalysts as the larger δ- on the hydride aids both templating of the approaching amine-borane (outer sphere mechanism) and protonation by the ligand or amine-borane N–H preceding H_2 loss (**Figure 23**).[110] This is facilitated by strong sigma donor ligands such as phosphines (e.g. MACHO pincer ligands or other aminophosphines). Strong sigma donor ligands trans to the metal hydride also increases donating ability, many metal ligand cooperative dehydropolymerisation catalysts exhibit strongly sigma donating trans hydrides. [54, 56, 84, 87, 110]

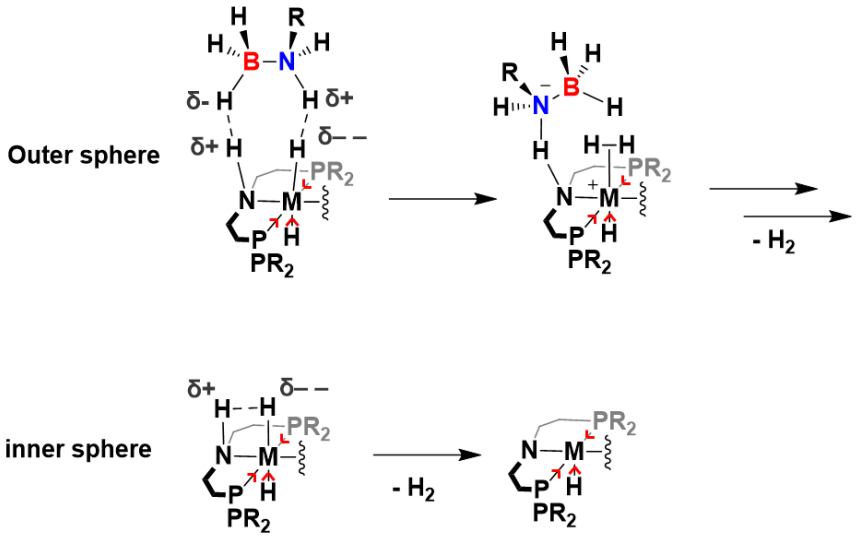

Figure 23. N–H bearing MACHO ligand cooperative dehydrogenation catalysts showing reaction geometries and inductive effects (red arrows) from strong sigma donors that increase hydride donating ability. [109, 110]

1.5.2 Metal centre effects

Most hydrogenation/dehydrogenation and amine-borane dehydropolymerisation catalysts are based on d^6 metal centres. Most amine-borane dehydropolymerisation catalysts operating by a metal ligand cooperative mechanisms have active catalytic species that have d^6 metal centres, which are Fe^{II}, Ru^{II}, Rh^{III}. [54, 56, 84, 87, 110] The energetic barriers to the operation of amido metal ligand cooperative dehydrogenation catalysts are primarily the substrate activation to add H_2 across the M–N bond from the approaching substrate, or the subsequent loss of dihydrogen across this same bond, and so the specific preference for 3d/4d d^6 metal centres lies here. [54, 56, 84, 87]

As mentioned previously, octahedral geometry presents the optimal orientation for amido metal ligand cooperative dehydrogenation catalysts. The low spin d^6 electronic configuration is the only commonly observed singlet spin configuration for octahedral geometry.[110] Examples of high spin states disfavouring small molecule binding and activation at metal centres have been reported.[111, 112] Low spin electronic configurations can be favoured for 3d metals such as Fe^{II} by strong field ligands such as phosphines (e.g. MACHO pincer ligands). [46, 113] This is also seen in nature where H_2 activating hydrogenase metalloenzymes contain strong field CN^- and CO ligands to retain low spin in 3d Fe and Ni metal centres (see **Figure 21**).[93, 114]

d^8 metal centres such as Ni^{II} are also low spin however they favour square planar complexes that are not as conducive to amido metal ligand cooperativity as octahedral geometry. This is due to the required deformation energy to bring the metal hydride and ligand N–H into the same plane, a necessity for the elimination of H_2 (**Figure 24**).[108] Consequently, although d^8 (and also d^7) square planar hydrogenation/dehydrogenation complexes with NH functionalised ligands exist, they are not thought to operate through ligand cooperative mechanisms. [108, 115] Utilising ligands where the cooperative functional group is coordinated adjacent to the M–H may allow cooperativity with d^8 metal centres and is an area requiring further work. [108]

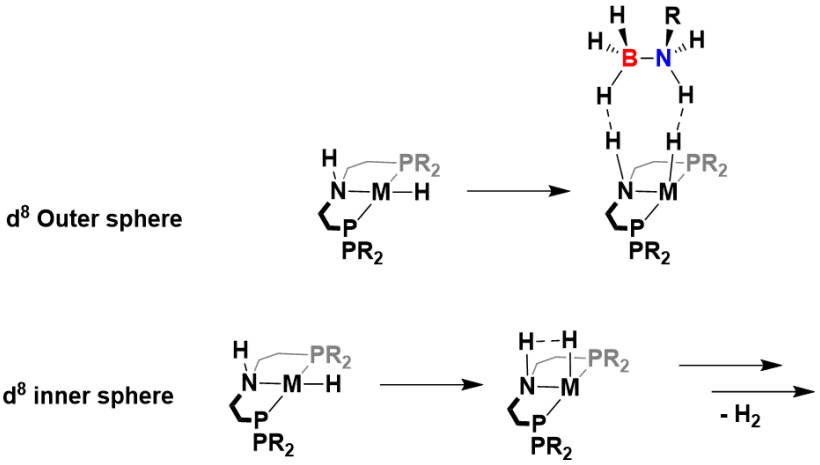

Figure 24. The conformational changes required for d^8 complexes to act as metal amine-amido ligand cooperative dehydrogenation catalysts with MACHO type ligands. The required migration of the metal hydride toward the ligand N–H effectuates an energy penalty to this mechanism, and so metal-only dehydrogenation mechanisms predominate. [108, 115]

Within d^6 metal complexes, periodic trends dictate the varying ability to act as effective hydrogenation/dehydrogenation catalysts. From Mn^{I} to Fe^{II} to Co^{III}, the free energy change for metal ligand cooperative dehydrogenation becomes more favourable as metal centre oxidation state and electronegativity increases, as the resulting hydride becomes more stable. [116] Simultaneously, the back donation ability of the metal from Mn^{I} to Fe^{II} to Co^{III} centre decreases, so the barrier to metal-only inner sphere dehydrogenation increases, further favouring a metal ligand cooperative mechanism (**Figure 25**).[117]

The row effect also plays a role in dehydrogenation catalyst effectiveness, with significant differences between 3d, 4d and 5d metals. Catalysis in 3d metals is complicated by the tendency to undergo single electron processes that may compete

with the intended two electron processes or even lead to catalyst decomposition. [114] Down the groups e.g. from Co^{III} to Rh^{III} to Ir^{III} metal centre back donation ability increases as radial extension increases due to better overlap with the substrate (e.g. H_2) antibonding orbitals. This results in more favourable heterolytic dihydrogen cleavage down the group (**Figure 25**).[115, 118] This more favourable hydrogen activation facilitates the dehydrogenation step in dehydrogenation catalysts, however amine-borane dehydropolymerisation is an acceptorless dehydrogenation where H_2 needs to be subsequently displaced from the catalyst. The increased back bonding ability of 5d metal centres such as Ir^{III} disfavours H_2 loss as the activated hydride is too stable. [68, 119] This is seen when comparing structurally identical Ir^{III} and Rh^{III} dehydropolymerisation catalysts with cooperative capable ligands, where the rhodium species operates via a metal-ligand cooperative mechanism, but the iridium does not due to a higher barrier to H_2 loss. [56, 68] Due to the increased stability of higher oxidation states in lower transition metal rows, this iridium catalyst can instead operate via an Ir^{III}/Ir^{V} oxidative addition/reductive elimination cycle that is inaccessible to Rh. [68] This is likely also the case for an osmium amine-borane dehydrogenation catalyst, operating via an Os^{II}/Os^{IV} cycle. [119-121]

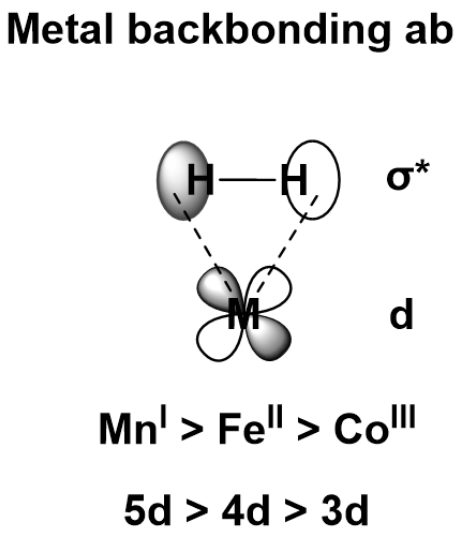

Figure 25. Transition metal d orbital backdonation to the σ* orbitals of hydride donor substrates. Back donation ability increases with decreasing oxidation state within the same electronic configuration (d^6) due to higher electron density at the metal centre and increases 5d > 4d > 3d due to increased d orbital radial extension leading to better overlap. [117, 118]

The balance between favourable substrate activation and favourable subsequent H_2 dissociation in an amine/amido metal ligand cooperative dehydropolymerisation catalyst is best found in second row (4d) transition metals (**Figure 26**).[118, 122] This, with the preference for low spin d^6 focuses the ideal metal centre properties on Ru^{II} and Rh^{III}. 3d metal centres Fe^{II} and Co^{III} can be similarly favourable if strong field ligands are used that disfavour high spin, and favour electron density donation into antibonding orbitals of approaching H_2-donor substrates. For a full analysis of metal centre effects, the ionic radius and ligand Lewis donor ability need to be considered as these vary from 3d to 4d and 5d metals, also playing a part in favouring or disfavouring metal ligand cooperative mechanisms. [115, 122]

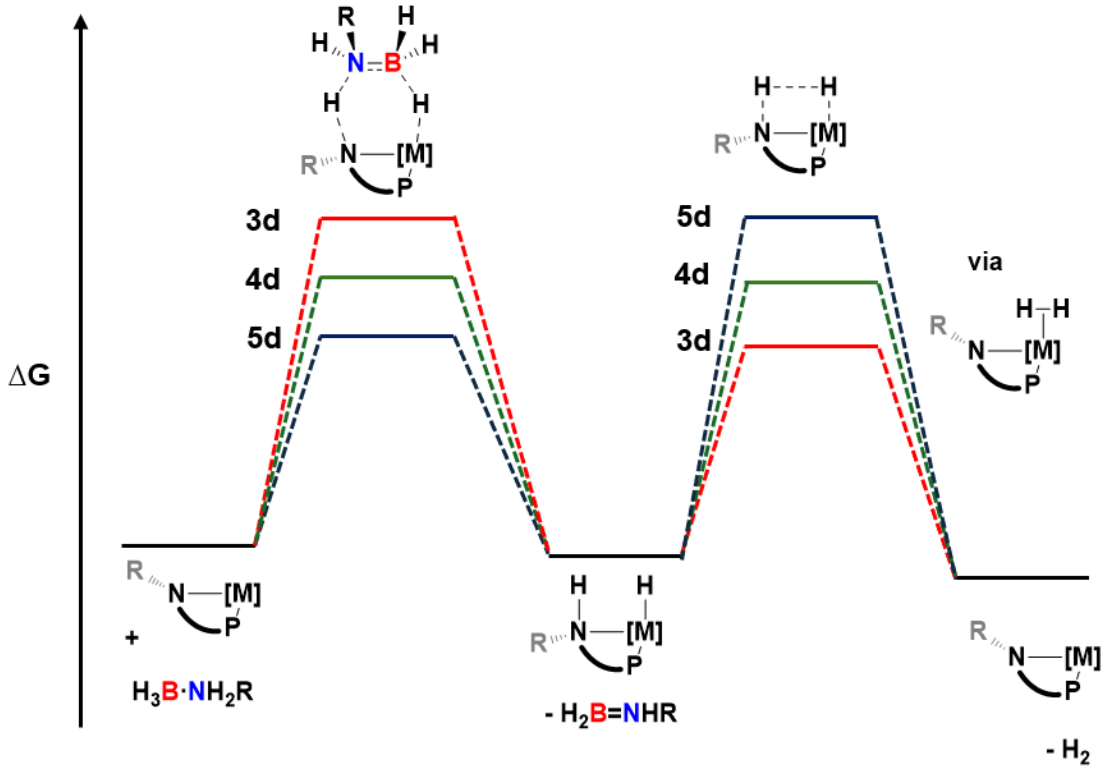

Figure 26. A simplified free energy diagram using the inner sphere metal amido amine-borane dehydrogenation mechanism as an example, showing generalised metal row effects on the barriers to amine-borane dehydrogenation (left) hydride loss as H_2 (right) for 3d, 4d & 4d metal centres. 5d dark blue, 4d green, 3d red. [118, 122]

1.6 Polyaminoborane materials applications

Inorganic polymers, including polyaminoboranes, are a more modern field than organic polymers such as polyolefins and often fulfil different needs. Whilst the ubiquitous organic polymers overwhelmingly fill the roles in modern life for structural applications due to their resilience and chemical inertness, inorganic polymers, although utilised significantly less frequently, have wide ranging physical properties suiting them to fill numerous roles. The main example of a commercially successful inorganic polymer is silicones (polysiloxanes, $(SiR_2O)_n$) which are used as high temperature thermal fluids, lubricants, and specialised adhesives. Many other known classes of inorganic polymers such as polysilazanes $(SiR_2NR)_n$), polyphosphazenes $((PR_2N)_n)$ and polythiazyl $((SN)_n)$ have been investigated for their physical and electrical properties such as thermal resistivity and electrical conductivity, however have yet to see use outside specialised applications. [123-125] For example, silicon based polymers and polyborazylenes (polymers with borazine monomers, $B_3N_3R_3$) are under development as preceramics for the synthesis of low-density silicon carbide and boron nitride respectively. [126, 127] Applications for which are high tensile strength and thermally resistant structural materials in aerospace technology. [128]

The initial focus of work on polyaminoborane synthesis was on its potential use as a hydrogen storage material, helping the transition away from fossil fuels as a portable energy source. Hydrogen itself is too low density to be used as a portable fuel, requiring high pressures to be viable which add unavoidable safety risks, along with the potential chemical explosive capacity. [129] Polyaminoboranes and the precursor amine-boranes were among the materials suggested due to the high mass percentage of H_2 (14 wt% for $(H_2BNH_2)_n$).[130] The hydrogen can be released thermally or by catalysis (as discussed previously in sections **1.1** and **1.2**) and by hydrolysis. [131] The difficulty comes with the regeneration of the subsequent BN material (e.g. polyborazylene) back to the amine-borane or polyaminoborane, which is thermodynamically uphill especially for the direct reaction with H_2. [132] Little progress has been made to surmount this obstacle, with the most viable process thus far involving the use of an excess of hydrazine in liquid ammonia under high pressures at 60 °C. [27]

The more recent focus for polyaminoborane applications is as a shapable preceramic for the improved synthesis of boron-nitride. [26] Boron nitrides are refractory materials

with high chemical resistance. Similarly to the isoelectronic carbon, boron nitrides can form multiple polymorphs: namely diamond-like cubic boron nitride (c-BN) and graphite-like hexagonal boron nitride (h-BN). Current synthetic techniques involve the heating of B_2O_3 and NH_3 at high temperatures to form amorphous boron nitride, followed by annealing and hot pressing at even higher temperatures. [133] By using polyaminoboranes as a preceramic, more complex BN materials such as porous structures and fibres may be attainable, using the polymer to template the structure which can then be thermolyzed into BN.

The homopolymer polyaminoboranes $(H_2BNH_2)_n$ and $(H_2BNHMe)_n$ are brittle materials with a glass transition temperatures close to their thermal decomposition points, and so are far from amenable to classical polymer processing techniques (melt casting, extrusion etc). [56] This is due to the large number of relatively strong dihydrogen bonding interactions between polymer chains (see **1.2**). If this dihydrogen bonding network could be disrupted, for example by the inclusion of bulkier monomers in a copolymer, the processability of the formed polyaminoboranes may improve, allowing for more thorough investigations of materials properties. The solubility effect of varying polyaminoborane *N*-substituents has been reported anecdotally, as larger pendant alkyl groups are introduced the solubility in non-polar solvents increases. [26, 45] The related polyolefins show similar effects, where even small amounts of long alkyl chain co-monomer (< 5%) introduced to polyethylene drastically reduces the crystallinity and melting temperature of the polymers. [134]

In order to fully explore the materials properties of polyaminoboranes such as glass transition temperature, solubility and ceramic yields upon pyrolysis, improved control over their synthesis needs to be demonstrated. The ability to selectively vary chain length, monomer ratios and crosslinking are critical to explore their full range of polyaminoborane materials properties, as is true with polyolefins. Metal ligand cooperative catalysts have been shown to be the best way to control polyaminoborane formation. Catalyst control and further mechanistic understanding of amine borane dehydropolymerisation is needed to be able to synthesize polyaminoboranes with tuneable properties, which would be a step toward taking these polymers from being of only academic interest to applications as functional materials.

References

1. A. L. Allred, *J. of Inorg. Nucl. Chem*, 1961, **17**, 215-221.
2. H. Umeyama and K. Morokuma, *J. Am. Chem. Soc.*, 1976, **98**, 7208-7220.
3. A. Haaland, *Angew. Chem. Int. Ed.*, 1989, **28**, 992-1007.
4. R. H. Crabtree, P. E. Siegbahn, O. Eisenstein, A. L. Rheingold and T. F. Koetzle, *Acc. Chem. Res.*, 1996, **29**, 348-354.
5. W. T. Klooster, T. F. Koetzle, P. E. M. Siegbahn, T. B. Richardson and R. H. Crabtree, *J. Am. Chem. Soc.*, 1999, **121**, 6337-6343.
6. W. M. Haynes, *CRC Handbook of Chemistry and Physics*, 2014.
7. R. M. Adams, J. Beres, A. Dodds and A. J. Morabito, *Inorg. Chem.*, 1971, **10**, 2072-2074.
8. X. Chen, J. C. Zhao and S. G. Shore, *Acc. Chem. Res.*, 2013, **46**, 2666-2675.
9. G. C. Andrews and T. C. Crawford, *Tetrahedron Lett.*, 1980, **21**, 693-696.
10. S. Lau, D. Gasperini and R. L. Webster, *Angew. Chem. Int. Ed.*, 2021, **60**, 14272-14294.
11. J. S. Wang and R. A. Geanangel, *Inorg. Chim. Acta.*, 1988, **148**, 185-190.
12. A. Kumar, T. M. Bhatti and A. S. Goldman, *Chem. Rev.*, 2017, **117**, 12357-12384.
13. H. Hirao and H. Fujimoto, *J. Phy. Chem. A.*, 2000, **104**, 6649-6655.
14. L. Pasumansky, D. Haddenham, J. W. Clary, G. B. Fisher, C. T. Goralski and B. Singaram, *J. Org. Chem.*, 2008, **73**, 1898-1905.
15. A. C. Stowe, W. J. Shaw, J. C. Linehan, B. Schmid and T. Autrey, *Phys. Chem. Chem. Phys.*, 2007, **9**, 1831-1836.
16. S. Frueh, R. Kellett, C. Mallery, T. Molter, W. S. Willis, C. King'ondu and S. L. Suib, *Inorg. Chem.*, 2011, **50**, 783-792.
17. C. W. Hamilton, R. T. Baker, A. Staubitz and I. Manners, *Chem. Soc. Rev.*, 2009, **38**, 279-293.
18. D. J. Heldebrant, A. Karkamkar, J. C. Linehan and T. Autrey, *Energy Environ. Sci.*, 2008, **1**, 156-160
19. T. B. Marder, *Angew. Chem. Int. Ed.*, 2007, **46**, 8116-8118.
20. F. H. Stephens, V. Pons and R. T. Baker, *Dalton Trans.*, 2007, 2613-2626.
21. M. G. Hu, R. A. Geanangel and W. W. Wendlandt, *Thermochim. Acta.*, 1978, **23**, 249-255.
22. A. Rossin and M. Peruzzini, *Chem. Rev.*, 2016, **116**, 8848-8872.
23. M. C. Denney, V. Pons, T. J. Hebden, D. M. Heinekey and K. I. Goldberg, *J. Am. Chem. Soc.*, 2006, **128**, 12048-12049.
24. D. Pun, E. Lobkovsky and P. J. Chirik, *Chem. Comm.*, 2007, 3297-3299.
25. T. Jurca, T. Dellermann, N. E. Stubbs, D. A. Resendiz-Lara, G. R. Whittell and I. Manners, *Chem. Sci.*, 2018, **9**, 3360-3366.
26. A. Staubitz, A. Presa Soto and I. Manners, *Angew. Chem. Int. Ed.*, 2008, **47**, 6212-6215.
27. A. D. Sutton, A. K. Burrell, D. A. Dixon, E. B. Garner, 3rd, J. C. Gordon, T. Nakagawa, K. C. Ott, J. P. Robinson and M. Vasiliu, *Science*, 2011, **331**, 1426-1429.
28. R. Komm, R. A. Geanangel and R. Liepins, *Inorg. Chem.*, 1983, **22**, 1684-1686.
29. T. Kobayashi, S. Gupta, M. A. Caporini, V. K. Pecharsky and M. Pruski, *J. Phys. Chem. C.*, 2014, **118**, 19548-19555.
30. I. Göttker-Schnetmann, P. S. White and M. Brookhart, *Organometallics*, 2004, **23**, 1766-1776.

31. A. Paul and C. B. Musgrave, *Angew. Chem. Int. Ed.*, 2007, **119**, 8301-8304.
32. V. Pons, R. T. Baker, N. K. Szymczak, D. J. Heldebrant, J. C. Linehan, M. H. Matus, D. J. Grant and D. A. Dixon, *Chem Comm.*, 2008, 6597-6599.
33. D. A. Resendiz-Lara, G. R. Whittell, E. M. Leitao and I. Manners, *Macromolecules*, 2019, **52**, 7052-7064.
34. M. Devillard, C. A. D. Pinheiro, E. Caytan, C. Roiland, C. Dinoi, I. Del Rosal and G. Alcaraz, *Adv. Synth. Catal.*, 2021, **363**, 2417-2426.
35. M. E. Bowden, I. W. M. Brown, G. J. Gainsford and H. Wong, *Inorg. Chim. Acta.*, 2008, **361**, 2147-2153.
36. A. Staubitz, M. E. Sloan, A. P. Robertson, A. Friedrich, S. Schneider, P. J. Gates, J. Schmedt auf der Gunne and I. Manners, *J. Am. Chem. Soc.*, 2010, **132**, 13332-13345.
37. D.P. Kim, K.T. Moon, J.G. Kho, J. Economy, C. Gervais and F. Babonneau, *Polym. Adv. Technol.*, 1999, **10**, 702-712.
38. K. J. R. Rosman and P. D. P. Taylor, *Pure Appl. Chem.*, 1998, **70**, 217-235.
39. T. Williams, *J. Mater. Sci.*, 1970, **5**, 811-820.
40. M. Ohring, *Engineering materials science*, Academic Press, Waltham, 1995.
41. A. L. Colebatch and A. S. Weller, *Chem. Eur. J.*, 2019, **25**, 1379-1390.
42. M. Trose, M. Reiss, F. Reiss, F. Anke, A. Spannenberg, S. Boye, A. Lederer, P. Arndt and T. Beweries, *Dalton Trans.*, 2018, **47**, 12858-12862.
43. T. Beweries and H. Helten, *Encyclopedia of Inorganic and Bioinorganic Chemistry*, 2020, 1-25.
44. C. A. De Albuquerque Pinheiro, C. Roiland, P. Jehan and G. Alcaraz, *Angew. Chem. Int. Ed.*, 2018, **57**, 1519-1522.
45. M. Devillard, C. A. De Albuquerque Pinheiro, E. Caytan, C. Roiland, C. Dinoi, I. Del Rosal and G. Alcaraz, *Adv. Synth. Catal.*, 2021, **363**, 2417-2426.
46. F. Anke, S. Boye, A. Spannenberg, A. Lederer, D. Heller and T. Beweries, *Chem. Eur. J.*, 2020, **26**, 7889-7899.
47. E. A. LaPierre, B. O. Patrick and I. Manners, *J. Am. Chem. Soc.*, 2019, **141**, 20009-20015.
48. E. A. K. Spearing-Ewyn, N. A. Beattie, A. L. Colebatch, A. J. Martinez-Martinez, A. Docker, T. M. Boyd, G. Baillie, R. Reed, S. A. Macgregor and A. S. Weller, *Dalton Trans.*, 2019, **48**, 14724-14736.
49. H. C. Johnson and A. S. Weller, *J. of Organomet. Chem.*, 2012, **721-722**, 17-22.
50. H. Helten, B. Dutta, J. R. Vance, M. E. Sloan, M. F. Haddow, S. Sproules, D. Collison, G. R. Whittell, G. C. Lloyd-Jones and I. Manners, *Angew. Chem. Int. Ed.*, 2013, **52**, 437-440.
51. H. Anane, A. Jarid, A. Boutalib, I. Nebot-Gil and F. Tomás, *J. Mol. Struct. THEOCHEM*, 1998, **455**, 51-57.
52. C. Laurence and J. Gal, *Lewis Basicity and Affinity Scales*, 2009, 1-69.
53. N. E. Stubbs, A. Schafer, A. P. Robertson, E. M. Leitao, T. Jurca, H. A. Sparkes, C. H. Woodall, M. F. Haddow and I. Manners, *Inorg. Chem.*, 2015, **54**, 10878-10889.
54. A. Glüer, M. Förster, V. R. Celinski, J. Schmedt auf der Günne, M. C. Holthausen and S. Schneider, *ACS. Catal.*, 2015, **5**, 7214-7217.
55. D. A. Resendiz-Lara, N. E. Stubbs, M. I. Arz, N. E. Pridmore, H. A. Sparkes and I. Manners, *Chem. Comm.*, 2017, **53**, 11701-11704.

56. C. N. Brodie, T. M. Boyd, L. Sotorrios, D. E. Ryan, E. Magee, S. Huband, J. S. Town, G. C. Lloyd-Jones, D. M. Haddleton, S. A. Macgregor and A. S. Weller, *J. Am. Chem. Soc.*, 2021, **143**, 21010-21023.
57. G. I. Peterson and T. L. Choi, *Chem. Sci.*, 2020, **11**, 4843-4854.
58. O. J. Metters, A. M. Chapman, A. P. Robertson, C. H. Woodall, P. J. Gates, D. F. Wass and I. Manners, *Chem. Comm.*, 2014, **50**, 12146-12149.
59. S. Bhunya, T. Malakar and A. Paul, *Chem. Commun.,* 2014, **50**, 5919-5922.
60. S. Bhunya, P. M. Zimmerman and A. Paul, *ACS. Catal.*, 2015, **5**, 3478-3493.
61. T. Malakar, L. Roy and A. Paul, *Chem. Eur. J.*, 2013, **19**, 5812-5817.
62. D. E. Ryan, K. A. Andrea, J. J. Race, T. M. Boyd, G. C. Lloyd-Jones and A. S. Weller, *ACS. Catal.*, 2020, **10**, 7443-7448.
63. A. Kumar, H. C. Johnson, T. N. Hooper, A. S. Weller, A. G. Algarra and S. A. Macgregor, *Chem. Sci.*, 2014, **5**, 2546-2553.
64. M. J. Cross, C. N. Brodie, D. G. Crivoi, J. C. Goodall, D. E. Ryan, A. J. Martinez-Martinez, A. Johnson and A. S. Weller, *Chem. Eur. J.*, 2023, **29**, e202302110.
65. A. P. Robertson, R. Suter, L. Chabanne, G. R. Whittell and I. Manners, *Inorg. Chem.*, 2011, **50**, 12680-12691.
66. A. Viola, J. Peron, K. Kazmierczak, M. Giraud, C. Michel, L. Sicard, N. Perret, P. Beaunier, M. Sicard, M. Besson and J. Y. Piquemal, *Cat. Sci. Tech.*, 2018, **8**, 562-572.
67. A. Johnson, A. J. Martinez-Martinez, S. A. Macgregor and A. S. Weller, *Dalton Trans.*, 2019, **48**, 9776-9781.
68. C. N. Brodie, L. Sotorrios, T. M. Boyd, S. A. Macgregor and A. S. Weller, *ACS. Catal.*, 2022, **12**, 13050-13064.
69. M. Rosello-Merino, J. Lopez-Serrano and S. Conejero, *J. Am. Chem. Soc.*, 2013, **135**, 10910-10913.
70. G. M. Adams, A. L. Colebatch, J. T. Skornia, A. I. McKay, H. C. Johnson, G. C. Lloyd Jones, S. A. Macgregor, N. A. Beattie and A. S. Weller, *J. Am. Chem. Soc.*, 2018, **140**, 1481-1495.
71. M. A. Esteruelas, A. M. López, M. Mora and E. Oñate, *ACS. Catal.*, 2014, **5**, 187-191.
72. T. M. Boyd, K. A. Andrea, K. Baston, A. Johnson, D. E. Ryan and A. S. Weller, *Chem. Comm.*, 2020, **56**, 482-485.
73. J. Tao and Y. Qi, *J. Organomet. Chem.*, 2013, **745-746**, 479-486.
74. J. W. Nugent, M. García-Melchor and A. R. Fout, *Organometallics*, 2020, **39**, 2917-2927.
75. E. A. LaPierre, B. O. Patrick and I. Manners, *J. Am. Chem. Soc.*, 2019, **141**, 20009-20015.
76. Y. Luo and K. Ohno, *Organometallics*, 2007, **26**, 3597-3600.
77. A. B. Chaplin and A. S. Weller, *Angew. Chem. Int. Ed.*, 2010, **49**, 581-584.
78. C. Peng, W. Liu and Y. Wang, *New J. of Chem.*, 2023, **47**, 6661-6672.
79. C. Gunanathan and D. Milstein, *Acc. Chem. Res.*, 2011, **44**, 588-602.
80. L. Luconi, U. B. Demirci, M. Peruzzini, G. Giambastiani and A. Rossin, *Sustain. Energ. Fuels*, 2019, **3**, 2583-2596.
81. Y. Zhang, Y. Zhang, Z.-H. Qi, Y. Gao, W. Liu and Y. Wang, *Int. J. Hydrogen Energ.*, 2016, **41**, 17208-17215.
82. I. Ortega-Lepe, A. Rossin, P. Sanchez, L. L. Santos, N. Rendon, E. Alvarez, J. Lopez-Serrano and A. Suarez, *Inorg. Chem.*, 2021, **60**, 18490-18502.
83. P. Hasche, J. Haak, F. Anke, C. Kubis, W. Baumann, H. J. Drexler, H. Jiao and T. Beweries, *Cat. Sci. Tech.*, 2021, **11**, 3514-3526.

84. A. N. Marziale, A. Friedrich, I. Klopsch, M. Drees, V. R. Celinski, J. Schmedt auf der Gunne and S. Schneider, *J. Am. Chem. Soc.*, 2013, **135**, 13342-13355.
85. S. Swinnen, V. S. Nguyen and M. T. Nguyen, *Chem. Phys. Lett.*, 2011, **513**, 195-200.
86. M. Kass, A. Friedrich, M. Drees and S. Schneider, *Angew. Chem. Int. Ed.*, 2009, **48**, 905-907.
87. N. Blaquiere, S. Diallo-Garcia, S. I. Gorelsky, D. A. Black and K. Fagnou, *J. Am. Chem. Soc.*, 2008, **130**, 14034-14035.
88. F. E. Paulik and J. F. Roth, *Chem. Comm. (London)*, 1968, 1578.
89. K. Ziegler, E. Holzkamp, H. Breil and H. Martin, *Angew. Chem. Int. Ed.*, 1955, **67**, 426-426.
90. P. Cossee, *J. Catal.*, 1964, **3**, 80-88.
91. P. M. Maitlis, A. Haynes, G. J. Sunley and M. J. Howard, *Dalton Trans.*, 1996, **11**, 2187-2196.
92. R. G. Matthews, M. Koutmos and S. Datta, *Curr. Opin. Struct. Biol.*, 2008, **18**, 658-666.
93. H. Ogata, W. Lubitz and Y. Higuchi, *J. Biochem.*, 2016, **160**, 251-258.
94. B. M. Hoffman, D. Lukoyanov, Z. Y. Yang, D. R. Dean and L. C. Seefeldt, *Chem. Rev.*, 2014, **114**, 4041-4062.
95. B. K. Werley, X. Hou, E. P. Bertonazzi, A. Chianese and T. W. Funk, *Organometallics*, 2023, **42**, 3053-3065.
96. H. M. Jung, S. T. Shin, Y. H. Kim, M. J. Kim and J. Park, *Organometallics*, 2001, **20**, 3370-3372.
97. Y. Shvo, D. Czarkie, Y. Rahamim and D. F. Chodosh, *J. Am. Chem. Soc.*, 1986, **108**, 7400-7402.
98. J. H. Choi, N. Kim, Y. J. Shin, J. H. Park and J. Park, *Tetrahedron Lett.*, 2004, **45**, 4607-4610.
99. T. Ohkuma, H. Ooka, S. Hashiguchi, T. Ikariya and R. Noyori, *J. Am. Chem. Soc.*, 1995, **117**, 2675-2676.
100. K. J. Haack, S. Hashiguchi, A. Fujii, T. Ikariya and R. Noyori, *Angew. Chem. Int. Ed.,* 1996, **36**, 285-288.
101. R. Noyori and S. Hashiguchi, *Acc. Chem. Res.*, 1997, **30**, 97-102.
102. R. Noyori and T. Ohkuma, *Angew. Chem. Int. Ed.*, 2001, **40**, 40-73.
103. R. Noyori, M. Yamakawa and S. Hashiguchi, *J. Org. Chem.*, 2001, **66**, 7931-7944.
104. M. D. Fryzuk, P. A. MacNeil and S. J. Rettig, *J. Am. Chem. Soc.*, 1987, **109**, 2803-2812.
105. V. Sinha, M. Trincado, H. Grutzmacher and B. de Bruin, *J. Am. Chem. Soc.*, 2018, **140**, 13103-13114.
106. S. Padmanaban, G. H. Gunasekar and S. Yoon, *Inorg. Chem.*, 2021, **60**, 6881-6888.
107. W. Jia, X. Chen, R. Guo, C. Sui-Seng, D. Amoroso, A. J. Lough and K. Abdur-Rashid, *Dalton Trans*, 2009, 8301-8307.
108. C. Hou, J. Jiang, Y. Li, Z. Zhang, C. Zhao and Z. Ke, *Dalton Trans*, 2015, **44**, 16573-16585.
109. W. Kuriyama, T. Matsumoto, O. Ogata, Y. Ino, K. Aoki, S. Tanaka, K. Ishida, T. Kobayashi, N. Sayo and T. Saito, *Org. Proc. Res. Dev.*, 2011, **16**, 166-171.
110. L. Alig, M. Fritz and S. Schneider, *Chem. Rev.*, 2019, **119**, 2681-2751.
111. J. P. Lomont, S. C. Nguyen and C. B. Harris, *Acc. Chem. Res.*, 2014, **47**, 1634-1642.

112. J. N. Harvey and R. Poli, *Dalton Trans.*, 2003, **21**, 4100-4106.
113. E. Alberico, P. Sponholz, C. Cordes, M. Nielsen, H. J. Drexler, W. Baumann, H. Junge and M. Beller, *Angew. Chem. Int. Ed.*, 2013, **52**, 14162-14166.
114. A. Fürstner, *ACS Cent. Sci.*, 2016, **2**, 778-789.
115. C. Hou, Y. Li and Z. Ke, *Inorg. Chim. Acta.*, 2020, **511**.
116. L. Zhou, D. Liu, H. Lan, X. Wang, C. Zhao, Z. Ke and C. Hou, *Cat. Sci. Tech.*, 2020, **10**, 169-179.
117. Y. Jing, Z. Ye, J. Su, Y. Feng, L.-B. Qu, Y. Liu and Z. Ke, *Cat. Sci. Tech.*, 2020, **10**, 5443-5447.
118. C. Hou, J. Jiang, S. Zhang, G. Wang, Z. Zhang, Z. Ke and C. Zhao, *ACS Catal.*, 2014, **4**, 2990-2997.
119. H. Jiao, K. Junge, E. Alberico and M. Beller, *J. Comput. Chem.*, 2016, **37**, 168-176.
120. M. A. Esteruelas, I. Fernández, A. M. López, M. Mora and E. Oñate, *Organometallics*, 2014, **33**, 1104-1107.
121. M. L. Buil, J. A. Cabeza, M. A. Esteruelas, S. Izquierdo, C. J. Laglera-Gandara, A. I. Nicasio and E. Onate, *Inorg. Chem.*, 2021, **60**, 16860-16870.
122. C. Wang, Q. Fan, G. Wang and Q. Zhu, *Mol. Catal.*, 2023, **547**.
123. C. R. Krüger and E. G. Rochow, *J. Polym. Sci. Part A: Gen. Pap.*, 1964, **2**, 3179-3189.
124. M. Goehring and D. Voigt, *Sci. Nat*, 1953, **40**, 482-482.
125. H. R. Allcock and R. L. Kugel, *J. Am. Chem. Soc.*, 1965, **87**, 4216-4217.
126. B. Toury and P. Miele, *J. Mat. Chem.*, 2004, **14**.
127. T. Isoda, H. Kaya, H. Nishii, O. Funayama, T. Suzuki and Y. Tashiro, *J. Inorg. Organomet. Polym.*, 1992, **2**, 151-160.
128. C. J. Simonsen Ginestra, C. Martinez-Jimenez, A. Matatyaho Ya'akobi, O. S. Dewey, A. D. Smith McWilliams, R. J. Headrick, J. A. Acapulco, L. R. Scammell, M. W. Smith, D. V. Kosynkin, D. M. Marincel, C. Park, S. H. Chu, Y. Talmon, A. A. Marti and M. Pasquali, *Nat. Commun.*, 2022, **13**, 3136.
129. T. B. Marder, *Angew. Chem. Int. Ed.*, 2007, **46**, 8116-8118.
130. A. Ledoux, P. Larini, C. Boisson, V. Monteil, J. Raynaud and E. Lacôte, *Angew. Chem. Int. Ed.*, 2015, **54**, 15744-15749.
131. U. B. Demirci, S. Bernard, R. Chiriac, F. Toche and P. Miele, *J. Power Sources*, 2011, **196**, 279-286.
132. M. H. Matus, K. D. Anderson, D. M. Camaioni, S. T. Autrey and D. A. Dixon, *J. Phys. Chem. A.*, 2007, **111**, 4411-4421.
133. S. Chakrabartty and S. Kumar, *Trans. Ind. Ceram. Soc.*, 1995, **54**, 48-51.
134. R. Alamo, R. Domszy and L. Mandelkern, *J. Phys. Chem.*, 1984, **88**, 6587-6595.

Chapter 2: The dehydropolymerisation of amine-boranes with group 9 $PN^{H}P$ catalysts

2. The dehydropolymerisation of amine-boranes with group 9 PN^HP catalysts

The tridentate MACHO ligands $NH(CH_2CH_2PR_2)_2$ are versatile components of many reported metal ligand cooperative catalysts, specifically in hydrogenation/dehydrogenation catalysis (**Figure 27**) (see section **1.4**). [1-3] The first reported MACHO catalyst 'RU-MACHO' [$Ru(PN^HPPh_2)(CO)ClH$] was developed for the catalytic reduction of esters by hydrogenation. [4] These catalysts generally have active species with M^{2+} d^6 metal centers and metal hydrides adjacent to the ligand NH. They operate via inner or outer sphere metal ligand cooperative mechanisms (see section **1.3**). [5-7]

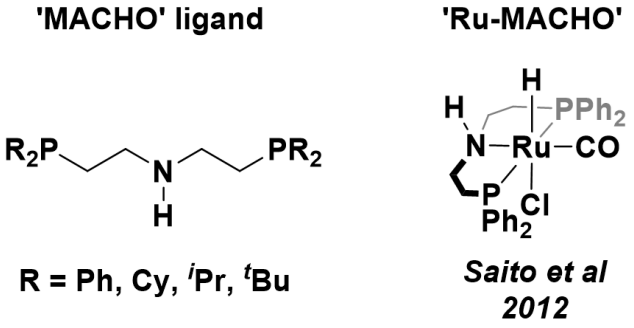

Figure 27. Left: The structure of tridentate aminophosphine MACHO ligands. Right: the first reported MACHO catalyst: Ru-MACHO. [4]

Catalysts with MACHO ligands have also been used for amine-borane dehydropolymerisation with group 8 and 9 metals (Fe, Ru, Co, Rh, Ir). [7-11] These MACHO catalysts can often be used at low loadings (< 0.5 mol%) and are particularly fast, for example the ruthenium catalyst $Ru(^i Pr\text{-}PN^HP)(PMe_3)H_2$ has a reported TOF of up to 20 s^{-1} for the dehydrogenation of $H_3B{\cdot}NH_2Me$. [5, 6] In one of the most recent developments, Weller et al. reported the MACHO-containing precatalyst $[Rh(^i Pr\text{-}PN^HP)(NBD)][Cl]$ (**1**) as a dehydropolymerisation precatalyst for methyl amine-borane ($H_3B{\cdot}NH_2Me$).

Complex **1** is a robust precatalyst that has been shown to be capable of catalyzing amine-borane dehydropolymerisation at very low catalyst loadings (0.01 mol%) and which remarkably works in air, despite the active catalyst species being highly air sensitive (**Figure 28**).[11] The activation route of the precatalyst **1**, specifically how the NBD placeholder ligand is lost and the metal centre is oxidized from Rh^I to Rh^{III}, is

currently not known. Initially there is an induction period to the dehydropolymerisation of $H_3B{\cdot}NH_2Me$ with **1** after which complexes Rh(*i*Pr-PN^{H}P)H_2Cl (**2**) and Rh(*i*Pr-PN^{H}P)H_3 (**3**) are observed by $^{31}P\{^1H\}$ NMR spectroscopy. [11] The dihydride chloride **2** can itself be used as a precatalyst, removing the induction period and expediting the formation of the catalytically active trihydride species Rh(*i*Pr-PN^{H}P)H_3 **3**, likely via a base-promoted hydride transfer from amine-borane (**Figure 28**).[11] This releases an equivalent of boronium salt $[H_2B(NMeH_2)_2][Cl]$ which can be observed by ^{11}B NMR.[11] Upon completion of amine-borane dehydropolymerisation, the active catalyst **3** converts back into the off-cycle species complex **2** as both species are in equilibrium, which is observed by post-catalysis in-situ $^{31}P\{^1H\}$ and ^1H NMR spectroscopies.[11]

Complex **3** is reported to operate via an outer-sphere ligand cooperative mechanism, where $H_3B{\cdot}NH_2Me$ forms a dihydrogen bonded outer sphere adduct across the Rh–H and adjacent N–H prior to dehydrogenation, as supported by DFT calculations (**Figure 29**).[11] This Rh MACHO system is reported to exhibit a first order dependance of rate on the catalyst concentration and an initial 'pseudo zeroth order' dependance on the concentration of $H_3B{\cdot}NH_2Me$. This is due to a pre-equilibrium involving $H_3B{\cdot}NH_2Me$ binding to the active catalyst species **3** that lies towards the dihydrogen bonded adduct **3·AB**, and so when $H_3B{\cdot}NH_2Me$ concentration decreases as catalysis progresses, the concentration of **3·AB** and therefore rate of dehydrogenation does not decrease until almost all of the $H_3B{\cdot}NH_2Me$ is consumed. [11]

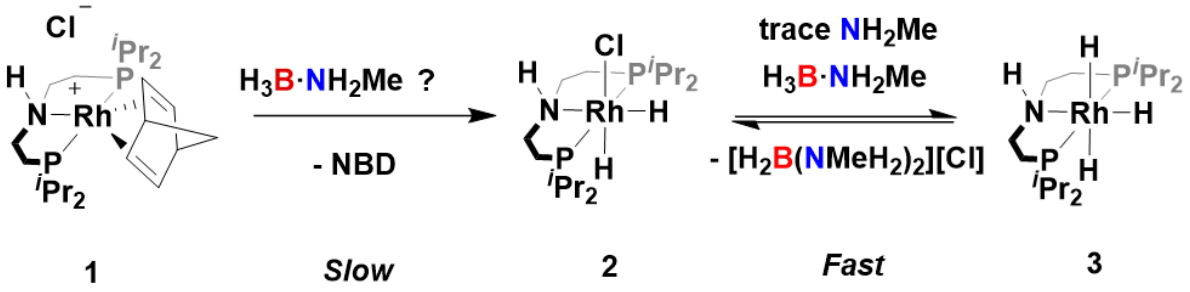

Figure 28. The activation of precatalyst **1** to precatalyst **2** via loss of the NBD ligand and the potential oxidative addition of H_2 from an amine-borane. The conversion of **2** to catalytically active species **3** via base-promoted hydride transfer from an amine-borane to form a metal hydride and an equivalent of boronium chloride. [11]

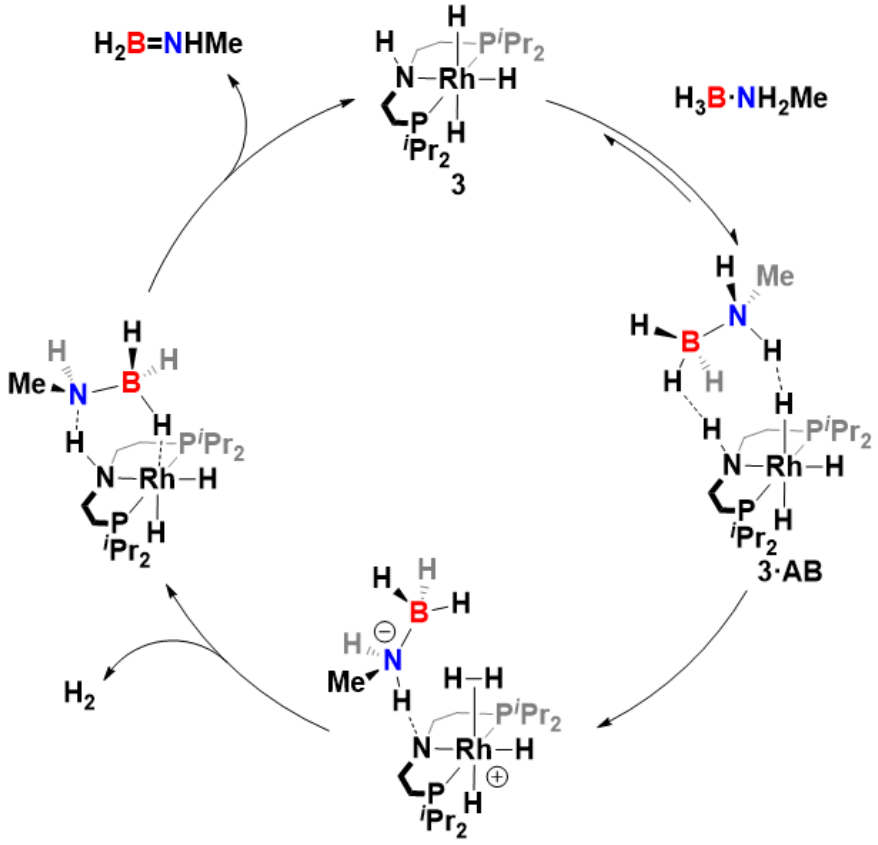

Figure 29. The proposed mechanism for the dehydrogenation of $H_3B{\cdot}NH_2Me$ catalyzed by Rh MACHO catalyst $Rh(PN^HP^iPr)H_3$ (**3**) with an outer-sphere mechanism.[11]

The aim of this chapter is to develop further the understanding of how the amine-borane dehydrogenation precatalysts **1** and **2** are activated and deactivated. This understanding will be then used to aid catalyst design. A better understanding of how these catalysts operate will also be used to attempt the dehydropolymerisation of *N*-alkyl substituted amine-boranes other than the already reported *N*-methyl. [11] It has previously been reported that dehydropolymerisation catalysts that are effective for $H_3B{\cdot}NH_2Me$ (such as $Ir(POCOP^tBu)H_2$) are often unable to dehydropolymerise amine-boranes with larger *N*-alkyl groups, which has been suggested but not proven to be a result of increased substrate steric bulk hindering catalyst turnover.[12,13] By understanding the reason for which substrate scope is limited for such dehydropolymerisation catalysts, the dehydropolymerisation of a wider range of amine-boranes and may be possible.

2.1 The dehydropolymerisation of amine-boranes with precatalysts [Rh(^{i}Pr-PN^{H}P)(NBD)][Cl] (1) and Rh(^{i}Pr-PN^{H}P)H$_2$Cl (2): background and methods

The catalytic dehydropolymerisation of amine-boranes can be monitored by multiple techniques that provide a wealth of information about the catalyst operation. The volume of hydrogen gas evolved during catalysis can be measured eudiometrically and plotted over time to provide reaction progress profiles, from which kinetic data can be extracted. The measurement of H_2 release is a proxy for measuring the transient aminoborane product of amine-borane dehydrogenation, which is rapidly polymerised immediately after formation. This method measures the rate of catalytic amine-borane dehydrogenation, which is the proposed rate determining process in the overall dehydropolymerisation. The reported energy barrier for the chain-end polymerisation of aminoboranes ($\Delta G^{\ddagger}$ = 7.8 kcal mol^{-1}) is significantly lower than the typical overall energy span for catalytic amine-borane dehydrogenation ($\Delta G^{\ddagger}$ = 15 – 25 kcal mol^{-1}) and therefore the rate of catalysis is related to that of the dehydrogenation step.[11, 14, 15]

An important consideration to be taken into account when interpreting the kinetic data obtained from H_2 gas evolution measurements is whether the overall dehydropolymerisation is 100% selective for polyaminoborane. The selective dehydropolymerisation of amine-boranes (to aminoboranes) releases 1 equivalent of H_2 gas per aminoborane monomer produced, however over-dehydrogenated products such as borazines result in the release of further H_2 (**Figure 30**). This selectivity is monitored by ^{11}B NMR spectroscopy and needs to be noted when using the recorded kinetic data to aid in mechanistic elucidation.

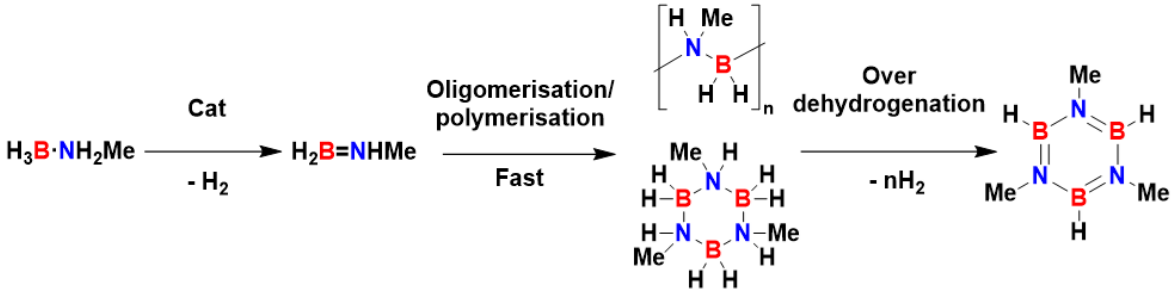

Figure 30. The catalytic dehydropolymerisation of $H_3B{\cdot}NH_2Me$ to cyclotriborazane or polyaminoborane via aminoborane $H_2B{=}NHMe$ releasing 1 equivalent of H_2. Further dehydrogenation (over dehydrogenation) is the release of further H_2 and the formation of products such as borazine.

NMR spectroscopy is important in tracking dehydropolymerisations as it allows for the monitoring of both catalyst and BN product speciation. ^{1}H and ^{31}P{^{1}H} NMR spectroscopies are particularly important for monitoring the catalyst speciation, i.e. precatalyst activation, resting-state identity and catalyst poisoning. ^{31}P{^{1}H} NMR spectroscopy allows for convenient identification and relative quantification of catalyst species when a phosphorous containing ligand (such as a MACHO ligand) is present. ^{1}H NMR spectroscopy can also be used to track speciation as most amine-borane dehydropolymerisation catalysts exhibit metal hydrides that typically lie up-field (negative ppm values) of the aliphatic region, which is obscured by solvent, amine-borane and polyaminoborane signals. [11, 16] ^{11}B NMR spectroscopy is used to track the conversion of amine-boranes into polyaminoboranes, alongside identifying side products, and calculating selectivities.

Mass spectrometry can also be used to track catalyst speciation, this is particularly useful if no spin active nuclei such as phosphorous are present in the ligands, or if no metal hydrides are present in the catalyst resting state. Active catalyst species during amine-borane dehydropolymerisation are however often transient reactive species that are prone to decomposition during analysis, such as by interaction with the mass spectrometer carrier solvent, and so this technique is less commonly used. Catalyst decomposition during mass spectrometric analysis can be partially mitigated by the coupling of the mass spectrometer to a glove box, preventing exposure to atmospheric oxygen and moisture. [17]

2.1.1 The effect of air on [Rh(^{i}Pr-PN^{H}P)(NBD)][Cl] (1) precatalyst activation

Precatalyst **1** is reported to be air-tolerant, such that dehydropolymerisations of $H_3B{\cdot}NH_2Me$ can be performed in air and form poly(*N*-methylaminoborane) with 98% selectivity. [11] Complex **1** is air stable, however the catalyst activation intermediate **2** and active species **3** are air sensitive. Dehydropolymerisations of $H_3B{\cdot}NH_2Me$ with precatalyst **1** exhibit an induction period (**Figure 31**) during which the precatalyst **1** is converted into the active catalytic species **3** (as measured by $^{31}P\{^{1}H\}$ NMR spectroscopy). [11] It was noted that this induction period was significantly reduced when catalysis is performed initially under an atmosphere of air rather than argon, however the reason why was not determined. This involved loading the catalyst and $H_3B{\cdot}NH_2Me$ into the reaction vessel with an initial atmosphere of air, which upon the initiation of catalysis was displaced by the H_2 produced.

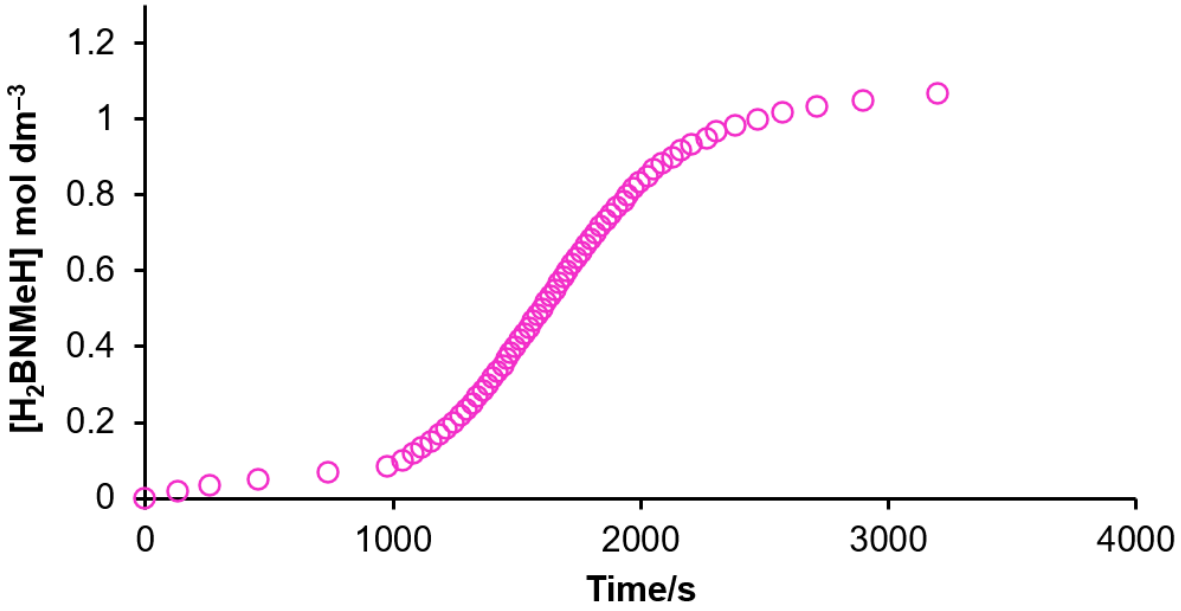

Figure 31. A typical hydrogen evolution plot for the dehydropolymerisation of $H_3B{\cdot}NH_2Me$ (1 mol dm^{-3} in THF) by precatalyst **1** (0.5 mol%) initially loaded under argon, showing an ~ 1000 s induction period.

The effect of air upon the activation of precatalyst **1** during the dehydropolymerisation of $H_3B{\cdot}NH_2Me$ was investigated by eudiometric measurements of H_2 evolution, with varying amounts of air present in the reaction vessel atmosphere prior to catalysis. Reactions were performed under otherwise identical conditions: 293 K, 1 mol dm^{-3} $H_3B{\cdot}NH_2Me$ in dry THF solvent (10 ppm of H_2O), with 0.5 mol% **1** relative to

$H_3B{\cdot}NH_2Me$ (**Figure 32**). The THF solvent was added to the solid precatalyst and $H_3B{\cdot}NH_2Me$ to initiate the reactions. Dehydropolymerisations were set up under an initial atmosphere of argon and various volumes of air (0, 2.5 cm^3, 5 cm^3) were injected into the solvent of the stirring reaction mixture. For reference, 2.5 cm^3 of air represents ~ 2 equivalents of O_2 to precatalyst **1**. A reaction initially set up in-air was also performed. The volume of hydrogen evolved from the catalysis runs was measured, which was used as a proxy for the effective aminoborane concentration produced during catalysis and plotted over time (**Figure 33**). As the initial *N*-methylamine borane concentration was 1 mol dm^{-3}, reaching an effective aminoborane concentration of 1 mol dm^{-3} represents the release of 1 equivalent of H_2 per amine-borane, as occurs in the selective formation of polyaminoborane.

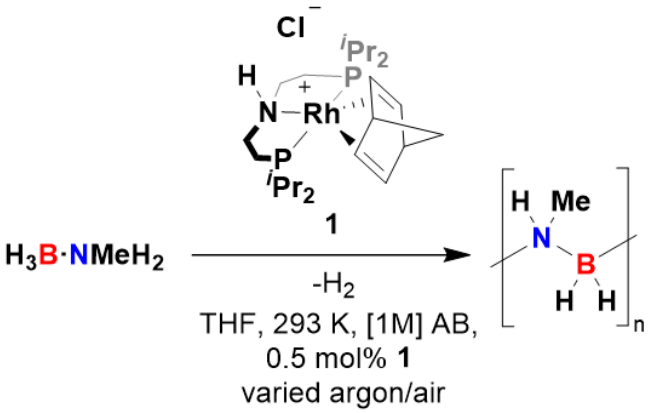

Figure 32. The dehydropolymerisation of methylamine borane (0.112 g, 1 mol dm^{-3} in THF) with precatalyst **1** (0.5 mol%), varying the reaction vessel atmosphere: argon (0 cm^3 air), argon + 2.5 cm^3 air, argon + 5 cm^3 air, air.

All kinetic profiles with complex **1** show an initial induction period, a pseudo zeroth order region of constant rate and finally a declaratory period. [11] A profound effect is seen with varying air present during catalysis, with reaction rate increasing and induction period decreasing as the amount of air is increased. The measured rate during the pseudo zeroth order region increases from $(4.4\pm0.03)x10^{-4}$ mol dm^{-3} s^{-1} under argon to $(1.8\pm0.07)x10^{-3}$ mol dm^{-3} s^{-1} when initially set up with a reaction vessel atmosphere of air. The induction period (time to the pseudo zeroth order region) decreases from ~ 2000 s under argon to ~ 200 s in air (**Figure 33**,**Table 1**). These together suggest that the presence of air (likely oxygen) is aiding the activation of precatalyst **1** toward active species **3**, reducing the time until catalysis initiates and also increasing the concentration of **3** during the active catalysis phase.

This hypothesis is supported by in-situ $^{31}P\{^{1}H\}$ NMR spectra recorded at the end of catalysis, which show precatalyst **1** still present at the end of catalysis (44.9 ppm, d, J_{PRh} = 125 Hz) when performed solely under argon, which decreases as the amount of air introduced increases (**Figure 34**). Concurrently the ^{31}P NMR signal from complex **2** (75.7 ppm, d, J_{PRh} = 115 Hz) increases as the amount of air introduced to the reaction increases, as measured at the end of catalysis (**Figure 34**). The measurement of the amount of complex **2** present after catalysis can be used as a proxy for the fraction of the added precatalyst **1** that is converted to the active catalyst species **3**. This is as **3** is reported to be fully converted back to off-cycle species **2** at the end of catalysis. [11] Only when catalysis is performed with an initial atmosphere wholly comprised of air is the conversion of **1** to **2** complete at the end of catalysis. This was also visually apparent as the precatalyst **1** (Rh^{I}) is yellow whereas **2** (Rh^{III}) is colorless; all catalysis reaction mixtures were still yellow after the completion of hydrogen evolution, except that which was set up initially with an atmosphere of air which was colorless.

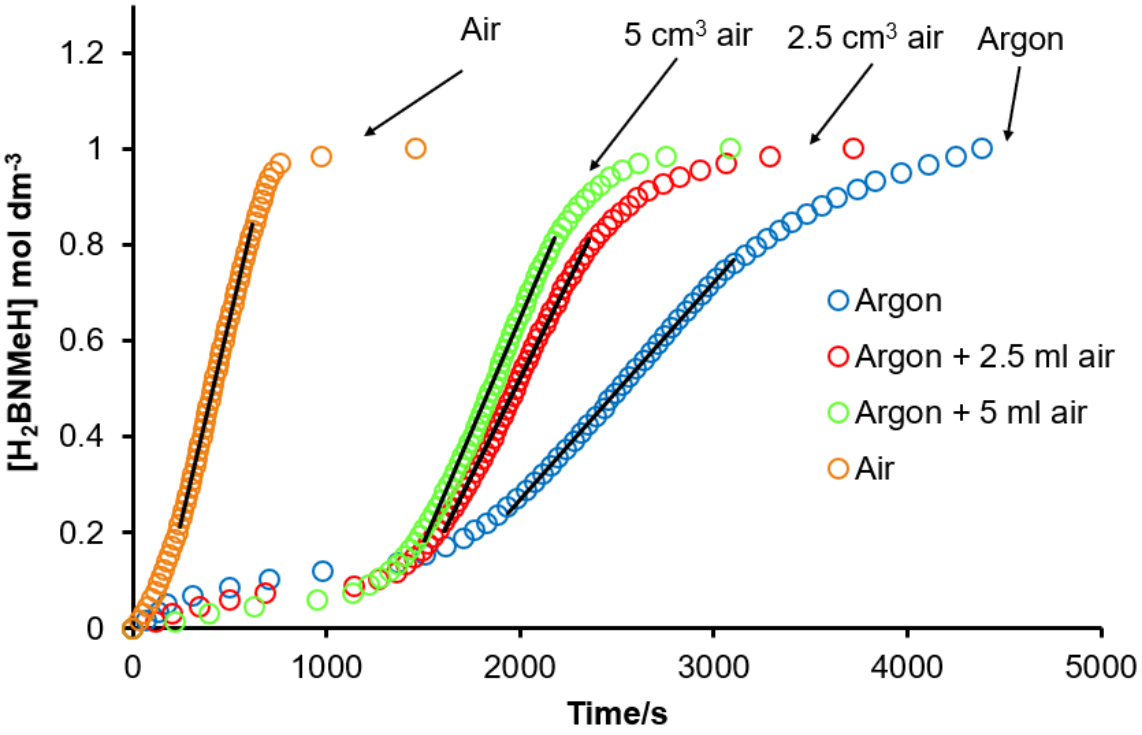

Figure 33. Effective $H_2B{=}NMeH$ concentration over time from eudiometric H_2 evolution measurement for the dehydropolymerisation of $H_3B{\cdot}NH_2Me$ (0.112 g, 1 mol dm^{-3} in THF) by precatalyst **1** (0.5 mol%) in THF with varying reaction vessel atmosphere: argon, argon + 2.5 cm^3 air, argon + 5 cm^3 air, air. Induction period is seen to decrease and rate of reaction increase as the amount of air present is increased.

Atmosphere	k_{obs} [a] (mol dm^{-3} s^{-1})	Amine borane conversion [b] (%)	Polymer selectivity [c] (%)	**1** conversion to **2** [d] (%)	Polymer M_n [e] (g mol^{-1})	Dispersity [f]
Ar	4.4x10^{-4} (±3x10^{-6})	95	99	44	25,600	1.7
Ar + 2.5 cm^3 air	9.2x10^{-4} (±7x10^{-6})	97	99	64	42,200	1.6
Ar + 5 cm^3 air	1.1x10^{-3} (±9x10^{-6})	97	99	74	53,000	1.5
Air	1.8x10^{-3} (7x10^{-6})	>99	94	100	81,000	1.7

Table 1. The dehydropolymerisation of methylamine borane (0.112 g, 1 mol dm^{-3} in THF) with precatalyst **1** (0.5 ml%), varying the reaction vessel atmosphere: argon, argon + 2.5 cm^3 air, argon + 5 cm^3 air, air. Rates [a] determined by eudiometric measurement. Amine-borane conversion [b] and polymer selectivity [c] determined by in-situ ^{11}B NMR spectroscopy at the end of catalysis, precatalyst **1** conversion to complex **2** [d] determined by in-situ ^{31}P{^{1}H} NMR spectroscopy, both measured after the end of hydrogen evolution. Polymer M_n [e] and dispersity [f] determined by GPC.

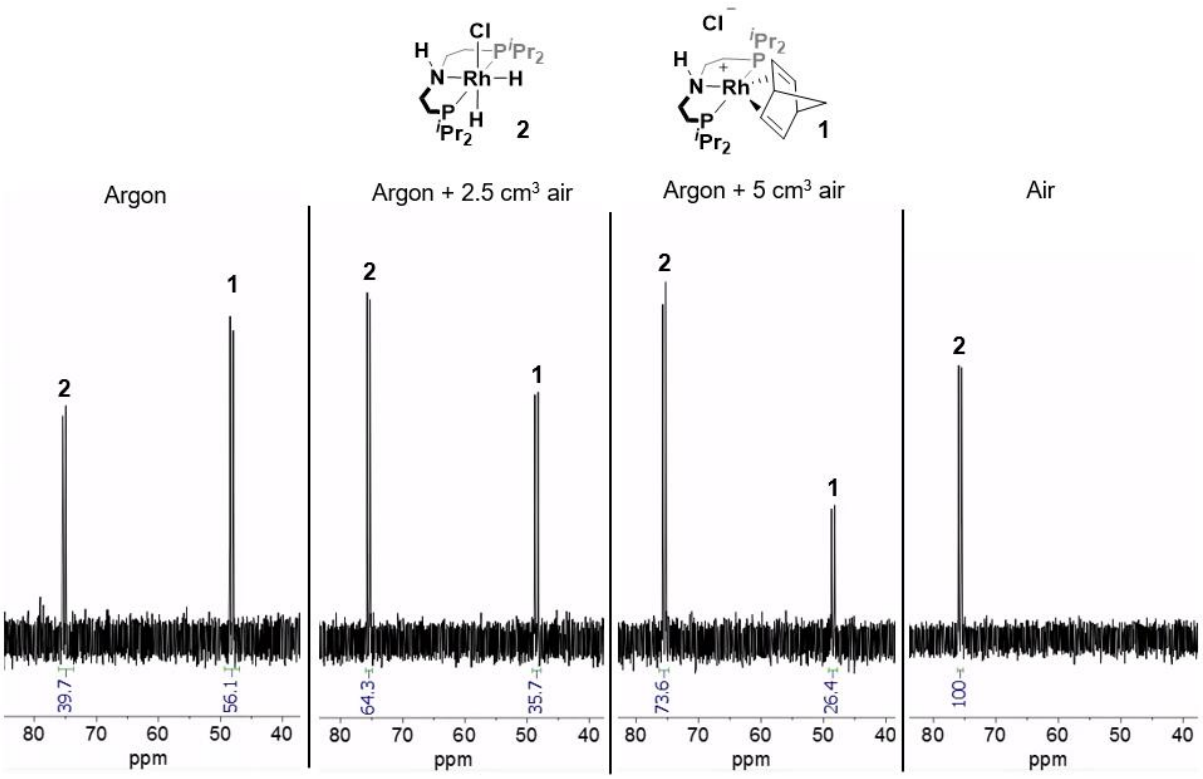

Figure 34. ^{31}P {^{1}H} NMR spectra recorded from in-situ aliquots at the end of the dehydropolymerisation of $H_3B{\cdot}NH_2Me$ (0.112 g, 1 mol dm^{-3} in THF) by precatalyst **1** (0.5 mol%) in THF with varying reaction vessel atmosphere: argon, argon + 2.5 cm^3 air, argon + 5 cm^3 air, air. Decreased intensity of precatalyst **1** and increased intensity of complex **2** is shown as the amount of air present increases.

As the conversion of precatalyst **1** into complex **2** is an irreversible process during catalysis, the NMR analyses suggest that air plays a constructive role in this conversion, possibly aiding loss of the NBD ligand. The oxidation of coordinated alkenes by oxygen with group 9 d^8 metal centers (Rh^I & Ir^I) has been reported, for example the release of 2-cyclooct-1-enone from $[Rh(C_2H_4)(COD)Cl_2]$ upon exposure to oxygen, however a mechanism for this reaction that is also applicable to NBD complexes has not been reported. [18, 19] An as-yet unidentified analogous process may occur during the air-assisted activation of precatalyst **1** during the induction period of amine-borane dehydropolymerisation.

In the absence of oxygen, the loss of NBD from precatalyst **1** may occur via metal assisted hydrogenation to NBE (norbornene). [20] The direct hydrogenation of complex **1** (to complex **2**) is however reported to be a slow process, requiring 7 days at 4 bar of H_2 in 1,2-DFB solution to reach completion, which may suggest another (faster) as-yet unidentified mechanism for NBD loss occurs during the induction period of amine-borane dehydrogenation in the absence of air.[11] Attempts to observe free NBD or its products (such as norbornene or norbornane) post catalysis by ^{1}H NMR spectroscopy were unsuccessful.

As measured by GPC, the molecular weight of the poly(*N*-methylaminoborane) is also affected by the presence of air during catalysis. Polymer M_n increases with increasing air present during dehydropolymerisation, from 25,600 g mol^{-1} under argon to 81,800 g mol^{-1} in air (**Table 1**). Conversion of $H_3B{\cdot}NH_2Me$ and selectivity for polymer (both approaching 100%) are unaffected as measured by ^{11}B NMR spectroscopy. Strong linear correlations are seen between the fractional amount of complex **2** observed at the end of catalysis with both the polymer M_n (R^2 = 0.9952) and k_{obs} (R^2 = 0.9965) (**Figure 35**).

The increase in polymer M_n cannot be attributed directly to the increased conversion of the precatalyst **1** to active catalyst **3**, as this process is proposed to release one equivalent of boronium species $[H_2B(NMeH_2)_2][Cl]$ per metal centre (**Figure 28**), this species acts as a chain transfer agent that limits polymer molecular weight. This has been reported by Weller et al. where increasing loadings of precatalyst **1** give larger k_{obs} values but the same polymer molecular weight. [11] A possible explanation for the increase in polymer M_n with increasing air present during catalysis is that air is

removing a chain terminating agent, and thus a polymer growth-limiting contaminant from catalysis, the possible identity of which will be discussed further in section **2.1.6**. The air introduced to these catalysis runs was not pre-dried and so water may also play a part in the variations seen.

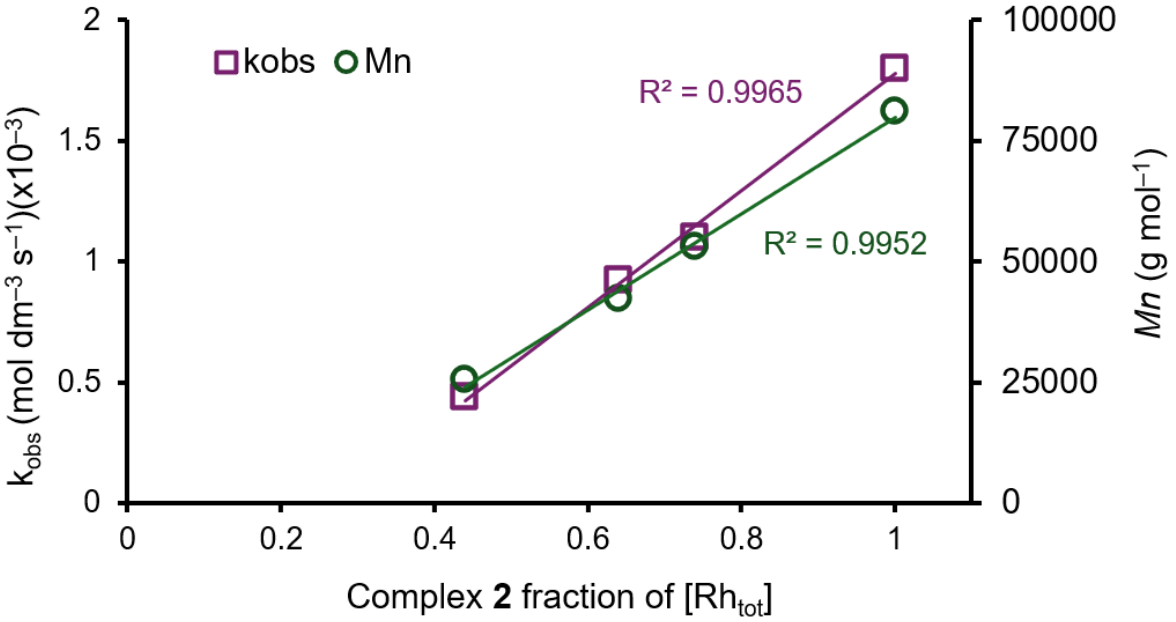

Figure 35. A plot of the measured k_{obs} and polyaminoborane M_n against the fractional amount of complex **2** at the end of catalysis (which varies with the amount of air added to the reaction), as measured by $^{31}P\{^1H\}$ NMR spectroscopy integrals. Strong linear correlations are shown between both M_n and k_{obs} with the fractional amount of **2** observed.

2.1.2 The effect of water on [Rh(^{i}Pr-PN^{H}P)(NBD)][Cl] (1) precatalyst activation

Water is also suggested to be a trace conponent during the dehydropolymerisation of $H_3B{\cdot}NH_2Me$ with precatalyst **1** that may affect catalyst activation and operation. It was noted by Weller et al. that when THF dried with a solvent still was used (5-10 ppm H_2O), a longer induction period was observed than when SPS dried THF was used (~35 ppm H_2O). [11] To further investigate this, dehydropolymerisations of $H_3B{\cdot}NH_2Me$ with precatalyst **1** (0.5 mol%, 0.005 mol dm^{-3}) were performed in THF solvent (2.5 cm^3, 1 mol dm^{-3} of $H_3B{\cdot}NH_2Me$) of varying water content (10, 50 & 100 ppm) under argon. These water contents as concentrations correspond to 0.00056, 0.0028 and 0.0056 mol dm^{-3} respectively, and so 100 ppm of water in the THF solvent represents ~ 1 equivalent of H_2O to precatalyst **1**. The hydrogen evolved over time was measured in an identical method to that described in **2.1.1** (**Figure 36**). It should be noted that the amount of water added to catalysis cannot be increased indefinitely, and at concentrations approaching that of the catalyst, the apparent catalytic hydrolysis of amine-boranes to form boric acid and H_2 can be observed by ^{11}B NMR spectroscopy. When ~ 400 equivalents of water to precatalyst **1** (at 0.5 mol% relative to $H_3B{\cdot}NH_2Me$, 0.005 mol dm^{-3} in 2.5 cm^3 of THF) was added to dehydropolymerisation rapid H_2 release was observed, and an in-situ ^{11}B NMR spectrum showed a broad peak at 20 ppm which corresponds to $B(OH)_3$. [21]

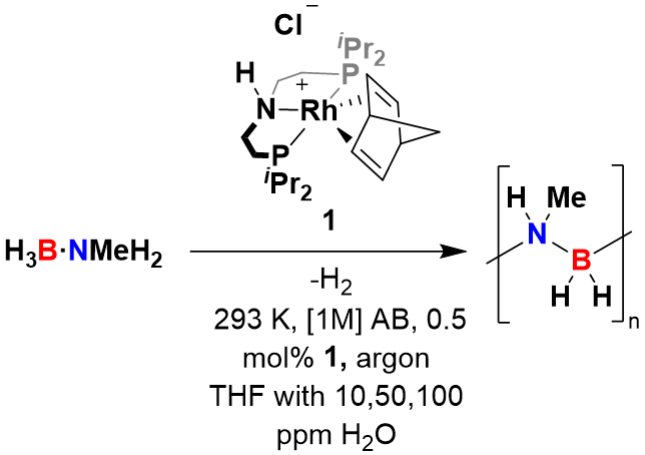

Figure 36. The dehydropolymerisation of methylamine borane (0.112 g, 1 mol dm^{-3} in THF) with precatalyst **1** (0.5 mol%), varying the water content of the solvent: 10, 50 & 100 ppm.

All catalytic runs show comparable profiles and no significant change in the length of the induction period. The rate of hydrogen evolution is observed to approximately double when THF water content is increased from 10 to 100 ppm, $(4.4\pm0.03)\times10^{-4}$ mol dm^{-3} s^{-1} to $(1.1\pm0.006)\times10^{-3}$ mol dm^{-3} s^{-1} (**Figure 37**). The lack of change in induction period suggests that the effect of water on catalysis is not the same as air, with the conversion of precatalyst **1** to complex **2** unlikely to be the primary cause of the increased rate. In-situ $^{31}P\{^{1}H\}$ NMR spectra recorded immediately after catalysis however show decreasing amounts of unactivated precatalyst **1** with increasing water concentration, from 44 % conversion to complex **2** at 10 ppm H_2O to 64% at 100 ppm of H_2O (**Figure 38**). A linear correlation (R^2 = 0.997) between water content during catalysis and the amount of complex **2** present at the end of catalysis is observed, however water appears to have a significantly reduced effect on this than the presence of air (**Figure 39**). The reason for this is currently unclear, as if water aided the conversion of complex **1** to complex **2** (and therefore active species **3**) during the induction period, shorter induction periods with increased water concentration should be observed however this is not the case.

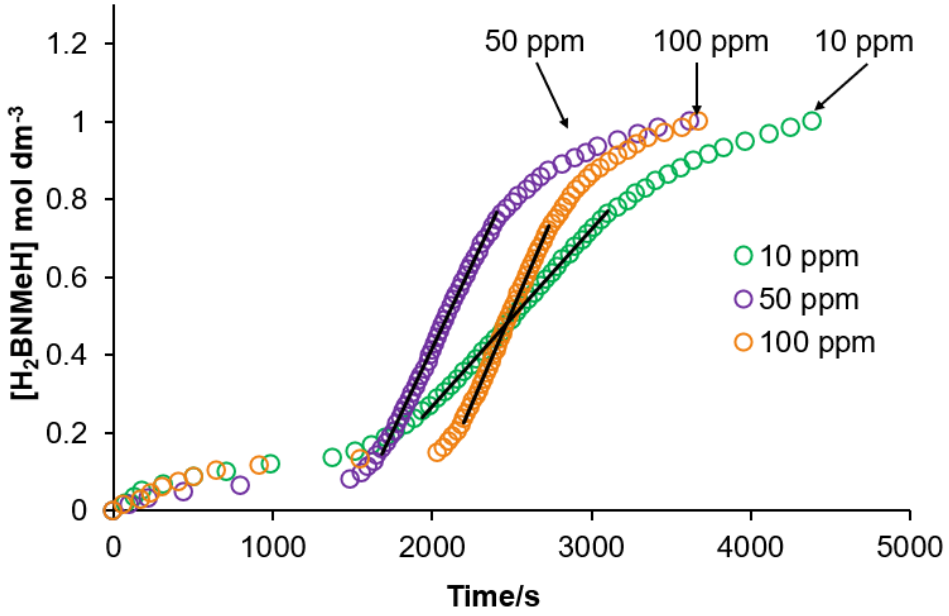

Figure 37. Effective $H_2B{=}NMeH$ concentration over time from eudiometric H_2 evolution measurement for the dehydropolymerisation of $H_3B{\cdot}NH_2Me$ (0.112 g, 1 mol dm^{-3} in THF) by precatalyst **1** (0.5 mol%, 0.005 mol dm^{-3}) in THF with varying water content of the solvent: 10, 50 & 100 ppm. Induction period is unchanged, and the rate of reaction increases as the amount of water present is increased.

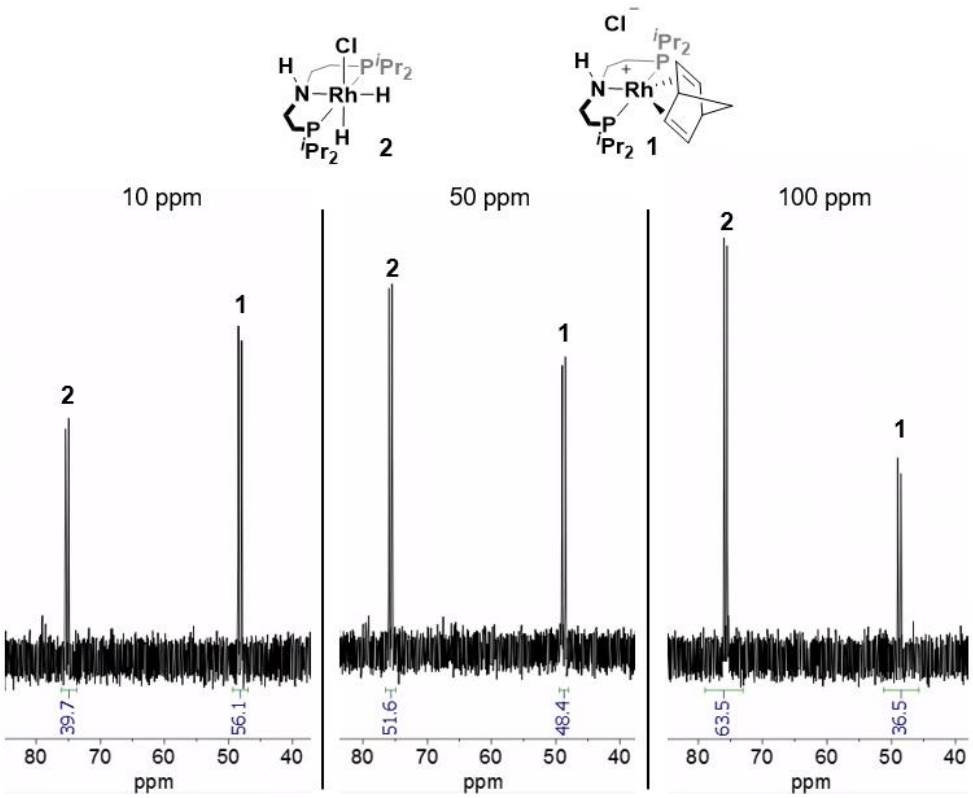

Figure 38. $^{31}P\{^{1}H\}$ NMR spectra recorded from in-situ aliquots at the end of the dehydropolymerisation of $H_3B{\cdot}NH_2Me$ (0.112 g, 1 mol dm^{-3} in THF) by precatalyst **1** (0.5 mol%) in THF with varying water content of the solvent: 10, 50 & 100 ppm. Decreased intensity of precatalyst **1** and increased intensity of complex **2** is shown as the amount of water present increases.

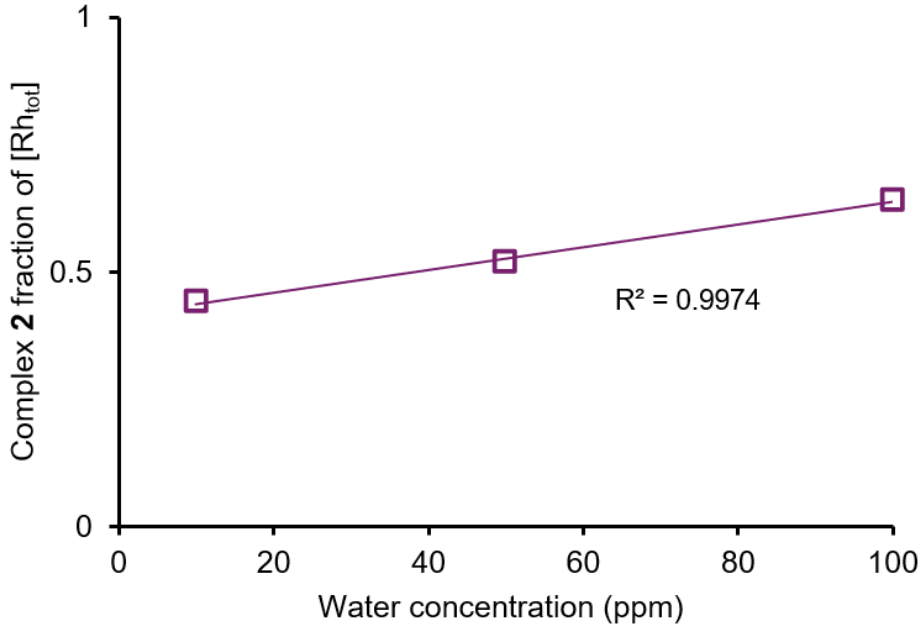

Figure 39. Water concentration in the THF used for the dehydropolymerisation of $H_3B{\cdot}NH_2Me$ (0.112 g, 1 mol dm^{-3}) with- precatalyst **1** (0.5 mol%) against the observed fractional amount of complex **2** at the end of catalysis, as measured by $^{31}P\{^{1}H\}$ NMR spectroscopy integrals

It is possible given the relationship between rate and catalyst that rather than directly reacting with precatalyst **1**, water may act as a co-catalyst for amine-borane dehydrogenation (with complex **3**) and therefore increase the rate of catalysis. Co-catalysts in amine/amido metal ligand cooperative hydrogenation and dehydrogenation have been reported, including the alcohol-assisted heterolytic cleavage of H_2 across a metal-amido bond.[22, 23] An analogous process may occur here where water may aid in the catalytic dehydrogenation of amine-boranes with active species **3**. Schneider et al. report the water-assisted heterolytic cleavage of H_2 across a metal-amido bond in a complex analogous to **3**: $Ru(PN^HP^iPr)(PMe_3)H_2$.[24] A similar effect may occur with catalyst **3** where water could form a hydrogen bonded adduct with catalyst **3** which lowers the barrier to amine-borane dehydrogenation, acting as a cocatalyst (**Figure 40**). As the reported turnover limiting step to catalytic dehydrogenation with catalyst **3** is $H_3B{\cdot}NH_2Me$ N–H activation, this is likely the mechanistic step that is facilitated by the presence of water (**Figure 40**).[11]

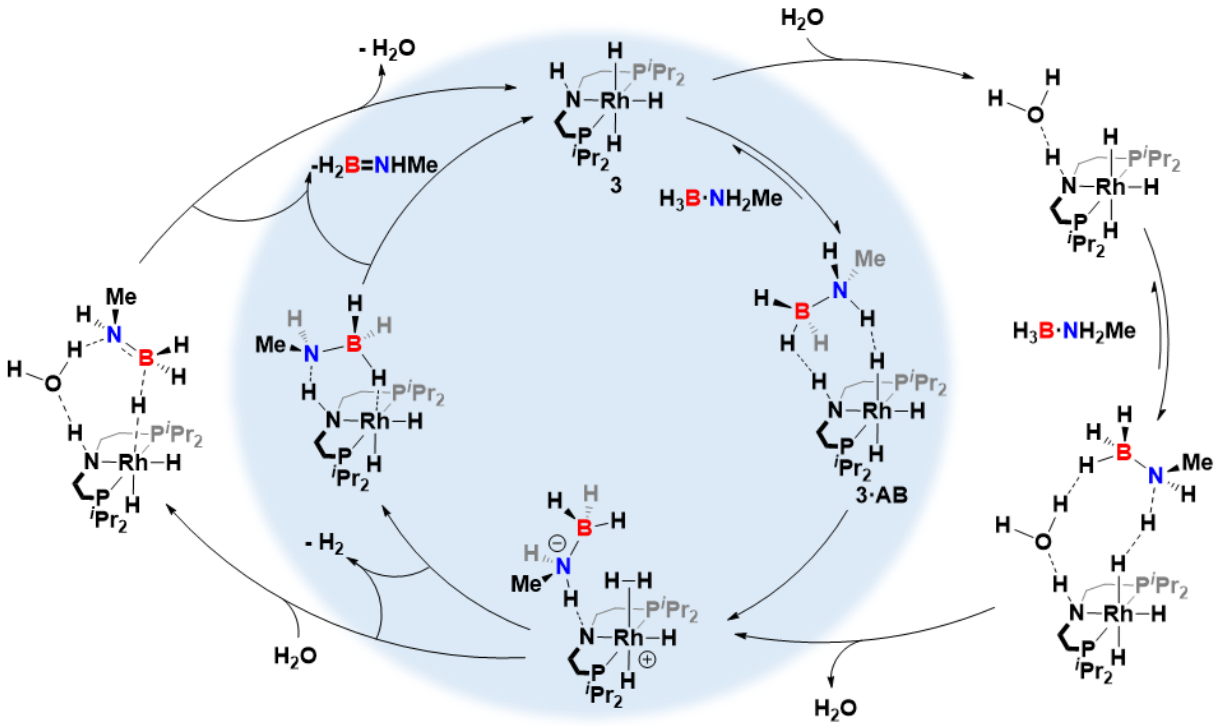

Figure 40. The reported mechanism for dehydrogenation of amine-boranes by catalyst **3** (highlighted in blue) and the proposed mechanism steps where water can act as a cocatalyst (outer, unhighlighted). Adapted from literature.[11]

The molecular weight of the formed polyaminoborane is also affected by the presence of varying amounts of water during catalysis. As mentioned vide supra, increasing the water concentration of the catalysis solvent leads to a marginally increased fractional amount of complex **2** present at the end of catalysis as measured by $^{31}P\{^{1}H\}$ NMR integrals, meaning an increased effective active catalyst (**3**) concentration during dehydropolymerisation. The amount of complex **2** present at the end of catalysis shows a strong linear correlation with increasing molecular weight (**Figure 41**), from an M_n of 25,600 g mol^{-1} with 44% complex **2** (10 ppm water) to 39,500 g mol^{-1} with 64% complex **2** (100 ppm water), as measured by GPC (**Table 2**). This trend is contrary to that reported by Weller et al. In the seminal report with precatalyst **1**, where under conditions of air and water exclusion with catalysis performed under an argon atmosphere, increasing the catalyst concentration has no effect on the polymer M_n. [11] As with air, this trend could also be explained by the reaction and sequestration of a chain terminating (therefore molecular weight limiting) contaminant present during catalysis by in this case water (see **2.1.6**). The trend could also be simply explained by the increased rate of catalysis with the presence of a water co-catalyst resulting in an increased rate of polymer chain propagation (as more aminoborane is available in a shorter time period), which outpaces chain termination.

THF water content (ppm)	k_{obs} [a] (mol dm^{-3} s^{-1})	Amine borane conversion [b] (%)	Polymer selectivity [c] (%)	**1** conversion to **2** [d] (%)	Polymer M_n [e] (g mol^{-1})	Dispersity [f]
10	$4.4x10^{-4}$ ($\pm 3x10^{-6}$)	95	99	44	25,600	1.7
50	$9.0x10^{-4}$ ($\pm 7x10^{-6}$)	96	99	52	32,000	1.6
100	$1.1x10^{-3}$ ($\pm 6x10^{-6}$)	95	99	64	39,500	1.6

Table 2. The dehydropolymerisation of methylamine borane (0.112 g, 1 mol dm^{-3} in THF) with precatalyst **1** (0.5 ml%), with varying water content of the solvent: 10, 50 & 100 ppm. Rates determined by eudiometric measurement [a]; amine-borane conversion [b] and polymer selectivity [c] determined by in-situ ^{11}B NMR spectroscopy at the end of catalysis, precatalyst **1** conversion to complex **2** [d] determined by in-situ $^{31}P\{^{1}H\}$ NMR spectroscopy, both measured after the end of hydrogen evolution. Polymer M_n [e] and dispersity [f] determined by GPC

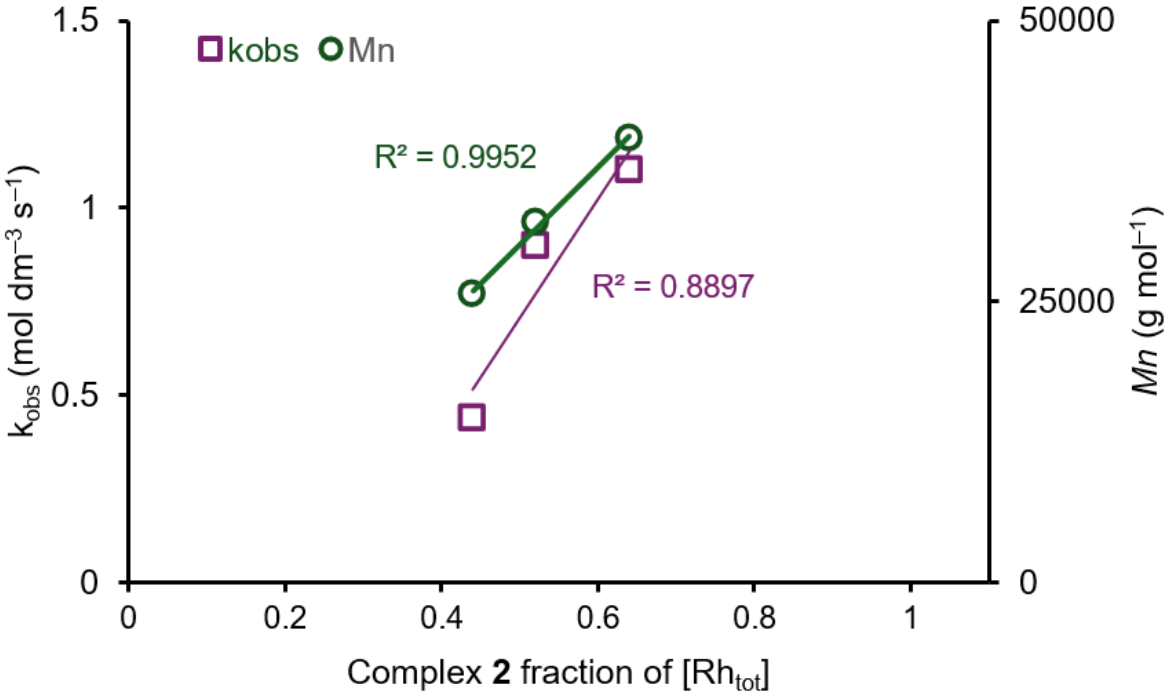

Figure 41. A plot of the measured k_{obs} and polyaminoborane M_n against the fractional amount of complex **2** at the end of catalysis (which varies with the amount of water added to the reaction), as measured by $^{31}P\{^1H\}$ NMR spectroscopy integrals. Strong linear correlations are shown between both M_n and k_{obs} with the fractional amount of complex **2** observed.

2.1.3 A summary of the effects of water and air on the dehydropolymerisation of *N*-methyl amine-borane with [Rh(*i*Pr-PN^{H}P)(NBD)][Cl] (1)

To summarise, the addition of air (likely dominated by the effect of oxygen) and to a more limited extent water increase the rate of the dehydropolymerisation of *N*-methyl amine-borane with precatalyst: from (4.4±0.03)x10^{-4} mol dm^{-3} s^{-1} (10 ppm water, under argon) to (1.8±0.007)x10^{-3} mol dm^{-3} s^{-1} with an initial reaction vessel atmosphere of air and to (1.1±0.006)x10^{-3} mol dm^{-3} s^{-1} when 100 ppm of H_2O is present (**Table 2**)**.** In the case of air, the increase in catalytic rate is likely due to more precatalyst being converted from the inactive NBD precatalyst **1** to complex **2** (and eventually the active species **3**). Air also decreases the induction period, potentially as it promotes the conversion of precatalyst **1** to complex **2**. These effects are possibly due to the oxygen in air aiding in the dissociation of norbornadiene from **1**, however this needs further investigation to identify what happens to the NBD after conversion of precatalyst **1** to complex **2**. Attempts to do this with ^{1}H NMR experiments have been unsuccessful due to the large number of peaks present from amine-borane dehydrocoupling products. The action of air (oxygen) on precatalyst **1** requires further investigation.

Increased addition of water and air also separately led to increases in the molecular weight of the polymer formed: from 25,600 g mol^{-1} (10 ppm water, under argon) to 81,000 g mol^{-1} with an initial reaction vessel atmosphere of air and to 39,500 g mol^{-1} when 100 ppm of H_2O is present. The increase in the degree of polymerisation of the formed poly(*N*-methylaminoborane) with increasing air and water during the dehydropolymerisation of *N*-methylamine borane with precatalyst **1** could be attributed to the reduction in concentration of a chain terminating species present in catalysis (see **2.1.6**).

Increasing water concentration of the solvent used in *N*-methylamine borane dehydropolymerisation with precatalyst **1** results in increased rate of catalysis and moderately increased conversion of precatalyst **1** to complex **2** measured at the end of catalysis (by ^{31}P{^{1}H} NMR spectroscopy), but no significant change in induction period length. This suggests that the action of water is not during the induction period, but during the active catalysis phase, possibly as a co-catalyst. This is supported by

comparing the data from dehydropolymerisations of *N*-methylamine borane with precatalyst **1**, where 100 ppm of H_2O or 2.5 cm^3 of air are added. Both show a 64% conversion of precatalyst **1** to the post-catalysis off cycle species **2** as measured by $^{31}P\{^1H\}$ NMR integrals at the end of catalysis, and so implicitly the same concentration of active species **3** was present during catalysis. With 2.5 cm^3 of air present during catalysis, in the pseudo zeroth order region the rate of dehydrogenation is $(9.2\pm0.07)x10^{-4}$ mol dm^{-3} s^{-1}. However when 100 ppm of water is present in the reaction mixture solvent, a higher rate of $(1.1\pm0.006)x10^{-3}$ mol dm^{-3} s^{-1} is observed. This strongly suggests that water can act as a rate-accelerating cocatalyst with active species **3**.

2.1.4 The attempted dehydropolymerisation of *N*-alkyl amine-boranes with precatalyst [Rh(^{i}Pr-PN^{H}P)(NBD)][Cl] (1)

Following on from the work of Weller et al. with precatalysts **1** and **2** for *N*-methylamine borane dehydropolymerisation, attempts were made to dehydropolymerise other *N*-alkyl amine-boranes. [11] As the catalytic dehydropolymerisation of *N*-propylamine borane has not been reported (the polymer poly(*N*-propylaminoborane) is reported by stoichiometric synthesis methods only), the reactivity of this substrate with precatalyst **1** was investigated. [25]

Dehydropolymerisations of $H_3B{\cdot}NH_2{}^nPr$ were attempted with precatalyst **1** at an amine-borane concentration of 1 mol dm^{-3} (0.182 g in 2.5 cm^3 of THF) and with a catalyst loading of 0.5 mol% (0.005 mol dm^{-3}) (**Figure 42**). The initial attempt performed under argon (with rigorous exclusion of air) resulted in no H_2 evolved after 1 hour, as measured eudiometrically. This is supported by the in-situ ^{11}B NMR spectrum recorded after 1 hour that shows primarily unreacted $H_3B{\cdot}NH_2{}^nPr$ at –18.9 ppm (**Figure 43**). Notably, small amounts of anions BH_4^- and $B_3H_8^-$ are observed in the ^{11}B NMR spectrum at <1 % of the total integral (– 37.7, pentet, J_{BH} = 82 Hz and – 29.6 Hz, nonet, J_{BH} = 33 Hz respectively, **Figure 43**).[26] These are not observed when precatalyst **1** is exposed to $H_3B{\cdot}NH_2Me$. The in-situ $^{31}P\{^1H\}$ NMR spectrum shows two species, unactivated precatalyst **1** (10% total integral) as a doublet (J_{PRh} = 126 Hz) at 48.8 ppm and a new rhodium-coupled species (90% total integral) as a doublet (J_{PRh} = 110 Hz) at 79.3 ppm (see **2.1.5**). [11] This suggests poisoning of the catalyst to form an inactive species seen at 79.3 ppm by ^{31}P NMR spectroscopy.

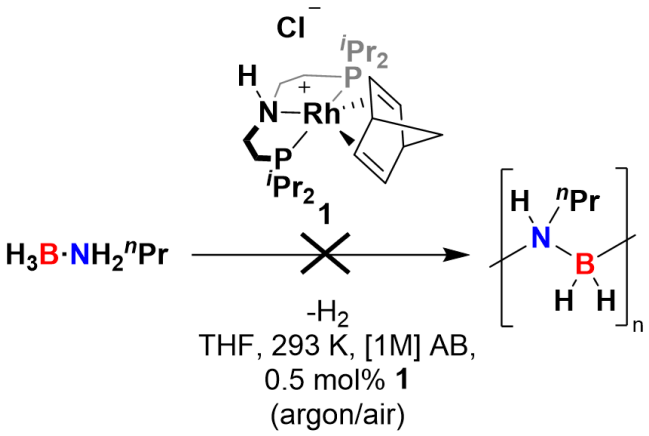

Figure 42. The attempted dehydropolymerisations of *N*-propylamine borane (0.182 g, 1 mol dm^{-3} in THF) with precatalyst **1** (0.5 mol%), varying the reaction vessel atmosphere: argon, air.

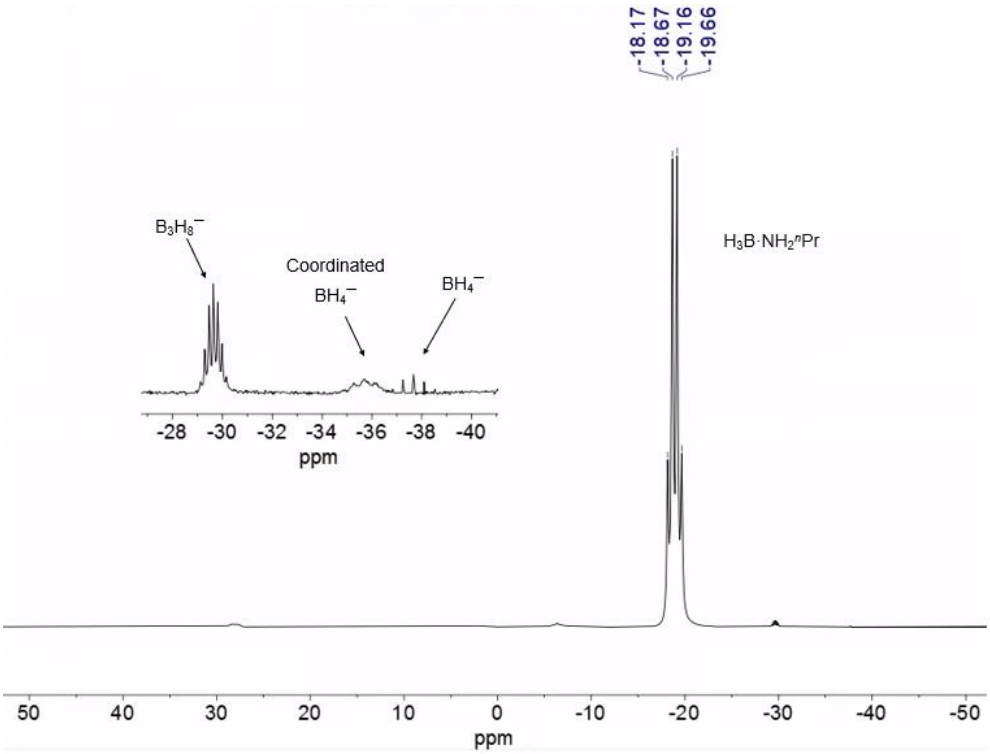

Figure 43. ^{11}B NMR spectrum recorded from an in-situ aliquot after one hour of the attempted dehydropolymerisation of $H_3B{\cdot}NH_2{}^nPr$ (0.182 g, 1 mol dm^{-3} in THF) by **1** (0.5 mol%) in THF. Primarily unreacted $H_3B{\cdot}NH_2{}^nPr$ is seen as a quartet corresponding to the BH_3, at –18.9 ppm. Inset shows trace amounts of BH_4^- and $B_3H_8^-$ anions.

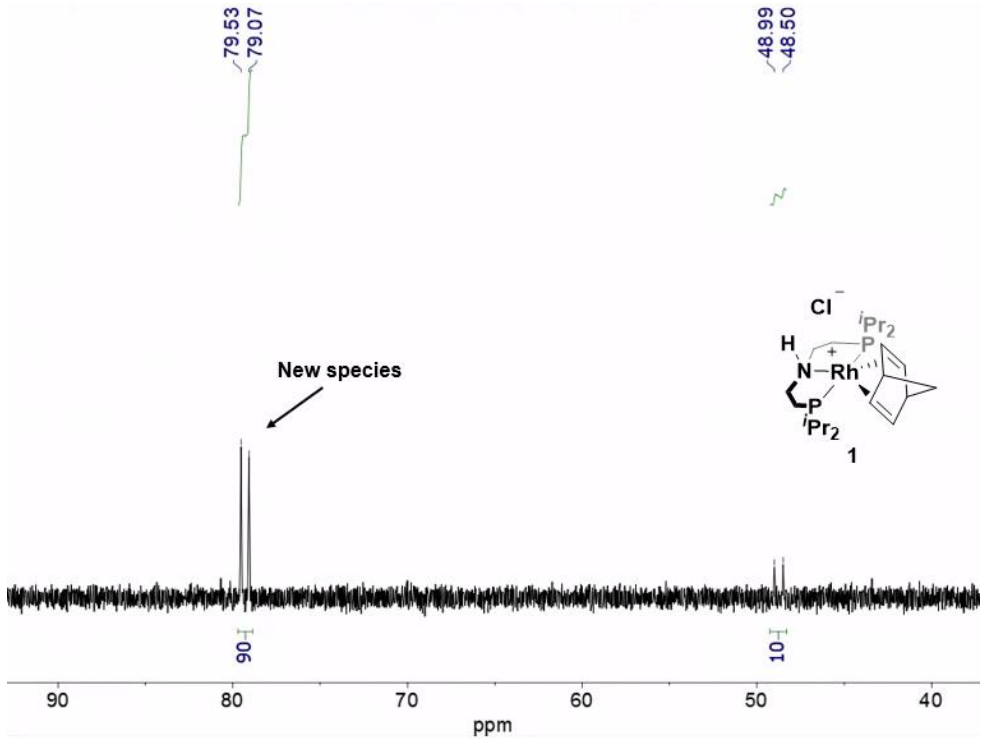

Figure 44. ^{31}P $\{^1H\}$ NMR spectrum recorded from an in-situ aliquot after one hour of the attempted dehydropolymerisation of $H_3B{\cdot}NH_2{}^nPr$ (0.182 g, 1 mol dm^{-3}) by **1** (0.5 mol%) in THF. 90% conversion of precatalyst **1** to a new species at 79.3 ppm is shown.

In an attempt to facilitate dehydropolymerisation of $H_3B{\cdot}NH_2{}^nPr$ with precatalyst **1** catalysis was also attempted where the reaction vessel was initially filled with air, as it was shown that this significantly increased rates of reaction and reduce induction periods with $H_3B{\cdot}NH_2Me$ (see **2.1.1**). $H_3B{\cdot}NH_2{}^nPr$ (0.182 g, 2.5 mmol) and precatalyst **1** (6.7 mg, 0.005 mmol, 0.5 mol%) were added to the reaction vessel in a glovebox under argon, the argon was then removed in-vacuo and air was allowed to enter (**Figure 42**). The THF solvent was added last to start the catalysis run.

After a ~500 s induction period, a partial evolution of H_2 was observed by eudiometric measurement, with only 0.35 equivalents of the starting $H_3B{\cdot}NH_2{}^nPr$ appears to have been dehydrogenated. A brief pseudo zeroth order region of catalysis ($(2.86\pm0.003)\times10^{-4}$ mol dm^{-3} s^{-1}) and then a deceleration of rate is shown (**Figure 45**). This partial dehydrogenation is also seen in the in-situ ^{11}B NMR spectrum recorded after 2000 seconds that shows primarily unreacted $H_3B{\cdot}NH_2{}^nPr$ at –18.9 ppm (41%) and a small amount of oligomer and/or *N,N,N*-tripropylborazane are present as a broad signal at –6.5 ppm (**Figure 46**).[27] Also present in the ^{11}B NMR are a doublet at 27.8 ppm corresponding to $HB(NH^nPr)_2$, [25] a broad singlet at 21.8 ppm corresponding to $B(OH)_3$ from the reaction with water (in the air) and an unknown signal at 1.8 ppm (**Figure 46**).[28, 29]

The solid obtained from this reaction mixture by precipitation with pentane was analysed by GPC and showed no evidence of polymer. A small amount of anion $[BH_4]^-$ is also observed in the ^{11}B NMR spectrum at <1 % of the total integral (– 37.7, pentet, J_{BH} = 82 Hz). The in-situ $^{31}P\{^1H\}$ NMR spectrum shows one organometallic species, a doublet (J_{PRh} = 110 Hz) at 79.3 ppm, the same species observed when the dehydropolymerisation of $H_3B{\cdot}NH_2{}^nPr$ was attempted under argon (**Figure 47**). A singlet at 57.1ppm is also seen by $^{31}P\{^1H\}$ NMR, lacking P-Rh coupling. This suggests that this corresponds to a non-coordinated phosphine, or more likely the corresponding phosphine oxide such as $(^iPr_2P(=O)CH_2CH_2)_2NH$. Free phosphine $(^iPr_2PCH_2CH_2)_2NH$ has a reported ^{31}P chemical shift of –1 ppm whereas $P(=O)Me_3$ has a more similar reported shift of 39.3 ppm. [30, 31] As this species is not present after dehydropolymerisations of $H_3B{\cdot}NH_2Me$ with precatalyst **1** that are performed with an initial reaction vessel atmosphere of air, it may correspond to a decomposition product of the newly formed organometallic species that is visible as a doublet at 79.3 ppm in the in-situ $^{31}P\{^1H\}$ NMR spectrum.

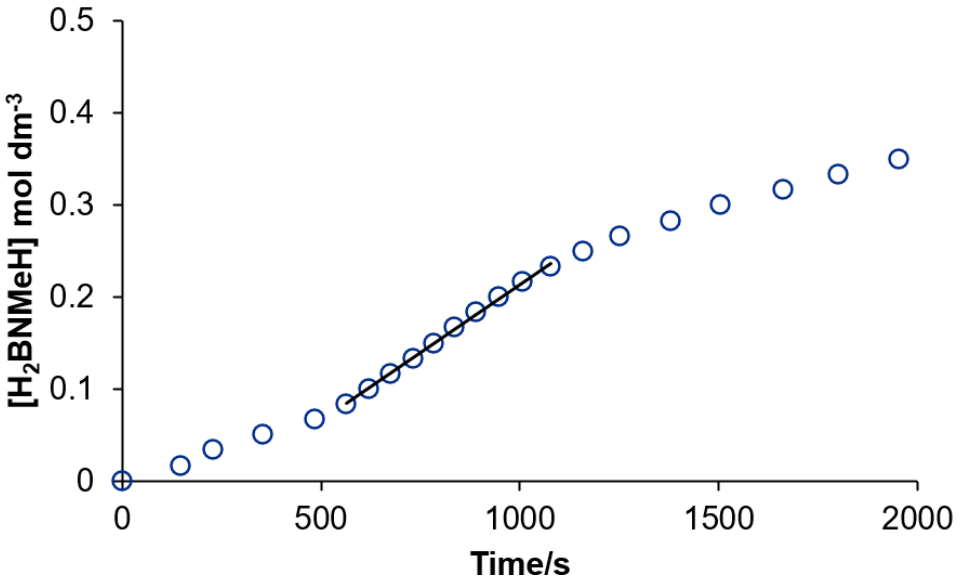

Figure 45. Effective $H_2B{=}NMeH$ concentration over time from eudiometric H_2 evolution measurement for the attempted dehydropolymerisation of $H_3B{\cdot}NH_2{}^nPr$ (0.182 g, 1 mol dm^{-3}) by precatalyst **1** (0.5 mol%) in THF with an initial atmosphere of air. An induction period is seen, followed by a short pseudo zeroth order catalysis period ($2.86x10^{-4}$ ± $3x10^{-6}$ mol dm^{-3} s^{-1}) and then a deceleration of rate.

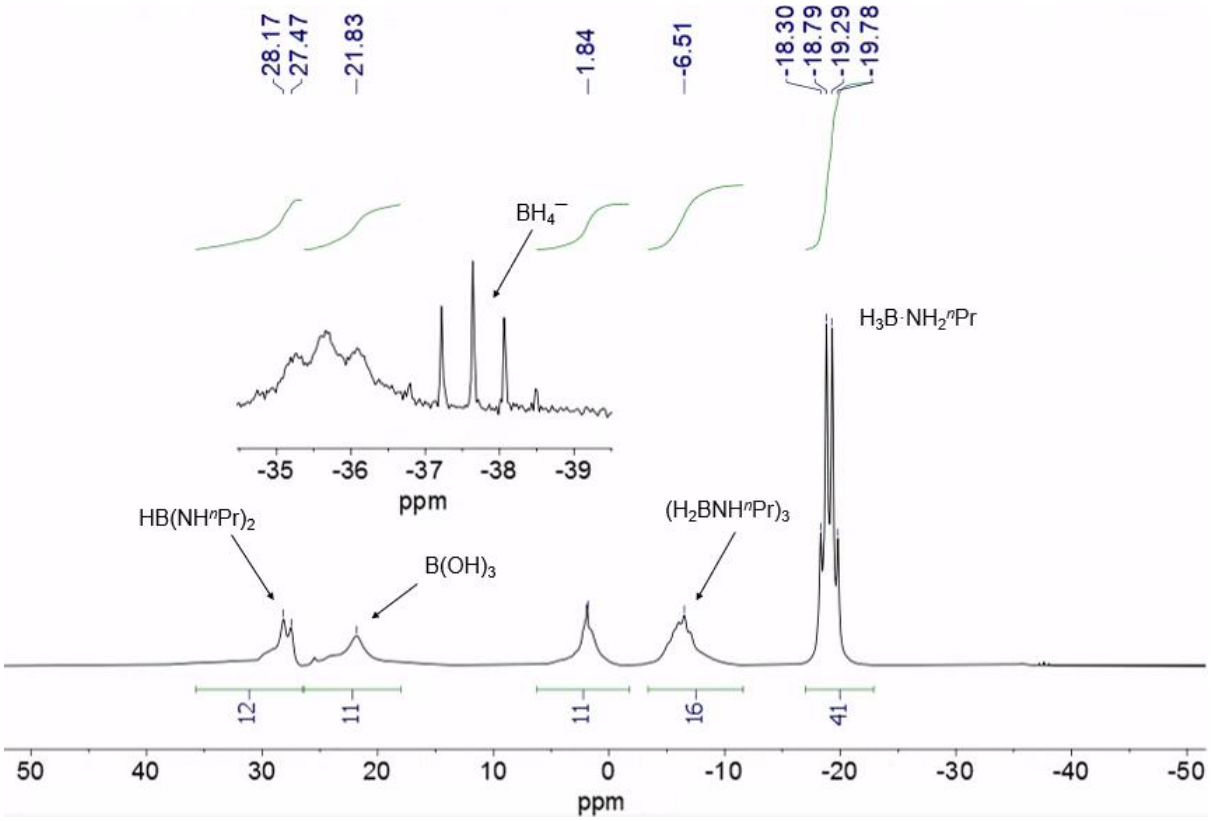

Figure 46. ^{11}B NMR spectrum recorded from an in-situ aliquot after one hour of the attempted dehydropolymerisation of $H_3B{\cdot}NH_2{}^nPr$ (0.182 g, 1 mol dm^{-3} in THF) by **1** (0.5 mol%) in THF. Primarily (41%) unreacted $H_3B{\cdot}NH_2{}^nPr$ is observed at –18.9 ppm. Small amounts of oligomer/*N,N,N*-tripropylborazane are present at – 6.5 ppm. [27] Inset shows trace amounts of BH_4^- as a pentet at – 37.7 ppm.

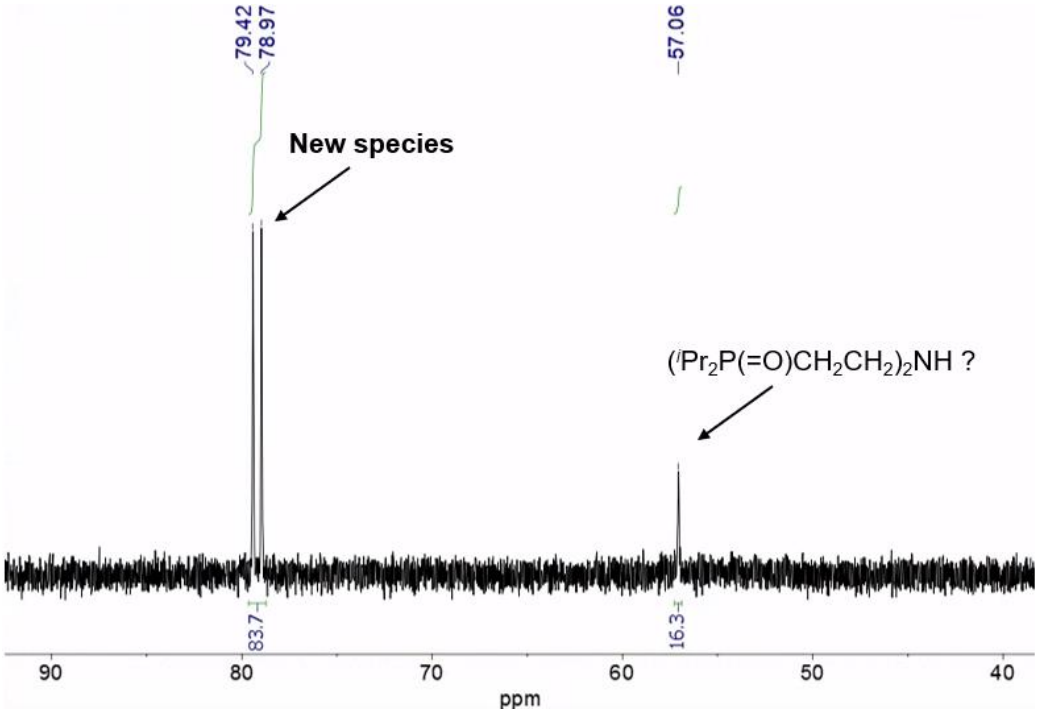

Figure 47. ^{31}P {^{1}H} NMR spectrum recorded from an in-situ aliquot after one hour of the attempted dehydropolymerisation of $H_3B{\cdot}NH_2{}^nPr$ (0.182 g, 1 mol dm^{-3}) by **1** (0.5 mol%) in THF, initially under air. Conversion of precatalyst **1** to a new species at 79.3 ppm is shown, alongside a singlet at 57.1 ppm, possibly indicative of free phosphine oxide after catalyst decomposition.

To summarize, the attempted dehydropolymerisation of $H_3B{\cdot}NH_2{}^nPr$ with precatalyst **1** using conditions that are efficacious with $H_3B{\cdot}NH_2Me$ are ineffective. Eudiometric measurements and ^{11}B NMR spectra show partial dehydrogenation with the absence of polymeric material and $^{31}P\{^{1}H\}$ NMR spectra show conversion of precatalyst **1** to a new rhodium species at – 79.3 ppm (J_{PRh} = 110 Hz) which appears to be catalytically inactive (**Figure 44**). The presence of air during catalysis appears to marginally improve the catalyst engagement with $H_3B{\cdot}NH_2{}^nPr$ as shown by ^{11}B NMR spectroscopy, however the products are unselective (**Figure 46**).

2.1.5 Identification of the catalyst speciation from the attempted dehydropolymerisation of $H_3B{\cdot}NH_2{}^nPr$ with precatalyst 1

During the attempted dehydropolymerisation of $H_3B{\cdot}NH_2{}^nPr$ (1 mol dm^{-3} in 2.5 cm^3 THF) with precatalyst **1** (0.5 mol%, 0.005 mol dm^{-3}) both in the presence of air and argon, conversion to a new rhodium-coupled species is observed in the $^{31}P\{^1H\}$ NMR spectrum at –79.3 ppm. Catalysis is impeded suggesting that this species is the result of catalyst decomposition. Small amounts (although likely significant relative to catalyst concentration) of BH_4^- (pentet, – 37.7 ppm) are observed in the in-situ ^{11}B NMR spectra after attempted dehydropolymerisation, and a broadened pentet is seen adjacent to this signal at –35.7 ppm with J_{BH} = 80 Hz, possibly corresponding to a coordinated borohydride (**Figure 46**).

The in-situ ^1H NMR spectrum recorded after attempted dehydropolymerisation of $H_3B{\cdot}NH_2{}^nPr$ with precatalyst **1** supports the formation of a borohydride complex, with a broad signal at – 2.37 ppm that is indicative of a coordinated borohydride (**Figure 49**), and almost identical to that seen by Schneider et al. for iron κ^1-borohydride complexes with the PN^HP MACHO ligand (–2.58, broad, **Figure 48**).[32] The in-situ ^1H NMR spectrum also shows two overlapping multiplets at –16.27 and –16.40 ppm that in total integrate to 2H relative to the 4H of the borohydride at –2.37 ppm (**Figure 49**). These signals correspond to rhodium hydrides that resemble those present in complex **2**. Together this NMR data suggests the formation of a rhodium κ^1-borohydride-dihydride complex.

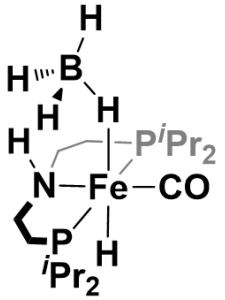

^1H NMR BH_4**:** – 2.58 ppm, broad

Schneider et al. 2013

Figure 48. The κ^1 borohydride complex $Fe(PN^HP^iPr)(CO)(BH_4)H$ reported by Schneider et al. [32]

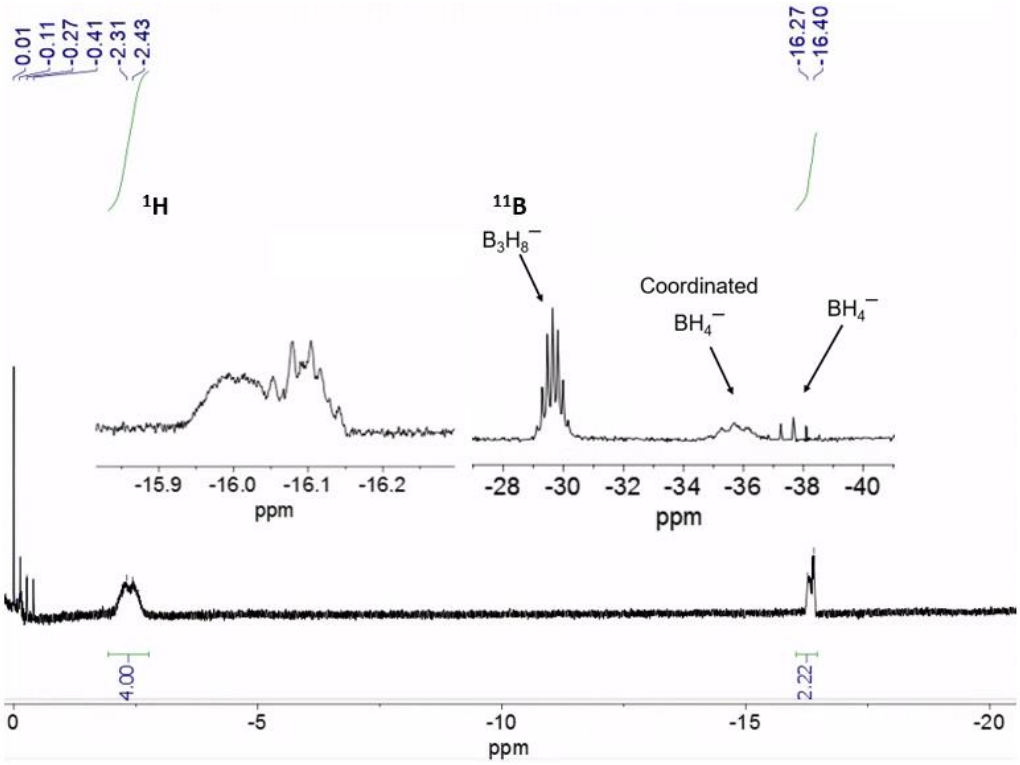

Figure 49. ^{1}H NMR spectrum recorded from an in-situ aliquot after one hour of the attempted dehydropolymerisation of $H_3B{\cdot}NH_2{}^{n}Pr$ (0.182 g, 1 mol dm^{-3} in THF) by **1** (0.5 mol%) in THF. 1:1:1:1 quartet at –0.16 ppm corresponds to free BH_4^-. The broad signal at –2.37 ppm corresponds to coordinated BH_4^- (4H) and the multiplets at –16.27 and –16.40 ppm correspond to rhodium hydrides (2H total). Left inset expands upon the overlapping hydride signals. Right inset shows the ^{11}B NMR signal

To confirm the tentative assignment of the rhodium κ^1-borohydride-dihydride complex, the species was synthesized independently. This was achieved via a modified procedure from Schneider et al. where **2** was reacted with a slight excess (1.2 eq.) of [^{n}Bu$_4$N][BH$_4$] in THF (**Figure 50**, see experimental for further details). [32] Complex **4** [Rh(PN^{H}P^{i}Pr)(κ^1-BH$_4$)H$_2$] was isolated as a crystalline solid in a 22% yield by evaporation of the reaction solvent THF, extraction of the solids with pentane and subsequent cooling to –20 °C overnight.

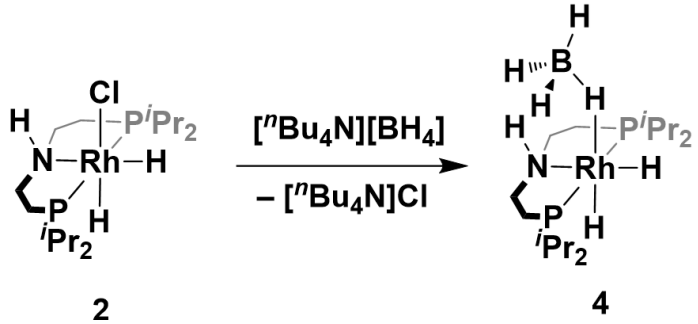

2 **4**

Figure 50. The synthesis of Rh(PN^{H}P^{i}Pr)(κ^1-BH$_4$)H$_2$ (**4**) from **2** and [^{n}Bu$_4$N][BH$_4$] in THF, adapted from literature procedure. [32]

The NMR spectra of the formed Rh(PN^{H}P^{i}Pr)(κ^{1}-BH_4)H_2 (**4**) match well with the species observed after attempted dehydropolymerisation of $H_3B{\cdot}NH_2{}^{n}Pr$ with precatalyst **1**. Both show a $^{31}P\{^{1}H\}$ NMR signal at ~79 ppm (d, J_{RhP} = 109 Hz), a ^{11}B NMR signal at – 35 ppm (br) and ^{1}H NMR hydride signals corresponding to a coordinated BH_4^- and two rhodium hydrides (**Figure 49**, **Figure 51**). The broad peak observed in the ^{1}H NMR spectrum of complex **4** (–2.37 ppm in THF, –1.36 ppm in benzene-d_6) corresponds to a collapsed 1:1:1:1 quartet of the coordinated BH_4 signals where the bridging and terminal hydrides are in fast exchange at 298 K (**Figure 51**).[33] This peak splits into bridging (–9.89 ppm, 1H) and terminal (–0.13 ppm, 3H) BH_4 hydrides upon cooling to 185 K (**Figure 52**).

Due to initial difficulties isolating complex **4** due to its high solubility in most solvents, variable temperature NMR studies were performed on an in-situ generated sample. Complex **4** was later isolated and room-temperature NMR spectra of the pure material were obtained. A single crystal x-ray diffraction structure was recorded of complex **4** confirming the presence of a κ^{1}-BH_4 and two hydrides, both cis and trans to the borohydride (**Figure 53**). The crystals were well-diffracting with an R_{int} of 0.031 for the space group P-1, and an R_1 of 0.079 that suggests good agreement between the model and observed diffraction data. The N–H and Rh–H hydrogen atoms were all located in the electron density map, allowed to ride on their parent atoms and freely refined. The B–H hydrogen atoms were also located in the electron density map and their bond distances were equally restrained to 1.1 Å.

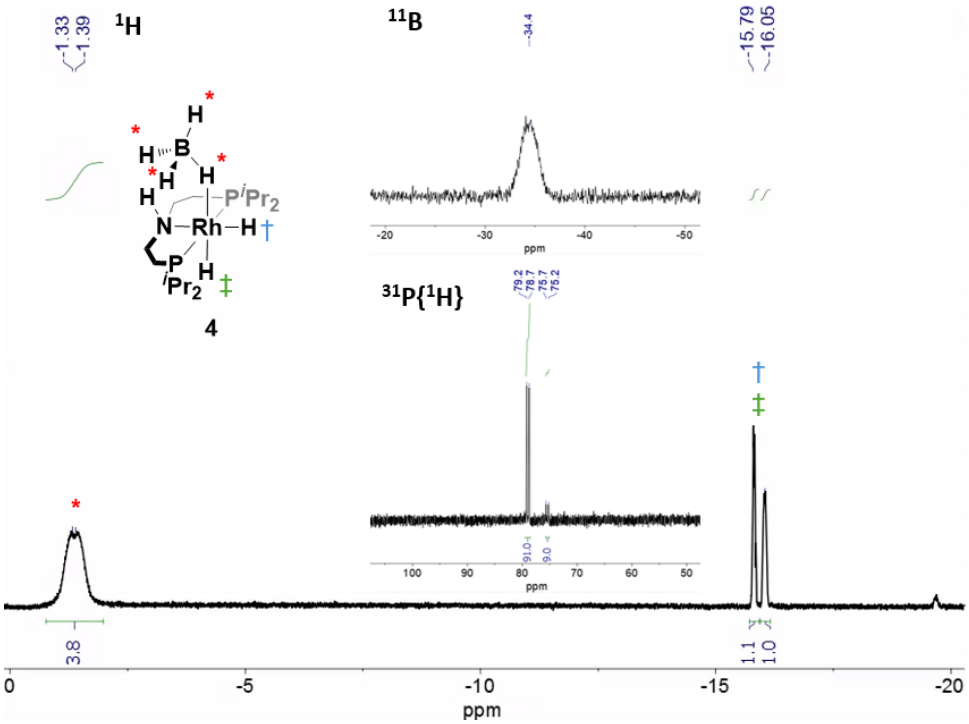

Figure 51. ^{1}H NMR spectrum of complex **4** showing the hydride region with peaks corresponding to BH_4 hydrides (*) and Rh-H hydrides († and ‡). Top inset: BH_4 signal at –34.4 ppm in the ^{11}B NMR spectrum. Bottom inset: ^{31}P{^{1}H} NMR spectrum showing a signal at 79.0 ppm for complex **4** alongside a trace of starting material complex **2** (75.5 ppm). All recorded in benzene-d_6, 298 K.

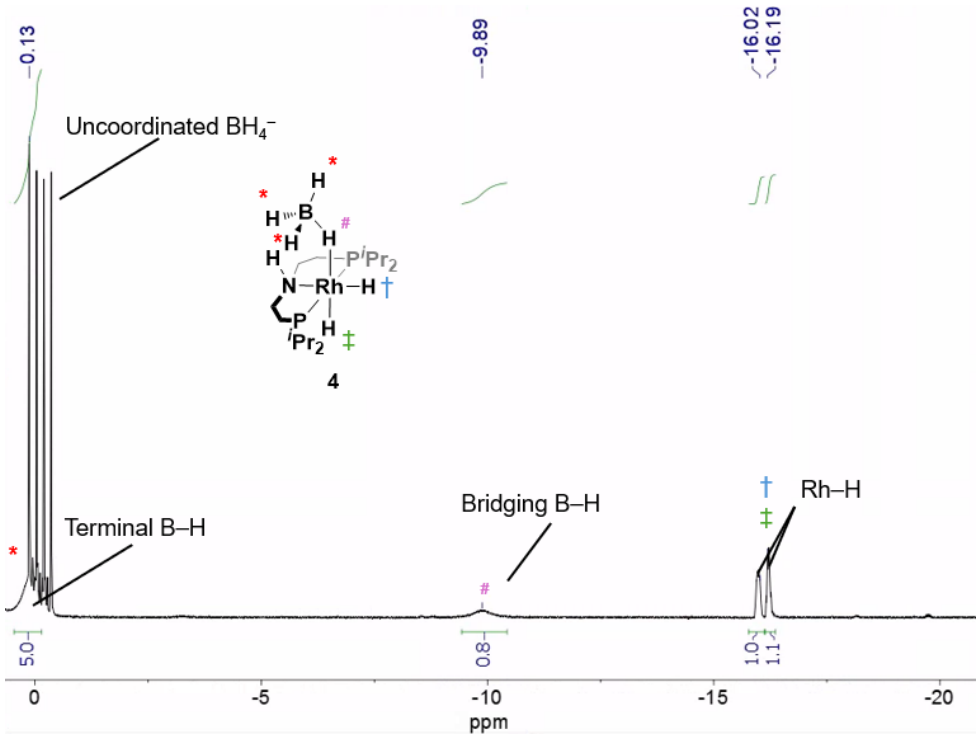

Figure 52. In-situ low-temperature in-situ ^{1}H NMR spectrum from the synthesis of complex **4** showing the hydride region with peaks corresponding to BH_4 hydrides and Rh-H hydrides († and ‡). Separation of the bridging (#, – 0.13 ppm) and terminal (*, – 9.89 ppm) BH_4 hydrides is observed. Recorded in THF, 185 K.

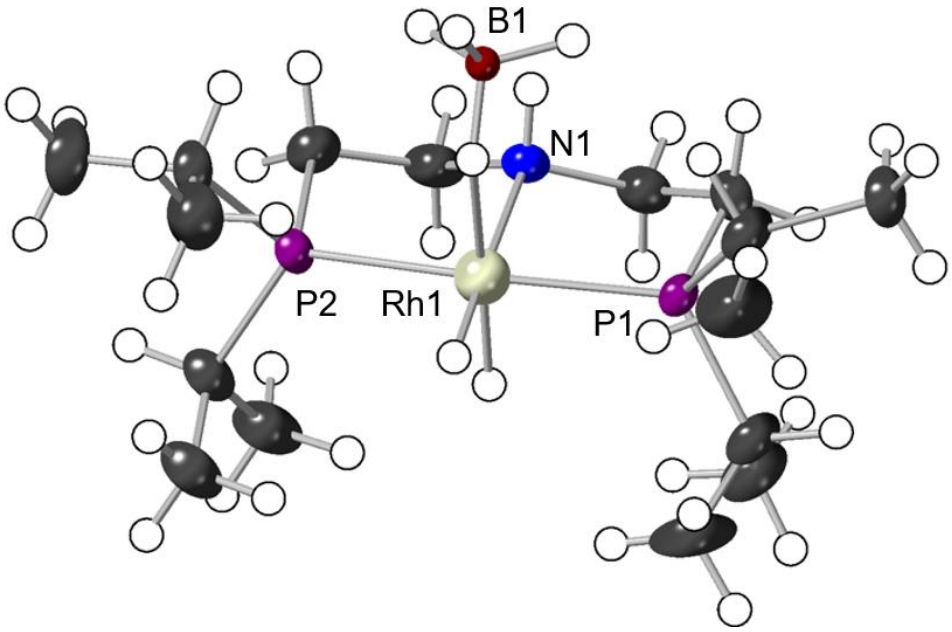

Figure 53. Molecular structure of Rh(PN^{H}P^{i}Pr)(κ^{1}-BH$_4$)H$_2$ (**4**) as determined by single crystal X-ray diffraction. Displacement ellipsoids are shown at the 50% probability level. Hydrogen atoms are placed in calculated positions. N–H, Rh–H and B–H were located in the Fourier difference map, allowed to ride the parent atoms and freely refined. Selected distances [Å], bond lengths [Å] and angles [°]: Rh(1)···B(1) 2.709(8), Rh(1) – N(1) 2.188(2), Rh(1) – P(1) 2.2677(7), Rh(1) – P(2) 2.2590(7), P(1) – Rh(1) – N(1) 84.32(7), P(1) – Rh(1) – P(2) 168.31(3), P(2) – Rh(1) – N(1) 85.25(7).

Metal borohydride complexes analogous to complex **4** have been previously reported as deactivated catalyst species observed during the dehydropolymerisation of H$_3$B·NH$_2$Me (**Figure 54**).[5, 12] Manners et al. report the rapid and complete poisoning of amine-borane dehydropolymerisation catalyst Ir(POCOP^{t}Bu)H$_2$ upon exposure to *N*-aryl amine-boranes such as H$_3$B·NPhH$_2$, forming BH$_3$-inactivated species Ir(POCOP^{t}Bu)(BH$_3$)H$_2$ (**Figure 54**).[34] No polyaminoboranes are formed and Ir(POCOP^{t}Bu)(BH$_3$)H$_2$ is reported to be a poor amine-borane dehydropolymerisation catalyst for amine-boranes, including H$_3$B·NH$_2$Me. [34, 35]

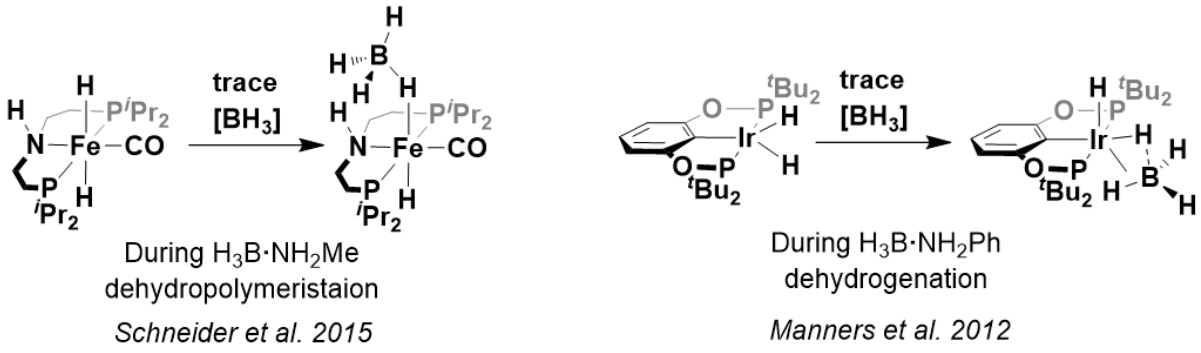

Figure 54. BH$_3$-deactivated catalyst species previously reported to form during amine-borane dehydeogenations. [5, 34]

When synthesised independently and added to methyl amine-borane, no catalytic activity is seen with complex **4**. This was evaluated by the addition of complex **4** (0.5 mol%) to $H_3B{\cdot}NH_2Me$ (1 mol dm^{-3} in THF) under argon, where after 3 hours no H_2 gas had been evolved and no conversion of the $H_3B{\cdot}NH_2Me$ was observed by ^{11}B NMR spectroscopy. The formation of complex **4** during attempted dehydropolymerisation of $H_3B{\cdot}NH_2{}^nPr$ is likely from BH_3 capping of the active species in catalysis, complex **3** ($Rh(^i Pr\text{-}PN^HP)H_3$), which fits well with the observation of catalysis starting but not reaching completion as evidenced by ^{11}B NMR and eudiometric measurements (**Figure 45**, **Figure 46**).

The importance of BH_3 capping to form complex **4**, apparently favouring the NH-adjacent rhodium hydride, is that the subsequent coordinated BH_4 may block the metal-ligand cooperative operation of the catalyst. The Rh–H and N–H templated approach of amine-borane substrates could then be hindered, thus preventing the dehydrogenation to form aminoboranes. The preference for the BH_4 formation adjacent to the ligand N–H is reported to be thermodynamically controlled in the related κ^1-BH_4 complex $Fe(^i Pr\text{-}PN^HP)(CO)(BH_4)H$, caused by dihydrogen-bonding between the adjacent B–H and N–H groups. [32] This is likely also the case in complex **4**.

2.1.6 The origin of BH_3 causing catalyst poisoning in amine-borane dehydropolymerisation.

The origin of the BH_3 that is observed to deactivate the active catalyst species **3** forming borohydride complex **4** during dehydropolymerisation is likely from B–N bond cleavage of the amine-borane substrate. The release of BH_3 in solution by amine-boranes has been investigated computationally and reported in the literature. The first proposed route is that of direct and reversible B–N bond cleavage of amine-boranes releasing an amine and solvation stabilised BH_3. [36] In this process amines are attacked by nucleophilic solvents such as THF via an S_N2 transition state, releasing $THF{\cdot}BH_3$ and an amine (**Figure. 55**). The stabilised Lewis adduct $THF{\cdot}BH_3$ allows the otherwise highly reactive BH_3 to persist in solution. The free energy barrier to this process is reported to be 27.5 kcal mol^{-1} with $H_3B{\cdot}NH_3$ in solution, and so dissociation is slow This reaction also has a positive $\Delta G°$, +14.6 kcal mol^{-1}, and so the equilibrium lies heavily against dissociation. [36] The subsequent BH_3 capping of complex **3** to form complex **4** is however likely to be irreversible and so drives further amine-borane dissociation.

As low catalyst loadings are used in dehydropolymerisation (typically <1 mol%), only a small amount of amine-borane dissociation is required to completely shut down catalytic activity. The apparent increased tendency for B–N bond cleavage and BH_3 release from $H_3B{\cdot}NH_2{}^n\text{Pr}$ relative to $H_3B{\cdot}NH_2\text{Me}$ is potentially due to the increased favourable solvation of the subsequently released amine $NH_2{}^n\text{Pr}$ compared to $NH_2\text{Me}$. This increased favourability for B–N bond cleavage in amine-boranes with larger *N*-alkyl substituents has been reported computationally. In gas-phase calculations *N*-alkyl amines such as $NH_2{}^n\text{Pr}$ bind more strongly to BH_3 than NH_3 (forming a stronger B–N bond), as expected with alkyl inductive effects promoting nitrogen lone-pair donation, however calculations modelling THF solvation reverse this trend. [36]

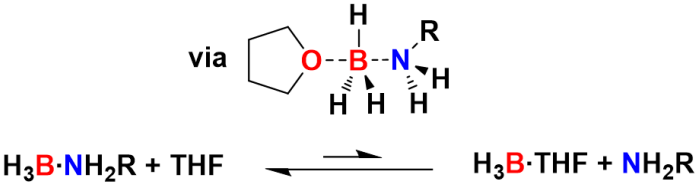

Figure. 55 The proposed reversible BH_3 transfer from an amine-borane to THF via an S_N2 type transition state. [36]

The second proposed route for spontaneous BH_3 formation is the oligomerisation and heterolysis of the aminoborane intermediate produced from amine-borane dehydrogenation. Aminoboranes are known to spontaneously oligomerise in solution forming products such as cyclotriborazane $(BH_2NH_2)_3$. [37] An intermediate in this process is the linear dimer $H_3B–NH_2–BH=NH_2$ which is reported to lose BH_3 to THF in solution via an S_N2 transition state in an overall exergonic process (ΔG^0 = – 3.5 kcal mol^{-1}). [38] This occurs in a process with a free energy barrier of 15.6 kcal mol^{-1}, releasing $THF·BH_3$ and $HB(NH_2)_2$ (**Figure 56**).[38] Tentative evidence for the occurrence of this process during the attempted dehydropolymerisation of $H_3B·NH_2{}^n$Pr with **1** is the presence of $HB(NH{}^n\text{Pr})_2$ in the in-situ ^{11}B NMR spectrum (27.8 ppm, d, J_{BH} = 125 Hz) (**Figure 46**).[25] The free energy barrier to this process with $H_3B·NH_3$ is reported to be significantly higher in non-coordinating solvents such as toluene (19.9 kcal mol^{-1}) due to the lack of a solvent-assisted pathway, however still accessible at ambient temperatures. [38]

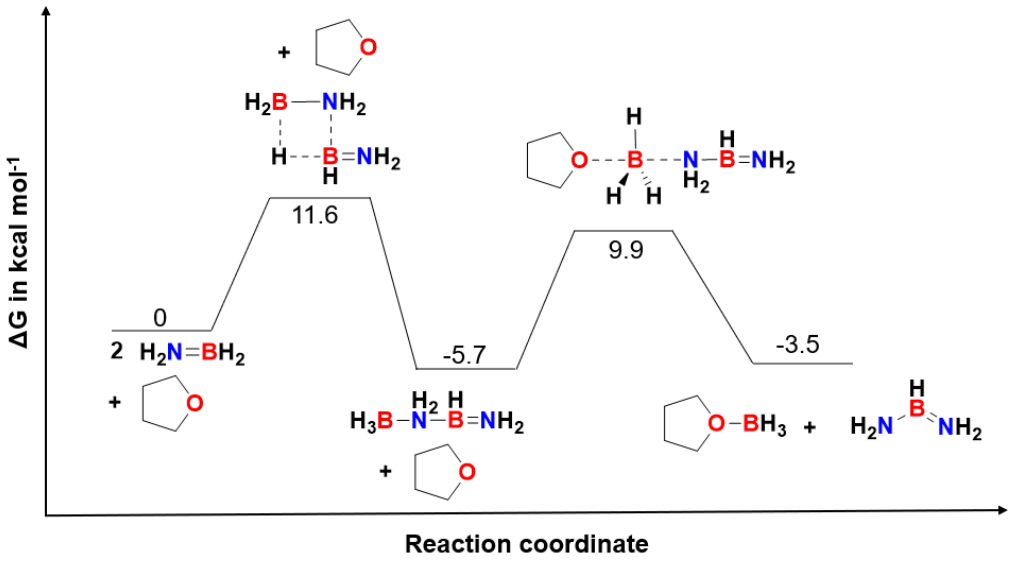

Figure 56. A free energy profile of the proposed oligomerisation and BH_3 transfer to THF of aminoborane $H_2B=NH_2$ in solution. [38]

The aminoborane dimerization to release BH_3 has a significantly lower free energy barrier than direct amine-borane B–N bond cleavage (15.6 vs 27.5 kcal mol^{-1}) however free aminoboranes only exist at low concentrations during dehydropolymerisation as a transient intermediate. [37, 38] It is possible that both of these processes contribute to the presence of BH_3 in solution and therefore the observed catalyst poisoning during dehydropolymerisation. As both processes are slow spontaneous dissociations, a

precatalyst such as **1** with a long induction period and low rate of amine-borane dehydrogenation (TOF ~ 0.01 s^{-1}) is understandably susceptible to significant catalyst poisoning over the course of dehydropolymerisation. It is apparent from the results presented in the first part of this chapter (and by Weller et al. in 2021) [11] that the induction period observed for dehydropolymerisation of amine-boranes with precatalyst **1** is likely due to the relatively slow loss of NBD from the complex. This induction period has been shown to shorten when catalysis is performed with exposure to air. A precatalyst without such a lengthy induction period may avoid some of this catalyst deactivation by limiting the time in the presence of the amine-borane, rapidly converting it to polymer.

The presence of BH_3 in the catalysis mixture may also affect the subsequent polyaminoborane molecular weight produced from amine-borane dehydropolymerisation. As BH_3 is Lewis acid, it may be capable of capping the nucleophilic nitrogen proposed to occur at the end of the growing polyaminoborane chain during head-to-tail aminoborane polymerisation. [39] This could explain the increasing polyaminoborane molecular weight observed after the dehydropolymerisation of methyl amine-borane with precatalyst **1** [Rh(*i*Pr-PN^HP)(NBD)][Cl] when increasing amounts of air or water were introduced (see **2.1.1** and **2.1.2**). This could be due to water and oxygen in air reacting with any BH_3 present and therefore removing this potential chain-terminating agent.

2.1.7 The attempted dehydropolymerisation of *N*-alkyl amine-boranes with precatalyst Rh(^{i}Pr-PN^{H}P)H$_2$Cl (2)

Precatalyst **2** is reported to catalyze the dehydropolymerisation of methyl amine-borane with no induction period and at slightly faster rates than precatalyst **1** during the active phase of catalysis: 2.7x10^{-3} mol dm^{-3} s^{-1} with precatalyst **2** and 1.9x10^{-3} mol dm^{-3} s^{-1} with precatalyst **1** (both at 0.5 mol%, 1 mol dm^{-3} of H$_3$B·NH$_2$Me in 2.5 cm^3 of THF, 293 K). [11] As discussed in section **2.1.6** the formation of the proposed catalyst poison BH$_3$ is a slow process, and so the use of a catalyst that is rapid and free of induction period may to some extent outpace catalyst deactivation to complex **4**. To evaluate this, dehydropolymerisations were attempted of *N*-methyl (control, previously reported) [11], *N*-ethyl and *N*-propyl amine-borane with precatalyst **2** (**Figure 57**).[11] In order to further increase the rate of dehydropolymerisation the catalyst loading was increased to 1 mol% and the amount of solvent used reduced from 2.5 cm^3 to 0.5 cm^3 of THF, increasing the absolute catalyst concentration (relative to attempted catalysis with precatalyst **1,** from 0.005 to 0.05 mol dm^{-3}). This also increases the amine-borane concentration during catalysis to 5 mol dm^{-3}, however this catalyst system shows a pseudo zeroth-order relationship to amine-borane concentration and so this alone should not affect the rate of catalysis. As catalysis in the presence of air improved engagement of precatalyst **1** with *N*-propyl amine-borane relative to under argon, the reactions with precatalyst **2** were also performed with an initial reaction vessel atmosphere of air.

Under these conditions with precatalyst **2** the dehydropolymerisation of all three amine-borane substrates show rapid gas evolution by eudiometric measurement, releasing ~1 equivalent of H$_2$ per amine-borane (**Figure 58**). Notably, the dehydropolymerisation of H$_3$B·NH$_2$^{n}Pr slows significantly toward the end of the reaction and fails to reach 1 equivalent of H$_2$ released per amine-borane (**Figure 58**, 0.95 eq.). The rates of dehydrogenation measured over the pseudo zeroth order regions decrease with increased amine-borane *N*-alkyl substituent size: (3.60±0.02)x10^{-2} mol dm^{-3} s^{-1} for methyl, (1.54±0.01)x10^{-2} mol dm^{-3} s^{-1} for ethyl and (3.55±0.04)x10^{-3} mol dm^{-3} s^{-1} for n-propyl (**Table 3**). This could be explained by increased formation of catalytically inactive complex **4** with increased amine-borane *N*-alkyl substituent size, as seen in the post-catalysis in-situ ^{31}P{^{1}H} NMR spectra (2.1% **4** for Me, 15.9% **4** for Et and

66.2% **4** for ^{n}Pr **Figure 59**). This suggests significantly increased propensity to release BH_3 for amine-boranes with larger *N*-alkyl substituents.

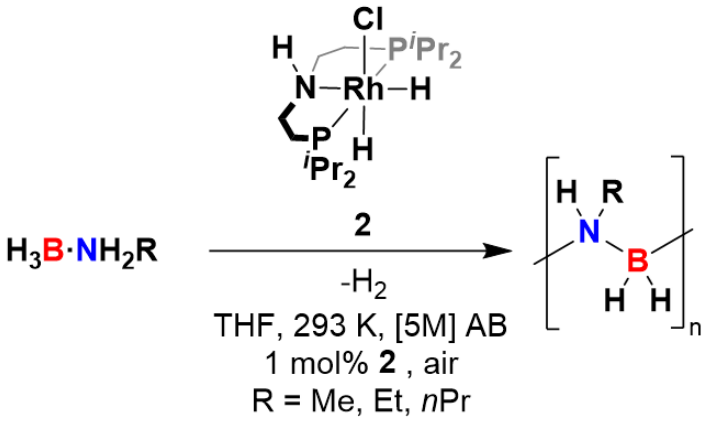

Figure 57. The attempted dehydropolymerisations of *N*-propylamine, *N*-ethyl and *N*-methyl amine-borane (0.182, 0.147 and 0.112 g respectively, 5 mol dm^{-3} in 0.5 cm^3 of THF) with precatalyst **2** (1 mol%, 0.05 mol dm^{-3}), with an initial reaction vessel atmosphere of air.

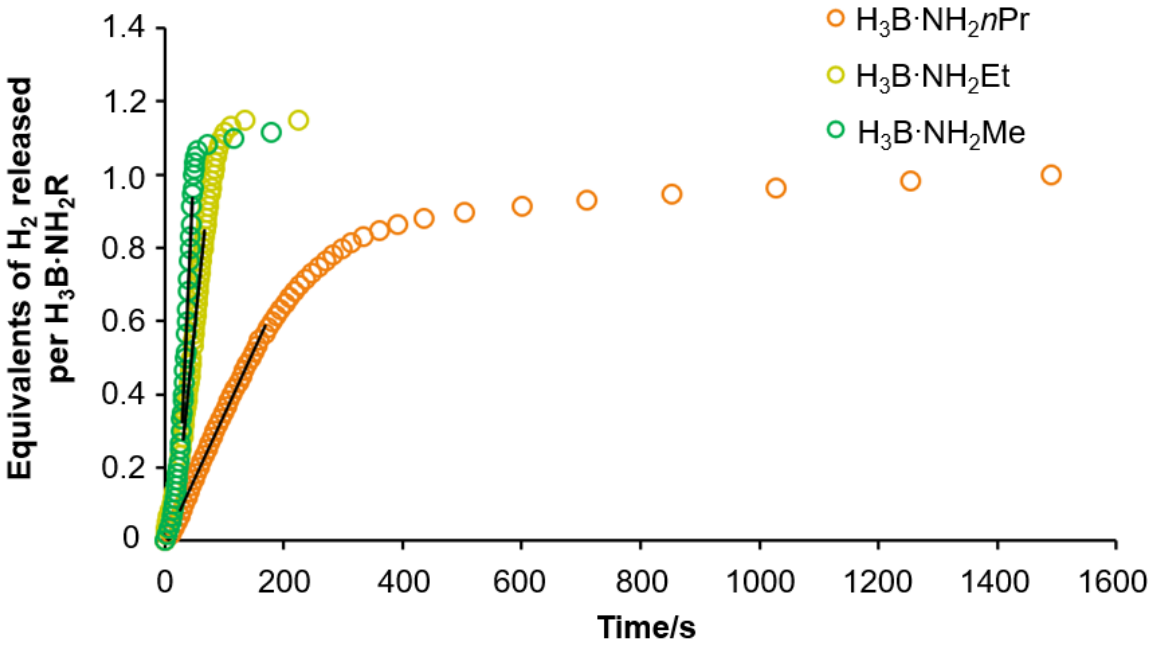

Figure 58. Effective $H_2B{=}NRH$ concentration over time from eudiometric H_2 evolution measurement for the dehydropolymerisations of *N*-propyl, *N*-ethyl and *N*-methyl amine-borane (0.182, 0.147 and 0.112 g respectively, 5 mol dm^{-3} in 0.5 cm^3 of THF) with precatalyst **2** (1 mol%, 0.05 mol dm^{-3}), with an initial reaction vessel atmosphere of air. Rates of reaction with each substrate follow the trend $H_3B{\cdot}NH_2Me$ > $H_3B{\cdot}NH_2Et$ > $H_3B{\cdot}NH_2{}^{n}Pr$.

Amine-borane	k_{obs} [a] (mol dm^{-3} s^{-1})	Amine-borane conversion [b] (%)	Polymer selectivity [c] (%)	**2** conversion to **4** [d] (%)	Polymer M_n [e] (g mol^{-1})	Dispersity
$H_3B{\cdot}NH_2Me$	3.60E–02 (± 2E–04)	95.1	97.7	2.1	33,500	1.7
$H_3B{\cdot}NH_2Et$	1.54E–02 (± 1E–04)	95.0	88.9	15.9	62,400	1.5
$H_3B{\cdot}NH_2{}^nPr$	3.55E–03 (± 4E–05)	92.4	78.3	66.2	51,200	1.5

Table 3. Data recorded from the dehydropolymerisations of $H_3B{\cdot}NRH_2$ (R = Me, Et, ^{n}Pr, 5 mol dm^{-3} in 0.5 cm^3 of THF) using **2** (1 mol%) initially under air. Rates [a] determined by eudiometric measurement; amine-borane conversion [b] and polymer selectivity [c] determined by in-situ ^{11}B NMR spectroscopy; precatalyst **2** conversions to complex **4** [d] determined by in-situ ^{31}P{^{1}H} NMR spectroscopy. Polymer M_n [e] and dispersity [f] determined by GPC.

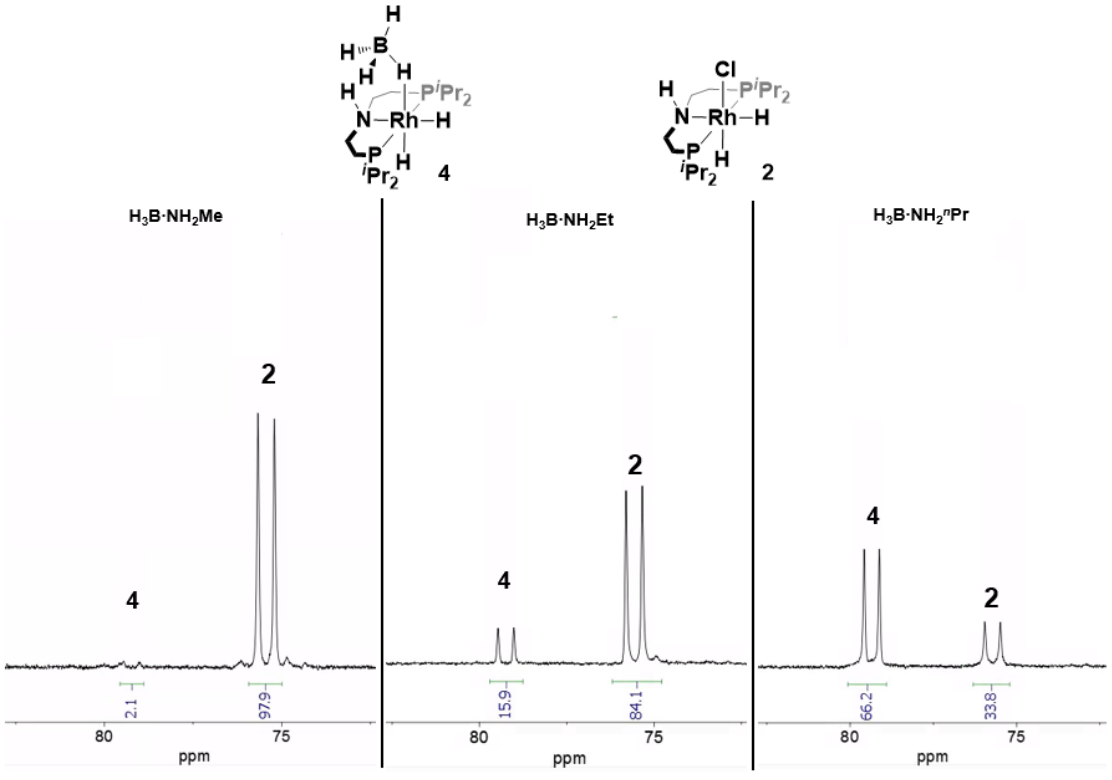

Figure 59. ^{31}P {^{1}H} NMR spectra recorded from in-situ aliquots at the end of the dehydropolymerisations of *N*-propylamine, *N*-ethyl and *N*-methyl amine-borane (0.182, 0.147 and 0.112 g respectively, 5 mol dm^{-3} in 0.5 cm^3 of THF) with precatalyst **2** (1 mol%), with an initial reaction vessel atmosphere of air. Increasing conversion of precatalyst **2** to complex **4** is observed with increased amine-borane *N*-alkyl substituent size.

Assuming that conversion of the active catalyst species **3** ($Rh(PN^{H}P)H_3$) to inactivated species **4** ($Rh(PN^{H}P)(BH_4)H_2$) is rapid at the onset of catalysis under these conditions, the amount of complex **2** ($Rh(PN^{H}P)H_2Cl$) detected by $^{31}P\{^{1}H\}$ NMR spectroscopy at the end of catalysis can be used to infer the amount of catalyst **3** that was present (not poisoned) during the active catalysis phase. Plotting this effective amount of catalyst **3** as a concentration against the measured rate of catalysis during the pseudo zero-order region shows a non-linear relationship (**Figure 60**). This suggests that the decrease in rate observed with increasing substrate *N*-alkyl substituent is not only due to catalyst poisoning, but also the dehydrogenation of the amine-boranes with larger pendant groups is intrinsically slower. If each amine-borane was dehydrogenated at the same rate, a linear correlation of rate and effective catalyst concentration that passed through (0,0) would be expected.

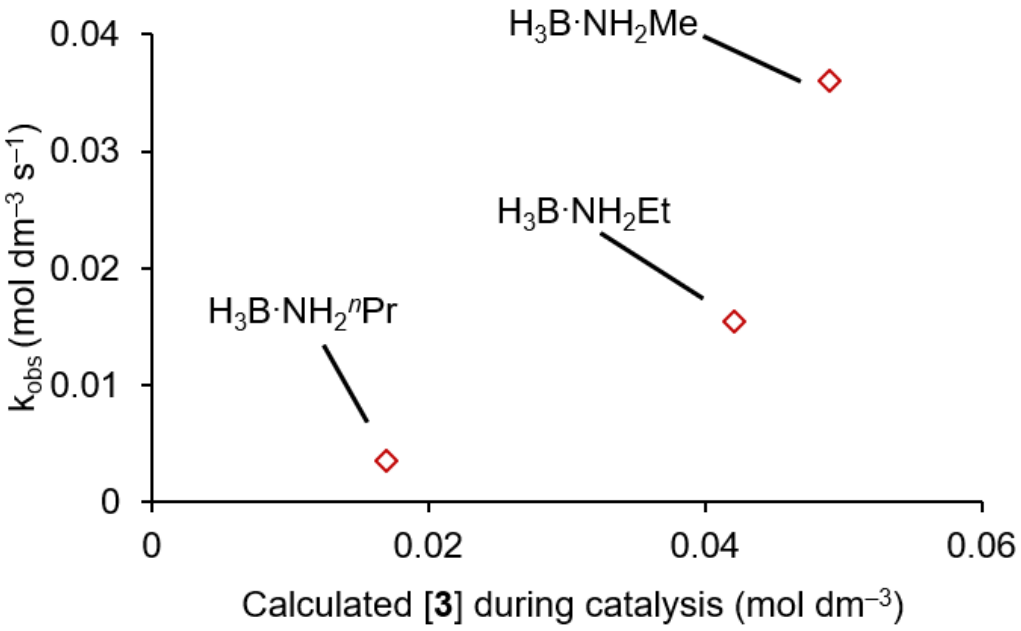

Figure 60. A plot of k_{obs} (mol dm^{-3} s^{-1}) as measured from H_2 evolution during the pseudo zeroth-order region of catalysis against the inferred concentration of active species **3** during catalysis (calculated from the fraction of poisoned species complex **4** visible by $^{31}P\{^{1}H\}$ NMR spectroscopy at the end of catalysis). Data points from the dehydropolymerisations of $H_3B{\cdot}NRH_2$ (R = Me, Et, ^{n}Pr, 5 mol dm^{-3} in 0.5 cm^3 of THF) using **2** (1 mol%, 0.05 mol dm^{-3}) initially under air.

In-situ ^{11}B NMR spectra of the reaction mixtures show broad peaks for all three dehydropoymerisations, at – 5.4, – 7.1 and – 6.7 ppm corresponding to $(H_2BNHMe)_n$, $(H_2BNHEt)_n$ and $(H_2BNH{}^{n}Pr)_n$ respectively. All three dehydropolymerisations show

>90% conversion of the amine-borane substrate by ^{11}B NMR integrals (**Table 3**). The selectivity for the respective polyaminoboranes decreases with increasing *N*-alkyl substituent size from 97.7% with Me to 78.3% with ^{n}Pr, corresponding to an increase in $B(OH)_3$, $HB(NH^{n}Pr)_2$ and other unidentified B-containing side products, as observed by ^{11}B NMR (**Table 3**). The observation of Me, Et and ^{n}Pr polyaminoboranes is supported by GPC measurement that show strong polymer peaks for the solid material precipitated with pentane from all three dehydropolymerisations (**Figure 61**).

This represents the first reported catalytic dehydropolymerisations of $H_3B{\cdot}NH_2Et$ and $H_3B{\cdot}NH_2{}^{n}Pr$ to form polyaminoboranes $(H_2BNH^{n}Pr)_n$ and $(H_2BNHEt)_n$. The successful catalytic synthesis of this polymer with precatalyst **2** and evidence for the formation of BH_3 poisoned catalyst species **4** suggests that the limitation to synthesizing a wider range of *N*-substituted polyaminoboranes is related to BH_3 release, rather than that repulsive steric interactions between bulkier amine-boranes and catalysts inhibit dehydrogenation as previously suggested in the literature. [12, 13] Also notable is that the $(H_2BNH^{n}Pr)_n$ GPC polymer peak exhibits a bimodal distribution (**Figure 61**). A possible explanation for this is that although complex **4** appears to be incapable of dehydrogenating amine-boranes, the hydrides present of the species may be capable of initiating head-to-tail polymerisation of aminoboranes. This would explain why a bimodal distribution is not seen from the dehydroplymerisation of $H_3B{\cdot}NH_2Et$ with precatalyst **2**, where significantly less complex **4** is formed (**Table 3**, **Figure 61**). A method of testing this hypothesis would be to add complex **4** to the dehydropolymerisation of $H_3B{\cdot}NH_2Me$ with precatalyst **2** and analyze the produced $(H_2BNHMe)_n$ by GPC to see if the expected bimodal distribution is produced.

The dispersity values of the $(H_2BNHEt)_n$ and $(H_2BNH^{n}Pr)_n$ formed with catalyst **2** (both 1.5) are significantly narrower than those synthesised by stoichiometric BH_2 transfer methods reported in the literature (2.6 and 2.1 respectively) representing a more controlled polymerisation. [25] The M_n of the polymer obtained varies from 33,500 g mol^{-1} for $(H_2BNHMe)_n$, 62,400 g mol^{-1} for $(H_2BNHEt)_n$ and 51,200 g mol^{-1} for $(H_2BNH^{n}Pr)_n$ (**Table 3**). Dividing these values by the respective repeat unit molecular weights for these polymers gives comparable degrees of polymerisation: 781, 1096 and 722 repeat units for $(H_2BNHMe)_n$, $(H_2BNHEt)_n$ and $(H_2BNH^{n}Pr)_n$ respectively.

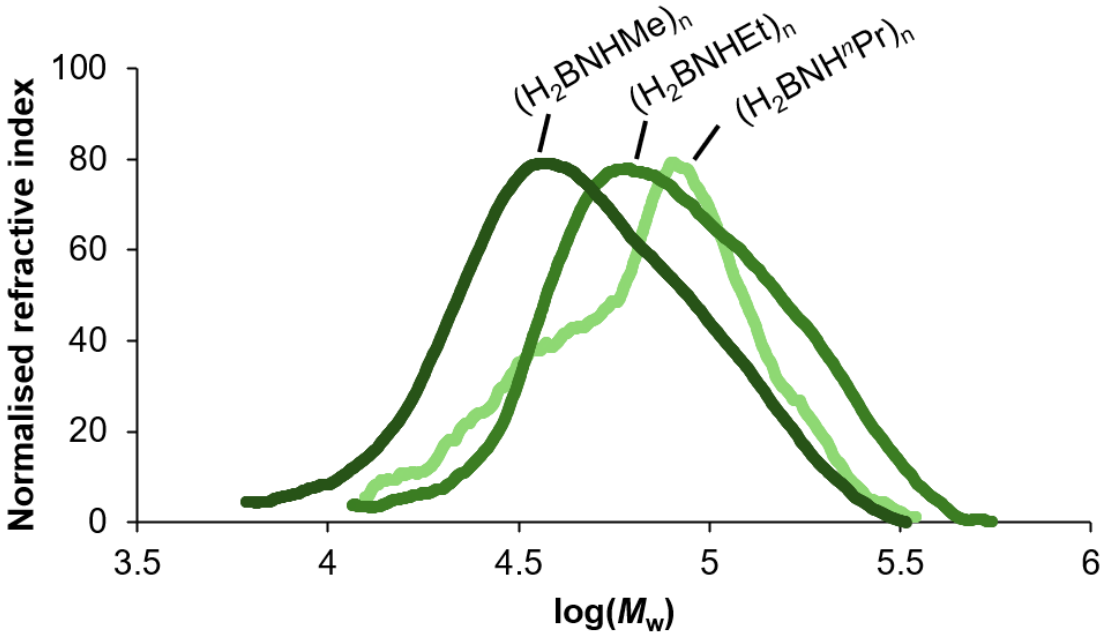

Figure 61. Overlaid normalised GPC traces of the polymers: poly(*N*-methylaminoborane), poly(*N*-ethylaminoborane) and poly(*N*-propylaminoborane) from the dehydropolymerisation of $H_3B{\cdot}NH_2Me$, $H_3B{\cdot}NH_2Et$ and $H_3B{\cdot}NH_2{}^nPr$, (5 mol dm^{-3} in 0.5 cm^3 of THF) by precatalyst **2** (1 mol%, 0.05 mol dm^{-3}) initially under air.

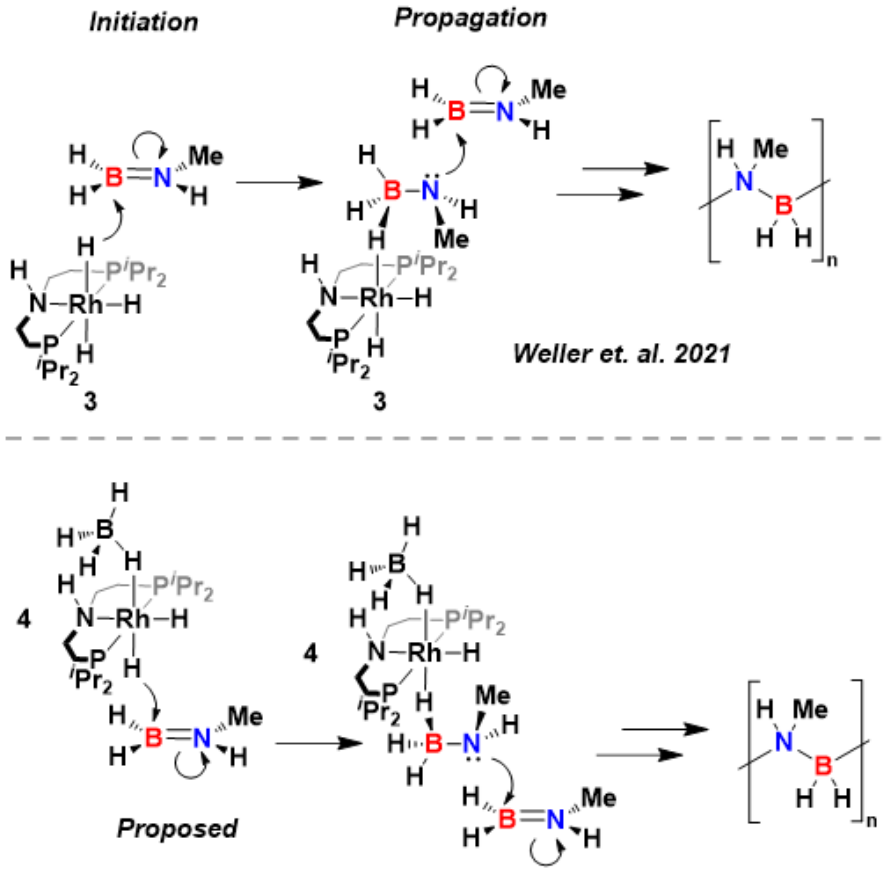

Figure 62. Top: The head-to-tail chain propagation aminoborane mechanism with complex **3** as an initiator proposed by Weller *et. al.* [11] **Bottom**: The proposed head-to-tail polymerisation of aminoboranes initiated by complex **4**.

2.1.8 The variation of reaction conditions to reduce catalyst poisoning in dehydropolymerisations with 2

To further improve dehydropolymerisations of *N*-ethyl and *N*-propyl amine-boranes the effect of various rection conditions on the relative conversion of precatalyst **2** to poisoned catalyst species **4** was investigated. The aim is to reduce the BH_3 poisoning of the active catalyst species **3** so that lower catalyst loadings than 1 mol% can be used to depolymerise these amine-boranes ($H_3B{\cdot}NH_2Me$ can be dehydropolymerised at 0.01 mol% of precatalyst **2**). [11] These trial dehydropolymerisations were performed on $H_3B{\cdot}NH_2Me$ or $H_3B{\cdot}NH_2Et$ at 1 mol dm^{-3} concentration with 0.5 mol% catalyst loading of precatalyst **2**. These conditions were chosen so that the conversion of the catalyst to poisoned species **4** was significant enough to be measured by $^{31}P\{^1H\}$ NMR integrals, but incomplete so that relative conversions can be compared (less than 100% complex **4** at the end of catalysis).

2.1.8.1 The effect of solvent choice on the substrate conversion and catalyst poisoning for dehydropolymerisations of *N*-methyl and *N*-ethyl amine-boranes with precatalyst 2

The dehydropolymerisation of $H_3B{\cdot}NH_2Me$ (1 mol dm^{-3}) with precatalyst **2** (0.5 mol%, 0.005 mol dm^{-3}) was performed in the following solvents: THF, 1,2-difluorobenzene and toluene. This was done to determine whether there was an effect on conversion to the deactivated species **4** (**Figure 63**). Toluene and 1,2-difluorobenzene (1,2-DFB) were chosen for this comparison as they are non-coordinating and have been used as amine-borane catalytic dehydropolymerisation solvents in the literature. [12, 40] The maximum solubility of $H_3B{\cdot}NH_2Me$ in 1,2-DFB and toluene is low, ~ 0.2 mol dm^{-3}, and so catalysis was performed as a slurry with an effective concentration of 0.2 mol dm^{-3}. For this reason, rates of catalysis from eudiometric measurements are not compared. Catalysis was complete in all 3 solvents in under 1000 s as observed by ^{11}B NMR spectroscopy and eudiometric measurements. In-situ $^{31}P\{^1H\}$ NMR spectra recorded at the end of catalysis show varying degrees of catalyst poisoning to species **4**, 47% with 1,2-DFB, 12% in THF and <5% in toluene (**Figure 64**).

The decrease in formation of complex **4** in toluene when compared to THF can be explained by the disfavouring of amine-borane B–N bond cleavage due to the lack of a coordinating-solvent mediated mechanism that lowers the energy barrier (see **Figure**

56). This is consistent for both of the proposed amine-borane BH_3 release mechanisms discussed in **2.1.6**, which operate via the formation of a solvent-BH_3 adduct (e.g. $THF{\cdot}BH_3$). [36, 38] The increase in conversion to complex **4** in 1,2-DFB when compared to THF is more difficult to explain, one possibility is that the $MeNH_2$ or $HB(NMeH)_2$ formed from methyl amine-borane BH_3 loss is most favourable solvated in 1,2-DFB. Irrespective of mechanism, 1,2-DFB appears to be a poor choice of solvent for amine-borane catalytic dehydropolymerisations due to the high proportion of catalyst which becomes poisoned by BH_3 capping.

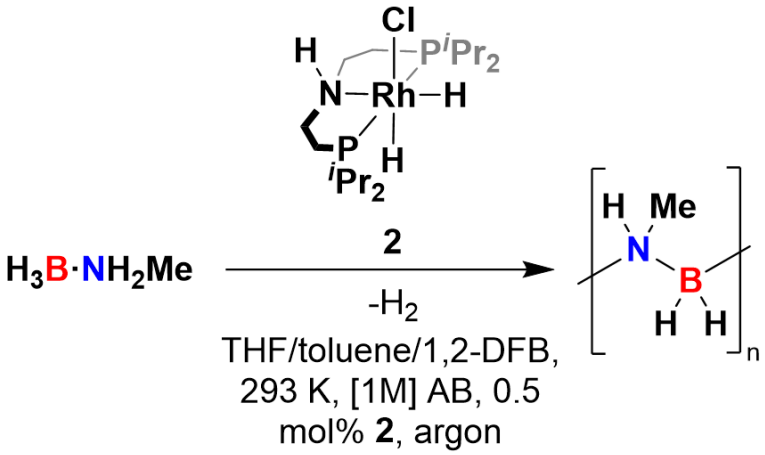

Figure 63. The dehydropolymerisations of *N*-methylamine borane (0.112 g, 1 mol dm^{-3}) with precatalyst **2** (0.5 mol%), varying the reaction solvent, using THF, toluene or 1,2-DFB.

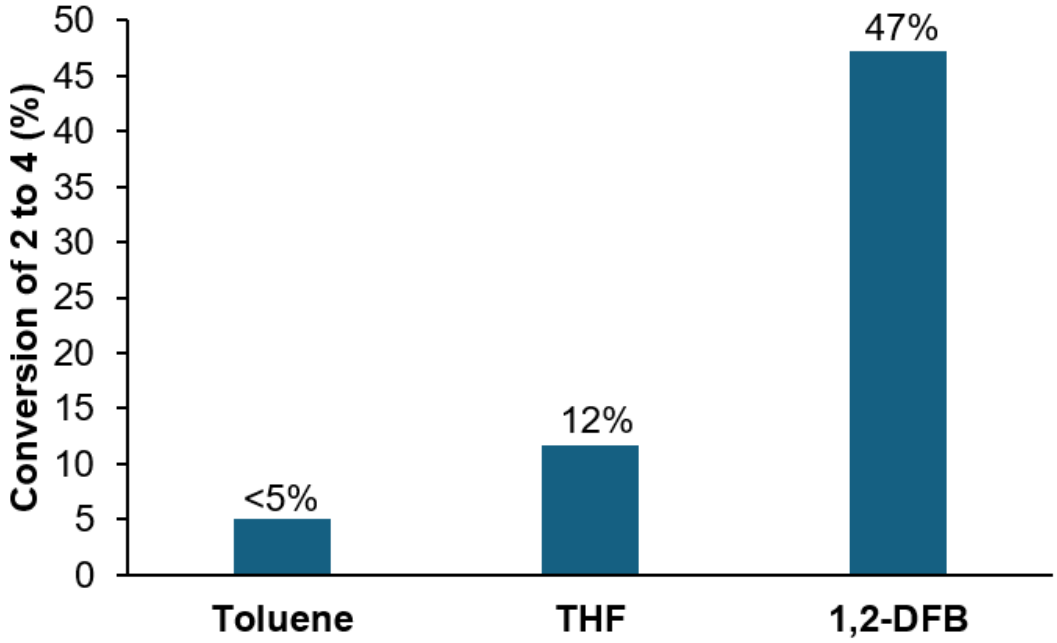

Figure 64. The percentage conversion of precatalyst **2** to poisoned species **4** during the dehydropolymerisation of $H_3B{\cdot}NH_2Me$ in solvents THF, toluene and 1,2-DFB. Values obtained from in-situ $^{31}P\{^1H\}$ NMR spectra integrals.

As toluene showed promise for reducing catalyst poisoning of precatalyst **2** to complex **4** (likely via active species **3**), dehydropolymerisations of $H_3B{\cdot}NH_2Et$, which appears to be more prone to BH_3 loss than $H_3B{\cdot}NH_2Me$, were attempted with precatalyst **2** at 0.5 mol% in toluene and THF (**Figure 65**). In THF the in-situ ^{11}B NMR spectrum recorded after 1 hour shows very little conversion of the $H_3B{\cdot}NH_2Et$, with integrals showing ~ 5% conversion to cyclic trimer $(H_2BNEtH)_3$ (**Figure 66**). Coordinated (in complex **4**) and uncoordinated borohydride alongside $B_3H_8^-$ can also be seen suggesting significant BH_3 production. Interestingly, the total integral for these BH_3-related species is very close to that of the $HB(NHEt)_2$ also present (0.35% and 0.37% of the total respectively (**Figure 66**). This is evidence for the release of BH_3 primarily from the rearrangement of aminoboranes, in this case two equivalents of $H_2B{=}NEtH$ forming one equivalent of BH_3 and one equivalent of $HB(NHEt)_2$ (see **2.1.6**). The presence of $B_3H_8^-$ which forms from BH_3 aggregation and the poor conversion of $H_3B{\cdot}NH_2Et$ indicate complete catalyst poisoning. [41] This is observed by an in-situ $^{31}P\{^1H\}$ NMR spectrum recorded after 1 hour that shows complex **4** as the only species present.

In toluene complete conversion of precatalyst **2** to poisoned species **4** was also observed by in-situ $^{31}P\{^1H\}$ NMR spectroscopy. The in-situ ^{11}B NMR spectrum however showed significantly higher conversion of the $H_3B{\cdot}NH_2Et$ substrate (66%), forming a mixture of $(H_2BNHEt)_n$ (– 6.8 ppm, br) and $H_3B{-}NHEt\text{-}BH_2{-}NH_2Et$ (BH_3, – 18.4 ppm, q; BH_2, – 6.8 ppm, t, **Figure 67**). The formation of $(H_2BNHEt)_n$ suggests that the catalyst persisted in solution longer in toluene than in THF, before ultimately forming **4**. The improved conversion of $H_3B{\cdot}NH_2Et$ by precatalyst **2** in toluene when compared to THF is similar to the reported improvement of $(H_3B{\cdot}NH_2CH_2SiMe_3)$ by $Fe(PN^HP\,^iPr)(CO)H_2$ in toluene vs THF. [12] It is likely that this iron catalyst is also forming a BH_3 capped complex, which is a known species, and this poisoning is limited in toluene. The poisoning of this iron catalyst is reported by Glüer et al. at low catalyst loadings with $H_3B{\cdot}NH_2Me$, forming $Fe(PN^HP^iPr)(CO)(\kappa^1\text{-}BH_4)H$ which is analogous to complex **4**. [5]

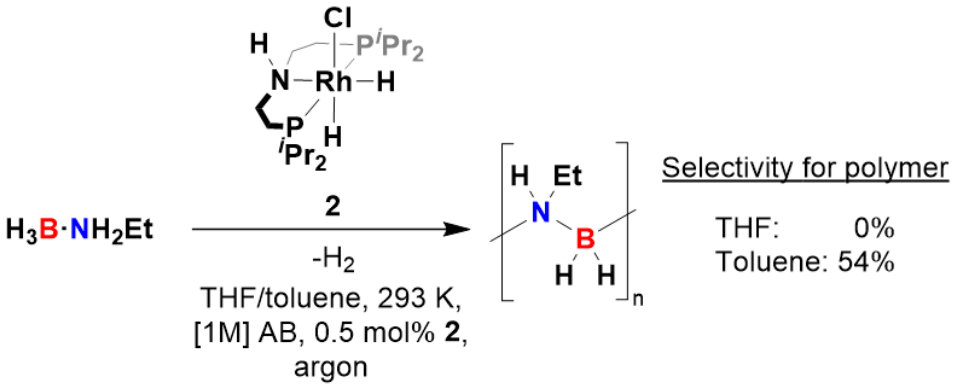

Figure 65. The attempted dehydropolymerisations of *N*-ethylamine borane (0.147 g, 1 mol dm^{-3}) with precatalyst **2** (0.5 mol%), varying the reaction solvent, using THF or toluene.

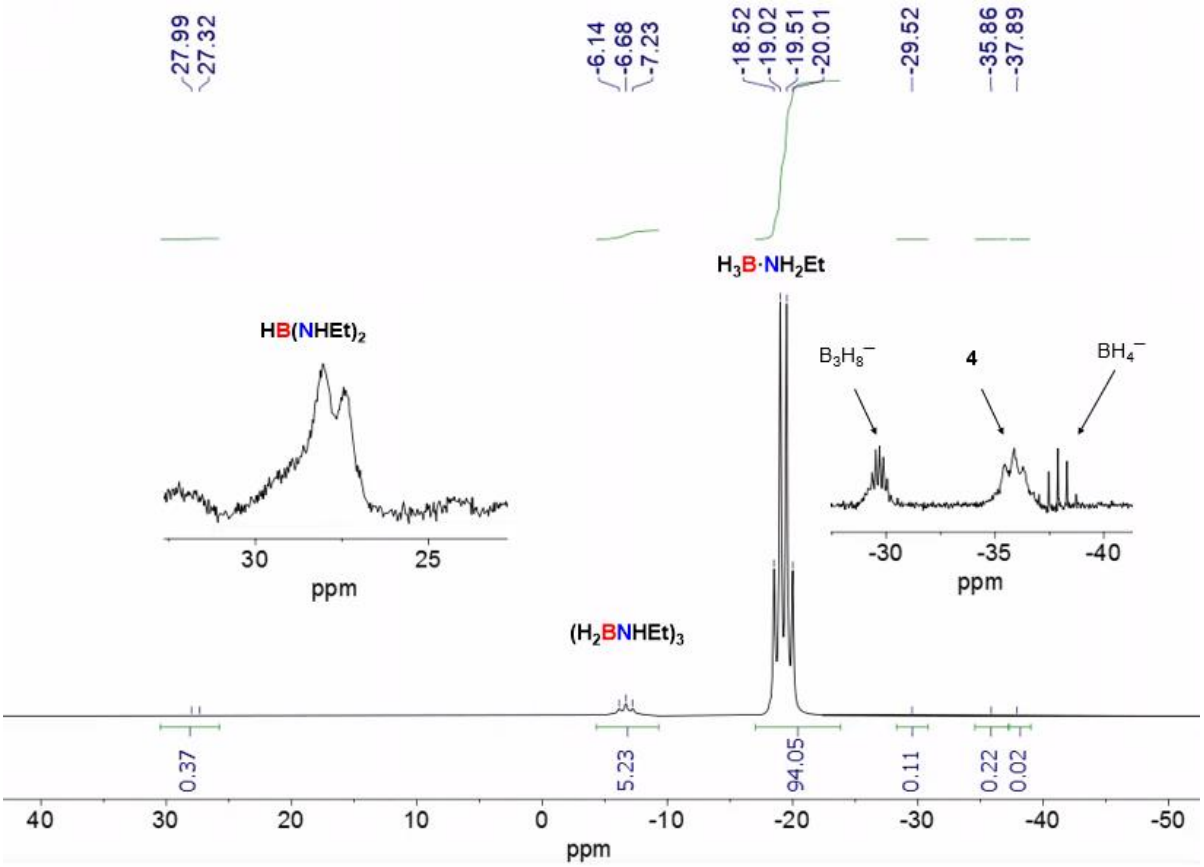

Figure 66. ^{11}B NMR spectrum recorded from an in-situ aliquot after one hour of the attempted dehydropolymerisation of $H_3B{\cdot}NH_2Et$ (0.147 g, 1 mol dm^{-3}) by **2** (0.5 mol%) in THF. Primarily unreacted $H_3B{\cdot}NH_2Et$ is seen as a quartet corresponding to the BH_3, at –18.9 ppm. The left inset shows the doublet corresponding to $HB(NHEt)_2$. The right inset shows $B_3H_8^-$, complex **4** and BH_4^- signals.

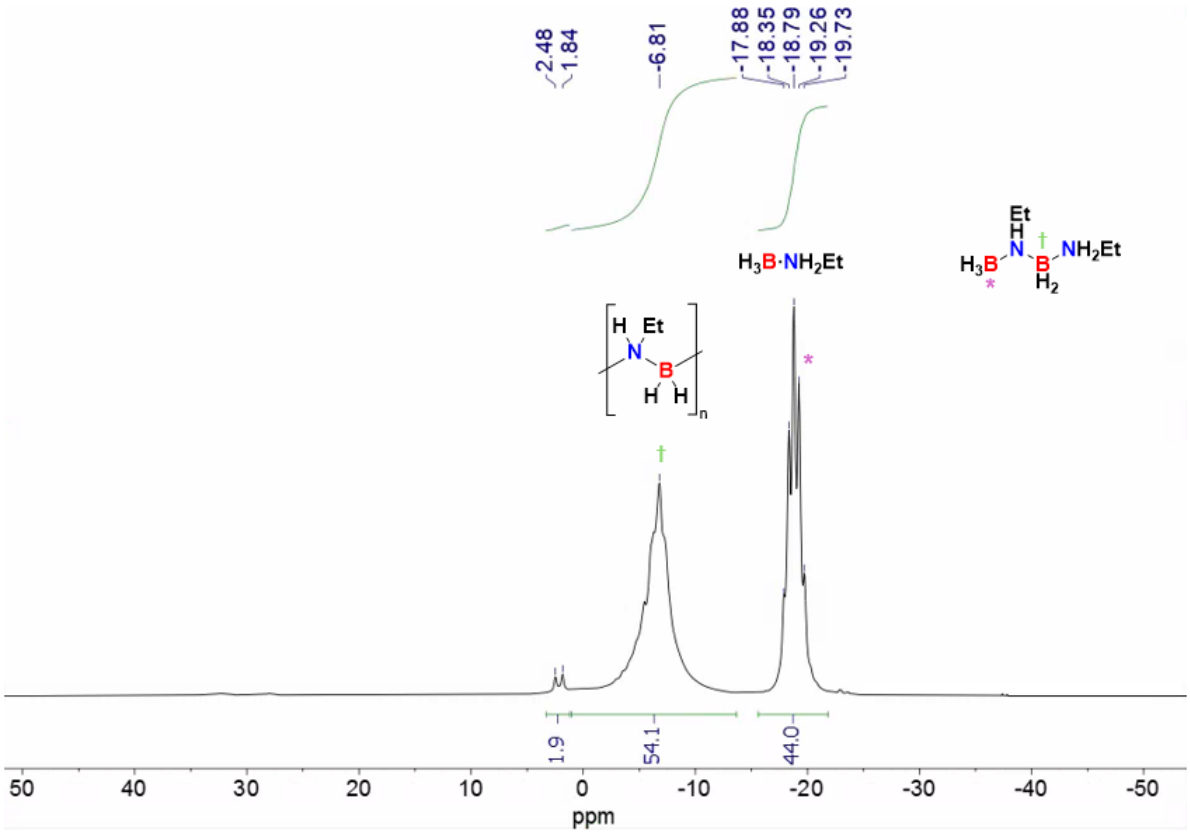

Figure 67. ^{11}B NMR spectrum recorded from an in-situ aliquot after one hour of the attempted dehydropolymerisation of $H_3B{\cdot}NH_2Et$ (0.147 g, 1 mol dm^{-3}) by precatalyst **2** (0.5 mol%) in toluene. Unreacted $H_3B{\cdot}NH_2Et$ is observed along with oligomer H_3B–$NHEt$-BH_2–NH_2Et and polymer $(H_2BNHEt)_n$.

2.1.8.2 The effect of added amines on the substrate conversion and catalyst poisoning for dehydropolymerisation of *N*-ethyl amine-borane with precatalyst 2

Glüer et al. also reported the use of in-situ NMe_2Et as a BH_3 scavenging agent to prevent catalyst poisoning and subsequently observed a 3-fold increase in maximum turnover number of the catalyst ($Fe(PN^HP^iPr)(CO)H_2$). [5] Dehydropolymerisations were performed on $H_3B{\cdot}NH_2Et$ at 1 mol dm^{-3} concentration in THF with 0.5 mol% catalyst loading of **2** and 5 equivalents to catalyst of NEt_3 or NH_2Et to evaluate their effectiveness as BH_3 scavenging agents (**Figure 68**).

In-situ ^{11}B NMR integrals after catalysis with the presence of 5 equivalents of NH_2Et showed most promise, with 87% conversion of the $H_3B{\cdot}NH_2Et$ substrate, forming primarily $(H_2BNHEt)_n$ alongside small amounts of $H_3B–NHEt–BH_2–NH_2Et$ and $HB(NHEt)_2$. This is a significant improvement over when precatalyst **2** is used without amine, where 6% conversion is observed by ^{11}B NMR spectroscopy and only $(H_2BNHEt)_3$ is formed (**Figure 66**). This suggests that $EtNH_2$ helps prolong the catalyst lifetime, likely by scavenging BH_3 (**Figure 69**). This is supported by the in-situ ^{31}P NMR spectra that show remaining precatalyst **2** at the end of catalysis, with 87% conversion to complex **4** rather than the 100% seen without NH_2Et (**Figure 70**). In this case it is likely that the precatalyst **2** observed at the end of catalysis was converted into the active species **3** and then upon the completion of catalysis is converted back to the off-cycle complex **2**, rather than being unreacted throughout. [11]

With 5 equivalents of NEt_3, lower conversion (63%) of $H_3B{\cdot}NH_2Et$ is observed by ^{11}B NMR spectroscopy, however significant amounts of $H_3B–NHEt\text{-}BH_2–NH_2Et$ are present which has an overlapping BH_3 signal with $H_3B{\cdot}NH_2Et$, meaning this conversion value is an underestimate (**Figure 69**).[42, 43] Large amounts of $H_3B{\cdot}NH_2Et$ are left unreacted. The observed presence of $H_3B{\cdot}NEt_3$ in the ^{11}B NMR spectrum could suggest BH_3 scavenging, however the direct displacement of BH_3 from $H_3B{\cdot}NH_2Et$ by NEt_3 is also likely to occur (**Figure 71**).[44] In-situ $^{31}P\{^1H\}$ NMR spectra show that despite the highest amount of precatalyst **2** remaining after catalysis with 5 equivalents of NEt_3 present (54 %), significant conversion to two new unidentified species is observed (77.0 ppm, d, 109 Hz & 73.2 ppm, dt, 106 Hz, 13 Hz, **Figure 72**).

The simultaneous presence of precatalyst **2** as observed by $^{31}P\{^{1}H\}$ NMR and unreacted $H_3B{\cdot}NH_2Et$ by ^{11}B NMR is difficult to explain as under other conditions, catalysis would promptly continue with the rapid conversion of **2** to the active trihydride species **3** [$Rh(PN^{H}P^{i}Pr)H_3$] (**Figure 71**, **Figure 72**). It is possible that during the activation process of precatalyst **2** where an amine-borane coordinates and is then deprotonated transferring a hydride and forming catalyst **3**, $H_3B{\cdot}NH_2Et$ is outcompeted by $H_3B{\cdot}NEt_3$ in coordinating to precatalyst **2**. As $H_3B{\cdot}NEt_3$ has no N–H protons it cannot undergo the same base-promoted hydride transfer to form active catalyst **3** (**Figure 73**). Overall, NEt_3 and NH_2Et both show improvements in amine-borane conversion when present during the dehydropolymerisation of $H_3B{\cdot}NH_2Et$ with precatalyst **2**, allowing the formation of polymer $(H_2BNHEt)_n$. NEt_3 is a less suitable additive than NH_2Et, as it appears to promote the formation of multiple unknown and apparently catalytically-inactive rhodium containing species observed by $^{31}P\{^{1}H\}$ NMR spectroscopy (**Figure 72**).

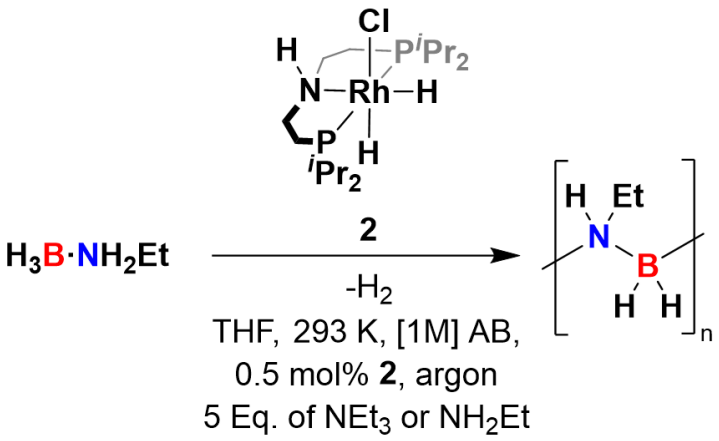

Figure 68. The attempted dehydropolymerisations of *N*-ethylamine borane (0.147 g, 1 mol dm^{-3} in THF) with precatalyst **2** (0.5 mol%), with 5 Eq. of added NEt_3 or NH_2Et as BH_3 scavengers.

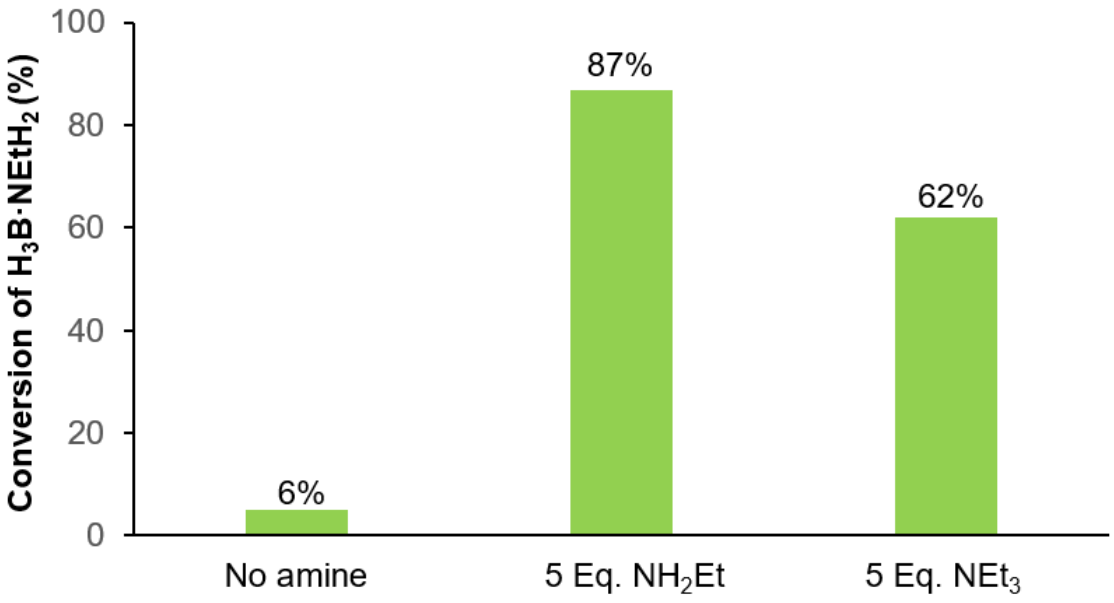

Figure 69. The percentage conversion of $H_3B{\cdot}NH_2Et$ to dehydrocoupled species as measured by in-situ ^{11}B NMR spectroscopy integrals from attempted dehydropolymerisations (0.147 g, 1 mol dm^{-3}) by precatalyst **2** (0.5 mol%) in THF. A comparison of BH_3 scavenging additives shows highest conversion of $H_3B{\cdot}NH_2Et$ when NH_2Et is present.

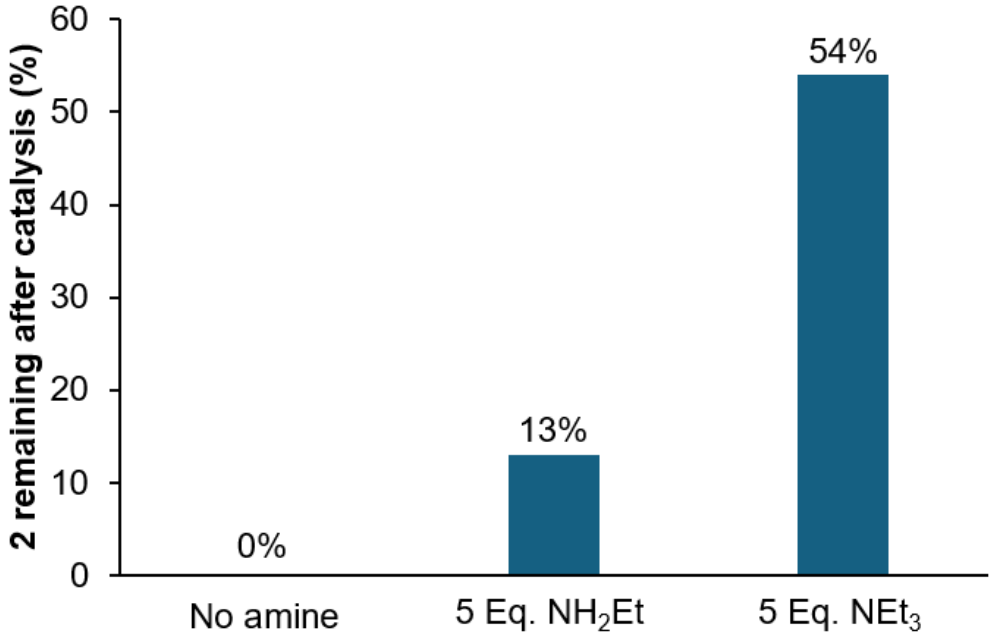

Figure 70. The percentage of precatalyst **2** remaining as measured by in-situ $^{31}P\{^1H\}$ NMR integrals after attempted dehydropolymerisations of $H_3B{\cdot}NH_2Et$ (0.147 g, 1 mol dm^{-3}) by precatalyst **2** (0.5 mol%) in THF. A comparison of BH_3 scavenging additives shows highest remaining quantity of precatalyst **2** when NEt_3 is present.

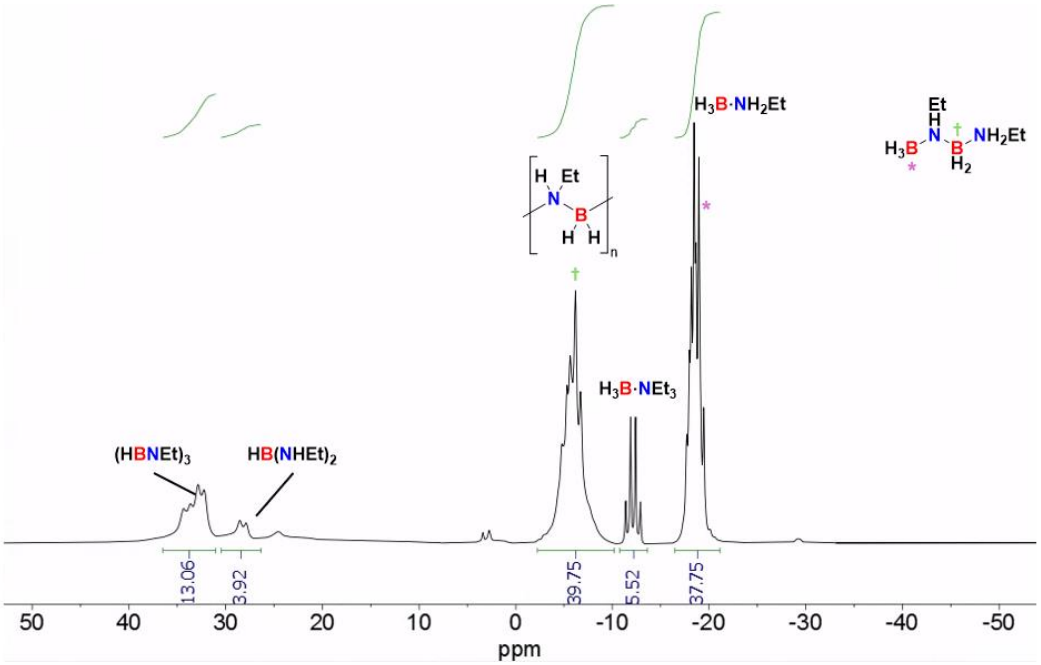

Figure 71. ^{11}B NMR spectrum recorded from an in-situ aliquot after one hour of the attempted dehydropolymerisation of $H_3B{\cdot}NH_2Et$ (0.147 g, 1 mol dm^{-3}) by precatalyst **2** (0.5 mol%) in THF with 5 Eq. of NEt_3. Unreacted $H_3B{\cdot}NH_2Et$ is observed along with oligomer H_3B–$NHEt$-BH_2–NH_2Et, *N,N,N*-triethylborazine $(HBNEt)_3$, $H_3B{\cdot}NEt_3$ and polymer $(H_2BNHEt)_n$. [45]

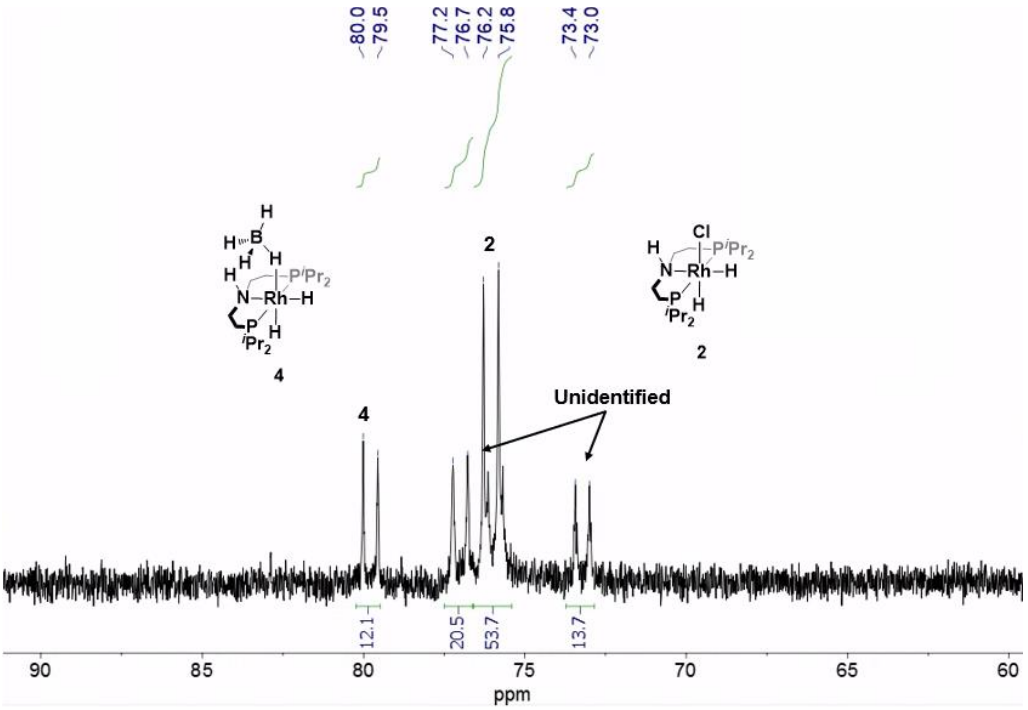

Figure 72. In-situ $^{31}P\{^1H\}$ NMR spectrum recorded after the attempted dehydropolymerisation of $H_3B{\cdot}NH_2Et$ (0.147 g, 1 mol dm^{-3}) by precatalyst **2** (0.5 mol%) in THF, with 5 Eq. of NMe_3 relative to precatalyst **2**. Complexes **2** and **4** are observed (76.1 ppm & 79.8 ppm respectively) alongside other unknown peaks at 77.0 and 73.2 ppm.

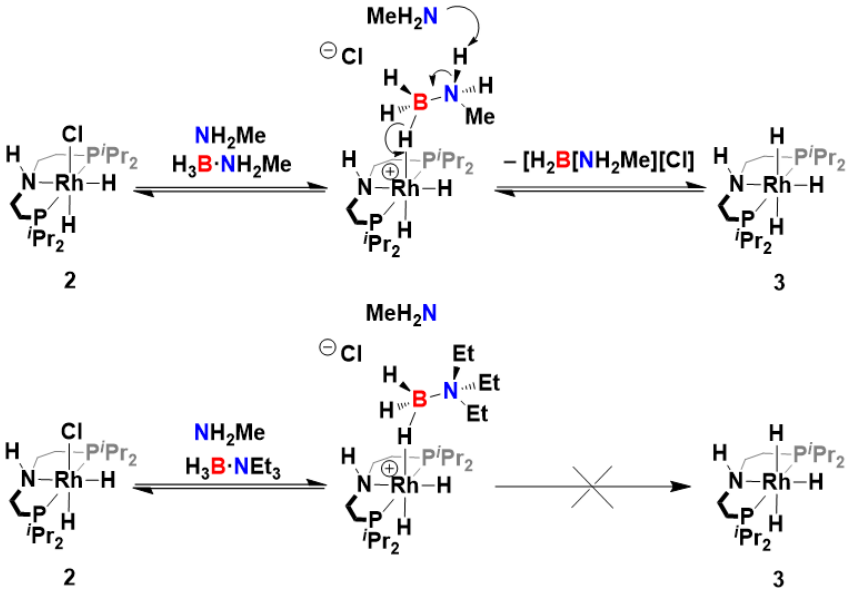

Figure 73. Top: The activation of precatalyst **2** to complex **3** via base-promoted hydride transfer from a sigma amine-borane complex intermediate proposed by Weller et al. [11] **Bottom:** The possible prevention of precatalyst (**2**) activation in the presence of $H_3B{\cdot}NEt_3$.

2.1.8.3 The effect of reaction temperature on the substrate conversion and catalyst poisoning for dehydropolymerisation of *N*-ethyl amine-borane with precatalyst 2

Resendiz-Lara et al. report the attempted dehydropolymerisation of *N*-substituted amine-borane $H_3B{\cdot}NH_2(CH_2)_4Ph$ with Ir(POCOP^{t}Bu)H_2 at 20 and –40 °C, showing that selectivity for the polymer $(H_2BNH(CH_2)_4Ph)_n$ is improved from 28 % at 20 °C to 45% at –40 °C. [46] Although it is not explicitly stated, it is likely that with $H_3B{\cdot}NH_2(CH_2)_4Ph$ this catalyst system is suffering from BH_3 poisoning, such as has been reported with $H_3B{\cdot}NH_2Ph$. [34] The reported increased selectivity for polyaminoborane with decreasing temperature for dehydropolymerisation may be the effect of a reduction in BH_3 release at lower temperatures. This was investigated by attempting dehydropolymerisations of $H_3B{\cdot}NH_2Et$ (1 mol dm^{-3}) with precatalyst **2** (0.5 mol%) in THF at temperatures 0, 20 and 40 °C (**Figure 74**).

At all three temperatures, complete catalyst poisoning was observed, with complex **4** as the only species observed by post-catalysis in situ $^{31}P\{^1H\}$ NMR spectra after 1 hour. At 20 and 40 °C little conversion of the $H_3B{\cdot}NH_2Et$ substrate was observed by in-situ ^{11}B NMR spectroscopy (6 and 5% respectively by relative integrals, **Figure 75**) and the only product formed was the cyclic trimer $(H_2BNHEt)_3$, indicative of rapid formation of the catalytically inactive complex **4**. At 0 °C significant conversion of the $H_3B{\cdot}NH_2Et$ substrate was observed by in-situ ^{11}B NMR spectroscopy (82% by relative integrals, **Figure 75**), with a broad peak at –6.7 ppm corresponding to polymer $(H_2BNHEt)_n$, with a small amount of overlapping oligomer $H_3B–NHEt\text{-}BH_2–NH_2Et$ (**Figure 76**). This suggests that catalyst poisoning to complex **4** was more gradual at 0 °C and therefore a significant proportion of the $H_3B{\cdot}NH_2Et$ substrate was dehydropolymerised to form $(H_2BNHEt)_n$ before the catalyst was fully taken offline. The effect of low temperature to decrease the formation of BH_3 capped complex **4** during catalysis is likely due to disfavouring B–N bond cleavage at lower temperatures. At –10 °C, activation of precatalyst **2** did not occur, as observed by in-situ $^{31}P\{^1H\}$ NMR spectroscopy.

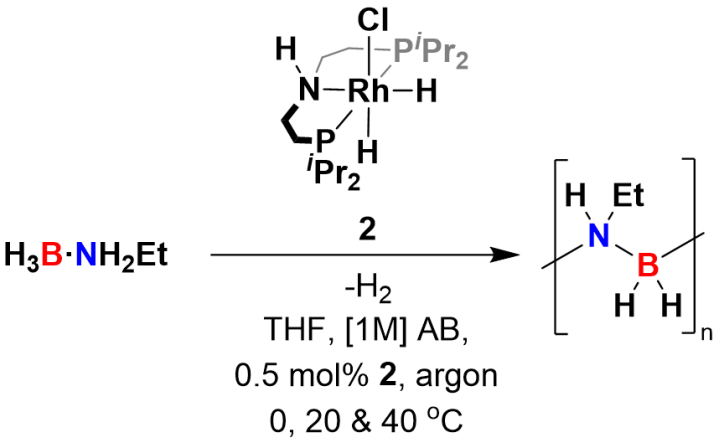

Figure 74. The attempted dehydropolymerisations of *N*-ethylamine borane (0.147 g, 1 mol dm^{-3} in THF) with precatalyst **2** (0.5 mol%), performed at 0, 20 and 40 °C.

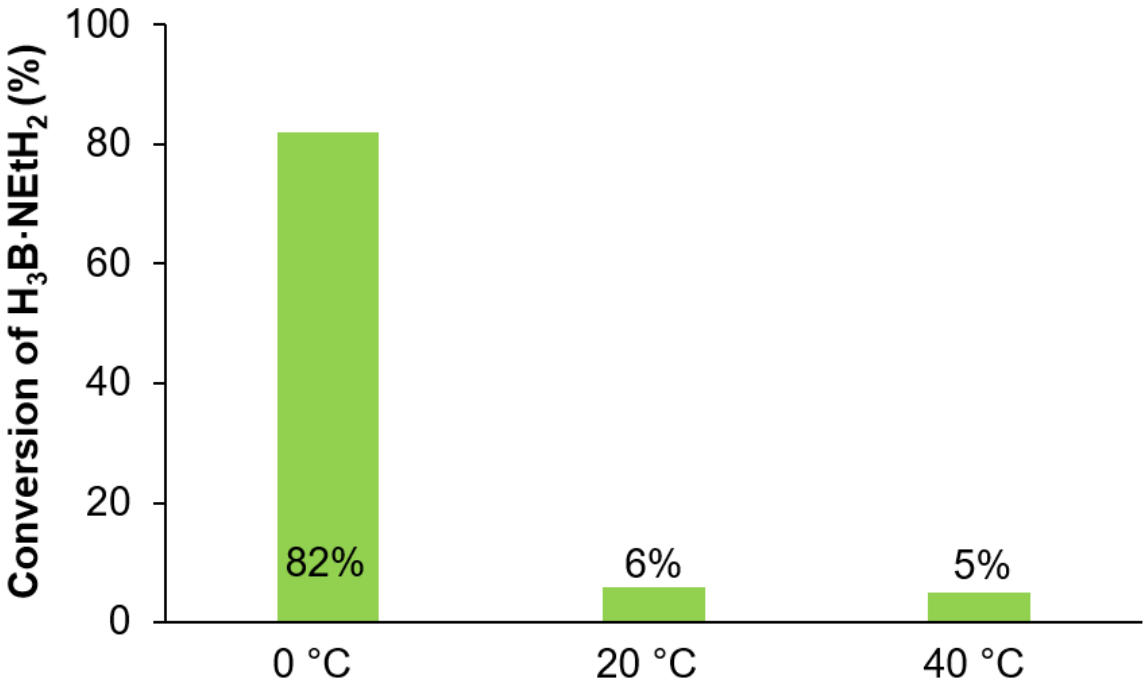

Figure 75. The percentage conversion of $H_3B{\cdot}NH_2Et$ to dehydrocoupled species as measured by in-situ ^{11}B NMR spectroscopy integrals from attempted dehydropolymerisations (0.147 g, 1 mol dm^{-3}) by precatalyst **2** (0.5 mol%) in THF at 0, 20 and 40 °C.

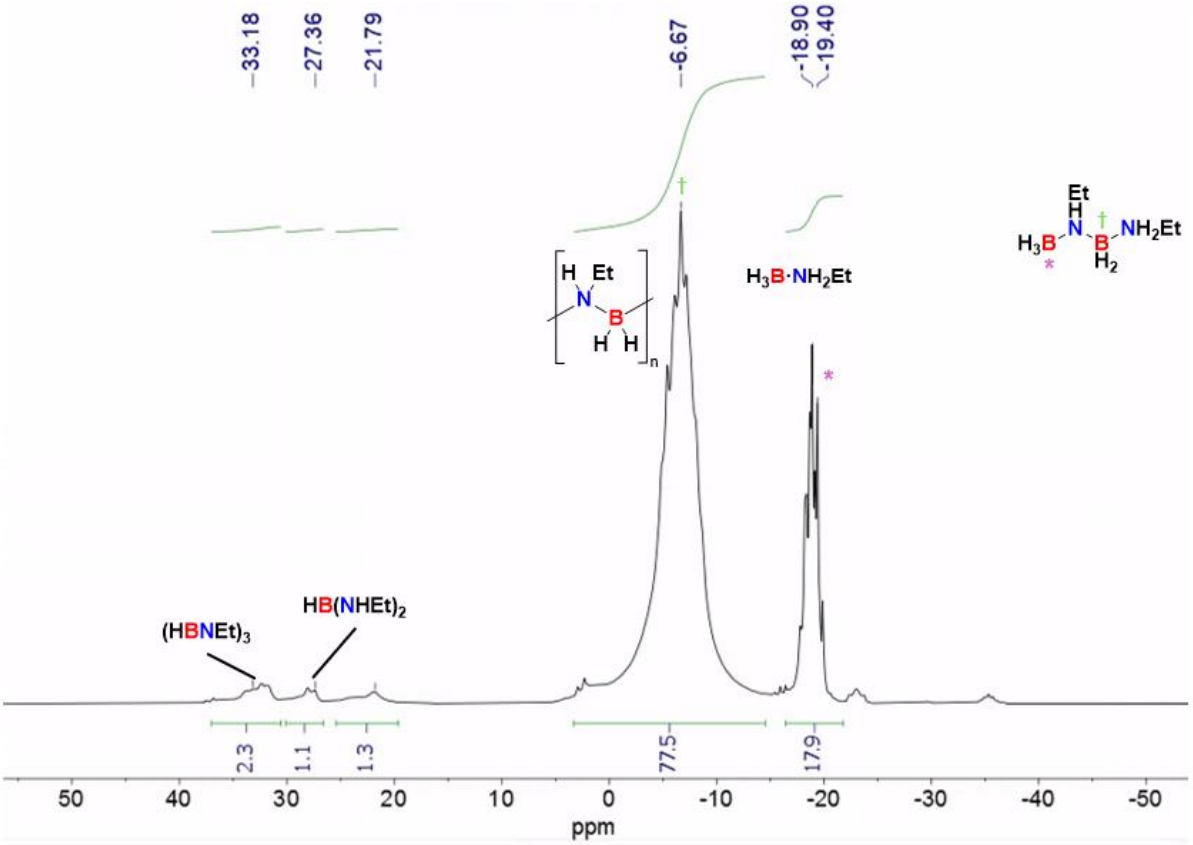

Figure 76. ^{11}B NMR spectrum recorded from an in-situ aliquot after one hour of the attempted dehydropolymerisation of $H_3B{\cdot}NH_2Et$ (0.147 g, 1 mol dm^{-3}) by precatalyst **2** (0.5 mol%) in THF at 0 °C. Unreacted $H_3B{\cdot}NH_2Et$ is observed along with oligomer H_3B–NHEt-BH_2–NH_2Et, *N,N,N*-triethylborazine $(HBNEt)_3$, $H_3B{\cdot}NEt_3$ and polymer $(H_2BNHEt)_n$. [45]

2.1.8.4 A summary of the effects of amine concentration, solvent and reaction temperature on the substrate conversion and catalyst poisoning for dehydropolymerisation of *N*-ethyl amine-borane with precatalyst 2

In this section several reaction condition variations have been shown to positively affect the efficacy of precatalyst **2** when used at 0.5 mol% (0.005 mol dm^{-3}) for dehydropolymerising *N*-alkyl substituted amine-borane $H_3B{\cdot}NH_2Et$, by helping delay the poisoning of the active species **3** by free BH_3 to catalytically inactive species **4**. The non-coordinating solvent toluene likely helps reduce BH_3 formation as it does not participate in either of the postulated BH_3 release mechanisms (amine-borane B–N bond cleavage and aminoborane oligomerisation-dissociation, **2.1.6**). In comparison THF is thought to facilitate these processes by lowering energy barriers, forming the Lewis adduct $THF{\cdot}BH_3$. [36, 38] This is apparent when comparing the conversion of $H_3B{\cdot}NH_2Et$ with THF vs toluene, where in toluene reaches 57% conversion with 94% polymer selectivity and THF reaches only 6% conversion with 0% polymer selectivity (as measured by ^{11}B NMR integrals, **Figure 77**). At the end of catalysis however both show complete conversion of the catalyst to inactive species **4** by $^{31}P\{^1H\}$ NMR spectroscopy (**Figure 78**).

Lowering the reaction temperature to 0 °C (when compared to 20 °C) during dehydropolymerisations significantly increases the conversion of $H_3B{\cdot}NH_2Et$ over the course of catalysis (from 6% with 0% polymer selectivity to 82% with 92% selectivity, **Figure 77**). The lower temperature likely slows the formation of borane capped species **4** (100% conversion to **4** was reached at both temperatures (**Figure 78**), possibly because there is a significant energy barrier to spontaneous BH_3 loss from amine-boranes in solution, which is less likely to be overcome if there is less thermal energy in the system. [36, 38] The addition of amine NH_2Et to the dehydropolymerisation of $H_3B{\cdot}NH_2Et$ with precatalyst **2** also helps prevent catalyst poisoning, showing a conversion of 87% to inactive species **4** at the end of catalysis in THF compared to 100% when performed with no added NH_2Et (**Figure 78**). NH_2Et may act as a BH_3 scavenging agent, re-forming $H_3B{\cdot}NH_2Et$. Understanding all of these observations is important, as the main challenge to the dehydropolymerisation of a broader amine-

borane substrate scope appears to minimise the aforementioned catalyst poisoning by BH_3.

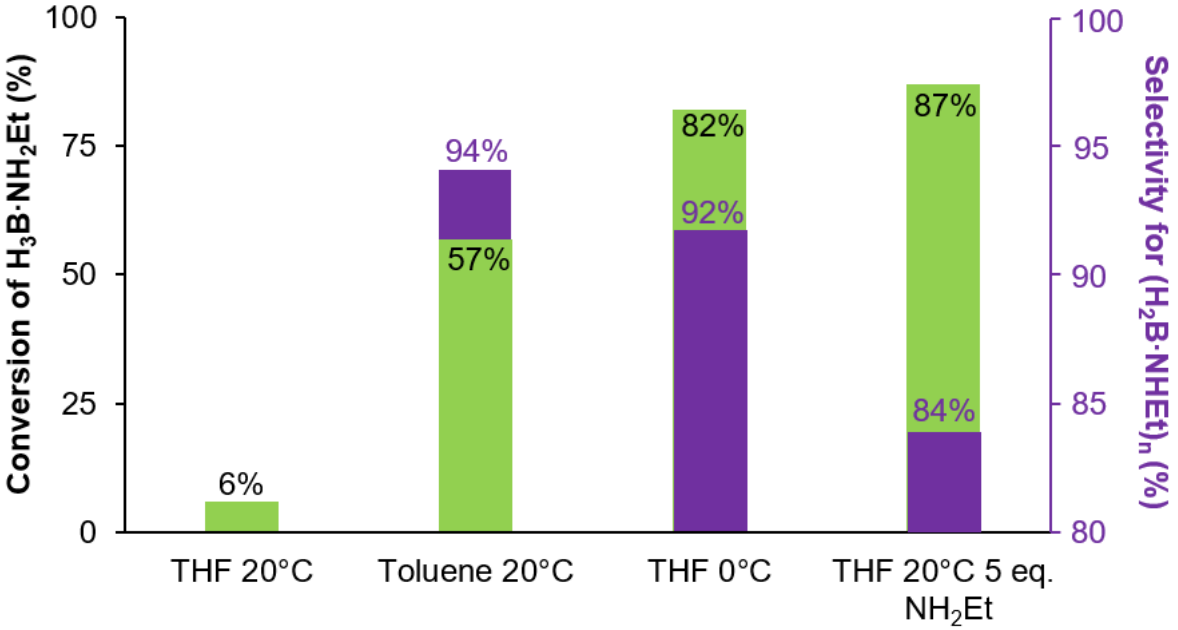

Figure 77. Green: The percentage conversion of $H_3B{\cdot}NH_2Et$ to dehydrocoupled species as measured by in-situ ^{11}B NMR spectroscopy integrals. **Purple:** The percentage selectivity for polymer $(H_2BNHEt)_n$ of dehydrocoupled species formed. Both as measured by in-situ ^{11}B NMR spectroscopy integrals from attempted dehydropolymerisations (0.147 g, 1 mol dm^{-3}) by precatalyst **2** (0.5 mol%, 0.005 mol dm^{-3}). Catalysis attempted with: THF at 20 °C, Toluene at 20 °C, THF at 0 °C and THF at 20 °C with 5 eq. (0.025 mol dm^{-3}) of NH_2Et.

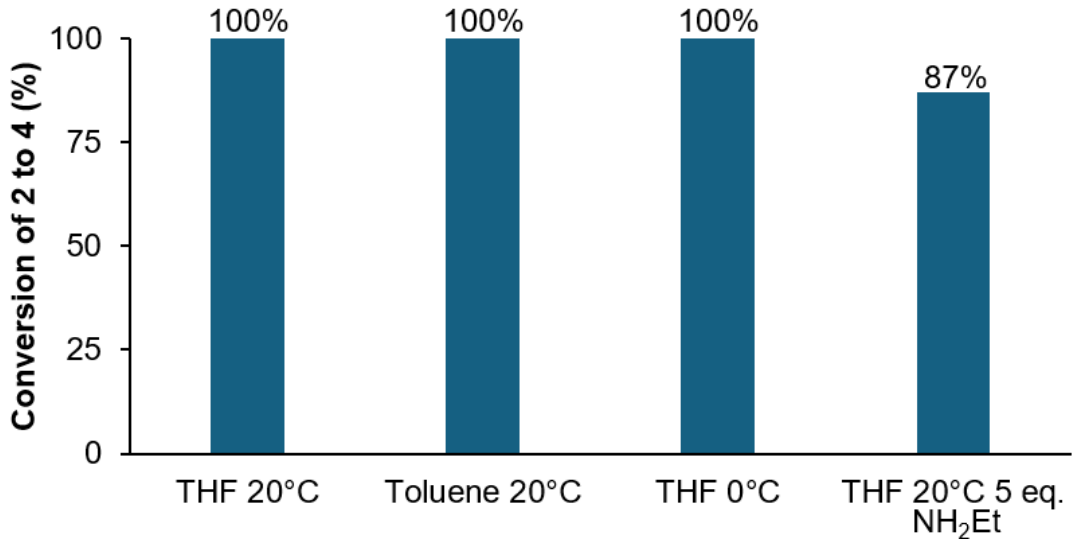

Figure 78. The percentage conversion of precatalyst **2** to inactivated species **4** as measured by in-situ ^{31}P NMR spectroscopy integrals from attempted dehydropolymerisations (0.147 g, 1 mol dm^{-3}) by precatalyst **2** (0.5 mol%, 0.005 mol dm^{-3}). Catalysis attempted with: THF at 20 °C, Toluene at 20 °C, THF at 0 °C and THF at 20 °C with 5 eq. (0.025 mol dm^{-3}) of NH_2Et.

In an attempt to selectively produce $(H_2BNHEt)_n$ from complete conversion of $H_3B{\cdot}NH_2Et$ by catalytic dehydropolymerisation with precatalyst **2**, all of the previously discussed advantageous reaction conditions were applied simultaneously: using toluene as a solvent; performing the reaction at 0 °C and adding 5 equivalents of NH_2Et relative to catalyst (**Figure 79**). The in-situ ^{11}B NMR spectrum recorded after the cessation of hydrogen evolution (as measured eudiometrically) shows the complete conversion of the $H_3B{\cdot}NH_2Et$ substrate, however no $(H_2BNHEt)_n$ is present. The main products that are observed are doublets corresponding to BH environments, *N,N,N*-triethylborazine, $(HBNEt)_3$ (31.8 ppm), $HB(NHEt)_2$ (27.6 ppm) and an unidentified species (33.3 ppm, **Figure 80**). A possible identity for the species at 33.3 ppm is a further dehydrogenated borazine oligomer such as 1,2-$(B_3N_3Et_3H_2)$, the unsubstituted derivative (NH) of which is reported to exhibit three very closely overlapped BH doublets at ~ 32 ppm and a very broad B singlet at ~ 30 ppm. [47]

The presence of *N,N,N*-triethylborazine and related products suggests over-dehydrogenation, where 2 equivalents of H_2 are lost from the $H_3B{\cdot}NH_2Et$ substrate. This likely occurs sequentially, where $(H_2BNHEt)_n$ and $(H_2BNHEt)_3$ that are formed first, continue to interact with the catalyst and are dehydrogenated. The in-situ $^{31}P\{^1H\}$ NMR spectrum shows the presence of both complex **2** (46%) and complex **4** (33%) alongside an unidentified J_{PRh} coupled species at 76 ppm (21%), the presence of complex **4** demonstrates that even under optimised conditions the issue BH_3 poisoning is still not entirely overcome (**Figure 81**). The combination of toluene as a solvent and either the addition of NH_2Et or performing catalysis at 0 °C should be further investigated to establish whether these conditions help prevent catalyst conversion to complex **4**, whilst maintaining selectivity for polyaminoborane $(H_2BNHEt)_n$.

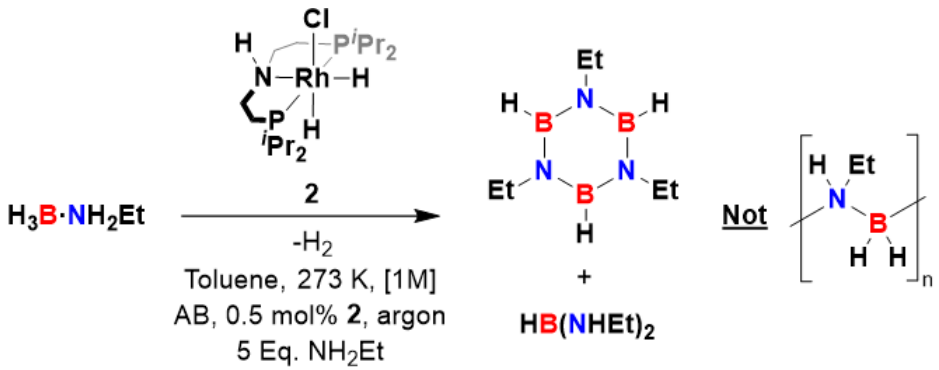

Figure 79. The attempted dehydropolymerisation of *N*-ethylamine borane (0.147 g, 1 mol dm^{-3} in toluene) with precatalyst **2** (0.5 mol%, 0.005 mol dm^{-3}), performed at 0 °C and with 5 equivalents of NH_2Et relative to catalyst present.

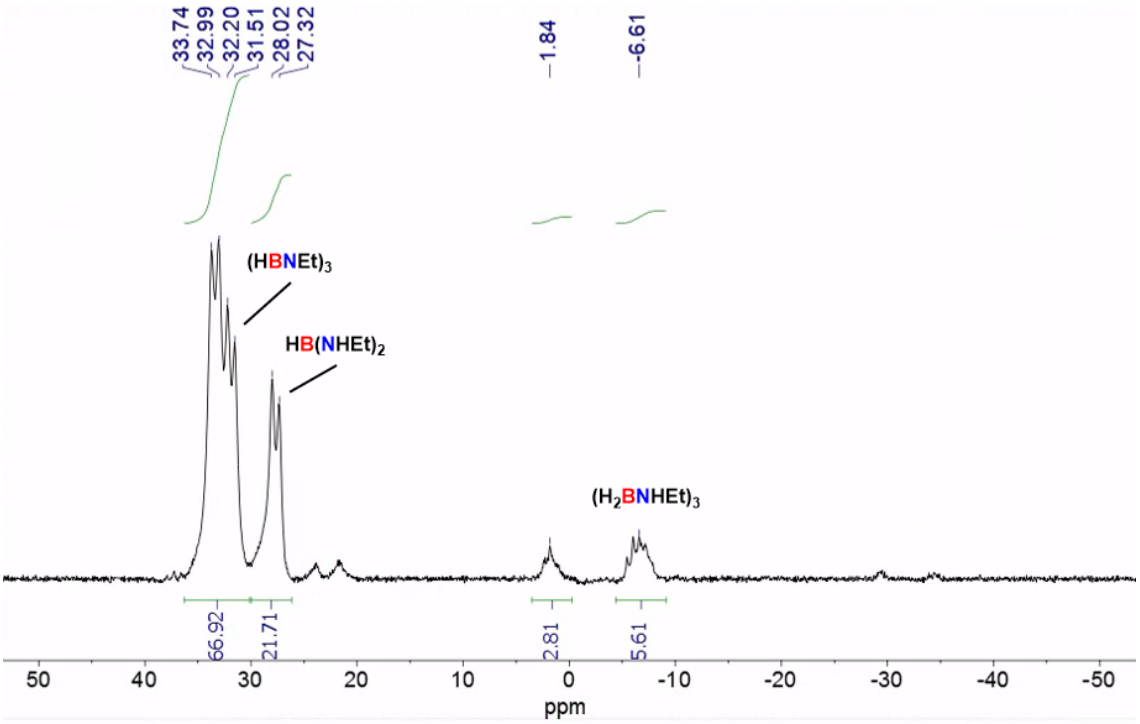

Figure 80. ^{11}B NMR spectrum recorded from an in-situ aliquot after one hour of the attempted dehydropolymerisation of $H_3B{\cdot}NH_2Et$ (0.147 g, 1 mol dm^{-3}) by precatalyst **2** (0.5 mol%) in toluene at 0 °C with 5 Eq. of added NH_2Et. *N,N,N*-triethylborazine $(HBNEt)_3$ is observed along with $HB(NHEt)_2$ as the major products, alongside an unidentified doublet at 33.3 ppm. [45, 48]

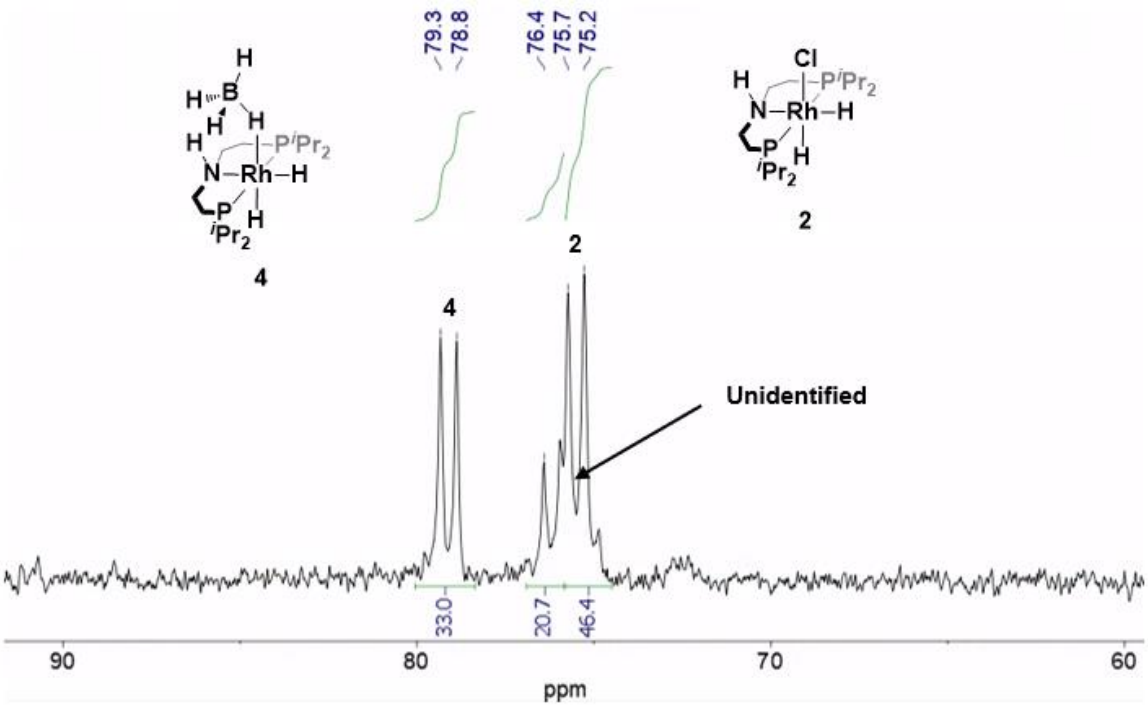

Figure 81. $^{31}P\{^1H\}$ NMR spectrum recorded from an in-situ aliquot after one hour of the attempted dehydropolymerisation of $H_3B{\cdot}NH_2Et$ (0.147 g, 1 mol dm^{-3}) by **2** (0.5 mol%) in toluene at 0 °C with 5 Eq. of added NH_2Et. Complexes **2** and **4** are observed, with an unidentified rhodium complex present at 76.0 ppm.

2.2 The dehydropolymerisation of amine-boranes with precatalysts Co(*i*Pr-PN^{H}P)Cl$_2$ (5), Co(Cy-PN^{H}P)Cl$_2$ (6) and Co(Cy-PN^{H}P)H$_2$Cl (7)

Due to apparent limitations for dehydropolymerisation scope with the rhodium precatalysts **1** and **2**, where the active catalytic species **3** appears to be rapidly poisoned by trace BH_3 in solution to form **4**, the analogous cobalt complexes were screened for their reactivity with *N*-propyl amine-borane. Co(*i*Pr-PN^{H}P)Cl$_2$ (**5**) and Co(Cy-PN^{H}P)Cl$_2$ (**6**) are reported by Boyd et al. to be competent dehydropolymerisation precatalysts for $H_3B{\cdot}NH_2Me$, capable of forming $(H_2BNHMe)_n$ selectively. [10] Unlike the rhodium PN^{H}P precatalysts **1** and **2**, the active species formed from cobalt precatalysts **5** and **6** appear to be intolerant of air, as catalysis does not proceed when initiated in the presence of air

Due to the paramagnetic nature of these catalysts and the subsequent difficulty performing NMR speciation studies, the mechanism of operation is not fully understood. It has been shown however that the *N*-methylated complex Co(*i*Pr-PN^{Me}P)Cl$_2$ is catalytically inactive, and therefore a metal-ligand cooperative mechanism is invoked. [10] The apparent approximate first-order rate dependence in amine-borane substrate for these catalysts compared to the pseudo zeroth-order for precatalysts **1** and **2** suggests a different mechanism of operation. [10, 11] Like precatalyst **2**, precatalysts **5** and **6** are thought to form cobalt hydride active catalytic species via base-promoted hydride transfer from amine-boranes, facilitated by amine. [10, 11]

2.2.1 The attempted dehydropolymerisation of $H_3B{\cdot}NH_2{}^nPr$ with $Co({}^iPr\text{-}PN^HP)Cl_2$ (5) & $Co(Cy\text{-}PN^HP)Cl_2$ (6)

Dehydropolymerisations of $H_3B{\cdot}NH_2{}^nPr$ (5 mol dm^{-3} in 0.5 cm^3 THF) were attempted with precatalysts **5** and **6** (0.5 mol%, 0.025 mol dm^{-3}), each activated with 2 equivalents of NH_2Me (**Figure 82**). These conditions are analogous to those reported for the dehydropolymerisation of $H_3B{\cdot}NH_2Me$ by pretacalysts **5** and **6** by Weller et al. [10]

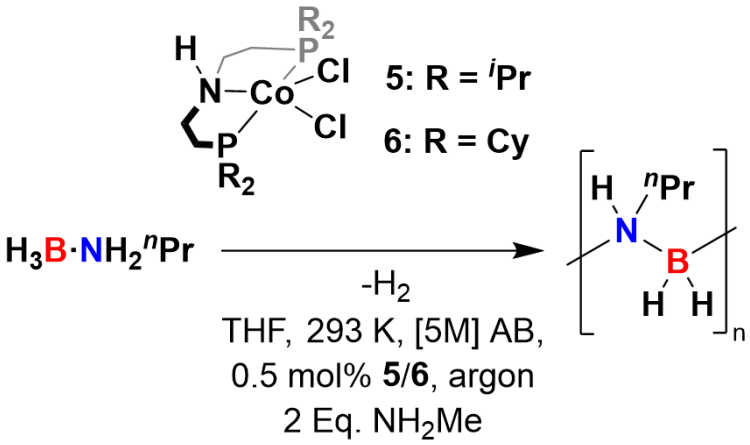

Figure 82. The attempted dehydropolymerisations of *N*-propylamine borane (0.182 g, 5 mol dm^{-3} in THF) with precatalysts **5** or **6** (0.5 mol%), performed with 2 equivalents of NH_2Me relative to catalyst present.

By eudiometric measurement both precatalysts showed rapid catalysis after a short ~ 100 s acceleratory period, followed by a slow decay in rate as part of an approximate first-order regime. Both catalysts cease H_2 evolution after approximately the same amount of time (~ 2000 s), however with precatalyst **6** significantly more hydrogen is released than for precatalyst **5** in this time: 0.75 and 0.35 equivalents per $H_3B{\cdot}NH_2{}^nPr$ respectively (**Figure 83**). This is also reflected in the initial rates of catalysis which are $(3.1\pm0.09)\times10^{-4}$ mol dm^{-3} s^{-1} for precatalyst **5** and $(1.2\pm0.01)\times10^{-3}$ mol dm^{-3} s^{-1} for precatalyst **6** (**Table 4**). This suggests that phosphine Cy groups on **6** make the dehydropolymerisation of $H_3B{\cdot}NH_2{}^nPr$ intrinsically faster than the ^iPr groups on **5**, as also seen with $H_3B{\cdot}NH_2Me$. [10]

The origin of this rate acceleration with Cy groups may be due to steric interactions between the phosphine substituents and molecules bound to the metal centre, where if the rate limiting step involves dissociation of the formed aminoborane or H_2, this may be favoured by higher steric congestion local to the metal. It should be noted however that isopropyl- and cyclohexyl- substituted phosphines have a very similar local steric

profile, the cyclohexyl group can be viewed as a peripheral extension on an isopropyl group, where the added bulk is distant from the phosphorous atom. [49] The relative electronic effect of varying ligand phosphine substituents will be investigated in section **2.2.2**.

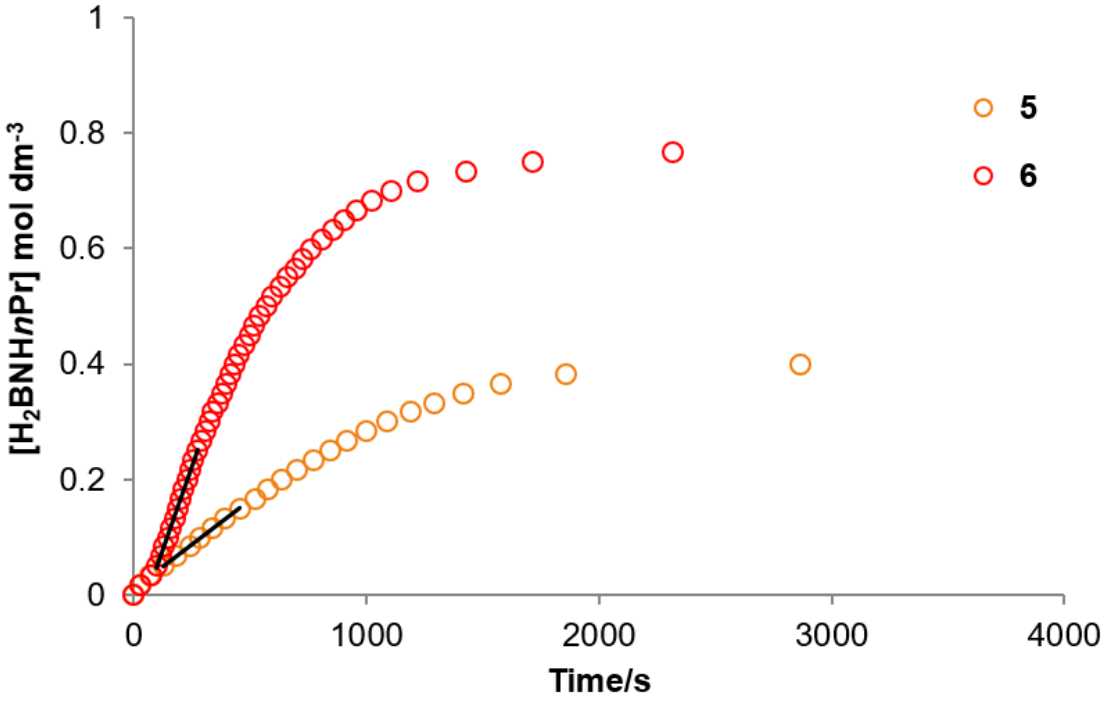

Figure 83. Effective $H_2B{=}NH^nPr$ concentration over time from eudiometric H_2 evolution measurement for the dehydropolymerisations of $H_3B{\cdot}NH_2{}^nPr$ (0.182g, 5 mol dm^{-3} in 0.5 cm^3 of THF) with precatalysts **5** and **6** (0.5 mol%), performed with 2 equivalents of NH_2Me relative to catalyst present. Precatalyst **6** shows a higher initial rate and higher overall conversion than precatalyst **5**.

Precatalyst	k_{obs} [a] (mol dm^{-3} s^{-1})	Amine borane conversion [b] (%)	Polymer selectivity [c] (%)	Polymer M_n [d] (g mol^{-1})	Dispersity [e]
5	3.1×10^{-4} ($\pm9\times10^{-6}$)	24	99	-	-
6	1.2×10^{-3} ($\pm1\times10^{-5}$)	48	95	61,100	1.4

Table 4. Data recorded from the dehydropolymerisations of $H_3B{\cdot}H_2{}^nPr$, 5 mol dm^{-3} in 0.5 cm^3 of THF) using precatalysts **5** and **6** (0.5 mol%). Rates determined by eudiometric measurement; polymer properties determined by GPC. Amine-borane conversion and polymer selectivity determined by in-situ ^{11}B NMR spectroscopy.

In-situ ^{11}B NMR spectra recorded after hydrogen evolution had ceased (~ 1 hour) show incomplete conversion of the $H_3B{\cdot}NH_2{}^nPr$ substrate to $(H_2BN{}^nPr)_n$ for both precatalysts **5** and **6**, with 24 and 48% conversion respectively, as measured by relative integrals (**Figure 84**, **Figure 85**). In ^{11}B NMR spectra recorded post-catalysis with both precatalysts **5** and **6** free BH_4^- is also observed, alongside two broad signals possibly corresponding to coordinated cobalt-borohydride complexes (–43.9 and –35.3 ppm, **Figure 84**, **Figure 85**). Co(^{i}Pr-PNP)(κ^2-BH_4) which would correspond to the BH_3 capping of a cobalt (I) hydride is a known compound, but the ^{11}B NMR is not reported. The analogous cobalt (II) and cobalt (III) borohydrides are unknown.[50] The presence of borohydride complexes suggests that like precatalyst **2**, precatalysts **5** and **6** are susceptible to BH_3 poisoning in solution before the dehydropolymerisation of $H_3B{\cdot}NH_2{}^nPr$ is complete.

The fact that both precatalysts **5** and **6** appear to be fully poisoned after approximately the same time frame (~ 2000 s), despite precatalyst **6** facilitating much more rapid dehydropolymerisation than precatalyst **5,** suggest that BH_3 formation may be independent of catalyst, such as in direct B–N bond cleavage of amine-boranes (see **2.1.6**). Catalysis with precatalyst **6** appears to further outpace BH_3 formation when compared to precatalyst **5**, therefore allowing for a higher amine-borane conversion before complete catalyst poisoning. GPC measurement of the material obtained from the precipitation of the reaction mixture with **5** showed no polymer signal, suggesting that oligomer of < 5000 g mol^{-1} was formed. GPC measurement of the corresponding material from catalysis with precatalyst **6** showed $(H_2BN{}^nPr)_n$ polymer with an M_n of 61,100 g mol^{-1} and a dispersity of 1.4 (**Table 4**). This is comparable to the $(H_2BNH{}^nPr)_n$ polymer made by precatalyst **2** (see **2.1.7**).

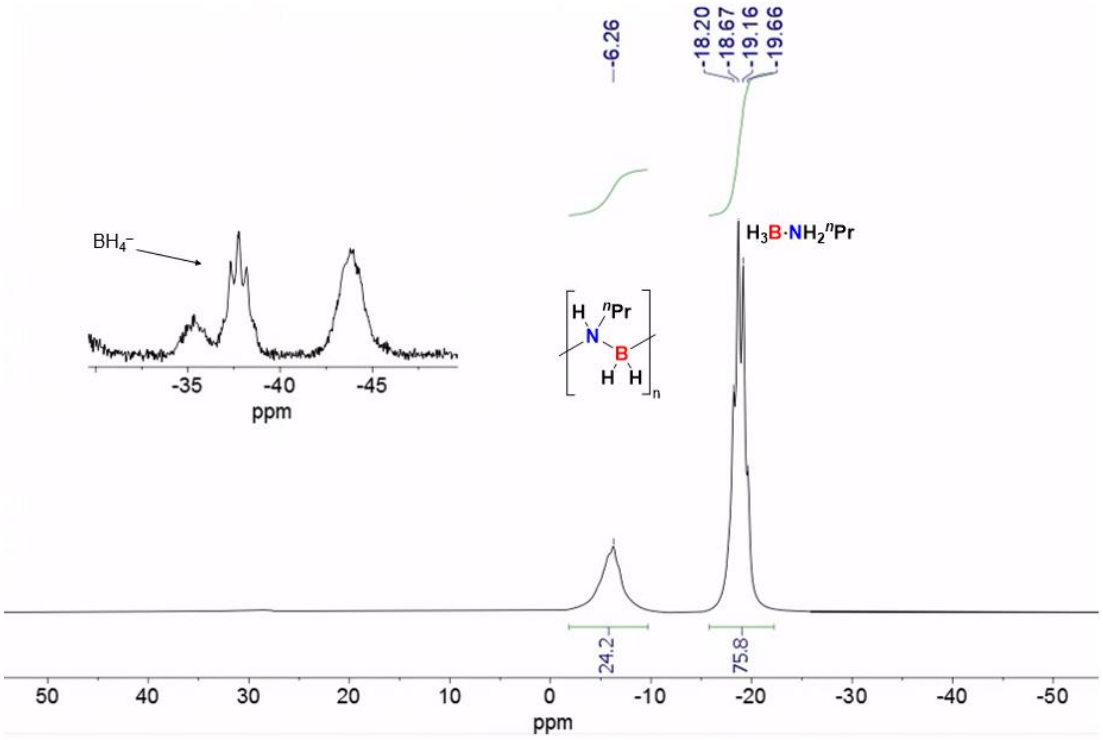

Figure 84. ^{11}B NMR spectrum recorded from an in-situ aliquot after one hour of the attempted dehydropolymerisation of $H_3B{\cdot}NH_2{}^nPr$ (0.182 g, 5 mol dm^{-3}) by **5** (0.5 mol%) in 0.5 cm^3 of THF. Unreacted $H_3B{\cdot}NH_2{}^nPr$ is observed along with a small amount of polymer $(H_2BNH{}^nPr)_n$. Inset shows free borohydride and two peaks tentatively assigned as cobalt borohydride complexes.

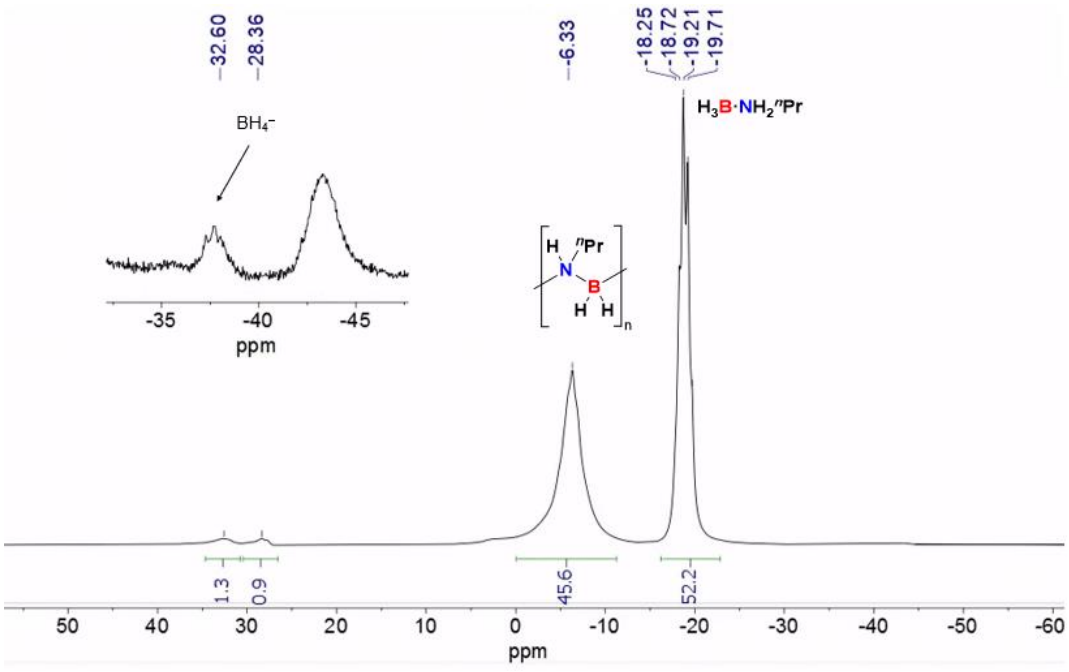

Figure 85. ^{11}B NMR spectrum recorded from an in-situ aliquot after one hour of the attempted dehydropolymerisation of $H_3B{\cdot}NH_2{}^nPr$ (0.182 g, 5 mol dm^{-3}) by **6** (0.5 mol%) in 0.5 cm^3 of THF. Unreacted $H_3B{\cdot}NH_2{}^nPr$ is observed along with polymer $(H_2BNH{}^nPr)_n$. Inset shows free borohydride and two peaks tentatively assigned as cobalt borohydride complexes.

2.2.2 The effect of phosphine substituent on PN^{H}P ligand donating ability and the attempted dehydropolymerisation of $H_3B{\cdot}NH_2Me$ with Rh(Cy-PN^{H}P)H_2Cl (7)

When comparing dehydropolymerisation of amine-boranes with precatalysts **5** and **6**, catalysis is significantly more rapid with the cyclohexyl substituted PN^{H}P ligand on precatalyst **6**. To investigate how PN^{H}P ligand phosphine substituents affect ligand σ-donating ability, the phosphine selenides of each ^{i}Pr-PN^{H}P, Cy-PN^{H}P and ^{t}Bu-PN^{H}P were synthesized (see experimental **4.2.2** to **4.2.4**). Analogous to the Tolman electronic parameter, P-Se NMR coupling constant can be used to evaluate the electron σ-donating ability of a phosphine. [51-53] This is demonstrated numerically where J_{PSe} is proportional to the inverse of the donor capacity of the phosphine (**Equation 1**). NMR coupling arises as a nuclear spin-spin interaction that is mediated by the electrons in a chemical bond, specifically of the *s* orbitals which have the highest radial distribution proximal to the nucleus (Fermi contact mechanism). High σ-donating ability of a phosphine relates to the lone pair that principally resides in the *p* orbital, and so a more electron withdrawn, poorer donating lone pair that resides closer to the nucleus in *s* orbitals exhibits a larger coupling constant when coupling to spin ½- ^{77}Se (8% abundance). [53]

$$^{1}J_{PSe} \propto \frac{1}{\sigma\,\text{donation}}$$

Equation 1. The relationship between phosphorous-selenium NMR coupling constant and phosphine lone pair σ-donation ability. [53]

The donating ability of a phosphine is affected by its bonded substituents, with alkyl groups increasing lone pair donation by inductive effects and hyperconjugation. More donating alkyl substituents lead to a smaller phosphorous selenium coupling that can be observed by ^{31}P NMR spectroscopy, where satellite signals appear around the corresponding phosphorous peak. The diselenides of ^{i}Pr-PN^{H}P, Cy-PN^{H}P and ^{t}Bu-PN^{H}P were synthesized and ^{31}P{^{1}H} NMR spectra recorded. The cyclohexyl derivative was found to have the smallest $^{1}J_{PSe}$ coupling constant (688 Hz) and therefore the most strongly σ-donating phosphines, the tertiary butyl and isopropyl derivatives had similar coupling constants suggesting similar σ-donating ability ($^{1}J_{PSe}$ = 693 and 695 Hz respectively, **Figure 86**).

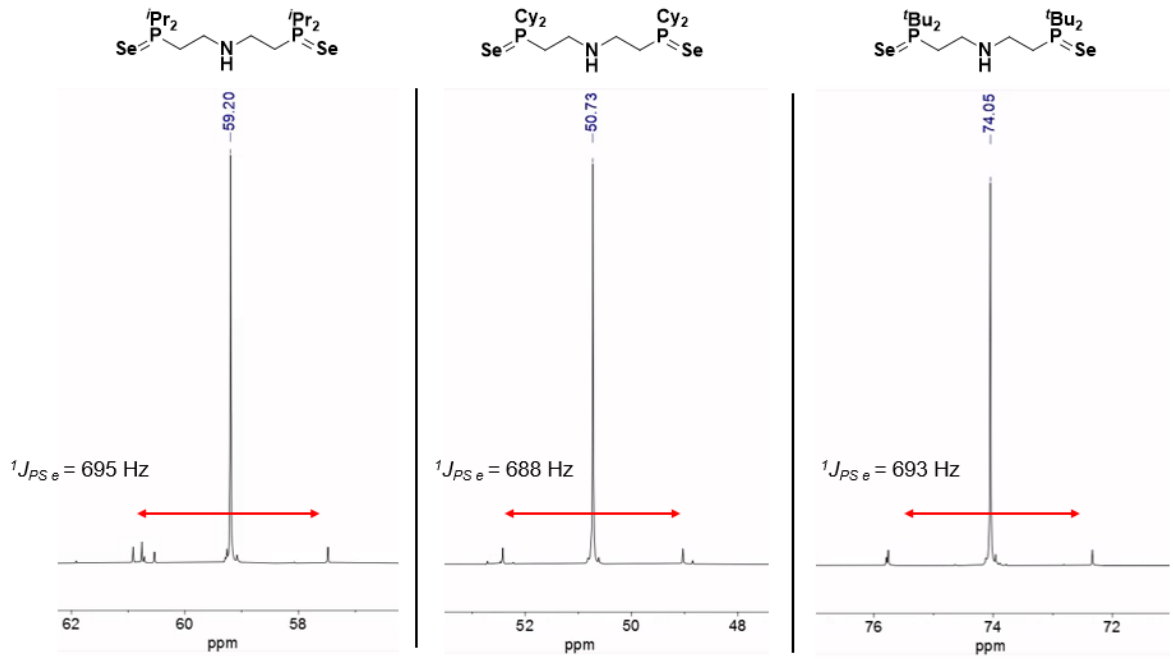

Figure 86. $^{31}P\{^1H\}$ NMR spectra of ^{i}Pr-PN^{H}P, Cy-PN^{H}P and ^{t}Bu-PN^{H}P diselenides, highlighting the P-Se coupling constant. Recorded in DCM-d_2 at 298 K.

From dehydropolymerisations with precatalysts **5** and **6** where the cyclohexyl-substituted precatalyst **6** led to faster rates of dehydrogenation, it was hypothesized that a stronger σ-donating ligand may lead to a more electron rich cobalt hydride, which in turn facilitates the higher rate of catalysis. With precatalyst **6**, this higher rate of catalysis appeared to outrun BH_3 catalyst poisoning and facilitate the dehydropolymerisation of bulkier amine-boranes (**2.2.1**, **Figure 83**). As the cyclohexyl-substituted phosphine was found to be the strongest σ-donating, the cyclohexyl derivative of precatalyst **2** was synthesized: Rh(Cy-PN^{H}P)H_2Cl (**7**). Precatalyst **7** was synthesized via the reported route for the synthesis of precatalyst **2** but using the ligand Cy-PN^{H}P instead of ^{i}Pr-PN^{H}P.[11]

Dehydropolymerisation of $H_3B{\cdot}NH_2Me$ by precatalysts **2** and **7** was performed as a direct comparison of phosphine ligand substituent effects, with 1 mol dm^{-3} of amine-borane in 2.5 cm^3 THF and 0.5 mol% of precatalyst (**Figure 87**). As previously reported, dehydropolymerisation of $H_3B{\cdot}NH_2Me$ with precatalyst **2** led to the selective production of $(H_2BNHMe)_n$, as observed by in-situ ^{11}B NMR spectroscopy (**Figure 88**).[11] The dehydropolymerisation of $H_3B{\cdot}NH_2Me$ with precatalyst **7** started more rapidly than that with precatalyst **2** but slowed toward completion, releasing less than 1 equivalent of H_2 per amine-borane. This can be seen in the in-situ ^{11}B NMR spectrum

where incomplete dehydropolymerisation is evident, with 20% of the $H_3B{\cdot}NH_2Me$ unreacted (**Figure 88**). Also seen by ^{11}B NMR is a broad signal at – 35.5 ppm, analogous to that exhibited by borohydride complex **4** (Rh(^{i}Pr-PN^{H}P)(κ^1-BH_4)H_2). This is mirrored by in-situ $^{31}P\{^1H\}$ NMR spectra which show primarily complex **2** after catalysis with precatalyst **2**, but with precatalyst **7** show an approximately 1:1 ratio of complex **7** and a new species at 69.7 ppm (d, 110 Hz, **Figure 89**). This new signal likely corresponds to the BH_3 capped species Rh(Cy-PN^{H}P)(κ^1-BH_4)H_2 (complex **Y**), a hypothesis supported by the fact that the Rh-P coupling constant is 110 Hz, the same as in complex **4**. Also supporting this idea is that a coordinated borohydride signal is seen in the ^{11}B NMR spectrum after catalysis with precatalyst **7**, that is similar to that seen for complex **4**. After catalysis with precatalyst **7**, a broad signal at – 2.1 ppm is observed in the ^1H NMR spectrum (**Figure 89**), analogous to that for the BH_4^- in complex **4** (both recorded in THF). Rh(Cy-PN^{H}P)(κ^1-BH_4)H_2 (complex **Y**) was not isolated or characterised.

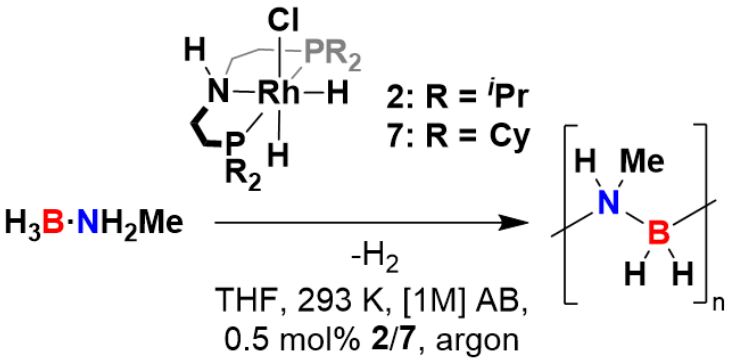

Figure 87. The attempted dehydropolymerisations of *N*-methylamine borane (0.112 g, 1 mol dm^{-3} in THF) with precatalysts **2** or **7** (0.5 mol%).

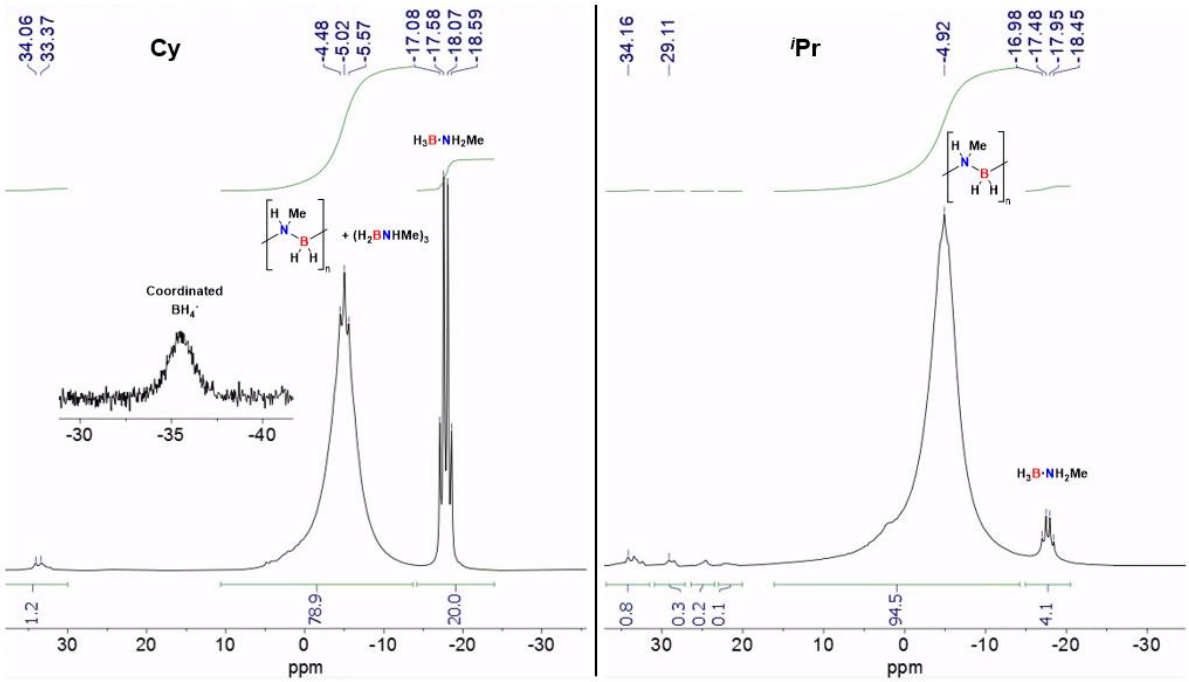

Figure 88. ^{11}B NMR spectra recorded from an in-situ aliquot after one hour of the attempted dehydropolymerisation of $H_3B{\cdot}NH_2Me$ (0.112 g, 1 mol dm^{-3}) by precatalyst **7** (Cy, left) or precatalyst **2** (^{i}Pr, right) (0.5 mol%) in 2.5 cm^3 of THF. In Cy, left with **7**, significant amounts of unreacted $H_3B{\cdot}NH_2Me$ are observed alongside polymer $(H_2BNHMe)_n$ and cyclic trimer $(H_2BNHMe)_3$. A broad signal at – 35.5 ppm corresponding to coordinated BH_4^- in a borohydride complex Is also seen. In (^{i}Pr, right) with precatalyst **2**, primarily $(H_2BNHMe)_n$ is observed.

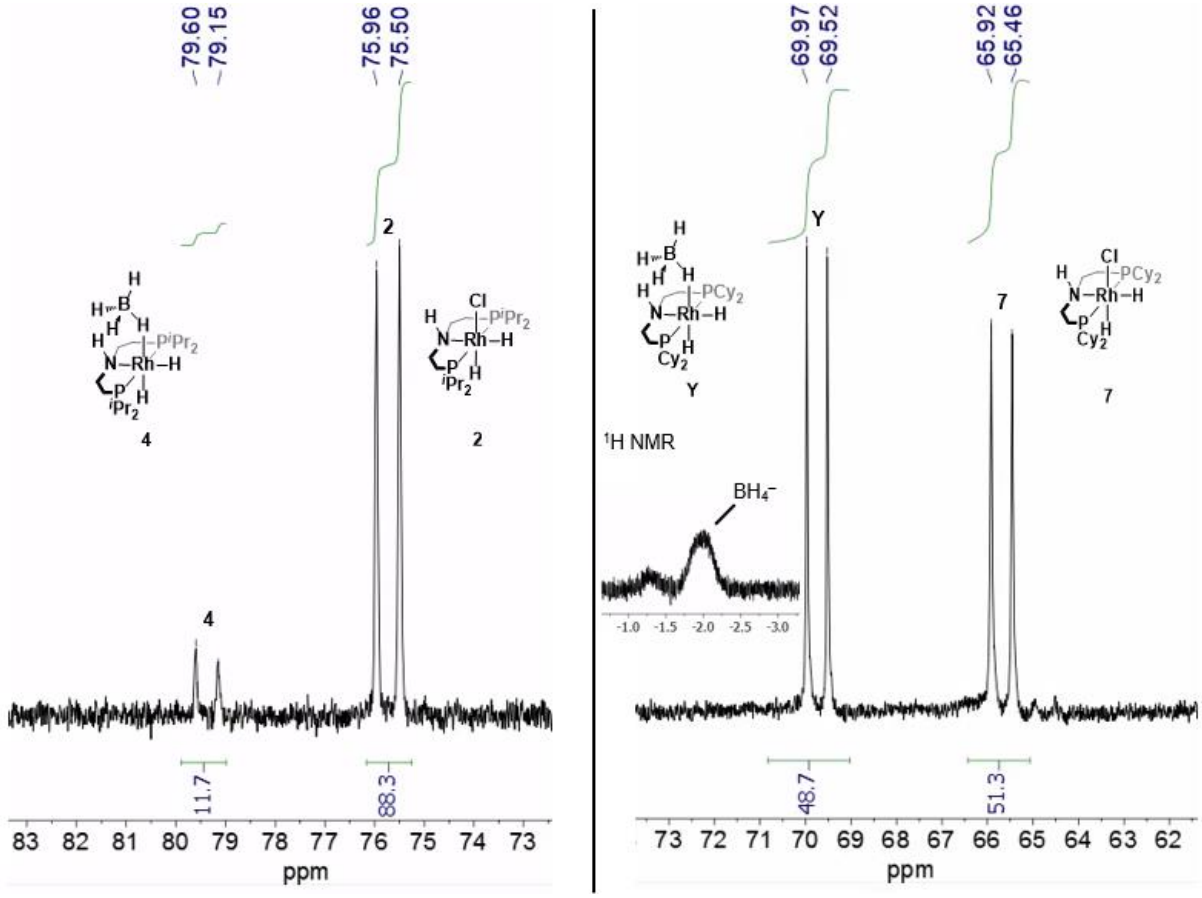

Figure 89. $^{31}P\{^1H\}$ NMR spectra recorded from in-situ aliquots after one hour of the attempted dehydropolymerisation of $H_3B{\cdot}NH_2Me$ (0.112 g, 1 mol dm^{-3}) by precatalysts **2** and **7** (0.5 mol%) THF. With precatalyst **2**, primarily complex **2** and a small amount of complex **4** are observed after catalysis. With precatalyst **7**, approximately 1:1 signals for complex **7** and the probable rhodium complex Rh(PN^{H}PCy)(κ^1-BH_4)H_2 (complex **Y**) at 69.7 ppm are observed after catalysis. The ^{1}H NMR spectrum inset for when precatalyst **7** is used shows the presence of coordinated BH_4^-,

2.2.3 A summary of metal centre and ligand phosphine substituent effects on the dehydropolymerisation of *N*-alkyl amine-boranes with group-9 MACHO catalysts

Overall, it appears that rather than improve substrate conversion as seen with the cobalt precatalysts **5** and **6**, cyclohexyl substitution for isopropyl on the PN^HP ligand of the rhodium system does not offer the same advantages (precatalysts **2** vs **7**). Precatalyst **7** appears to be more susceptible to BH_3 poisoning than precatalyst **2** as shown by the increased conversion to the apparent corresponding borohydride complex Rh(Cy-PN^HP)(κ^1-BH_4)H_2 (complex **Y**). The stronger inductive effect for the Cy substituted ligand phosphines on precatalyst **7** when compared to ^{i}Pr substituted phosphines on precatalyst **2**, likely make the corresponding hydrides on the active catalytic species formed from precatalyst **7** (likely Rh(Cy-PN^HP)H_3, analogous to complex **3** Rh(^{i}Pr-PN^HP)H_3) more nucleophilic than on the active catalytic species formed from precatalyst **2** (**3**, Rh(^{i}Pr-PN^HP)H_3). This may increase the propensity to attack the electrophilic BH_3 and accelerate catalyst poisoning in precatalyst **7** compared to precatalyst **2**.

Why the opposite trend is seen with the cobalt precatalysts **5** and **6**, where the Cy-substituted precatalyst **6** appears to be more resistant to BH_3 than ^{i}Pr-substituted precatatalyst **5** and reaches a higher conversion of $H_3B{\cdot}NH_2{}^n$Pr under the same conditions, is more difficult to explain. This is possibly related to how ligand substituent steric interactions affect the mechanism of each catalyst, such as if the rate limiting step is a dissociative process which may be favored by high local steric bulk. An investigation into this would likely require kinetic measurements (i.e. Eyring analysis) from each of the **2**, **7**, **5**, & **6** precatalysts alongside a thorough computational comparison to evaluate how MACHO-ligand phosphine substituents affect the mechanism of amine-borane dehydrogenation with Rh and Co metal centres.

References

1. P. A. Dub and J. C. Gordon, *Nat. Rev. Chem.*, 2018, **2**, 396-408.
2. S. Padmanaban, G. H. Gunasekar and S. Yoon, *Inorg. Chem.*, 2021, **60**, 6881-6888.
3. J. B. Curley, C. Hert, W. H. Bernskoetter, N. Hazari and B. Q. Mercado, *Inorg. Chem.*, 2022, **61**, 643-656.
4. W. Kuriyama, T. Matsumoto, O. Ogata, Y. Ino, K. Aoki, S. Tanaka, K. Ishida, T. Kobayashi, N. Sayo and T. Saito, *Org. Process Res. Dev.*, 2011, **16**, 166-171.
5. A. Glüer, M. Förster, V. R. Celinski, J. Schmedt auf der Günne, M. C. Holthausen and S. Schneider, *ACS. Catal.*, 2015, **5**, 7214-7217.
6. A. N. Marziale, A. Friedrich, I. Klopsch, M. Drees, V. R. Celinski, J. Schmedt auf der Gunne and S. Schneider, *J. Am. Chem. Soc.*, 2013, **135**, 13342-13355.
7. C. N. Brodie, L. Sotorrios, T. M. Boyd, S. A. Macgregor and A. S. Weller, *ACS. Catal.*, 2022, **12**, 13050-13064.
8. F. Anke, D. Han, M. Klahn, A. Spannenberg and T. Beweries, *Dalton Trans.*, 2017, **46**, 6843-6847.
9. M. Kass, A. Friedrich, M. Drees and S. Schneider, *Angew. Chem. Int. Ed.*, 2009, **48**, 905-907.
10. T. M. Boyd, K. A. Andrea, K. Baston, A. Johnson, D. E. Ryan and A. S. Weller, *Chem. Commun.*, 2020, **56**, 482-485.
11. C. N. Brodie, T. M. Boyd, L. Sotorrios, D. E. Ryan, E. Magee, S. Huband, J. S. Town, G. C. Lloyd-Jones, D. M. Haddleton, S. A. Macgregor and A. S. Weller, *J. Am. Chem. Soc.*, 2021, **143**, 21010-21023.
12. F. Anke, S. Boye, A. Spannenberg, A. Lederer, D. Heller and T. Beweries, *Chem. Eur. J.*, 2020, **26**, 7889-7899.
13. A. Staubitz, M. E. Sloan, A. P. Robertson, A. Friedrich, S. Schneider, P. J. Gates, J. Schmedt auf der Gunne and I. Manners, *J. Am. Chem. Soc.*, 2010, **132**, 13332-13345.
14. S. Bhunya, T. Malakar and A. Paul, *Chem. Commun.*, 2014, **50**, 5919-5922.
15. E. M. Titova, E. S. Osipova, A. A. Pavlov, O. A. Filippov, S. V. Safronov, E. S. Shubina and N. V. Belkova, *ACS Catal.*, 2017, **7**, 2325-2333.
16. Y. Ruiz-Morales, G. Schreckenbach and T. Ziegler, *Organometallics*, 1996, **15**, 3920-3923.
17. A. T. Lubben, J. S. McIndoe and A. S. Weller, *Organometallics*, 2008, **27**, 3303-3306.
18. B. R. James and E. Ochiai, *Can. J. Chem.*, 1971, **49**, 975-976.
19. J. P. Collman, M. Kubota and J. W. Hosking, *J. Am. Chem. Soc.*, 1967, **89**, 4809-4811.
20. M. A. Esteruelas, J. Herrero, M. Martín, L. A. Oro and V. c. M. Real, *J. Organomet. Chem.*, 2000, **599**, 178-184.
21. L. M. Aguilera-Saez, J. R. Belmonte-Sanchez, R. Romero-Gonzalez, J. L. Martinez Vidal, F. J. Arrebola, A. Garrido Frenich and I. Fernandez, *Analyst.*, 2018, **143**, 4707-4714.
22. R. Hartmann and P. Chen, *Angew. Chem. Int. Ed.*, 2001, **40**, 3581-3585.

23. A. Hadzovic, D. Song, C. M. MacLaughlin and R. H. Morris, *Organometallics*, 2007, **26**, 5987-5999.
24. A. Friedrich, M. Drees, J. Schmedt auf der Gunne and S. Schneider, *J. Am. Chem. Soc.*, 2009, **131**, 17552-17553.
25. C. A. De Albuquerque Pinheiro, C. Roiland, P. Jehan and G. Alcaraz, *Angew. Chem. Int. Ed.*, 2018, **57**, 1519-1522.
26. T. G. Hill, R. A. Godfroid, J. P. White and S. G. Shore, *Inorg. Chem.*, 1991, **30**, 2952-2954.
27. C. K. Narula, J. F. Janik, E. N. Duesler, R. T. Paine and R. Schaeffer, *Inorg. Chem.*, 1986, **25**, 3346-3349.
28. T. Jurca, T. Dellermann, N. E. Stubbs, D. A. Resendiz-Lara, G. R. Whittell and I. Manners, *Chem. Sci.*, 2018, **9**, 3360-3366.
29. B. L. Davis, B. D. Rekken, R. Michalczyk, E. B. Garner, 3rd, D. A. Dixon, H. Kalviri, R. T. Baker and D. L. Thorn, *Chem. Commun.*, 2013, **49**, 9095-9097.
30. Z. E. Clarke, P. T. Maragh, T. P. Dasgupta, D. G. Gusev, A. J. Lough and K. Abdur-Rashid, *Organometallics*, 2006, **25**, 4113-4117.
31. B. Maryasin and H. Zipse, *Phys. Chem. Chem. Phys.*, 2011, **13**, 5150-5158.
32. I. Koehne, T. J. Schmeier, E. A. Bielinski, C. J. Pan, P. O. Lagaditis, W. H. Bernskoetter, M. K. Takase, C. Wurtele, N. Hazari and S. Schneider, *Inorg. Chem.*, 2014, **53**, 2133-2143.
33. S. Selvarasu, G. Joshi, D. Senthurpandi, M. Nethaji, E. D. Jemmis and B. R. Jagirdar, *Organometallics*, 2024, **43**, 2755-2766.
34. H. Helten, A. P. Robertson, A. Staubitz, J. R. Vance, M. F. Haddow and I. Manners, *Chem. Eur. J.*, 2012, **18**, 4665-4680.
35. M. C. Denney, V. Pons, T. J. Hebden, D. M. Heinekey and K. I. Goldberg, *J. Am. Chem. Soc.*, 2006, **128**, 12048-12049.
36. R. G. Potter, D. M. Camaioni, M. Vasiliu and D. A. Dixon, *Inorg. Chem.*, 2010, **49**, 10512-10521.
37. P. M. Zimmerman, A. Paul, Z. Zhang and C. B. Musgrave, *Inorg. Chem.*, 2009, **48**, 1069-1081.
38. T. Malakar, S. Bhunya and A. Paul, *Chem. Eur. J.*, 2015, **21**, 6340-6345.
39. D. E. Ryan, K. A. Andrea, J. J. Race, T. M. Boyd, G. C. Lloyd-Jones and A. S. Weller, *ACS Catal.*, 2020, **10**, 7443-7448.
40. E. A. K. Spearing-Ewyn, N. A. Beattie, A. L. Colebatch, A. J. Martinez-Martinez, A. Docker, T. M. Boyd, G. Baillie, R. Reed, S. A. Macgregor and A. S. Weller, *Dalton Trans.*, 2019, **48**, 14724-14736.
41. X. M. Chen, N. Ma, Q. F. Zhang, J. Wang, X. Feng, C. Wei, L. S. Wang, J. Zhang and X. Chen, *J. Am. Chem. Soc.*, 2018, **140**, 6718-6726.
42. A. P. Robertson, E. M. Leitao, T. Jurca, M. F. Haddow, H. Helten, G. C. Lloyd-Jones and I. Manners, *J. Am. Chem. Soc.*, 2013, **135**, 12670-12683.
43. M. T. Mock, R. G. Potter, M. J. O'Hagan, D. M. Camaioni, W. G. Dougherty, W. S. Kassel and D. L. DuBois, *Inorg. Chem.*, 2011, **50**, 11914-11928.
44. P. Veeraraghavan Ramachandran and A. S. Kulkarni, *RSC Adv.*, 2014, **4**.
45. Y. Yamamoto, K. Miyamoto, J. Umeda, Y. Nakatani, T. Yamamoto and N. Miyaura, *J. Organomet. Chem.*, 2006, **691**, 4909-4917.
46. D. A. Resendiz-Lara, G. R. Whittell, E. M. Leitao and I. Manners, *Macromolecules*, 2019, **52**, 7052-7064.
47. P. J. Fazen, E. E. Remsen, J. S. Beck, P. J. Carroll, A. R. McGhie and L. G. Sneddon, *Chem. Mater.*, 1995, **7**, 1942-1956.
48. O. T. Beachley, *Inorg. Chem.*, 1968, **8**, 981-985.

49. L. P. Wolters, R. Koekkoek and F. M. Bickelhaupt, *ACS Catal.*, 2015, **5**, 5766-5775.
50. T. M. Townsend, W. H. Bernskoetter, G. W. Brudvig, N. Hazari, H. M. C. Lant and B. Q. Mercado, *Polyhedron*, 2020, **177**.
51. U. Beckmann, D. Süslüyan and P. C. Kunz, *Phosphorus, Sulfur, Silicon, Relat. Elem.*, 2011, **186**, 2061-2070.
52. C. A. Tolman, *Chem. Rev.*, 1977, **77**, 313-348.
53. P. W. Dyer, J. Fawcett, M. J. Hanton, R. D. W. Kemmitt, R. Padda and N. Singh, *Dalton Trans.*, 2003, 104-113.

Chapter 3: The dehydropolymerisation of methyl amine-borane with group 8 $H_2NCH_2CH_2P^iPr_2$ catalysts

3. The dehydropolymerisation of methyl amine-borane with group 8 $H_2NCH_2CH_2P^iPr_2$ catalysts

The aminophosphines $^iPr_2PCH_2CH_2NH_2$ (R = ^{i}Pr, ^{t}Bu) were first reported as ligands for ruthenium-based ketone hydrogenation catalysts such as Ru($^iPr_2PCH_2CH_2NH_2$)$_2Cl_2$ (**8**), where their very low catalyst loadings (as low as 0.0001 mol%) and operation under mild conditions (e.g. 40 °C) was noted.[1] Complex **8** was later used as a precatalyst by Fagnou et al. for the rapid dehydrogenation of $H_3B{\cdot}NH_3$ and $H_3B{\cdot}NH_2Me$ where up to 2 equivalents of H_2 per amine-borane were released, however under the conditions reported dehydrocoupling was unselective and did not primarily form polyaminoboranes. [2] The suggested mechanism of operation in both of these cases where **8** acts as a precatalyst is the same: H_2 transfer to or from a ruthenium hydride active catalyst, facilitated by an adjacent nitrogen atom in a ligand cooperative fashion (see section **1.4**) (**Figure 90**).[2, 3]

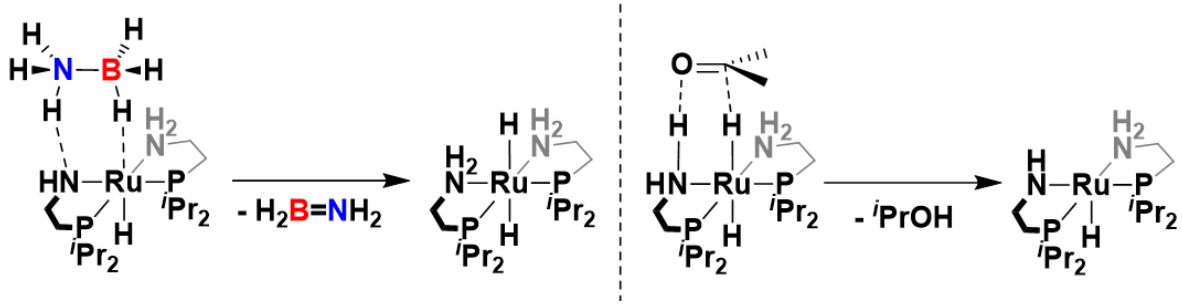

Figure 90. Left: the proposed metal-ligand cooperative dehydrogenation of ammonia borane across a ruthenium nitrogen bond in a ruthenium aminophosphine amido hydride complex, forming an aminoborane and a ruthenium dihydride. [2] **Right:** the proposed metal-ligand cooperative hydrogenation of a ketone (acetone) by an adjacent ruthenium aminophosphine amine and hydride, forming isopropanol and a ruthenium amido hydride. [3, 4]

Interestingly, in dehydrogenations of amine-boranes with complex **8** the first equivalent of hydrogen was released extremely rapidly, in some cases <10 s, possibly forming polyaminoboranes which are then further dehydrogenated. This first equivalent of H_2 was released significantly faster than by MACHO-based group 9 catalysts such as **2** (Rh(^{i}Pr-PN^{H}P)H_2Cl), **5** (Co(^{i}Pr-PN^{H}P)Cl_2), or **6** (Co(Cy-PN^{H}P)Cl_2) for which dehydropolymerisations typically take ~1000 s to reach completion. [2, 5, 6] This made complex **8** a good candidate for the dehydropolymerisation of larger *N*-alkyl substituted amine-boranes, where outpacing poisoning by BH_3 is key (see **2.1.6**), if the selectivity of the catalyst could be tuned to prevent over-dehydrogenation. The ^{t}Bu derivative of

8 ($Ru(^tBu_2PCH_2CH_2NH_2)_2Cl_2$) has been reported to unselectively dehydrocouple *sec*-butylamine-borane, releasing up to 2 equivalents of H_2, when heated above 60 °C. [7]

Another advantage to rapid catalysis may be the ability to form polyaminoboranes with a higher degree of polymerisation (longer chain length). The degree of polymerisation (*DP)* for a simplified chain growth mechanism (such as in anionic chain polymerisation) is proportional to the rate of chain propagation divided by the rate of chain termination (**Equation 2**).[8] This may mean that for a fast dehydrogenation catalyst such as **8**, assuming that chain termination is catalyst-independent, high degrees of polymerisation for the formed polyaminoboranes may be possible. For the catalytic dehydropolymerisation of amine-boranes, the calculated energy barrier to the chain-end polymerisation of aminoboranes ($\Delta G^{\ddagger}$ = 7.8 kcal mol^{-1}) [9] is much lower than the typical free energy barrier to amine-borane dehydrogenation ($\Delta G^{\ddagger}$ = 15 – 25 kcal mol^{-1}) [2, 5, 10], and therefore at a first approximation the rate of polymer chain propagation is dependent on the rate of catalytic dehydrogenation in which the aminoborane monomer is formed.

$$DP \propto \frac{k[Prop]}{k[Term]}$$

Equation 2. The relationship between the rates of chain termination and chain propagation with the degree of polymerisation for a chain polymerisation mechanism.[8]

Under the conditions used by Fagnou et al. where **8** (0.5 mol%) is activated by 30 equivalents of ^tBuOK, polyaminoborane $(H_2BNHMe)_n$ was formed with low selectivity from $H_3B{\cdot}NH_2Me$ (mol dm^{-3} in THF) only when the reaction was stopped after 1 equivalent of H_2 was released. However, unselectively dehydrocoupled products such as borazines were formed if the reaction was allowed to continue, overall releasing 2 equivalents of H_2.[2] Complex **8** was evaluated as an amine-borane dehydropolymerisation catalyst in a subsequent publication by Manners et al., where $(H_2BNHMe)_n$ was formed from $H_3B{\cdot}NH_2Me$ when catalysis was performed at –20 °C. [11] The polymer formed was analyzed by GPC where it was found to be of low molecular weight and relatively wide dispersity (M_n = 9000 g mol^{-1}, dispersity = 2.5). [11] It was also reported that the active catalyst species generated by **8** seemed to attack polymer

$(H_2BNHMe)_n$ in solution at temperatures above –10 °C, likely forming trimethylborazine $(HBNMe)_3$, however no further details were given. [11]

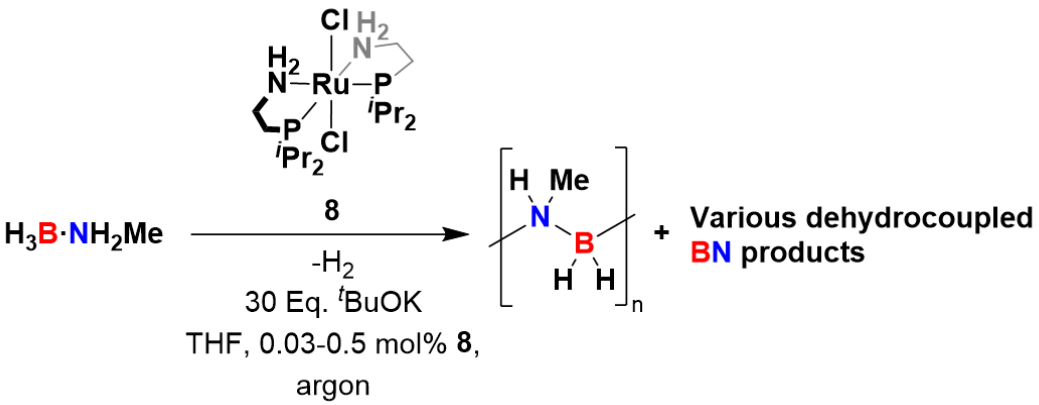

Figure 91. The reported dehydrocoupling of $H_3B{\cdot}NH_2Me$ by precatalyst **8**. [2, 11]

3.1 The dehydropolymerisation of $H_3B{\cdot}NH_2Me$ with 8 and ^tBuOK

In an attempt to use complex **8** to synthesize polyaminoboranes selectively, the dehydropolymerisation of $H_3B{\cdot}NH_2Me$ was performed under varying conditions: 30 equivalents (the same as used by Fagnou et al. and Manners *et al*), 2 equivalents or no ^tBuOK were used, with 0.33 mol% of precatalyst **8** and 1 mol dm^{-3} of $H_3B{\cdot}NH_2Me$ in THF solution (**Figure 92**).[2, 11] For reaction of **8** with 30 equivalents of ^tBuOK prior to addition to the amine-borane, dehydrogenation was immediate and at a rate too fast for eudiometric measurement, resulting in some of the produced H_2 escaping from the bottom of the eudiometric apparatus before the water could be displaced. This resulted in no recorded hydrogen evolution plot. Approximately 1 equivalent of H_2 was released in under 5 seconds, with a further 0.5 equivalents released over the course of 3 minutes. An in-situ ^{11}B NMR spectrum recorded after 5 minutes showed the presence of a wide range of dehydrocoupled products similar to that reported by Fagnou et al. These varied from $(H_2BNHMe)_n$ short chain oligomers, linear dimer $H_3BNHMeBH_2NH_2Me$ and $(HBNMe)_3$ to borazines and $HB(NHMe)_2$ (**Figure 93**).[2]

Reaction of **8** with only 2 equivalents of ^tBuOK before addition to the $H_3B{\cdot}NH_2Me$, resulted in no induction period and the immediate extremely rapid release of ~1 equivalent H_2. This was rapid enough for some of the produced H_2 to escape from the bottom of the eudiometric apparatus before the water could be displaced. The in-situ ^{11}B NMR spectrum recorded after H_2 evolution had ceased showed the selective formation (>99 %) of polyaminoborane $(H_2BNHMe)_n$ and compete conversion of the $H_3B{\cdot}NH_2Me$ (**Figure 94**). This polymer was precipitated from the reaction mixture with pentane and analyzed by GPC, which found a M_n of 70,500 g mol^{-1} and $Đ$ of 1.8.

When only precatalyst **8** was used without added ^tBuOK, a long induction period of ~ 4 hours was observed where no catalysis took place, after which 1 equivalent of H_2 was released in under 5 seconds. The induction period length made recording kinetic data via producing a hydrogen evolution plot difficult. The in-situ ^{11}B NMR spectrum recorded after H_2 evolution had ceased, showed the selective formation of polyaminoborane $(H_2BNHMe)_n$ and complete conversion of the $H_3B{\cdot}NH_2Me$ substrate (**Figure 95**). The polyaminoborane precipitated from this reaction mixture with pentane was analyzed by GPC and found to have an M_n of 50,000 g mol^{-1} and a dispersity of 1.5, comparable to the polymers produced by Rh MACHO precatalysts **1** and **2**.

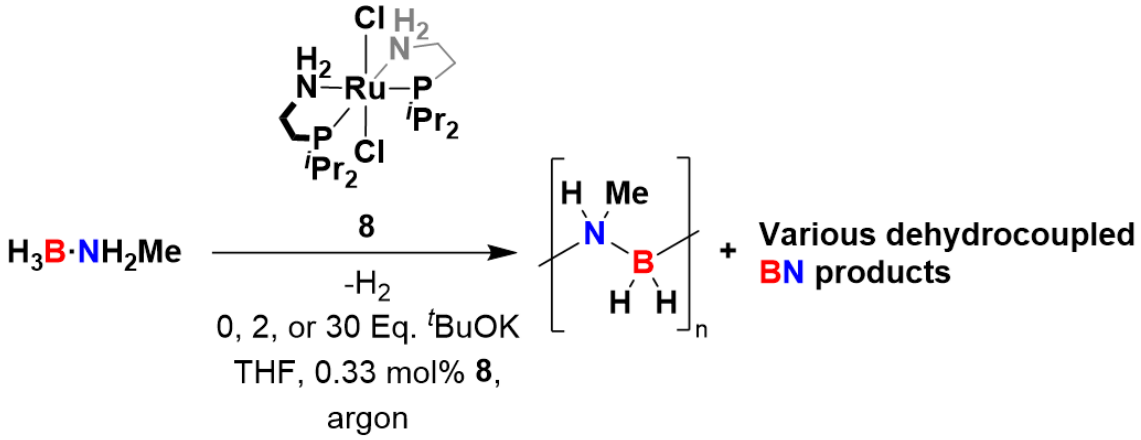

Figure 92. The attempted dehydropolymerisation of $H_3B{\cdot}NH_2Me$ (1 mol dm^{-3} in THF) by precatalyst **8** (0.33 mol%) with varying ^{t}BuOK added: 0, 2 or 30 equivalents.

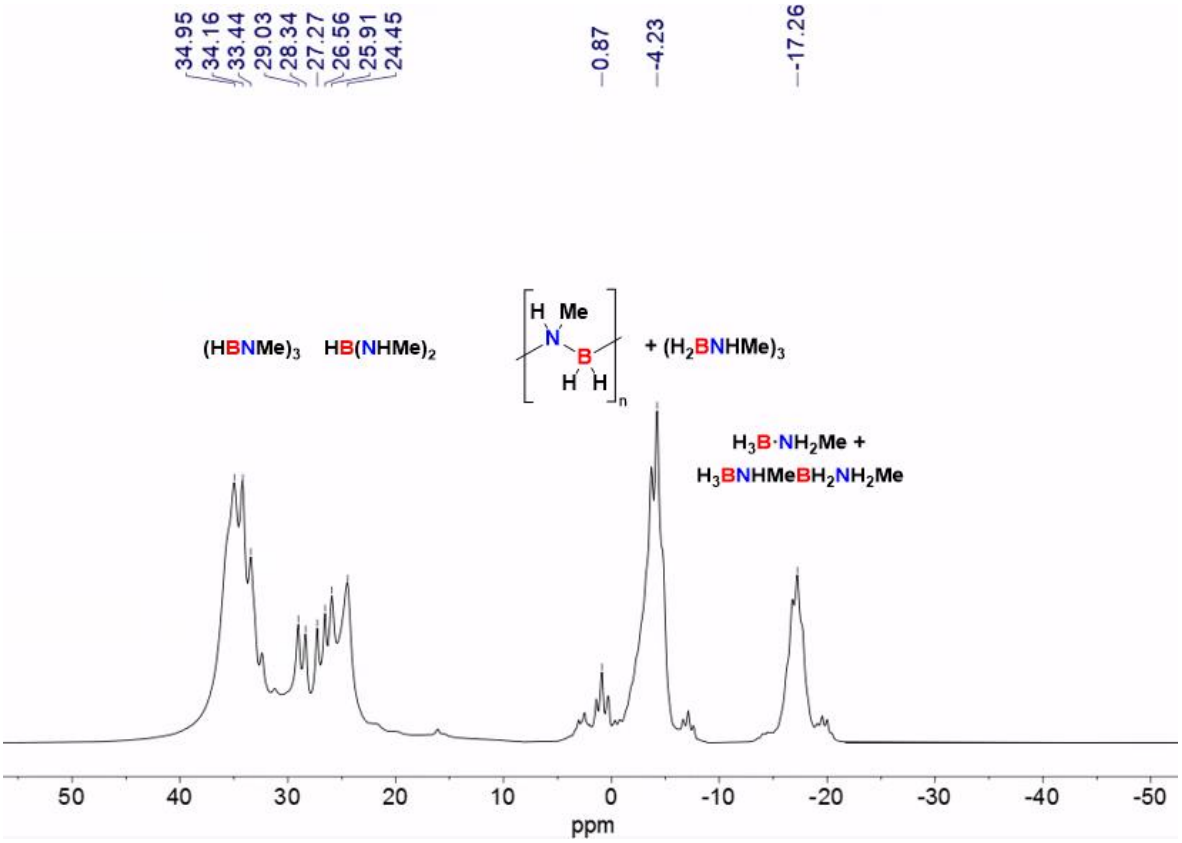

Figure 93. In-situ ^{11}B NMR spectrum from the unselective dehydrocoupling of $H_3B{\cdot}NH_2Me$ (1 mol dm^{-3} in THF) by **8** (0.33 mol%), with 30 equivalents of ^{t}BuOK added. A mixture of dehydrocoupled products is observed.

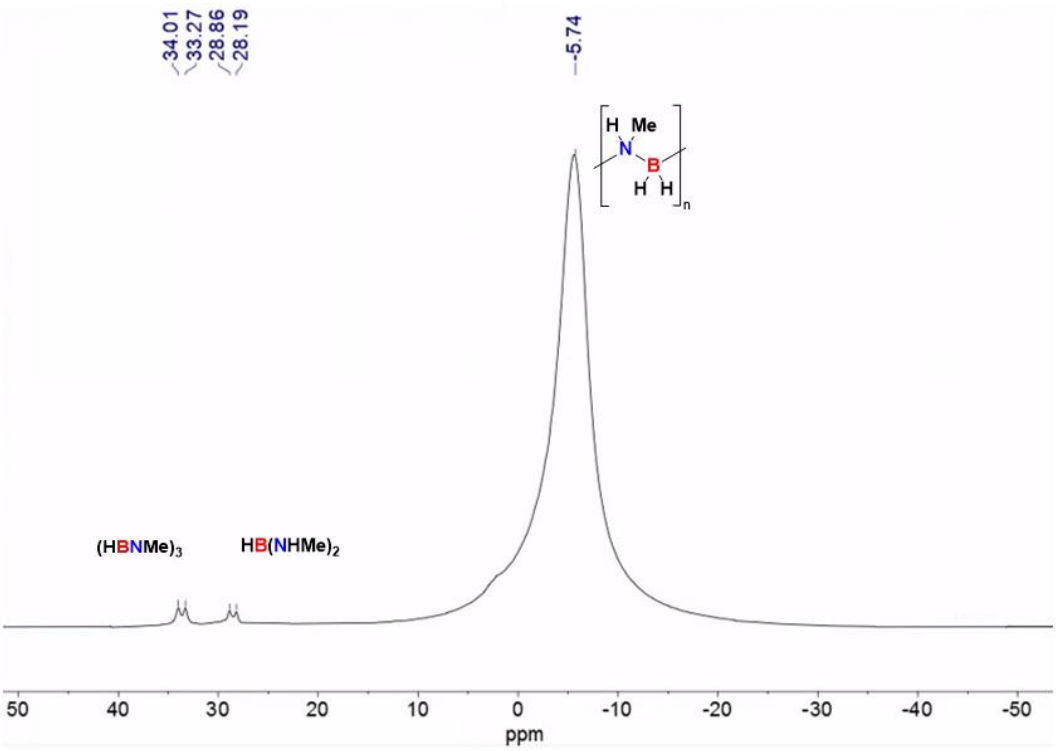

Figure 94. In-situ ^{11}B NMR spectrum from the selective dehydropolymerisation of $H_3B{\cdot}NH_2Me$ (1 mol dm^{-3} in THF) by **8** (0.33 mol%), with 2 equivalents of ^{t}BuOK added. Primarily polyaminoborane $(H_2BNHMe)_n$ is observed, very small amounts of $HB(NHMe)_2$ and borazine $(HBNMe)_3$ are also formed.

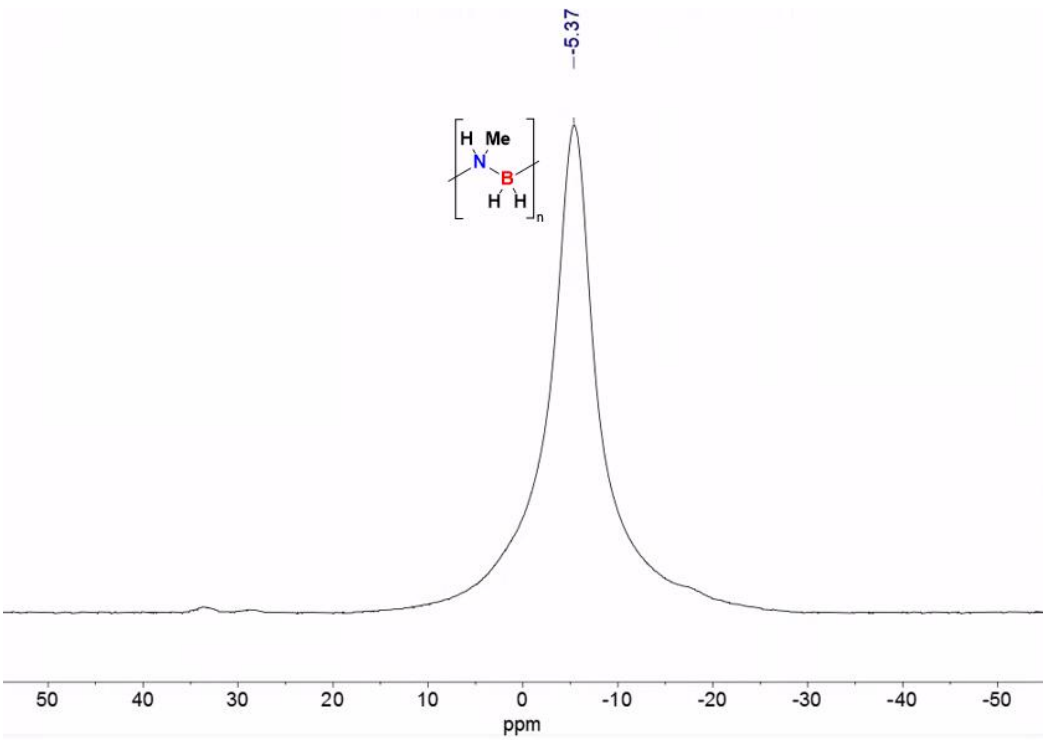

Figure 95. In-situ ^{11}B NMR spectrum from the selective dehydropolymerisation of $H_3B{\cdot}NH_2Me$ (1 mol dm^{-3} in THF) by **8** (0.33 mol%), with no ^{t}BuOK added. Only polyaminoborane $(H_2BNHMe)_n$ is observed.

These results show for the first time that ruthenium aminophosphine complex **8** can be effectively used for the selective dehydropolymerisation of amine-borane $H_3B{\cdot}NH_2Me$. Precatalyst **8** shows significantly higher rates of catalysis than previously reported dehydropolymerisation precatalysts such as **1** and **2**, with complete hydrogen evolution completed in under 10 seconds compared to **1** and **2** which typically take > 1500 and 500 seconds respectively (all at 0.3 – 0.5 mol% with 1 mol dm^{-3} $H_3B{\cdot}NH_2Me$ in THF). [5] Kinetic data from this catalyst system will be discussed in detail later in the section **3.3**. When activated with ^{t}BuOK, **8** rapidly forms an active catalytic species, which when in the presence of excess ^{t}BuOK (30 equivalents) appears to over-dehydrogenate amine-boranes releasing >1 equivalent of H_2. This was demonstrated by adding **8** (0.5 mol%) and 30 equivalents of ^{t}BuOK to a pre-prepared sample of polyaminoborane $(H_2BNHMe)_n$, upon which H_2 was released rapidly and the in-situ ^{11}B NMR spectrum recorded showed an array of products similar to that when **8** and 30 equivalents of ^{t}BuOK is added to $H_3B{\cdot}NH_2Me$ (see supplementary **Figure S1**). $(H_2BNHMe)_n$ is not rapidly dehydrogenated by ^{t}BuOK alone. In-situ $^{31}P\{^1H\}$ NMR spectra were recorded for these preliminary experiments and the speciation of this catalyst system will be discussed later (see **3.5**).

3.2 The activation of precatalyst 8 with 2 equivalents of ^{t}BuOK to form *P,P-trans*-Ru(^{i}Pr$_2$PCH$_2$CH$_2$NH)$_2$ (9)

To understand the activation of **8** with ^{t}BuOK, an investigation into the speciation was performed. Upon the addition of 2 equivalents of ^{t}BuOK to a THF solution of **8** in an NMR tube, the solution slowly turned from a pale orange to a deep pink over the course of 15 minutes. This pink solution was analyzed by ^{31}P{^{1}H} NMR spectroscopy, where conversion of **8** (65 ppm) to a new phosphorous-containing species at 70.5 ppm was observed (**Figure 97**).[1] The ^{1}H NMR spectrum showed no hydride signals in the region of 0 to –40 ppm. This newly formed species was extremely sensitive to air, with rapid decomposition resulting in dark green coloration of the solution and loss of ^{31}P{^{1}H} NMR signals. This reaction was scaled up to use 20 mg of **8**, and the THF solvent then removed in-vacuo. The dark pink residue was then extracted in a small amount of pentane and cooled to –80 °C for two days to induce crystallization (see experimental **4.3.3** for further details).

The resulting extremely air sensitive pink crystals were analyzed by single crystal x-ray crystallography and a crystal structure obtained (**Figure 96**). The molecular structure showed a square-planar complex formed by the dehydro-dehalogenation of **8**, where the aminophosphine ligands had rearranged from the cis-phosphine configuration to having trans-phosphines. The crystals were well-diffracting, with an R_{int} of 0.029 for the space group P-1. The R_1 of 0.034 suggests excellent agreement between the observed and calculated structure factors, validating the model. The N–H protons, located in the electron density map, were found to lie along the Ru–N–C plane with the sum of all angles around N1 = 360°. This suggests that the N atom is sp^2-hybridised. The Ru–N distance was also found to be significantly shorter than in **8** (1.931(2) Å vs 2.174(3) Å), suggesting a bond order higher than 1. [1] This allowed assignment of this species to be the bis-amido ruthenium complex *P,P-trans*-Ru(^{i}Pr$_2$PCH$_2$CH$_2$NH)$_2$ (**9**). The isopropyl CH$_3$ carbon atoms do not make a close approach to the ruthenium atom, with the minimum Ru···C distance being 3.7 Å. This suggests no agostic or anagostic interactions are present with the ligand isopropyl groups, which typically show M···C distances of significantly less than 3.5 Å for 4d metals. [12] No residual electron density was detected above and below the P–Ru–N plane, ruling out the possibility of a hydride complex such as *P,P-trans*-Ru(^{i}Pr$_2$PCH$_2$CH$_2$NH)$_2$(H)$_2$.[13-16]

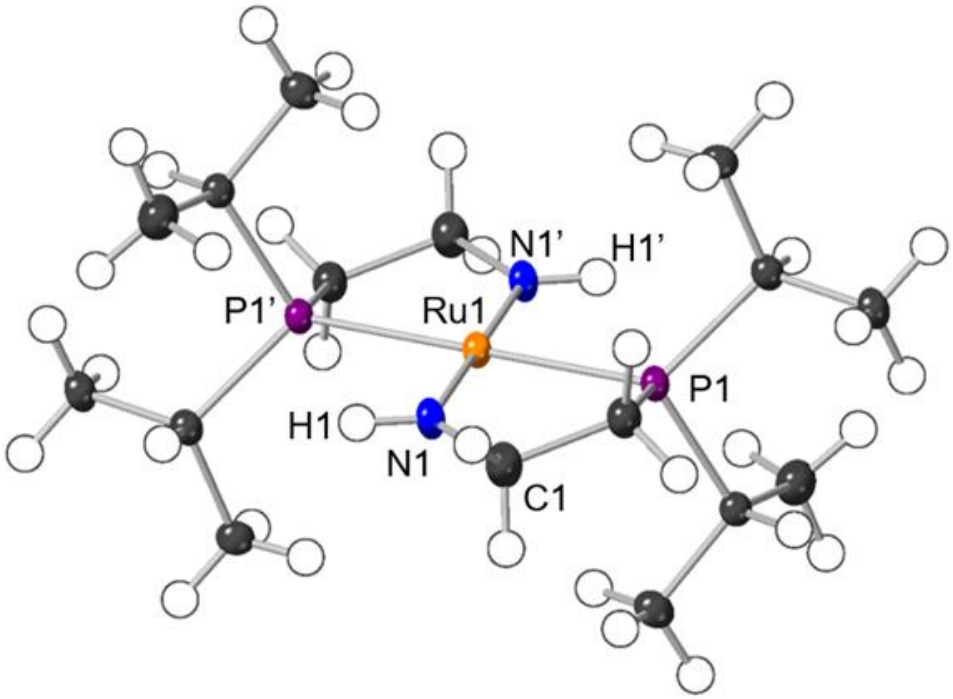

Figure 96. Molecular structure of *P,P-trans*-Ru(^{i}Pr$_2$PCH$_2$CH$_2$NH)$_2$ (**9**) as determined by single crystal X-ray diffraction. Displacement ellipsoids are shown at the 50% probability level. Hydrogen atoms are placed in calculated positions apart from H1/H1' that was located in the final difference map. Selected bond lengths [Å] and angles [°]: Ru(1) – N(1) 1.931(2), Ru(1) – P(1) 2.2943(6), C(1) – N(1) 1.473(3); P(1) – N(1) – Ru(1) 82.45(7), P(11) – Ru(1) – N(1) 97.55(7), N(1) – Ru(1) – N(11) 180.0, P(1) – Ru(1) – P(11) 180.00(3), C(1) – N(1) – Ru(1) 127.67(18).

^{31}P{^{1}H} and ^{1}H NMR analysis of the bulk sample of complex **9** supported the structural assignment. Upon dissolution in cyclohexane-d$_{12}$, a single peak is observed in the ^{31}P{^{1}H} NMR spectrum at 74.4 ppm that corresponds to equivalent ligand phosphines. The ^{1}H NMR spectrum shows a broad signal at 5.95 ppm corresponding to the N–H protons (2H), this is significantly shifted from complex **8** which has a shift of 3.65 ppm for its NH$_2$ protons (4H), further supporting suggestion that the ligand N atoms are sp^2-hybridised.[1] Only two isopropyl CH$_3$ environments are present in the ^{1}H NMR spectrum, suggesting high symmetry in solution as strongly roofed doublets of doublets at 1.37 and 1.22 ppm (both J_{HH} = 7.0 Hz, J_{HP} = 7.0 Hz). These signals collapse to doublets upon phosphorous decoupling. No hydride signals were detected in the ^{1}H NMR spectrum (0 to – 40 ppm) (see experimental **4.3.3** for further details). The reaction of 1 equivalent of ^{t}BuOK (instead of 2 equivalents) with complex **8** results in a mixture of **8** and **9** observed by ^{31}P{^{1}H} NMR spectroscopy (**Figure 97**). No mono-amido intermediate is observed suggesting that it is not isolable.

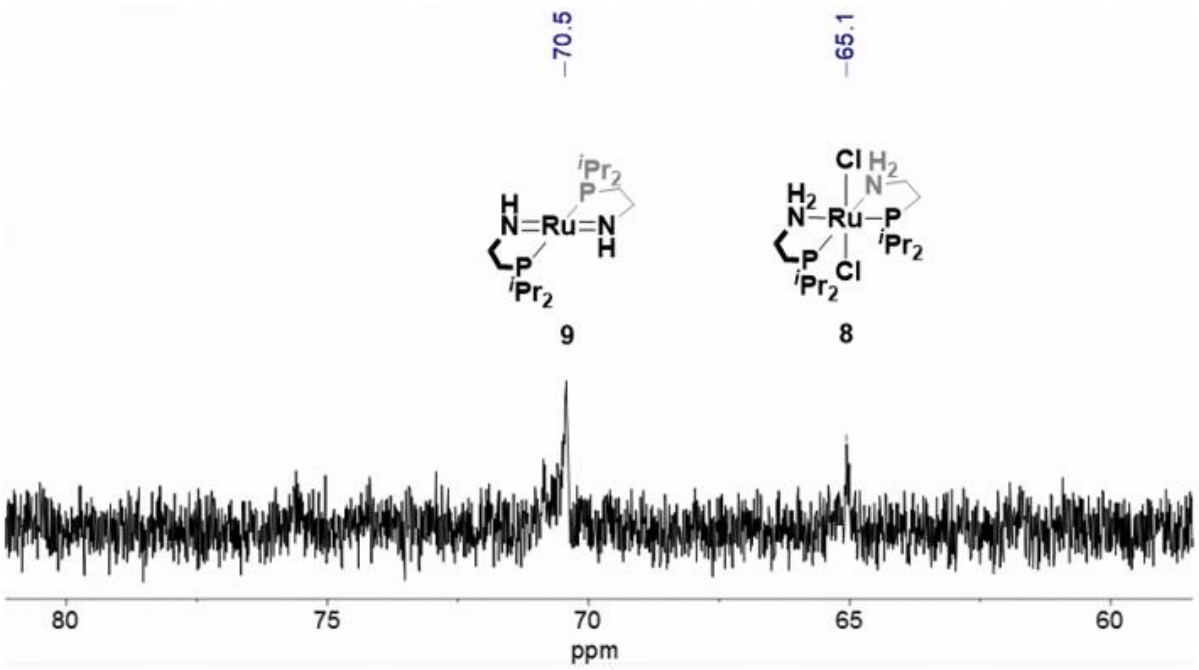

Figure 97. $^{31}P\{^{1}H\}$ NMR spectrum of the NMR scale reaction between **8** and 1 equivalent of ^{t}BuOK, showing some unreacted **8** at 65 ppm and a new peak at 70.5 ppm corresponding to **9**.

3.2.1 The proposed electronic structure of 9

The structure of **9** is of fundamental interest due to its unusual combination of d^6 electron count at the ruthenium and square-planar geometry. This combination is rare, and even more so that the complex is low-spin (S = 0). Other known Ru d^6 square-planar complexes are based on mono-amido MACHO ligands such as $Ru[N(CH{=}CHP^tBu_2)_2]Cl$ and $Ru\{N[Si(CH_3)_2CH_2P^tBu_2]_2\}Cl$ and are paramagnetic with S = 1 (**Figure 98**). [13-15] The first example of a low-spin, square-planar d^6 ruthenium complex, reported by Schneider et al., is MACHO complex $Ru[N(CH_2CH_2P^tBu_2)_2]Cl$. It is reported to be stabilised in the S = 0 spin state by the strong π-donation from the filled nitrogen p_z orbital into the ruthenium non-bonding d_{xz} orbital.

The diamagnetic nature of complex **9** was determined by ^1H NMR spectroscopy where no peak shifting or broadening was observed, which would be expected for a paramagnetic species (S > 0). [16-18] To the best of my knowledge complex **9** represents the newest example of a d^6, square-planar, low spin complex, where only two are previously reported ($Ru[N(CH_2CH_2P^tBu_2)_2]Cl$ and $[Ir\{N(CH_2CH_2P^tBu_2)_2\}Cl][PF_6]$),and is the second ever featuring a ruthenium centre (**Figure 98**).[15, 19-21]

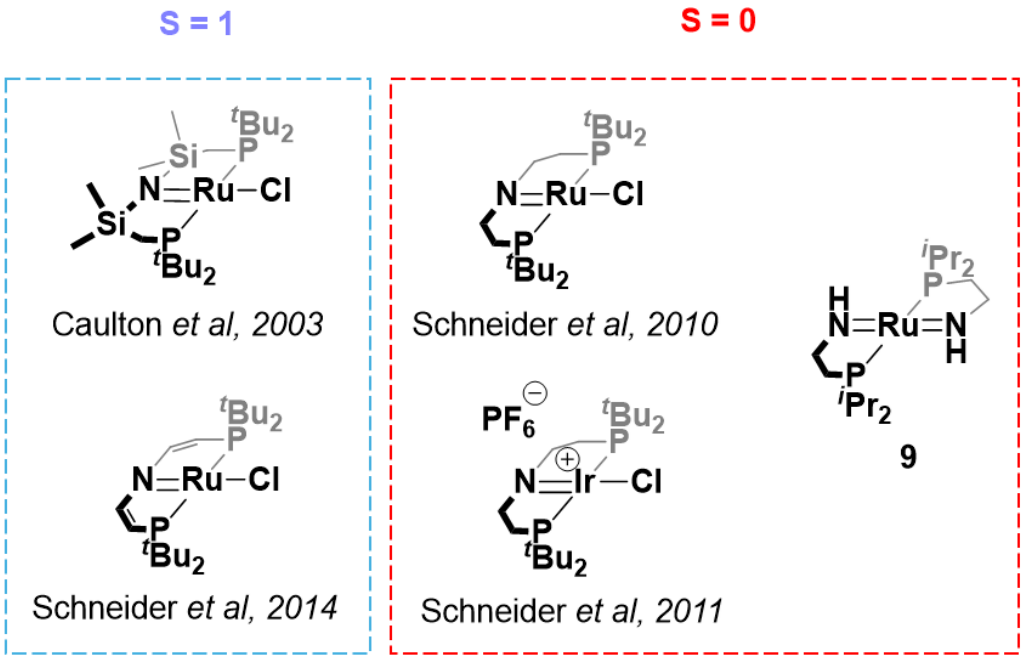

Figure 98. Examples of reported square-planar d^6 ruthenium complexes, showing two examples of S = 1 and the only example of S = 0: $Ru[N(CH_2CH_2P^tBu_2)_2]Cl$. [14, 15, 19] $[Ir\{N(CH_2CH_2P^tBu_2)_2\}Cl][PF_6]$ was also included as the only other reported low spin square-planar d^6 complex. [20]

Group theory and the molecular structure observed by single crystal x-ray crystallography can be used to construct a simple ligand field splitting diagram for complex **9** that helps to explain its unusual electronic properties**.** This can be done by approximating D_{4h} symmetry for the strictly square planar complex, and by assuming the strong σ-donation from the ligand phosphines and amines to be approximately equal.

In a σ-only model for a square-planar d^6 complex the d_{xy}, d_{yz} and d_{xz} orbitals are non-bonding due to the lack of overlap with the ligand orbitals and are of similar relative energies (**Figure 99**). The d_{z^2} orbital is of a slightly higher energy and is weakly-antibonding in combination with the ligand s orbitals. Populating this ligand field splitting diagram with 6 d electrons and 8 electrons from ligand σ-donation gives a paramagnetic (S = 1) 14 electron complex (**Figure 99**).[23] This results in the d_{z^2} orbital being singly occupied, resulting in a triplet (S = 1) ground state.

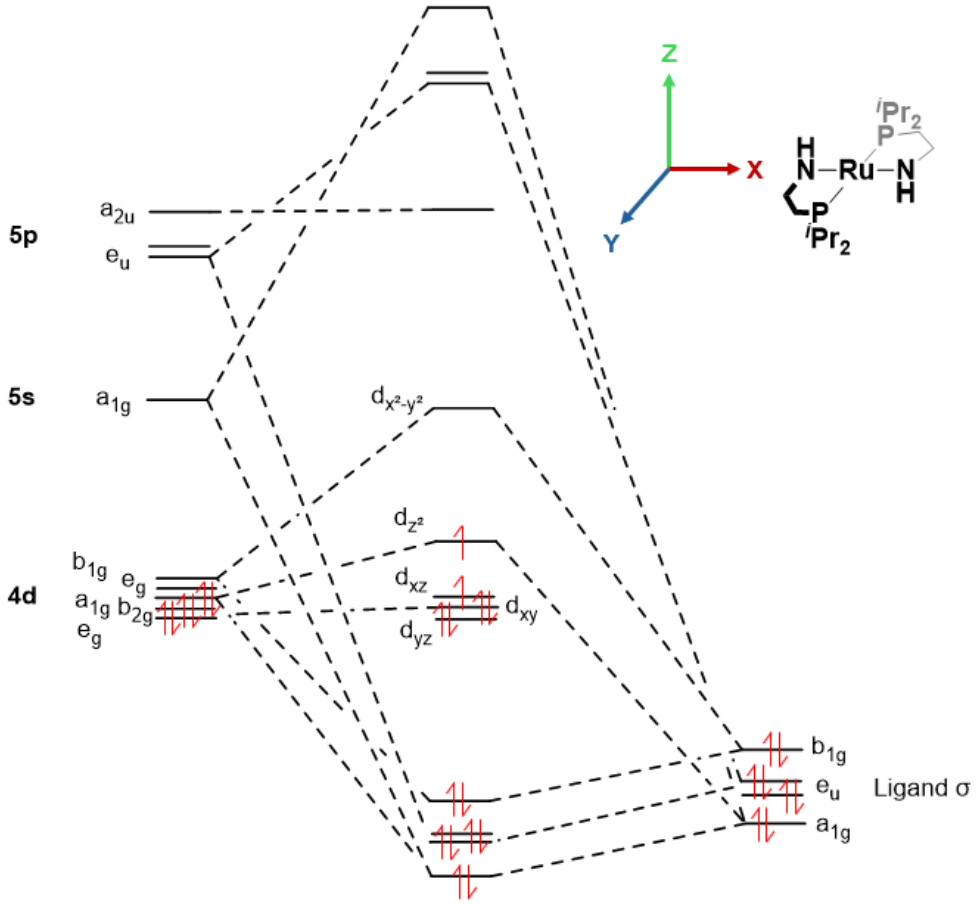

Figure 99. The ligand field splitting diagram of a square planar (D_{4h}) 4d transition metal complex with a d^6 metal centre, considering only ligand σ-donation. The resulting 14 electron complex is in a triplet state where S = 1.

By constructing a ligand field splitting diagram that invokes π-bonding, such as from the amido ligands in complex **9**, the effect on the relative energy levels of d-orbitals explains the observed diamagnetism. In the case of complex **9**, only one set of populated ligand p orbitals are of the correct geometry to form π-bonding interactions with a d-orbital, which are the amido p_z orbitals with e_g symmetry (**Figure 100**). Strong π-donation into the d_{xz} orbital such as by an amido ligand forms a bonding and an antibonding interaction, where the antibonding interaction becomes the new LUMO. In the newly formed orbital arrangement with strong enough π-donors, the energy gap between the d_{xz} and the d_{z^2} becomes larger than the spin pairing energy and so a singlet (S = 0) ground state results (**Figure 100**).[19] This is the apparent case for **9**. Populating this diagram with the 6 4d electrons from the Ru^{II} centre, 6 electrons from the ligand σ-donation and 2 electrons from the ligand amido π-donation gives a total electron count of 16 (**Figure 100**). Although 4 electrons are available in total from the two amido p_z orbital lone pairs, only one d-orbital of appropriate symmetry and orientation is available to donate into (d_{xz}), meaning that a total of two electrons are donated from the two amido ligands.

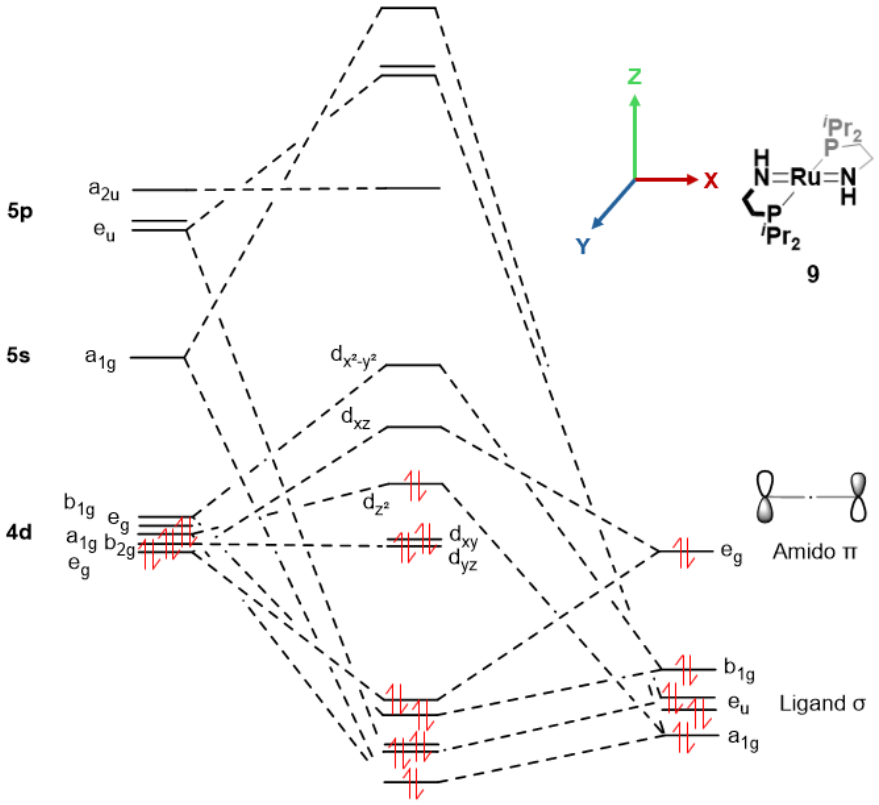

Figure 100. The ligand field splitting diagram of a square planar (D_{4h}) 4d transition metal complex with a d^6 metal centre, with ligand σ and π-donation. The resulting 16 electron complex is in a singlet state where S = 0.

In complex **9**, the strong π-interaction between amido ligand p_z orbitals and the ruthenium d_{xz} orbital strengthens the ruthenium-nitrogen bond. This matches what is observed in the x-ray crystal structure of complex **9**, where the Ru–N bond distance (1.931(2) Å) is shorter than the single bond seen in complex **8** (2.174(3) Å). The Ru–N bond length in complex **9** is typical of Ru(II) amido complexes (~ 1.9 Å). [19, 22]

Orbital energy and electron density isosurface DFT calculations courtesy of Prof. Stuart Macgregor at the University of St. Andrews, optimised from the recorded single crystal x-ray crystal structure of complex **9**, show clearly the Ru–N π-bonding interaction in the HOMO-5, analogous to that reported by Schneider et al. for Ru(N{CH_2CH_2P*t*Bu_2}$_2$)Cl (**Figure 101**).[19] The corresponding antibonding interaction between the d_{xz} and amido p_z orbitals is the LUMO.

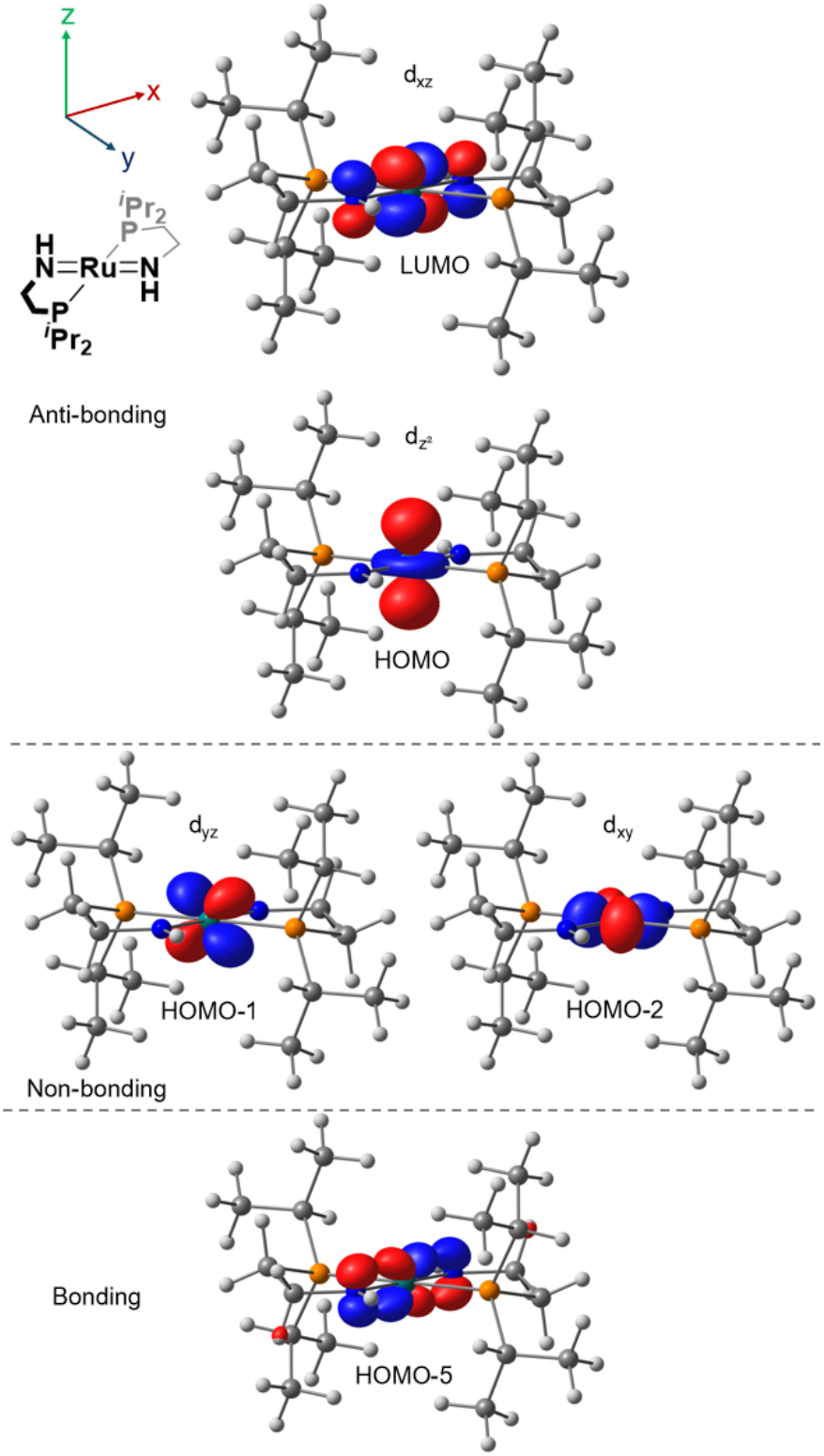

Figure 101. Calculated electron density isosurface models for selected orbitals in **9**, arranged decreasing orbital energy from top to bottom. The π-bonding interaction between the amido p_z orbitals and the ruthenium d_{xz} is seen as the HOMO-5. The corresponding out of phase antibonding interaction is seen as the LUMO. The fifth d-orbital $d_{x^2-y^2}$ (not shown) is the LUMO+1. Courtesy of Prof. Stuart Macgregor at the University of St. Andrews.

3.2.2 Decomposition of 9 into $Ru_2H(\mu_2,\kappa^1\text{-}NHCH_2CH_2P^iPr_2)_2(\mu_2,\kappa^1\text{-}NCH_2CH_2P^iPr_2)(\kappa^2\text{-}^iPr_2PCH_2CH_2NH_2)$ (10)

Complex **9** undergoes facile dimerisation in solution in C_6D_{12} over the timescale of a few hours, turning from pink to a brown colouration. Alkane C_6D_{12} was chosen as the NMR solvent to rule out solvent-induced decomposition of the very reactive complex **9** and to prevent obscuring of the aliphatic region in the ^1H NMR spectrum. The $^{31}P\{^1H\}$ NMR spectrum of this brown solution shows the presence of 4 separate phosphorous environments of approximately equal intensity integrals (60.3, 68.3, 75.1 and 77.6 ppm, all multiplets, **Figure 102**). The ^1H NMR spectrum of this solution shows the presence of a metal-hydride signal at –11.56 ppm that exhibits a complex splitting pattern; the $^1H\{^{31}P\}$ NMR spectrum of this signal shows a sharp singlet suggesting coupling to multiple inequivalent phosphorous environments (**Figure 103**). The hydride splitting pattern was simulated and found to be an overlapped dddd, resulting from coupling to all four inequivalent phosphorous environments with constants J_{HP} = 12, 15, 36 & 61 Hz. The coupling to all 4 phosphorous environment was confirmed by ^1H-^{31}P HMBC NMR spectra. These ^1H and $^{31}P\{^1H\}$ NMR spectrum signals all belong to a single new species, complex **10.**

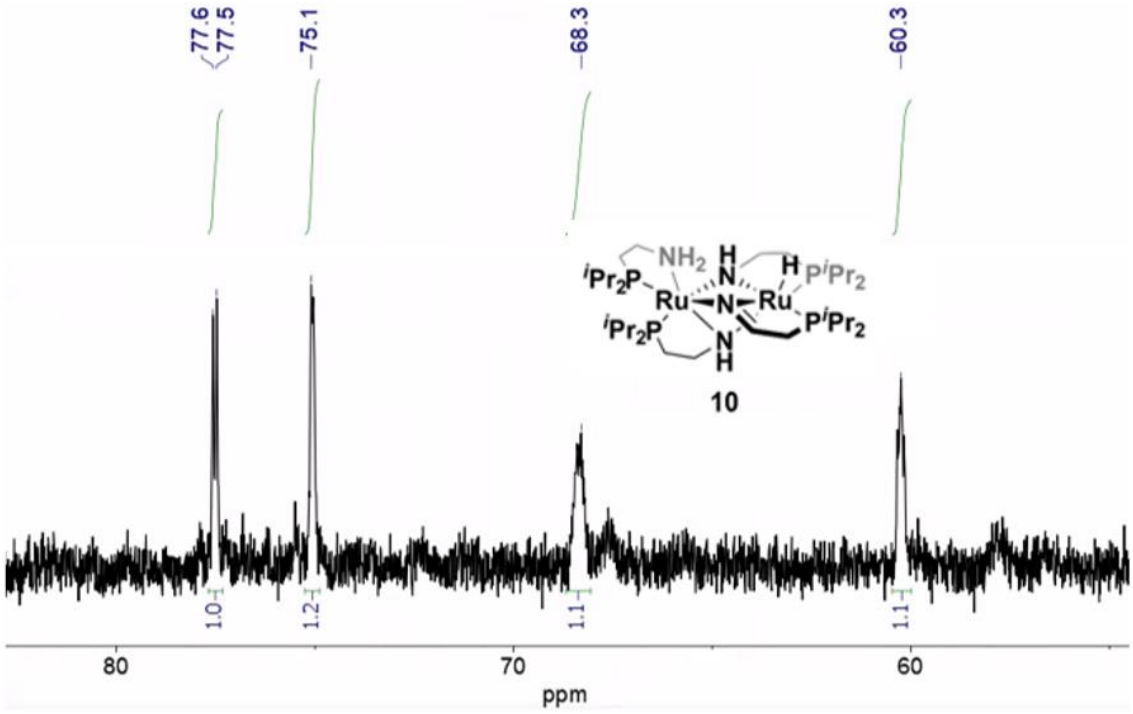

Figure 102. $^{31}P\{^1H\}$ NMR spectrum of a sample of **9** left in solution for 12 hours, showing 4 phosphorous environments corresponding to **10**. Recorded in C_6D_{12} at 298 K.

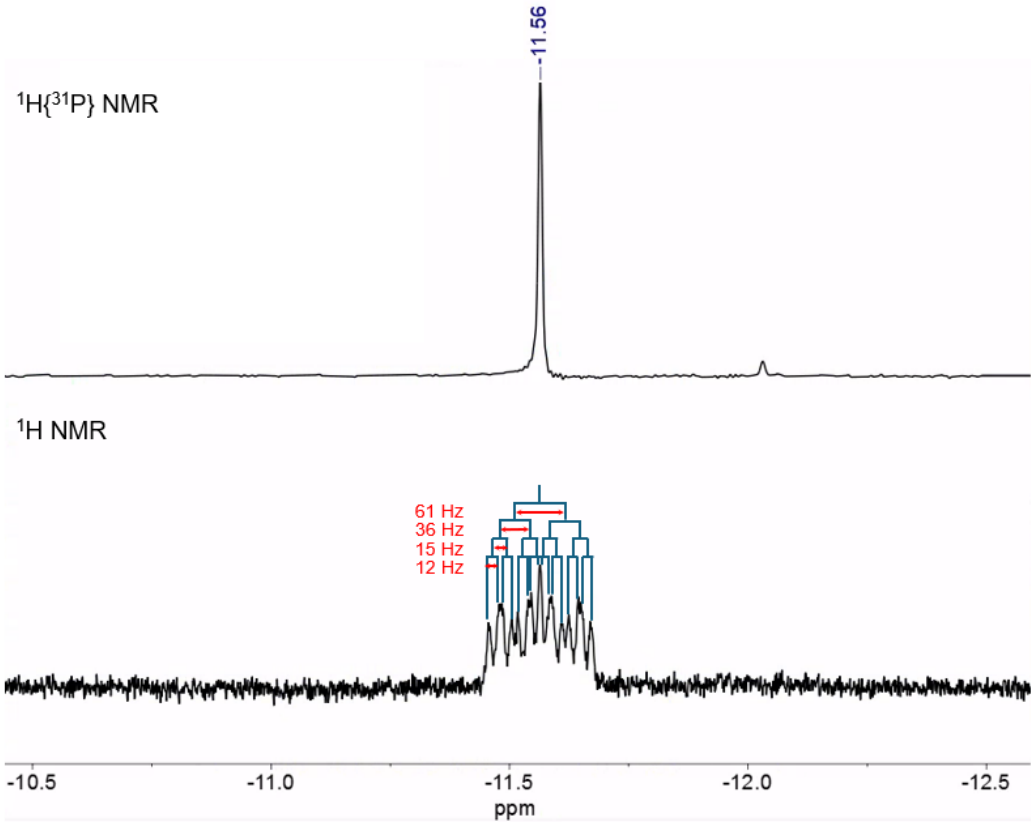

Figure 103. Top: $^{1}H\{^{31}P\}$ NMR spectrum of the ruthenium hydride in **10**, showing a sharp singlet. Bottom: ^{1}H NMR spectrum of the ruthenium hydride in **10**, showing a complex splitting pattern corresponding to coupling to 4 inequivalent phosphorous environments.

To identify the product formed, **9** was left as a concentrated pentane solution overnight, before cooling to –80 °C to grow crystals (see **4.3.4** for details). The resulting brown crystals were analyzed by single crystal x-ray diffraction and a crystal structure was obtained (**Figure 104**). This allowed assignment of this species to be the dimeric ruthenium complex $Ru_2H(\mu_2,\kappa^1\text{-}NHCH_2CH_2P^iPr_2)_2(\mu_2,\kappa^1\text{-}NCH_2CH_2P^iPr_2)(\kappa^2\text{-}{}^iPr_2PCH_2CH_2NH_2)$ (**10**) which exhibits two ruthenium atoms bridged by 3 aminophosphine ligand derived nitrogen atoms. The Ru···Ru distance is 3.004 Å, longer than would be expected for a ruthenium–ruthenium bond (2.6 – 2.8 Å). [23-25] A hydride is present on one of the ruthenium atoms, transferred from the β carbon at the nitrogen end of one of the aminophosphine ligands (**Figure 104**). The crystals were well-diffracting with an Rint of 0.0435 for the space group P-1, and an R1 of 0.0290 that suggests good agreement between the model and observed diffraction data. The full characterisation details for **10**, including 2D-NMR and mass spectrometry are reported in the experimental **4.3.4**.

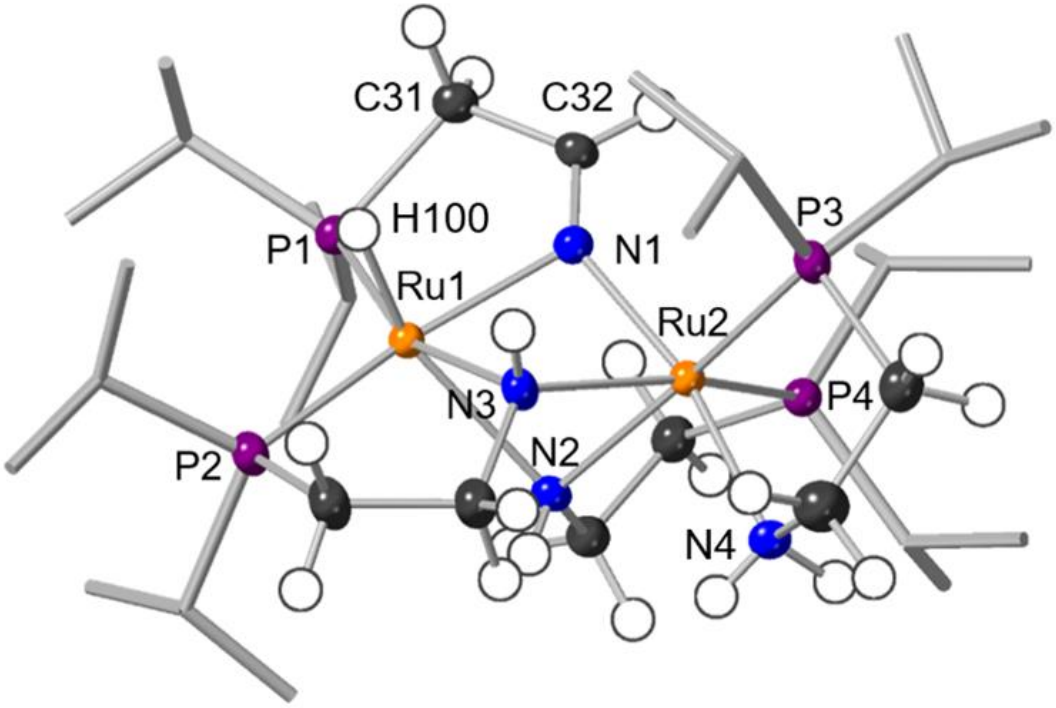

Figure 104. Molecular structure of **10** as determined by single crystal X-ray diffraction. Displacement ellipsoids are shown at the 50% probability level. N–H, Ru–H (H 100) and H32a were located in the difference map and freely refined. All other hydrogen atoms are placed in calculated positions. Selected bond lengths [Å] and angles [°]: N(1) – C(32) 1.263(3), Ru(1) – N(2) 2.059(2), Ru(2) – N(2) 2.159(2), Ru(1) – N(3) 2.159(2), Ru(2) – N(3) 2.178(2), Ru(2) – N(4) 2.178(2), Ru(1) – N(1) 2.059(2), Ru(1) ··· Ru(2) 3.004, C(31) – C(32) – N(4) 120.0(2).

Schneider et al. reported the decomposition of Ru(N{$CH_2CH_2P^tBu_2$}$_2$)Cl (analogous to **9**) via the beta-hydride elimination from the ligand backbone adjacent to the nitrogen atom to form a secondary aldimine and a ruthenium hydride (**Figure 105**).[19] It is likely that **9** also undergoes beta-hydride elimination to form an intermediate monomeric ruthenium hydride which subsequently reacts with a second equivalent of **9** forming the diruthenium species **10** (**Figure 105**). Complex **10** is not catalytically active for the dehydropolymerisation of methyl amine-borane despite featuring an adjacent ligand N–H and Ru–H (N3–H and Ru1–H100), this may be due to significant steric hinderance to the approach of methyl amine-borane caused by the surrounding ^{i}Pr groups and ligand backbones.

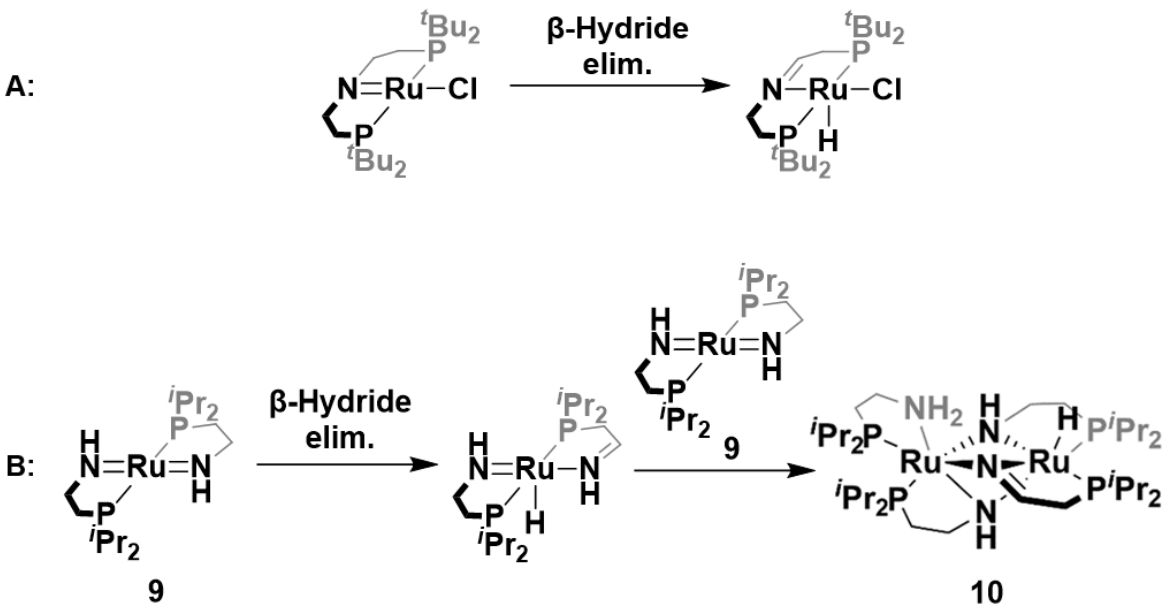

Figure 105. A: the reported decomposition by beta-hydride elimination of the d^6 ruthenium square-planar of Ru(N{$CH_2CH_2P^tBu_2$}$_2$)Cl. [19] B: the proposed beta-hydride elimination and subsequent dimerization of **9** to form diruthenium species **10** with a ruthenium hydride and coordinated aldimine ligand.

3.3 Kinetic analysis of the dehydropolymerisation of $H_3B{\cdot}NH_2Me$ with 8 and ^tBuOK

As the dehydropolymerisation of $H_3B{\cdot}NH_2Me$ with complex **8** at 0.33 mol% with 2 equivalents of ^tBuOK was extremely rapid (1 equivalent of H_2 was released in under 5 seconds) and showed no induction period, catalysis at lower catalyst loadings was attempted in order to record eudiometric hydrogen evolution data as well as establish a lower limit to catalyst loading. Recording eudiometric hydrogen evolution data plots allows for the kinetic analysis of the dehydrogenation step in dehydropolymerisations with complex **8**, which helps to provide the evidence necessary to propose a catalytic mechanism. With 30 equivalents of ^tBuOK, Fagnou et al. reported the activity of complex **8** with $H_3B{\cdot}NH_3$ at 0.03 mol%.[2]

Dehydropolymerisations of $H_3B{\cdot}NH_2Me$ (1 mol dm^{-3} in THF) were attempted with complex **8** (0.01, 0.02, 0.03, 0.04 & 0.05 mol%), which was reacted with 2 equivalents of ^tBuOK to form complex **9** before addition to catalysis (**Figure 106**). The instability of **9** precludes the use of catalyst stock solutions. With 0.02 – 0.05 mol% catalyst loading of complex **8**, 1 equivalent of H_2 was released as measured eudiometrically. This is concordant with in-situ ^{11}B NMR spectra recorded after catalysis which showed complete conversion of $H_3B{\cdot}NH_2Me$ to polymer $(H_2BNHMe)_n$. Hydrogen evolution plotted over time showed lengthy induction periods (800 – 2000 s), that decreased with increasing catalyst loading, followed by a short period of rapid H_2 release (**Figure 107**). This is in contrast to when 0.33 mol% of **8** with 2 equivalents of ^tBuOK was used, for which no induction period was observed.

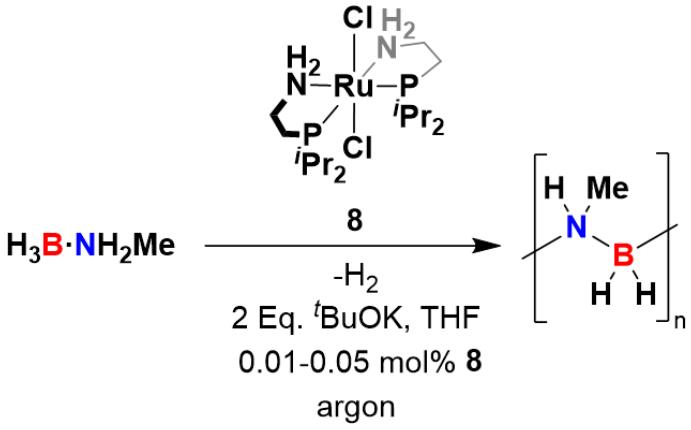

Figure 106. The dehydropolymerisation of $H_3B{\cdot}NH_2Me$ (1 mol dm^{-3} in THF) by precatalyst **8** with varying catalyst loading (0.01 – 0.05 mol%). 2 equivalents of ^tBuOK were added to activate the precatalyst.

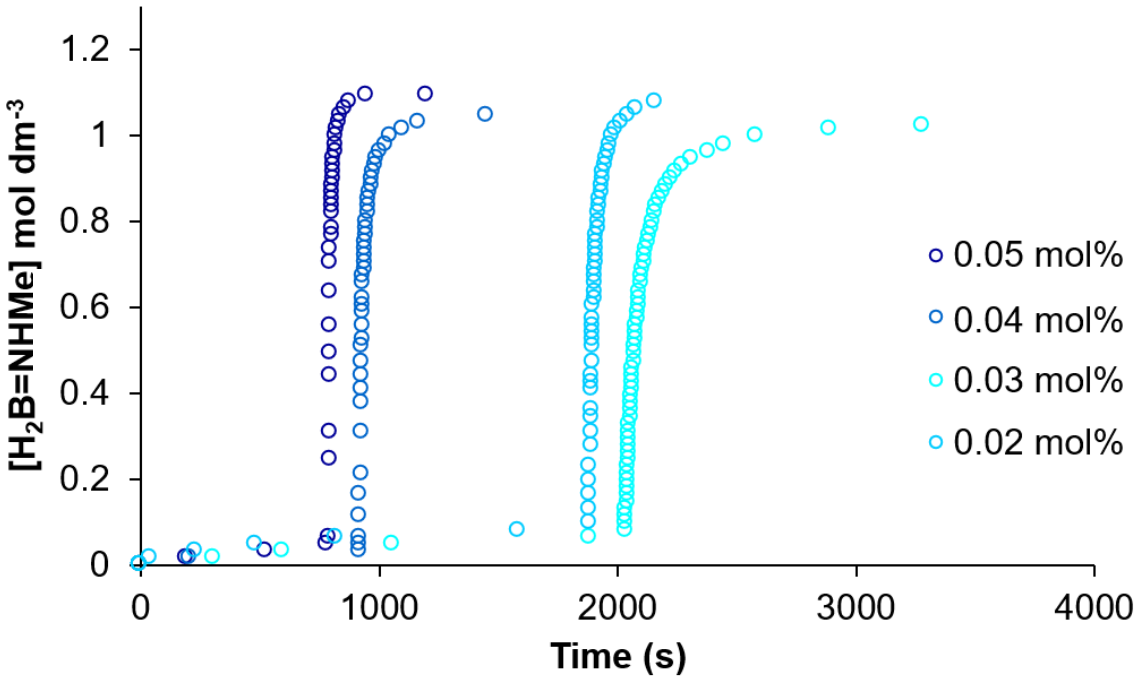

Figure 107. Effective $H_2B{=}NMeH$ concentration over time from eudiometric H_2 evolution measurement for the dehydropolymerisation of $H_3B{\cdot}NH_2Me$ (0.112 g, 1 mol dm^{-3} in THF) by **8** (0.02-0.05 mol%) with 2 equivalents of ^{t}BuOK to catalyst. Induction period is observed to decrease and rate of reaction increase as the amount of catalyst used is increased.

At 0.01 mol%, catalysis does not initiate, no H_2 is released and no conversion of the $H_3B{\cdot}NH_2Me$ substrate is observed by ^{11}B NMR. The ^{11}B NMR spectrum of the sample remained unchanged after 24 hours, showing no evidence of slow dehydropolymerisation. This suggests the presence of a catalyst poison present at very low concentrations which completely deactivates the active catalyst species when less than 0.02 mol% (0.0002 mol dm^{-3}) of **8** is added (discussed further in section **3.5.3**). In-situ $^{31}P\{^1H\}$ NMR spectra recorded after catalysis with 0.05 mol% of **8** show the complete conversion of **8** (65 ppm) to a new species with a signal at 89 ppm (**Figure 108**). No corresponding hydride signals are observed by in-situ ^{1}H NMR. In-situ $^{31}P\{^1H\}$ NMR spectra recorded on catalysis with below 0.05 mol% **8** show no phosphorous signals as the concentration is too low.

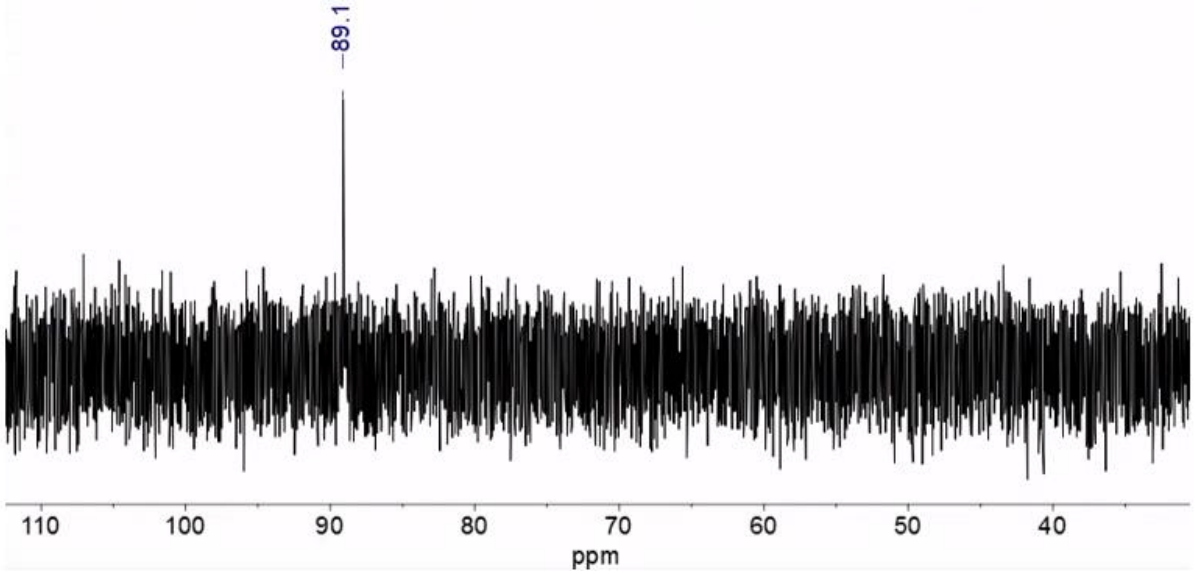

Figure 108. In-situ $^{31}P\{^{1}H\}$ NMR spectrum recorded after catalytic dehydropolymerisation of $H_3B{\cdot}NH_2Me$ (1 mol dm^{-3} in THF) by precatalyst **8** (0.05 mol%) and 2 equivalents to catalyst of ^{t}BuOK. Precatalyst **8** is not observed (singlet, 65 ppm) and a new species is present, singlet, 89 ppm.

The formed polyaminoborane $(H_2BNHMe)_n$ was precipitated from these catalysis runs with an excess of pentane and then analyzed by GPC. The M_n of these polymers is significantly higher than the reactions run at 0.33 mol% catalyst loading but show no clear trend with changes in catalyst concentration (M_n = 89,700 – 141,600 g mol^{-1}, **Table 5**). The M_w is approximately constant at ~ 200,000 g mol^{-1} except for the lowest catalyst loading 0.02 mol% for which the polymer is shorter (M_w = 136,900 g mol^{-1}). The exact reason for this variation in M_w is unclear, however it is likely related to the catalyst poisoning that prevents catalytic activity when using 0.01 mol% of **8**.

Catalyst	$H_3B{\cdot}NMeH_2$ concentration (mol dm^{-3})	Catalyst mol%	$[Ru]_{total}$ (mol dm^{-3})	M_n (g mol^{-1})	M_w (g mol^{-1})	Đ
8 + 2 ^{t}BuOK	1	0.05	0.0005	117,200	200,700	1.71
8 + 2 ^{t}BuOK	1	0.04	0.0004	141,600	202,600	1.43
8 + 2 ^{t}BuOK	1	0.03	0.0003	131,700	201,400	1.48
8 + 2 ^{t}BuOK	1	0.02	0.0002	87,900	136,900	1.56

Table 5. Polymer data obtained by GPC analysis of the $(H_2BNHMe)_n$ formed by the catalytic dehydropolymerisation of $H_3B{\cdot}NH_2Me$ (1 mol dm^{-3} in THF) by **8** (0.02 – 0.05 mol%) with 2 equivalents to catalyst of ^{t}BuOK.

3.3.1 Determination of the order in catalyst and substrate for the dehydropolymerisation of amine-boranes with in-situ generated 9

Hydrogen evolution plots recorded when using **8** activated with two equivalents of ^{t}BuOK to catalyst (generating **9** in-situ) for the dehydropolymerisation of $H_3B{\cdot}NH_2Me$ show an induction period followed by an initially rapid and constant rate of catalysis, and the rate of hydrogen evolution then decreases over the course of the reaction. This is best exemplified in the 0.03 mol% catalysis trace in **Figure 107**. This either suggests a positive order in $H_3B{\cdot}NH_2Me$ substrate for catalysis with this system, where the rate decreases as $H_3B{\cdot}NH_2Me$ concentration decreases, or that the catalyst speciation is changing over the course of the reaction. Previously discussed precatalysts **5** and **6** (Co(^{i}Pr-PN^{H}P)Cl_2 and Co(Cy-PN^{H}P)Cl_2) show a first order dependance on amine-borane concentration, whereas precatalysts **1** and **2** ([Rh(^{i}Pr-PN^{H}P)(NBD)]Cl and Rh(^{i}Pr-PN^{H}P)H_2Cl) show pseudo zero-order in amine-borane. [5, 6] When the substrate in a reaction exhibits first-order reaction kinetics, plotting the natural logarithm of the substrate concentration over time gives a straight line with gradient – kt, where k is the reaction rate constant. This can be derived by integrating the first order rate law (**Equation 3**).

Taking the eudiometric hydrogen evolution data from the dehydropolymerisation of $H_3B{\cdot}NH_2Me$ with **8** plus 2 equivalents of ^{t}BuOK (0.02 – 0.05 mol%) and plotting the data as a function of the natural logarithm of $H_3B{\cdot}NH_2Me$ concentration over time gives the decay profiles shown in **Figure 109**. $H_3B{\cdot}NH_2Me$ concentration can be inferred, as H_2 production is in theory a 1:1 process with $H_3B{\cdot}NH_2Me$ dehydrogenation. The profiles start at a normalized time = 0, and as initial $H_3B{\cdot}NH_2Me$ concentration is 1 mol dm^{-3}, at $\ln[H_3B{\cdot}NH_2Me] = 0$. These decay profiles do not show the linearity expected for a first order dependence of $H_3B{\cdot}NH_2Me$ on catalytic rate. Most notably, the lowest catalyst loading plot in **Figure 109** (0.02 mol%) exhibits a deceleratory curvature over the course of the reaction. This is significantly less deceleration than would be expected for a higher order in substrate (e.g. $[H_3B{\cdot}NH_2Me]^2$). This method of determining order in substrate assumes that the components of the rate law such as catalyst active species remain at steady state concentration, which may not be the case.

One interpretation that could explain the observed rate data is that of saturation kinetics. The substrate $H_3B{\cdot}NH_2Me$ may form an adduct with the active catalyst species in a pre-equilibrium prior to the rate-limiting step. If this equilibrium lies in favor of adduct formation, the $H_3B{\cdot}NH_2Me$ substrate appears pseudo zero-order at high concentration relative to the catalyst concentration. As dehydropolymerisation progresses and $H_3B{\cdot}NH_2Me$ concentration drops significantly, the pseudo zero-order regime may then end due to reduced catalyst adduct formation, therefore resulting in a decrease in rate (and dependance on $[H_3B{\cdot}NH_2Me]$). Such a scenario has been previously reported by Weller et al. for the Rh MACHO catalyst system **3** ($Rh(PN^HP\text{-}^iPr)H_3$) where the formation of an outer-sphere dihydrogen bonded adduct $Rh(PN^HP\text{-}^iPr)H_3{\cdot}H_3B{\cdot}NH_2Me$ results in a pseudo zero-order rate dependence on $H_3B{\cdot}NH_2Me$ concentration. [5]

$$Rate = -\frac{d[A]}{dt} = k[A]^1$$

$$\therefore$$

$$ln[A] = -kt + ln[A]_0$$

Equation 3. The first-order rate law for a reaction and its integrated form that can be plotted in the form y = mx + c to give a straight line. [A] is the concentration of substrate at any given time (t), $[A]_0$ is the initial substrate concentration.

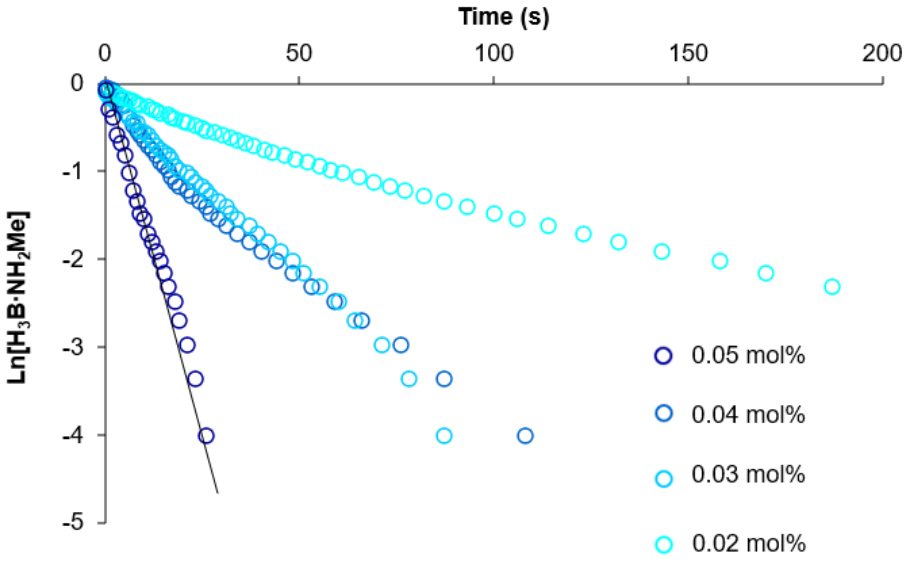

Figure 109. Plots of $ln[H_3B{\cdot}NH_2Me]$ against time where all plots are time normalized so that catalysis starts at t = 0. Original data from eudiometric H_2 evolution measurement for the dehydropolymerisation of $H_3B{\cdot}NH_2Me$ (0.112 g, 1 mol dm^{-3} in

THF) by **8** (0.02-0.05 mol%) with 2 equivalents of ^{t}BuOK to catalyst, generating **9** in-situ.

The eudiometric hydrogen evolution data from catalysis runs with varying catalyst concentration can also be used to determine the order in catalyst. Initial rates of reaction can be measured for each catalyst loading (0.02 – 0.05 mol%) and assuming that all other rate law components are the same between catalysis runs, the effect of catalyst concentration on rate can be found. The initial rates of these catalyst runs were measured by mathematically modelling the hydrogen evolution plot curves (moles of H_2 released against time) and differentiating the approximated functions at time = 0 s. These initial rates were then plotted against catalyst concentration (**Figure 110**). These initial rates however do not show a linear correlation with catalyst concentration (initial concentration of in-situ formed **9,** [cat]) and show a non-zero intercept. One explanation for this is that a low concentration of inhibitor present ([inhb]) is reducing the true catalyst concentration by irreversible poisoning. [26]

The experimental evidence that catalysis did not proceed at 0.01 mol% (0.0001 mol dm^{-3}) of **9** but was rapid at 0.02 mol% (0.0002 mol dm^{-3}) provided upper and lower limits to the concentration of the catalyst inhibitor. By plotting the measured initial rates of catalysis against [cat]-[inhb] and varying [inhb] between 0.0001 and 0.0002 mol dm^{-3}, a linear correlation with an intercept close to (0, 0) was found when [inhb] = 0.00016 mol dm^{-3} (0.016 mol% equivalent) (**Figure 110**).

To provide evidence of the proposed inhibitor concentration of 0.00016 mol dm^{-3} present during catalysis, a dehydropolymerisation of $H_3B{\cdot}NH_2Me$ was attempted with **8** + 2 equivalents of ^{t}BuOK (generating **9**) at 0.016 mol% (0.00016 mol dm^{-3}). The hydrogen evolution plot generated by eudiometric measurement shows that with 0.016 mol% (0.00016 mol dm^{-3}) of precatalyst **9**, catalysis immediately halts after initiation suggesting that this catalyst concentration is close to the inhibitor concentration (~0.00016 mol dm^{-3}) and provides further evidence for the presence of an inhibitor (**Figure 111**). The dehydropolymerisation of $H_3B{\cdot}NH_2Me$ with **8** + 2 equivalents of ^{t}BuOK (generating **9**) at 0.015 mol% (0.00015 mol dm^{-3}) was also attempted, for which no initiation of catalysis was observed after 3 hours. The possible identity of the proposed inhibitor will be discussed later (see **3.5.3**). Overall, the linear correlation between initial rate [cat]-[inhb] suggests a first-order dependence on catalyst concentration. This means that the rate limiting step in the mechanism for amine-

borane dehydropolymerisation with **9** likely involves the reaction of an active catalyst species that is derived from **9**.

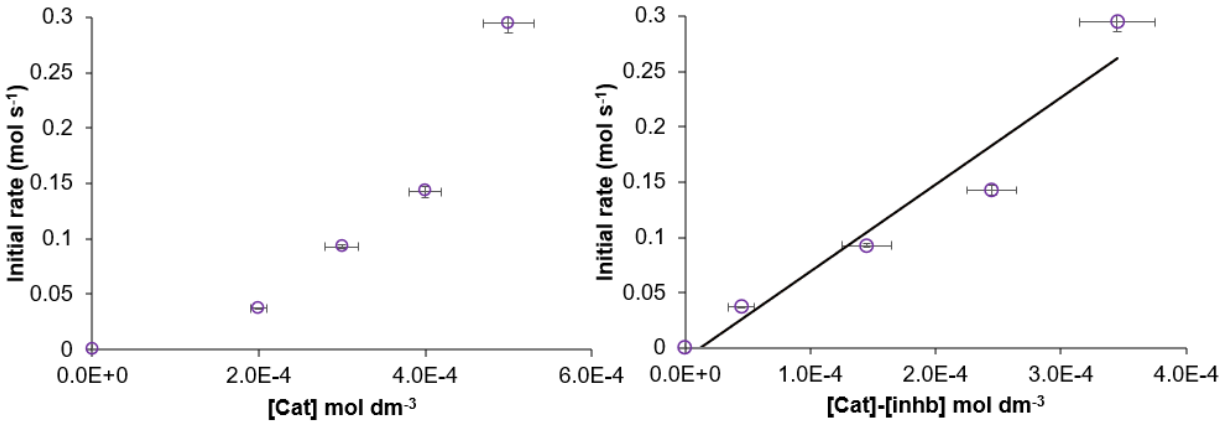

Figure 110. Left: a plot of initial rates of hydrogen evolution measured eudiometrically against catalyst concentration [cat] for the dehydropolymerisation of $H_3B{\cdot}NH_2Me$ (0.112 g, 1 mol dm^{-3} in THF) by **8** (0.02-0.05 mol%) with 2 equivalents of ^{t}BuOK to catalyst, generating **9** in-situ. Right: the same catalysis initial rate data plotted against an adjusted catalyst concentration [cat]–[inhb], where [inhb] is the concentration of a proposed catalyst inhibitor/poison assumed to be 0.00016 mol dm^{-3}. The initial rates of these catalyst runs were measured by mathematically modelling the hydrogen evolution plot curves and differentiating the approximated functions at time = 0 s

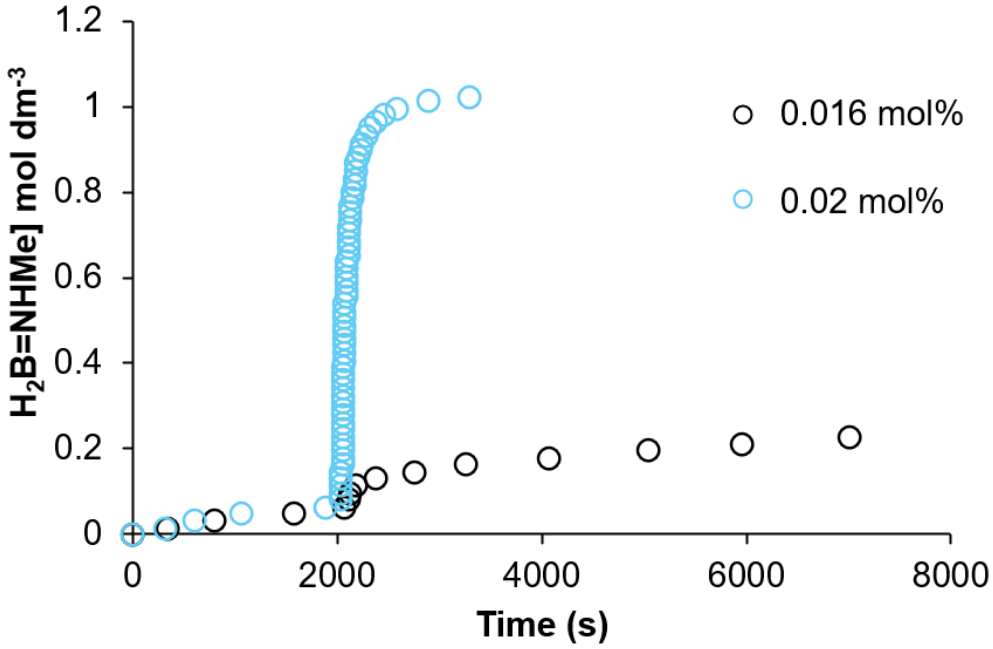

Figure 111. Effective $H_2B{=}NMeH$ concentration over time from eudiometric H_2 evolution measurement for the dehydropolymerisation of $H_3B{\cdot}NH_2Me$ (0.112 g, 1 mol dm^{-3} in THF) by **8** (0.02 and 0.016 mol%) with 2 equivalents of ^{t}BuOK to catalyst. Catalysis initiates and reaches completion for 0.02 mol% but halts immediately after initiation with 0.016 mol%.

An attempt was also made to evaluate the order in catalyst concentration for $H_3B{\cdot}NH_2Me$ dehydropolymerisation with **9** utilising variable time normalisation analysis (VTNA) to provide a qualitative assessment. [27] The amount of H_2 released was plotted against $t[cat]^n$ where t is time, [cat] is catalyst concentration and n is the order in catalyst. The value of n was varied to find a value for which the plots at different catalyst concentrations overlapped, thus qualitatively finding the order in catalyst for the rate law. Applying this to the dehydropolymerisations of $H_3B{\cdot}NH_2Me$ with **9** (made from **8** + 2 equivalents of ^{t}BuOK) at catalyst loadings 0.02 – 0.05 mol% showed initially a best overlap for $[cat]^2$ (**Figure 112**).

When considering the proposed catalyst inhibitor concentration discussed vide supra by subtracting its proposed concentration (0.00016 mol dm^{-3}) from the catalyst concentration, $[cat]^1$ exhibits the closest overlap of the plotted data (**Figure 112**). The overlap for $[cat]^1$ is however a poor fit, especially toward the end of the catalysis run hydrogen evolution plots. This can be explained by the same mechanism which causes an initial pseudo zeroth-order rate dependence on the concentration of $H_3B{\cdot}NH_2Me$: saturation kinetics where the catalyst forms an adduct with $H_3B{\cdot}NH_2Me$ in a pre-equilibrium prior to the rate limiting step. This would cause a shift in the concentration of the active catalyst resting state ($H_3B{\cdot}NH_2Me$ bound adduct) as the reaction progresses and $H_3B{\cdot}NH_2Me$ concentration decreases, meaning that VTNA may be unsuitable to assess order in catalyst for this system

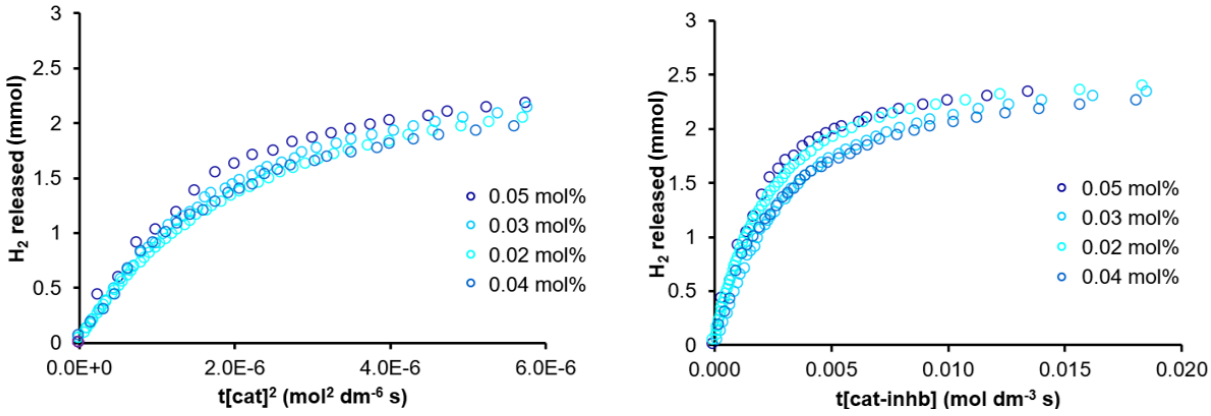

Figure 112. Left: VTNA plot showing mmol of H_2 released against $t[cat]^2$ for the dehydropolymerisation of $H_3B{\cdot}NH_2Me$ (0.112 g, 1 mol dm^{-3} in THF) by **8** (0.02-0.05 mol%) with 2 equivalents of ^{t}BuOK to catalyst, generating **9**. Right: VTNA plot showing moles of H_2 released against t[cat-inhb] for the dehydropolymerisation of $H_3B{\cdot}NH_2Me$ (0.112 g, 1 mol dm^{-3} in THF) by **8** (0.02-0.05 mol%) with 2 equivalents of ^{t}BuOK to catalyst, generating **9**. [inhb] is approximated to be 0.00016 mol dm^{-3} based on low catalyst loading experiments.

3.4 The dehydropolymerisation of $H_3B{\cdot}NH_2Me$ with 8 and NH_2Me

In solution complex **9** exhibits high reactivity and long-term instability, with spontaneous decomposition via beta-hydride elimination and dimerization to the catalytically inactive **10** (see section **3.2.2**), which is visible by ^{1}H NMR spectroscopy at low concentration almost immediately after the preparation of **9**. This means that using ^{t}BuOK to activate amine-borane dehydropolymerisation precatalyst **8** is inconvenient. Catalyst stock solutions are needed to produce the accurate concentrations used to investigate the order in catalyst on the rate of dehydropolymerisation. As the instability of complex **9** precludes the use of stock solutions, specific concentrations of **9** must be produced by the reaction of **8** and ^{t}BuOK immediately prior to catalysis each time hydrogen evolution data (catalytic rate) is to be measured. This method of catalyst preparation introduces an intrinsic error in catalyst concentration, exacerbated by the low catalyst concentrations used.

To circumvent this issue and facilitate a more accurate measurement of the relationship between catalytic rate and catalyst concentration, activation of **8** via other methods was sought. The activation of dehydropolymerisation precatalysts via base-promoted hydride transfer to form a metal-hydride is reported in the literature, where primary amines are commonly used as/act as the base. [5, 6, 28] This occurs via deprotonation by the amine of a metal amine-borane complex (see introduction **1.3.2**), which can be stable or transient species. Such is the case for precatalysts **5** and **6**.

Dehydropolymerisations of $H_3B{\cdot}NH_2Me$ (0.112 g, 1 mol dm^{-3} in THF) were attempted with **8** (0.033 mol% catalyst loading) and various amounts of added NH_2Me (as a 2 mol dm^{-3} solution in THF, 3, 15, 30 & 75 equivalents to catalyst, corresponding to 0.001, 0.005, 0.01 and 0.025 mol dm^{-3}, **Figure 113**).

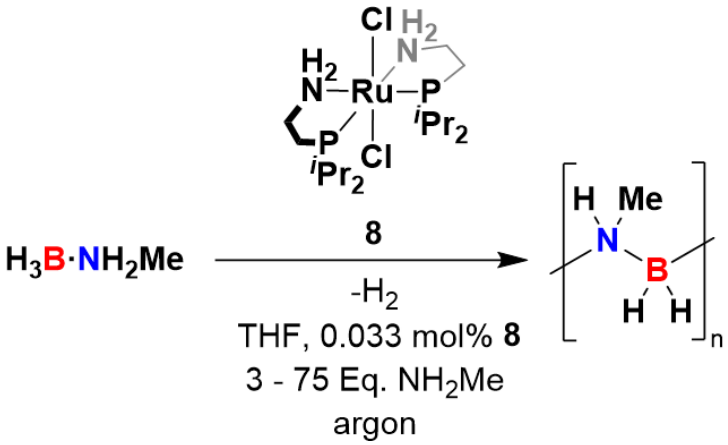

Figure 113. The dehydropolymerisation of $H_3B{\cdot}NH_2Me$ (0.112 g, 1 mol dm^{-3} in 2.5 cm^3 THF) by precatalyst **8** with varying amounts NH_2Me of added to activate the precatalyst (3 – 75 equivalents).

Eudiometric hydrogen evolution data was measured and plotted for the $H_3B{\cdot}NH_2Me$ dehydropolymerisation with **8** when amine concentration was varied to allow for kinetic analysis (**Figure 114**). With increasing NH_2Me concentration the induction period is shown to significantly decrease, from ~1600 s with 3 equivalents to ~200 s with 75 equivalents. High rates of catalysis are observed when 30 and 75 equivalents of NH_2Me are used meaning that the hydrogen evolution plot data density is low, precluding the comparison of initial rates of reaction, however the H_2 evolution profiles show that the rate of catalysis is significantly accelerated with increasing amine concentration (**Figure 114**). Comparing the initial rates of catalysis for **8** (0.03 mol%) + 2 equivalents of ^{t}BuOK and **8** (0.033 mol%) + 15 equivalents of NH_2Me, 0.03 and 0.24 mol dm^{-3} s^{-1} respectively, it is clear that the presence of an amine such as NH_2Me has a profound acceleratory effect on amine-borane dehydrogenation.

Measuring over the initial linear pseudo zero-order region, the turnover frequency of catalysis when using ^{t}BuOK and **8** (0.03 mol%) is 121 s^{-1}, whereas with **8** (0.033 mol%) + 15 equivalents of NH_2Me TOF = 660 s^{-1}. This represents the highest TOF thus far reported for a dehydropolymerisation catalyst. [29, 30] It should be noted that due to the fact that the catalyst concentrations are not equal for these reactions they are not wholly comparable, however the increased rate of reaction when 15 equivalents of NH_2Me are used to activate **8** cannot be solely accounted for by the increased catalyst concentration (0.0003 to 0.00033 mol dm^{-3}). The turnover frequency measured for the dehydropolymerisation of $H_3B{\cdot}NH_2Me$ with **8** (0.04 mol%, 0.0004 mol dm^{-3} in THF) + 2 equivalents of ^{t}BuOK was measured at 119 s^{-1} over the pseudo zero-order region.[36-38]

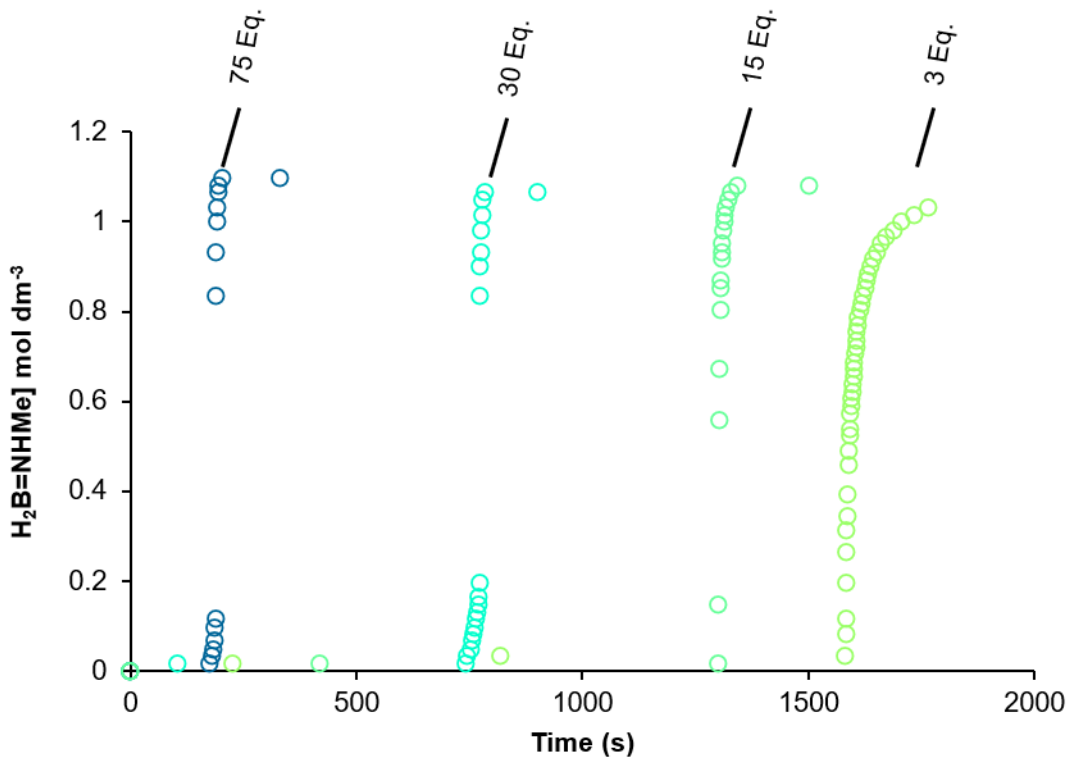

Figure 114. Effective $H_2B{=}NMeH$ concentration over time from eudiometric H_2 evolution measurement for the dehydropolymerisation of $H_3B{\cdot}NH_2Me$ (0.112 g, 1 mol dm^{-3} in 2.5 cm^3 THF) by precatalyst **8** (0.033 mol%) with varying amounts NH_2Me of added to activate the precatalyst (3 – 75 equivalents). Rate is seen to increase, and induction period decrease with increasing amine concentration.

A possible explanation for the acceleratory effect of NH_2Me on the dehydropolymerisation of $H_3B{\cdot}NH_2Me$ with **8** is that amines such as NH_2Me may act as co-catalysts for amine-borane dehydropolymerisation, alongside being precatalyst activators. It has been reported that water and alcohols are capable of templating the heterolysis of H_2 across a ruthenium-amido bond by forming a hydrogen bonded adduct with the catalyst, this lowers the free energy barrier to H_2 activation by as much as 8 kcal mol^{-1}.[31-33] A similar mechanism may occur here, where additional amine may facilitate the dehydrogenation of amine-boranes, decreasing the barrier to reaction and therefore increasing the rate of catalysis (**Figure 115**). It is unlikely that this process is a trimolecular reaction, but rather NH_2Me and the active catalyst species form a hydrogen bonded adduct, which then reacts with $H_3B{\cdot}NH_2Me$. To test this mechanism the effect of tertiary amines on the rate of reaction should be investigated, as tertiary amines should not be able to facilitate the proton shuttling suggested in **Figure 115** and therefore not significantly affect rate. No reaction was observed between complex **8** and NH_2Me in the absence of an amine-borane, and complex **9** is unlikely to be an intermediate in precatalyst activation with NH_2Me.

Another possibility could be that NH_2Me may facilitate the loss of H_2 from an adjacent ligand N–H and Ru–H across the ruthenium nitrogen bond by acting as a proton shuttle, thereby a ruthenium amido bond that can go on to dehydrogenate an amine-borane. This is effectively the microscopic reverse of templating H_2 heterolysis by water and alcohols that has been previously reported (**Figure 115**). This would imply that the rate limiting step in amine-borane dehydrogenation with **8** involves H_2 loss from the catalyst.

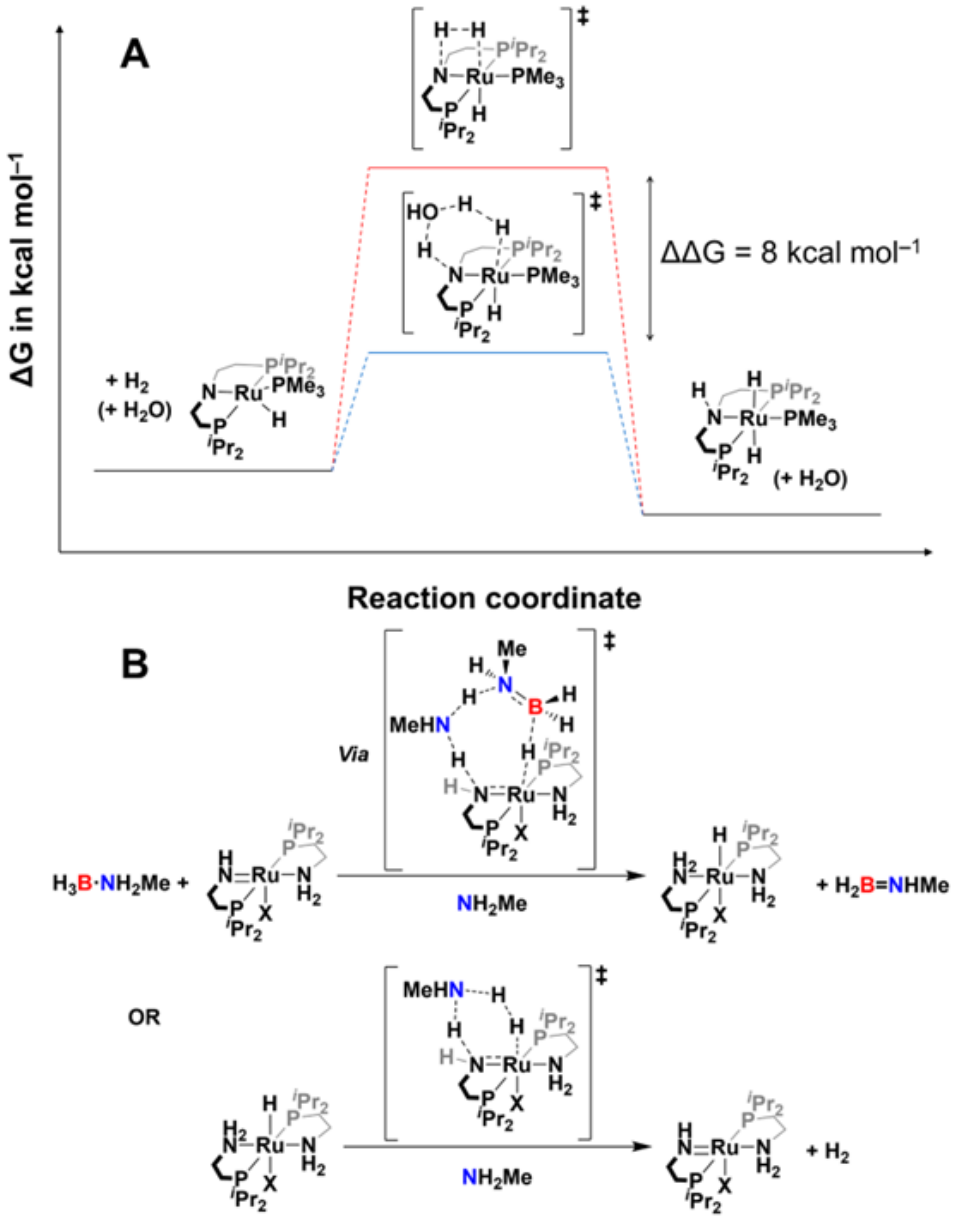

Figure 115. A: The reported lower activation barrier for H_2 across the ruthenium–nitrogen bond of Ru(^{i}Pr-PNP)(PMe$_3$)H when mediated by a water adduct, figure adapted from literature reference. [31] B: the proposed amine-mediated amine-borane dehydrogenation/catalyst dehydrogenation, involving ruthenium amido species related to the active catalyst proposed by Fagnou et al. [2]

With increasing NH_2Me concentration polyaminoborane M_n was recorded to increase, from 108,000 g mol^{-1} with 3 equivalents to 153,900 g mol^{-1} with 30 equivalents (relative to catalyst, **Table 6**). It is possible that this represents the sequestration of a polyaminoborane chain termination agent such as free BH_3 from solution by NH_2Me. Another possibility is that the increased rate of catalysis when NH_2Me is present, which leads to an increased rate of aminoborane production, outpaces the rate of polyaminoborane chain termination and leads to a higher degree of polymerisation.

Catalyst	$H_3B{\cdot}NMeH_2$ concentration (mol dm^{-3})	Catalyst mol%	Catalyst concentration (mol dm^{-3})	$MeNH_2$ concentration (mol dm^{-3})	M_n (mol dm^{-3})	M_w (mol dm^{-3})	Đ
8	1	0.033	0.00033	0.025	133,300	228,600	1.71
8	1	0.033	0.00033	0.01	153,900	245,500	1.60
8	1	0.033	0.00033	0.005	126,100	191,100	1.52
8	1	0.033	0.00033	0.001	108,000	153,100	1.42

Table 6. Polymer data obtained by GPC analysis of the $(H_2BNHMe)_n$ formed by the catalytic dehydropolymerisation of $H_3B{\cdot}NH_2Me$ (1 mol dm^{-3} in THF) by **8** (0.033 mol%) varying added NH_2Me (3 – 75 equivalents, 0.001 – 0.025 mol dm^{-3}).

3.4.1 Kinetic analysis of the dehydropolymerisation of $H_3B{\cdot}NH_2Me$ with 8 and NH_2Me

From this point on, 0.01 mol dm^{-3} of NH_2Me with **8** (30 eq. to catalyst when at 0.033 mol% loading) was used as the standard amount of NH_2Me for activating this dehydropolymerisation catalyst. This volume of NH_2Me (12.5 µL of 2 mol dm^{-3} in THF) was large enough to add repeatably, while keeping the rate of catalysis low enough so that H_2 evolution could be measured eudiometrically.

To further understand the role that amines such as NH_2Me play when present during the dehydropolymerisation of amine-boranes by precatalyst **8**, the normalised H_2 evolution data recorded at varying amine concentrations was plotted as moles of H_2 released against t[amine]^n (VTNA), where t is time, [amine] is concentration of NH_2Me in mol dm^{-3} and n is order in terms of the rate law. [27] The catalysis with **8** and 3 equivalents (0.001 mol dm^{-3}) of NH_2Me was not included due its relatively very low rate of catalysis, possibly due to incomplete catalyst activation when only a small excess of NH_2Me is used. The best qualitative overlap of the data was when n = 1, suggesting that the rate of catalysis has a first-order dependance on the concentration of NH_2Me (**Figure 116**). This value however is uncertain due to only 3 concentrations evaluated and an imperfect VTNA overlap, likely due to the high rates of reaction leading to lower accuracy when measuring H_2 evolution eudiometrically.

A positive order (tentatively first order) in NH_2Me concentration is supportive of the amine-mediated mechanism for amine-borane dehydrogenation proposed in **Figure 115**, and may suggest that the turnover-limiting step for the catalytic cycle involves either is loss of H_2 from a hydrogenated catalyst species or dehydrogenation of the amine-borane. This turnover-limiting step may have a lowered energy barrier when amine is present leading to the increased rate with increasing NH_2Me concentration. The presence of all three components in the rate law could suggest the formation of an adduct between amine and catalyst, before rate-limiting dehydrogenation of the amine-borane occurs.

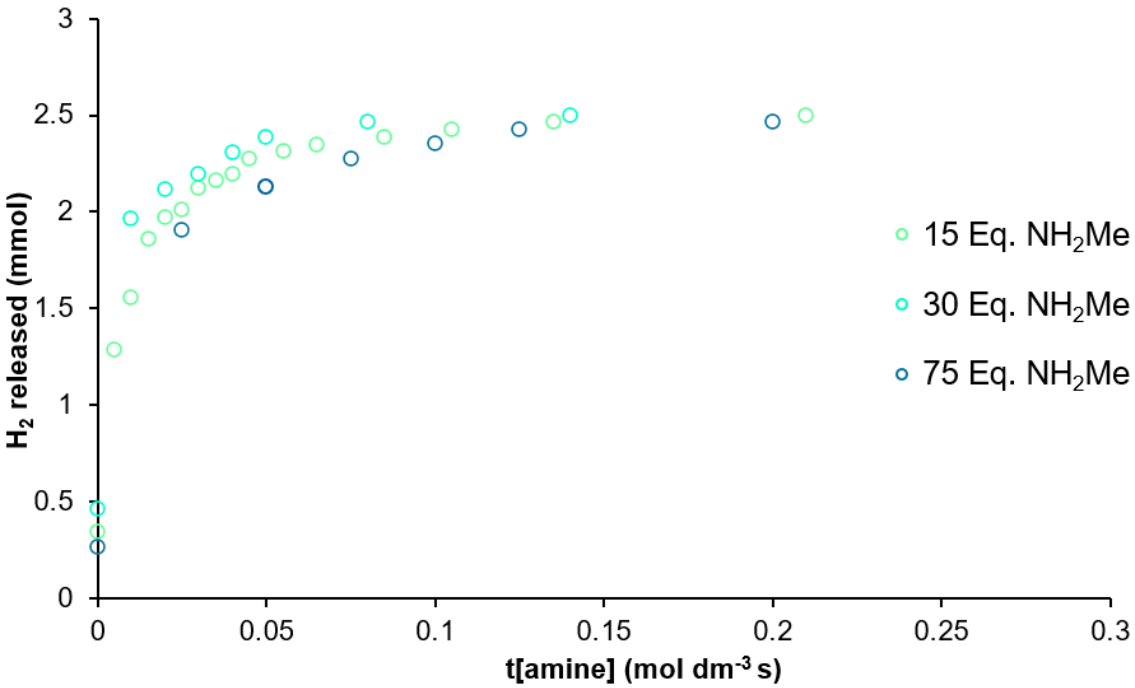

Figure 116. VTNA plot showing mmol of H_2 released against t[amine] for the dehydropolymerisation of $H_3B{\cdot}NH_2Me$ (0.112 g, 1 mol dm^{-3} in THF) by **8** (0.033 mol%, 0.00033 mol dm^{-3}) with 15, 30 and 75 equivalents to catalyst of NH_2Me (0.005, 0.01 and 0.025 mol dm^{-3} respectively).

As precatalyst **8** is stable in solution over long periods of time and can be readily activated at low concentration with NH_2Me in the presence of amine-boranes to form an active catalytic species, the order of catalyst for the dehydropolymerisation of $H_3B{\cdot}NH_2Me$ was investigated using stock solutions of **8**. Dehydropolymerisations of $H_3B{\cdot}NH_2Me$ (0.112 g, 1 mol dm^{-3} in THF) with **8** (0.01 – 0.033 mol%) in the presence of 0.01 mol dm^{-3} of NH_2Me were performed under these conditions and H_2 evolution measured eudiometrically (**Figure 117**). Catalyst loadings of **8** higher than 0.033 mol% were not used due to the rate of H_2 evolution exceeding that which could be measured accurately by the eudiometric methods.

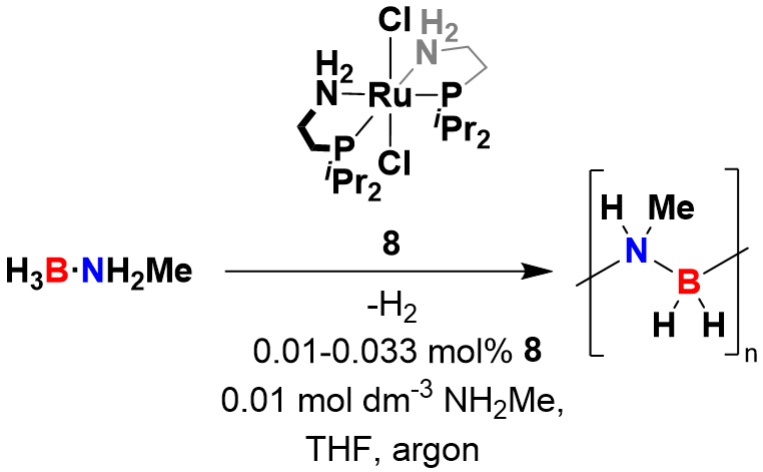

Figure 117. The dehydropolymerisation of $H_3B{\cdot}NH_2Me$ (0.112 g, 1 mol dm^{-3} in 2.5 cm^3 THF) by precatalyst **8** (0.01 – 0.033 mol%) with 0.01 mol dm^{-3} of NH_2Me of added to activate the precatalyst.

As catalyst concentration was increased the induction period decreased, as was seen with **8** + 2 equivalents of ^{t}BuOK (see **3.3**). Notably, the lowest effective catalyst loading was 0.01 mol%, slightly lower than the 0.02 mol% when **8** + 2 equivalents of ^{t}BuOK was used. This is possibly due to avoiding the extremely reactive complex **9** which could be rapidly and disproportionately poisoned by trace contaminants. This means that the effective inhibitor concentration [inhb] is lower when 0.01 mol dm^{-3} of NH_2Me is used as an initiator when compared to 2 equivalents of ^{t}BuOK, despite the true concentration of the trace contaminant species likely being constant in all cases. The possible identity of this trace inhibitor will be discussed in section **3.5.3**.

The initial rates of catalysis were plotted against catalyst concentration for the catalytic runs at each catalyst loading, excluding those at 0.0297 and 0.033 mol% as the high rates and therefore sparsity of data points lead to low accuracy at t = 0. This shows a non-linear correlation between rate and [cat] that does not pass through 0 (**Figure 119**). As with when **8** + 2 equivalents of ^{t}BuOK was used, this can be accounted for by assuming an inhibitor concentration [inhb] of 8.5×10^{-5} mol dm^{-3}. When plotting initial rate against [cat–inhb], a direct correlation is seen suggesting a first-order dependence of rate on true catalyst concentration (**Figure 119**). To confirm this proposed inhibitor concentration, dehydropolymerisations were also performed at 0.008 and 0.009 mol% (**Figure 120**). Catalysis initiates but only reaches 80% conversion for 0.009 mol% and does not initiate for 0.008 mol%, strongly suggesting that the effective inhibitor

concentration is between these values and matching the value of 8.5×10^{-5} mol dm^{-3} determined from initial rates.

The polyaminoboranes obtained from the dehydropolymerisation of $H_3B{\cdot}NH_2Me$ with **8** and 0.01 mol dm^{-3} of NH_2Me was analyzed by GPC and found to have M_n values of around 150,000 g mol^{-1} with a dispersity of 1.5 - 1.6 for all catalyst concentrations used (**Figure 121**). This is likely due to the activation of **8** with NH_2Me and $H_3B{\cdot}NH_2Me$ to form a ruthenium hydride species via base-promoted hydride transfer. This also produces an equivalent of boronium $[H_2B(NHMe)_2][Cl]$ which is reported to act as a chain transfer agent, and has a concentration intrinsically linked with the likely polymerisation initiator species that is the ruthenium hydride. Changing catalyst concentration therefore simultaneously affects the initiation and termination steps of aminoborane polymerisation. [5]

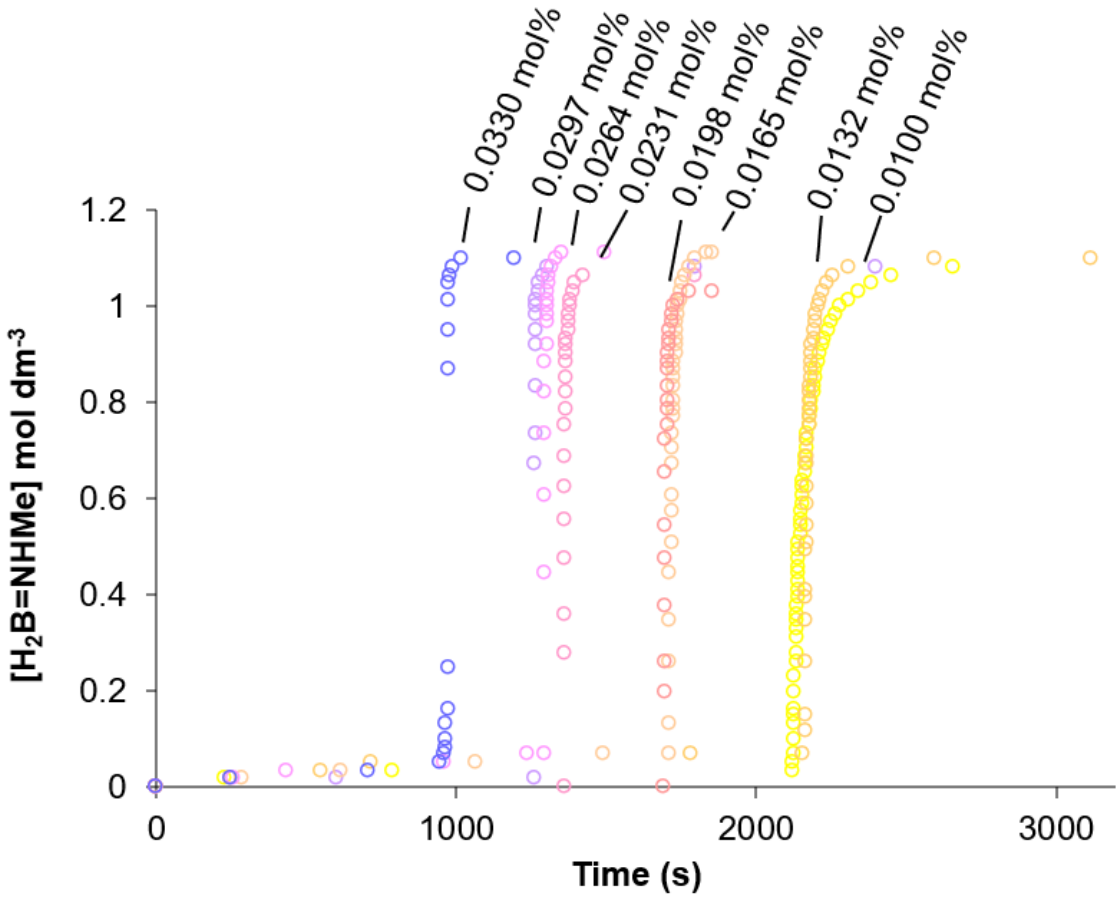

Figure 118. Effective $H_2B{=}NMeH$ concentration over time from eudiometric H_2 evolution measurement for the dehydropolymerisation of $H_3B{\cdot}NH_2Me$ (0.112 g, 1 mol dm^{-3} in 2.5 cm^3 THF) by precatalyst **8** (0.01-0.033 mol%), with 0.01 mol dm^{-3} of NH_2Me added to activate the precatalyst. Rate is seen to increase, and induction period decrease with increasing catalyst concentration.

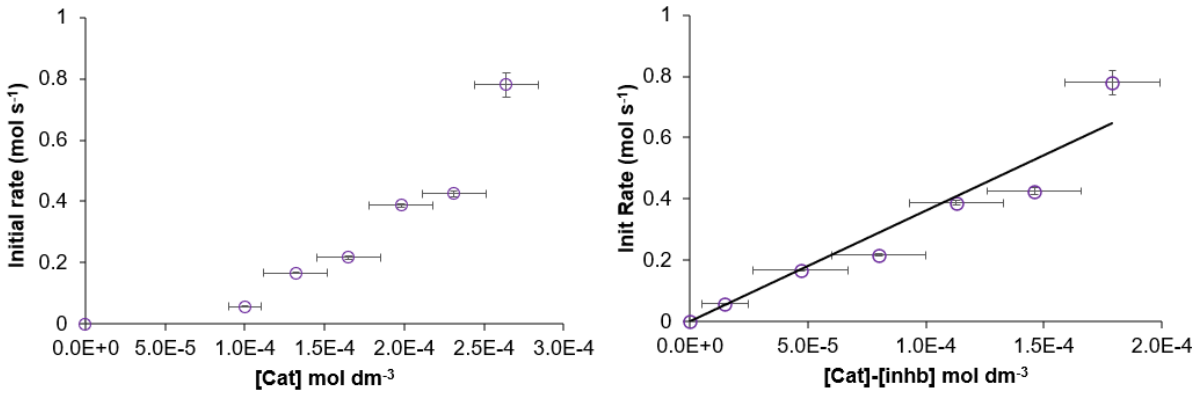

Figure 119. Left: a plot of initial rates of hydrogen evolution measured eudiometrically against catalyst concentration [cat] for the dehydropolymerisation of $H_3B{\cdot}NH_2Me$ (0.112 g, 1 mol dm^{-3} in THF) by **8** (0.01-0.0264 mol%) with 0.01 mol dm^{-3} of NH_2Me. Right: the same catalysis initial rate data plotted against an adjusted catalyst concentration [cat]–[inhb], where [inhb] is the concentration of a proposed catalyst inhibitor/poison assumed to be $8.5x10^{-5}$ mol dm^{-3}.

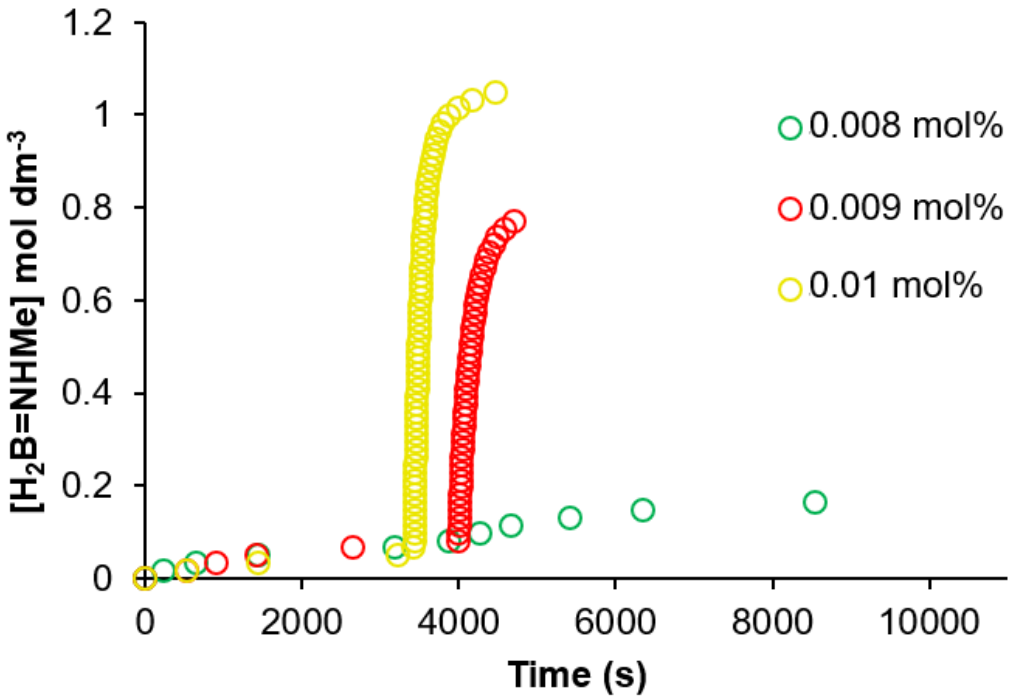

Figure 120. Effective $H_2B{=}NMeH$ concentration over time from eudiometric H_2 evolution measurement for the dehydropolymerisation of $H_3B{\cdot}NH_2Me$ (0.112 g, 1 mol dm^{-3} in THF) by **8** (0.01, 0.009 and 0.008 mol%) with 0.01 mol dm^{-3} of NH_2Me. Catalysis initiates and reaches completion with 0.01 mol%, reaches partial dehydrogenation with 0.009 mol% and halts immediately after initiation with 0.008 mol%.

Catalyst	$H_3B{\cdot}NH_2Me$ concentration (mol dm^{-3})	Catalyst mol%	Catalyst concentration (mol dm^{-3})	NH_2Me concentration (mol dm^{-3})	M_n (mol dm^{-3})	M_w (mol dm^{-3})	Đ
8	1	0.0330	0.000330	0.01	153,800	241,100	1.57
8	1	0.0297	0.000297	0.01	151,800	224,600	1.48
8	1	0.0264	0.000264	0.01	154,300	240,600	1.56
8	1	0.0231	0.000231	0.01	159,700	246,600	1.54
8	1	0.0198	0.000198	0.01	171,600	207,200	1.53
8	1	0.0165	0.000165	0.01	149,800	229,900	1.54
8	1	0.0132	0.000132	0.01	147,100	235,100	1.60
8	1	0.0100	0.000100	0.01	152,600	242,400	1.59

Figure 121. Polymer data obtained by GPC analysis of the $(H_2BNHMe)_n$ formed by the catalytic dehydropolymerisation of $H_3B{\cdot}NH_2Me$ (1 mol dm^{-3} in THF) by **8** (0.01 – 0.033 mol%, 0.0001 – 0.00033 mol dm^{-3}) with 0.01 mol dm^{-3} of NH_2Me.

The order in catalyst when NH_2Me is used as an initiator was further investigated by plotting the H_2 evolution data at the varied catalyst loadings (0.01 – 0.0264 mol%) in the VTNA format, with normalized mmol of H_2 released against normalized $t[cat]^n$. Under these conditions the concentration of the catalyst was varied whilst the concentration of NH_2Me was maintained at 0.01 mol dm^{-3}. This plot qualitatively showed the best overlap where n = 3, suggesting a third-order dependance on catalyst concentration (**Figure 122**). However when accounting for the inhibitor concentration of $8.5x10^{-5}$ mol dm^{-3} determined from initial rates and low catalyst loading experiments, the best VTNA profile fit corresponds to n = 1 (**Figure 122**), suggesting a first order dependence in catalyst concentration on rate. This is in agreement with the initial rates measurements plotted against catalyst concentration and in agreement with the order in catalyst found for **8** + 2 equivalents of ^{t}BuOK (see **3.3.1**).

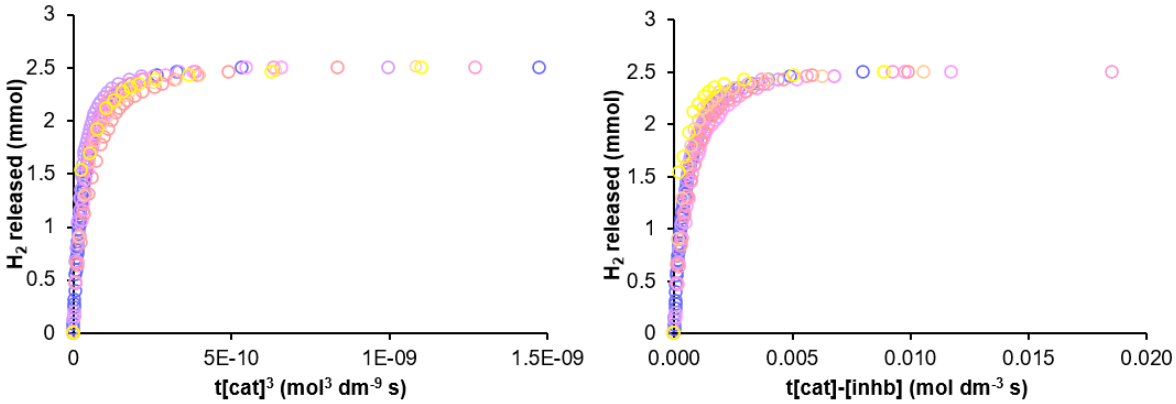

Figure 122. Left: VTNA plot showing mmol of H_2 released against t[cat]^3 for the dehydropolymerisation of $H_3B{\cdot}NH_2Me$ (0.112 g, 1 mol dm^{-3} in THF) by **8** (0.01-0.0264 mol%) with 0.01 mol dm^{-3} of NH_2Me. Right: VTNA plot showing moles of H_2 released against t[cat-inhb] for the dehydropolymerisation of $H_3B{\cdot}NH_2Me$ (0.112 g, 1 mol dm^{-3} in THF) by **8** (0.01-0.0264 mol%) with 0.01 mol dm^{-3} of NH_2Me. [inhb] is approximated to be 8.5x10^{-5} mol dm^{-3} based on low catalyst loading experiments.

3.5 Speciation during amine-borane dehydropolymerisation with 8

To aid in building a catalytic cycle for catalyst system **8** during the dehydropolymerisation of $H_3B{\cdot}NH_2Me$, the speciation was investigated via NMR spectroscopy when using both ^{t}BuOK and NH_2Me as activators. Post-catalysis this is done by in-situ ^{1}H and ^{31}P{^{1}H} NMR spectroscopy at 298 K. Observing speciation during the induction period and during catalysis is more difficult due to the large volumes of hydrogen produced and the very short (seconds) active catalysis period during which sampling takes place. To address these issues, in-situ aliquots were taken from dehydropolymerisations during the induction and active catalysis phases and rapidly cooled to – 90 °C, effectively pausing catalysis whilst preserving catalyst speciation.

3.5.1 Induction period speciation during amine-borane dehydropolymerisation with 8

In order to be able to sample catalysis during the rapid hydrogen evolution phase whilst using a concentration of catalyst high enough to be detectable by NMR spectroscopy, 0.0003 mol dm^{-3} (0.03 mol%) for **8** + 2 equivalents of ^{t}BuOK and at 0.00033 mol dm^{-3} (0.033 mol%) for **8** with 0.01 mol dm^{-3} of NH_2Me were found to be the ideal middle ground reaction conditions (**Figure 123**), where catalyst species NMR signals were weak but observable.

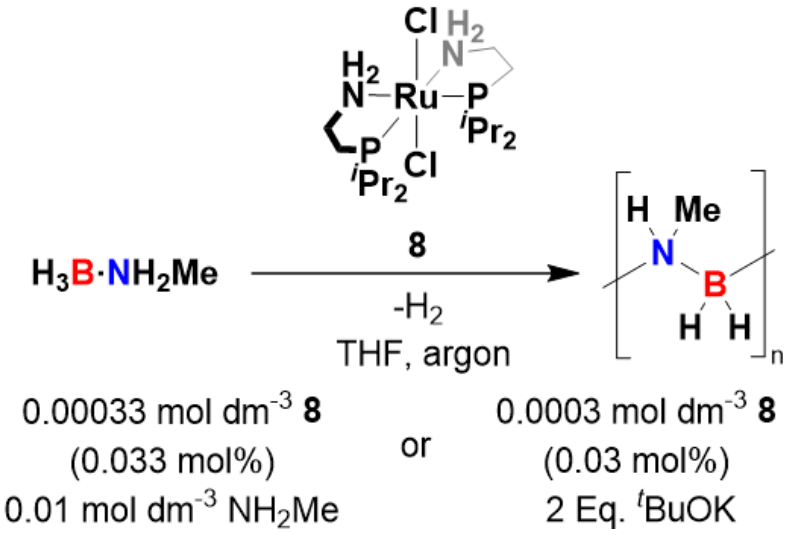

Figure 123. The dehydropolymerisation of $H_3B{\cdot}NH_2Me$ (0.112 g, 1 mol dm^{-3} in 2.5 cm^3 THF) by precatalyst **8** with either 2 equivalents of ^{t}BuOK (forming **9**) or 0.01 mol dm^{-3} of NH_2Me to activate. NMR spectroscopy speciation study.

In-situ $^{31}P\{^{1}H\}$ NMR spectroscopy at –90 °C of samples taken during the induction periods of catalysis with **8** activated with either 2 equivalents of ^{t}BuOK or 0.01 mol dm^{-3} of NH_2Me show the presence of a new species, a singlet at 89 ppm (**Figure 124**). The induction period aliquot was taken 500 s into the induction period for both precatalyst activation methods and suggests rapid conversion into the same species. This further is confirmed by in-situ ^{1}H NMR spectra also recorded at –90 °C (512 scans), which show a signal in the hydride region at –19.6 ppm (t, J_{HP} = 27 Hz, **Figure 125**). This signal collapses to a singlet upon phosphorous decoupling of the ^{1}H NMR spectrum. This signal likely corresponds to a Ru–H that is coupled to two equivalent phosphorous environments. The shift of this hydride is typical of that seen in octahedral Ru(II) complexes- with aminophosphine ligands where the hydride is trans to a weak field ligand: e.g. Cl^- not H^- such as in $RuHCl(PPh_3)_2(N(Me)_2CH_2CH_2N(Me)_2)$ (–18.5 ppm) .[34, 35] This suggests the structure of this species, henceforth referred to as **11** is: Ru(^{i}PrCH$_2$CH$_2$NH$_2$)(H)(X) (**Figure 125**).

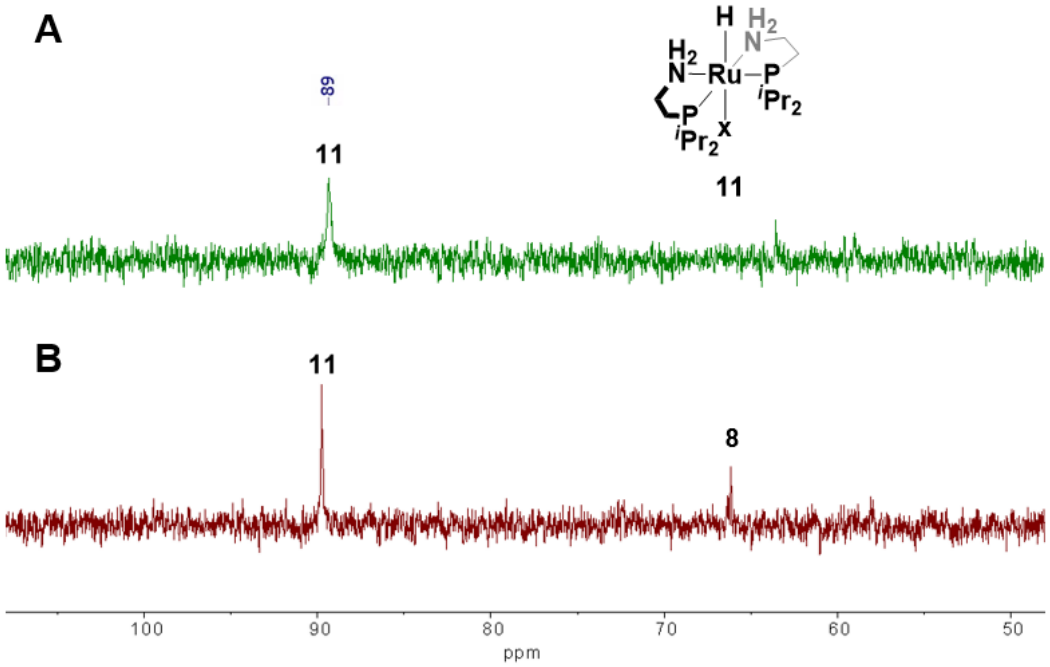

Figure 124. In-situ $^{31}P\{^{1}H\}$ NMR spectra taken during the induction period of the dehydropolymerisation of $H_3B{\cdot}NH_2Me$ with **8**. A: **8** activated with 0.01 mol dm^{-3} of NH_2Me. B: **8** activated with 2 equivalents of ^{t}BuOK, forming **9** in-situ. Both show the same speciation, a singlet at 89 ppm. B shows a small amount of unactivated **8** at ~ 65 ppm. Both recorded in THF at –90 °C, 512 scans with a starting catalyst concentration of $3.0x10^{-4}$ mol dm^{-3}.

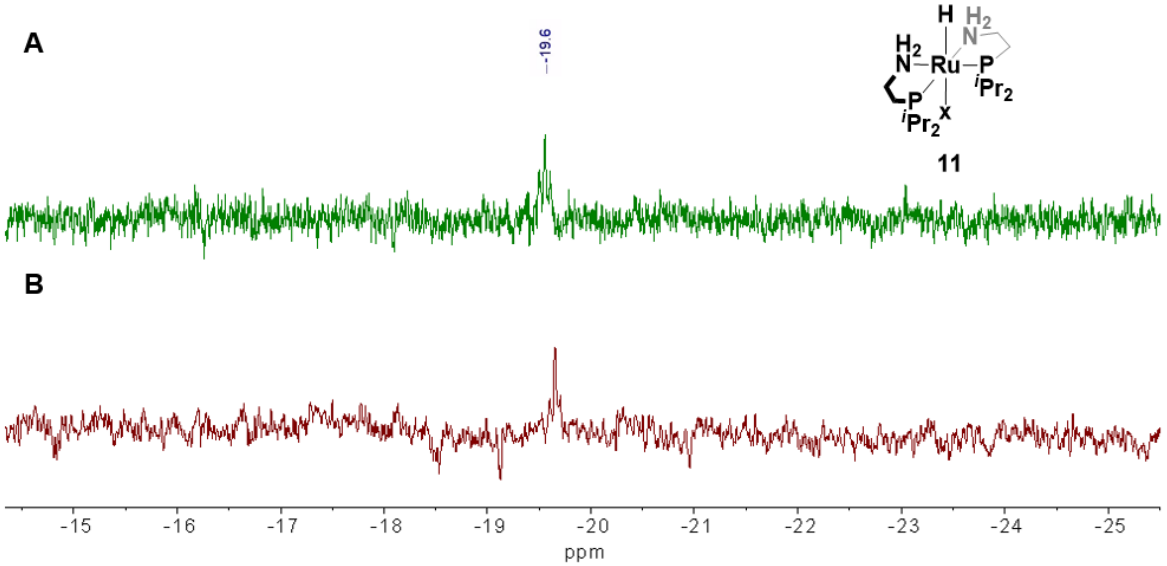

Figure 125. In-situ ^{1}H NMR spectra taken during the induction period of the dehydropolymerisation of $H_3B{\cdot}NH_2Me$ with **8**. A: **8** activated with 0.01 mol dm^{-3} of NH_2Me. B: **8** activated with 2 equivalents of ^{t}BuOK, forming **9** in-situ. Both showing the same speciation, a triplet at – 19.6 ppm with J_{HP} = 27 Hz corresponding to a Ru–H (**11**). Both recorded in THF at – 90 °C, 512 scans with a starting catalyst concentration of $3x10^{-4}$ mol dm^{-3}.

3.5.2 The identity and formation of 11 during the induction period of amine-borane dehydropolymerisation with 8

In an attempt to synthesize the species observed during the induction period of the dehydropolymerisation of $H_3B{\cdot}NH_2Me$ with **8**, tentatively identified as structurally resembling Ru($^{i}Pr_2PCH_2CH_2NH_2$)(H)(X) (**11**), stoichiometric hydrogenations of **9** with hydrogen sources was investigated. These include H_2 gas (see section **3.5.4**) which is produced during the dehydrogenatation of amine-boranes, $H_3B{\cdot}NH_2Me$ and ^{i}PrOH which is used as a H_2 source in transfer hydrogenations. [4]

The reaction of **9** (generated in-situ from **8** and 2 equivalents of ^{t}BuOK) in THF and 5 equivalents of ^{i}PrOH resulted in the rapid color change from pink to yellow. The in-situ $^{31}P\{^{1}H\}$ NMR spectrum of the reaction mixture showed the complete conversion of **9** to a new species with a singlet at 89 ppm (**Figure 126**). The corresponding ^{1}H NMR spectrum showed a broad signal at – 21.8 ppm (**Figure 126**). The reaction mixture was evaporated under argon flow due to decomposition on exposure to vacuum, and the resulting yellow solids extracted into the minimum volume of pentane (see experimental for details). This pentane solution was then cooled to –90 °C to grow crystals, from which a single crystal x-ray diffraction crystal structure was obtained.

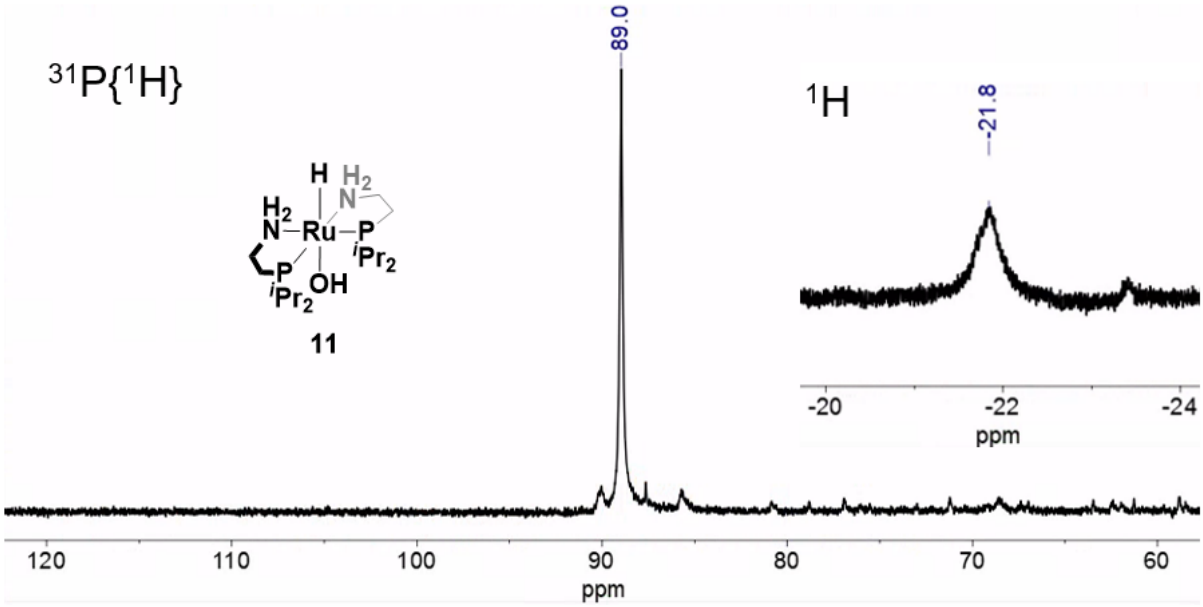

Figure 126. In-situ $^{31}P\{^{1}H\}$ NMR spectrum of the reaction between **9** (generated in-situ from **8** and 2 equivalents of ^{t}BuOK) and 5 equivalents of ^{i}PrOH, showing a new signal at 89 ppm, corresponding to *P,P-cis*-Ru($^{i}Pr_2PCH_2CH_2NH_2$)$_2$(OH)H (**11**). Inset: In-situ ^{1}H NMR spectrum of the same reaction showing a hydride signal at – 21.8 ppm, corresponding to *P,P-cis*-Ru($^{i}Pr_2PCH_2CH_2NH_2$)$_2$(OH)H (**11**). Both recorded in THF-H_8 at 298 K.

The crystal structure was found to be *P,P-cis*-Ru(^{i}Pr$_2$PCH$_2$CH$_2$NH$_2$)$_2$(OH)H · (^{i}PrOH)$_2$ where the OH ligand is trans to the hydride, and is hydrogen bonded by 2 equivalents of ^{i}PrOH (**Figure 127**). A single-crystal x-ray diffraction crystal structure was also obtained of the un-solvated form *P,P-cis*-Ru(^{i}Pr$_2$PCH$_2$CH$_2$NH$_2$)$_2$(OH)H, crystals of which were isolated by fractional crystallisation of the isopropanol solvate in pentane at –90 °C (see experimental **4.3.5** for details). In the isopropanol solvated structure *P,P-cis*-Ru(^{i}Pr$_2$PCH$_2$CH$_2$NH$_2$)$_2$(OH)H · (^{i}PrOH)$_2$ (P-1, R_{int} = 0.0446, R_1 = 0.0354) the ruthenium hydride, and OH proton were located in the electron density map and freely refined. The two isopropanol molecules form a birfurcated hydrogen bonded motif with the hydroxyl group. In the unsolvated structure *P,P-cis*-Ru(^{i}Pr$_2$PCH$_2$CH$_2$NH$_2$)$_2$(OH)H ($P3_2$, R_{int} = 0.0355, R_1 = 0.0361) the ruthenium hydride was located in the electron density map and freely refined. The OH proton was not located so was affixed and allowed to ride on the oxygen atom.

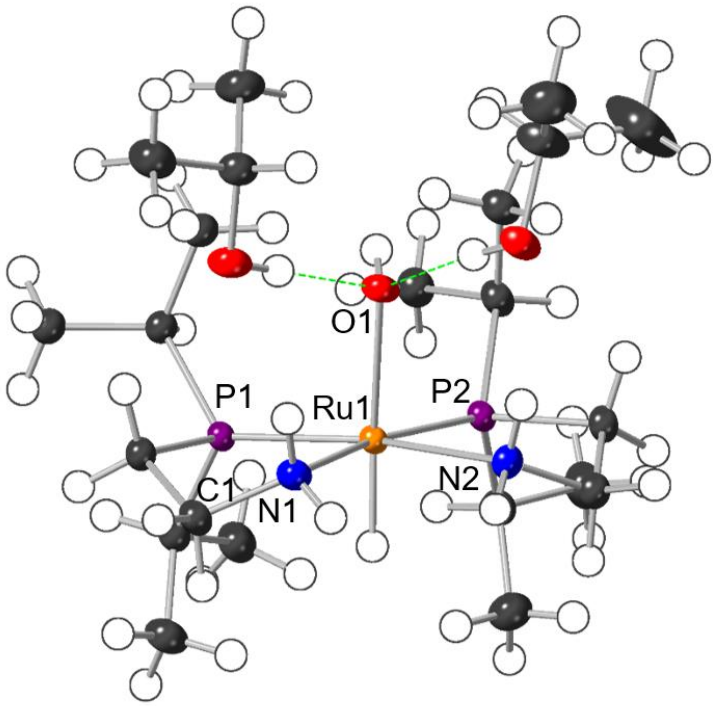

Figure 127. Molecular structure of *P,P-cis*-Ru(^{i}Pr$_2$PCH$_2$CH$_2$NH$_2$)$_2$(OH)H·(^{i}PrOH)$_2$ (**11**·(^{i}PrOH)$_2$) as determined by single crystal X-ray diffraction. Displacement ellipsoids are shown at the 50% probability level. Hydrogen atoms are placed in calculated positions. Selected bond lengths [Å] and angles [°]: Ru(1) –O(1) 2.2795(18), Ru(1) – N(1) 2.186(2), Ru(1) – N(2) 2.186(2), Ru(1) – P(1) 2.2499(6), Ru(1) – P(2) 2.2477(6), C(1) – N(1)1.476(3), P(1) – Ru(1) – N(1) 83.52(6), C(1) – N(1) – Ru(1) 113.57(15), O(1) – Ru(1) – N(1) 81.13(8), O(1) – Ru(1) – P(1) 101.22(5).

An ^{1}H NMR spectrum of the isolated unsolvated *P,P-cis*-Ru($^{i}Pr_2PCH_2CH_2NH_2)_2(OH)H$ was recorded at –80 °C in THF-d_8 which showed the broad hydride signal resolved into a triplet at –22.7 ppm with a coupling constant of J_{HP} = 27 Hz (**Figure 128**). Morris et al. have also reported a Ru(II) trans hydroxy hydride complex (trans-Ru(H)(OH)($PPh_3)_2${$NH_2C(Me)_2C(Me)_2NH_2$}) that exhibits a similar ^{1}H NMR hydride shift of – 17.4 ppm and also decomposes on exposure to vacuum. [36]

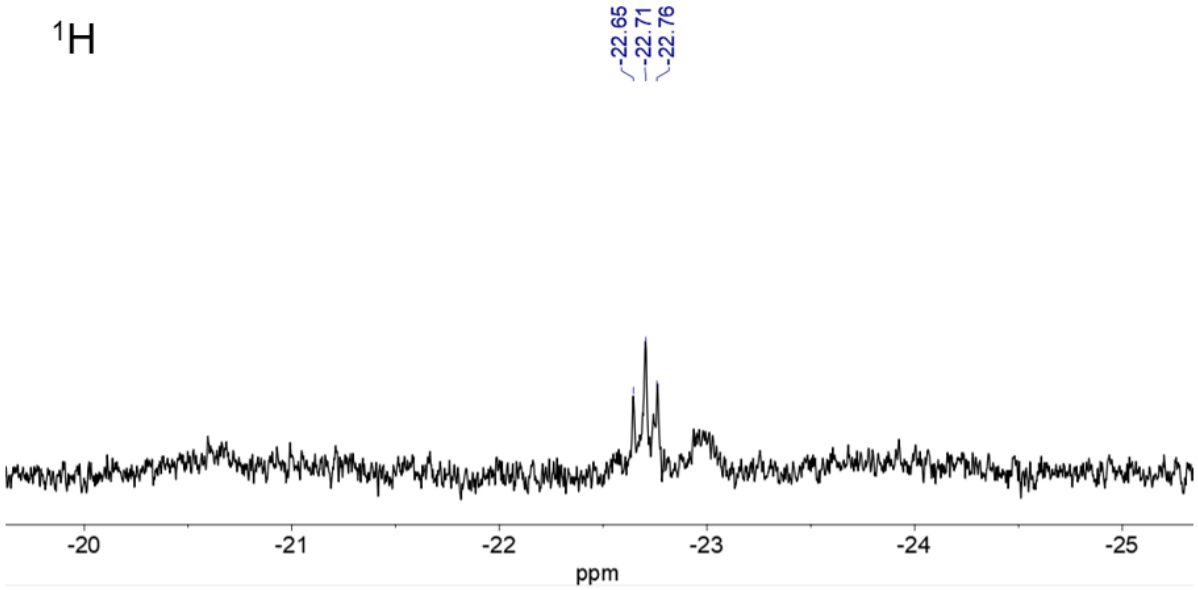

Figure 128. ^{1}H NMR spectrum of **11** showing a triplet at – 22.7 ppm corresponding to the phosphorous coupled ruthenium hydride, J_{HP} = 27 Hz. Recorded in THF-d_8 at –80 °C. The broad signal adjacent to the hydride triplet is likely the hydride of partially-solvated complex **11**.

The coupling constant of J_{HP} = 27 Hz for the ^{1}H NMR spectroscopy signal of the hydride for *P,P-cis*-Ru($^{i}Pr_2PCH_2CH_2NH_2)_2(OH)H$ matches that of the hydride signal seen during the induction period of dehydropolymerisation of $H_3B{\cdot}NH_2Me$ with **8** (activated with either 2 equivalents of ^{t}BuOK or 0.01 mol dm^{-3} of NH_2Me) (**Figure 125**). This along with the matching $^{31}P\{^{1}H\}$ NMR spectroscopy signal at 89 ppm (**Figure 124**, **Figure 126**) suggests that the identity of **11** seen during the induction period of catalysis is *P,P-cis*-Ru($^{i}Pr_2PCH_2CH_2NH_2)_2(OH)H$. The shift of isolated **11** is similar to but does not match that observed in the induction period (–19.6 vs – 21.8 ppm; **Figure 125**, **Figure 126**). This can be attributed to hydrogen bonding interactions in the catalysis reaction mixture and differing degrees of solvation, which are known to significantly affect the hydride ^{1}H chemical shift of Ru(II) trans hydride-hydroxide complexes. [36]

Complex **11** could be formed from complex **9** by the addition of 1 equivalent of H_2 from an amine-borane across one of the ruthenium amido bonds and one equivalent of water across the other ruthenium amido bond. The origin of this trace water is likely in the reaction THF solvent, which was measured by Karl Fischer analysis to be ~ 10 ppm. This corresponds to 5.0×10^{-4} mol dm^{-3} H_2O, higher than the concentration of **8** in a dehydropolymerisation at 0.03 mol% (3×10^{-4} mol dm^{-3}). A possible additional source of water is the back-diffusion of water vapour from the water-filled burette used to measure H_2 evolution. A control experiments performed without this apparatus, instead using a bleed needle, showed a significantly decreased induction period (500 s, compared to ~1500 s when attached to the water filled burette). The rapid formation of **11** likely leads to the observed induction period to amine-borane dehydropolymerisation, with H_2O acting an inhibitor before **11** is converted into the active catalyst. The addition of trace H_2O across ruthenium amido bonds to form off-cycle ruthenium hydroxide species during catalysis has been previously proposed for Noyori-type metal-ligand transfer hydrogenation catalysts. [37, 38]

During the induction period prior to amine-borane dehydropolymerisation, **11** is likely converted into the active catalyst species when all water present is consumed, possibly by the reaction of the OH on **11** with amine-boranes to form boron oxyhydrides which are then eliminated (**Figure 129**). The postulated mono-amido ruthenium hydride intermediate species in this mechanism (Ru(^{i}Pr$_2$PCH$_2$CH$_2$NH)(^{i}Pr$_2$PCH$_2$CH$_2$NH$_2$)H, **A**) was proposed by Fagnou et al. as a possible on-cycle species for the dehydrogenation of amine-boranes with **8**, and analogous species have been isolated and proven to play a role in catalytic transfer hydrogenation reactions. [2, 34] The reaction of trans hydroxy hydride complexes of other group 8 metals with aminoboranes to form boroxide complexes has been previously reported. [39] The catalytic hydrolysis of amine-boranes by Ru(II) complexes, where Ru–OH species are detected in-situ has also been reported. [40]

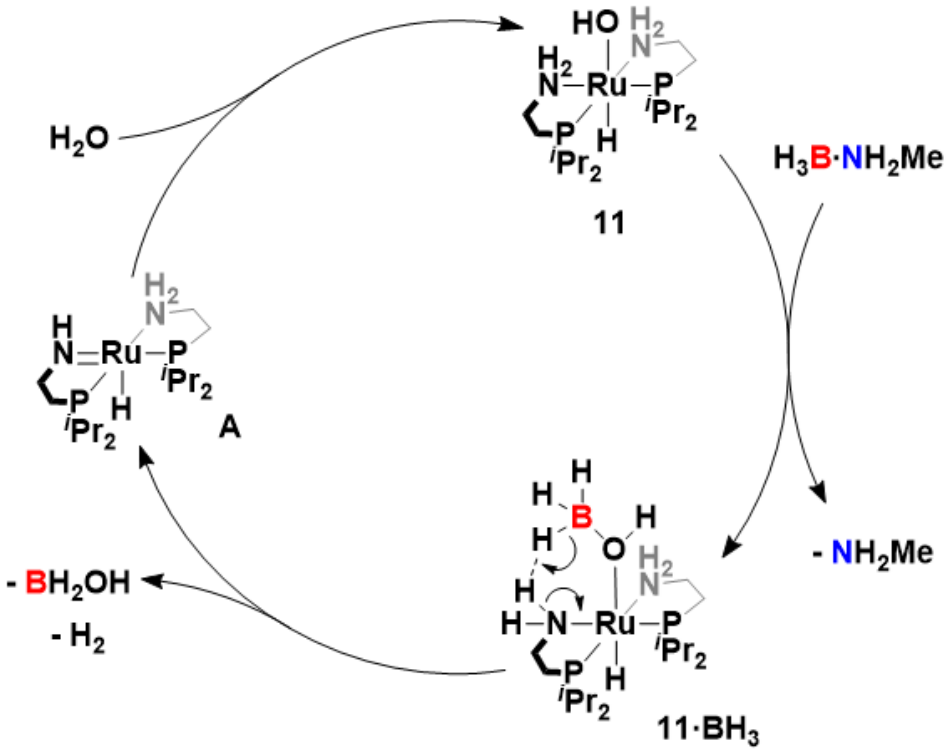

Figure 129. A hypothetical catalytic cycle for the processing of water by hydrolysis of amine-boranes, catalysed by **11**. Such a mechanism may operate during the induction period of amine-borane dehydropolymerisation with **8**.

To test the theory that the induction period observed prior to catalysis is due to the processing of a trace contaminant (such as water) a recharge experiment was performed. This involved the initial catalysis (charge 1) where $H_3B{\cdot}NH_2Me$ (0.112 g, 2.5 mmol as a 1 mol dm^{-3} solution in THF) was dehydropolymerised by **8** (0.033 mol%, 0.00033 mol dm^{-3}) activated by 0.01 mol dm^{-3} of NH_2Me. An induction period of 1500 s was observed before rapid hydrogen evolution commenced (**Figure 130**). Upon cessation of hydrogen evolution, the entire reaction mixture was then transferred onto a second equivalent of solid $H_3B{\cdot}NH_2Me$ (0.112 g, 2.5 mmol). Upon exposure to this second equivalent of $H_3B{\cdot}NH_2Me$ there was no induction period and rapid catalysis immediately commenced (**Figure 130**). This supports the theory that the cause of the induction period (likely water) is completely removed by the time catalysis initiates. The second period of catalysis exhibits a lower rate than the first, although this may be due to saturation of the reaction mixture with $(H_2BNHMe)_n$ resulting in delayed dissolution of the $H_3B{\cdot}NH_2Me$, and also a significant increase in reaction mixture viscosity.

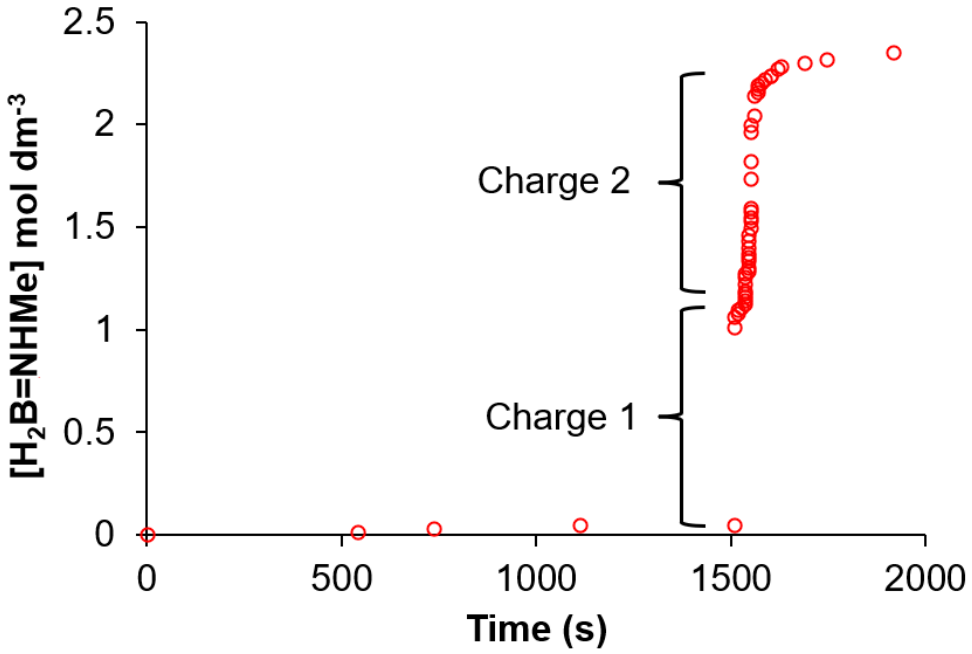

Figure 130. The H_2 evolution plot obtained from the dehydropolymerisation of methylamine-borane by *P,P-cis*-Ru(^{i}Pr$_2$CH$_2$CH$_2$NH$_2$)$_2$Cl$_2$ (**8**) with 0.01 mol dm^{-3} of MeNH$_2$, followed by a further charge of methylamine borane. The first charge shows the typical long induction period. The second charge shows almost no induction period. Catalyst loading at 0.033 mol% relative to methyl amine-borane (0.00033 mol dm^{-3} catalyst), 1 mol dm^{-3} methylamine borane in THF in each charge.

To further assess the effect of water on the dehydropolymerisation of H$_3$B·NH$_2$Me with precatalyst **8** (*P,P-cis*-Ru(^{i}Pr$_2$CH$_2$CH$_2$NH$_2$)$_2$Cl$_2$, activated with 2 equivalents of ^{t}BuOK forming **9**), catalysis was performed with varying water content. The THF solvent dried on a Na/benzophenone still that was used throughout this chapter had a water content measured by Karl Fischer analysis to be ~ 10 ppm, this was further dried over NaH and then stored on a potassium mirror for 3 months to provide an extremely low water content solvent. Separately, THF with a high water content was prepared (0.15 mol dm^{-3}, ~ 2700 ppm) which was 500 equivalents to the catalyst loading added to amine-borane dehydropolymerisation (0.0003 mol dm^{-3}).

When dehydropolymerisation was performed in THF dried over a potassium mirror, almost no induction period was observed and hydrogen evolution from rapid catalysis was observed immediately upon addition of the catalyst solution (**9**, *P,P-trans*-Ru(^{i}Pr$_2$PCH$_2$CH$_2$NH)$_2$ in THF) (**Figure 131**). In THF with ~ 2700 ppm of water present, a significantly extended induction period of over 11,000 s, after which catalysis proceeded and ~ 1 eq. of H_2 was released from the H$_3$B·NH$_2$Me (**Figure 131**). These are in comparison to dehydropolymerisation performed in the standard ~10 ppm of

H_2O THF for which the induction period was typically 1000 – 1500 s (**Figure 131**). This further strengthens the evidence that the presence of water is intrinsic to the induction period observed when precatalyst **8** (*P,P-cis*-Ru(^{i}Pr$_2$CH$_2$CH$_2$NH$_2$)$_2$Cl$_2$) and its derivatives are used in amine-borane dehydropolymerisation, apparently due to the formation of the catalytically-dormant water bound species **11** (*P,P-cis*-Ru(^{i}Pr$_2$PCH$_2$CH$_2$NH$_2$)$_2$(OH)H). This appears to be the case regardless of whether precatalyst **8** is activated by NH_2Me or by ^{t}BuOK (via species **9**) where species **11** forms during the induction period of catalysis with both activation methods.

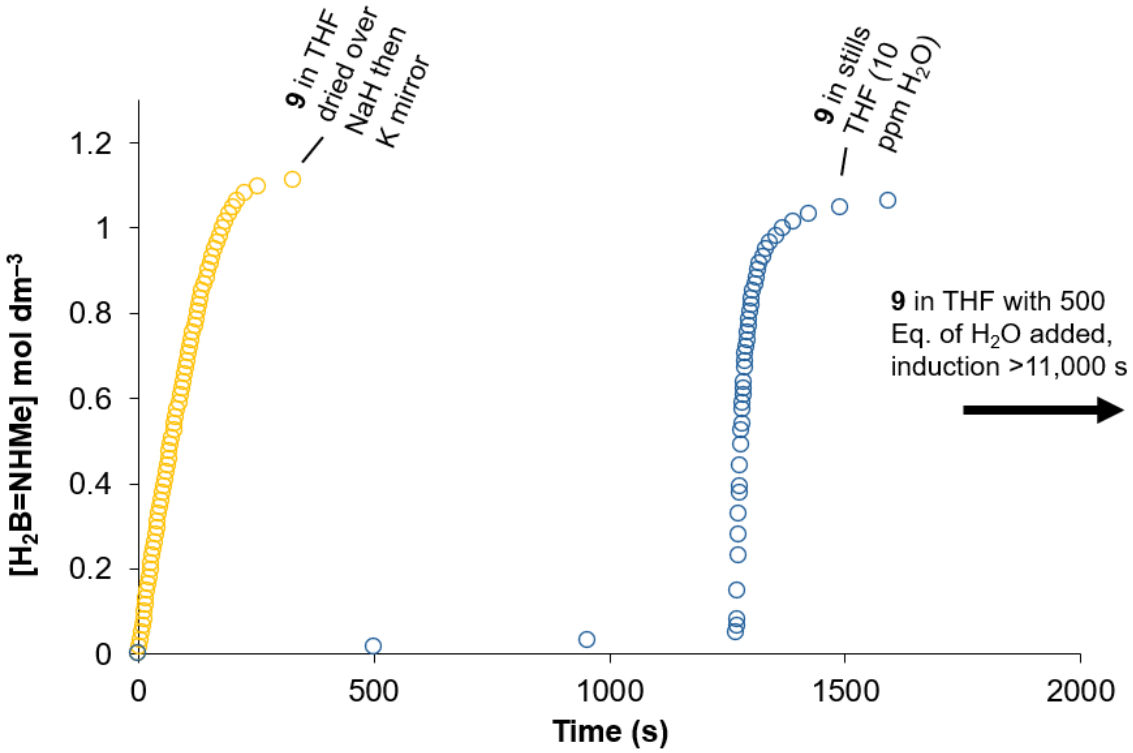

Figure 131. Effective H_2B=NMeH concentration over time from eudiometric H_2 evolution measurement for the dehydropolymerisation of $H_3B{\cdot}NH_2Me$ (0.112 g, 1 mol dm^{-3} in THF) **9** (0.03 mol%, generated in-situ from the reaction of **8** with 2 equivalents of ^{t}BuOK) with THF solvent with differing water content, varying from exceptionally dry (> 5 ppm) to 10 ppm and 2700 ppm. The effect of increased induction period with increasing water present is shown.

3.5.2.1 The dehydropolymerisation of $H_3B{\cdot}NH_2Me$ with 11 as a precatalyst

To provide more evidence that **11** is indeed the species seen during the induction period of the dehydropolymerisation of $H_3B{\cdot}NH_2Me$ with **8**, independently prepared **11** was used as a precatalyst. **11** was generated in-situ from the reaction of **8** with 2 equivalents of ^{t}BuOK (forming **9**) and then 5 equivalents of ^{i}PrOH. This solution (corresponding to 0.03 mol%) was then added to $H_3B{\cdot}NH_2Me$ (1 mol dm^{-3} in 2.5 cm^3 in THF) and the hydrogen evolution over time plotted to be compared with the other precatalysts **8** and **9** (**Figure 132**). **11** as a precatalyst shows a similar hydrogen evolution profile to when **8** and **9** are used as precatalysts and shows a comparable induction period, making **11** a good candidate for the species observed during the induction period of catalysis (**Figure 132**). The formed $(H_2BNHMe)_n$ polymer was precipitated from these catalysis runs with pentane and analyzed by GPC. The $(H_2BNHMe)_n$ obtained from **9** and **11** as precatalysts show almost identical M_n and dispersity, adding further evidence to the hypothesis that **11** is formed by the action of trace water on **9** during the induction period of catalysis (**Table 7**).

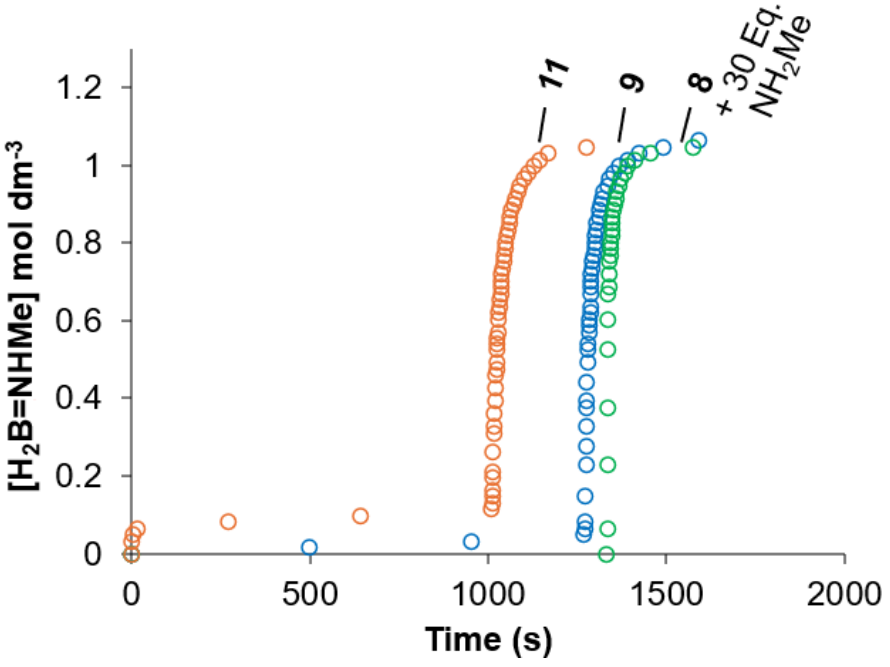

Figure 132. Effective $H_2B{=}NMeH$ concentration over time from eudiometric H_2 evolution measurement for the dehydropolymerisation of $H_3B{\cdot}NH_2Me$ (0.112 g, 1 mol dm^{-3} in THF) by **8** (0.033 mol%, with 30 equivalents of NH_2Me to catalyst (0.01 mol dm^{-3})), **9** (0.03 mol%, generated in-situ from the reaction of **8** with 2 equivalents of ^{t}BuOK) and **11** (0.03 mol%, generated in-situ from the reaction of **8** with 2 equivalents of ^{t}BuOK and then 5 equivalents of ^{i}PrOH).

Catalyst	$H_3B{\cdot}NMeH_2$ concentration (mol dm^{-3})	Catalyst mol%	Catalyst concentration (mol dm^{-3})	$MeNH_2$ concentration (mol dm^{-3})	M_n (mol dm^{-3})	Đ
11	1	0.03	0.0003	-	132,600	1.45
9	1	0.03	0.0003	-	138,700	1.46
8	1	0.033	0.0003	0.01	153,800	1.57

Table 7. Polymer data obtained by GPC analysis of the $(H_2BNHMe)_n$ formed by the catalytic dehydropolymerisation of $H_3B{\cdot}NH_2Me$ (1 mol dm^{-3} in THF) by **8** (0.033 mol%, with 30 equivalents of NH_2Me to catalyst (0.01 mol dm^{-3})), **9** (0.03 mol%, generated in-situ from the reaction of **8** with 2 equivalents of ^{t}BuOK) and **11** (0.03 mol%, generated in-situ from the reaction of **8** with 2 equivalents of ^{t}BuOK and then 5 equivalents of ^{i}PrOH).

3.5.3 Catalyst speciation during the active catalysis phase of amine-borane dehydropolymerisation with 8

Analogous to the speciation investigation of the induction period, in-situ NMR spectra were recorded during the hydrogen-producing active catalysis phase of $H_3B{\cdot}NH_2Me$ dehydropolymerisation with **8** (activated by 2 equivalents of *t*BuOK or 0.01 mol dm^{-3} of NH_2Me). These in-situ samples were also cooled rapidly to –90 °C to pause catalysis during NMR analysis whilst preserving catalyst speciation.

During the active catalysis phase, a new species is observed by in-situ $^{31}P\{^1H\}$ NMR spectroscopy as a singlet at 84 ppm (**Figure 133**) different to that observed during the induction period (89 ppm, **11**). The corresponding in-situ ^1H NMR spectrum shows the presence of a very weak and broad hydride resonance at –12.2 ppm (**Figure 134**). These signals are present when both precatalyst activation methods are used and visible at the same chemical shift across multiple runs. The low concentration and short timescale of this apparent observed catalyst resting state during dehydropolymerisation makes definitive assignment difficult. The singular phosphorous signal in the $^{31}P\{^1H\}$ NMR spectrum suggests that there is one ligand phosphorous environment and that by extension the aminophosphine ligands are symmetrical. This species will be henceforth referred to as complex **12** and the possible identity of which will be discussed vide infra.

The reduced signal to noise ratios for catalyst speciation ^1H NMR signals during the active catalysis phase compared to the induction period could reflect the removal of the catalyst at this stage by the inhibitor that was invoked to explain the observation of no catalytic activity when less than 0.01 mol% of **8** was used (or 0.016 mol% with **9**, see **3.3.1** and **3.4.1**). The absence of corresponding ^1H and ^{31}P NMR signals for the inhibited species could suggest that a paramagnetic species is formed. Ruthenium (III) complexes and many ruthenium (IV) complexes are paramagnetic and can be formed by the reaction of ruthenium (II) complexes with oxygen. [34, 41] A trace of oxygen corresponding to a solution concentration of around $1x10^{-4}$ mol dm^{-3} could account for the inhibitor affect seen by kinetic analysis, for which the corresponding catalyst decomposition would not be observed by NMR spectroscopy.

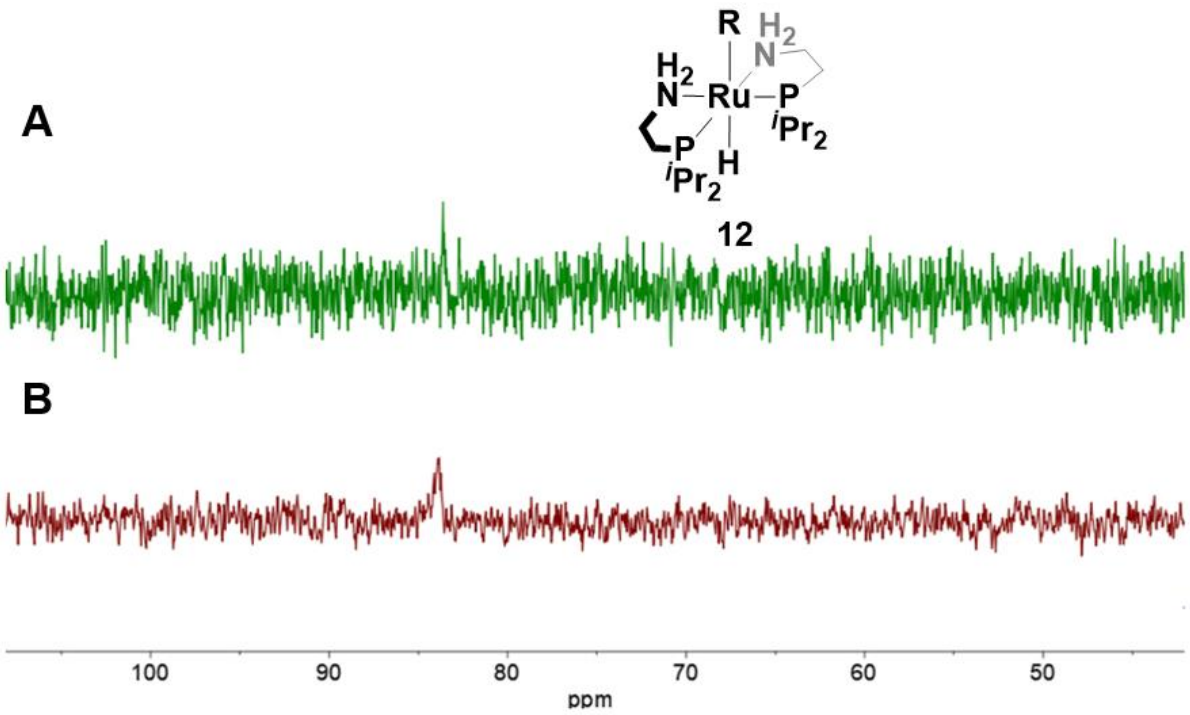

Figure 133. In-situ $^{31}P\{^{1}H\}$ NMR spectra taken during the active catalysis period of the dehydropolymerisation of $H_3B{\cdot}NH_2Me$ with **8**. A: **8** activated with 30 equivalents (0.01 mol dm^{-3}) of NH_2Me. B: **8** activated with 2 equivalents of ^{t}BuOK, forming **9** in-situ. Both show the same speciation, a singlet at 84 ppm. Both recorded in THF at – 90 °C, 512 scans with a starting catalyst concentration of $3x10^{-4}$ mol dm^{-3}.

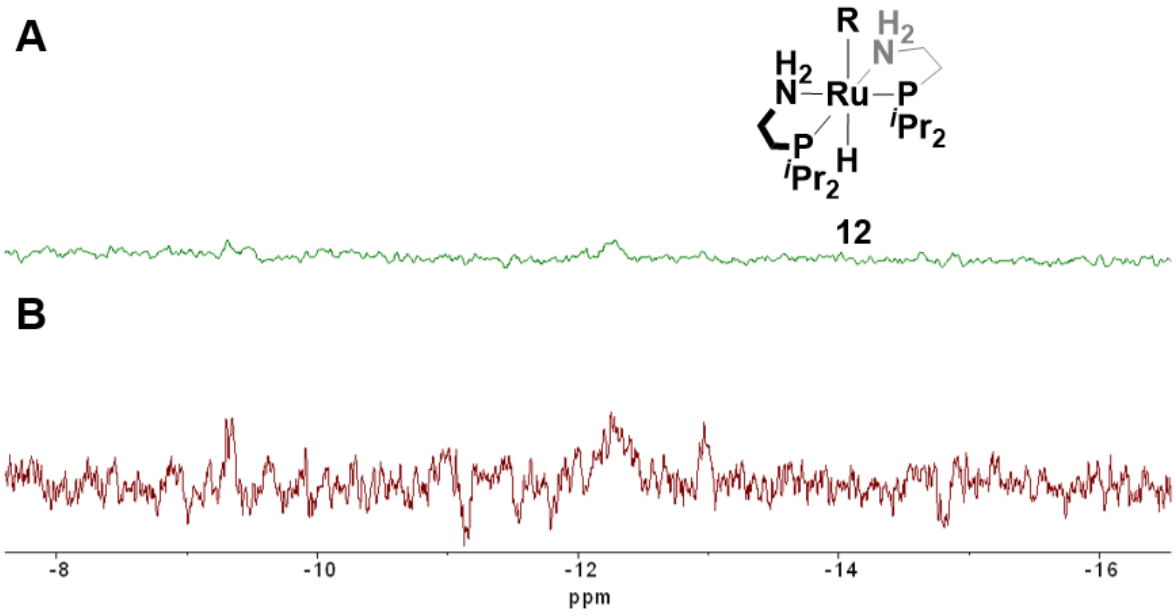

Figure 134. In-situ ^{1}H NMR spectra taken during the active catalysis period of the dehydropolymerisation of $H_3B{\cdot}NH_2Me$ with **8**. A: **8** activated with 30 equivalents (0.01 mol dm^{-3}) of NH_2Me. B: **8** activated with 2 equivalents of ^{t}BuOK, forming **9** in-situ. Both show the same speciation, a broad signal at – 12.2 ppm. Both recorded in THF at – 90 °C, 512 scans with a starting catalyst concentration of $3x10^{-4}$ mol dm^{-3}.

To aid with the identification of the catalyst speciation (complex **12**) during dehydropolymerisation of $H_3B{\cdot}NH_2Me$ with **8**, a comparison of reported Ru(II) aminophosphine ^1H NMR spectroscopic hydride shifts was performed. For the reaction of complex **9** with an excess of a H_2 source such as $H_3B{\cdot}NH_2Me$ a ruthenium dihydride could be expected from the addition of H_2 across both Ru-amido bonds, such dihydride species are reported for ruthenium transfer hydrogenation catalysts. [42, 43] The chemical shift of the ruthenium hydride observed during dehydropolymerisation (**12**, –12.2 ppm) is however between that for ruthenium octahedral trans dihydride complexes (–5 to –8 ppm) [31, 34, 43, 44] and that of ruthenium octahedral or trigonal bipyramidal monohydride complexes (–15 to –25 ppm) [34, 43, 44] with aminophosphine ligands (**Figure 135**). Octahedral ruthenium aminophosphine complexes with cis hydrides also have ^1H NMR shifts of around –5 ppm and would require an isomerization from a trans dihydride, which is reported to be a slow process in analogous complexes. [43, 45]

Amongst reported ruthenium (II) aminophosphine hydride complexes, a general trend can be seen where stronger sigma donating ligands trans to the hydride result in a less negative shift by ^1H NMR spectroscopy (**Figure 135**).[34, 43, 46-48] From this trend it can be inferred that complex **12**, which is seen by in-situ ^1H NMR spectroscopy during the active phase of dehydropolymerisation catalysis with **8** and **9**, has a ruthenium hydride that is trans to a medium-strength sigma-donating ligand. The broad ^1H NMR signal of this species (~ 190 Hz FWHM) could signify the presence of a fluxional process or hydrogen bonding. This observed species which may be the catalyst resting state will be referred to as **12** ($Ru(^iPr_2PCH_2CH_2NH_2)_2(R)H$), where R is a currently unidentified X-type sigma donating ligand (**Figure 135**).

There are two main possibilities for the identity of **12**. The first of which is where R is an equivalent of aminoborane $H_2B{=}NHMe$ that is bound across the Ru–N bond, with the nitrogen donating a lone pair into the aminoborane boron and a B–H forming a 3 centre two electron bond with the ruthenium (**Figure 136**). An analogous complex has been reported by Schneider et al. with a MACHO ligand: $[Ru(H)(PMe_3)\{(\mu\text{-}H)HB(NMe_2)N(CH_2CH_2P^iPr_2)_2\}]$ (**Figure 135**) that exhibits a similar hydride ^1H NMR spectroscopic shift (–13.6 ppm) to that of complex **12** (–12.2 ppm). [47] In the complex reported by Schneider et al., the BH hydrides are difficult to observe due to broadening, presumably caused by exchanging which of the B–H bonds is coordinated to the ruthenium. If complex **12** exhibits an analogous structure, this would explain the lack

of observable BH hydrides (around 0 – 5 ppm) and the broad hydride signal.[47] A bound aminoborane would however result in 2 ligand phosphorous environments, and only 1 is observed, so this is unlikely to be the identity of **12**. Of note is that related metal-bound aminoborane complexes have been invoked as the first step in metal-out head-to-tail aminoborane polymerisation.[5, 9, 49]

The second possibility is that complex **12** is a trans-dihydride where R is H^-, and the hydride ^1H NMR signal is shifted by adduct formation with $H_3B{\cdot}NH_2Me$. The $H_3B{\cdot}NH_2Me$ could bind via dihydrogen bonding across the Ru–N bond as $Ru(^iPr_2PCH_2CH_2NH_2)_2(H)_2{\cdot}H_3B{\cdot}NH_2Me$ (**Figure 136**). Both hydrides must form transient adducts with $H_3B{\cdot}NH_2Me$ for only 1 hydride shift to be present in the ^1H NMR spectrum, as seen for complex **12**. This adduct formation is also supported by the apparent initial zero-order in $H_3B{\cdot}NH_2Me$ concentration observed during kinetic analysis, which could suggest a pre-equilibrium of binding $H_3B{\cdot}NH_2Me$ to the catalyst before the rate limiting step. A similar scenario has been reported by Weller et al. in which rhodium MACHO complex **3** ($Rh(^iPr\text{-}PN^HP)H_3$) forms a dihydrogen bonded adduct with $H_3B{\cdot}NH_2Me$ during dehydropolymerisation, which leads to a pseudo zero order in $[H_3B{\cdot}NH_2Me]$ and shifts the hydride signals as observed by ^1H NMR spectroscopy.[5]

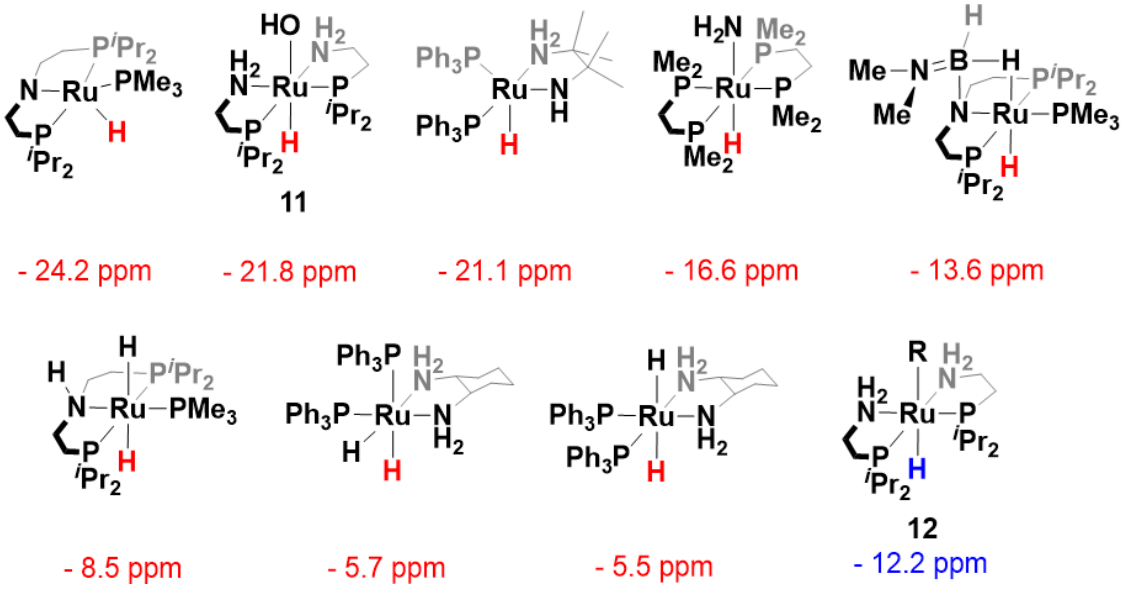

Figure 135. ^1H NMR shifts for a variety of reported ruthenium (II) aminophosphine complexes. Shifts given for the hydrides coloured in red.[34, 43, 46-48] The general inferred structure for the species observed by ^1H NMR spectroscopy during the active catalysis phase of dehydropolymerisation of $H_3B{\cdot}NH_2Me$ with **8** and **9** is shown as **12**, with its hydride highlighted in blue.

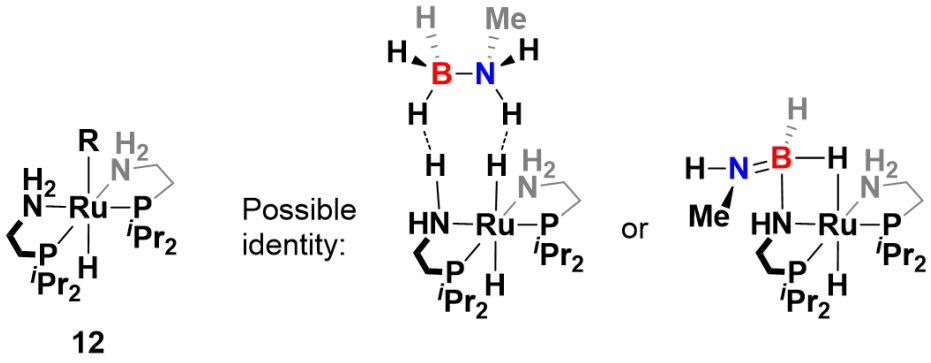

Figure 136. Possible identities of complex **12**: a trans dihydride which forms a transient amine-borane dihydrogen bonded adduct Ru(^{i}Pr$_2$PCH$_2$CH$_2$NH$_2$)$_2$(H)$_2$·H$_3$B·NH$_2$Me or a mono amido hydride which is irreversibly bound to an equivalent of aminoborane H$_2$B=NHMe.

3.5.4 The hydrogenation of 9 with H_2 to form a ruthenium hydride

In an attempt to understand the catalyst speciation observed during the active catalysis period, the synthesis of the hypothetical trans dihydride complex Ru(^{i}Pr$_2$PCH$_2$CH$_2$NH$_2$)$_2$H$_2$ was attempted by reacting **9** (made in-situ from **8** + 2 equivalents of ^{t}BuOK) in a THF-d$_8$ solution with H_2 gas at 4 bar (**Figure 137**). Complete conversion was observed by $^{31}P\{^1H\}$ NMR spectroscopy, where a new species observed as a singlet at 92.8 ppm was observed (**Figure 138**). The corresponding ^1H NMR spectrum at 298 K showed the presence of two overlapped hydride signals, a triplet at – 9.13 ppm (J_{HP} = 16 Hz) and a broad signal at – 9.21 ppm (**Figure 138**). The singular signal in the $^{31}P\{^1H\}$ NMR spectrum and triplet splitting of hydride suggest identical ligand phosphorous environments and therefore symmetrical aminophosphine ligands. At –90 °C these hydride signals resolve into dt: – 9.05 ppm (dt, J_{HP} = 16 Hz, J_{HH} = 4 Hz), – 9.43 ppm (dt, J_{HP} = 16 Hz, J_{HH} = 4 Hz) (**Figure 138**). The ^1H NMR spectrum of the formed species also suggests symmetrical aminophosphine ligands, showing only two CH_2 resonances from the ligand backbones (**Figure 139**).

The broad hydride signal observed in the ^1H NMR spectrum is likely the result of a rapid exchange process (**Figure 138**). This has been observed for the ruthenium trans-dihydride Ru(^{i}Pr-PN^{H}P)(PMe$_3$)H$_2$ in the presence of a trace proton source such as water where one of the ^1H NMR hydride signals is broadened by exchange (**Figure 141**).[31] Such trace water was observed during the induction period of catalysis, forming *P,P-cis*-Ru(^{i}Pr$_2$PCH$_2$CH$_2$NH$_2$)$_2$(OH)H (**11**). This exchange-induced broadening is further supported by the sharpening of the observed hydride signals upon cooling to 193 K, thus slowing the exchange process (**Figure 138**). This exchange process could also be the rapid interconversion of the proposed dihydride complex Ru(^{i}Pr$_2$PCH$_2$CH$_2$NH$_2$)$_2$H$_2$ to the corresponding mono-amido dihydrogen complex Ru(^{i}Pr$_2$PCH$_2$CH$_2$NH$_2$)(^{i}Pr$_2$PCH$_2$CH$_2$NH)(H$_2$) (**Figure 141**).[50]

The ruthenium species observed at 92.8 ppm in the $^{31}P\{^1H\}$ NMR spectrum (tentatively Ru(^{i}Pr$_2$PCH$_2$CH$_2$NH$_2$)$_2$H$_2$) could not be isolated due to the rapid decomposition to multiple unidentified species when the H_2 atmosphere was removed, likely via facile H_2 dissociation. The NMR spectra of this species (^{31}P NMR: 92.8 ppm, ^1H NMR: ~ – 9.1 ppm) differ significantly from what is observed during the active catalysis phase of

$H_3B{\cdot}NH_2Me$ dehydropolymerisation with **8** (^{31}P NMR: 84.0 ppm, ^{1}H NMR: –12.2 ppm) and so is unlikely to be the same species as the apparent catalyst resting state **12**. [55]

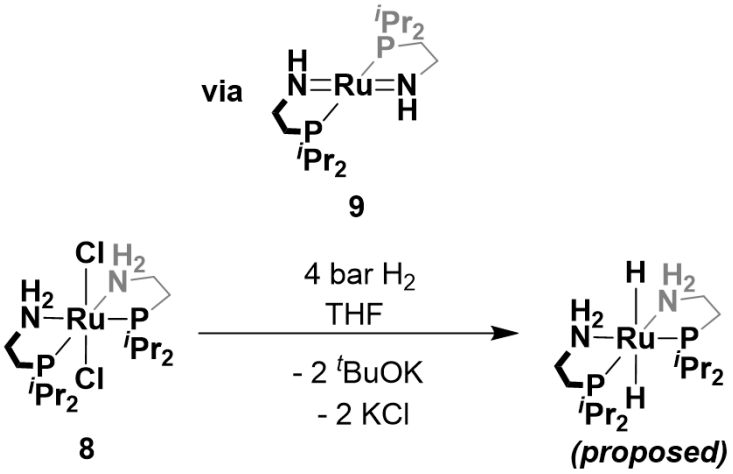

Figure 137. The reaction of **9** (generated in-situ from **8** + 2 equivalents of ^{t}BuOK) and an excess of H_2 gas, to form the proposed trans dihydride species Ru($^{i}Pr_2PCH_2CH_2NH_2)_2H_2$.

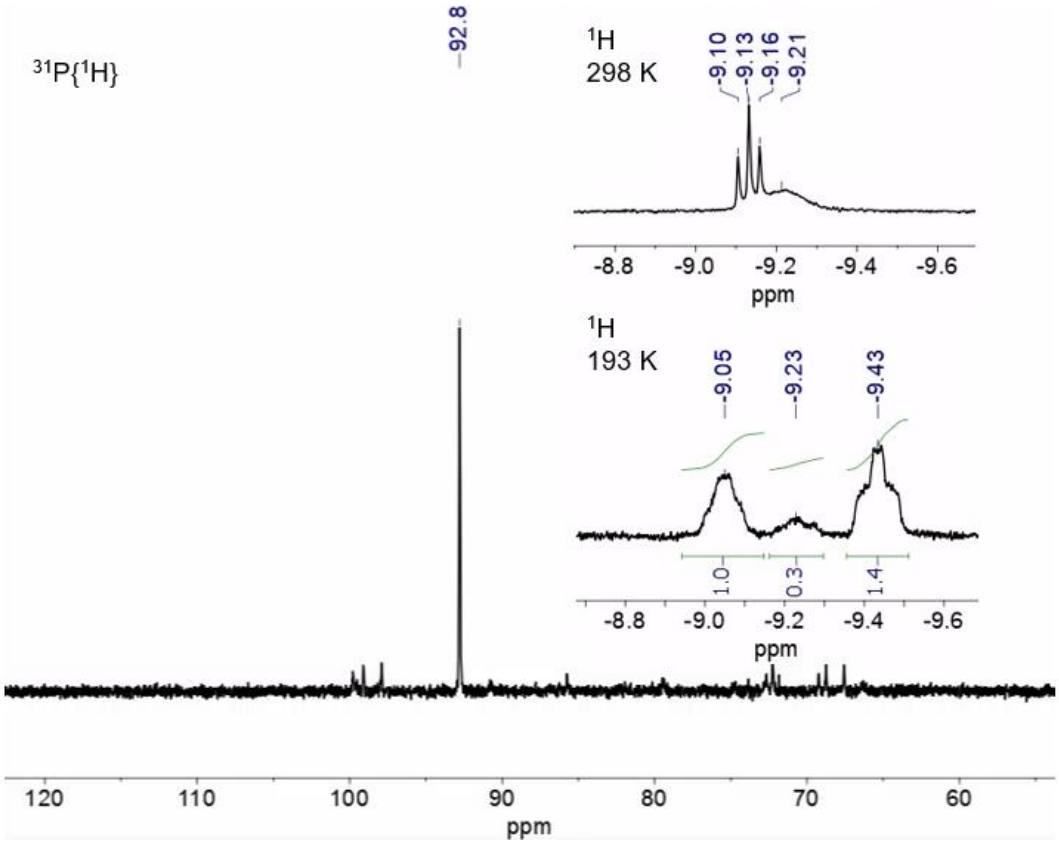

Figure 138. In-situ $^{31}P\{^{1}H\}$ NMR spectrum of the reaction between **9** (generated in-situ from **8** and 2 equivalents of ^{t}BuOK) and an excess of H_2 at 4 bar, showing a new signal at 92.8 ppm, possibly corresponding to *P,P-cis*-Ru($^{i}Pr_2PCH_2CH_2NH_2)_2H_2$. Inset: in-situ ^{1}H NMR spectra showing expansions of the observed hydrides at 298 K and when cooled to 193 K. Both recorded in THF-d_8.

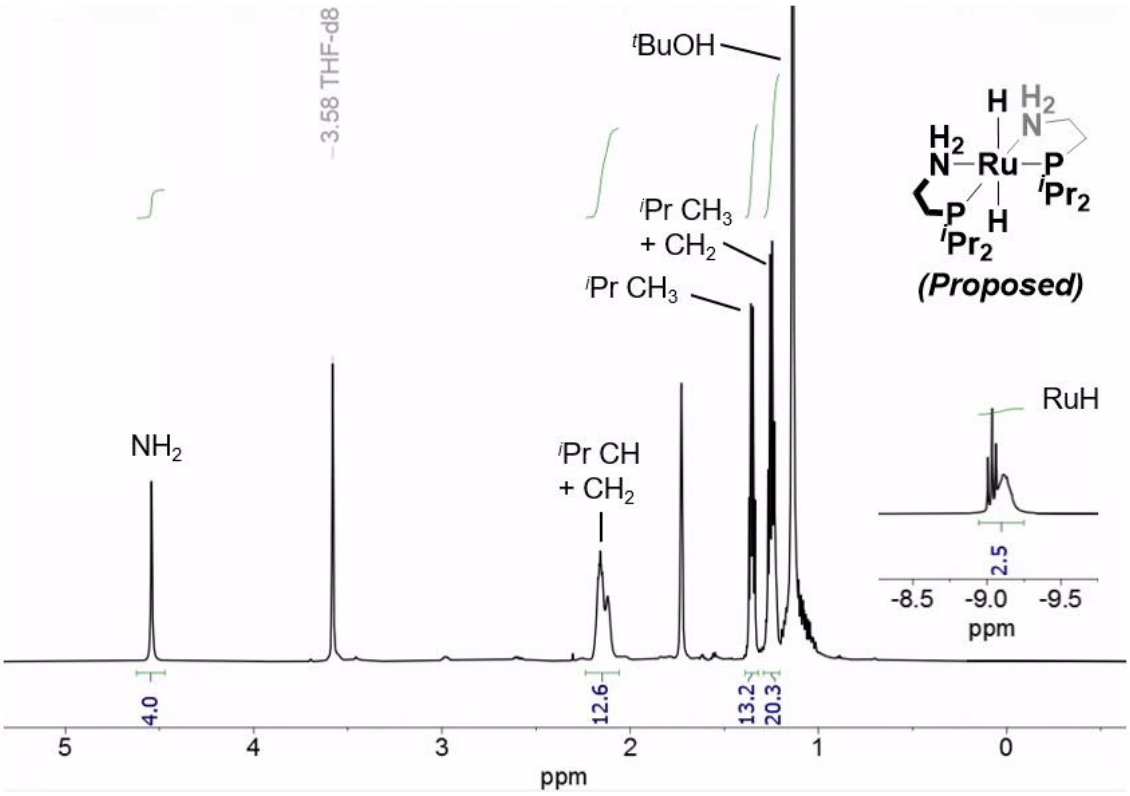

Figure 139. In-situ ^{1}H NMR spectrum of the reaction between **9** (generated in-situ from **8** and 2 equivalents of ^{t}BuOK) and an excess of H_2 at 4 bar, showing signals possibly corresponding to *P,P-cis*-Ru($^{i}Pr_2PCH_2CH_2NH_2)_2H_2$. Inset: in-situ ^{1}H NMR spectra showing an expansion of the observed hydrides at 298 K. Recorded in THF-d_8.

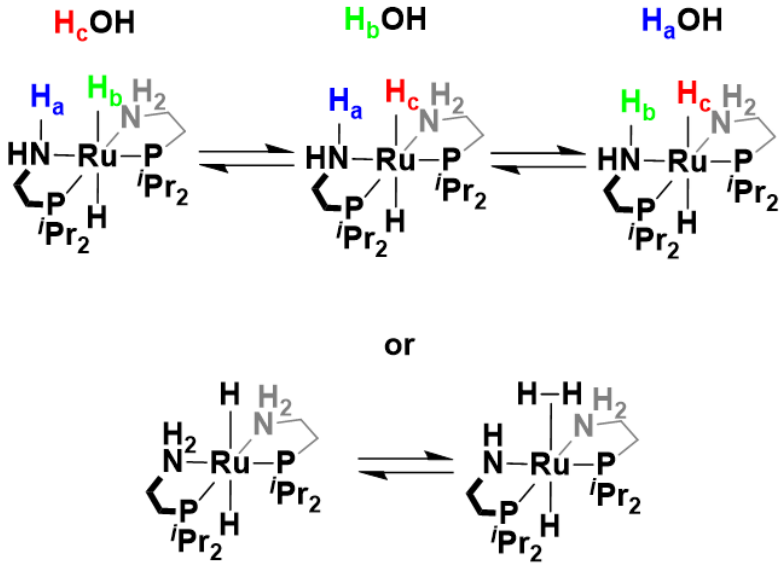

Figure 140. Possible exchange processes with *P,P-cis*-Ru($^{i}Pr_2PCH_2CH_2NH_2)_2H_2$ that could lead to the observed broadening of the hydride shift in the room-temperature ^{1}H NMR spectrum.

3.6 The reaction of 8 with borohydride to form ruthenium hydride *P,P-cis*-Ru(^{i}Pr$_2$PCH$_2$CH$_2$NH$_2$)$_2$(κ^1-BH$_4$)H (13)

As the direct hydrogenation of **9** failed to produce a ruthenium hydride spectroscopically resemblant of **12** seen during the active catalysis phase of $H_3B{\cdot}NH_2Me$ dehydropolymerisation with **8**, other hydrogen donors were considered. For hydrogenation and transfer hydrogenation catalysis, trans ruthenium hydride borohydride complexes have been reported as competent precatalysts that are structurally related to the proposed trans-dihydride active species (effectively BH_3 capped). [51-53] The reported syntheses of such compounds involve the reaction of a ruthenium chloride complex with an excess of $NaBH_4$ in the presence of an alcohol. [51, 54]

A solution of **8** in ^{i}PrOH was reacted with 5 equivalents of $NaBH_4$, the solvent was then evaporated in-vacuo and the residue extracted with toluene (**Figure 141**, see experimental for details). This toluene extract was layered with pentane to form a crystalline solid which was interrogated by single-crystal x-ray diffraction. The structure of the formed ruthenium complex was found to be *P,P-cis*-Ru(^{i}Pr$_2$PCH$_2$CH$_2$NH$_2$)$_2$(κ^1-BH$_4$)H (**13**) as determined by single crystal x-ray diffraction (**Figure 142**). The crystals were well diffracting with an R_{int} of 0.0966 for the space group P2$_1$/c, and an R_1 of 0.0630 that suggests good agreement between the model and observed diffraction data. Two crystallographically independent molecules of complex **13** are present in the unit cell. The Ru–H and B–H hydrides were all located in the electron density map; however these were lightly constrained to have equal bond distances in both inequivalent **13** molecules in the unit cell.

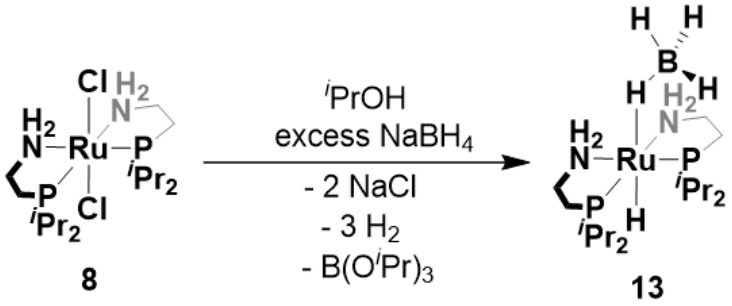

Figure 141. The synthesis of **13** from the reaction of **8** with an excess of $NaBH_4$ in the presence of ^{i}PrOH.

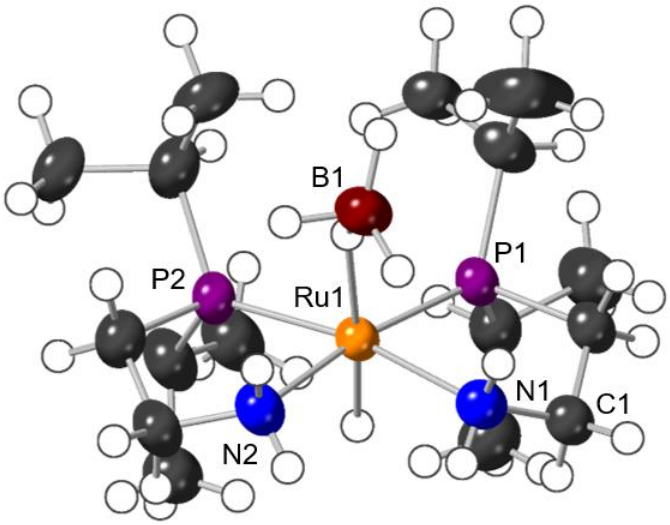

Figure 142. Molecular structure of *P,P-cis*-Ru(^{i}Pr$_2$PCH$_2$CH$_2$NH$_2$)$_2$(κ^1-BH$_4$)H (**13**) as determined by single crystal X-ray diffraction. Displacement ellipsoids are shown at the 50% probability level. Hydrogen atoms are placed in calculated positions other than the Ru–H and B–H hydrides which were located in the electron density map. Selected distances [Å], bond lengths [Å] and angles [°]: Ru(1)···B(1) 2.859(9), Ru(1) – N(1) 2.192(7), Ru(1) – N(2) 2.189(8), Ru(1) – P(1) 2.253(2), Ru(1) – P(2) 2.245(2), C(1) – N(1) 1.485(11), P(1) – Ru(1) – N(1) 83.8(2), C(1) – N(1) – Ru(1) 112.2(6).

Isolated crystalline **13** was also investigated by ^{1}H, ^{11}B and ^{31}P{^{1}H} NMR spectroscopies. NMR data for **13** show a single phosphorous environment by ^{31}P{^{1}H} NMR spectroscopy at 93.4 ppm (singlet) and two hydride signals by ^{1}H NMR spectroscopy: 1.55 ppm (br, 4H, BH_4) and – 17.26 ppm (t, J_{HP} = 24 Hz 1H, Ru–H) (**Figure 143**). The BH_4 signal in the proton NMR sharpens slightly upon ^{11}B decoupling (**Figure 143**). Complex **13** is not observed during the dehydropolymerisation of $H_3B{\cdot}NH_2Me$ with complex **8**, discounting it as the catalytic resting state. Attempts to abstract the BH_3 from **13** to from a trans-dihydride complex such as *P,P-cis*-Ru(^{i}Pr$_2$PCH$_2$CH$_2$NH$_2$)$_2$H$_2$ with the nucleophiles: NH_2Me, NEt_3, DABCO and ^{t}BuOK were unsuccessful, resulting in no reaction.

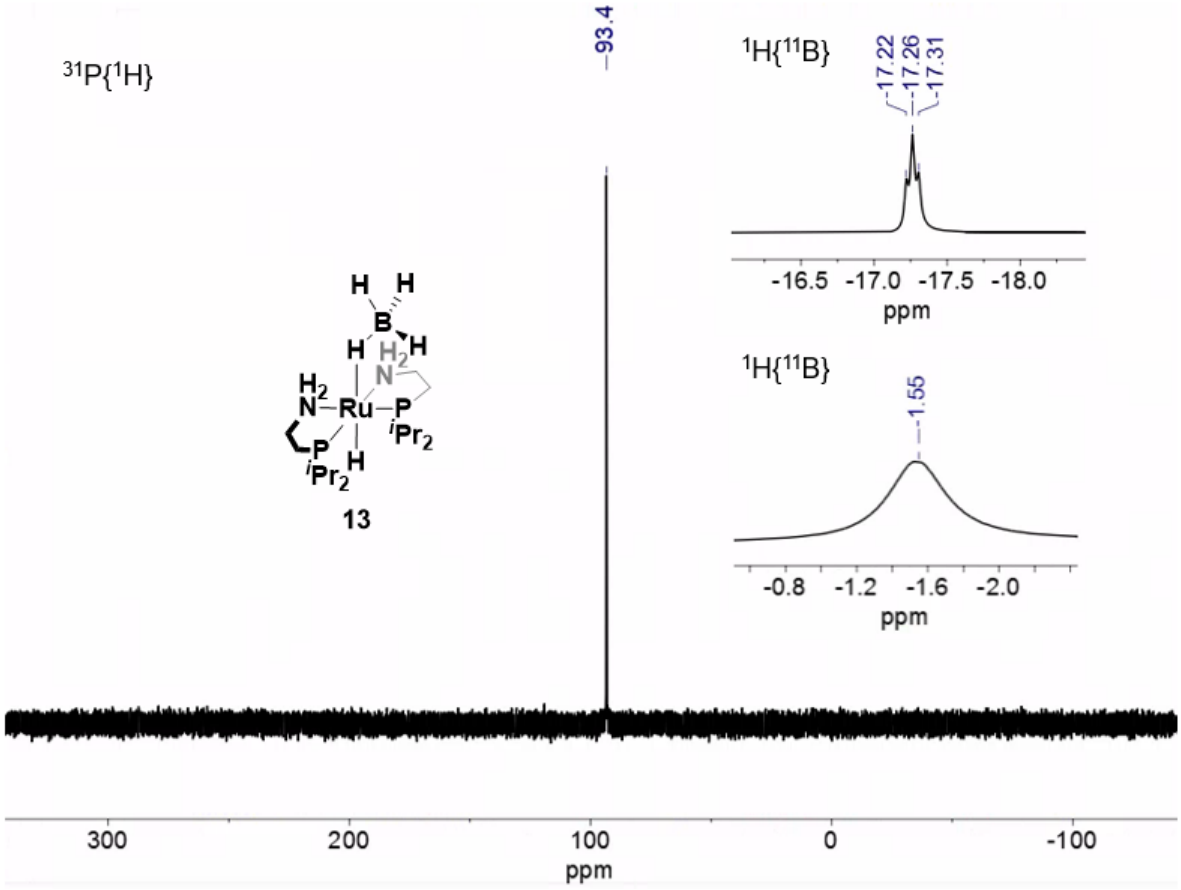

Figure 143. $^{31}P\{^{1}H\}$ NMR spectrum of isolated **13** showing a singlet at 93.4 ppm. Inset: in-situ $^{1}H\{^{11}B\}$ NMR spectra showing expansions of the observed hydrides Ru–H and Ru–H–BH_3. Both recorded in benzene-d_6 at 298 K

3.6.1 *P,P-cis*-Ru(^{i}Pr$_2$PCH$_2$CH$_2$NH$_2$)$_2$(κ^1-BH$_4$)H (13) as a precatalyst to amine-borane dehydropolymerisation

As ruthenium trans hydride borohydride complexes are known to function as competent precatalysts for the hydrogenation and transfer hydrogenation of small molecules, the use of **13** as an amine-borane dehydropolymerisation catalyst was evaluated. Complex **13** (0.03 mol%) with 0.01 mol dm^{-3} of NH_2Me was used to dehydropolymerise $H_3B{\cdot}NH_2Me$ (1 mol dm^{-3} in THF) and the hydrogen evolved was measured eudiometrically (**Figure 144**). Similarly to **8**, without the addition of excess NH_2Me to the catalyst no dehydropolymerisation of $H_3B{\cdot}NH_2Me$ by **13** was observed, suggesting that the amine is critical to bring the catalyst online. As NH_2Me does not directly react with **13**, the precatalyst activation must involve the presence of both NH_2Me and $H_3B{\cdot}NH_2Me$. As with complexes **8** and **9** as precatalysts, complex **13** fully and rapidly dehydropolymerised the $H_3B{\cdot}NH_2Me$ in under 30 seconds after an induction period (**Figure 145**). This induction period (~ 1000 seconds) was shorter than that typically seen with **8** and **9** at similar catalyst loadings (> 1300 seconds at 0.03 mol%), however it should be noted that these induction periods for these catalysts can be stochastic, varying by ± 300 s between runs.

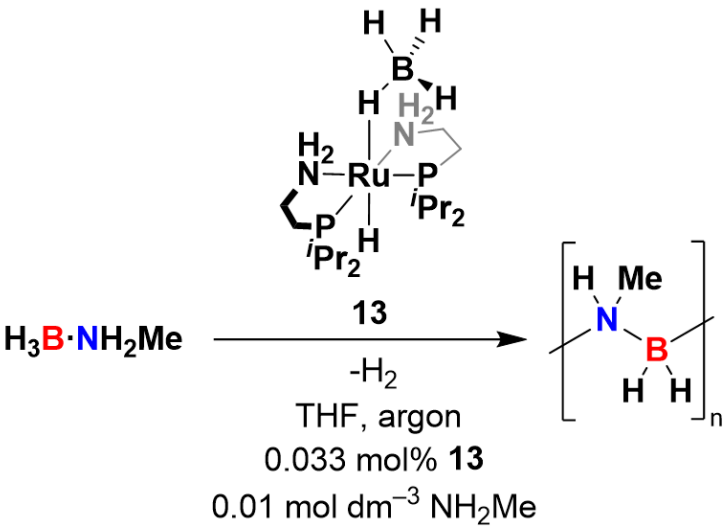

Figure 144. The dehydropolymerisation of $H_3B{\cdot}NH_2Me$ (0.112 g, 1 mol dm^{-3} in 2.5 cm^3 THF) by precatalyst **13** with 0.01 mol dm^{-3} of NH_2Me to activate.

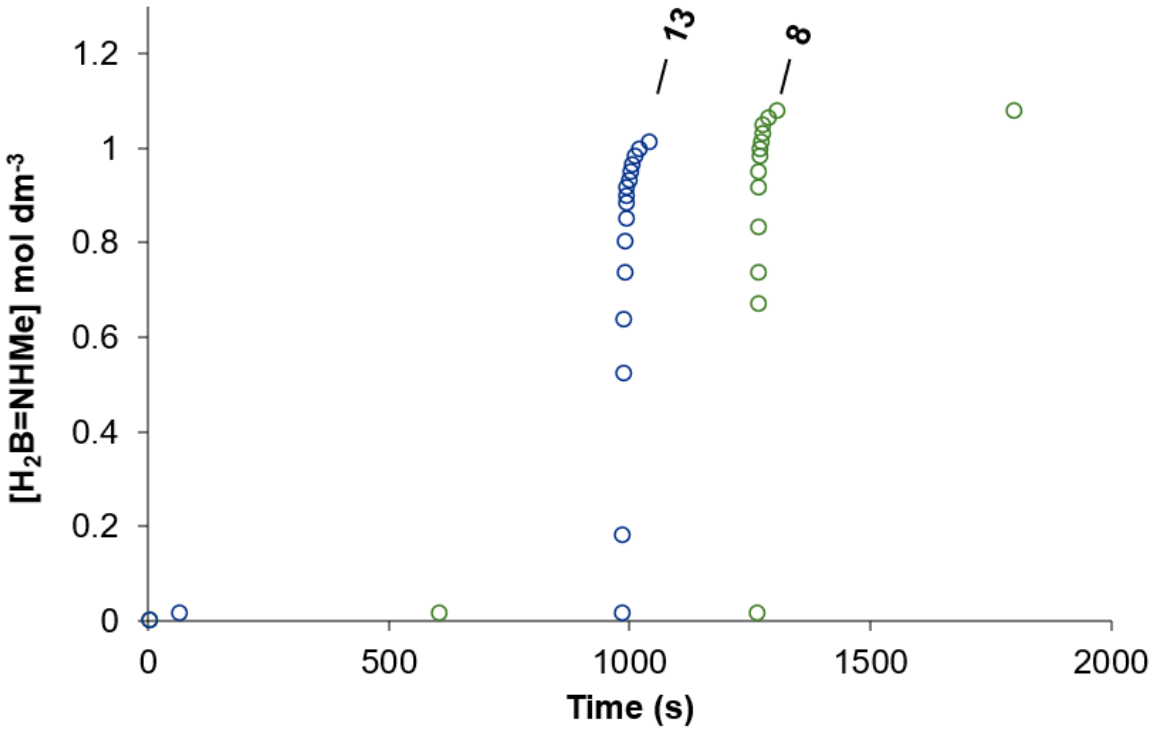

Figure 145. Effective $H_2B{=}NMeH$ concentration over time from eudiometric H_2 evolution measurement for the dehydropolymerisation of $H_3B{\cdot}NH_2Me$ (0.112 g, 1 mol dm^{-3} in THF) by **8** and **13** (0.0297 and 0.03 mol% respectively), with 0.01 mol dm^{-3} of NH_2Me. A shorter induction period is seen with **13** (1000 s) compared to **8** (1300 s).

To confirm that precatalyst **13** operates in the same way as **8** and **9** during the dehydropolymerisation of amine-boranes, an in-situ NMR study was performed in an identical fashion to those described previously in this chapter for precatalysts **8** and **9** (–90 °C in THF-H_8). In-situ aliquots were taken from the induction period and active catalysis regions during the dehydropolymerisation of $H_3B{\cdot}NH_2Me$ with **13** + 0.01 mol dm^{-3} of NH_2Me.

During the induction period a singlet is observed in the $^{31}P\{^1H\}$ NMR spectrum at –89.2 ppm and a triplet is observed in the ^1H NMR spectrum at – 19.56 ppm (J_{HP} = 27 Hz, **Figure 146**). These signals match those seen during the induction periods when **8** and **9** are used as precatalysts, corresponding to the hydroxy-hydride complex **11** which is formed by the reaction with trace water. This provides strong evidence that all three dehydropolymerisation catalysts (**8**, **9**, and **13**) are rapidly converted to complex **11** during the induction period of amine-borane dehydropolymerisation and therefore operate by the same mechanism. Further evidence for this is provided by the in-situ NMR signals observed during the active catalysis phase for the dehydropolymerisation

of $H_3B{\cdot}NH_2Me$ with **13** + 0.01 mol dm^{-3} of NH_2Me. The in-situ $^{31}P\{^1H\}$ NMR spectrum shows a singlet at 84.5 ppm and the ^1H NMR spectrum shows a broad resonance –12.19 ppm which corresponds to a ruthenium hydride (complex **12**) (**Figure 147**). These signals also match those seen during the active catalysis periods when **8** and **9** are used as precatalysts.

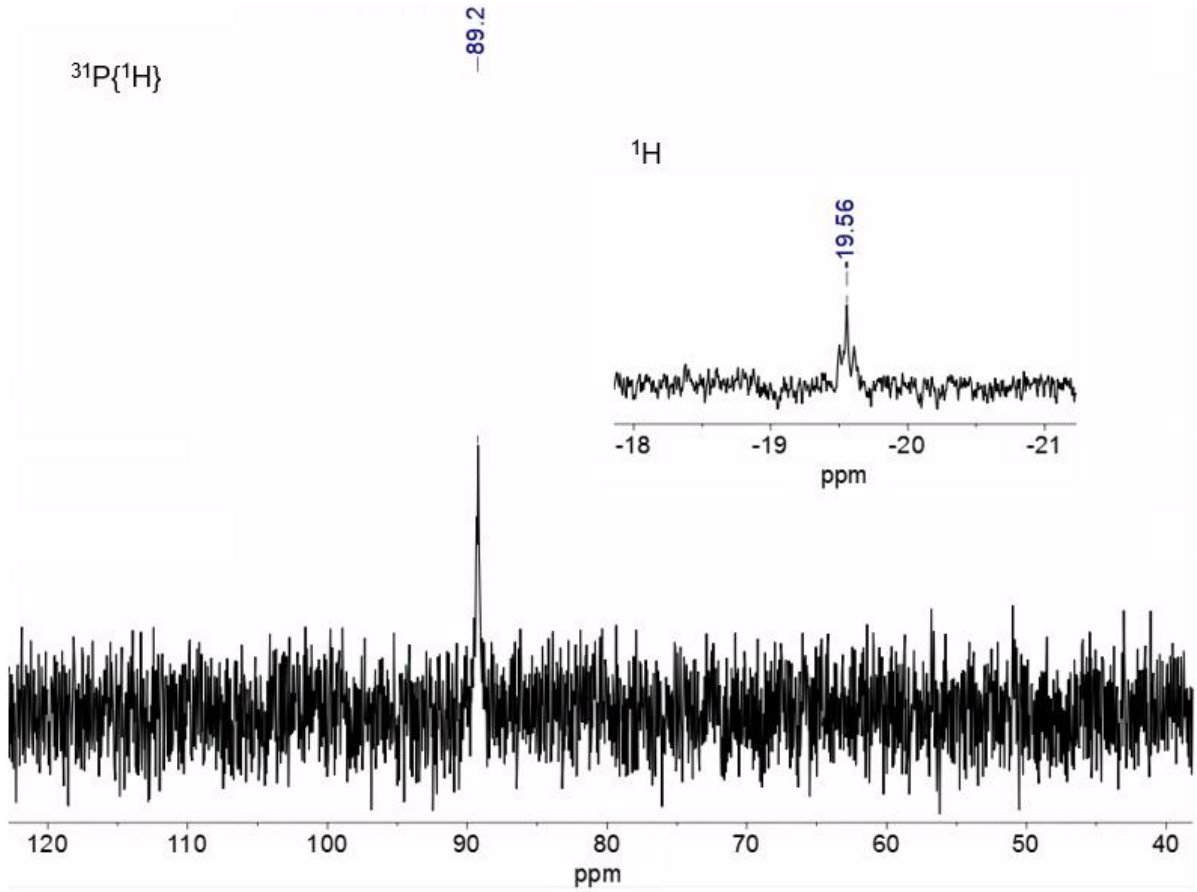

Figure 146. In-situ $^{31}P\{^1H\}$ NMR spectrum taken during the induction period of the dehydropolymerisation of $H_3B{\cdot}NH_2Me$ with **13** activated with 0.01 mol dm^{-3} of NH_2Me, showing a singlet at 89.2 ppm which corresponds to **11**. Inset: ^1H NMR spectrum recorded in-situ during the induction period of the same dehydropolymerisation, showing a triplet at –19.56 Hz (J_{HP} = 27 Hz) which corresponds to the ruthenium hydride of **11**. Both recorded in THF at –90 °C, 512 scans with a starting catalyst concentration of $3.3x10^{-4}$ mol dm^{-3}.

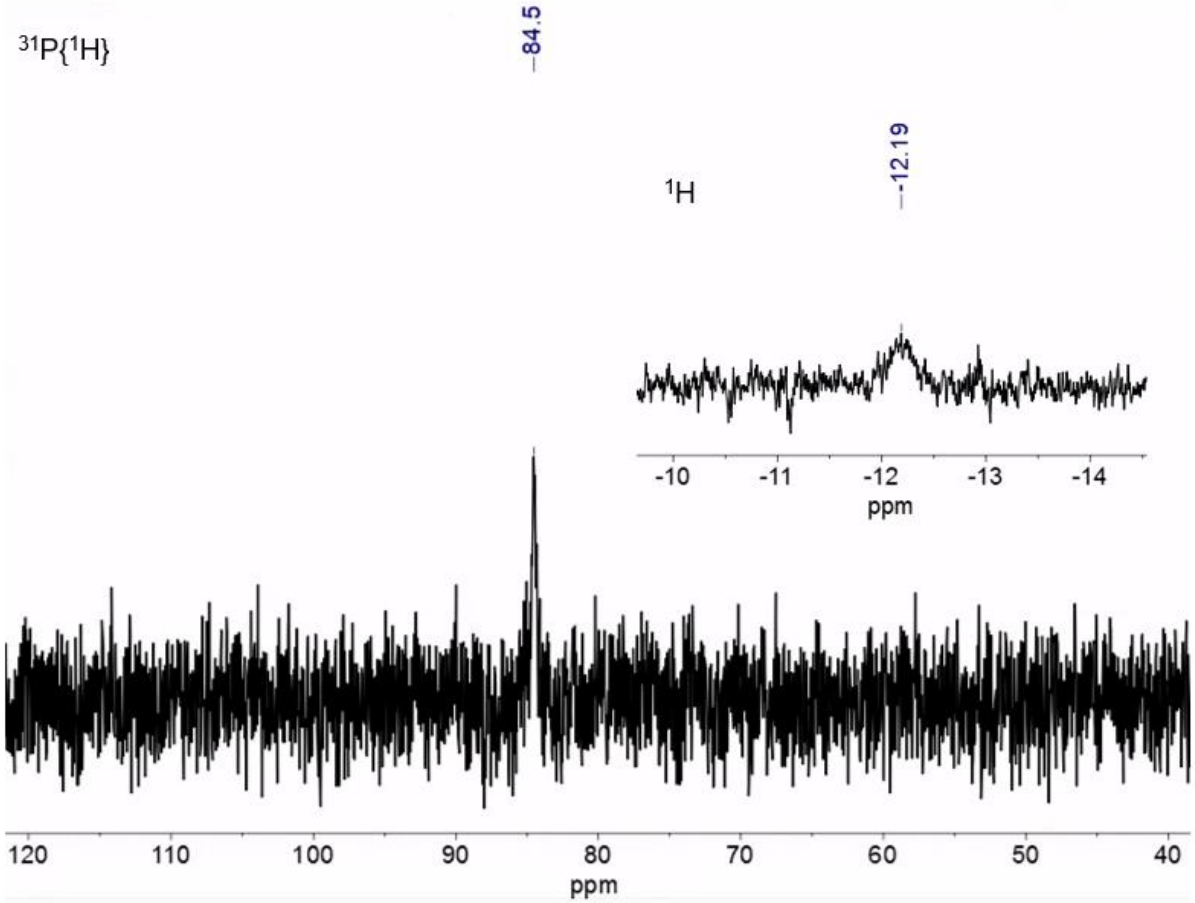

Figure 147. In-situ $^{31}P\{^{1}H\}$ NMR spectrum taken during the active catalysis period of the dehydropolymerisation of $H_3B{\cdot}NH_2Me$ with **13** activated with 0.01 mol dm^{-3} of NH_2Me, showing a singlet at 84.5 ppm (**12**). Inset: ^{1}H NMR spectrum recorded in-situ during the active catalysis period of the same dehydropolymerisation, showing a broad signal at – 12.19 Hz (**12**). Both recorded in THF at –90 °C, 512 scans with a starting catalyst concentration of $3.3x10^{-4}$ mol dm^{-3}.

The shorter induction period by precatalyst **13** compared to **8** when both were activated by NH_2Me could support the idea that the processing of trace water, by reaction with boranes, occurs during the induction period and that the BH_3 bound to the precatalyst **13** aids this (see **3.5.2**). This should be further investigated by the addition of $BH_3{\cdot}THF$ to the dehydropolymerisation of amine-boranes as a possible way to remove the induction period seen with all of the ruthenium precatalysts discussed herein. The activity of borohydride complex **13** as a dehydropolymerisation catalyst is of significant interest as the related rhodium borohydride complex **4** ($Rh(PN^{H}P^{i}Pr)(\kappa^{1}\text{-}BH_4)H_2$), formed by catalyst poisoning of active species **3** ($Rh(PN^{H}P^{i}Pr)H_3$) upon exposure to bulkier amine-boranes such as $H_3B{\cdot}NH_2{}^{n}Pr$, does not show activity (see chapter 2, **2.1.4**). This may mean these ruthenium precatalysts are more suited to the dehydropolymerisation of a wider range of amine-boranes (vide infra).

3.7 Possible mechanisms for the dehydropolymerisation of amine-boranes with precatalysts 8, 9 and 13

3.7.1 Precatalyst activation and induction period

NMR spectroscopic speciation investigations carried out during the induction period of the dehydropolymerisation of amine-borane $H_3B{\cdot}NH_2Me$ with **8**, **9**, and **13** show that all of these prectalaysts are rapidly converted into the hydroxy hydride species **11**, likely by the reaction with trace water present in the reaction solvent. **11** can be inferred to form via the heterolysis of a H_2O molecule across a ruthenium amido bond, and so a precursor to **11** could be the mono amido monohydride complex Ru(^{i}Pr$_2$PCH$_2$CH$_2$NH)(^{i}Pr$_2$PCH$_2$CH$_2$NH$_2$)H (**A**) (**Figure 148**), which was proposed to be a catalytically relevant species by Fagnou et al. in the seminal report on the dehydrogenation of amine-boranes by **8** with ^{t}BuOK. [2] This species may form part of a water-processing catalytic cycle in which boranes are slowly catalytically hydrolysed to form boron oxyhydrides such as BH_2OH and eventually boric acid during the induction period of amine-borane dehydropolymerisation (**Figure 148**).[40] This process likely continues until the majority of the water present is used up, upon which amine-borane dehydrogenation starts. [45]

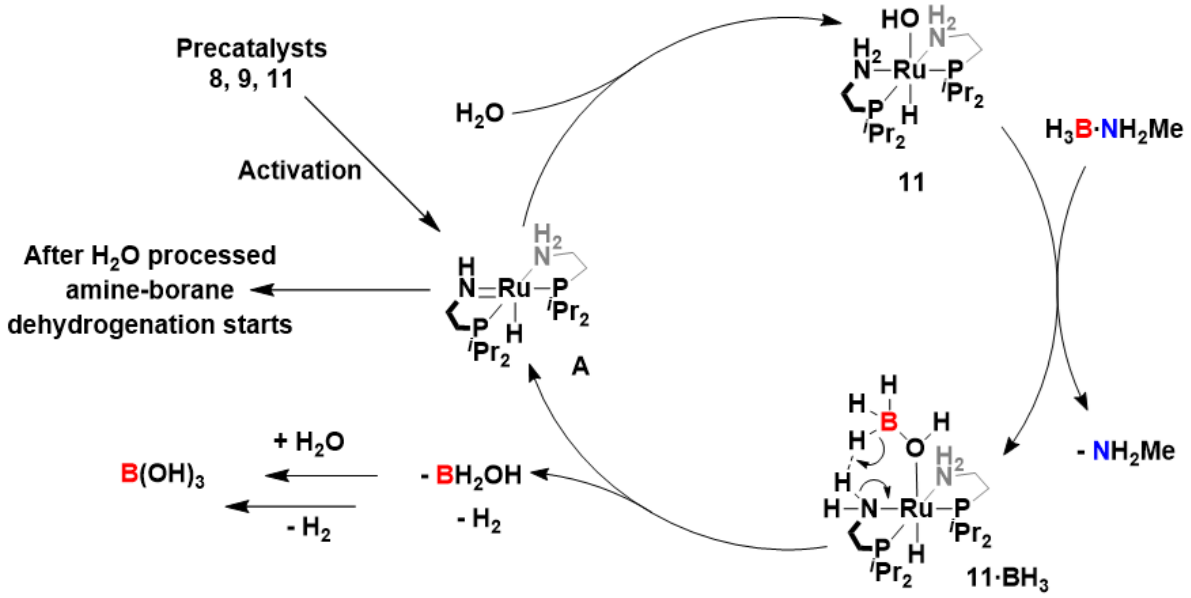

Figure 148. A hypothetical catalytic cycle for the processing of water by hydrolysis of amine-boranes, catalysed by **11**. Such a mechanism may operate during the induction period of amine-borane dehydropolymerisation with **8**, **9** and **13**.

The routes by which the precatalysts **8**, **9**, and **13** are activated and eventually form **11** is likely significantly different. Bis-amido complex **9** could react with an amine-borane adding an equivalent of H_2 across one ruthenium amido bond, forming complex **A** (Ru(^{i}Pr$_2$PCH$_2$CH$_2$NH)(^{i}Pr$_2$PCH$_2$CH$_2$NH$_2$)H), followed by the rapid heterolysis of water to form **11** (**Figure 149**). During the activation of metal halide precatalysts for amine-borane dehydropolymerisation, base promoted hydride transfer from amine-boranes has been suggested as a formation mechanism for metal hydride species. [5, 55, 56] This often involves an amine as the base, which deprotonates a transient sigma bonded amine-borane complex, resulting a transfer of a B–H hydride to the metal and releasing an equivalent of ammonium salt and aminoborane (or a boronium salt). [5, 55, 56] This may occur during the activation of precatalyst **8** in the presence of NH_2Me and amine-boranes, forming the transient dihydride Ru(^{i}Pr$_2$PCH$_2$CH$_2$NH$_2$)H$_2$, which then can lose H_2, a process which is likely facile (see **3.5.4**) to form the mono-amido hydride Ru(^{i}Pr$_2$PCH$_2$CH$_2$NH)(^{i}Pr$_2$PCH$_2$CH$_2$NH$_2$)H (**A**) (**Figure 149**). This could then heterolytically cleave water to form **11**. The activation of borohydride complex **13** could involve initial hydrolysis of the BH_4 by trace water, forming the trans-dihydride complex Ru(^{i}Pr$_2$PCH$_2$CH$_2$NH$_2$)H$_2$, however the exact mechanism is unclear and further investigation into the reactivity of complex **13** is required.

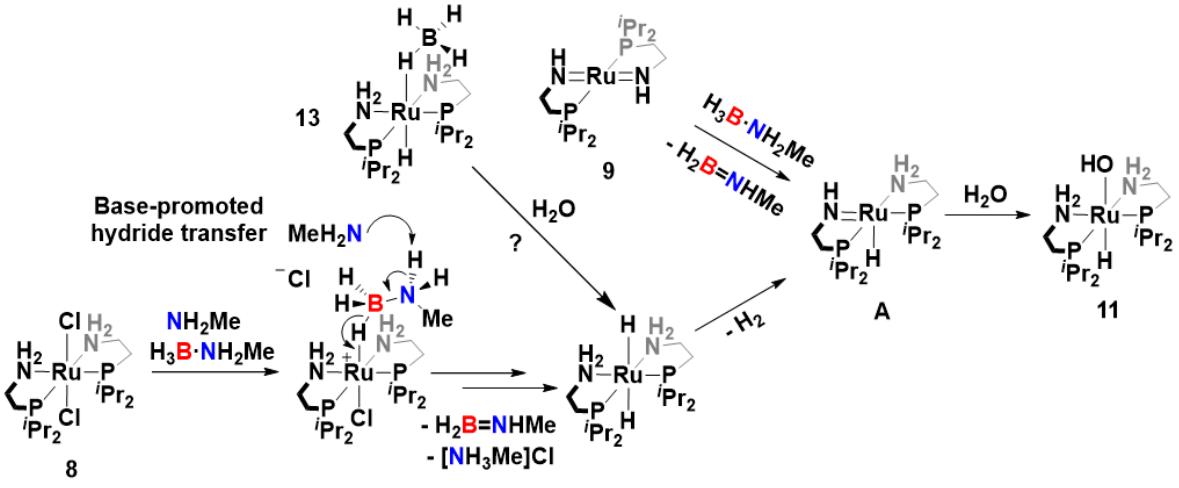

Figure 149. Proposed mechanisms for the activation of precatalysts **8** and **9** leading to the formation of **11** during the induction period of amine-borane dehydropolymerisation.

3.7.2 Potential amine-borane dehydrogenation mechanisms

Kinetic investigations into the dehydropolymerisation of amine-boranes by precatalyst **9** suggests that the rate law for dehydrogenation (as measured by H_2 evolution) has a first order dependence in catalyst concentration and follows saturation kinetics with regards to amine-borane concentration (initially pseudo zeroth-order). This implies that the rate determining step in the dehydrogenation mechanism involves interaction between the catalyst and amine-borane, which are likely involved in an adduct forming pre-equilibrium. This is contrary to the seminal report by Fagnou et al. that suggested via purely in-silico work that the rate determining step for amine-borane dehydrogenation was H_2 elimination from the dihydride complex intermediate Ru(^{i}Pr$_2$PCH$_2$CH$_2$NH$_2$)H$_2$. [2, 29]

The increase in the rate of catalytic dehydrogenation of $H_3B{\cdot}NH_2Me$ by **8** in the presence of NH_2Me (a positive order) suggests that NH_2Me can also play a role in the rate determining step of dehydrogenation. One interpretation of these kinetic investigations is that the rate determining step for this catalytic cycle is dehydrogenation of a bound amine-borane, which can be facilitated with a lower $\Delta G^{\ddagger}$ by the presence of an amine co-catalyst. An inner-sphere amine-borane dehydrogenation mechanism that takes these observations into account can be envisioned, where $H_3B{\cdot}NH_2Me$ could form a reversable adduct with mono amido hydride complex Ru(^{i}Pr$_2$PCH$_2$CH$_2$NH)(^{i}Pr$_2$PCH$_2$CH$_2$NH$_2$)H (**A**) prior to rate-limiting dehydrogenation, leading to a pseudo zero order in [$H_3B{\cdot}NH_2Me$]. This adduct (**A·AB**) would then be the catalyst resting state. An equivalent of H_2 is then transferred to from across the B–N bond of an amine-borane to across the Ru–N amido bond of the mono amido hydride complex Ru(^{i}Pr$_2$PCH$_2$CH$_2$NH)(^{i}Pr$_2$PCH$_2$CH$_2$NH$_2$)H (**A**) in the rate limiting step forming Ru(^{i}Pr$_2$PCH$_2$CH$_2$NH$_2$)H$_2$ (**Figure 150**). This could be facilitated by a hydrogen-bonded amine acting as a proton-shuttle co-catalyst, aiding in transferring a proton from the amine-borane nitrogen to the catalyst amido nitrogen (**Figure 150**). A similar effect has been reported where hydrogen-bonded water can aid in the heterolysis of H_2 across a ruthenium amido bond. [31]

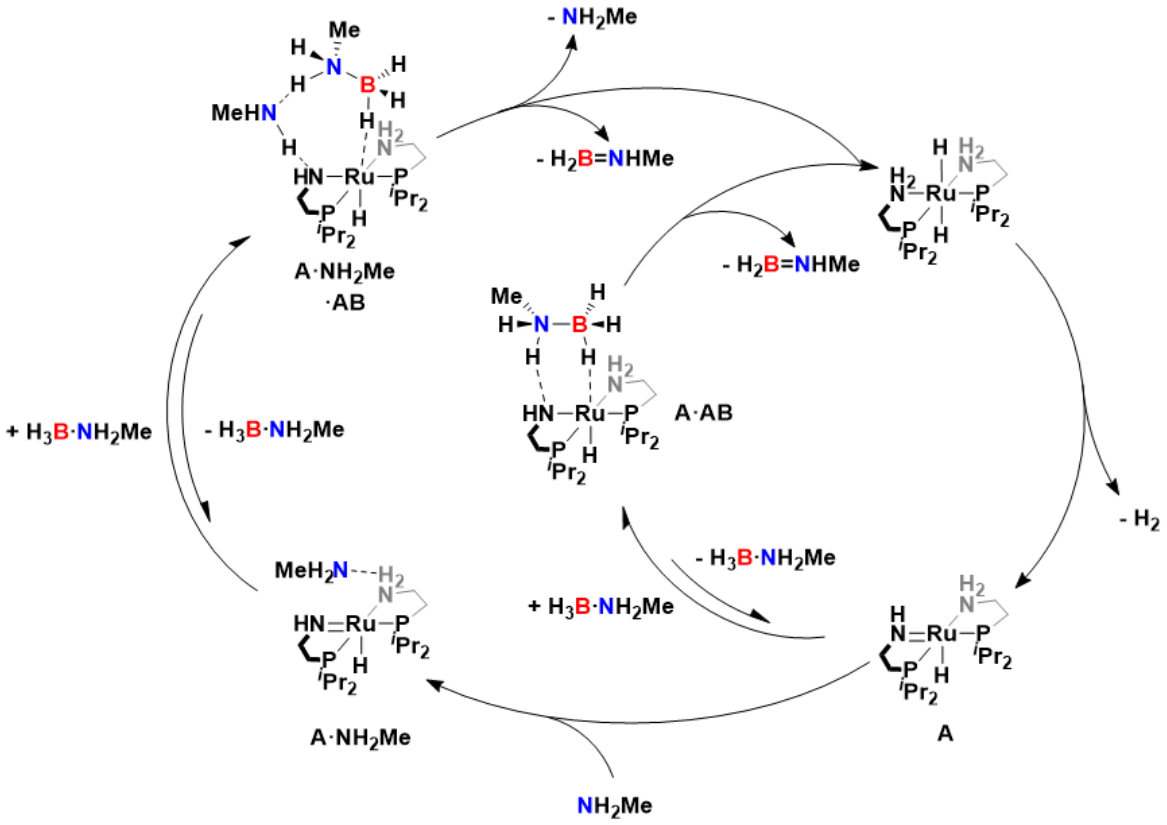

Figure 150. A proposed inner-sphere metal ligand cooperative mechanism for the dehydrogenation of $H_3B{\cdot}NH_2Me$ by Ru(^{i}Pr$_2$PCH$_2$CH$_2$NH)(^{i}Pr$_2$PCH$_2$CH$_2$NH$_2$)H (**A**), with a dehydrogenation step that can involve NH_2Me as a proton shuttle co-catalyst when present.

One problem with this proposed inner-sphere mechanism is that it relies on the spontaneous H_2 dissociation from the trans dihydride complex Ru(^{i}Pr$_2$PCH$_2$CH$_2$NH$_2$)H$_2$, a process for which the barrier has been calculated by Fagnou et al. to be $\Delta G^{\ddagger}$ = 22.7 kcal mol^{-1}, which corresponds to a $t_{1/2}$ of 1.37 s.[2] If the inner sphere mechanism has amine-borane activation as the rate limiting step (as suggested by kinetic analyses) then the energetic barrier to this step must be even higher than that calculated for hydrogen loss, which is not conducive with the very high rates of reaction (overall TOF of up to 660 s^{-1}) exhibited by this catalyst system. This mechanism is also not supported by the speciation observed mid-catalysis by NMR spectroscopy, which suggests that the catalyst resting state (**12**) could be an amine-borane adduct of a trans dihydride complex such as Ru(^{i}Pr$_2$PCH$_2$CH$_2$NH$_2$)H$_2$·($H_3B{\cdot}NH_2Me$) (see section **3.5.3**).

The outer-sphere dehydrogenation of amine-boranes is a potential alternative mechanism that avoids the necessity for direct loss of H_2 from dihydride complex

Ru(^{i}Pr$_2$PCH$_2$CH$_2$NH$_2$)H$_2$. This mechanism involves the protonation of a hydride on Ru(^{i}Pr$_2$PCH$_2$CH$_2$NH$_2$)H$_2$ by the amine of a hydrogen-bonded amine-borane (bound in a pre-equilibrium), forming a sigma dihydrogen complex intermediate (**Figure 151**). This is followed by H$_2$ dissociation and then amine-borane B–H bond activation (**Figure 151**). This mechanism is proposed by Schneider et al. to account for the rapid dehydrogenation of amine-boranes by Ru(^{i}Pr-PN^{H}P)(PMe$_3$)H$_2$, for which the rate law has an apparent first order dependence on the concentration of both catalyst and amine-borane (**Figure 151**).[29] In this catalytic cycle, amine-borane N–H activation and subsequent H$_2$ loss are rate-limiting with a reported energy barrier of $\Delta G^{\ddagger}$ = 12.5 kcal mol^{-1}. [29]

An analogous outer-sphere amine-borane dehydrogenation mechanism can be drawn for the trans-dihydride Ru(^{i}Pr$_2$PCH$_2$CH$_2$NH$_2$)H$_2$, which is likely accessible from precatalysts **8**, **9** and **13** (**Figure 152**). The proposed rate-limiting N–H activation transition state in this mechanism, like the inner sphere mechanism discussed vide supra, has the possibility of including an amine co-catalyst as a proton shuttle, in this case during the protonation of a ruthenium hydride to form a sigma bonded dihydrogen complex (**Figure 152**).

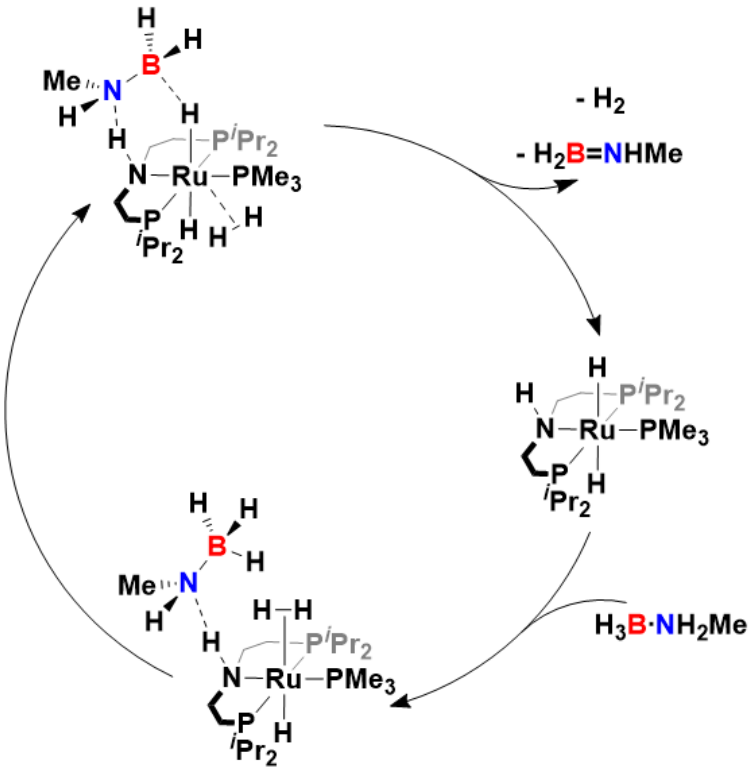

Figure 151. The reported outer-sphere mechanism for the dehydrogenation of amine-boranes with Ru(^{i}Pr-PN^{H}P)(PMe$_3$)H$_2$. [29]

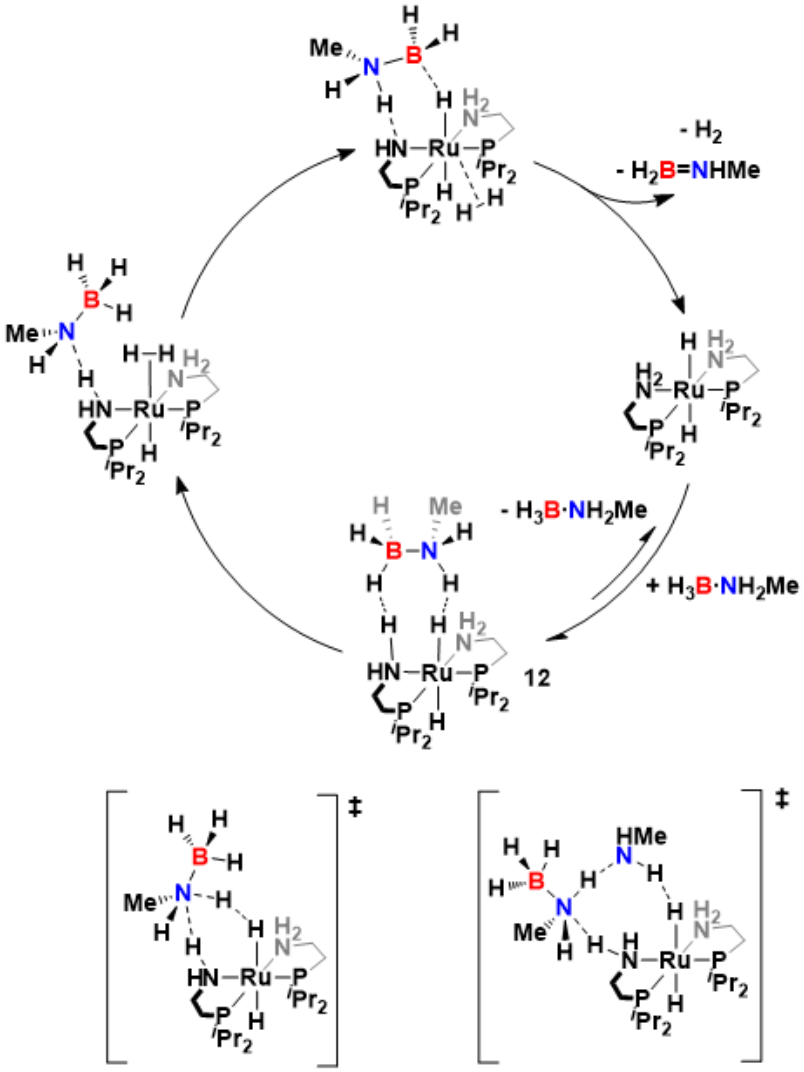

Figure 152. A proposed outer-sphere metal ligand cooperative mechanism for the dehydrogenation of $H_3B{\cdot}NH_2Me$ by $Ru(^iPr_2PCH_2CH_2NH_2)H_2$. Bottom: Possible transition states for the amine-borane N–H activation step, with the possibility of involving NH_2Me as a proton shuttle co-catalyst when present.

3.8 Conclusions

It has been demonstrated that complex **8** is an exceptional precatalyst for the catalytic dehydropolymerisation of methylamine-borane at very low catalyst loadings (0.01 – 0.02 mol%), exhibiting the highest reported turnover frequency (at the time of writing) measured at 660 s^{-1} in the presence of amine NH_2Me. This high rate of reaction leads to a polyaminoborane $(H_2BNHMe)_n$ of high M_n (>100,000 g mol^{-1}), likely due to the rapid production of the aminoborane monomer which allows for chain growth polymerisation to proceed at a much higher rate than chain termination. Possible mechanisms and active catalyst species have been identified and related to those previously reported for analogous catalysts.

The use of amine NH_2Me as a co-catalyst to **8** has been established to result in a significant increase in catalyst rate, for which a mechanism has been proposed where hydrogen bonded NH_2Me assists in proton transfer at the rate limiting step. Although amine has been shown to be important in the activation of dehydropolymerisation catalysts, its role as a co-catalyst has not been investigated thoroughly. [28, 55]

The synthesis and characterisation of highly reactive bis-amido complex **9** is of fundamental interest due to its rare combination of square planar geometry, d^6 electro count and low spin. This is only the second reported complex with this combination. [19]

3.9 Future work

To gain more insight into the mechanism of amine-borane dehydrogenation by catalysts derived from complex **8,** Eyring analysis should be performed form when both NH_2Me and ^tBuOK are used to activate **8**. This would involve recording catalysis rate data at a range of temperatures. This would help better determine the nature of the rate-limiting step for the mechanism of operation for these catalysts.

Kinetic isotope analysis may also help identify the catalysis rate limiting step. By using $D_3B{\cdot}NH_2Me$, $D_3B{\cdot}ND_2Me$ and $H_3B{\cdot}ND_2Me$ as substrates alongside $H_3B{\cdot}NH_2Me$, then comparing the catalysis rate may offer evidence for whether B–H or N–H bond activation are rate-limiting.[5] This however may be difficult due to the long induction period observed for the reported precatalysts, during which time D/H scrambling may occur. As the induction period for catalysis likely involved multiple proton and hydride transfers, the time taken before catalysis initiates may also show an isotope effect.

The so-far unobserved-directly mono-amido ruthenium hydride species **A** (Ru(^{i}Pr$_2$PCH$_2$CH$_2$NH)(^{i}Pr$_2$PCH$_2$CH$_2$NH$_2$)H) should be a future target complex to synthesize as it is invoked both in the activation of all the precatalysts (**8**, **9**, and **13**) and the inner-sphere mechanism of amine-borane dehydrogenation. The synthesis of **A** is not possible by the reaction of complex **9** with only 1 equivalent of H_2 as it is likely more reactive than **9**, resulting in over-hydrogenation. One possible route to this compound would be the formation of Ru(^{i}Pr$_2$PCH$_2$CH$_2$NH$_2$)ClH from the reaction of the ligand ^{i}Pr$_2$PCH$_2$CH$_2$NH$_2$ with commercially available Ru(PPh$_3$)$_3$ClH, from which HCl could be extracted by one equivalent of ^{t}BuOK, forming **A**. [3] This would have to be performed with the strictest exclusion of water due to the apparent propensity of **A** to react with trace moisture to form **11** (*P,P-cis*-Ru(^{i}Pr$_2$PCH$_2$CH$_2$NH$_2$)(OH)H).

The profound effect that the presence of even trace water has on elongating the induction period of amine-borane dehydropolymerisation has been demonstrated to be caused by the formation of a catalytically dormant water bound species **11** (*P,P-cis*-Ru(^{i}Pr$_2$PCH$_2$CH$_2$NH$_2$)(OH)H). Further investigation through stoichiometric reactions with water scavenging reagents should be performed to determine exactly how **11** is then converted to the active catalytic species. An example would be how **11** reacts with free BH_3 in THF solution. The water-bound state of these amine ligated metal-ligand cooperative catalysts is also of broader interest to the operation of

hydrogenation/transfer hydrogenation transfer in general, where the occurrence of analogous species should be investigated. [36]

This preliminary investigation has identified the capability for precatalysts derived from complex **8** to form high molecular weight polyaminoborane by the dehydropolymerisation of $H_3B{\cdot}NH_2Me$. The molecular weights (M_n) reported herein vary between 90,000 – 170,000 g mol^{-1} depending on the reaction conditions precatalyst used and activation method. The highest molecular weights were observed in the presence of excess NH_2Me to catalyst, and so this should be a starting point from which reaction optimisation to form the highest molecular weight polyaminoborane should be investigated. This should include variation in reaction temperature, solvent and reactant concentrations.

References

1. W. Jia, X. Chen, R. Guo, C. Sui-Seng, D. Amoroso, A. J. Lough and K. Abdur-Rashid, *Dalton Trans.*, 2009, 8301-8307.
2. N. Blaquiere, S. Diallo-Garcia, S. I. Gorelsky, D. A. Black and K. Fagnou, *J. Am. Chem. Soc.*, 2008, **130**, 14034-14035.
3. K. Abdur-Rashid, R. Guo, A. J. Lough, R. H. Morris and D. Song, *Adv. Synth. Catal.*, 2005, **347**, 571-579.
4. S. E. Clapham, A. Hadzovic and R. H. Morris, *Coord. Chem. Rev.*, 2004, **248**, 2201-2237.
5. C. N. Brodie, T. M. Boyd, L. Sotorrios, D. E. Ryan, E. Magee, S. Huband, J. S. Town, G. C. Lloyd-Jones, D. M. Haddleton, S. A. Macgregor and A. S. Weller, *J. Am. Chem. Soc.*, 2021, **143**, 21010-21023.
6. T. M. Boyd, K. A. Andrea, K. Baston, A. Johnson, D. E. Ryan and A. S. Weller, *Chem. Commun.*, 2020, **56**, 482-485.
7. S. S. Mal, F. H. Stephens and R. T. Baker, *Chem Commun.*, 2011, **47**, 2922-2924.
8. G. Odian, *Principles of Polymerization*, Wiley, India Pvt. Limited, 2004.
9. S. Bhunya, T. Malakar and A. Paul, *Chem Commun.*, 2014, **50**, 5919-5922.
10. E. M. Titova, E. S. Osipova, A. A. Pavlov, O. A. Filippov, S. V. Safronov, E. S. Shubina and N. V. Belkova, *ACS Catal.*, 2017, **7**, 2325-2333.
11. A. Staubitz, M. E. Sloan, A. P. Robertson, A. Friedrich, S. Schneider, P. J. Gates, J. Schmedt auf der Gunne and I. Manners, *J. Am. Chem. Soc.*, 2010, **132**, 13332-13345.
12. M. Brookhart, M. L. Green and G. Parkin, *Proc. Natl. Acad. Sci. USA*, 2007, **104**, 6908-6914.
13. S. Alvarez and J. Cirera, *Angew. Chem. Int. Ed.*, 2006, **45**, 3012-3020.
14. B. Askevold, M. M. Khusniyarov, W. Kroener, K. Gieb, P. Muller, E. Herdtweck, F. W. Heinemann, M. Diefenbach, M. C. Holthausen, V. Vieru, L. F. Chibotaru and S. Schneider, *Chem. Eur. J.*, 2015, **21**, 579-589.
15. L. A. Watson, O. V. Ozerov, M. Pink and K. G. Caulton, *J. Am. Chem. Soc.*, 2003, **125**, 8426-8427.
16. J. Abbenseth, M. Diefenbach, S. C. Bete, C. Wurtele, C. Volkmann, S. Demeshko, M. C. Holthausen and S. Schneider, *Chem. Commun.*, 2017, **53**, 5511-5514.
17. P. O. Lagaditis, B. Schluschass, S. Demeshko, C. Wurtele and S. Schneider, *Inorg. Chem.*, 2016, **55**, 4529-4536.
18. E. J. Hawrelak, W. H. Bernskoetter, E. Lobkovsky, G. T. Yee, E. Bill and P. J. Chirik, *Inorg. Chem.*, 2005, **44**, 3103-3111.
19. B. Askevold, M. M. Khusniyarov, E. Herdtweck, K. Meyer and S. Schneider, *Angew. Chem. Int. Ed.*, 2010, **49**, 7566-7569.
20. J. Meiners, M. G. Scheibel, M. H. Lemee-Cailleau, S. A. Mason, M. B. Boeddinghaus, T. F. Fassler, E. Herdtweck, M. M. Khusniyarov and S. Schneider, *Angew. Chem. Int. Ed.,* 2011, **50**, 8184-8187.
21. B. Askevold, M. M. Khusniyarov, W. Kroener, K. Gieb, P. Muller, E. Herdtweck, F. W. Heinemann, M. Diefenbach, M. C. Holthausen, V. Vieru, L. F. Chibotaru and S. Schneider, *Chem. Eur. J*, 2015, **21**, 579-589.
22. K. J. Haack, S. Hashiguchi, A. Fujii, T. Ikariya and R. Noyori, *Angew. Chem. Int. Ed.*, 1997, **36**, 285-288.

23. A. Sinha, M. Majumdar, M. Sarkar, T. Ghatak and J. K. Bera, *Organometallics*, 2013, **32**, 340-349.
24. T. Mayer and H.C. Böttcher, *Polyhedron*, 2014, **69**, 240-243.
25. J. A. K. Howard, S. A. R. Knox, N. J. Terrill and M. I. Yates, *J. Chem. Soc., Chem. Commun.*, 1989, **0**, 640-642.
26. C. Alamillo-Ferrer, G. Hutchinson and J. Bures, *Nat. Rev. Chem.*, 2023, **7**, 26-34.
27. J. Bures, *Angew. Chem. Int. Ed.*, 2016, **55**, 16084-16087.
28. D. E. Ryan, K. A. Andrea, J. J. Race, T. M. Boyd, G. C. Lloyd-Jones and A. S. Weller, *ACS Catal.*, 2020, **10**, 7443-7448.
29. A. N. Marziale, A. Friedrich, I. Klopsch, M. Drees, V. R. Celinski, J. Schmedt auf der Gunne and S. Schneider, *J Am. Chem. Soc.*, 2013, **135**, 13342-13355.
30. A. L. Colebatch and A. S. Weller, *Chem. Eur. J.*, 2019, **25**, 1379-1390.
31. A. Friedrich, M. Drees, J. Schmedt auf der Gunne and S. Schneider, *J. Am. Chem. Soc.*, 2009, **131**, 17552-17553.
32. M. Ito, M. Hirakawa, K. Murata and T. Ikariya, *Organometallics*, 2001, **20**, 379-381.
33. A. Hadzovic, D. Song, C. M. MacLaughlin and R. H. Morris, *Organometallics*, 2007, **26**, 5987-5999.
34. K. Abdur-Rashid, S. E. Clapham, A. Hadzovic, J. N. Harvey, A. J. Lough and R. H. Morris, *J. Am. Chem. Soc.*, 2002, **124**, 15104-15118.
35. Z. Han, L. Rong, J. Wu, L. Zhang, Z. Wang and K. Ding, *Angew. Chem. Int. Ed.*, 2012, **51**, 13041-13045.
36. D. E. Prokopchuk, A. Collado, A. J. Lough and R. H. Morris, *Dalton Trans*, 2013, **42**, 10214-10220.
37. A. M. R. Hall, P. Dong, A. Codina, J. P. Lowe and U. Hintermair, *ACS Catal.*, 2019, **9**, 2079-2090.
38. R. J. Hamilton and S. H. Bergens, *J. Am. Chem. Soc.*, 2006, **128**, 13700-13701.
39. A. Antiñolo, M. A. Esteruelas, C. García-Yebra, J. Martín, E. Oñate and A. Ramos, *Organometallics*, 2018, **38**, 310-318.
40. A. Telleria, C. Vicent, V. San Nacianceno, M. A. Garralda and Z. Freixa, *ACS Catal.*, 2017, **7**, 8394-8405.
41. G. Albertin, S. Antoniutti, M. Bortoluzzi, J. Castro and V. Ferraro, *Dalton Trans.*, 2018, **47**, 9173-9184.
42. M. D. Fryzuk, M. J. Petrella, R. C. Coffin and B. O. Patrick, *C. R. Chimie*, 2002, **5**, 451-460.
43. R. Abbel, K. Abdur-Rashid, M. Faatz, A. Hadzovic, A. J. Lough and R. H. Morris, *J. Am. Chem. Soc.*, 2005, **127**, 1870-1882.
44. M. Bertoli, A. Choualeb, A. J. Lough, B. Moore, D. Spasyuk and D. G. Gusev, *Organometallics*, 2011, **30**, 3479-3482.
45. J. A. Ayllón, C. Gervaux, S. Sabo-Etienne and B. Chaudret, *Organometallics*, 1997, **16**, 2000-2002.
46. M. Kass, A. Friedrich, M. Drees and S. Schneider, *Angew. Chem. Int. Ed.*, 2009, **48**, 905-907.
47. A. Friedrich, M. Drees and S. Schneider, *Chem. Eur. J.*, 2009, **15**, 10339-10342.
48. A. W. Kaplan, J. C. M. Ritter and R. G. Bergman, *J. Am. Chem. Soc.*, 1998, **120**, 6828-6829.

49. F. Anke, D. Han, M. Klahn, A. Spannenberg and T. Beweries, *Dalton Trans.*, 2017, **46**, 6843-6847.
50. R. H. Crabtree, *Chem. Rev.*, 2016, **116**, 8750-8769.
51. R. Guo, X. Chen, C. Elpelt, D. Song and R. H. Morris, *Org. Lett.*, 2005, **7**, 1757-1759.
52. R. Guo, R. H. Morris and D. Song, *J Am Chem Soc*, 2005, **127**, 516-517.
53. C. A. Sandoval, T. Ohkuma, K. Muniz and R. Noyori, *J. Am. Chem. Soc.*, 2003, **125**, 13490-13503.
54. D. G. Gusev, F. M. Dolgushin and M. Y. Antipin, *Organometallics*, 2000, **19**, 3429-3434.
55. E. A. K. Spearing-Ewyn, N. A. Beattie, A. L. Colebatch, A. J. Martinez-Martinez, A. Docker, T. M. Boyd, G. Baillie, R. Reed, S. A. Macgregor and A. S. Weller, *Dalton Trans.*, 2019, **48**, 14724-14736.
56. P. Hasche, J. Haak, F. Anke, C. Kubis, W. Baumann, H.-J. Drexler, H. Jiao and T. Beweries, *Cat. Sci. Tech.*, 2021, **11**, 3514-3526.

Chapter 4: The selective catalytic synthesis of $(H_2BNHEt)_n$ and $(H_2BNH^nPr)_n$

4. The selective catalytic synthesis of $(H_2BNHEt)_n$ and $(H_2BNH^nPr)_n$

4.1 The dehydropolymerisation of $H_3B{\cdot}NH_2{}^nPr$ and $H_3B{\cdot}NH_2Et$ with 8 when activated with NH_2Me

Following on from the successful dehydropolymerisations of $H_3B{\cdot}NH_2Me$ to form $(H_2BNHMe)_n$ with precatalysts derived from **8**, the dehydropolymerisations of *n*-alkyl substituted amine-boranes $H_3B{\cdot}NH_2Et$ and $H_3B{\cdot}NH_2{}^nPr$ was investigated. The understanding gained about catalyst poisoning during the dehydropolymerisations of $H_3B{\cdot}NH_2Et$ and $H_3B{\cdot}NH_2{}^nPr$ with the rhodium aminophosphine precatalysts such as **2** (see chapter 2), aided the optimization of the reaction conditions for using these amine-boranes as substrates with the ruthenium based precatalysts discussed in this chapter. From the rhodium-based precatalyst work it was established that rapid catalysis and the presence of an amine helped in reducing the poisoning of metal-hydride catalyst species by free BH_3, which is released by amine-boranes in solution via B–N bond cleavage and forms catalytically inactive borohydride complexes such as $Rh(PN^HP^iPr)(\kappa^1\text{-}BH_4)H_2$ (**4**).

As the ruthenium on-cycle catalyst species derived from precatalyst **8** during dehydropolymerisation of amine-boranes feature hydrides, they are likely to be susceptible to poisoning by BH_3, forming catalytically inactive borohydride complexes (analogous to the Rh catalysts). For the above reasons, the attempts to dehydropolymerise $H_3B{\cdot}NH_2{}^nPr$ and $H_3B{\cdot}NH_2Et$ were performed with **8** activated by NH_2Me, which has been demonstrated to show the fastest catalysis with $H_3B{\cdot}NH_2Me$ of the precatalysts and activation routes assessed. The hypothesis was that by optimizing for rapid catalysis, the rate of dehydropolymerisation for $H_3B{\cdot}NH_2{}^nPr$ and $H_3B{\cdot}NH_2Et$ with **8** could outpace any catalyst poisoning by BH_3.

4.1.1 The attempted dehydropolymerisation of $H_3B{\cdot}NH_2{}^nPr$ with 8 at low catalyst loading (0.033 mol%), with NH_2Me

The initial attempt to dehydropolymerise $H_3B{\cdot}NH_2{}^nPr$ (0.182 g in 2.5 cm^3 THF, 1 mol dm^{-3}) with **8** was done at 0.033 mol%, activated with NH_2Me at 0.01 mol dm^{-3} (30 equivalents of NH_2Me to **8**) (**Figure 153**). These are the same conditions for which $H_3B{\cdot}NH_2Me$ was rapidly dehydropolymerised after a ~ 700 s induction period. No H_2 evolution was observed by eudiometric measurements after 3 hours and so an aliquot was extracted, on which in-situ ^1H, ^{11}B and $^{31}P\{^1H\}$ NMR spectra were recorded.

Due to the low initial catalyst concentration of **8** used ($3.3x10^{-4}$ mol dm^{-3}), no hydride signal was observed by ^1H NMR spectroscopy and no $^{31}P\{^1H\}$ signal was observed. By ^{11}B NMR spectroscopy, the $H_3B{\cdot}NH_2{}^nPr$ substrate was observed unreacted (**Figure 154**). Trace BH_4^- and $B_3H_8^-$ (– 37.5, pentet, J_{BH} = 82 Hz and – 29.0 Hz, nonet, J_{BH} = 33 Hz respectively) were also observed by ^{11}B NMR spectroscopy, possibly formed from BH_3 which was released by B–N bond cleavage of the $H_3B{\cdot}NH_2{}^nPr$ (**Figure 154**).[1] It is likely that under these conditions the catalyst is poisoned, forming a catalytically inactive species.

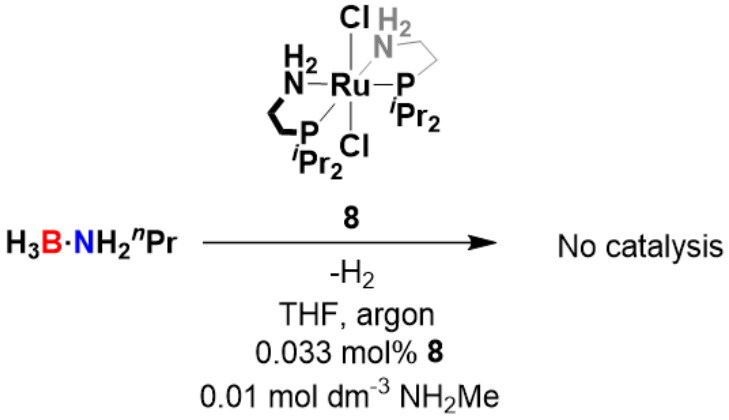

Figure 153. The attempted dehydropolymerisation of $H_3B{\cdot}NH_2{}^nPr$ (0.182 g in 2.5 cm^3 THF, 1 mol dm^{-3}) with **8** (0.033 mol%), activated by 0.01 mol dm^{-3} NH_2Me. No catalysis was observed.

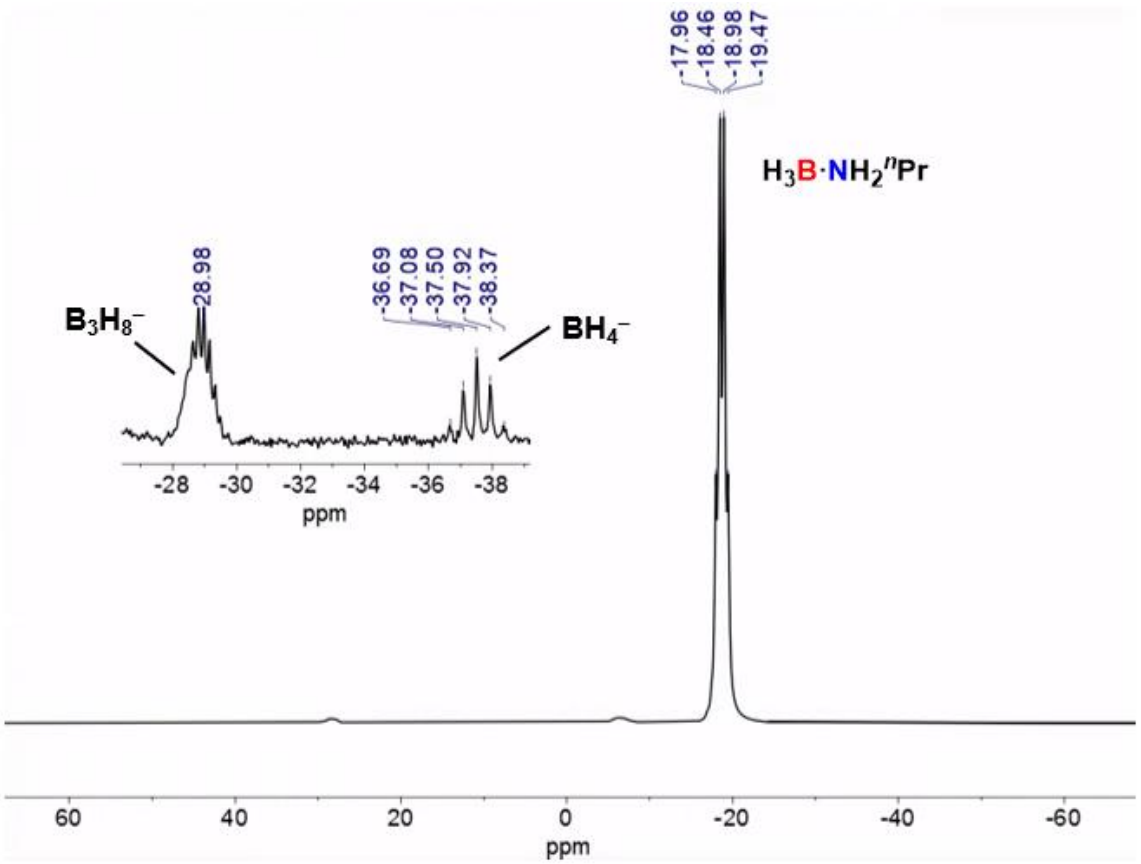

Figure 154. The in-situ ^{11}B recorded of the attempted dehydropolymerisation of $H_3B{\cdot}NH_2{}^nPr$ (0.182 g in 2.5 cm^3 THF, 1 mol dm^{-3}) with **8** (0.033 mol%), activated by 0.01 mol dm^{-3} NH_2Me. The unreacted $H_3B{\cdot}NH_2{}^nPr$ is observed as a quartet at – 18.72 ppm (J_{BH} = 94 Hz). Inset: expansion showing the presence of $B_3H_8^-$ and BH_4^-. Recorded in THF-H_8 at 298 K. [1]

4.1.2 The attempted dehydropolymerisation of $H_3B{\cdot}NH_2{}^nPr$ with 8 at high catalyst loading (0.33 mol%), with NH_2Me

In an attempt to overcome the apparent catalyst poisoning of **8** when attempting to dehydropolymerise $H_3B{\cdot}NH_2{}^nPr$, the catalyst loading was increased tenfold to 0.33 mol%. For comparison, this catalyst loading of **8** was capable of catalyzing the complete dehydropolymerisation of $H_3B{\cdot}NH_2Me$ in under 5 seconds and with no induction period (see chapter 3). Dehydropolymerisation was also attempted in toluene, as well as THF, as toluene attenuated catalyst poisoning by BH_3 in the rhodium catalyst systems (see chapter 2).

Dehydropolymerisation of $H_3B{\cdot}NH_2{}^nPr$ (0.182 g, 1 mol dm^{-3} in 2.5 cm^3 of toluene or THF) was attempted with **8** at 0.33 mol% catalyst loading, activated with 0.01 mol dm^{-3} of NH_2Me (3 equivalents of NH_2Me to **8**) (**Figure 155**). With THF and 0.33 mol% **8**, no H_2 evolution was observed by eudiometric measurement after 3 hours, similarly to with 0.033 mol%, and no significant conversion of the $H_3B{\cdot}NH_2{}^nPr$ was observed by ^{11}B NMR. The in-situ $^{31}P\{^1H\}$ NMR showed partial conversion (87 %) of **8** to a new organometallic species with a pair of highly roofed doublets: 83.9 ppm (d, J_{PP} = 18 Hz), 82.7 ppm (d, J_{PP} = 18 Hz) and henceforth referred to as **14** (**Figure 156**). This likely corresponds to two ligand phosphine environments that couple to each other, either as chemically inequivalent ligands on a single ruthenium center, or possibly as part of a dimer. The small coupling constant of 18 Hz likely corresponds to phosphines in a cis-configuration around the metal center. In the corresponding in-situ ^1H NMR spectrum, a single hydride was seen as a broad singlet at – 15.92 ppm (60 Hz FWHM), likely from **14** (**Figure 156**). No broad ^1H signal between 0 and – 5 ppm that would be expected for a Ru-bound κ^1- or κ^2-BH_2 complex is observed. [2, 3] As **14** was present alongside unreacted $H_3B{\cdot}NH_2{}^nPr$, it is likely that it does not catalyze the dehydropolymerisation of amine-boranes and represents a poisoned catalyst species. The trans hydride-borohydride complex **13** is not observed in the $^{31}P\{^1H\}$, ^1H or ^{11}B in-situ NMR spectra.

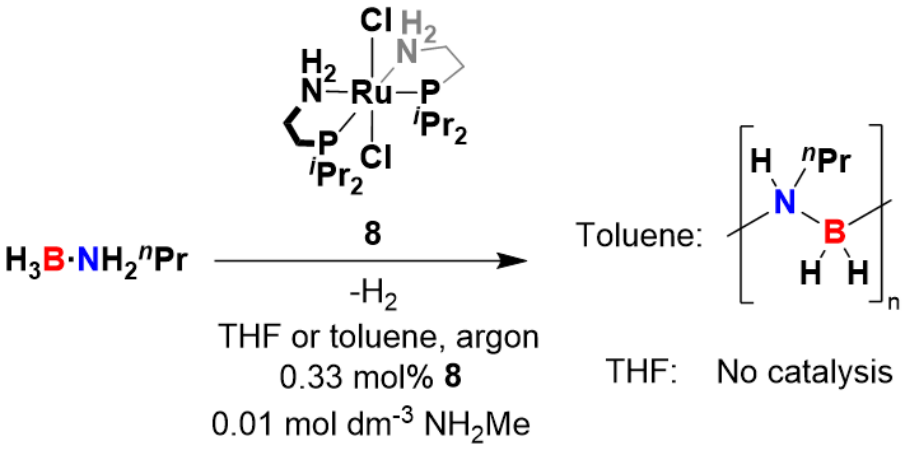

Figure 155. The attempted dehydropolymerisation of $H_3B{\cdot}NH_2{}^nPr$ (0.182 g in 2.5 cm^3 THF/toluene, 1 mol dm^{-3}) with **8** (0.33 mol%), activated by 0.01 mol dm^{-3} NH_2Me. No catalysis was observed with THF, complete conversion to polymer $(H_2B{=}NH^nPr)_n$ was observed with toluene by ^{11}B NMR.

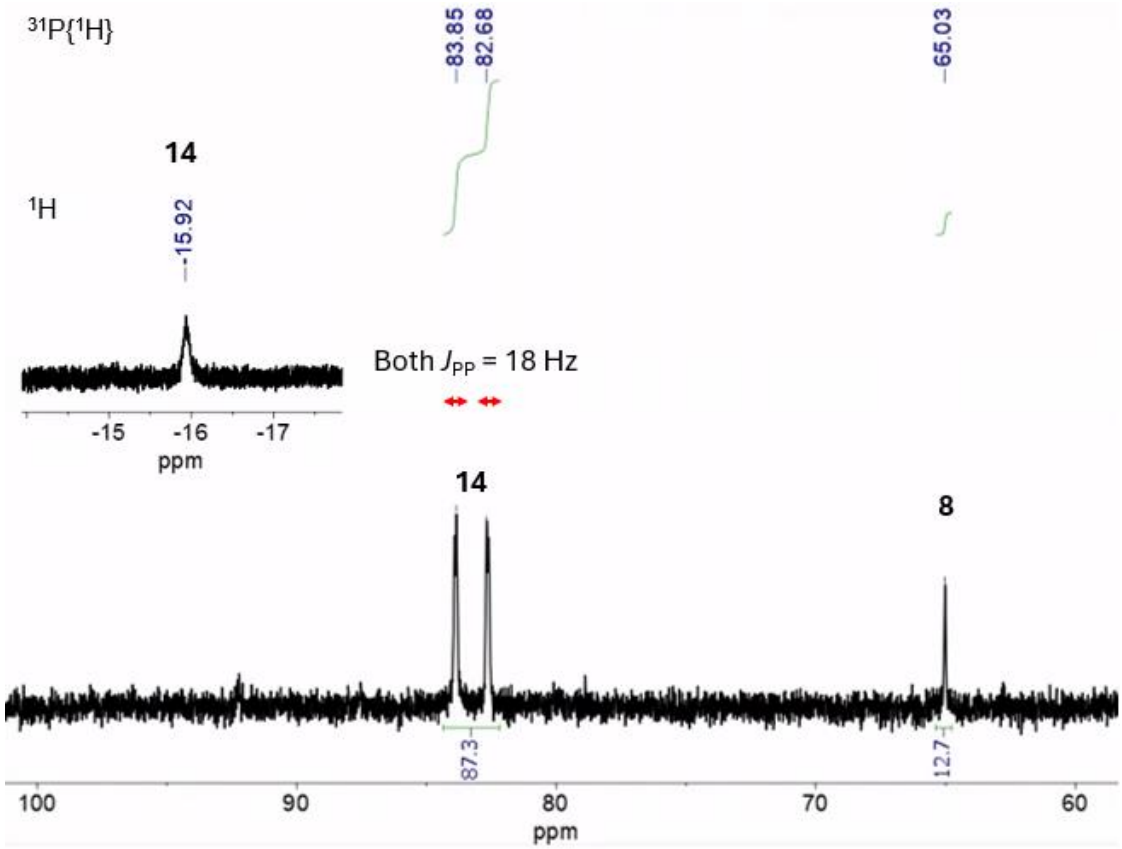

Figure 156. The in-situ $^{31}P\{^1H\}$ NMR spectrum recorded after the attempted dehydropolymerisation of $H_3B{\cdot}NH_2{}^nPr$ (0.182 g in 2.5 cm^3 THF, 1 mol dm^{-3}) with **8** (0.33 mol%), activated by 0.01 mol dm^{-3} NH_2Me, showing primarily **14** and some unreacted **8**. Inset: expanded in-situ ^1H NMR spectrum from the same reaction showing a hydride signal. Both recorded in THF-H_8 at 298 K.

A possible identity for **14** is *P,P-cis*-Ru(^{i}Pr$_2$PCH$_2$CH$_2$NH$_2$)(κ^3-^{i}Pr$_2$PCH$_2$CH$_2$NHBH$_3$)H, where the BH_3 is datively bonded to one of the ligand N atoms, and forms a sigma bond between a B–H and the ruthenium atom (**Figure 157**). This could form via the BH_3 capping of the mono amido hydride Ru(^{i}Pr$_2$PCH$_2$CH$_2$NH$_2$)(^{i}Pr$_2$PCH$_2$CH$_2$NH)H, where the amido lone pair acts as a Lewis base. Analogous complexes have been reported for iron and ruthenium with MACHO ligands (**Figure 157**).[4, 5] This would explain the lack of obvious B–H signals for **14** in the ^{1}H NMR spectrum, as the terminal B–H shift would likely be positive and obscured by the solvent and amine-borane signals.[4] The bridging B–H–Ru would be very broad, particularly if the BH_3 unit is rotating at room temperature, which could result in the signal broadening into baseline.[4, 5] Recording a ^{1}H{^{11}B} spectrum would help determine if a bridging B–H–Ru is present.

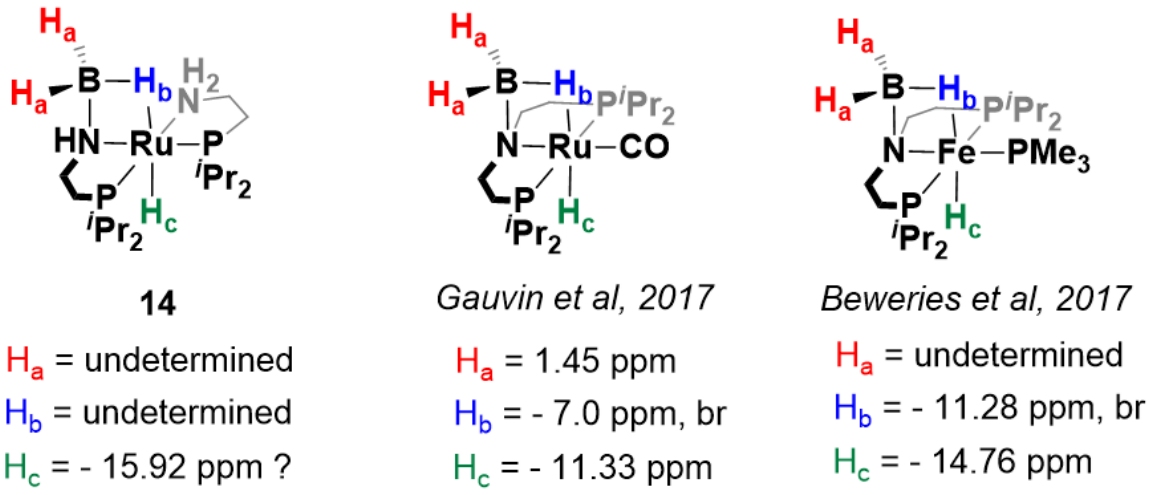

Figure 157. The possible structure of **14** and the reported group 8 MACHO complexes where the ligand nitrogen is capped by BH_3.[4, 5]

The equivalent dehydropolymerisation performed in toluene as a solvent (1 mol dm^{-3} $H_3B{\cdot}NH_2{}^{n}Pr$ in 2.5 cm^3 of toluene, 0.33 mol% **8** and 0.01 mol dm^{-3} NH_2Me) resulted in a 300 s induction period, followed by the release of ~ 1 equivalent of H_2 from the $H_3B{\cdot}NH_2{}^{n}Pr$ substrate in 2 seconds. This was more rapid than could be measured eudiometrically. The in-situ ^{11}B NMR spectrum recorded after the completion of H_2 evolution showed the almost complete conversion of the $H_3B{\cdot}NH_2{}^{n}Pr$ substrate into the polymer $(H_2BNH^{n}Pr)_n$, appearing as a broad signal at – 6.9 ppm (**Figure 158**). After catalysis was complete the reaction mixture was dried in vacuo to remove the toluene solvent and the residue analyzed by GPC. The $(H_2BNH^{n}Pr)_n$ formed was found to have

a M_n of 101,700 g mol^{-1} and a dispersity of 1.44, comparable to the $(H_2BNHMe)_n$ polymers formed by this catalyst system.

The in-situ $^{31}P\{^1H\}$ NMR spectrum recorded at the end of the dehydropolymerisation of $H_3B{\cdot}NH_2{}^nPr$ in toluene shows a similar species to **14** that was observed in THF: two roofed signals at 83.8 ppm and 82.2 ppm (both d, J_{PP} = 18 Hz) (**Figure 159**). No $^{31}P\{^1H\}$ signal corresponding to **8** is observed suggesting complete conversion into the new species. The in-situ ^1H NMR shows the same hydride signal as when the reaction was performed in THF, shifted slightly to – 15.74 ppm and corresponding to **14** (**Figure 159**).

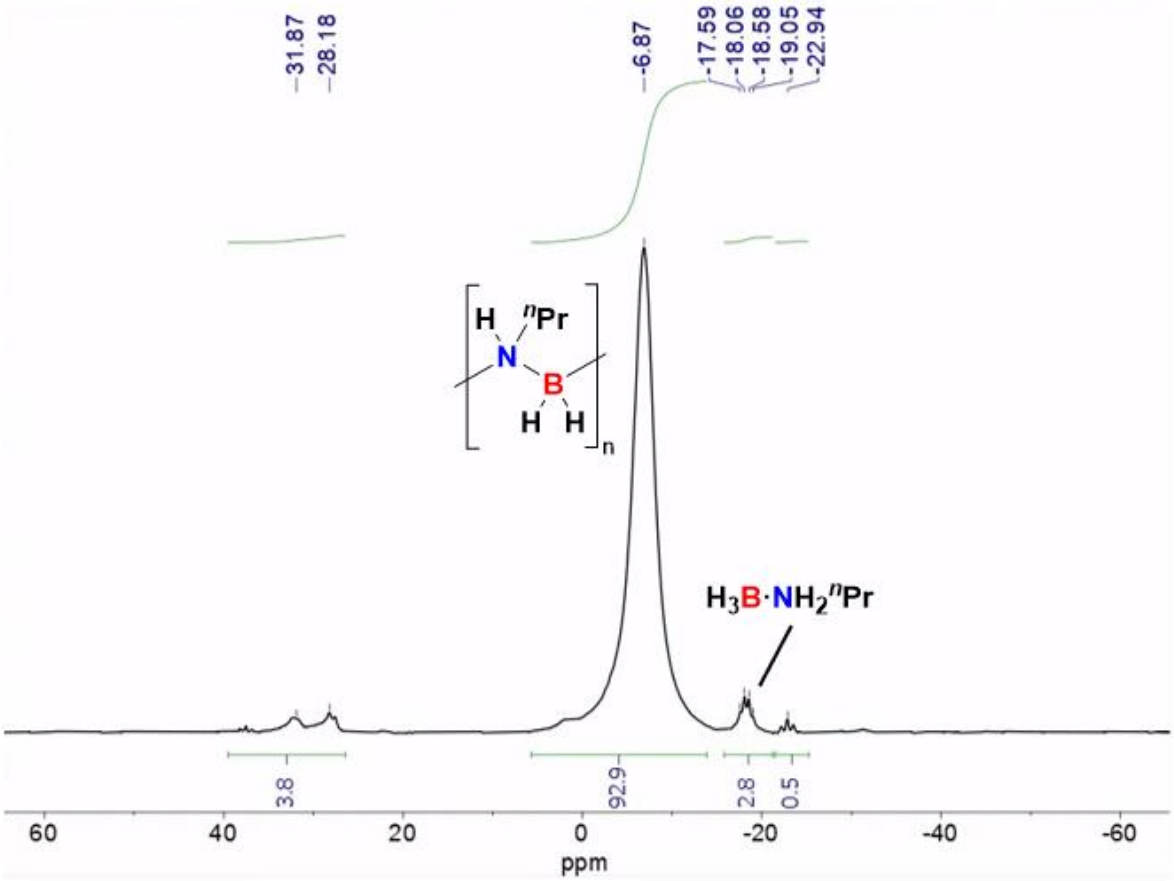

Figure 158. In-situ ^{11}B spectrum recorded after H_2 evolution ceased for the dehydropolymerisation of $H_3B{\cdot}NH_2{}^nPr$ (0.182 g in 2.5 cm^3 toluene, 1 mol dm^{-3}) with **8** (0.33 mol%), activated by 0.01 mol dm^{-3} NH_2Me. The primary species is $(H_2BNH^nPr)_n$, seen as a broad signal a – 6.9 ppm. Recorded in toluene-H_8 at 298 K.

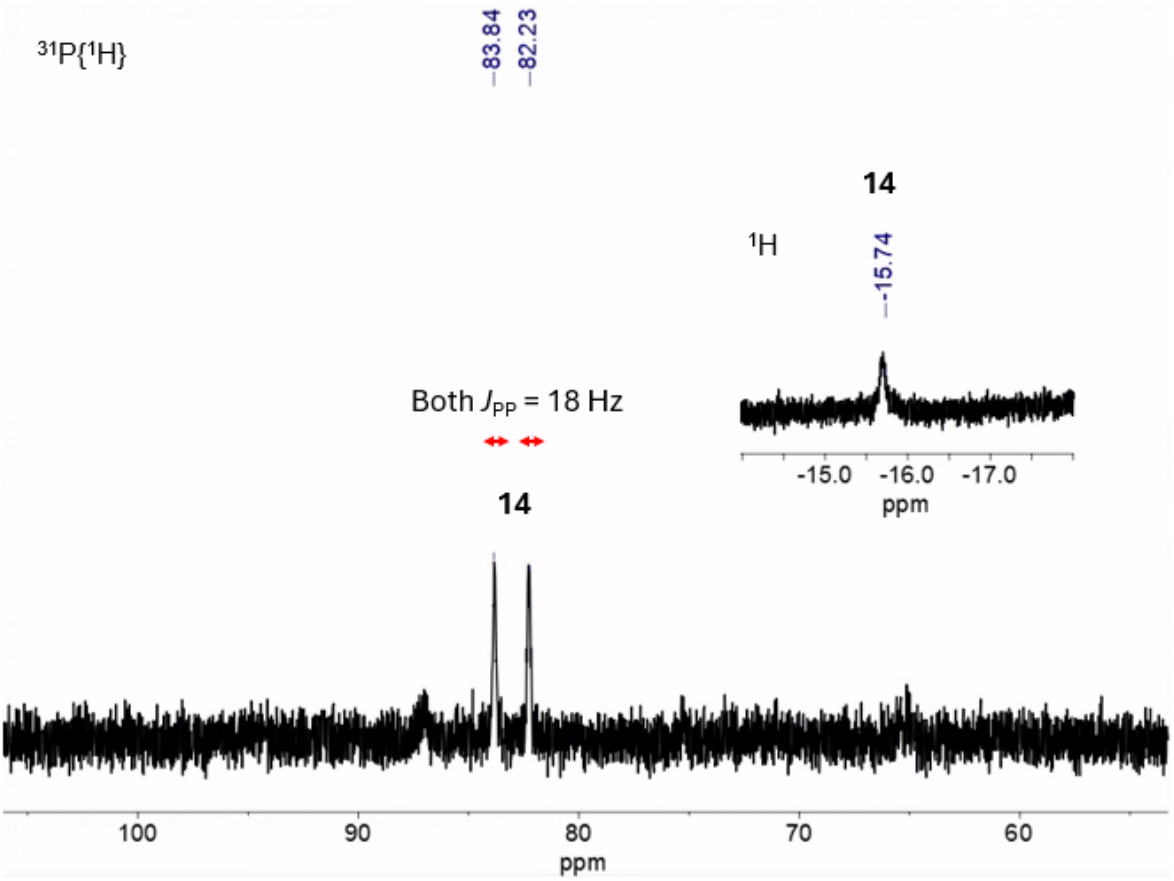

Figure 159. The in-situ $^{31}P\{^{1}H\}$ NMR spectrum recorded after the attempted dehydropolymerisation of $H_3B{\cdot}NH_2{}^{n}Pr$ (0.182 g in 2.5 cm^3 of toluene, 1 mol dm^{-3}) with **8** (0.33 mol%), activated by 0.01 mol dm^{-3} NH_2Me. Inset: expanded in-situ ^{1}H NMR spectrum from the same reaction showing a hydride signal. Recorded in toluene-H_8 at 298 K.

4.1.3 The dehydropolymerisation of $H_3B{\cdot}NH_2{}^nPr$ and $H_3B{\cdot}NH_2{}^nPr$ with 8 at high catalyst loading (0.5 mol%), with NH_2Me

In an attempt to increase the degree of polymerisation, the reaction conditions for the dehydropolymerisation of $H_3B{\cdot}NH_2{}^nPr$ were optimized by increasing the catalyst loading to 0.5 mol% of **8** and increasing the NH_2Me concentration to 0.05 mol dm^{-3} (10 equivalents relative to **8**). $H_3B{\cdot}NH_2Et$ was also evaluated as a substrate. In the previous investigation using 0.33 mol% of **8** to dehydropolymerise $H_3B{\cdot}NH_2{}^nPr$, the only species observed by $^{31}P\{^1H\}$ NMR spectroscopy at the end of catalysis was the likely catalytically inactive species **14**, suggesting that the catalyst was almost completely poisoned (possibly by BH_3) at 0.33 mol% loading. The higher concentration of NH_2Me was used in an attempt to sequester more BH_3 and therefore prolong the catalyst lifespan.

$H_3B{\cdot}NH_2{}^nPr$ and $H_3B{\cdot}NH_2Et$ (0.182 and 0.147 g respectively, in 2.5 cm^3 of toluene, 1 mol dm^{-3}) were dehydropolymerised by **8** (0.5 mol%) in toluene with 0.05 mol dm^{-3} of NH_2Me to activate the precatalyst (**Figure 160**). Both substrates showed the release of ~1 equivalent of H_2 by eudiometric measurements after an induction period: ~150 s for $H_3B{\cdot}NH_2{}^nPr$ and ~550 s for $H_3B{\cdot}NH_2Et$ (**Figure 161**). The release of ~1 equivalent of H_2 from $H_3B{\cdot}NH_2{}^nPr$ took 20 s, and from $H_3B{\cdot}NH_2Et$ took 5 s (**Figure 161**). In-situ ^{11}B NMR spectra recorded after catalysis show complete conversion of the respective amine-boranes, primarily into the polymers $(H_2BNHEt)_n$ (–7.16 ppm) and $(H_2BNH{}^nPr)_n$ (–6.79 ppm) as products (94 and 85 % selectivity respectively) (**Figure 162**).

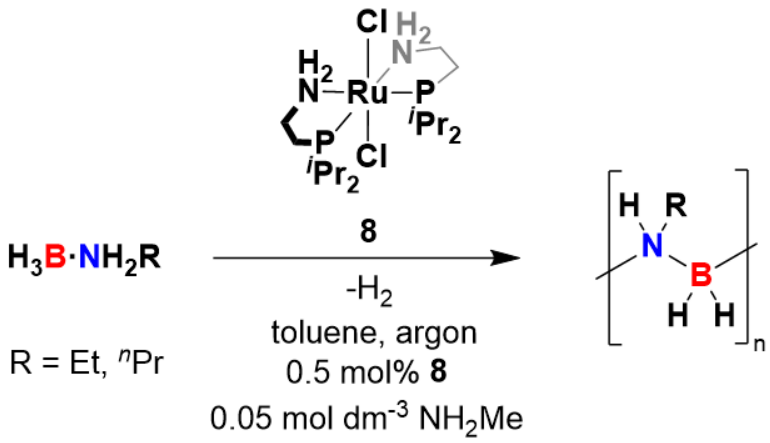

Figure 160. The dehydropolymerisation of $H_3B{\cdot}NH_2Et$ and $H_3B{\cdot}NH_2{}^nPr$ (0.147 and 0.182 g respectively in 2.5 cm^3 toluene, 1 mol dm^{-3}) with **8** (0.5 mol%), activated by 0.05 mol dm^{-3} NH_2Me. Complete conversion to polymers $(H_2BNHEt)_n$ and $(H_2BNH{}^nPr)_n$ was observed with toluene by ^{11}B NMR.

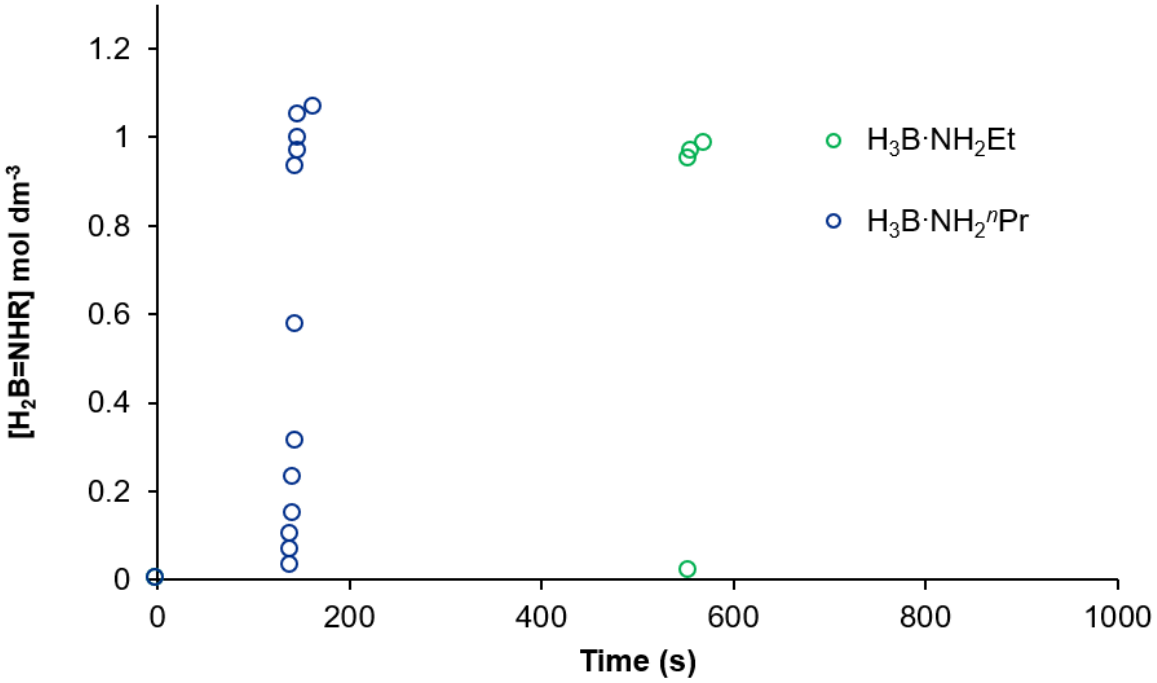

Figure 161. Effective $H_2B{=}NHR$ (R = Et, ^nPr) concentration over time from eudiometric H_2 evolution measurement for the dehydropolymerisations of $H_3B{\cdot}NH_2Et$ and $H_3B{\cdot}NH_2{}^nPr$ (0.147 and 0.182 g respectively, 1 mol dm^{-3} in toluene) by **8** (0.5 mol%), with 0.05 mol dm^{-3} of NH_2Me. A shorter induction period is seen with $H_3B{\cdot}NH_2{}^nPr$ (150 s) compared to $H_3B{\cdot}NH_2Et$ (550 s). $H_3B{\cdot}NH_2{}^nPr$ exhibits a lower rate of catalysis when compared with $H_3B{\cdot}NH_2Et$.

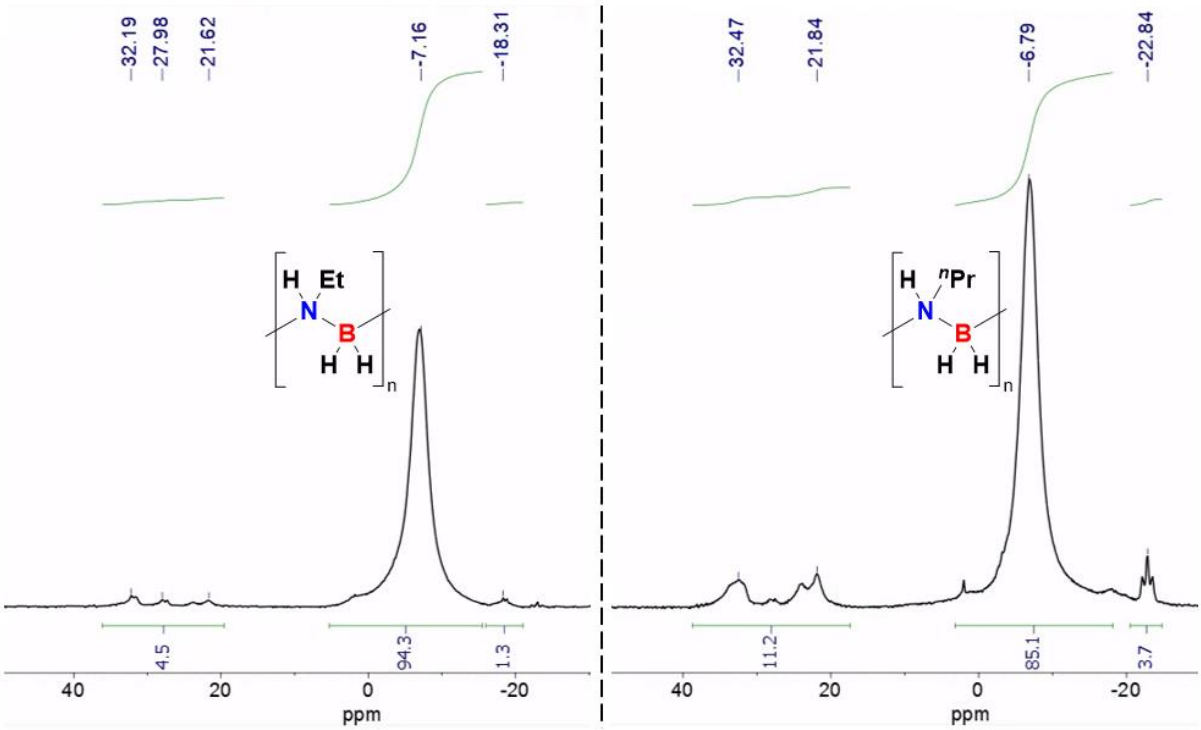

Figure 162. In-situ ^{11}B NMR spectra recorded after the dehydropolymerisations of $H_3B{\cdot}NH_2Et$ and $H_3B{\cdot}NH_2{}^nPr$ (0.147 and 0.182 g respectively, 1 mol dm^{-3} in toluene) by **8** (0.5 mol%), with 0.05 mol dm^{-3} of NH_2Me. **Left**: $H_3B{\cdot}NH_2Et$ dehydropolymerisation showing primarily $(H_2BNHEt)_n$. **Right**: $H_3B{\cdot}NH_2{}^nPr$ dehydropolymerisation showing primarily $(H_2BNH{}^nPr)_n$. Both recorded in toluene-H_8 at 298 K.

The in-situ $^{31}P\{^1H\}$ spectra recorded after catalysis show diverging speciation. For the dehydropolymerisation of $H_3B{\cdot}NH_2{}^nPr$, signals at 83.8 and 82.3 ppm are observed by $^{31}P\{^1H\}$ NMR spectroscopy corresponding to **14**, the only species observed. The hydride of **14** is also observed by ^1H NMR spectroscopy at – 15.70 ppm. This is the same as observed for when 0.33 mol% of **8** was used showing that the increase in catalyst loading and amine concentration does not prevent conversion to **14**, likely indicative that **14** can be formed post-catalysis. For the dehydropolymerisation of $H_3B{\cdot}NH_2Et$, 3 signals are seen by $^{31}P\{^1H\}$ NMR spectroscopy: two unidentified at 75.3 and 80.1 ppm, and **11** (*P,P-cis*-Ru(^{i}Pr$_2$PCH$_2$CH$_2$NH$_2$)$_2$(OH)H) at 88.6 ppm (**Figure 163**). The corresponding ^1H NMR spectrum shows 4 hydride signals: 3 unidentified at – 9.78, – 11.76 and – 15.83 ppm, with – 20.01 likely corresponding to **11** (**Figure 163**). No **14** is seen and no equivalent species with inequivalent phosphorous environments that are coupled. The reason for the differing catalyst speciation is not currently understood.

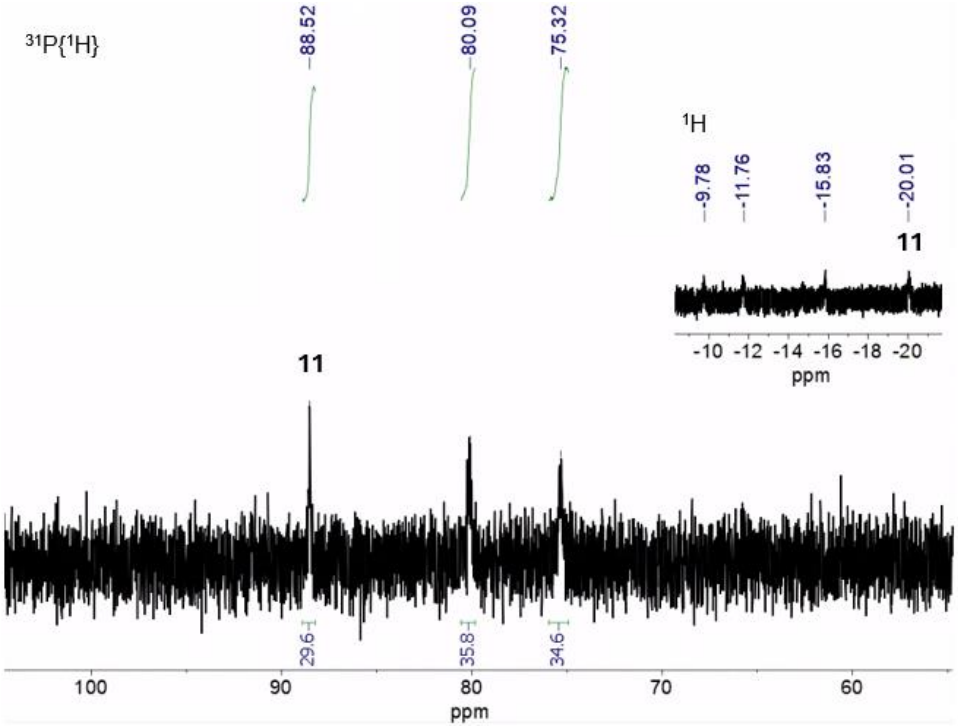

Figure 163. The in-situ $^{31}P\{^{1}H\}$ NMR spectrum showing multiple P containing species recorded after the dehydropolymerisation of $H_3B{\cdot}NH_2Et$ (0.147 g in 2.5 cm^3 of toluene, 1 mol dm^{-3}) with **8** (0.5 mol%), activated by 0.05 mol dm^{-3} NH_2Me. Inset: expanded in-situ ^{1}H NMR spectrum from the same reaction showing multiple hydride signals. Recorded in toluene-H_8 at 298 K.

The polymers $(H_2BNH^nPr)_n$ and $(H_2BNHEt)_n$ were isolated from the dehydropolymerisation reaction mixtures by removal of the toluene solvent and other volatile compounds in-vacuo. The resulting yellow solids were analyzed by GPC (**Figure 164**). The polymers were found to have M_n values of 115,800 g mol^{-1} for $(H_2BNH^nPr)_n$ and 118,600 g mol^{-1} for $(H_2BNHEt)_n$, corresponding to degrees of polymerisation ~ 1600 and ~ 2000 respectively. This is an approximate two-fold increase in polymer chain length when compared to the $(H_2BNHEt)_n$ and $(H_2BNH^nPr)_n$ synthesized by rhodium-based catalysts (see chapter 2).

Catalyst	Amine-borane	$H_3B{\cdot}NH_2R$ concentration (mol dm^{-3})	Catalyst mol%	Catalyst concentration (mol dm^{-3})	$MeNH_2$ concentration (mol dm^{-3})	M_n (mol dm^{-3})	M_w (mol dm^{-3})	Đ
8	$H_3B{\cdot}NH_2Et$	1	0.5	0.05	0.05	118,600	166,800	1.41
8	$H_3B{\cdot}NH_2{}^nPr$	1	0.5	0.05	0.05	115,800	160,400	1.39

Figure 164. Polymer data obtained by GPC analysis of the $(H_2BNHEt)_n$ and $(H_2BNH^nPr)_n$, formed by the dehydropolymerisations of $H_3B{\cdot}NH_2Et$ and $H_3B{\cdot}NH_2{}^nPr$ (0.147 and 0.182 g respectively, 1 mol dm^{-3} in toluene) by **8** (0.5 mol%), with 0.05 mol dm^{-3} of NH_2Me.

4.2 The NMR spectra of polyaminoboranes $(H_2BNHEt)_n$ and $(H_2BNH^nPr)_n$

Due to the moderate selectivity (> 85% by ^{11}B NMR integrals) for the corresponding *N*-alkyl polyaminoboranes formed by the dehydropolymerisation of $H_3B{\cdot}NH_2Et$ and $H_3B{\cdot}NH_2{}^nPr$ by **8** activated by NH_2Me, the NMR spectra of the isolated materials could be recorded in $CDCl_3$. The ^{11}B NMR spectra of $(H_2BNHEt)_n$ and $(H_2BNH^nPr)_n$ show broad peaks at – 7.14 and – 6.89 ppm respectively, matching well with the reported shifts of these polymers synthesized by stoichiometric methods (both reported at ~ – 7 ppm). [6, 7] The ^1H NMR spectrum of $(H_2BNHEt)_n$ consists of 5 signals: two signals at 2.65 and 2.47 ppm corresponding to inequivalent CH_2 protons, a broad NH signal at 2.51 ppm, a very broad BH_2 signal at 1.76 ppm and a sharp terminal CH_3 signal at 1.24 ppm (**Figure 165**). The ^1H NMR spectrum of $(H_2BNH^nPr)_n$ consists of 7 signals: a broad NH signal at 2.71 ppm, a pair of inequivalent CH_2 environments at 2.47 and 2.35 ppm, a pair of inequivalent CH_2 environments at 1.78 and 1.60 ppm, a very broad BH_2 signal at 1.70 ppm and a sharp terminal CH_3 signal at 0.85 ppm (**Figure 166**). These were confirmed by a ^1H-^1H COSY spectra and by comparison to the literature, the ^1H shifts match well with the reported literature values. [6, 7] $^{11}B\{^1H\}$ and $^1H\{^{11}B\}$ NMR spectra were not recorded.

The inequivalent geminal CH_2 protons on the alpha and beta carbons of $(H_2BNHEt)_n$ and $(H_2BNH^nPr)_n$ alkyl chains are reported to be due to proximity to the BN backbone hindering rotation. [7] A distinct explanation is that the polyaminoboranes formed exhibit stereochemically identical aminoborane monomer units (so-called isotactic) and that the alkyl CH_2 protons are therefore diastereotopic. Such isotacticity would require a significant free energy penalty to the formation of the stereo-random (atactic) or alternating stereochemical (atactic) polyaminoboranes. The tacticity of polyaminoboranes is at the time of writing yet to be convincingly elucidated. [7, 8]

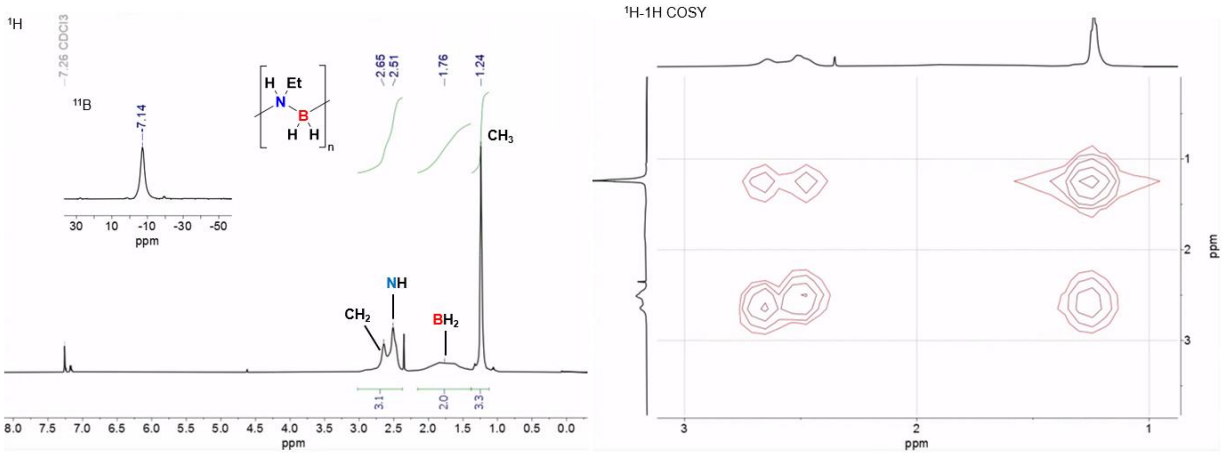

Figure 165. Left: ^{1}H NMR spectrum of $(H_2BNHEt)_n$, inset showing ^{11}B NMR spectrum. **Right:** ^{1}H-^{1}H COSY spectrum of $(H_2BNHEt)_n$ showing correlations between CH_2, CH_3 and NH resonances.

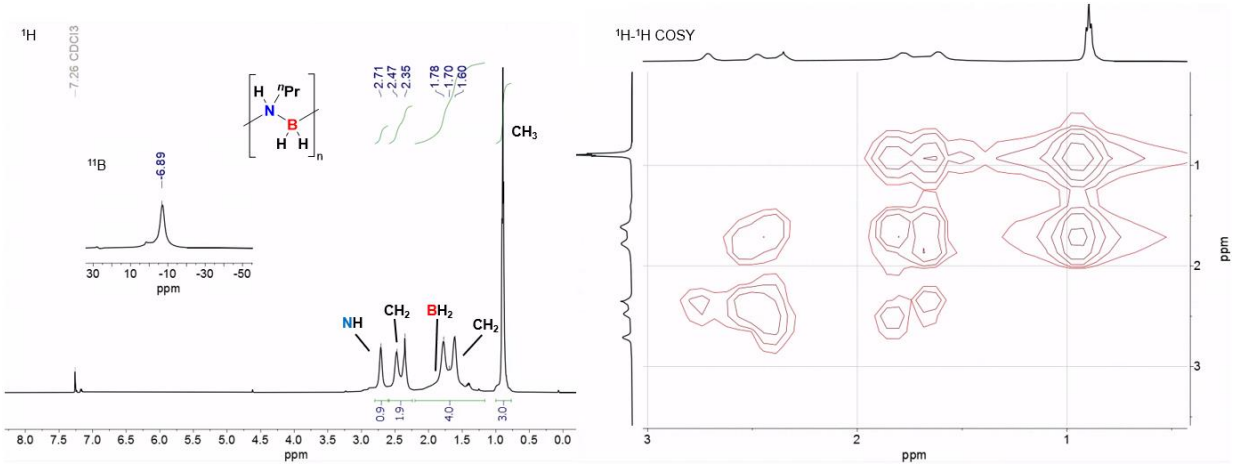

Figure 166. Left: ^{1}H NMR spectrum of $(H_2BNH^{n}Pr)_n$, inset showing ^{11}B NMR spectrum. **Right:** ^{1}H-^{1}H COSY spectrum of $(H_2BNH^{n}Pr)_n$ showing correlations between CH_3 – CH_2, CH_2 – CH_2, and CH_2 – NH resonances.

4.3 The future materials properties investigation of polyaminoboranes $(H_2BNHEt)_n$ and $(H_2BNH^nPr)_n$

Due to time constraints, the effect of substituting methyl groups for ethyl and *n*-propyl in *N*-alkyl polyaminoboranes on the bulk properties of these materials was unfortunately not investigated. The use of **8** as a competent precatalyst for the dehydropolymerisation of $H_3B{\cdot}NH_2Et$ and $H_3B{\cdot}NH_2{}^nPr$ to form high molecular weight $(H_2BNHEt)_n$ and $(H_2BNH^nPr)_n$ provides the first step toward this aim.

The glass transition temperature (T_g) of the most frequently reported polyaminoborane $(H_2BNHMe)_n$ is reported to be significantly above room-temperature (varying between 50 and 110 °C), as a result is $(H_2BNHMe)_n$ is very brittle. [9] This is likely due to strong intermolecular and intramolecular dihydrogen bonding between $(H_2BNHMe)_n$ chains, resulting in extensive crystalline domains. [9, 10] The inclusion of bulkier aminoborane monomers in polyaminoborane chains may disrupt the extended dihydrogen bonding network and result in lower T_g values, resulting in a more plastic and processable polymers. The decrease in T_g with increasing alkyl side chain length has been reported for the related polyolefins and polyphosphinoboranes. [11] The inclusion of 1-octene monomers at 3.6% incorporation in polyethylene chains is reported to halve the crystallinity, and is halved again upon reaching 12.3% 1-octene incorporation. [12] It may therefore be possible to decrease the crystallinity of $(H_2BNHMe)_n$ by substituting in a fraction of longer alkyl chain aminoborane units, with the aim of lowering T_g. Some examples of *N*-alkyl polyaminoborane copolymers have been reported, though the effect of varying co-monomer inclusion on materials properties has not been investigated. [6, 13]

Anecdotally, the $(H_2BNH^nPr)_n$ obtained from the dehydropolymerisation of $H_3B{\cdot}NH_2{}^nPr$ by **8** formed flexible films upon deposition by the evaporation of the toluene reaction solvent (see supplementary figures). This is in contrast to $(H_2BNHMe)_n$ which is reported to form extremely brittle films upon drop-casting from THF. [9] The quantitative measurement of T_g for $(H_2BNHEt)_n$ and $(H_2BNH^nPr)_n$ is yet to be performed and should be measured using differential scanning calorimetry.

4.4 Conclusions and future work

Precatalyst **8** when used at > 0.33 mol% catalyst loading and in the presence of NH_2Me (0.05 mol dm^{-3}) was shown to be capable of selectively dehydropolymerising $H_3B{\cdot}NH_2Et$ and $H_3B{\cdot}NH_2{}^nPr$, forming polyaminoboranes $(H_2BNHEt)_n$ and $(H_2BNH{}^nPr)_n$ selectively. This is a significant advancement over current dehydropolymerisation catalysts which are mainly limited to $(H_2BNHMe)_n$, and catalysts with broader scope often require higher catalyst loadings (> 1 mol%) or neat amine-boranes.[13,14] To investigate the effect on materials properties (such as T_g, melting point, solubility) of longer pendant alkyl chains on polyaminoboranes, a range of copolymers where *N*-methylaminoborane is the primary monomer and is supplemented by varying amounts of *N*-n-propylaminoborane should be synthesized. This will likely be more easily attainable than the synthesis of the homopolymer $(H_2BNH{}^nPr)_n$ due to the reduced release of BH_3 by B–N bond cleavage during dehydropolymerisation and is likely possible using precatalyst **8** in the presence of excess NH_2Me.

The dehydropolymerisation of a wider range of *N*-substituted amine-boranes should be attempted with the methodology described in this chapter, this should not be limited to *N*-alkyl substituents but also include those with potential for functionalization. The post-synthetic functionalization of polyaminoboranes is yet to be investigated, despite being commonplace with other classes of polymers.[15,16] The synthesis of polyaminoboranes with pendant functional groups has seldom been reported. One notable example is the brief description of copolymer formation using methyl amine-borane and hydrazine bis-borane in Manners seminal paper on catalytic polyaminoborane synthesis.[13] This was suggested to crosslink the typically linear polyaminoborane chains and therefore raised the ceramic yield upon thermal decomposition (forming boron nitride).[13] Future targets could include polyaminoboranes with pendant allyl or propargyl groups (likely as copolymers with *N*-methyl aminoborane) which could be used tune the extent of crosslinking between polymer chains, and therefore bulk materials properties.

References

1. T. G. Hill, R. A. Godfroid, J. P. White and S. G. Shore, *Inorg. Chem.*, 1991, **30**, 2952-2954.
2. S. Selvarasu, G. Joshi, D. Senthurpandi, M. Nethaji, E. D. Jemmis and B. R. Jagirdar, *Organometallics*, 2024, **43**, 2755-2766.
3. I. Koehne, T. J. Schmeier, E. A. Bielinski, C. J. Pan, P. O. Lagaditis, W. H. Bernskoetter, M. K. Takase, C. Wurtele, N. Hazari and S. Schneider, *Inorg. Chem.*, 2014, **53**, 2133-2143.
4. D. H. Nguyen, G. Raffa, Y. Morin, S. Desset, F. Capet, V. Nardello-Rataj, F. Dumeignil and R. M. Gauvin, *Green Chem.*, 2017, **19**, 5665-5673.
5. F. Anke, D. Han, M. Klahn, A. Spannenberg and T. Beweries, *Dalton Trans.*, 2017, **46**, 6843-6847.
6. C. A. De Albuquerque Pinheiro, C. Roiland, P. Jehan and G. Alcaraz, *Angew. Chem. Int. Ed.*, 2018, **57**, 1519-1522.
7. M. Devillard, C. A. De Albuquerque Pinheiro, E. Caytan, C. Roiland, C. Dinoi, I. Del Rosal and G. Alcaraz, *Adv. Synth. Catal.*, 2021, **363**, 2417-2426.
8. M. J. Cross, C. N. Brodie, D. G. Crivoi, J. C. Goodall, D. E. Ryan, A. J. Martinez-Martinez, A. Johnson and A. S. Weller, *Chem. Eur. J.*, 2023, **29**, e202302110.
9. C. N. Brodie, T. M. Boyd, L. Sotorrios, D. E. Ryan, E. Magee, S. Huband, J. S. Town, G. C. Lloyd-Jones, D. M. Haddleton, S. A. Macgregor and A. S. Weller, *J. Am. Chem. Soc.*, 2021, **143**, 21010-21023.
10. A. Staubitz, M. E. Sloan, A. P. Robertson, A. Friedrich, S. Schneider, P. J. Gates, J. Schmedt auf der Gunne and I. Manners, *J. Am. Chem. Soc.*, 2010, **132**, 13332-13345.
11. H. Cavaye, F. Clegg, P. J. Gould, M. K. Ladyman, T. Temple and E. Dossi, *Macromolecules*, 2017, **50**, 9239-9248.
12. A. Alizadeh, L. Richardson, J. Xu, S. McCartney, H. Marand, Y. W. Cheung and S. Chum, *Macromolecules*, 1999, **32**, 6221-6235.
13. A. Staubitz, A. Presa Soto and I. Manners, *Angew. Chem. Int. Ed.*, 2008, **47**, 6212-6215.
14. T. Jurca, T. Dellermann, N. E. Stubbs, D. A. Resendiz-Lara, G. R. Whittell and I. Manners, *Chem. Sci.*, 2018, **9**, 3360-3366.
15. N. K. Boaen and M. A. Hillmyer, *Chem. Soc. Rev.*, 2005, **34**, 267-275.
16. M. A. Gauthier, M. I. Gibson and H. A. Klok, *Angew. Chem. Int. Ed.*, 2009, **48**, 48-58.

Chapter 5: Experimental

5. Experimental methods

5.1 General experimental methods

All manipulations, unless otherwise stated were performed under an argon atmosphere, utilising Schlenk techniques on a dual vacuum/inlet J. Youngs tap manifold. All reactions were performed in J. Youngs tap glass ampoules, dried overnight in an oven overnight at 120 °C prior to use, unless otherwise specified. Cannulas were also dried overnight at 120 °C prior to use. Low temperature crystallisations of organometallic compounds (< 0 °C) were performed in J. Youngs tap glass ampoules, using a J. Youngs tap piston made of borosilicate glass to prevent thermal contraction from causing the seal to fail. All organometallic compounds were stored in an MBraun glovebox under an Argon atmosphere.

Solvents *n*-pentane, *n*-hexane, dichloromethane and toluene were dried using a Grubbs-type solvent purification system, degassed by 3 freeze-pump-thaw cycles and backfilled with argon.[1] Dichloromethane and toluene were stored over 3 Å molecular sieves. THF and Et_2O were dried by reflux over sodium/benzophenone in a solvent still under a nitrogen atmosphere and distilled, before being degassing with 3 freeze-pump-thaw cycles and backfilled with argon. THF and Et_2O were then stored over 3 Å molecular sieves. The THF was measured by Karl-Fischer analysis and found to contain 10 ppm residual H_2O. Extra dried THF (water free) was prepared by taking the THF distilled from sodium/benzophenone and storing it over a potassium mirror for 3 months. 1,2-Difluorobenzene was dried by reflux over CaH_2 benzophenone in a solvent still under a nitrogen atmosphere and distilled, before being degassing with 3 freeze-pump-thaw cycles and backfilled with argon. It was then stored over 3 Å molecular sieves. Deionised water was degassed by sparging with argon before use.

Deuterated solvents were purchased from Cambridge Isotope Laboratories, with the exception of $CDCl_3$ which was purchased from Sigma-Aldrich and used as supplied. Toluene-d_8 and benzene-d_6 were dried over CaH_2 and stored over 3 Å molecular sieves. CD_2Cl_2 was dried over CaH_2 and vacuum distilled prior to use. THF-d_8 was dried over Na/benzophenone, vacuum distilled and stored over a potassium mirror. C_6D_{12} was dried over CaH_2, vacuum distilled and stored over 3 Å molecular sieves. ^{i}PrOD-d_7 was dried over sodium (5 mol%), vacuum distilled and stored over 3 Å molecular sieves.

$H_3B{\cdot}NH_2Me$ was purchased from Boron Specialities LLC and recrystallised before use from Et_2O by dissolving in the minimum solvent and the cooling to –20 °C. $H_3B{\cdot}NH_2Et$ and $H_3B{\cdot}NH_2{}^nPr$ were prepared by literature methods, and then and recrystallised from Et_2O, by dissolving in the minimum solvent and the cooling to –20 °C, before use.[2] CaH_2 and benzophenone were obtained from Sigma-Aldrich and used as supplied. Potassium and sodium were obtained from Sigma-Aldrich and washed with *n*-hexane before use.

5.1.1 NMR spectroscopic measurements

NMR spectra were recorded on a 600 MHz Bruker Ultra-shield NMR spectrometer or a 500 MHz Bruker Avance III NMR spectrometer at 298 K, unless otherwise specified. Low-temperature NMR spectra were recorded on the 500 MHz Bruker Avance III NMR spectrometer and utilised a liquid nitrogen heat exchanger to cool the flow gas. All chemical shifts (δ) are reported in ppm and coupling constants (*J*) reported in Hz. ^1H, $^1H\{^{31}P\}$, $^1H\{^{11}B\}$ and $^{13}C\{^1H\}$ NMR spectra were referenced to residual solvent signals. $^{31}P\{^1H\}$ NMR spectra were referenced externally to 85% H_3PO_4. ^{11}B and $^{11}B\{^1H\}$ NMR spectra were referenced externally to 15% $Et_2O{\cdot}BF_3$ in $CDCl_3$. ^{11}B and $^{11}B\{^1H\}$ NMR spectra were corrected for the boron content in the borosilicate glass NMR tubes by subtraction of a blank, recorded on empty NMR tubes.

5.1.2 Gel permeation chromatography (GPC)

GPC was performed on a Malvern Viscotek GPCmax chromatograph fitted with a refractive index (RI) detector. The triple-column (3x LT4000 plus guard column) setup was contained within an oven (35 °C) and consisted of a porous styrene divinylbenzene copolymer with a maximum pore size of 1.500 Å. THF containing 0.1% w/w $[NBu_4]Br$ was used as the eluent at a flow rate of 1.0 mL min^{-1}. Samples were dissolved in the eluent (2.0 mg mL^{-1}), filtered (0.2 μm pore size) and run immediately. The calibration was conducted using a series of monodisperse polystyrene standards (M_n = 9630 – 476,800 g mol^{-1}) obtained from Sigma–Aldrich.

5.1.3 Mass spectrometry

Mass spectrometry was performed on purified materials (ESI-MS) and recorded on a Bruker HCTultra PTM Discovery with an attached custom-built glovebox. The carrier solvent was THF, flowing at 180 μL h^{-1}. The nebulizer was set at 2.9 psi and argon gas

at 2.0 l/min at a temp of 60 °C. End plate offset was set at -500 V and capillary at 4500 V.

5.1.4 Infra-red spectroscopy (IR)

IR spectroscopy was performed in an MBraun glovebox under an argon atmosphere with a Bruker ALPHA II Compact FT-IR Spectrometer (ATR).

5.1.5 UV-vis spectroscopy

UV-vis spectroscopy was performed in THF solutions at 293 K using a Jasco V-560 spectrophotometer. Analysis was performed in a J. Youngs quartz UV cuvette with a pathlength of 1 cm and with the strict exclusion of air and water.

5.2 Chapter 2 experimental methods and data

NH_2Me (2 mol dm^{-3} in THF), NH_2Et (2 mol dm^{-3} in THF), $NH_2{}^nPr$ (neat), NEt_3 (neat), tetrabutylammonium borohydride and elemental selenium powder were purchased from Sigma-Aldrich and used as supplied. $(^iPr_2PCH_2CH_2)_2NH$ (10% w/v in THF), $(^tBu_2PCH_2CH_2)_2NH$ (10% w/v in THF) and $(Cy_2PCH_2CH_2)_2NH$ (solid) were purchased from Sigma-Aldrich and used as supplied.

Rh(^{i}Pr-PN^{H}P)(NBD)][Cl] (**1**), Rh(^{i}Pr-PN^{H}P)H_2Cl (**2**), Co(^{i}Pr-PN^{H}P)Cl_2 (**5**) and Co(Cy-PN^{H}P)Cl_2 (**6**) were prepared via reported literature methods. [3, 4]

5.2.1 Synthesis and characterisation of Rh(^{i}Pr-PN^{H}P)(κ^{1}-BH$_4$)H$_2$ (4)

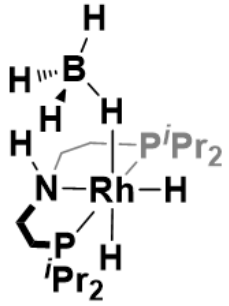

4

100 mg of **2**, Rh(^{i}Pr-PN^{H}P)H$_2$Cl, 0.23 mmol) and 69 mg (0.27 mmol, 1.2x excess) of [NBu$_4$][BH$_4$] was dissolved in 5 cm^3 of THF and stirred for 30 minutes. The THF was then evaporated under argon flow and the solids extracted with the minimum pentane, which was filtered off. The pentane solution was then cooled to – 20 °C overnight to afford colorless crystals of Rh(^{i}Pr-PN^{H}P)(κ^{1}-BH$_4$)H$_2$ (**4**), 21 mg, (22% yield). The low isolated yield is likely due to the high solubility of **4** even at low temperature in pentane.

^{1}H NMR (600 MHz, benzene-d$_6$) δ 3.90 (t, br, J_{HH} = 11 Hz, 1H, NH), 2.71 (m, 2H, ^{i}Pr CH), 2.50 (m, 2H, NH–CH$_2$), 1.86 (m, 2H, P–CH$_2$), 1.72 (m, 2H, ^{i}Pr CH), 1.64 (m, 2H, NH–CH$_2$), 1.57 (m, 2H, P–CH$_2$), 1.43 (dd, J = 16.5 Hz, 7.6 Hz, ^{i}Pr CH$_3$), 1.04 (dd, J = 15.5 Hz, 7.1 Hz, ^{i}Pr CH$_3$), 0.99 (dd, J = 12.8 Hz, 6.8 Hz, ^{i}Pr CH$_3$), 0.84 (dd, J = 14.3 Hz, 7.3 Hz, ^{i}Pr CH$_3$), – 1.37 (br, 4H, BH$_4$), – 15.81 (m, 1H, Rh–H), – 16.05 (m, br, 1H, Rh–H). A NOESY experiment was not recorded and so signals above and below the P–Rh–N plane were not distinguished.

^{13}C{^{1}H} NMR (151 MHz, benzene-d$_6$) δ 52.85 (t, J_{CP} = 3.5 Hz, NH–CH$_2$), 31.29 (t, J_{CP} = 9.1 Hz, P–CH$_2$), 27.43 (t, J_{CP} = 12.4 Hz, ^{i}Pr CH), 22.27 (dd, J = 9.5 Hz, 12.0 Hz, ^{i}Pr CH), 21.44 (t, J_{CP} = 3.9 Hz, ^{i}Pr CH$_3$), 20.97 (t, J_{CP} = 4.0 Hz, ^{i}Pr CH$_3$), 18.59 (s, ^{i}Pr CH$_3$), 17.05 (s, ^{i}Pr CH$_3$).

^{31}P{^{1}H} NMR (243 MHz, benzene-d$_6$) δ 79.0 (d, J_{PRh} = 109 Hz).

^{11}B NMR (193 MHz, benzene-d$_6$) δ – 34.4 (br, BH$_4$).

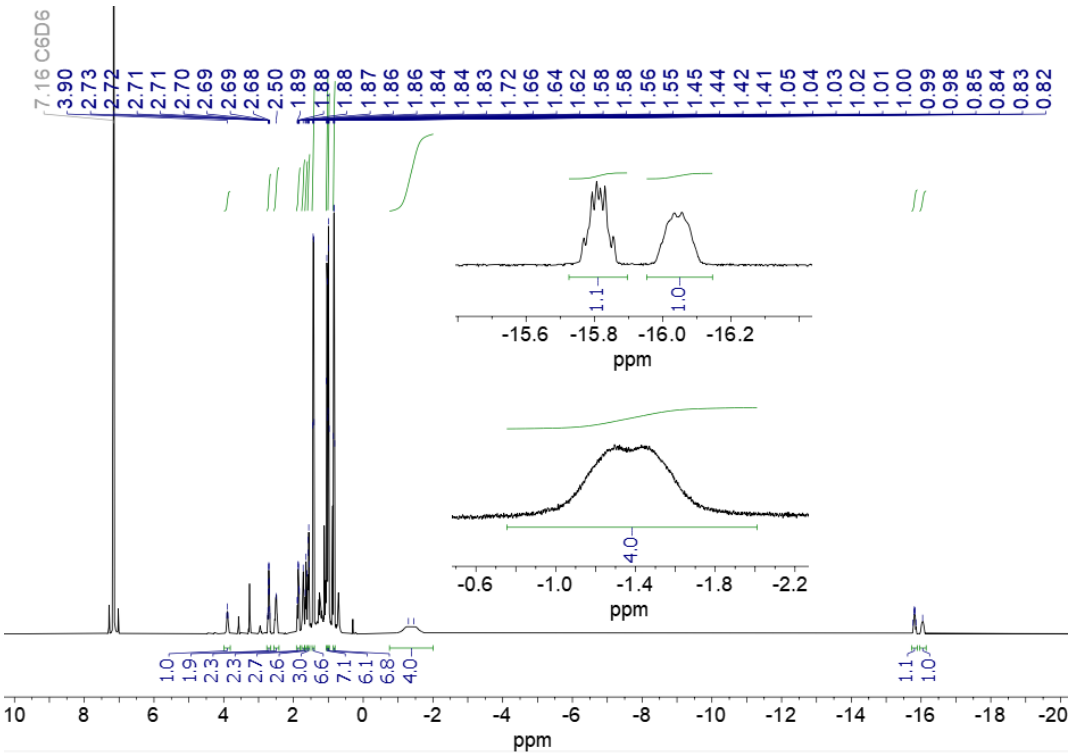

Figure 167. ^{1}H NMR spectrum of Rh(^{i}Pr-PN^{H}P)(κ^{1}-BH_4)H_2 (**4**), insets showing Rh–H and BH_4 signals. Traces of NBu_4 are present in the aliphatic region. Recorded in benzene-d_6 at 298 K.

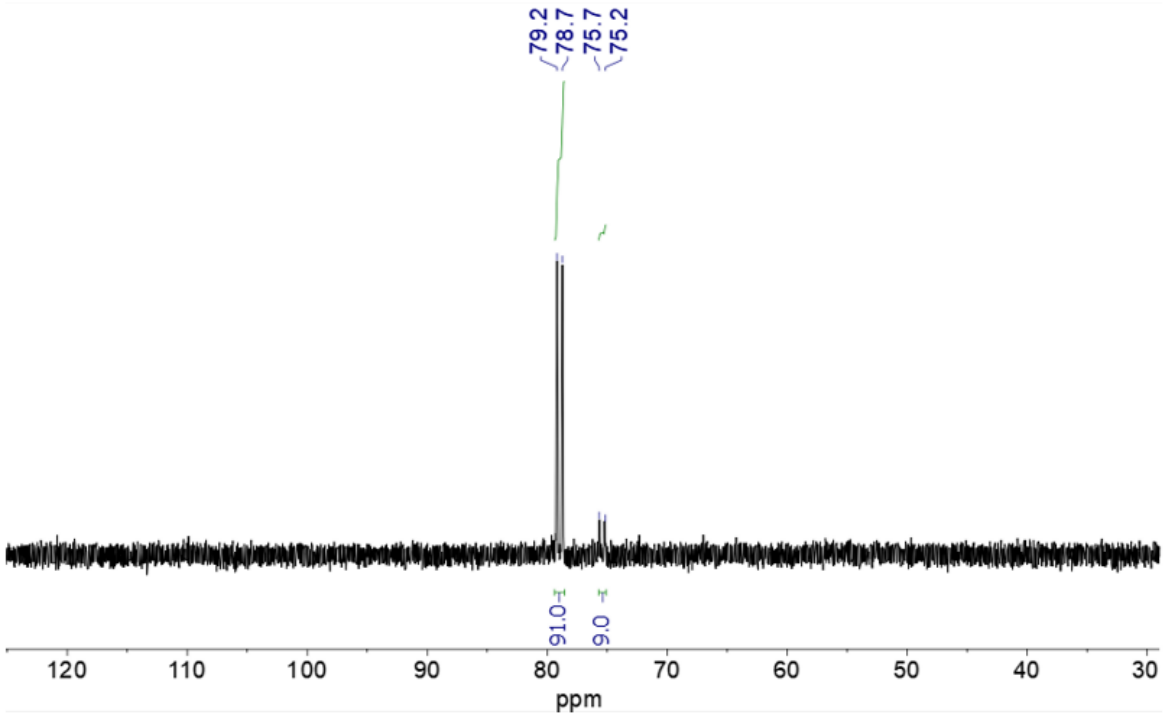

Figure 168. ^{31}P{^{1}H} NMR spectrum of Rh(^{i}Pr-PN^{H}P)(κ^{1}-BH_4)H_2 (**4**) showing a doublet at 79.0 ppm (J_{PRh} = 109 Hz). A small amount of starting material Rh(^{i}Pr-PN^{H}P)H_2Cl (**2**) is present as a doublet at 75.5 ppm (J_{PRh} = 116 Hz). Recorded in benzene-d_6 at 298 K.

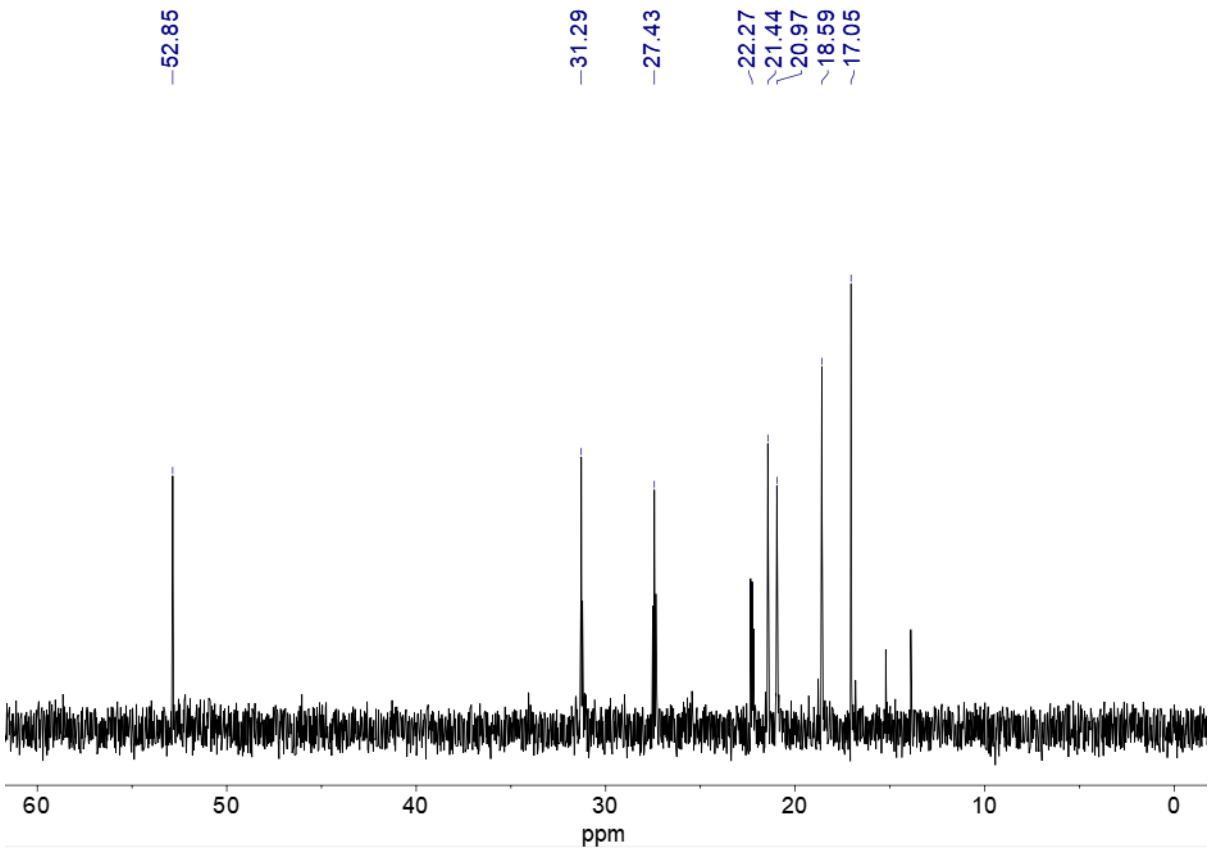

Figure 169. $^{13}C\{^{1}H\}$ NMR of Rh(PN^{H}P^{i}Pr)(κ^{1}-BH_4)H_2 (**4**). Recorded in benzene-d_6 at 298 K.

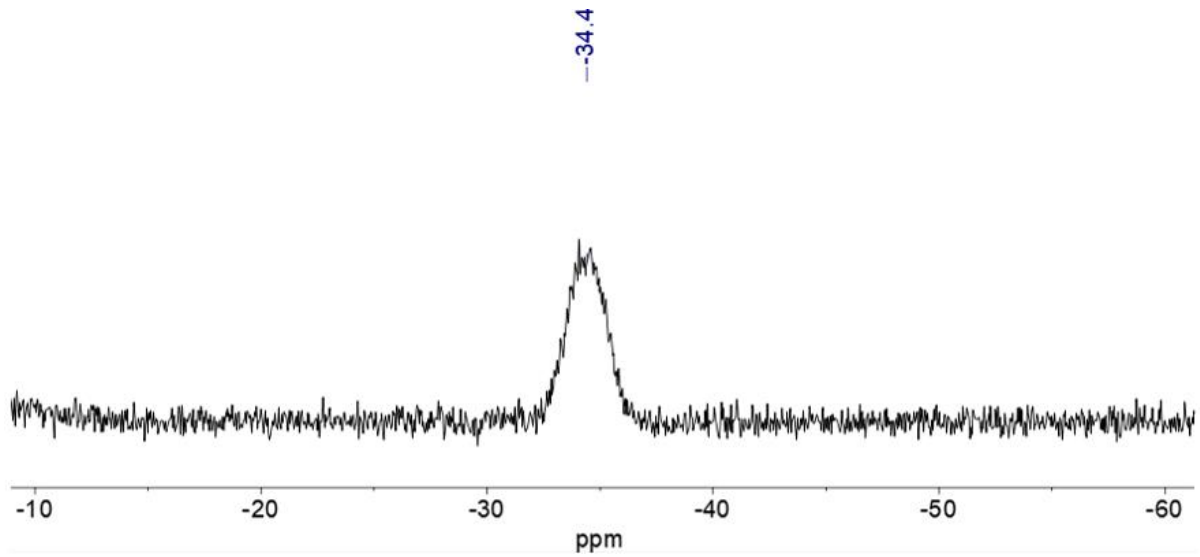

Figure 170. ^{11}B NMR of Rh(^{i}Pr-PN^{H}P)(κ^{1}-BH_4)H_2 (**4**). Recorded in benzene-d_6 at 298 K.

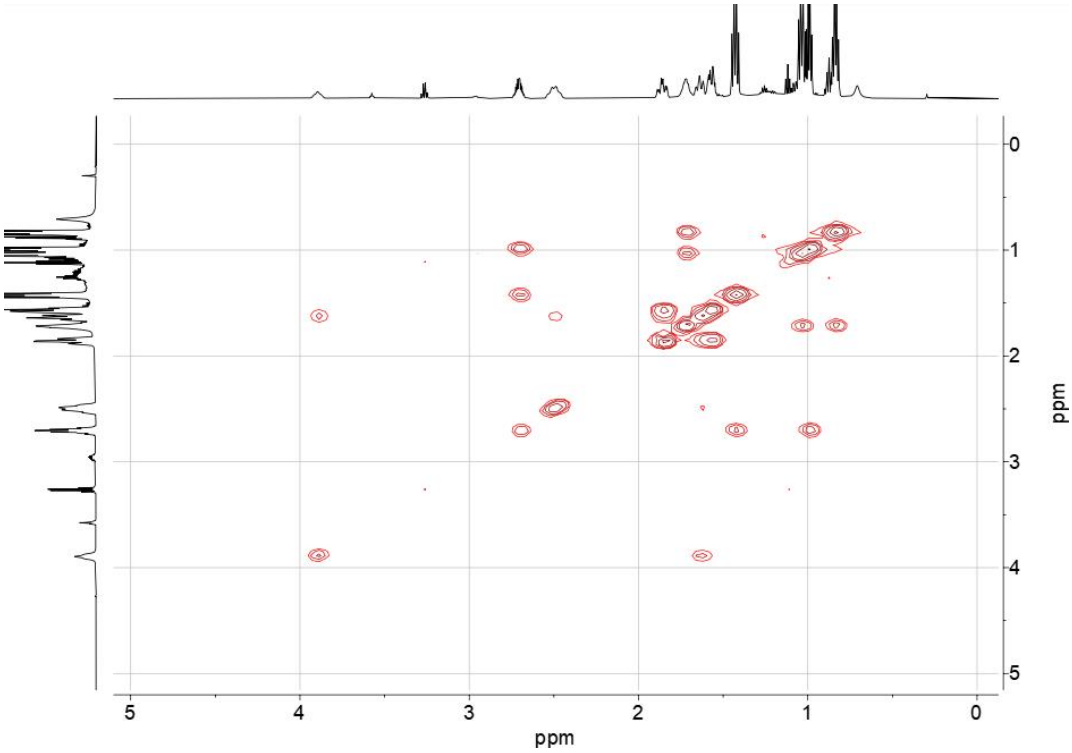

Figure 171. $^{1}H^{1}H$ COSY NMR spectrum of Rh(^{i}Pr-PN^{H}P)(κ^{1}-BH_4)H_2 (**4**). Recorded in benzene-d_6 at 298 K.

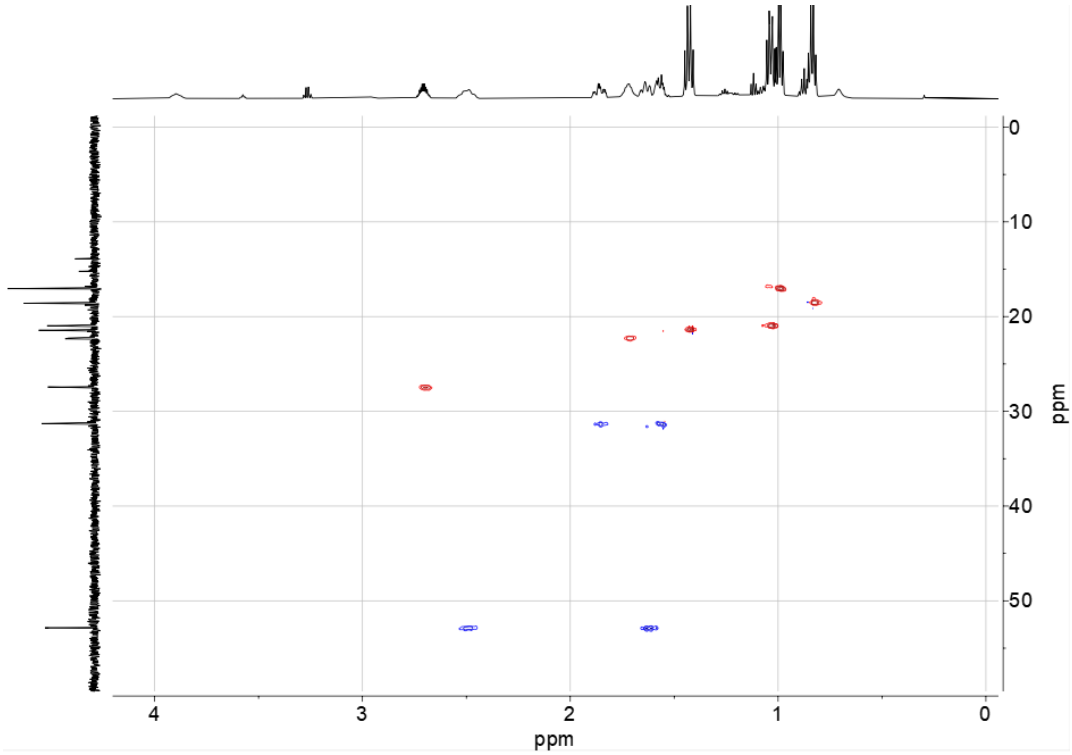

Figure 172. $^{13}C^{1}H$ HSQC NMR spectrum of Rh(^{i}Pr-PN^{H}P)(κ^{1}-BH_4)H_2 (**4**). Recorded in benzene-d_6 at 298 K.

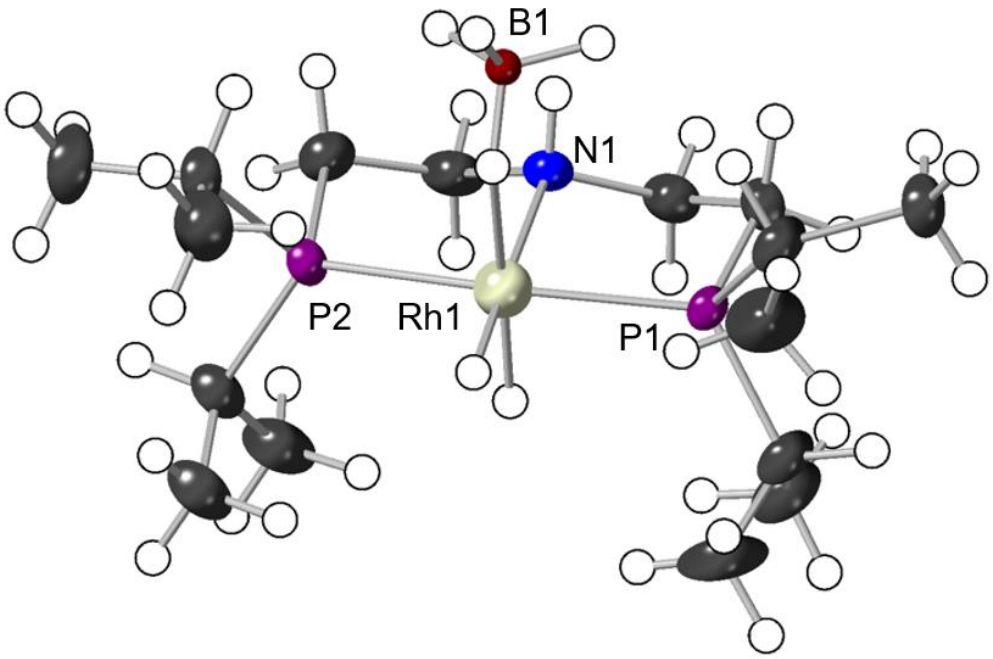

Figure 173. Molecular structure of Rh(PN^{H}P^{i}Pr)(κ^{1}-BH$_4$)H$_2$ (**4**) as determined by single crystal X-ray diffraction. Displacement ellipsoids are shown at the 50% probability level. Hydrogen atoms are placed in calculated positions. N–H, Rh–H and B–H were located in the Fourier difference map, allowed to ride the parent atoms and freely refined. Selected distances [Å], bond lengths [Å] and angles [°]: Rh(1)···B(1) 2.709(8), Rh(1) – N(1) 2.188(2), Rh(1) – P(1) 2.2677(7), Rh(1) – P(2) 2.2590(7), P(1) – Rh(1) – N(1) 84.32(7), P(1) – Rh(1) – P(2) 168.31(3), P(2) – Rh(1) – N(1) 85.25(7).

5.2.2 Synthesis and characterisation of {^{i}Pr$_2$P(=Se)CH$_2$CH$_2$}$_2$NH

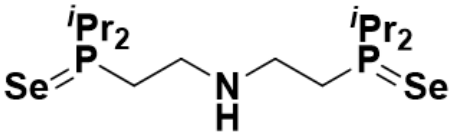

(^{i}Pr$_2$PCH$_2$CH$_2$)$_2$NH (55 µl, 10% w/v in THF, 0.016 mmol) was added to a Youngs tap NMR tube containing a vast excess of grey selenium (~ 10 mg, 0.12 mmol). The THF was then removed *in-vacuo*. CD_2Cl_2 (0.5 cm^3) was then transferred via a distillation bridge *in-vacuo*. The Youngs tap NMR tube was then agitated in an ultrasound bath for 1 hour at room temperature. The product {^{i}Pr$_2$P(=Se)CH$_2$CH$_2$}$_2$NH was not isolated and characterised by NMR spectroscopy in-situ.

^{1}H NMR (500 MHz, CD_2Cl_2, 298 K) δ_H 2.91 (dt, *J* = 11.4, 7.4, Hz, 4H, CH_2), 2.14 (dsep, *J* = 9.0, 7.0 Hz, 4 H, ^{i}Pr CH), 2.05 (br, s, 1H, NH) 2.00 (t, *J* = 10.3, 7.4 Hz, 4 H, CH_2), 1.20 (dd, *J* = 7.0, 6.5 Hz, 12 H, ^{i}Pr CH_3), 1.16 (dd, *J* = 7.0, 6.2 Hz, 12 H, ^{i}Pr CH_3).

^{13}C{^{1}H} NMR (126 MHz, CD_2Cl_2, 298 K) δ_C 45.3 (s, N-CH_2), 27.9 (d, *J* = 42 Hz, $CH(CH_3)_2$), 25.3 (d, *J* = 38.8 Hz, P-CH_2), 17.0 (d, *J* = 6 Hz, CH_3).

^{31}P{^{1}H} NMR (203 MHz, CD_2Cl_2, 298 K) δ_P 59.2 (s, 2 P, P=Se). ^{77}Se satellites: (d, J_{PSe} = 695 Hz)

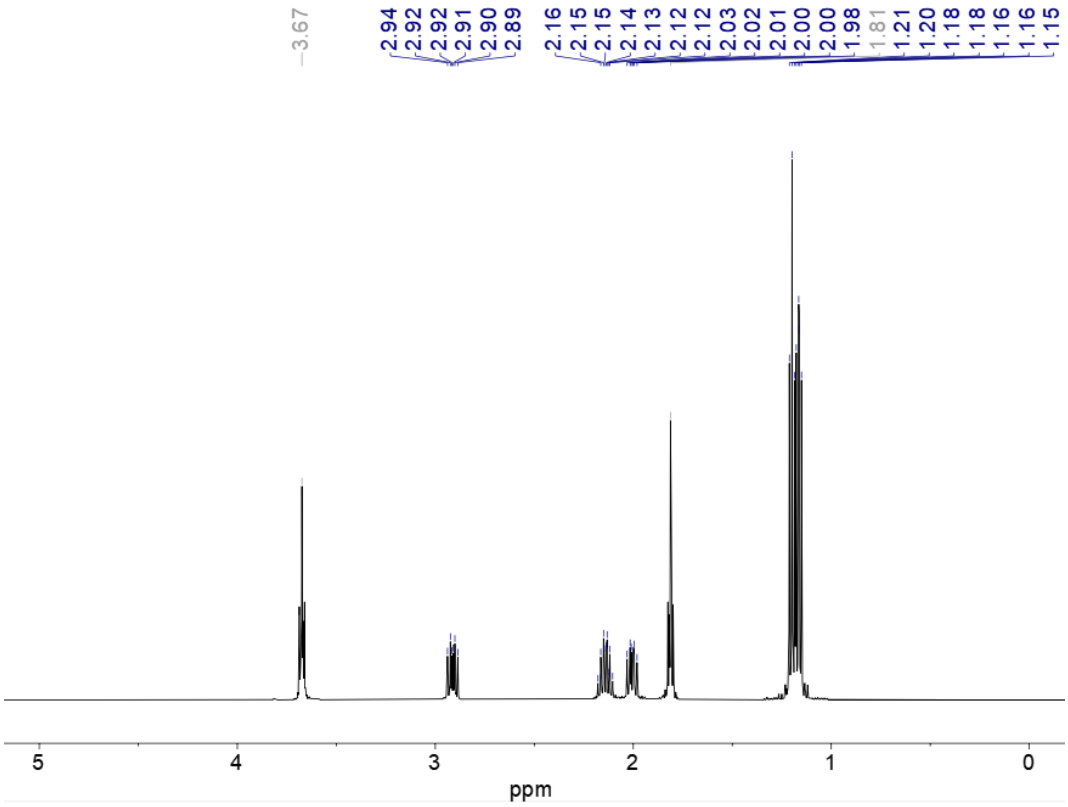

Figure 174. ^{1}H NMR of $\{^{i}Pr_2P(=Se)CH_2CH_2\}_2NH$. Residual THF signals from the synthesis are seen at 3.67 and 1.81 ppm. Recorded in CD_2Cl_2 at 298 K.

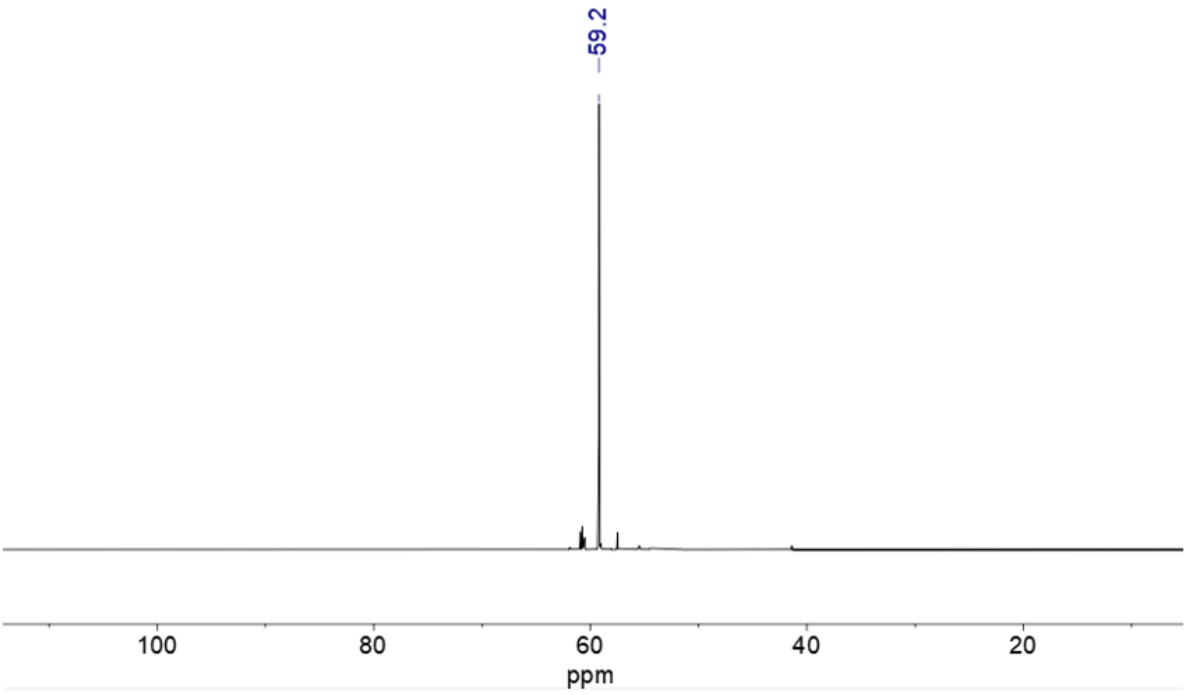

Figure 175. $^{31}P\{^{1}H\}$ NMR spectrum of $\{^{i}Pr_2P(=Se)CH_2CH_2\}_2NH$, showing satellite peaks corresponding to ^{31}P – ^{77}Se coupling of 695 Hz. Recorded in CD_2Cl_2 at 298 K.

5.2.3 Synthesis and characterisation of $\{Cy_2P(=Se)CH_2CH_2\}_2NH$

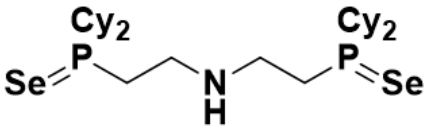

$(Cy_2PCH_2CH_2)_2NH$ (5 mg, 0.011 mmol) was added to a Youngs tap NMR tube containing a vast excess of grey selenium (~ 10 mg, 0.12 mmol). CD_2Cl_2 (0.5 cm^3) was then transferred via a distillation bridge *in-vacuo*. The Youngs tap NMR tube was then agitated in an ultrasound bath for 1 hour at room temperature. The product $\{Cy_2P(=Se)CH_2CH_2\}_2NH$ was not isolated and characterised by NMR spectroscopy in-situ.

$^1H\{^{31}P\}$ NMR (500 MHz, CD_2Cl_2, 298 K) δ_H 2.92 (t, *J* = 7 Hz, 4 H, CH_2), 2.05 (t, *J* = 7 Hz, 4 H, CH_2), 1.91 (s, br, 1 H, NH), 1.16 – 2.01 (44 H, Cy),

$^{13}C\{^1H\}$ NMR (126 MHz, CD_2Cl_2, 298 K) δ_C 45.4 (s, N-CH_2), 37.5 (d, *J* = 41 Hz, Cy CH), 26.1-27.1 (20 C, Cy CH_2), 24.7 (d, *J* = 39 Hz, 2 C, P-CH_2).

$^{31}P\{^1H\}$ NMR (203 MHz, CD_2Cl_2, 298 K) δ_P 50.7 (s, 2 P, P=Se). ^{77}Se satellites: (d, J_{PSe} = 688 Hz)

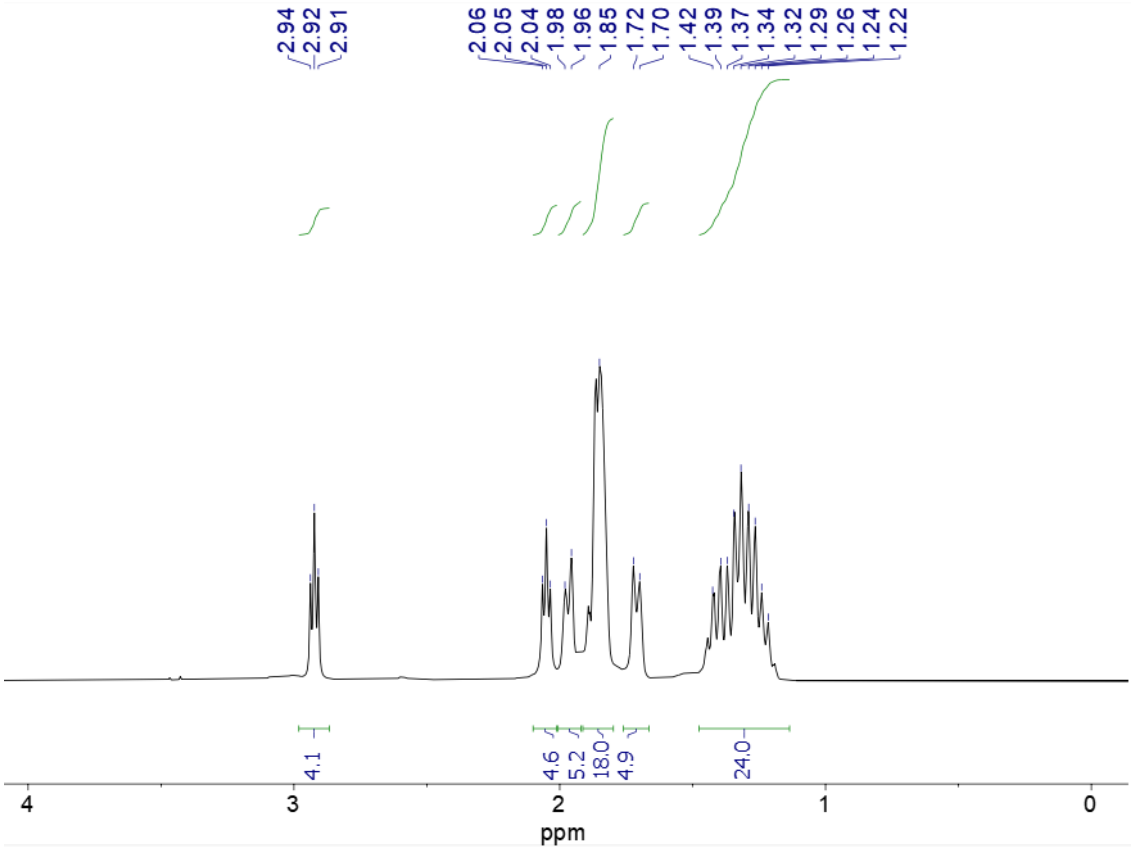

Figure 176. $^{1}H\{^{31}P\}$ NMR spectrum of $\{Cy_2P(=Se)CH_2CH_2\}_2NH$. Recorded in CD_2Cl_2 at 298 K.

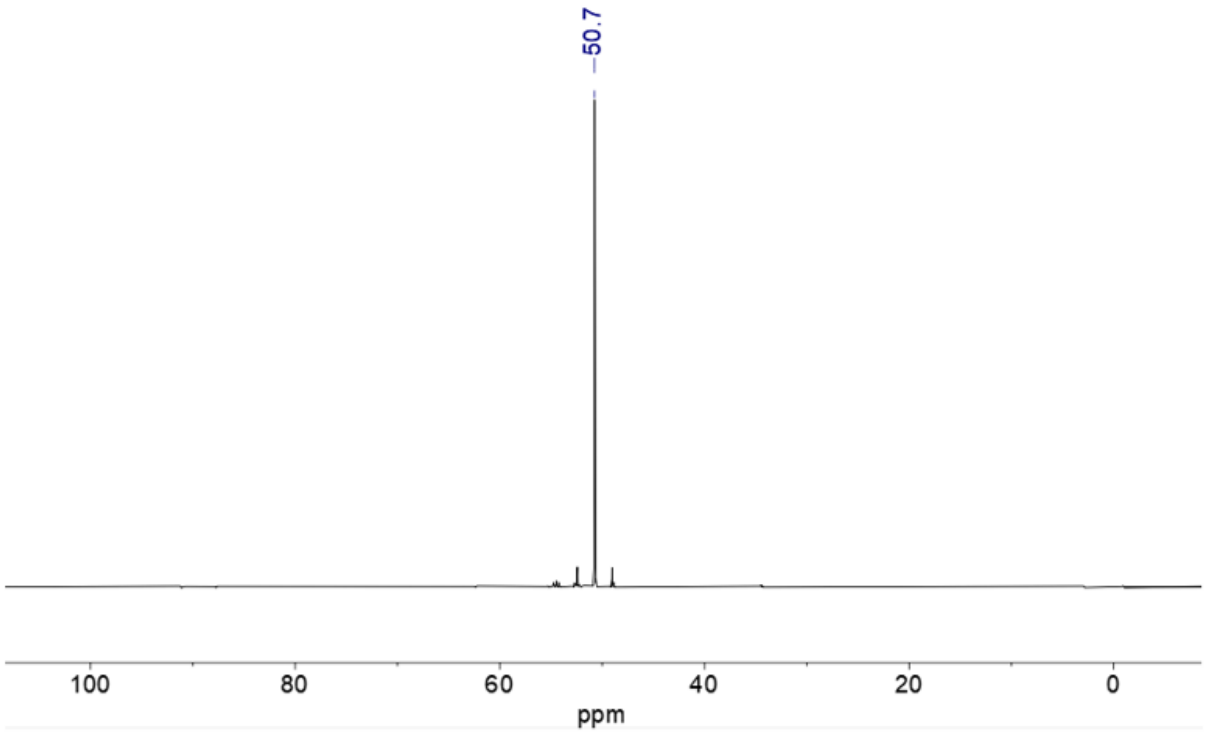

Figure 177. $^{31}P\{^{1}H\}$ NMR spectrum of $\{Cy_2P(=Se)CH_2CH_2\}_2NH$, showing satellite peaks corresponding to ^{31}P – ^{77}Se coupling of 688 Hz. Recorded in CD_2Cl_2 at 298 K.

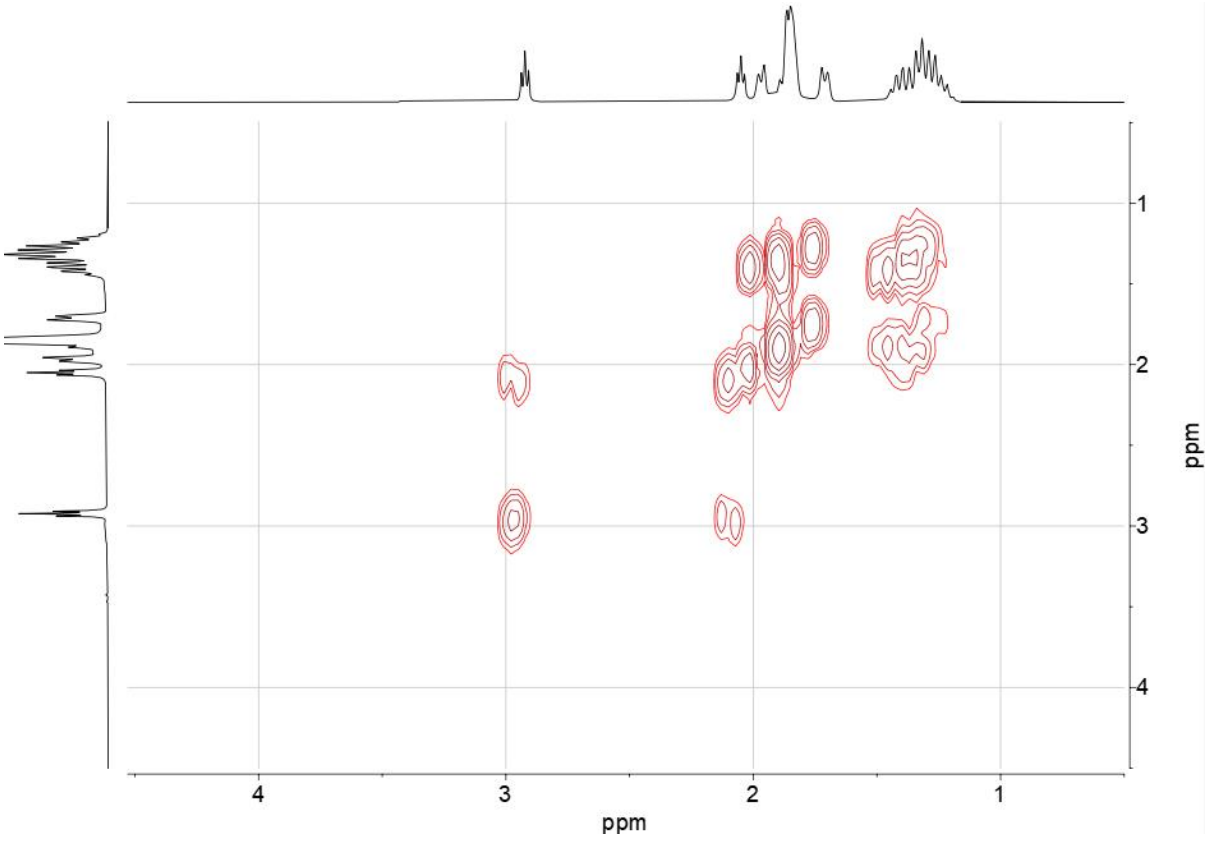

Figure 178. $^{1}H^{1}H$ COSY NMR spectrum of $\{Cy_2P(=Se)CH_2CH_2\}_2NH$. Recorded in CD_2Cl_2 at 298 K.

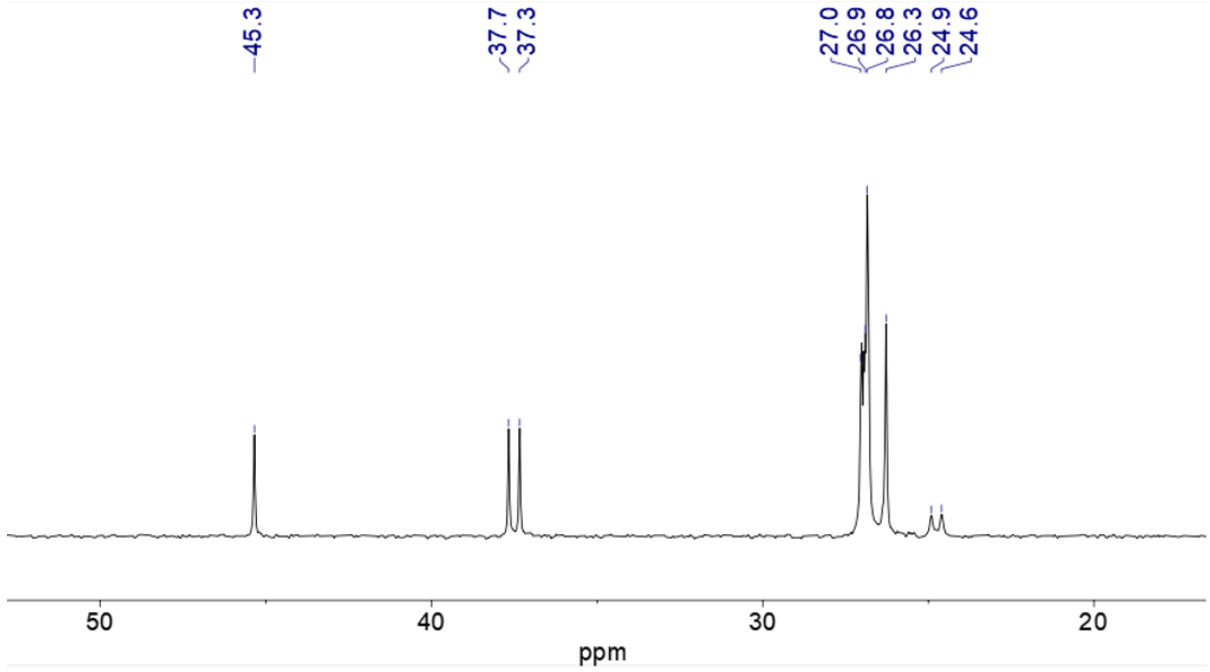

Figure 179. $^{13}C\{^{1}H\}$ NMR spectrum of $\{Cy_2P(=Se)CH_2CH_2\}_2NH$. Recorded in CD_2Cl_2 at 298 K.

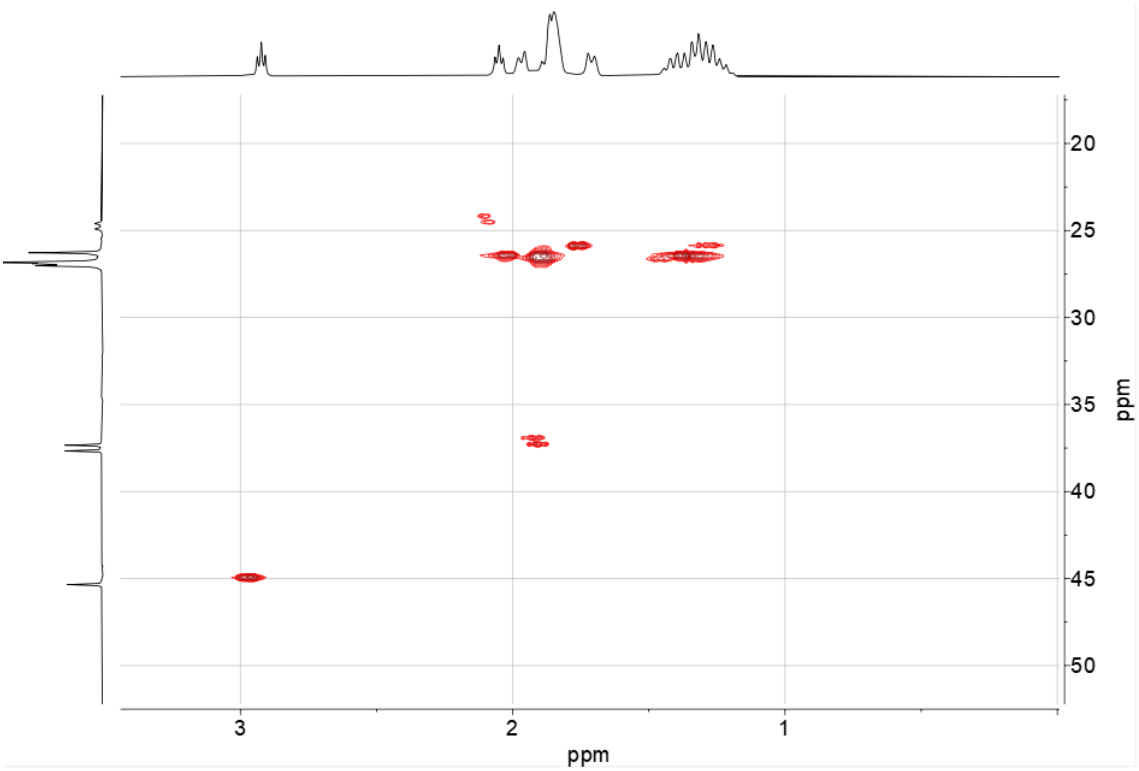

Figure 180. $^{1}H^{13}C$ HMBC NMR spectrum of $\{Cy_2P(=Se)CH_2CH_2\}_2NH$. Recorded in CD_2Cl_2 at 298 K.

5.2.4 Synthesis and characterisation of {^{t}Bu$_2$P(=Se)CH$_2$CH$_2$}$_2$NH

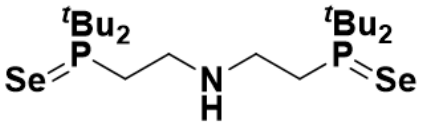

(^{t}Bu$_2$PCH$_2$CH$_2$)$_2$NH (55 µl, 10% w/v in THF, 0.014 mmol) was added to a Youngs tap NMR tube containing a vast excess of grey selenium (~ 10 mg, 0.12 mmol). The THF was then removed *in-vacuo*. CD_2Cl_2 (0.5 cm^3) was then transferred via a distillation bridge *in-vacuo*. The Youngs tap NMR tube was then agitated in an ultrasound bath for 1 hour at room temperature. The product {^{t}Bu$_2$P(=Se)CH$_2$CH$_2$}$_2$NH was not isolated and characterised by NMR spectroscopy in-situ.

^{1}H NMR (500 MHz, CD_2Cl_2, 298 K) δ_H 2.97 (t, *J* = 7 Hz, 4 H, CH_2), 2.13 (s, br, 1 H, NH), 2.07 (t, *J* = 7 Hz, 4 H, CH_2), 1.33 (s, 36 H, CH_3).

^{13}C{^{1}H} NMR (126 MHz, CD_2Cl_2, 298 K) δ_C47.0 (s, N-CH_2), 37.3 (d, *J* = 34 Hz, C(CH_3)$_3$), 27.9 (s, CH_3), 22.2 (d, *J* = 35 Hz, P-CH_2).

^{31}P{^{1}H} NMR (203 MHz, CD_2Cl_2, 298 K) δ_P 74.0 (s, 2 P, P=Se). ^{77}Se satellites: (d, J_{PSe} = 693 Hz)

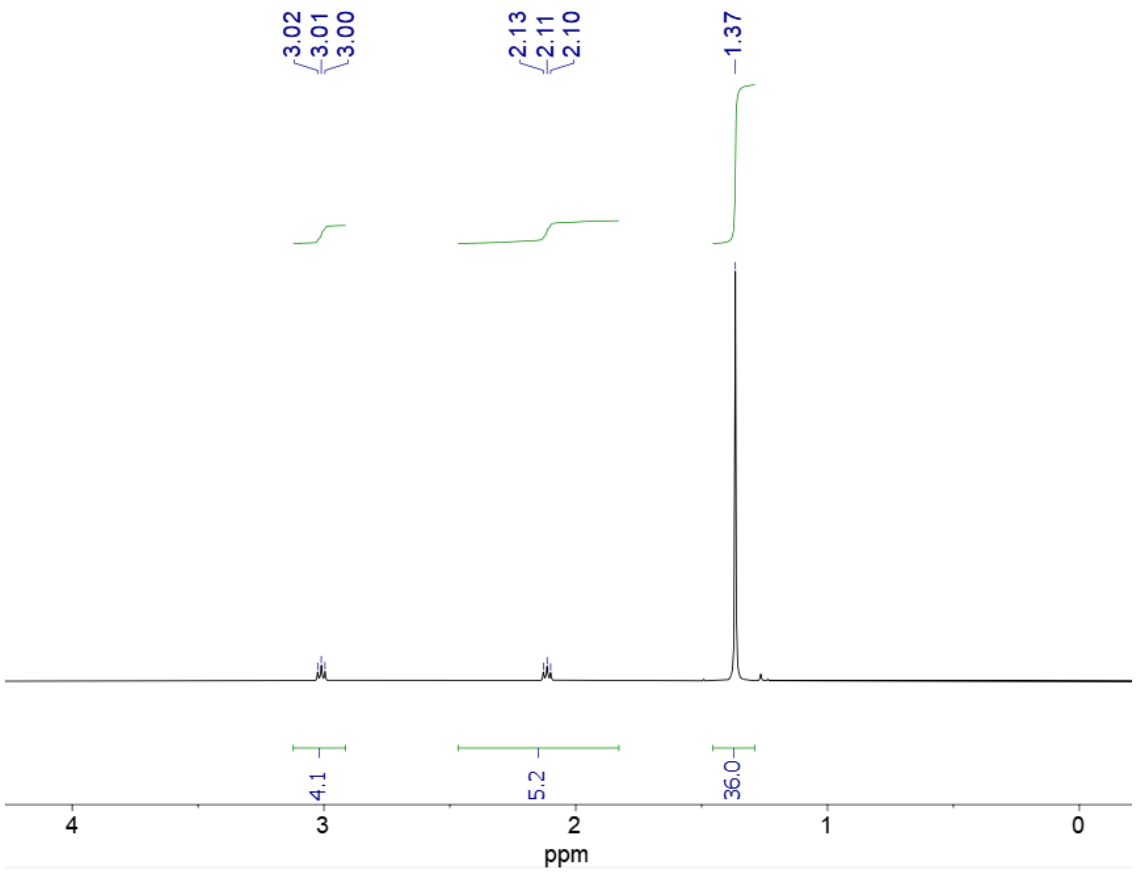

Figure 181. ^{1}H NMR spectrum of {^{t}Bu$_2$P(=Se)CH$_2$CH$_2$}$_2$NH. Recorded in CD_2Cl_2 at 298 K.

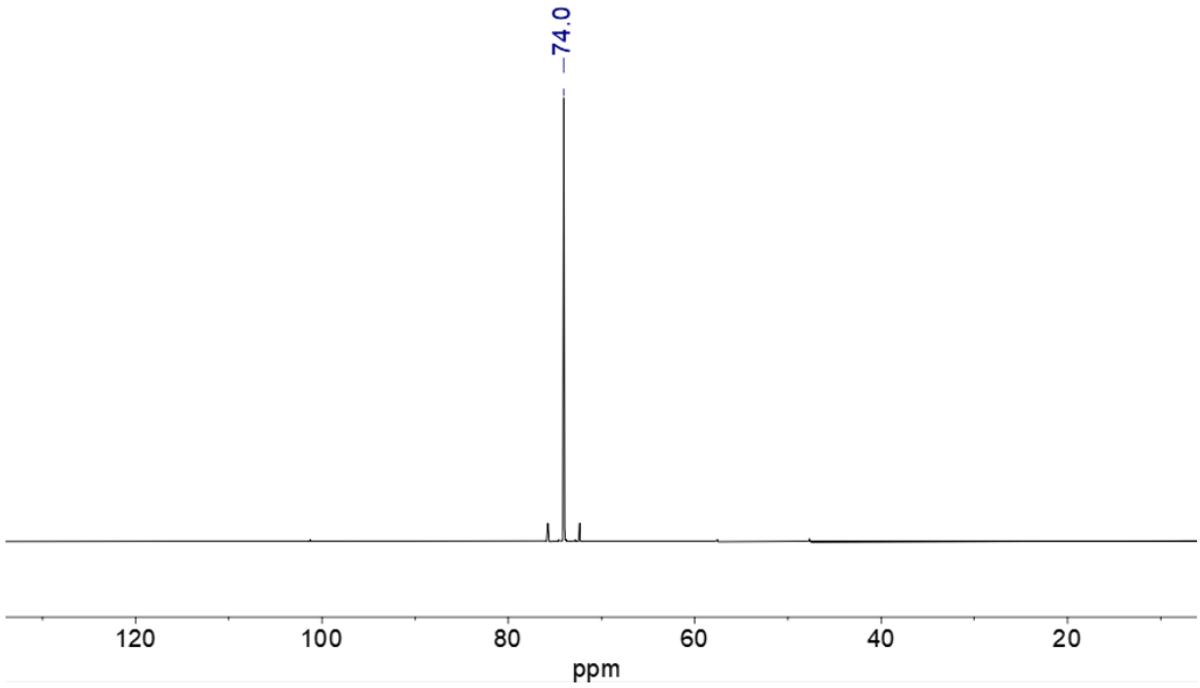

Figure 182. ^{31}P{^{1}H} NMR spectrum of {^{t}Bu$_2$P(=Se)CH$_2$CH$_2$}$_2$NH, showing satellite peaks corresponding to ^{31}P – ^{77}Se coupling of 693 Hz. Recorded in CD_2Cl_2 at 298 K.

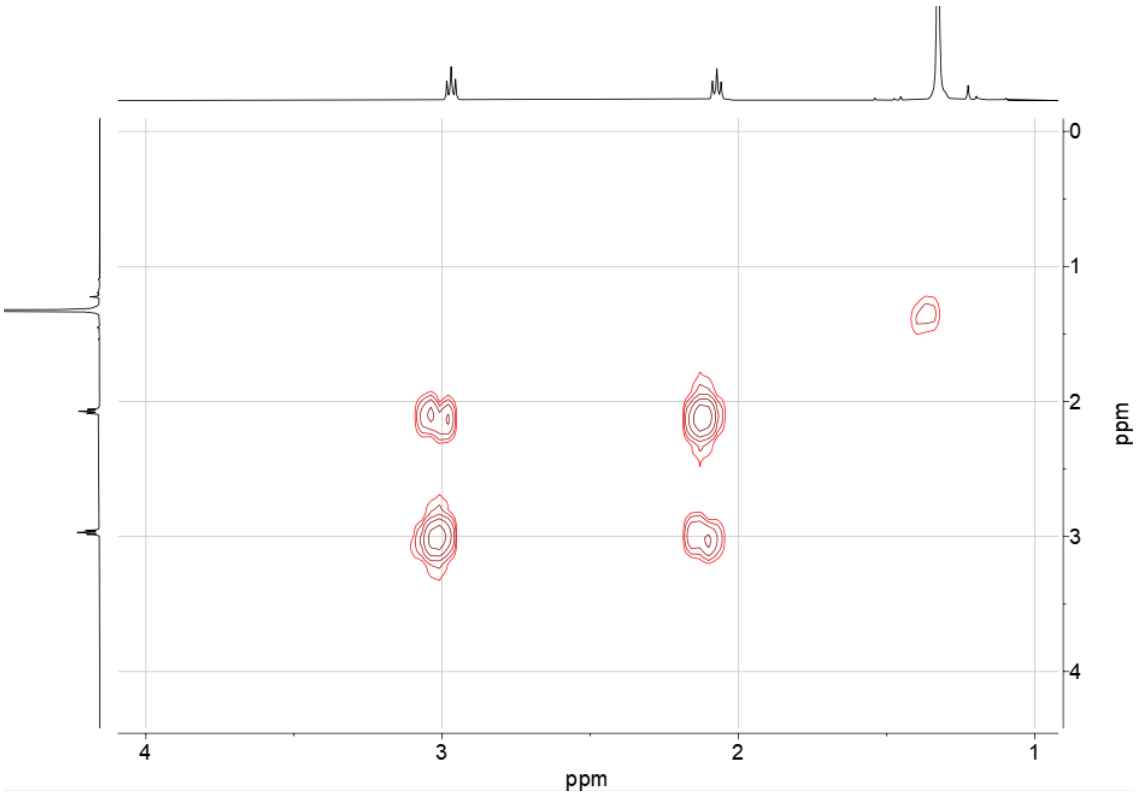

Figure 183. $^{1}H^{1}H$ COSY NMR spectrum of $\{^{t}Bu_2P(=Se)CH_2CH_2\}_2NH$. Recorded in CD_2Cl_2 at 298 K.

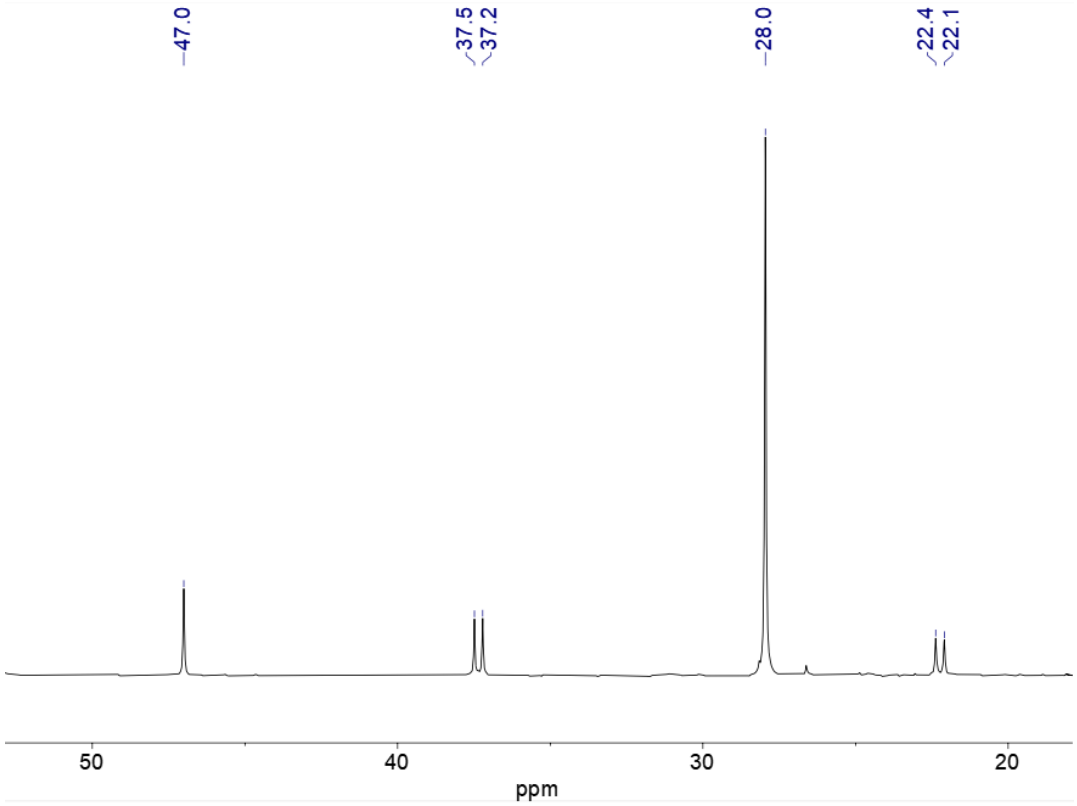

Figure 184. $^{13}C\{^{1}H\}$ NMR spectrum of $\{^{t}Bu_2P(=Se)CH_2CH_2\}_2NH$. Recorded in CD_2Cl_2 at 298 K.

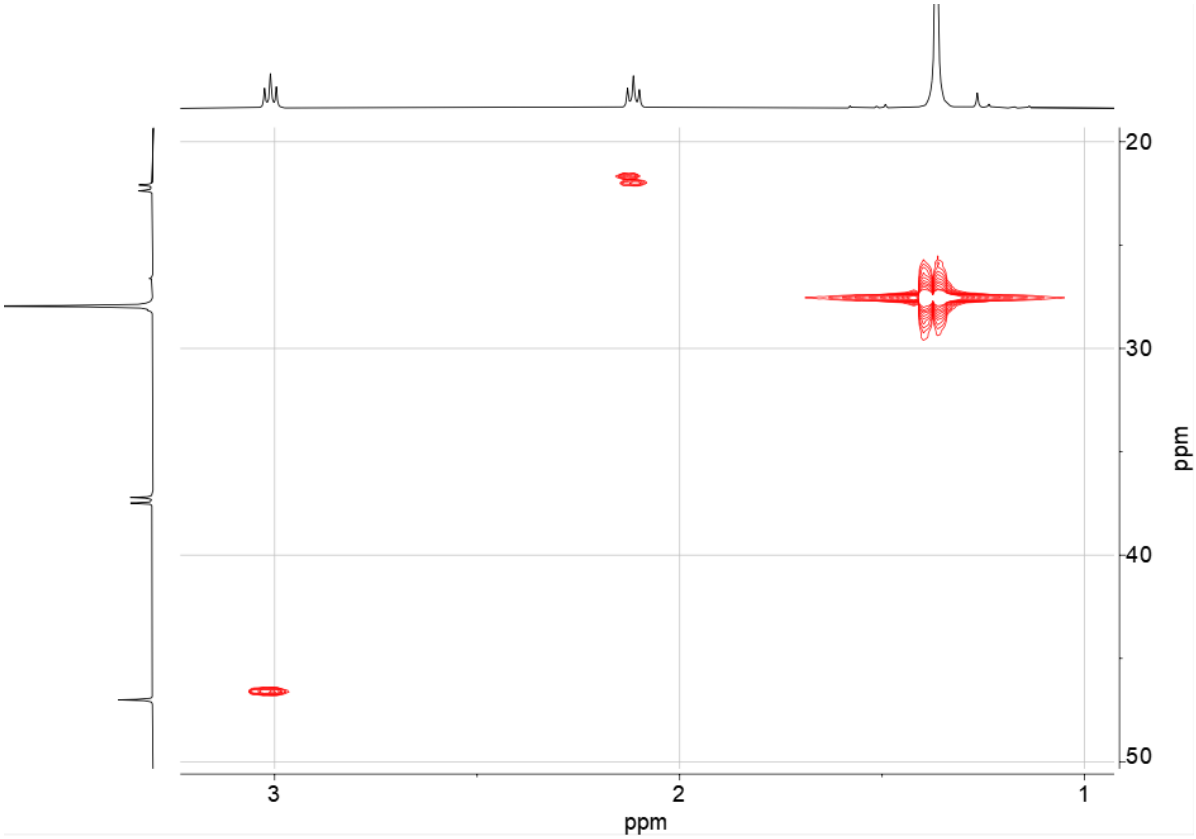

Figure 185. $^{13}C^{1}H$ HMBC NMR spectrum of $\{^{t}Bu_2P(=Se)CH_2CH_2\}_2NH$. Recorded in CD_2Cl_2 at 298 K.

5.2.5 Synthesis and characterisation of Rh{κ^3-($Cy_2PCH_2CH_2)_2NH$}H_2Cl (7)

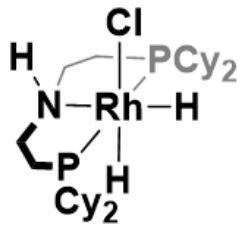

7

An ampoule with stirrer was charged with $(Cy_2PCH_2CH_2)_2NH$ (0.175 g, 0.38 mmol). A separate ampoule was charged with $[Rh(COD)Cl]_2$ (0.0925 g, 0.19 mmol). 5 cm^3 of dry 1,2-difluorobenzene was then added to the $[Rh(COD)Cl]_2$, and the resulting solution was transferred into the $(Cy_2PCH_2CH_2)_2NH$ resulting in an orange solution. The reaction mixture was then degassed by 3 freeze-pump-thaw cycles. The reaction mixture was then stirred under an atmosphere of 4 bar H_2 for 24 hours at room temperature. After 24 hours, the reaction mixture was again degassed by 3 freeze-pump-thaw cycles and the stirred under 4 bar H_2 for a further 24 hours, resulting in a white precipitate and yellow supernatant. The supernatant was then removed via filtration and the white solid was washed with degassed pentane (3 x 2 cm^3) then dried *in-vacuo*. The solid was then recrystallised by dissolution in dry 1,2-difluorobenzene and then layering with dry pentane, forming x-ray quality crystals of Rh{κ^3-($Cy_2PCH_2CH_2)_2NH$}H_2Cl (**7**) (0.143 g, 63% yield).

^{1}H NMR (600 MHz, benzene-d_6, 298 K) δ_H 3.60 (t, br, *J* = 10 Hz, 1 H, N–H), 2.88 (m, 2 H, H–C($CH_3)_2$), 2.72-2.86 (overlapping multiplets, 4 H) 1.15-2.00 (many overlapping Cy & backbone multiplets, 42 H), – 15.68 (m, br, 1 H, Rh–H), – 19.71 (m, br, 1 H, Rh-H).

^{13}C{^{1}H} NMR (151 MHz, benzene-d_6, 298 K) δ_C 52.8 (t, *J* = 3.7 Hz, N–CH_2), 36.9 (t, *J* = 11.6 Hz, Cy CH), 34.0 (t, 12 Hz, Cy CH), 32.3 (t, *J* = 2.4 Hz, Cy CH_2), 31.5 (t, *J* = 3 Hz, Cy CH_2), 31.0 (t, *J* = 8.6 Hz, P–CH_2), 28.7 (s, Cy CH_2), 28.5 (s, Cy CH_2), 27.9 (t, *J* = 4.6 Hz, Cy CH_2), 27.3 (t, *J* = 10.1 Hz, P–CH_2), 27.0 (s, Cy CH_2), 26.8 (t, *J* = 6.4 Hz,), 26.6 (s, Cy CH_2).

^{31}P{^{1}H} NMR (600 MHz, benzene-d_6, 298 K) δ_P 65.8 (d, J_{RhP} = 112 Hz, 2 P, Rh–P).

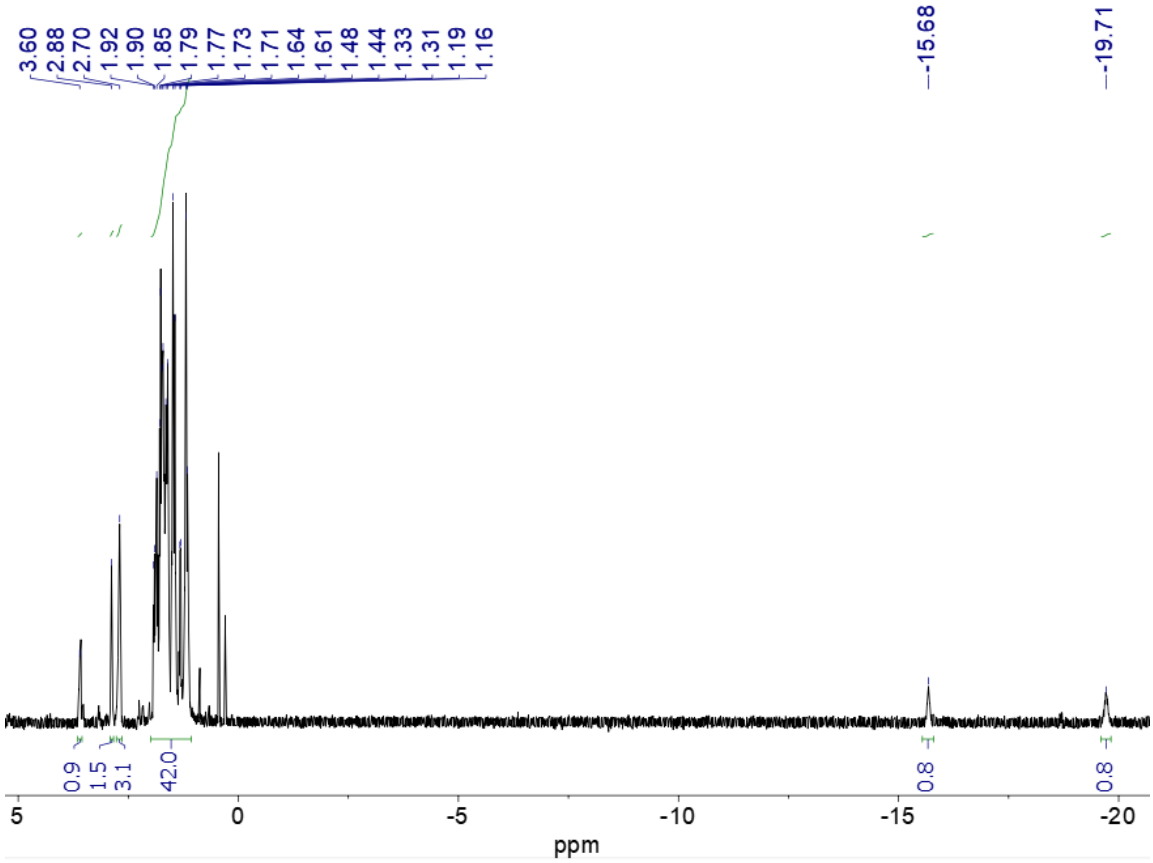

Figure 186. ^{1}H NMR spectrum of Rh{κ^{3}-($Cy_2PCH_2CH_2)_2NH$}H_2Cl (**7**), showing hydride resonances at – 15.68 and – 19.71 ppm. Recorded in benzene-d_6 at 298 K.

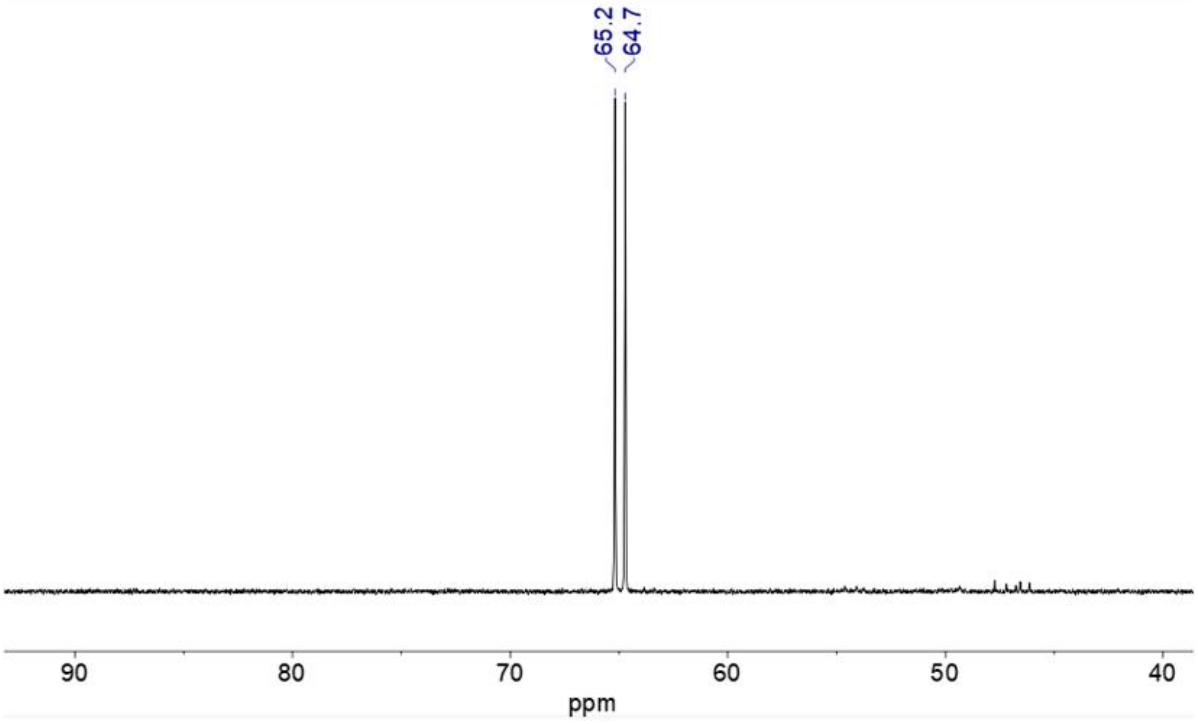

Figure 187. $^{31}P\{^{1}H\}$ NMR spectrum of Rh{κ^{3}-($Cy_2PCH_2CH_2)_2NH$}H_2Cl (**7**). Recorded in benzene-d_6 at 298 K.

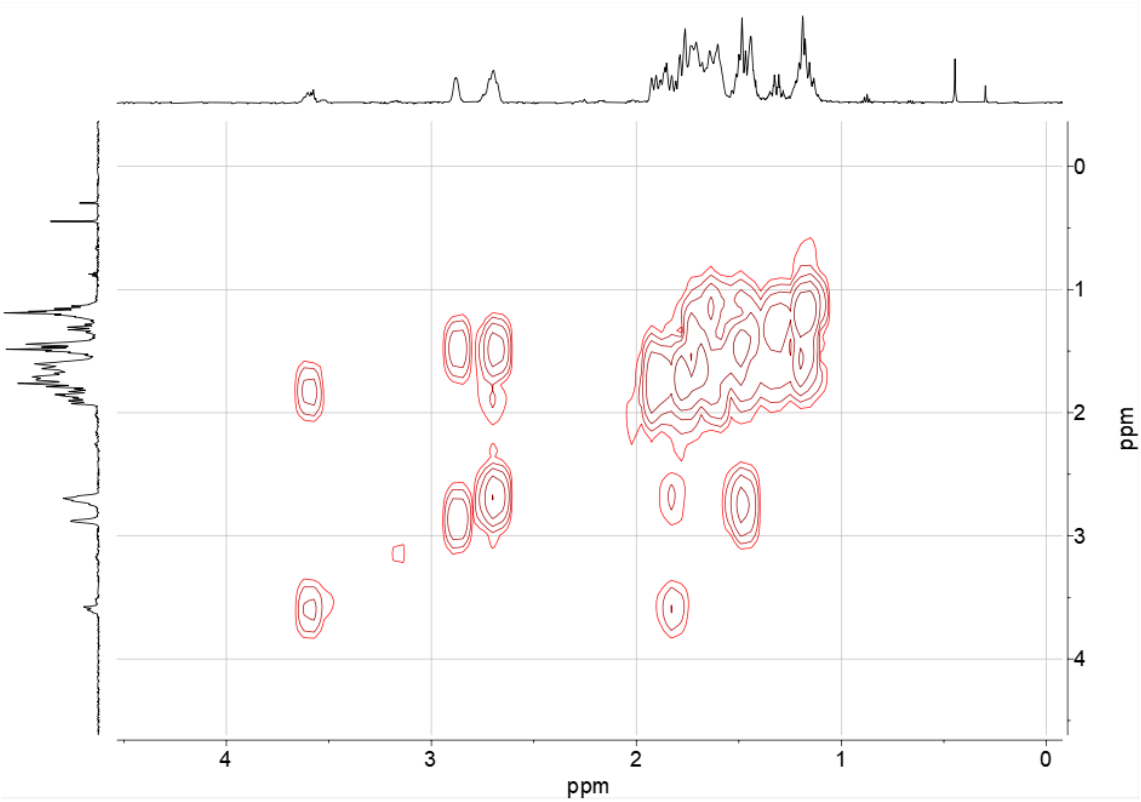

Figure 188. $^{1}H^{1}H$ COSY NMR spectrum showing the aliphatic region of Rh{κ^{3}-($Cy_2PCH_2CH_2)_2NH$}H_2Cl (**7**). Recorded in benzene-d_6 at 298 K.

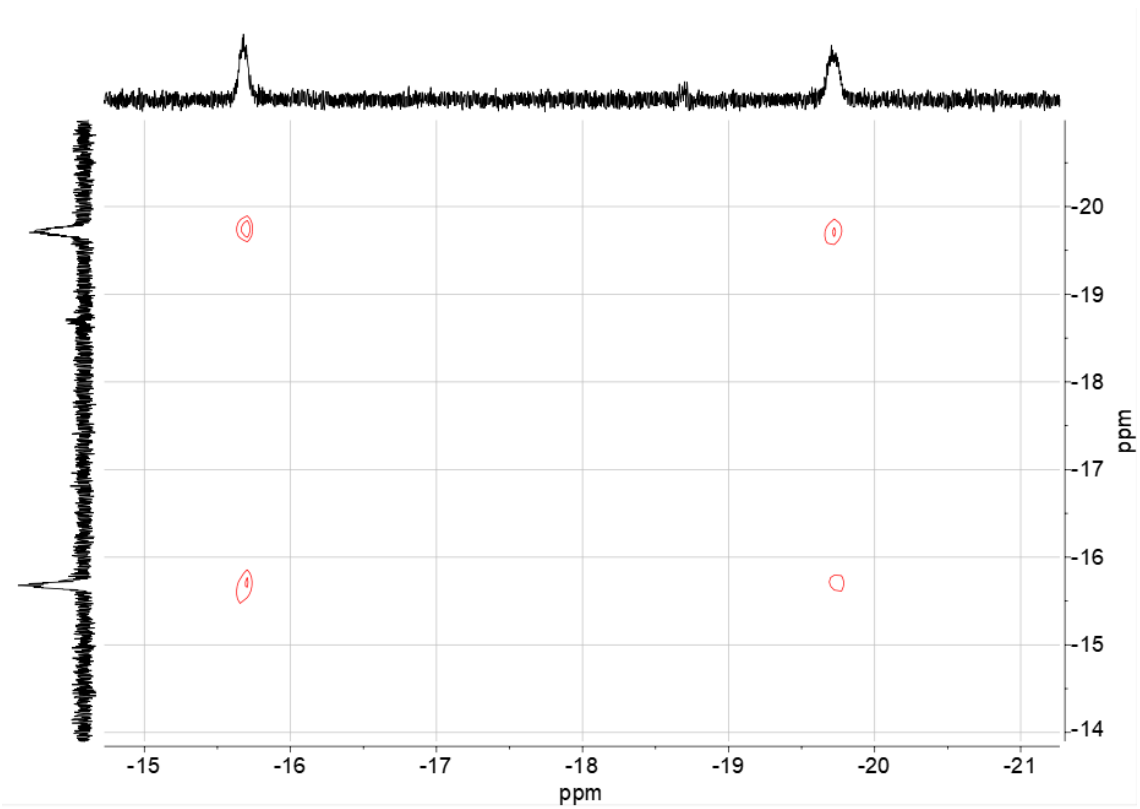

Figure 189. $^{1}H^{1}H$ COSY NMR spectrum showing the hydride region of Rh{κ^{3}-($Cy_2PCH_2CH_2)_2NH$}H_2Cl (**7**). Recorded in benzene-d_6 at 298 K.

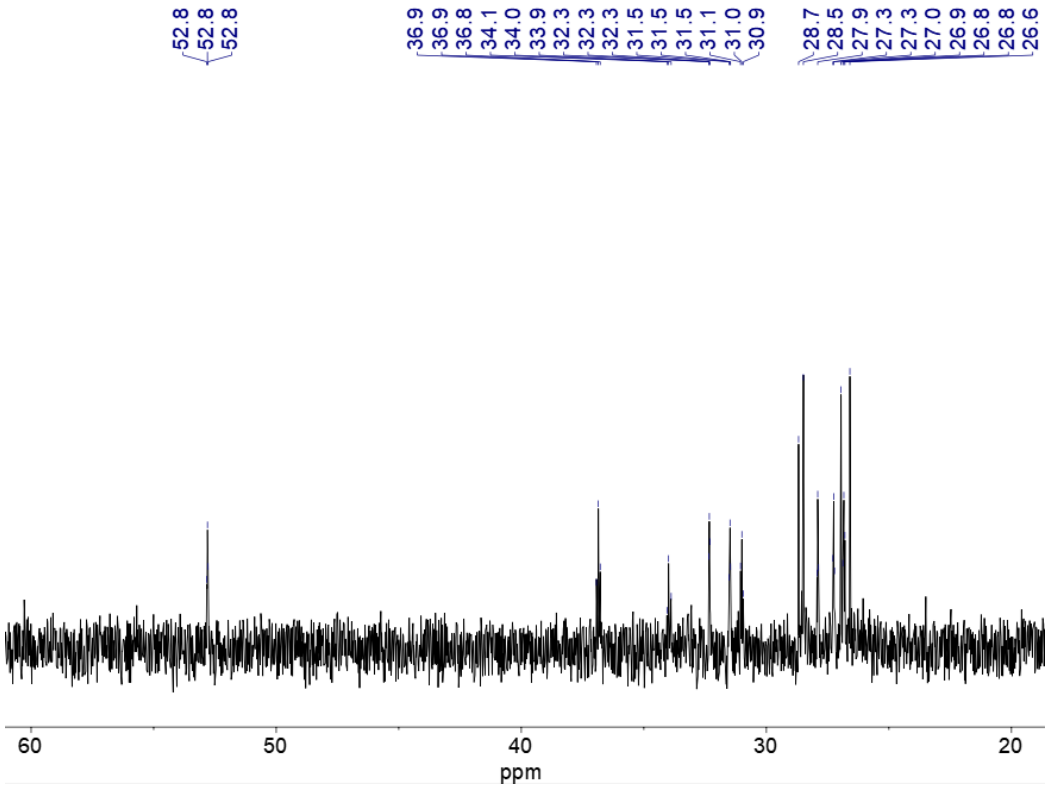

Figure 190. $^{13}C\{^{1}H\}$ NMR spectrum of Rh{κ^3-($Cy_2PCH_2CH_2)_2NH$}H_2Cl (**7**). Recorded in benzene-d_6 at 298 K.

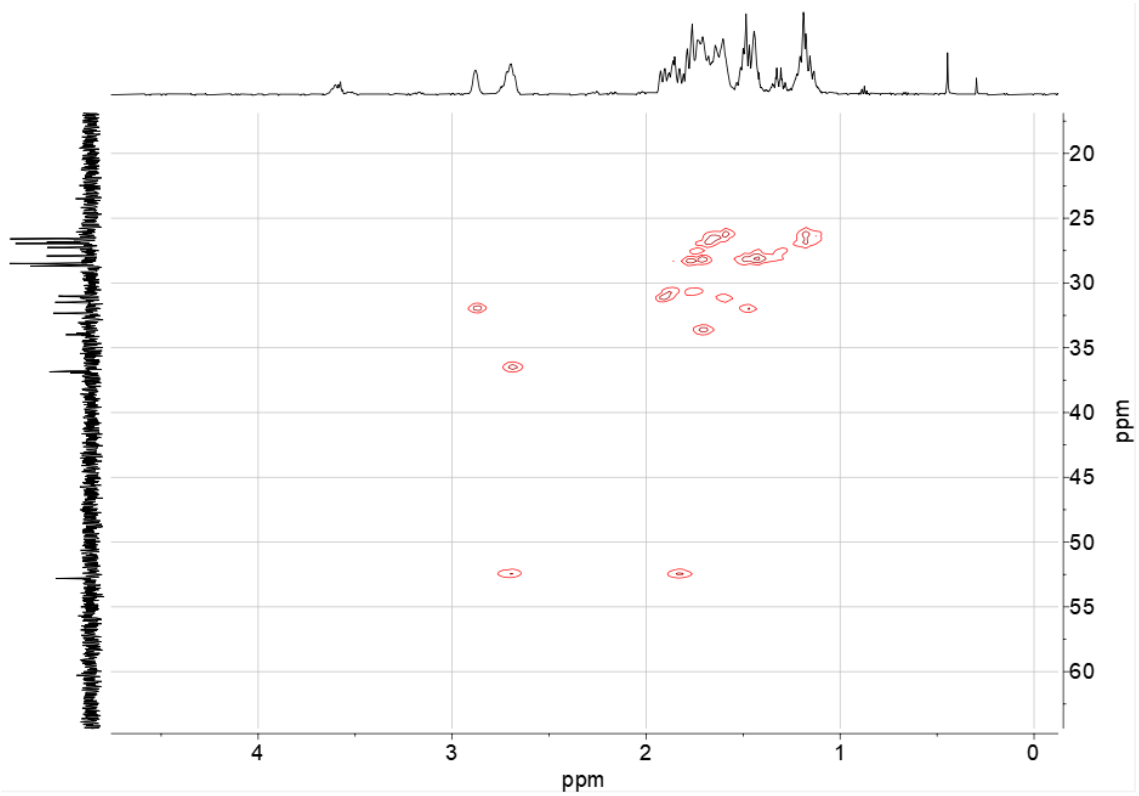

Figure 191. $^{13}C^{1}H$ HMBC NMR spectrum of Rh{κ^3-($Cy_2PCH_2CH_2)_2NH$}H_2Cl (**7**). Recorded in benzene-d_6 at 298 K.

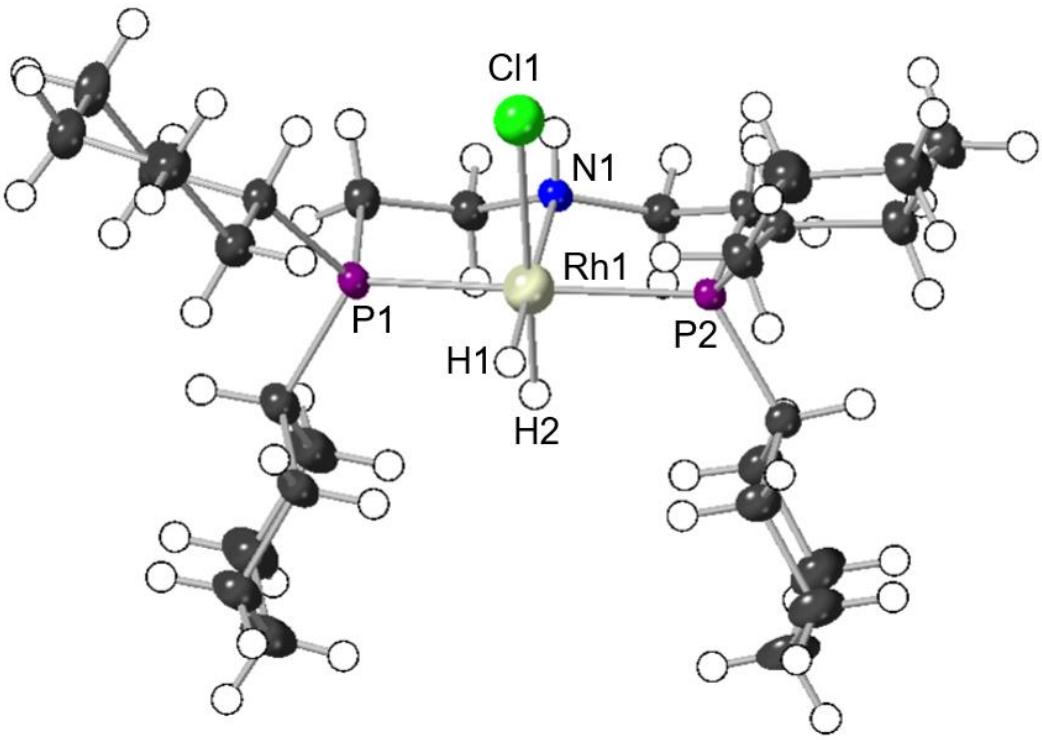

Figure 192. Molecular structure of Rh{κ^3-$(Cy_2PCH_2CH_2)_2NH$}H_2Cl (**7**) as determined by single crystal X-ray diffraction. Displacement ellipsoids are shown at the 50% probability level. Hydrogen atoms are placed in calculated positions. N–H and Rh–H were located in the Fourier difference map, allowed to ride the parent atoms and freely refined. Selected distances [Å], bond lengths [Å] and angles [°]: Rh(1) – P(1) 2.2793(6), Rh(1) – P(2) 2.2729(6), Rh(1) – N(1) 2.190(2), Rh(1) – Cl(1) 2.5036(6), P(1) – Rh(1) – N(1) 84.53(6), P(2) – Rh(1) – N(1) 84.16(6), P(1) – Rh(1) – P(2) 167.07(2), N(1) – Rh(1) – Cl(1) 89.88(6), P(1) – Rh(1) – Cl1 93.18(2), H(1) – Rh(1) – H(2) 88.3(14).

5.2.6 The dehydropolymerisation of methyl amine-borane with Rh(*i*Pr-PN^{H}P)(NBD)][Cl] (1) under argon

112 mg (2.5 mmol) of recrystallised methyl amine-borane and 6.7 mg (0.0125 mmol, 0.5 mol%) of Rh(*i*Pr-PN^{H}P)(NBD)][Cl] (**1**) were weighed into a jacketed Schlenk under argon, which was then temperature equilibrated to 20 °C and connected to an upturned water-filled burette to collect the produced H_2 gas. To initiate catalysis, 2.5 cm^3 of THF was added to the amine-borane and precatalyst (resulting in a concentration of 1 mol dm^{-3} of methyl amine-borane), which was then stirred at 400 rpm. After an induction period (typically ~ 1500 s), the yellow reaction mixture turned rapidly colourless and H_2 gas was evolved. The volume of evolved H_2 was recorded by the burette. Upon completion of H_2 evolution, an *in-situ* NMR sample was taken and analysed by ^{1}H, $^{31}P\{^{1}H\}$ and ^{11}B NMR spectroscopies. The catalysis mixture was then quenched in-air by the addition of ~ 50 cm^3 of pentane, resulting in the precipitation of white poly(*N*-methylaminoborane). The polymer was isolated by filtration and dried in-vacuo to give a white solid, 0.076 g (68% recovered yield), > 99% conversion and selectivity observed by in-situ ^{11}B NMR spectroscopy. This poly(*N*-methylaminoborane) was then analysed by GPC (M_n = 25,600 g mol^{-1}, dispersity = 1.7).

5.2.7 The dehydropolymerisation of methyl amine-borane with Rh(*i*Pr-PN^{H}P)(NBD)][Cl] (1) in air

112 mg (2.5 mmol) of recrystallised methyl amine-borane and 6.7 mg (0.0125 mmol, 0.5 mol%) of Rh(*i*Pr-PN^{H}P)(NBD)][Cl] (**1**) were weighed into a jacketed Schlenk under argon, which was then evacuated and refilled with air. The jacketed Schlenk was then temperature equilibrated to 20 ˚C and connected to an upturned water-filled burette to collect the produced H_2 gas. To initiate catalysis, 2.5 cm^3 of THF was added to the amine-borane and precatalyst (resulting in a concentration of 1 mol dm^{-3} of methyl amine-borane), which was then stirred at 400 rpm. After an induction period (typically ~ 100 s), the yellow reaction mixture turned rapidly colourless and H_2 gas was evolved. The volume of evolved H_2 was recorded by the burette. Upon completion of H_2 evolution, an *in-situ* NMR sample was taken and analysed by ^{1}H, $^{31}P\{^{1}H\}$ and ^{11}B NMR spectroscopies. The catalysis mixture was then quenched in-air by the addition of ~ 50 cm^3 of pentane, resulting in the precipitation of white poly(*N*-methylaminoborane). The polymer was isolated by filtration and dried in-vacuo to give a white solid, 0.069 g (63% recovered yield), > 99% conversion and 94% selectivity observed by in-situ ^{11}B NMR spectroscopy. This poly(*N*-methylaminoborane) was then analysed by GPC (M_n = 81,000 g mol^{-1}, dispersity = 1.7).

5.2.8 The attempted dehdyropolymerisation of *n*-propyl amine-borane with Rh(*i*Pr-PN^{H}P)(NBD)][Cl] (1)

182 mg (2.5 mmol) of recrystallised *n*-propyl amine-borane and 6.7 mg (0.0125 mmol, 0.5 mol%) of Rh(*i*Pr-PN^{H}P)(NBD)][Cl] (**1**) were weighed into a jacketed Schlenk either under argon or air, which was then temperature equilibrated to 20 ˚C and connected to an upturned water-filled burette to collect the produced H_2 gas. To initiate catalysis, 2.5 cm^3 of THF was added to the amine-borane and precatalyst (resulting in a concentration of 1 mol dm^{-3} of methyl amine-borane), which was then stirred at 400 rpm. The volume of evolved H_2 was recorded by the burette. Upon completion of H_2 evolution, an *in-situ* NMR sample was taken and analysed by ^{1}H, $^{31}P\{^{1}H\}$ and ^{11}B NMR spectroscopies. Incomplete dehydropolymerisation was observed by ^{11}B NMR spectroscopy when performed in-air (60% conversion to various dehydrocoupled products), no conversion was observed when performed under argon.

5.2.9 The dehdyropolymerisation of methyl, ethyl and *n*-propyl amine-borane with Rh(^{i}Pr-PN^{H}P)H$_2$Cl (2)

112, 0.147 or 0.182 mg (2.5 mmol) of recrystallised methyl, ethyl or *n*-propyl amine-borane respectively, and 11.1 mg (0.0125 mmol, 1 mol%) of Rh(^{i}Pr-PN^{H}P)H$_2$Cl (**2**) were weighed into a jacketed Schlenk under argon, which was then evacuated and refilled with air. The jacketed Schlenk was then temperature equilibrated to 20 °C and connected to an upturned water-filled burette to collect the produced H_2 gas. To initiate catalysis, 0.5 cm^3 of THF was added to the amine-borane and precatalyst (resulting in a concentration of 5 mol dm^{-3} of amine-borane), which was then stirred at 400 rpm. The volume of evolved H_2 was recorded by the burette. Upon completion of H_2 evolution, an *in-situ* NMR sample was taken and analysed by ^{1}H, ^{31}P{^{1}H} and ^{11}B NMR spectroscopies. The catalysis mixture was then quenched in-air by the addition of ~ 50 cm^3 of pentane, resulting in the precipitation of white poly(*N*-methylaminoborane), poly(*N*-ethylaminoborane) or poly(*N*-*n*-propylaminoborane). The polymer was isolated by filtration and dried in-vacuo to give off-white solids: poly(*N*-methylaminoborane) 0.095 g, 86 % yield; poly(*N*-ethylaminoborane) 0.073 g, 50% yield; poly(*N*-*n*-propylaminoborane) 0.085 g, 45% yield. The polymers were then analysed by GPC: poly(*N*-methylaminoborane) M_n = 33,500 g mol^{-1}, dispersity = 1.7; poly(*N*-ethylaminoborane) M_n = 62,400 g mol^{-1}, dispersity = 1.5; poly(*N*-*n*-propylaminoborane) M_n = 51,200 g mol^{-1}, dispersity = 1.5.

5.2.10 The dehdyropolymerisation of ethyl amine-borane with Rh(*i*Pr-PN^{H}P)H$_2$Cl (2), varying the solvent

0.147 mg (2.5 mmol) of recrystallised ethyl amine-borane, and 5.6 mg (0.0125 mmol, 0.5 mol%) of Rh(*i*Pr-PN^{H}P)H$_2$Cl (**2**) were weighed into a jacketed Schlenk under argon. The jacketed Schlenk was then temperature equilibrated to 20 °C and connected to an upturned water-filled burette to collect the produced H_2 gas. To initiate catalysis, 2.5 cm^3 of the chosen solvent (THF, 1,2-difluorobenzene or toluene) was added to the amine-borane and precatalyst (resulting in a concentration of 1 mol dm^{-3} of amine-borane), which was then stirred at 400 rpm. The volume of evolved H_2 was recorded by the burette. Upon completion of H_2 evolution, an *in-situ* NMR sample was taken and analysed by ^{1}H, ^{31}P{^{1}H} and ^{11}B NMR spectroscopies. As these experiments were performed to investigate how much of the catalyst was converted to poisoned species Rh(PN^{H}P*i*Pr)(κ^{1}-BH$_4$)H$_2$ (**4**), poly(*N*-ethylaminoborane) was often not formed and so the products were not analyzed by GPC. <5% conversion to **4** in toluene, 12% conversion to **4** in THF and 47% conversion to **4** in 1,2-difluorobenzene (as measured by ^{31}P{^{1}H} NMR integrals).

5.2.11 The dehydropolymerisation of ethyl amine-borane with Rh(^{i}Pr-PN^{H}P)H$_2$Cl (2), varying the reaction temperature

0.147 mg (2.5 mmol) of recrystallised ethyl amine-borane, and 5.6 mg (0.0125 mmol, 0.5 mol%) of Rh(^{i}Pr-PN^{H}P)H$_2$Cl (**2**) were weighed into a jacketed Schlenk under argon. The jacketed Schlenk was then temperature equilibrated to 0, 20 or 40 ˚C via a recirculating cooler and connected to an upturned water-filled burette to collect the produced H_2 gas. To initiate catalysis, 2.5 cm^3 of THF was added to the amine-borane and precatalyst (resulting in a concentration of 1 mol dm^{-3} of amine-borane), which was then stirred at 400 rpm. The volume of evolved H_2 was recorded by the burette. Upon completion of H_2 evolution, an *in-situ* NMR sample was taken and analysed by ^{1}H, ^{31}P{^{1}H} and ^{11}B NMR spectroscopies. As these experiments were performed to investigate how much of the ethyl amine-borane was converted at different temperatures, poly(*N*-ethylaminoborane) was not always formed (e.g. at 20 and 40 °C) and so the products were not analyzed by GPC. Conversion of the ethyl amine-borane was measured by ^{11}B NMR integrals at each temperature as follows: 82% at 0 °C; 6% at 20 °C; 5% at 40 °C.

5.2.12 The dehydropolymerisation of ethyl amine-borane with Rh(^{i}PrPN^{H}P)H_2Cl (2), varying the amine added

0.147 mg (2.5 mmol) of recrystallised ethyl amine-borane, and 5.6 mg (0.0125 mmol, 0.5 mol%) of Rh(^{i}Pr-PN^{H}P)H_2Cl (**2**) were weighed into a jacketed Schlenk under argon. The jacketed Schlenk was then temperature equilibrated to 20 °C and connected to an upturned water-filled burette to collect the produced H_2 gas. To initiate catalysis, 2.5 cm^3 of THF was added to the amine-borane and precatalyst (resulting in a concentration of 1 mol dm^{-3} of amine-borane), followed by 5 equivalents to catalyst (0.0625 mmol) of the chosen amine (9 µl of NEt_3 or 31 µl of 2 mol dm^{-3} NH_2Me in THF). The reaction mixture was then was then stirred at 400 rpm. The volume of evolved H_2 was recorded by the burette. Upon completion of H_2 evolution, an *in-situ* NMR sample was taken and analysed by ^{1}H, ^{31}P{^{1}H} and ^{11}B NMR spectroscopies. As these experiments were performed to investigate how much of the ethyl amine-borane was converted with different amines and additives, poly(*N*-ethylaminoborane) was not formed in significant quantities and so the products were not analyzed by GPC. Conversion of the ethyl amine-borane was measured by ^{11}B NMR integrals with each additive as follows: 0% at with no amine added; 13% with 5 Eq. of NH_2Me; 54% with 5 Eq. of NEt_3.

5.2.13 The attempted dehydropolymerisation of *n*-propyl amine-borane with Co(^{i}Pr-PN^{H}P)Cl$_2$ (5) & Co(Cy-PN^{H}P)Cl$_2$ (6)

0.182 mg (2.5 mmol) of recrystallised *n*-propyl amine-borane, and either Co(^{i}Pr-PN^{H}P)Cl$_2$ (**5**, 5.4 mg, 0.0125 mmol, 0.5 mol%) or Co(Cy-PN^{H}P)Cl$_2$ (**6**, 7.4 mg, 0.0125 mmol, 0.5 mol%), were weighed into a jacketed Schlenk under argon. The jacketed Schlenk was then temperature equilibrated to 20 °C and connected to an upturned water-filled burette to collect the produced H_2 gas. To initiate catalysis, 0.5 cm^3 of THF was added to the amine-borane and precatalyst (resulting in a concentration of 5 mol dm^{-3} of amine-borane), followed by 2 equivalents to catalyst of NH_2Me (13 µl of 2 mol dm^{-3} in THF). The reaction mixture was then was then stirred at 400 rpm. The volume of evolved H_2 was recorded by the burette. Upon completion of H_2 evolution, an *in-situ* NMR sample was taken and analysed by ^{1}H, ^{31}P{^{1}H} and ^{11}B NMR spectroscopies. The catalysis mixtures were then quenched in-air by the addition of ~ 50 cm^3 of pentane, resulting in the precipitation of grey poly(*N*-methylaminoborane) when Co(PN^{H}PCy)Cl$_2$ (**6**) was used, likely contaminated with metallic cobalt from catalyst decomposition. The polymer was isolated by filtration and dried in-vacuo to give a grey solid, 0.031 g (18% recovered yield), 48% conversion and 95% selectivity observed by in-situ ^{11}B NMR spectroscopy. This poly(*N*-methylaminoborane) was then analysed by GPC (M_n = 61,100 g mol^{-1}, dispersity = 1.4) (**Figure 193**).

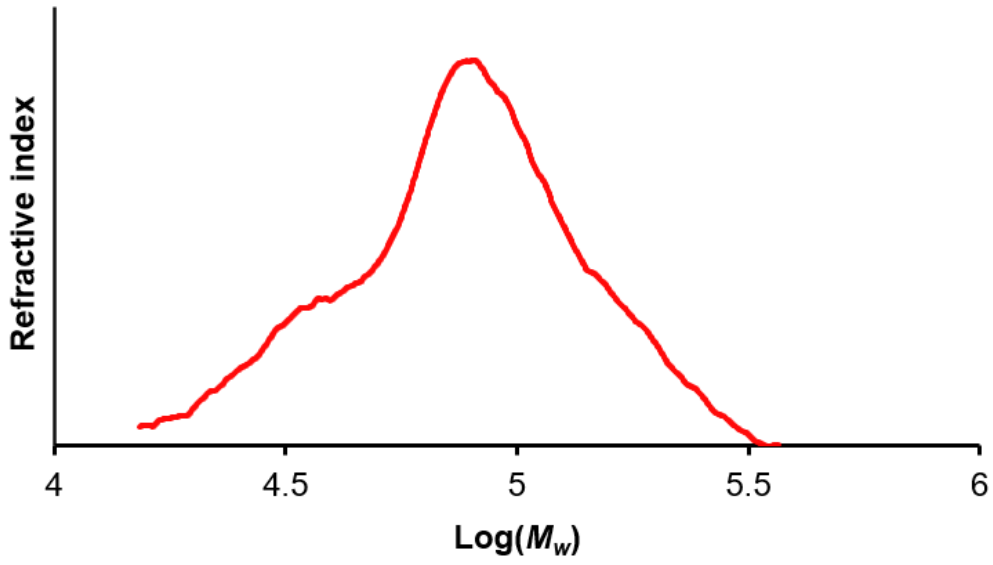

Figure 193. GPC trace of the polymer poly(*N*-*n*-propylaminoborane) from the dehydropolymerisation of $H_3B{\cdot}NH_2nPr$ (5 mol dm^{-3} in 0.5 cm^3 of THF) by Co(Cy-PN^{H}P)Cl$_2$ (6) (0.5 mol%) with 2 equivalents to catalyst of NH_2Me.

5.2.14 The attempted dehydropolymerisation of methyl amine-borane by Rh(PN^{H}PCy)H$_2$Cl (7)

112 mg (2.5 mmol) of recrystallised methyl amine-borane and 7.6 mg (0.0125 mmol, 0.5 mol%) of Rh(PN^{H}PCy)H$_2$Cl (**7**) were weighed into a jacketed Schlenk under argon. The jacketed Schlenk was then temperature equilibrated to 20 °C and connected to an upturned water-filled burette to collect the produced H_2 gas. To initiate catalysis, 2.5 cm^3 of THF was added to the amine-borane and precatalyst (resulting in a concentration of 1 mol dm^{-3} of methyl amine-borane), which was then stirred at 400 rpm. After an induction period (~ 800 s), H_2 gas was rapidly evolved. The volume of evolved H_2 was recorded by the burette. Upon completion of H_2 evolution, an *in-situ* NMR sample was taken and analysed by ^{1}H, ^{31}P{^{1}H} and ^{11}B NMR spectroscopies. Due to the ^{11}B NMR analysis showing incomplete conversion of the methyl amine-borane (80% by integrals) and the formation of cyclic oligomer (triplet at – 5 ppm) it was determined that Rh(PN^{H}PCy)H$_2$Cl (**7**) is an inferior dehydropolymerisation precatalyst when compared to Rh(PN^{H}P^{i}Pr)H$_2$Cl (**2**), and so the polymer formed was not analysed.

5.3 Chapter 3 and 4 experimental methods and data

^{t}BuOK was purchased from Sigma-Aldrich and sublimed (1x10^{-2} mbar, 80 °C) before use. $NaBH_4$ purchased from Sigma-Aldrich and used as supplied. Hexamethyldisilazane was dried over CaH_2 and vacuum distilled before use. ^{i}PrOH was dried over CaH_2, vacuum distilled and stored over 3 Å molecular sieves for 1 week before use, after which no residual water was observed by ^{1}H NMR spectroscopy. $^{i}Pr_2PCH_2CH_2NH_2$ and $[Ru(COD)Cl_2]_n$ were prepared by literature methods. [5, 6]

Some of the synthetic procedures relating to chapter 3 have been published: M. J. Cross, A. M. Sajjad, S. A. Macgregor, A. S. Weller, *Angew*. *Chem*., 2025, **64**, e202500019.

5.3.1 Synthesis and characterisation of *P,P-cis*-Ru(^{i}Pr$_2$PCH$_2$CH$_2$NH$_2$)$_2$Cl$_2$ (8)

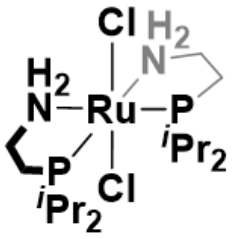

8

The synthesis of *P,P-cis*-Ru($^{i}Pr_2PCH_2CH_2NH_2)_2Cl_2$ (**8**) was adapted from the reported method. [5] 0.500 g (3.1 mmol) of $^{i}Pr_2PCH_2CH_2NH_2$ was dissolved in 6 cm^3 of toluene and added to 0.434 g (1.55 mmol) of $[Ru(COD)Cl_2]_n$ with stirring. The reaction was then heated in a sealed ampoule at 115 °C for 12 hours. The resulting orange reaction mixture was left to cool to room temperature, upon which orange crystals formed. 18 cm^3 of Et_2O was then added and the mixture was stirred for 1 hour. The resulting orange solid was then filtered off and dried *in-vacuo*. From this precipitate x-ray quality crystals for both the *P,P-cis* and *P,P-trans* isomers were obtained from manual separation by eye. **Figure 194** shows the structure, as determined by single crystal x-ray diffraction, of the previously unreported *P,P-trans* isomer. The structure of the *P,P-cis*-isomer has been reported. [5] The filtrate was reduced in volume by half *in-vacuo* and ~20 cm^3 of pentane was added to give an orange precipitate, which was filtered off, dried *in-vacuo* and combined with the previously collected solids. All of the solid

obtained was then re-dissolved in the minimum of boiling toluene (~8 cm^3) and heated with stirring in a sealed ampoule at 115 °C for 48 hours to convert all of the minor product *P,P-trans* into the major product *P,P-cis*, as monitored by $^{31}P\{^1H\}$ NMR (*P,P-trans* was typically present at ~ 20% by $^{31}P\{^1H\}$ NMR integrals). The reaction mixture was allowed to cool to room temperature before being further cooled to –20 °C. The orange solid formed was filtered off and dried *in-vacuo* to obtain the *P,P-cis*-Ru(^{i}Pr$_2$PCH$_2$CH$_2$NH$_2$)$_2$Cl$_2$ (**8**) product (0.550 g, 72% yield).

^1H, $^{31}P\{^1H\}$ NMR data for the cis isomer *P,P-cis*-Ru(^{i}Pr$_2$PCH$_2$CH$_2$NH$_2$)$_2$Cl$_2$ (**8**) matches that reported by Abdur-Rashid et al. [5]

P,P-trans-Ru(^{i}Pr$_2$PCH$_2$CH$_2$NH$_2$)$_2$Cl$_2$, (**8** trans-isomer), $^{31}P\{^1H\}$ NMR (600 MHz, THF-H_8) δ 50.8 ppm (s).

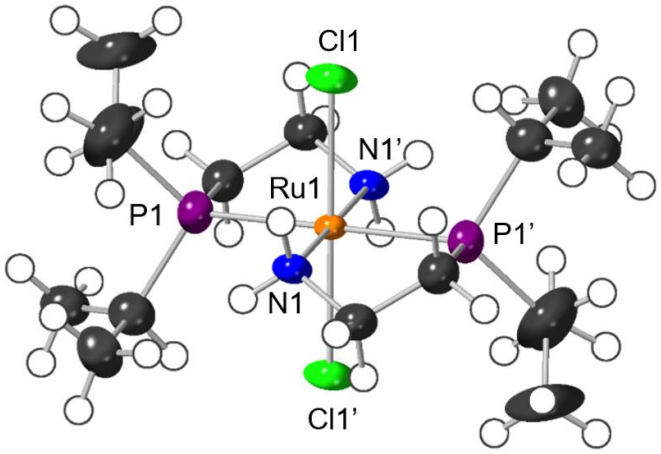

Figure 194. Molecular structure of minor product *P,P-trans*-Ru(^{i}Pr$_2$PCH$_2$CH$_2$NH$_2$)$_2$Cl$_2$ (**8** trans-isomer) as determined by single crystal X-ray diffraction. Displacement ellipsoids are shown at the 50% probability level. Hydrogen atoms are placed in calculated positions. Selected bond lengths [Å] and angles [°]: Ru(1) – N(1) 2.142(4), Ru(1) – N(1') 2.142(4), Ru(1) – P(1) 2.3288(17), Ru(1) – P(1') 2.3288 (17), C(1) – N(1) 1.477(7); P(1) – Ru(1) – N(1) 81.72(14), C(1) – N(1) – Ru(1) 114.7(4), Cl(1) – Ru(1) – Cl(1') 180.0(0), Cl(1) – Ru(1) – N(1) 90.91(13).

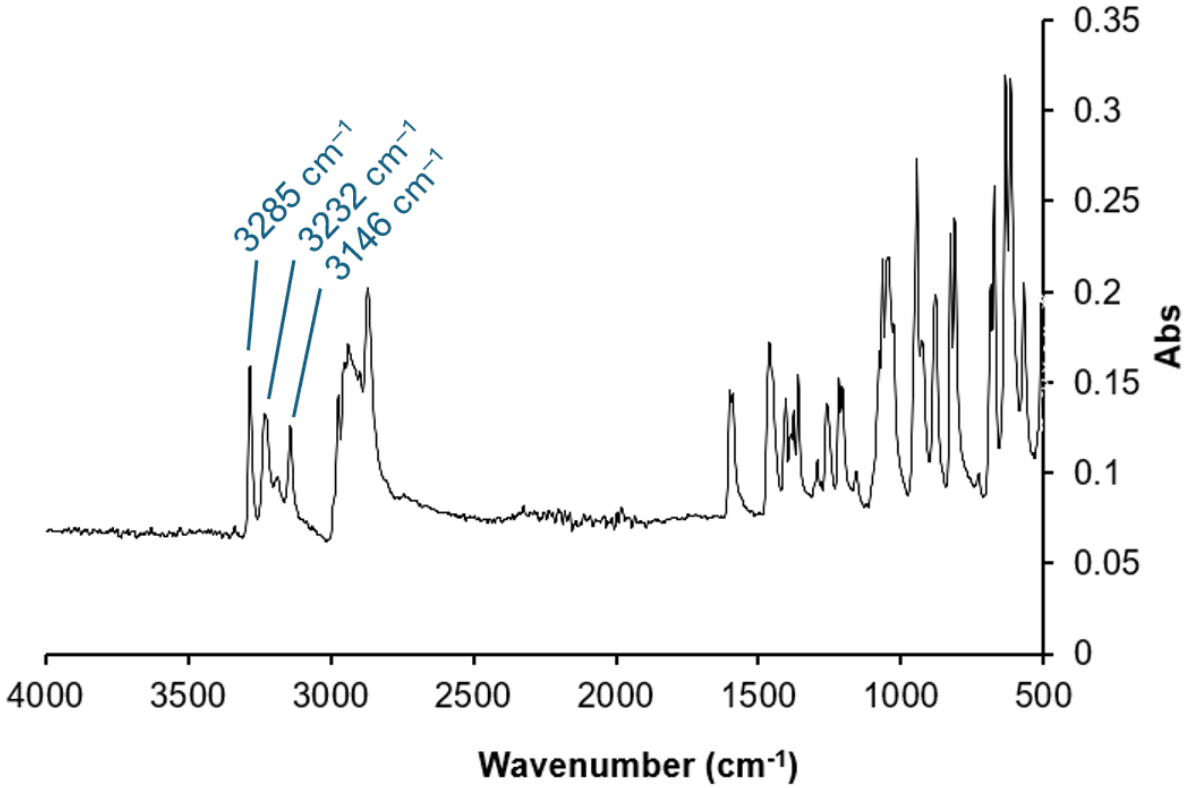

Figure 195. ATR IR spectrum recorded of *P,P-cis*-Ru(^{i}Pr$_2$PCH$_2$CH$_2$NH$_2$)$_2$Cl$_2$ (**8**). Ligand N–H stretches are observed between 3100 and 3200 cm^{-1}.

5.3.3 Synthesis and characterisation of *P,P-trans*-Ru(^{i}Pr$_2$PCH$_2$CH$_2$NH)$_2$ (9)

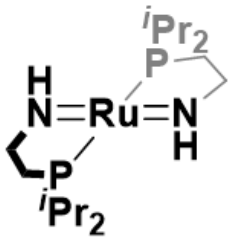

9

20 mg (0.04 mmol) of *P,P-cis*-Ru(^{i}Pr$_2$PCH$_2$CH$_2$NH$_2$)$_2$Cl$_2$ (**8**) and 9.1 mg (0.08mmol) of ^{t}BuOK were dissolved in 2 cm^3 of THF and stirred for 30 minutes. Over the course of 30 minutes the reaction colour turned from orange to deep pink and a small amount of white precipitate formed. The THF was then removed *in-vacuo* and 1 cm^3 of pentane was added. The resulting deep-red pentane solution was filtered off and cooled to –80 ºC. After 48 hours at –80 ºC deep-red, x-ray quality crystals, had formed. The mother liquor was removed via filtration at –80 ºC and the crystals were dried *in-vacuo* to obtain very air-sensitive *P,P-trans*-Ru(^{i}Pr$_2$PCH$_2$CH$_2$NH)$_2$ (**9**) product (3 mg, 18% yield). The conversion of *P,P-cis*-Ru(^{i}Pr$_2$PCH$_2$CH$_2$NH$_2$)$_2$Cl$_2$ (**8**) to *P,P-trans*-Ru(^{i}Pr$_2$PCH$_2$CH$_2$NH)$_2$ (**9**) was quantitative, as observed by ^{31}P{^{1}H} NMR of an in-situ aliquot of the THF reaction mixture analysed after 30 minutes of stirring. The low isolated yield obtained was due to the very high solubility of *P,P-trans*-Ru(^{i}Pr$_2$PCH$_2$CH$_2$NH)$_2$ (**9**) in pentane, and the pervasive and relatively fast decomposition by dimerization to **10**. Thus, isolated *P,P-trans*-Ru(^{i}Pr$_2$PCH$_2$CH$_2$NH)$_2$ (**9**) samples were used immediately once synthesised.

P,P-trans-Ru(^{i}Pr$_2$PCH$_2$CH$_2$NH)$_2$ (**9**) was dissolved in cyclohexane-d$_{12}$ for analysis by NMR spectroscopy, as it reacts with an CD$_2$Cl$_2$ to decompose to form unidentified products. Residual solvent peaks in THF-d$_8$ overlap with compound peaks hindering accurate integrals.

^{1}H NMR (600 MHz, cyclohexane-d$_{12}$) δ 5.95 (s, br, 2H, NH), 2.48 (apparent sept of apparent t J_{HH} = 7.0 Hz J_{HP} = 1.7 Hz, 4H, ^{i}Pr CH), 1.77 (m, 4H, CH$_2$), 1.58 (m, 4H, CH$_2$), 1.32 (dd, J_{HH} = 7.0 Hz, J_{HP} = 7.0 Hz, 12H, ^{i}Pr CH$_3$), 1.27 (dd, J_{HH} = 7.0 Hz, J_{HP} = 7.0 Hz, 12H, ^{i}Pr CH$_3$).

^{31}P{^{1}H} NMR (600 MHz, cyclohexane-d$_{12}$) δ 74.4 (s).

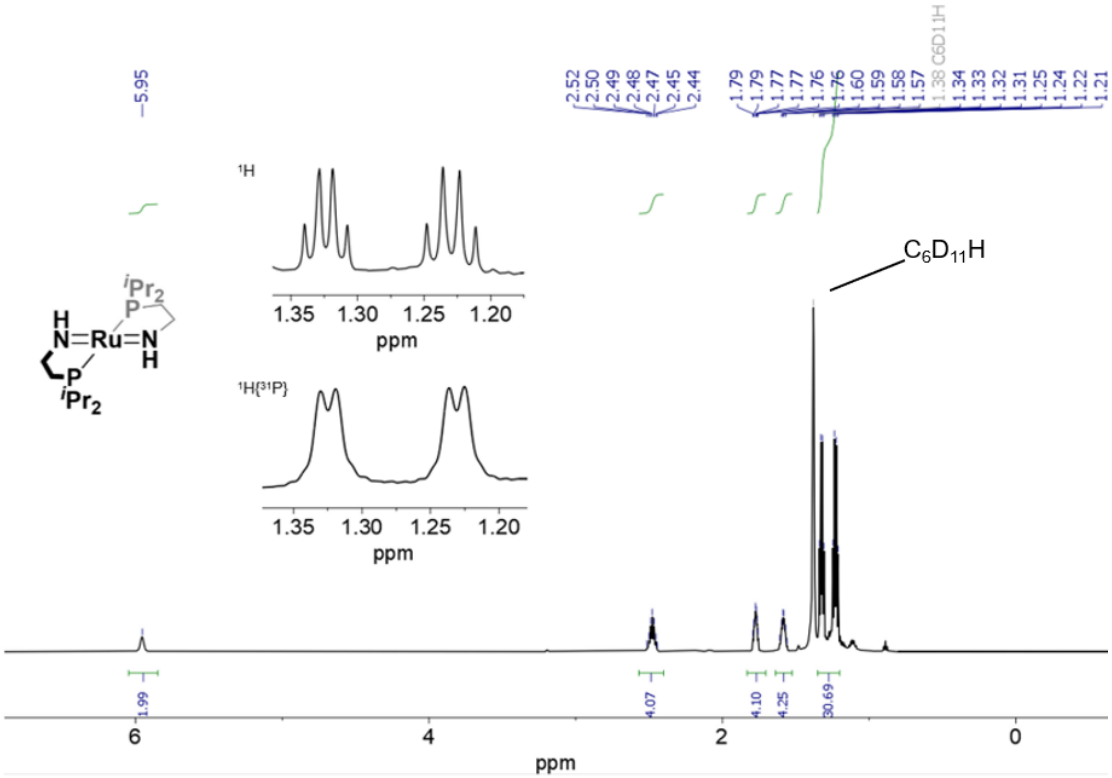

Figure 196. ^{1}H NMR spectrum of *P,P-trans*-Ru(^{i}Pr$_2$PCH$_2$CH$_2$NH)$_2$ (**9**) recorded 10 minutes after dissolution. Left inset showing ^{i}Pr CH$_3$ ^{1}H{^{31}P} and ^{1}H signals. dd collapse to d upon phosphorous decoupling. Recorded in cyclohexane-d$_{12}$ at 298 K. Right inset shows the ^{i}Pr CH sharpening to an apparent septet of apparent triplets when recorded in THF-d$_8$ at 298 K.

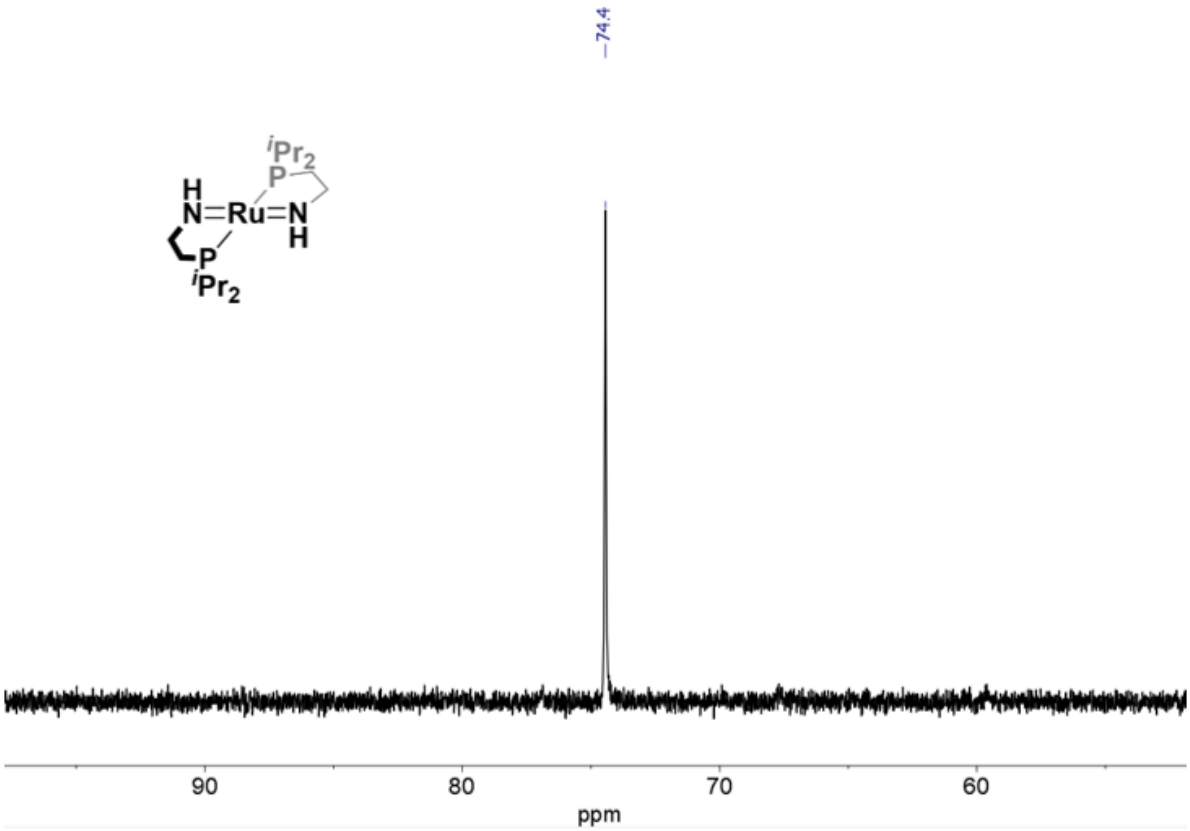

Figure 197. $^{31}P\{^{1}H\}$ NMR spectrum of *P,P-trans*-Ru($^{i}Pr_2PCH_2CH_2NH)_2$ (**9**). Recorded in cyclohexane-d_{12} at 298 K.

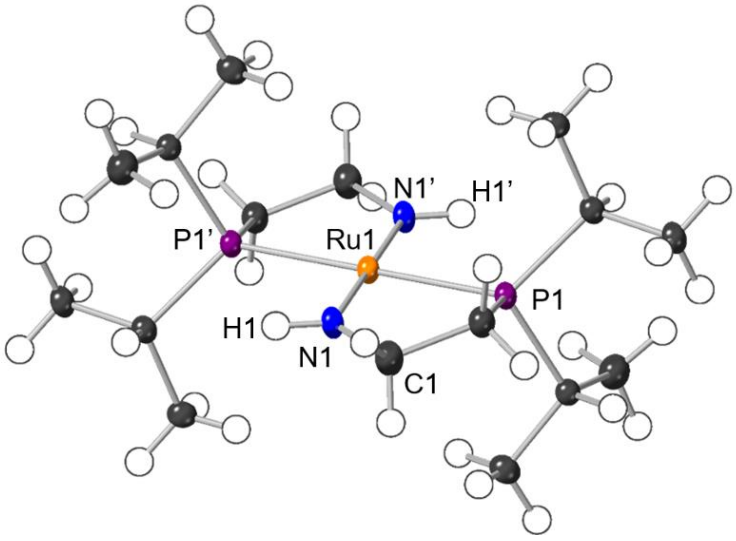

Figure 198. Molecular structure of *P,P-trans*-Ru($^{i}Pr_2PCH_2CH_2NH)_2$ (**9**) as determined by single crystal X-ray diffraction. Displacement ellipsoids are shown at the 50% probability level. Hydrogen atoms are placed in calculated positions apart from H1/H1' that was located in the final difference map. Selected bond lengths [Å] and angles [°]: Ru(1) – N(1) 1.931(2), Ru(1) – P(1) 2.2943(6), C(1) – N(1) 1.473(3); P(1) – N(1) – Ru(1) 82.45(7), P(1^{1}) – Ru(1) – N(1) 97.55(7), N(1) – Ru(1) – N(1^{1}) 180.0, P(1) – Ru(1) – P(1^{1}) 180.00(3), C(1) – N(1) – Ru(1) 127.67(18).

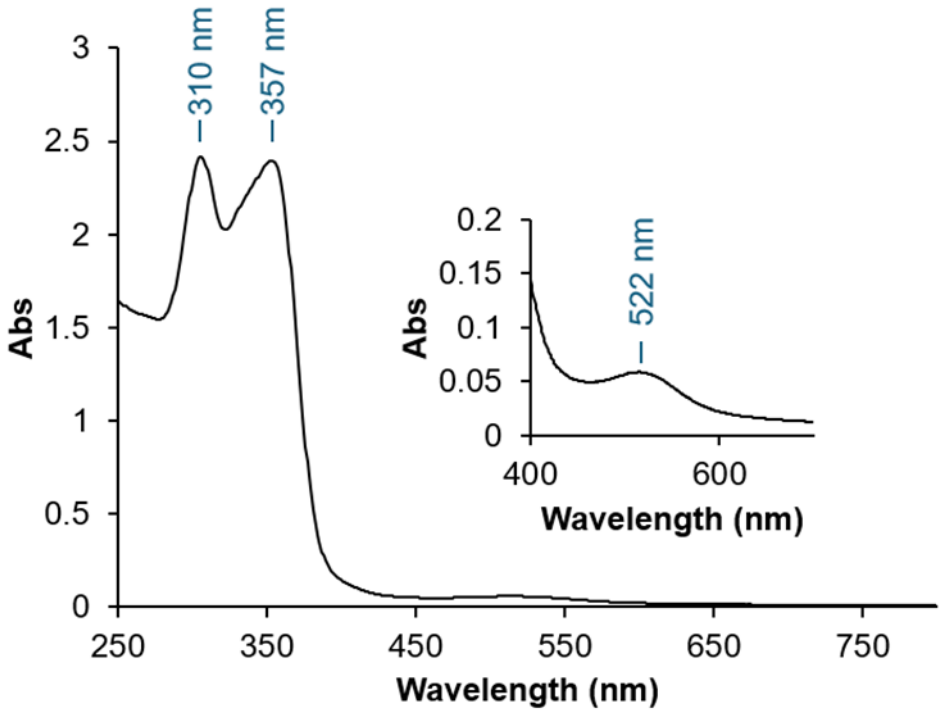

Figure 199. UV-Vis spectrum of *P,P-trans*-Ru(^{i}Pr$_2$PCH$_2$CH$_2$NH)$_2$ (**9**), recorded at 1x10^{-4} mol dm^{-3} in THF at 298 K, 1 cm pathlength in a sealed J. Youngs UV cuvette. Inset shows a broad absorbance at 522 nm (ε = 579 mol dm^{-3} cm^{-1}), likely corresponding to a d–d transition. Sharp, strong absorbances at 310 and 357 nm (ε = 23620 and 23680 mol dm^{-3} cm^{-1} respectively) likely correspond to ligand-metal charge transfer bands.

5.3.4 Synthesis and characterisation of Ru(^{i}Pr$_2$PCH$_2$CH$_2$NH)$_2$ dimer Ru$_2$H(μ$_2$,κ^1-NHCH$_2$CH$_2$P^{i}Pr$_2$)$_2$(μ$_2$,κ^1-NCH$_2$CH$_2$P^{i}Pr$_2$)(κ^2-^{i}Pr$_2$PCH$_2$CH$_2$NH$_2$) (10)

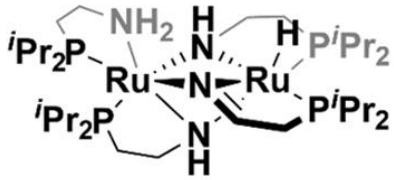

10

100 mg (0.20 mmol) of *P,P-cis*-Ru(^{i}Pr$_2$PCH$_2$CH$_2$NH$_2$)$_2$Cl$_2$ (**8**) and 45.5 mg (0.40 mmol) of ^{t}BuOK were dissolved in 5 cm^3 of THF and stirred for 1 hour at room temperature (293 K), forming *P,P-trans*-Ru(^{i}Pr$_2$PCH$_2$CH$_2$NH)$_2$ (**9**), as measured by ^{31}P(^{1}H) NMR spectroscopy. The resulting pink mixture was filtered, and the filtrate evaporated to dryness *in-vacuo*. The solids were dissolved in 0.5 cm^3 of pentane to give a pink solution which was left to stand at room temperature for 1 week, after which the solution had turned light-brown. The solution was then cooled to –80 ºC to give pale-yellow coloured x-ray quality crystals of the product (25 mg, 29% yield). Quantitative conversion of *P,P-trans*-Ru(^{i}Pr$_2$PCH$_2$CH$_2$NH)$_2$ (**9**) to Ru$_2$H(μ$_2$-NHCH$_2$CH$_2$P^{i}Pr$_2$)$_2$(μ$_2$-NCH$_2$CH$_2$P^{i}Pr$_2$)(^{i}Pr$_2$PCH$_2$CH$_2$NH$_2$) (**10**) is observed by ^{31}P{^{1}H} NMR spectroscopic analysis of the pentane solution after standing for 1 week. The low yield obtained was due to the very high solubility of very air-sensitive Ru$_2$H(μ$_2$-NHCH$_2$CH$_2$P^{i}Pr$_2$)$_2$(μ$_2$-NCH$_2$CH$_2$P^{i}Pr$_2$)(^{i}Pr$_2$PCH$_2$CH$_2$NH$_2$) (**10**) in pentane.

^{1}H NMR (600 MHz, cyclohexane-d$_{12}$) 7.73 (ddd, J_{HP} = 35.8 Hz, J_{HH} = 8.5, 4.9 Hz, 1H, N=C*H*), 3.92 (m, 1H, N=CC*H*$_2$), 3.52 (m, 1H, N=CC*H*$_2$), 2.82-0.72 (multiple overlapping CH$_2$ backbone, ^{i}Pr CH and CH$_3$ resonances), –11.56 (dddd, J_{HP} = 12 Hz, J_{HP} = 15 Hz, J_{HP} = 36 Hz, J_{HP} = 61 Hz , 1H, RuH)

^{1}H NMR (600 MHz, benzene-d$_6$) 8.05 (ddd, J_{HP} = 35.8 Hz, J_{HH} = 8.5, 4.9 Hz, 1H, N=C*H*), 3.91 (m, 1H, N=CC*H*$_2$), 3.51 (m, 1H, N=CC*H*$_2$), 2.70-0.50 (multiple overlapping CH$_2$ backbone, ^{i}Pr CH and CH$_3$ resonances), –11.52 (dddd, J_{HP} = 12 Hz, J_{HP} = 15 Hz, J_{HP} = 36 Hz, J_{HP} = 61 Hz , 1H, RuH)

^{31}P{^{1}H} NMR (600 MHz, benzene-d$_6$) δ 77.1 (d, J_{PP} = 22.3 Hz, 1P), 74.6 (m, 1P), 68.1 (dd, J_{PP} = 54.3 Hz, 25.3 Hz, 1P), 60.2 (dd, J_{PP} = 26.0 Hz, 16.5 Hz, 1P).

$^{31}P\{^{1}H\}$ NMR (600 MHz, cyclohexane-d_{12}) δ 77.5 (d, J_{PP} = 22.3 Hz, 1P), 75.1 (m, 1P), 68.3 (dd, J_{PP} = 54.3 Hz, 25.3 Hz, 1P), 60.3 (dd, J_{PP} = 26.0 Hz, 16.5 Hz, 1P)

Mass spectrum (ESI+) expected: 844.31 observed: 845.42, $[M+H]^+$.

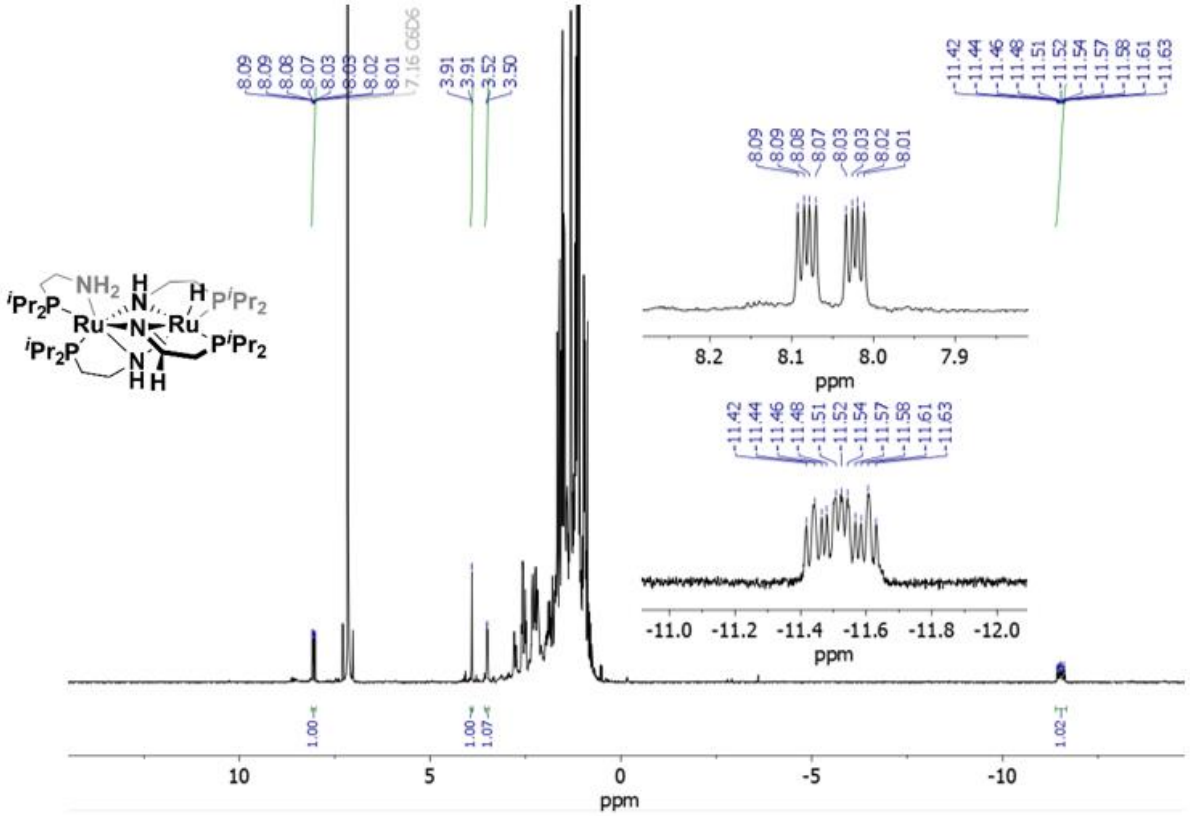

Figure 200. ^{1}H NMR spectrum of $Ru_2H(\mu_2\text{-}NHCH_2CH_2P^iPr_2)_2(\mu_2\text{-}NCH_2CH_2P^iPr_2)(^iPr_2PCH_2CH_2NH_2)$ (**10**), highlighting the hydride peak at –11.52 ppm (dddd with couplings J_{HP} = 12 Hz, J_{HP} = 15 Hz, J_{HP} = 36 Hz, J_{HP} = 61 Hz) and the imine alpha proton at 8.05 ppm. Recorded in benzene-d_6 at 298 K.

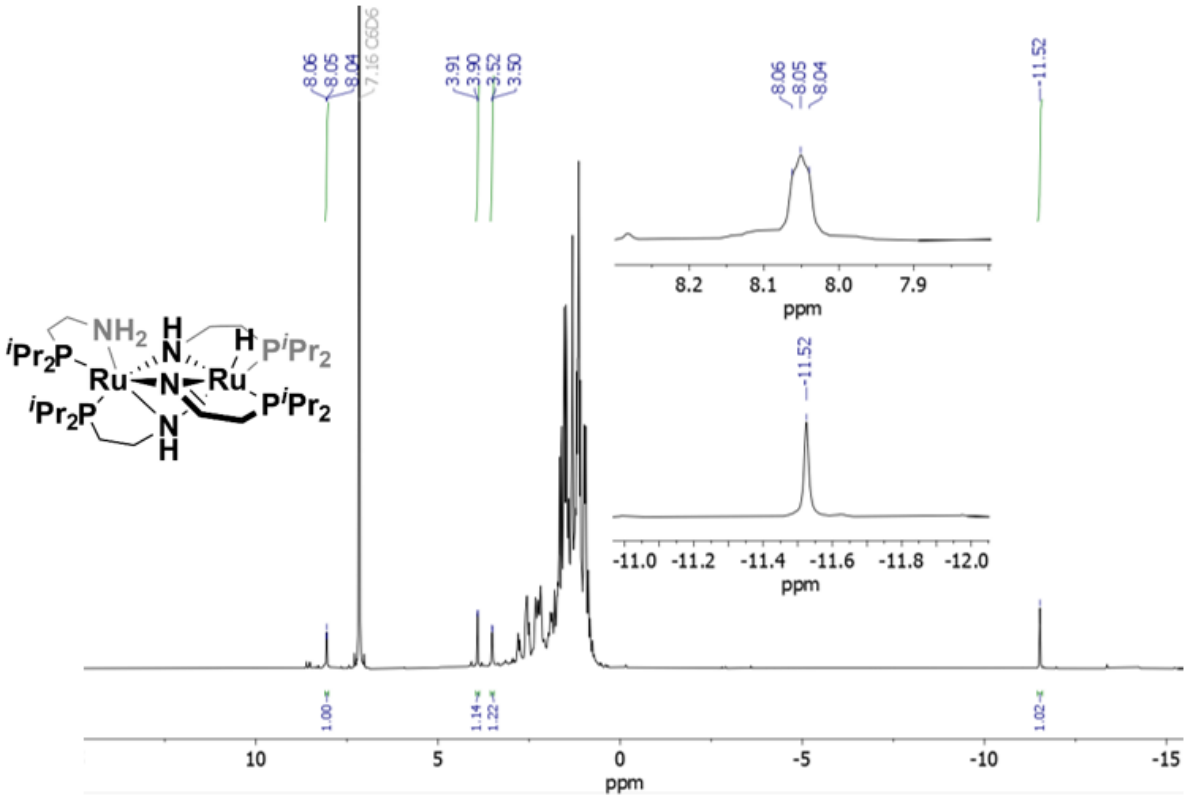

Figure 201. $^{1}H\{^{31}P\}$ NMR spectrum of $Ru_2H(\mu_2\text{-}NHCH_2CH_2P^iPr_2)_2(\mu_2\text{-}NCH_2CH_2P^iPr_2)(^iPr_2PCH_2CH_2NH_2)$ (**10**), highlighting the hydride peak at –11.52 ppm collapsed to a singlet, and the imine alpha proton at 8.05 ppm collapsed to a dd. Recorded in benzene-d_6 at 298 K.

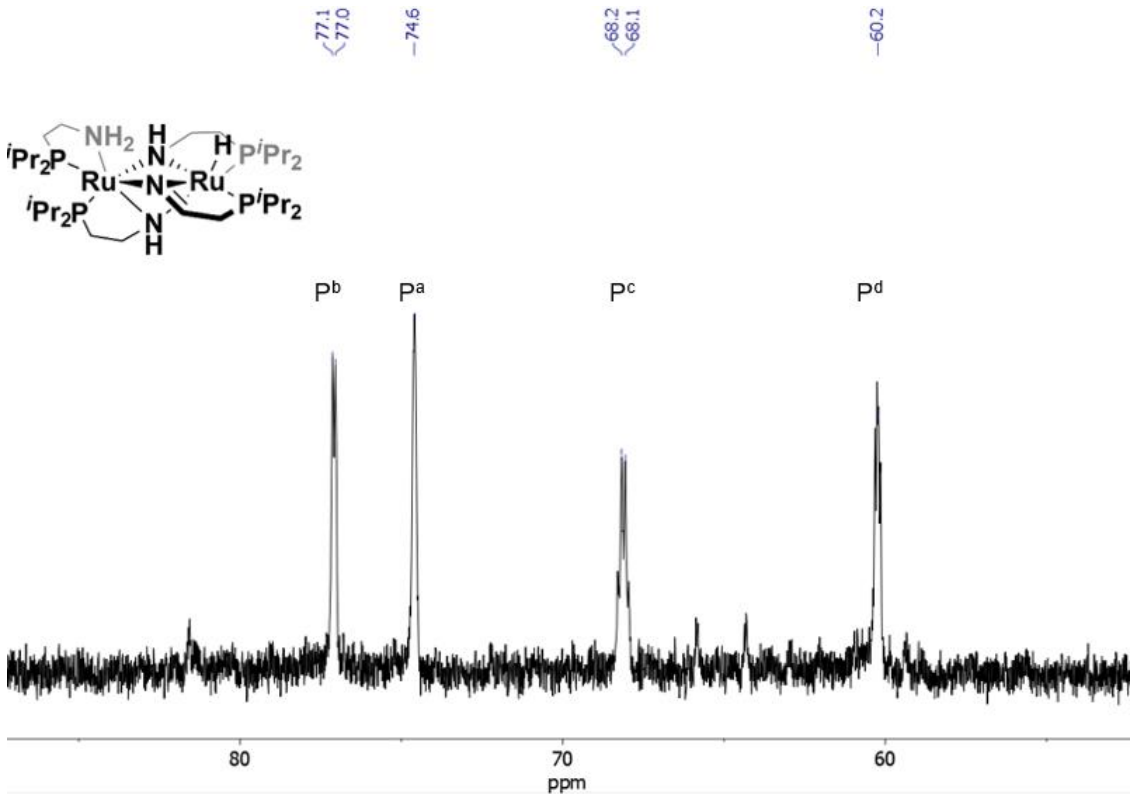

Figure 202. $^{31}P\{^{1}H\}$ NMR spectrum of $Ru_2H(\mu_2\text{-}NHCH_2CH_2P^iPr_2)_2(\mu_2\text{-}NCH_2CH_2P^iPr_2)(^iPr_2PCH_2CH_2NH_2)$ (**10**) showing 4 phosphorous environments. Recorded in benzene-d_6 at 298 K.

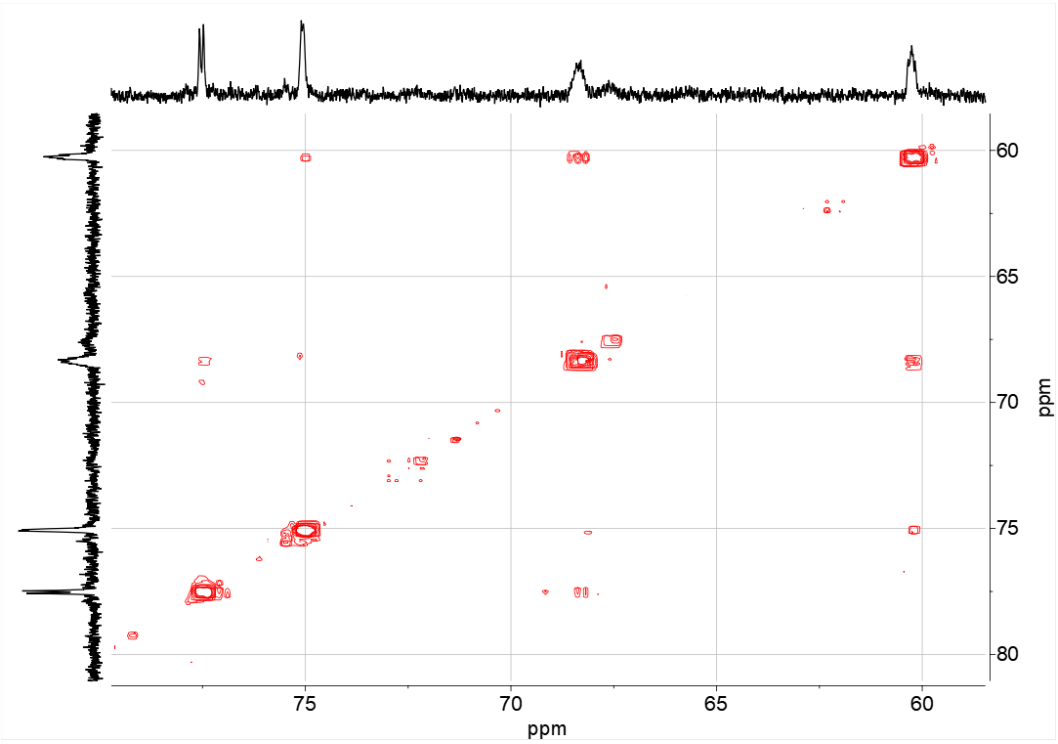

Figure 203. $^{31}P\text{-}^{31}P$ COSY 2D NMR spectrum of $Ru_2H(\mu_2\text{-}NHCH_2CH_2P^iPr_2)_2(\mu_2\text{-}NCH_2CH_2P^iPr_2)(^iPr_2PCH_2CH_2NH_2)$ (**10**) showing varied coupling between phosphorous environments. Recorded in Cyclohexane-d_{12} at 298 K.

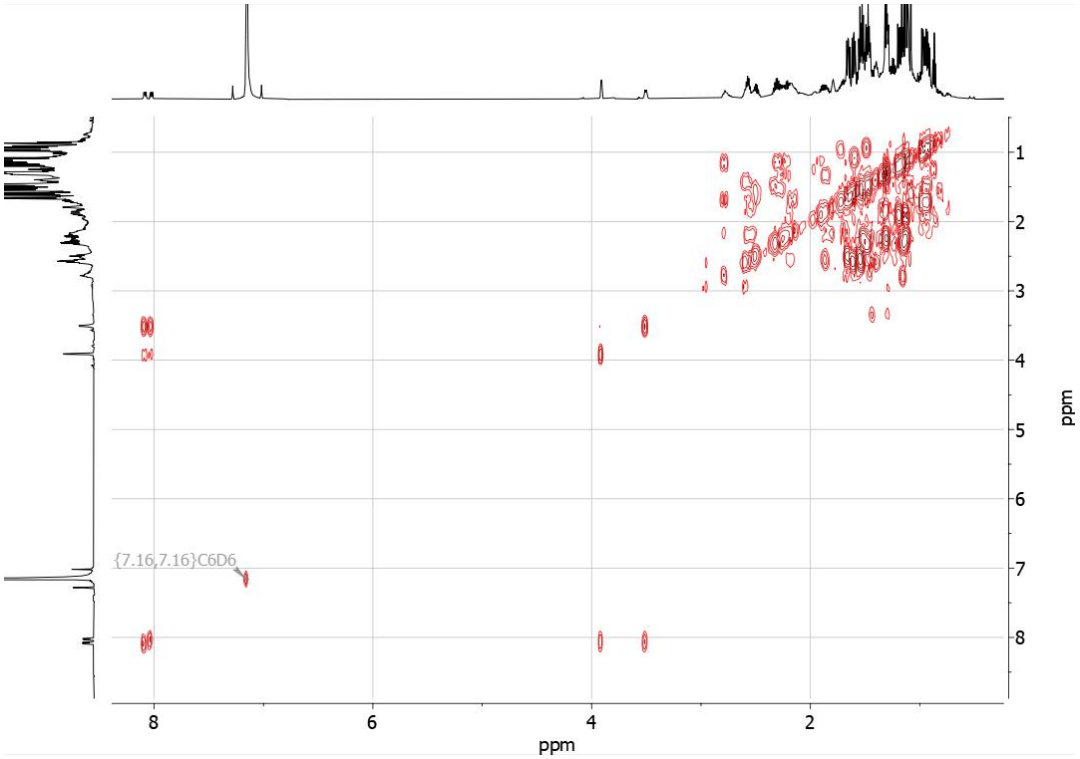

Figure 204. ^{1}H-^{1}H COSY 2D NMR spectrum of $Ru_2H(\mu_2\text{-}NHCH_2CH_2P^iPr_2)_2(\mu_2\text{-}NCH_2CH_2P^iPr_2)(^iPr_2PCH_2CH_2NH_2)$ (**10**). Recorded in benzene-d_6 at 298 K.

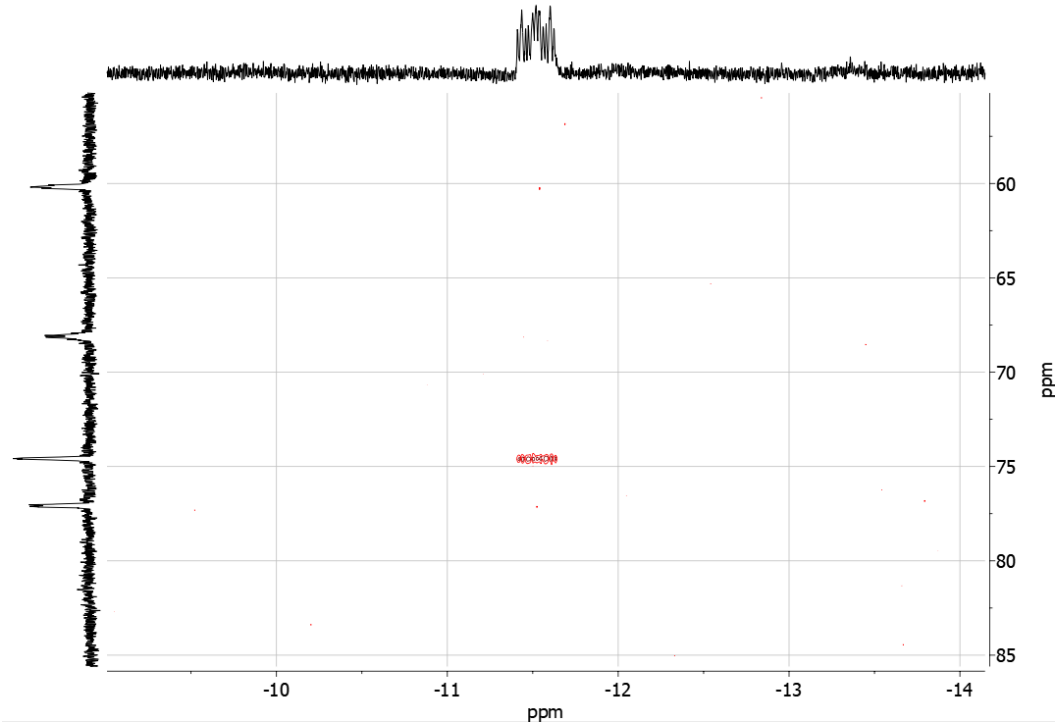

Figure 205. ^{1}H-^{31}P HMBC 2D NMR spectrum of the $Ru_2H(\mu_2\text{-}NHCH_2CH_2P^iPr_2)_2(\mu_2\text{-}NCH_2CH_2P^iPr_2)(^iPr_2PCH_2CH_2NH_2)$ (**10**) hydride showing coupling to 1 phosphorous environment. CNST13 = 5 Hz. Recorded in benzene-d_6 at 298 K.

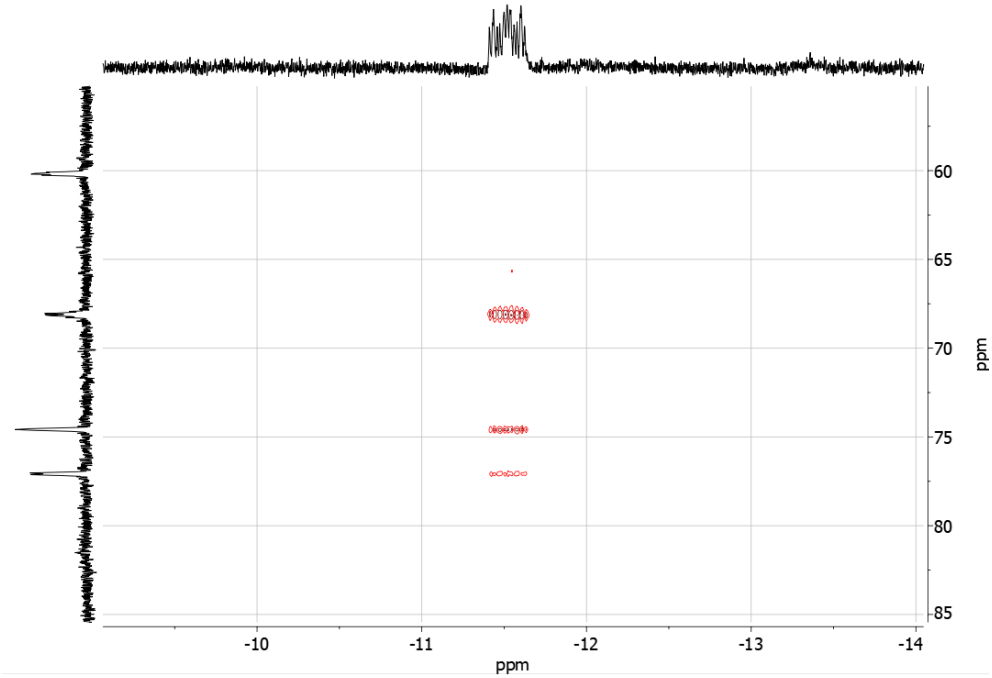

Figure 206. ^{1}H-^{31}P HMBC 2D NMR spectrum of the $Ru_2H(\mu_2\text{-}NHCH_2CH_2P^iPr_2)_2(\mu_2\text{-}NCH_2CH_2P^iPr_2)(^iPr_2PCH_2CH_2NH_2)$ (**10**) hydride showing coupling to 3 phosphorous environments. CNST13 = 30 Hz. Recorded in benzene-d_6 at 298 K.

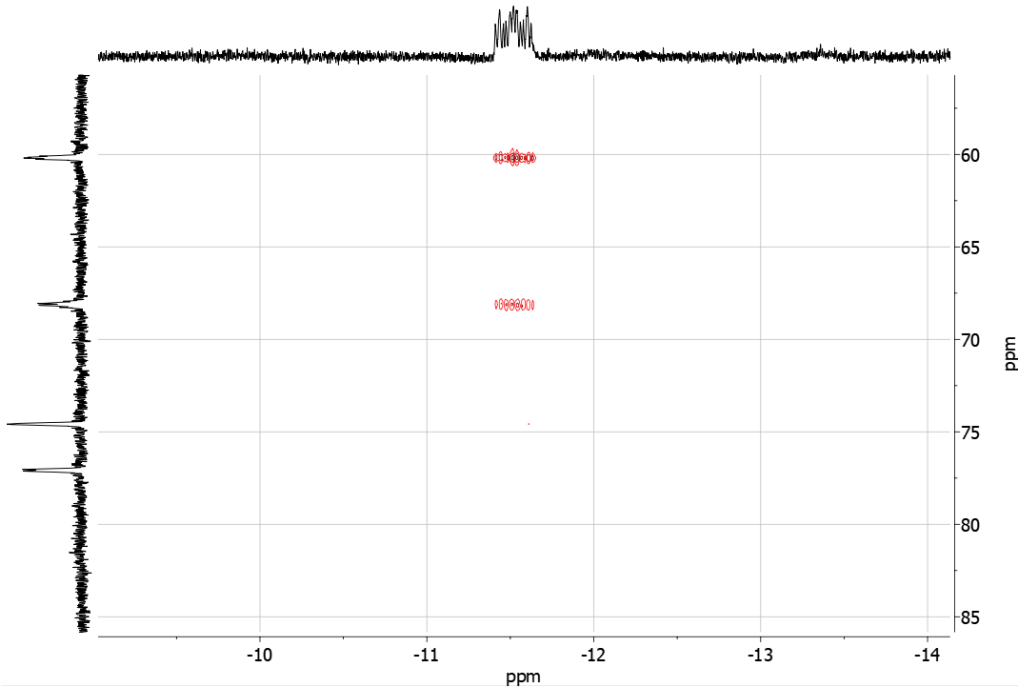

Figure 207. ^{1}H-^{31}P HMBC 2D NMR spectrum of the $Ru_2H(\mu_2\text{-}NHCH_2CH_2P^iPr_2)_2(\mu_2\text{-}NCH_2CH_2P^iPr_2)(^iPr_2PCH_2CH_2NH_2)$ (**10**) hydride showing coupling to 2 phosphorous environments. CNST13 = 50 Hz. Recorded in benzene-d_6 at 298 K.

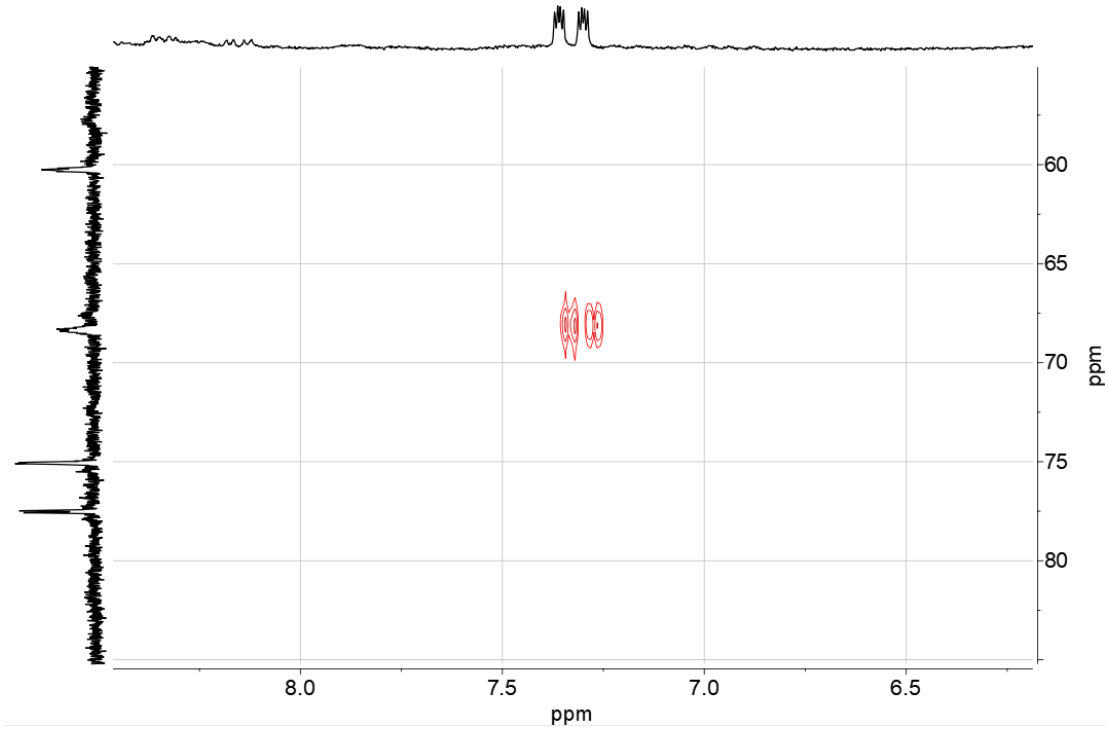

Figure 208. ^{1}H-^{31}P HMBC 2D NMR spectrum of the $Ru_2H(\mu_2\text{-}NHCH_2CH_2P^iPr_2)_2(\mu_2\text{-}NCH_2CH_2P^iPr_2)(^iPr_2PCH_2CH_2NH_2)$ (**10**) N=CH. CNST13 = 36 Hz. Recorded in cyclohexane-d_{12} at 298 K.

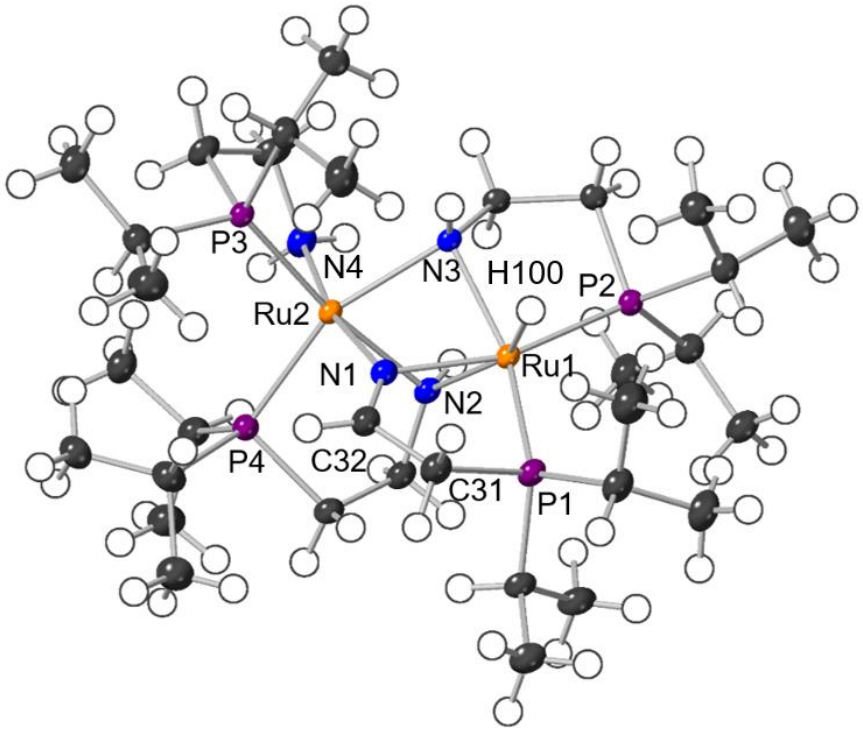

Figure 209. Molecular structure of $Ru_2H(\mu_2\text{-}NHCH_2CH_2P^iPr_2)_2(\mu_2\text{-}NCH_2CH_2P^iPr_2)(^iPr_2PCH_2CH_2NH_2)$ (**10**) as determined by single crystal X-ray diffraction. Displacement ellipsoids are shown at the 50% probability level. Hydrogen atoms are placed in calculated positions. Selected bond lengths [Å] and angles [°]: N(1) – C(32) 1.263(3), Ru(1) – N(2) 2.059(2), Ru(2) – N(2) 2.159(2), Ru(1) – N(3) 2.159(2), Ru(2) – N(3) 2.178(2), Ru(2) – N(4) 2.178(2), Ru(1) – N(1) 2.059(2), Ru(1) ··· Ru(2) 3.004, C(31) – C(32) – N(4) 120.0(2).

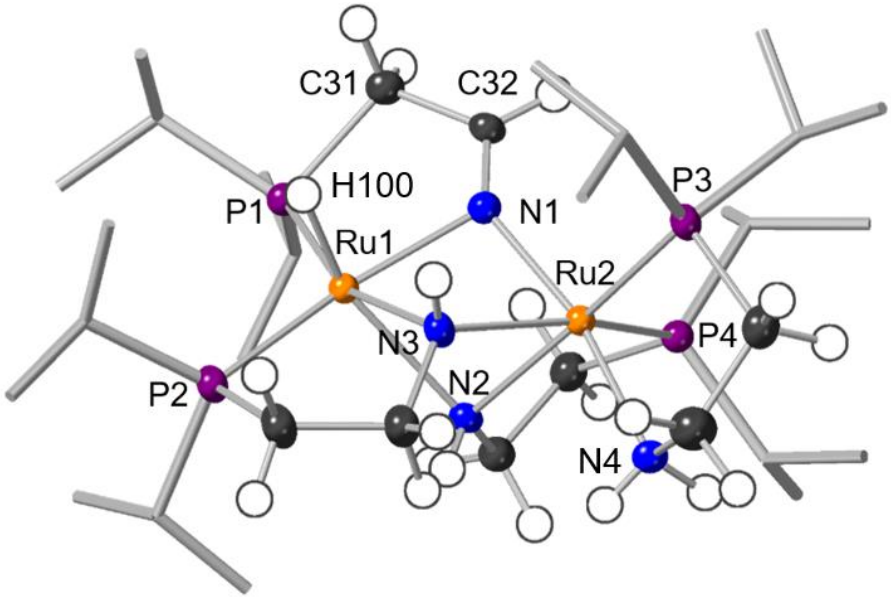

Figure 210. Alternative view of the molecular structure of $Ru_2H(\mu_2\text{-}NHCH_2CH_2P^iPr_2)_2(\mu_2\text{-}NCH_2CH_2P^iPr_2)(^iPr_2PCH_2CH_2NH_2)$ (**10**) as determined by single crystal X-ray diffraction with the ^{i}Pr groups simplified for clarity. Displacement ellipsoids are shown at the 50% probability level.

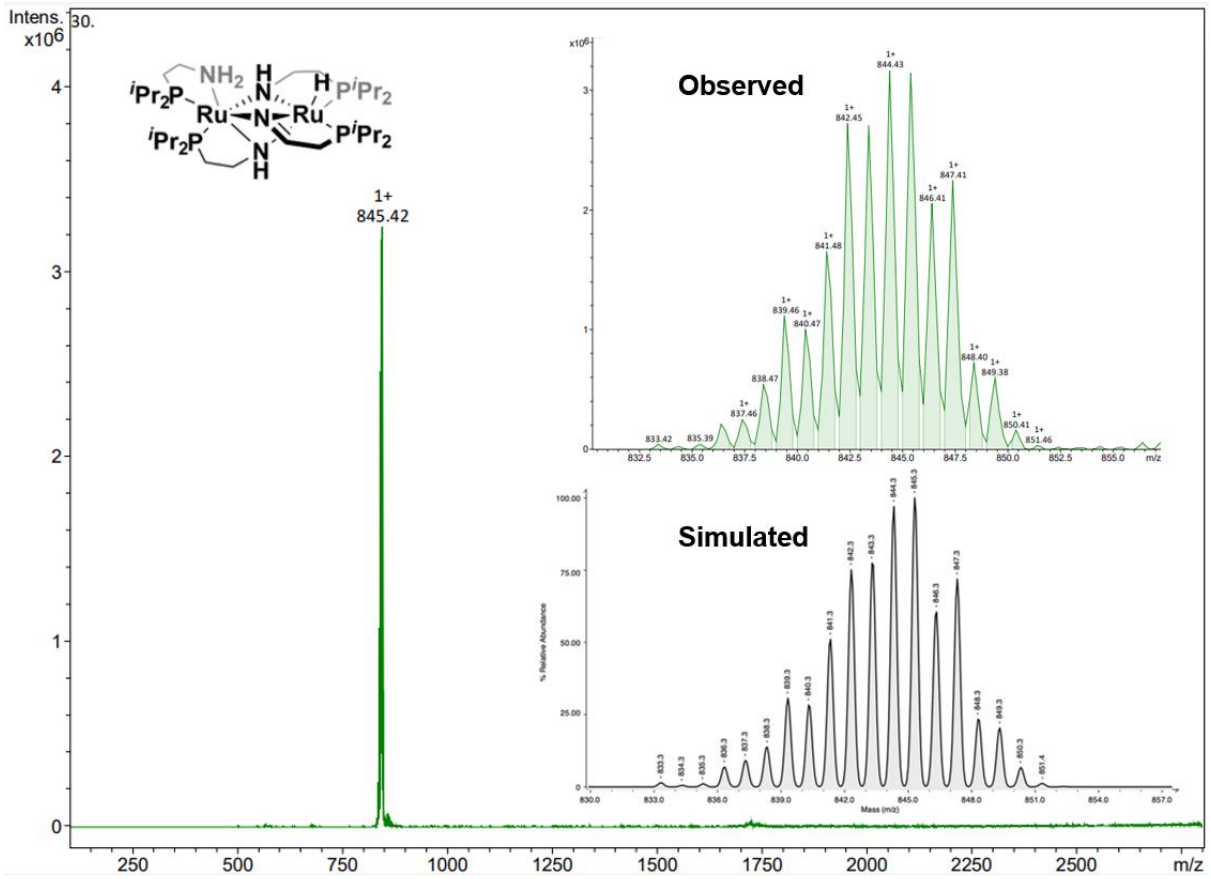

Figure 211. ESI+ mass spectrum of $Ru_2H(\mu_2\text{-}NHCH_2CH_2P^iPr_2)_2(\mu_2\text{-}NCH_2CH_2P^iPr_2)(^iPr_2PCH_2CH_2NH_2)$ (**10**) showing the molecular ion $[M+H]^+$ at m/z = 845.42. Recorded in THF. Inset shows an expanded view of the observed molecular ion and the simulated isotope pattern, showing a good fit.

5.3.5 Synthesis and characterisation of *P,P-cis*-Ru(^{i}Pr$_2$PCH$_2$CH$_2$NH$_2$)$_2$(OH)H (11)

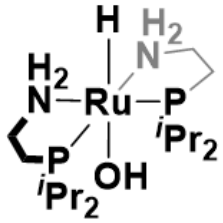

11

20 mg (0.04 mmol) of *P,P-cis*-Ru(^{i}Pr$_2$PCH$_2$CH$_2$NH$_2$)$_2$Cl$_2$ (**8**) and 9 mg (0.08 mmol) of ^{t}BuOK were dissolved in 2 cm^3 of THF, 16 µl of ^{i}PrOH (20 mmol) was added and the mixture was stirred for 1 hour, during which the solution changed colour from pink to yellow. Quantitative conversion to *P,P-cis*-Ru(^{i}Pr$_2$PCH$_2$CH$_2$NH$_2$)$_2$(OH)H (**11**) is observed by ^{31}P{^{1}H} NMR. After 1 hour the THF solvent was removed under an argon flow, as decomposition is observed when exposed to vacuum as seen by a large number of phosphorous environments in the ^{31}P{^{1}H} NMR spectrum. 0.5 cm^3 of pentane was added to the remaining solids and the solution was filtered. The yellow filtrate was then cooled to –80 ºC to give yellow coloured x-ray quality crystals of *P,P-cis*-Ru(^{i}Pr$_2$PCH$_2$CH$_2$NH$_2$)$_2$(OH)H·(^{i}PrOH)$_2$ (**11**·(^{i}PrOH)$_2$) which were pure material as measured by solution NMR spectroscopy (3 mg, 17%). The low yield obtained was due to the very high solubility in pentane, 100% conversion observed by ^{31}P{^{1}H} NMR. Whilst at –80 ºC the mother liqueur was separated from the crystals and kept at –80 ºC for 48 hours, upon which x-ray quality crystals of solvent-free *P,P-cis*-Ru(^{i}Pr$_2$PCH$_2$CH$_2$NH$_2$)$_2$(OH)H (**11**) were obtained as a mixture with the ^{i}PrOH solvate (NMR spectroscopy). Crystals suitable for analysis by single crystal X-ray diffraction were selected by eye from this mixture. Bulk samples such as those analysed by NMR and IR spectroscopies can be observed in varying degrees of solvation depending on the time exposed to argon flow and age of the sample: *P,P-cis*-Ru(^{i}Pr$_2$PCH$_2$CH$_2$NH$_2$)$_2$(OH)H·(^{i}PrOH)$_{0-x}$ where x = 2.

P,P-cis-Ru(^{i}Pr$_2$PCH$_2$CH$_2$NH$_2$)$_2$(OH)H·(^{i}PrOH)$_2$ (**11**·(^{i}PrOH)$_2$) ^{1}H NMR (600 MHz, benzene-d$_6$): 3.92 (sept, 6 Hz, 2H, ^{i}PrOH CH), 3.08 (d, br, 12 Hz, 2H, N–CH$_2$), 2.40 (m, 2H, N-CH$_2$), 2.13 (m, 2H, ^{i}Pr CH), 1.81 (m, 2H, ^{i}Pr CH), 1.44 (overlapping m, 4H, CH$_2$), 1.23 (dd, 7 Hz, 12 Hz, 6H, ^{i}Pr CH$_3$), 1.14 (overlapping m, 18H, ^{i}PrOH CH$_3$ 6 Hz

and ^{i}Pr CH_3), 1.08 (dd, 13 Hz, 7 Hz, 6H, ^{i}Pr CH_3), 1.03 (dd, 10 Hz, 6 Hz, 6H, ^{i}Pr CH_3), –21.70 (s, br, 1H, Ru-H). The byproduct from synthesis acetone is also commonly observed by ^{1}H NMR at 1.55 ppm as a singlet.

Hydrogen bonding and rapid exchange at the NMR timescale made assignment of the OH and NH protons difficult. They are tentatively identified as: ~4.20 (s, br, 1H, Ru-OH), ~3.80 (s, br, 4H, NH_2). The exact shift of these signals varies with the level of solvation of the complex, the hydride shift also varies slightly from – 21.70 to – 21.47 ppm. The NH_2 and OH signals show no coupling to any other in the ^{1}H^{1}H COSY spectrum and to no ^{13}C signal in the ^{1}H^{13}C HMBC.

^{31}P{^{1}H} NMR (600 MHz, benzene-d_6) δ 89.2 (s, 2P).

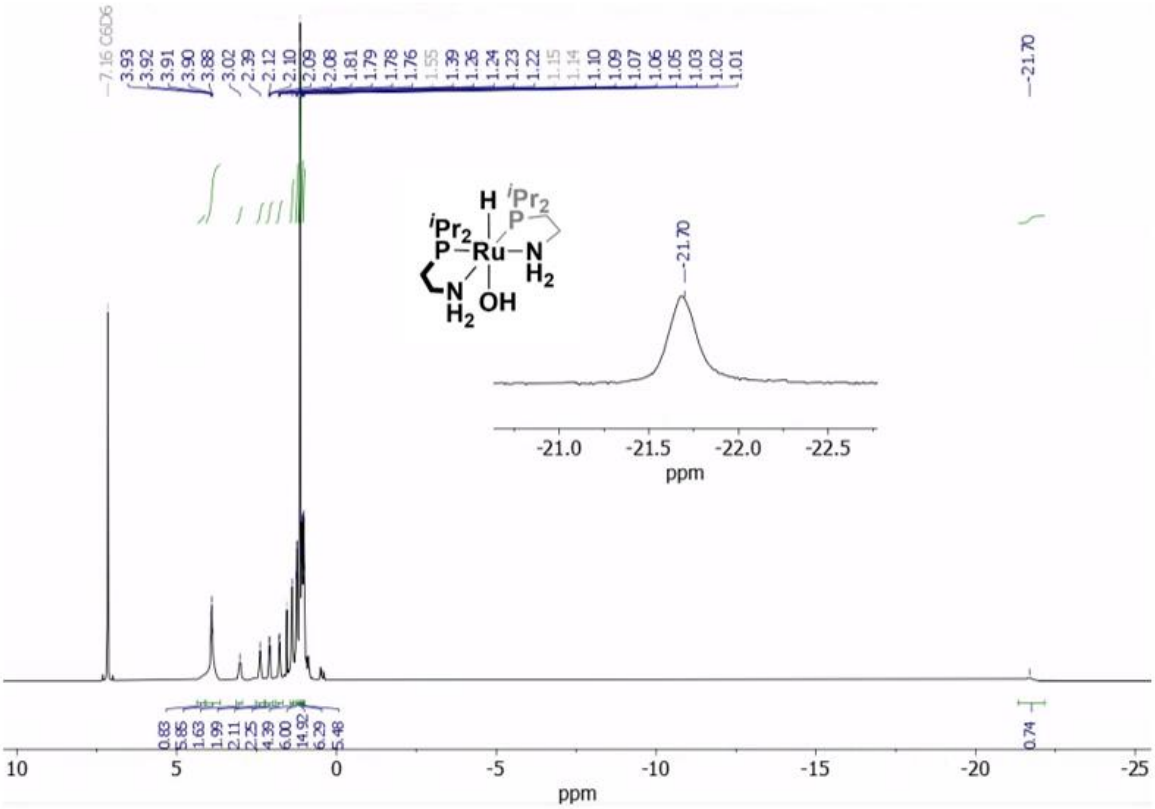

Figure 212. ^{1}H NMR of *P,P-cis*-Ru(^{i}Pr$_2$PCH$_2$CH$_2$NH$_2$)$_2$(OH)H·(^{i}PrOH)$_2$ (**11**·(^{i}PrOH)$_2$), ^{i}Pr CH_3 signal (1.15 ppm) from isopropanol relative integrals at ~ 12 allow assignment of the bis-solvated form. The hydride signal at –21.70 ppm is highlighted in the inset. Residual acetone as a byproduct of synthesis is present at 1.55 ppm. Recorded in benzene-d_6 at 298 K.

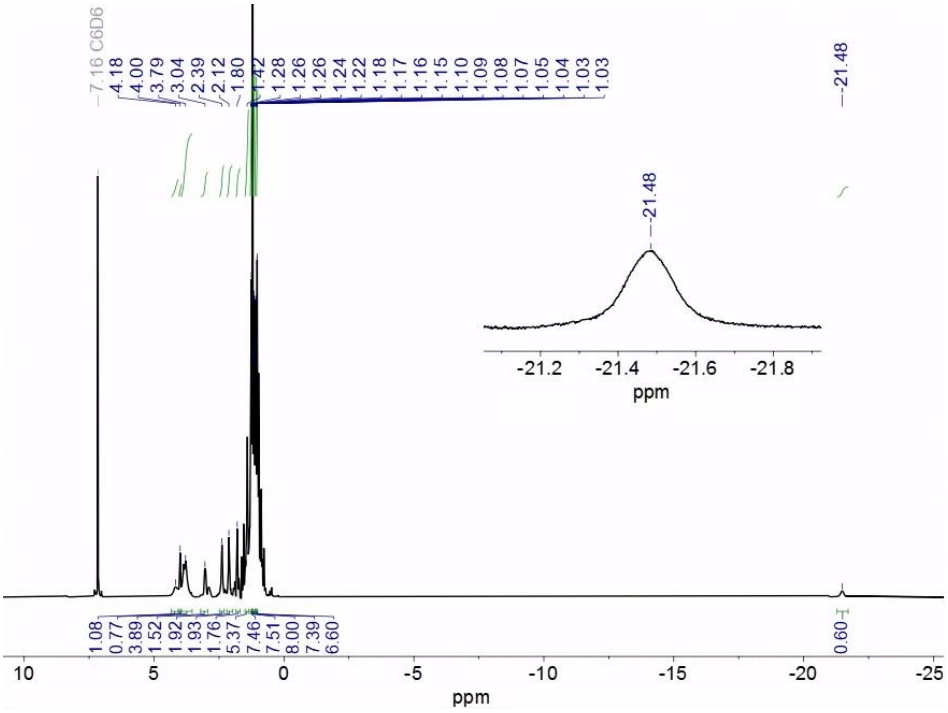

Figure 213. ^{1}H NMR of *P,P-cis*-Ru(^{i}Pr$_2$PCH$_2$CH$_2$NH$_2$)$_2$(OH)H·(^{i}PrOH), ^{i}Pr CH$_3$ signal (1.15 ppm) from isopropanol relative integrals at ~ 6 allow assignment of the mono-solvated form. This material was used for the IR measurements. The hydride signal at –21.48 ppm is highlighted in the inset. Recorded in benzene-d$_6$ at 298 K.

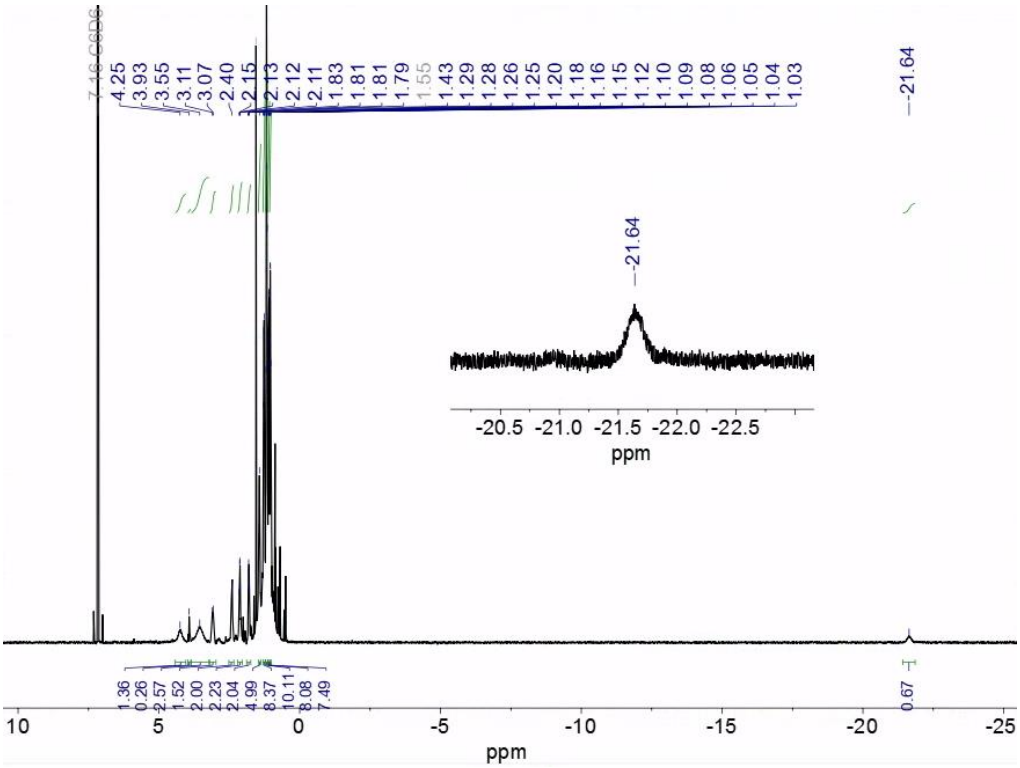

Figure 214. ^{1}H NMR of *P,P-cis*-Ru(^{i}Pr$_2$PCH$_2$CH$_2$NH$_2$)$_2$(OH)H (**11**), un-solvated form. Residual acetone as a byproduct of synthesis is present at 1.55 ppm. The hydride signal at – 21.64 ppm is highlighted in the inset. Recorded in benzene-d$_6$ at 298 K.

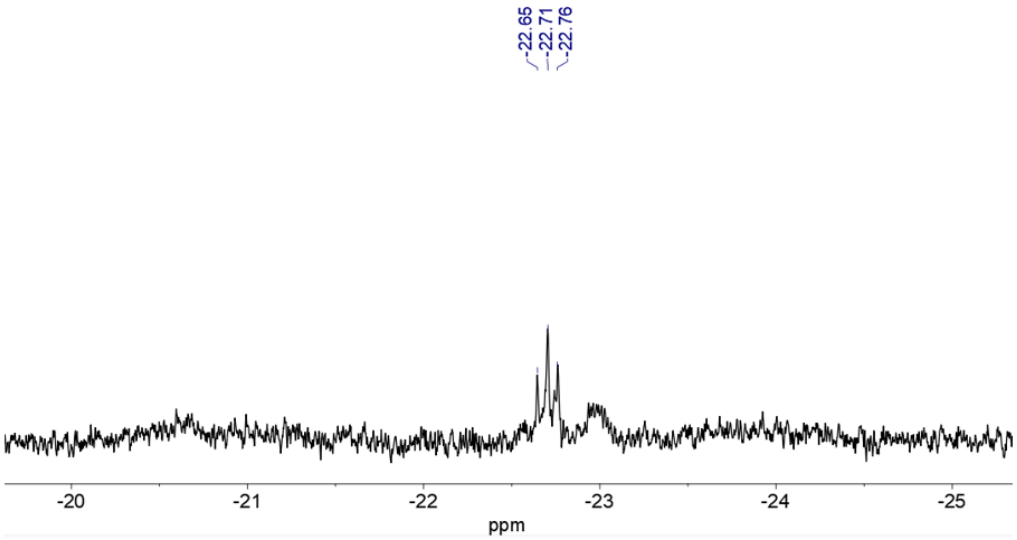

Figure 215. The ^{1}H NMR of *P,P-cis*-Ru($^{i}Pr_2PCH_2CH_2NH_2)_2(OH)H\cdot(^{i}PrOH)_2$ (**11**·(^{i}PrOH)$_2$) showing the hydride as a triplet at – 22.71 ppm with J_{HP} = 27 Hz when at 193 K. Recorded in THF-d_8 at 298 K. The smaller additional adjacent peak may correspond to **11** with a different level of solvation. [7]

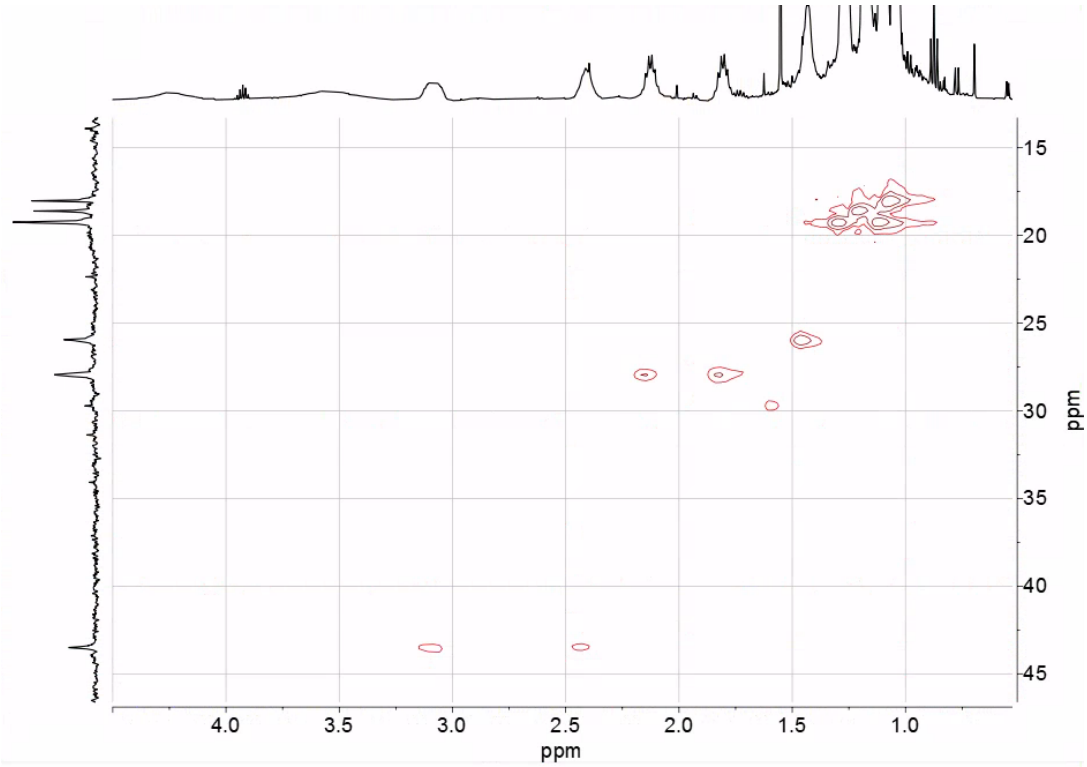

Figure 216. $^{1}H^{31}C$ HMBC 2D NMR spectrum of *P,P-cis*-Ru($^{i}Pr_2PCH_2CH_2NH_2)_2(OH)H$ (**11**), un-solvated form, showing lack of coupling to ^{13}C environments for the RuOH signal at 4.23 ppm and NH_2 at 3.53 ppm. Recorded in C_6D_6 at 298 K.

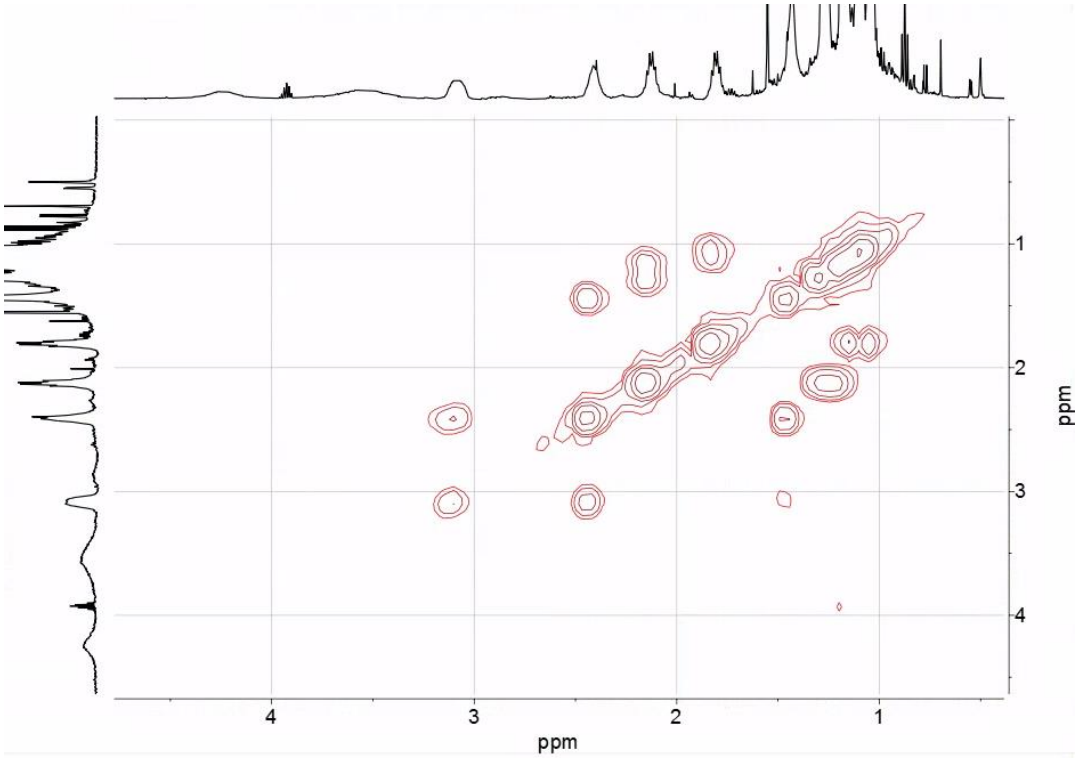

Figure 217. $^{1}H^{1}H$ COSY 2D NMR spectrum of *P,P-cis*-Ru($^{i}Pr_2PCH_2CH_2NH_2)_2$(OH)H (**11**), un-solvated form, showing lack of coupling to other ^{1}H environments for the RuOH signal at 4.23 ppm and NH_2 at 3.53 ppm. Recorded in C_6D_6 at 298 K.

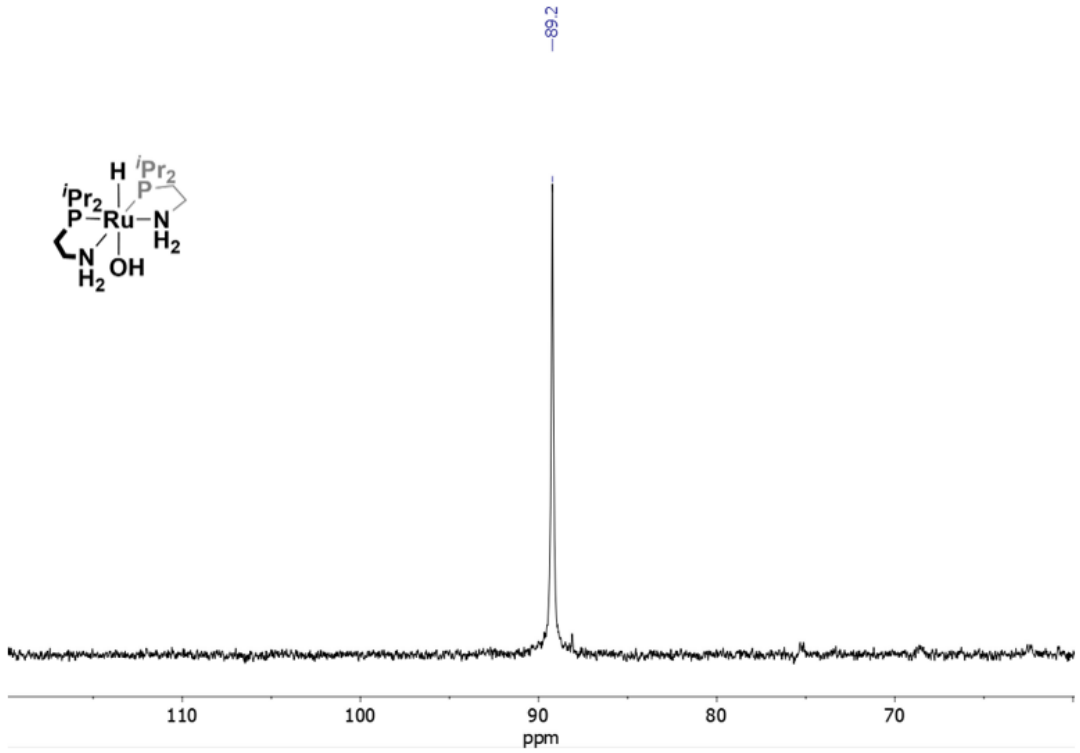

Figure 218. $^{31}P\{^{1}H\}$ NMR of *P,P-cis*-Ru($^{i}Pr_2PCH_2CH_2NH_2)_2$(OH)H·($^{i}PrOH)_2$ (**11**·($^{i}PrOH)_2$), recorded in benzene-d_6 at 298 K.

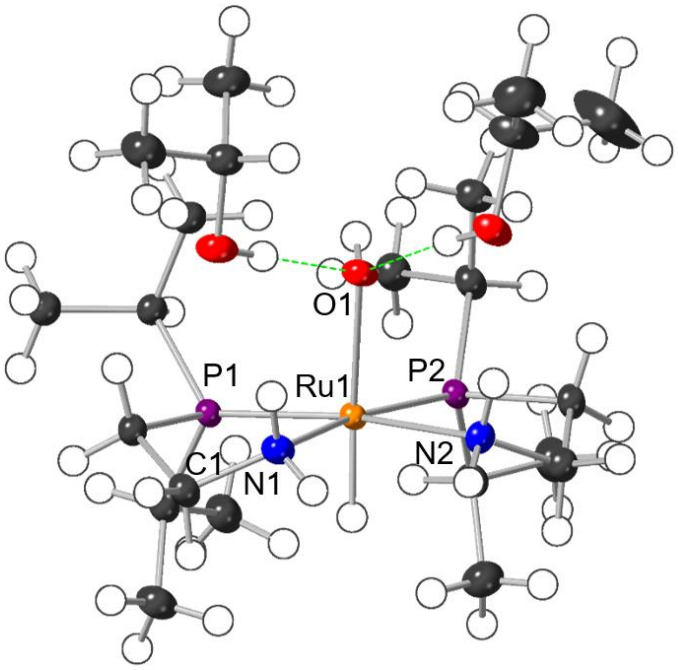

Figure 219. Molecular structure of *P,P-cis*-Ru(^{i}Pr$_2$PCH$_2$CH$_2$NH$_2$)$_2$(OH)H·(^{i}PrOH)$_2$ (**11**·(^{i}PrOH)$_2$) as determined by single crystal X-ray diffraction. Displacement ellipsoids are shown at the 50% probability level. Hydrogen atoms are placed in calculated positions. Selected bond lengths [Å] and angles [°]: Ru(1) –O(1) 2.2795(18), Ru(1) – N(1) 2.186(2), Ru(1) – N(2) 2.186(2), Ru(1) – P(1) 2.2499(6), Ru(1) – P(2) 2.2477(6), C(1) – N(1)1.476(3), P(1) – Ru(1) – N(1) 83.52(6), C(1) – N(1) – Ru(1) 113.57(15), O(1) – Ru(1) – N(1) 81.13(8), O(1) – Ru(1) – P(1) 101.22(5).

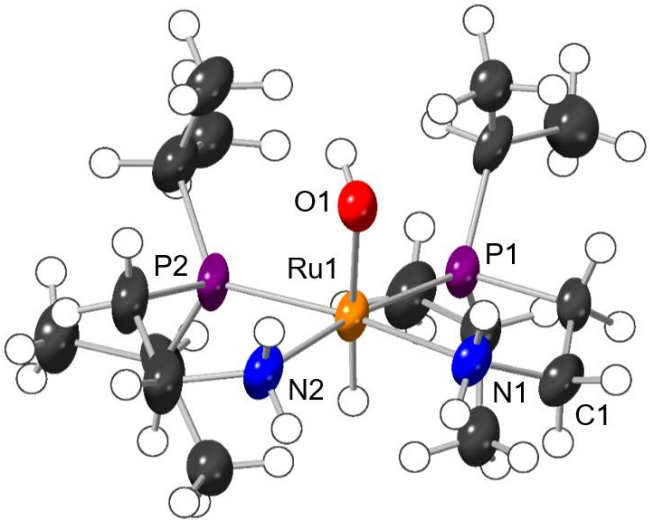

Figure 220. Molecular structure of unsolvated *P,P-cis*-Ru(^{i}Pr$_2$PCH$_2$CH$_2$NH$_2$)$_2$(OH)H (**11**), as determined by single crystal X-ray diffraction. Displacement ellipsoids are shown at the 50% probability level. Hydrogen atoms are placed in calculated positions. Selected bond lengths [Å] and angles [°]: Ru(1) –O(1) 2.260(8), Ru(1) – N(1) 2.176(9), Ru(1) – N(2) 2.20(3), Ru(1) – P(1) 2.228(3), Ru(1) – P(2) 2.233(3), C(1) – N(1)1.51(4), P(1) – Ru(1) – N(1) 84.0(3), C(1) – N(1) – Ru(1) 115.6(10), O(1) – Ru(1) – N(1) 77.0(3), O(1) – Ru(1) – P(1) 104.9(2).

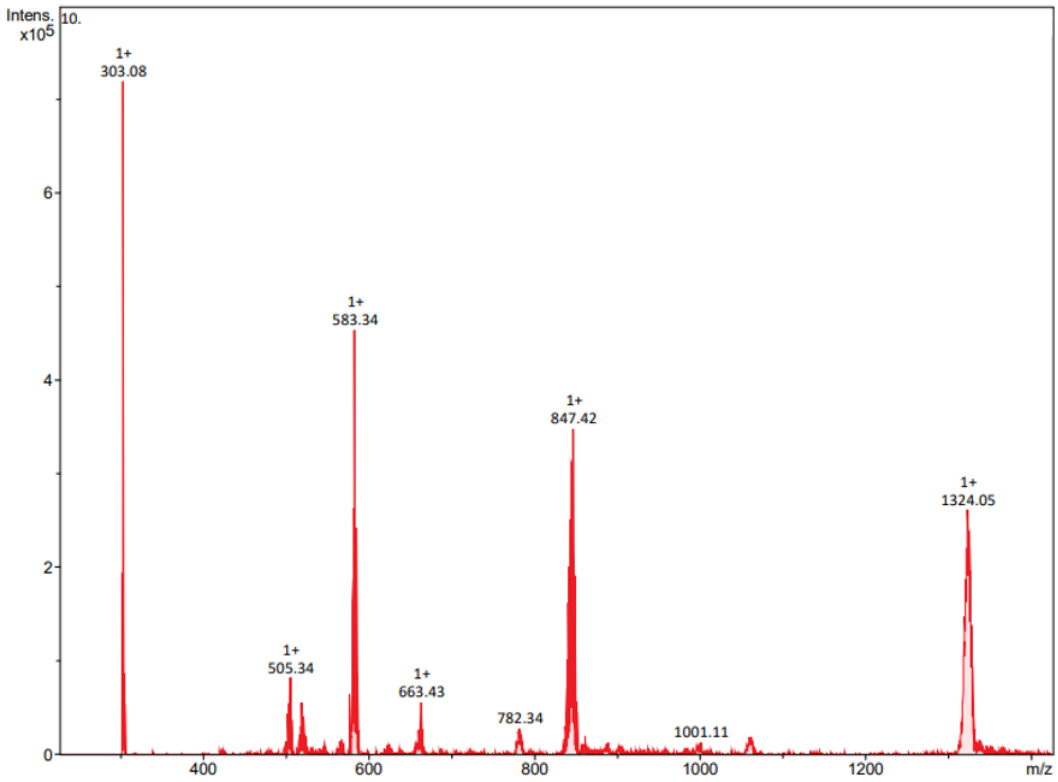

Figure 221. ESI+ mass spectrum measured of *P,P-cis*-Ru(^{i}Pr$_2$PCH$_2$CH$_2$NH$_2$)$_2$(OH)H (**11**), showing decomposition during analysis. Species observed at m/z 847.42 is likely a ruthenium dimer, corresponding to the dimerization of *P,P-cis*-Ru(^{i}Pr$_2$PCH$_2$CH$_2$NH$_2$)$_2$(OH)H (11) with the loss of 2 molecule of H_2O and 1 molecule of H_2 ([M+H]$^+$, $Ru_2N_4P_4C_{16}H_{78}$), likely due to the high vacuum within the mass spectrometer. The mass peak at 303.08 m/z is likely to be the plasticiser oleamide [M+Na]$^+$. The mass peaks at 583.34 and 1324.05 m/z are unidentified mono- and poly-ruthenium species respectively, as evidenced by isotope patterns.

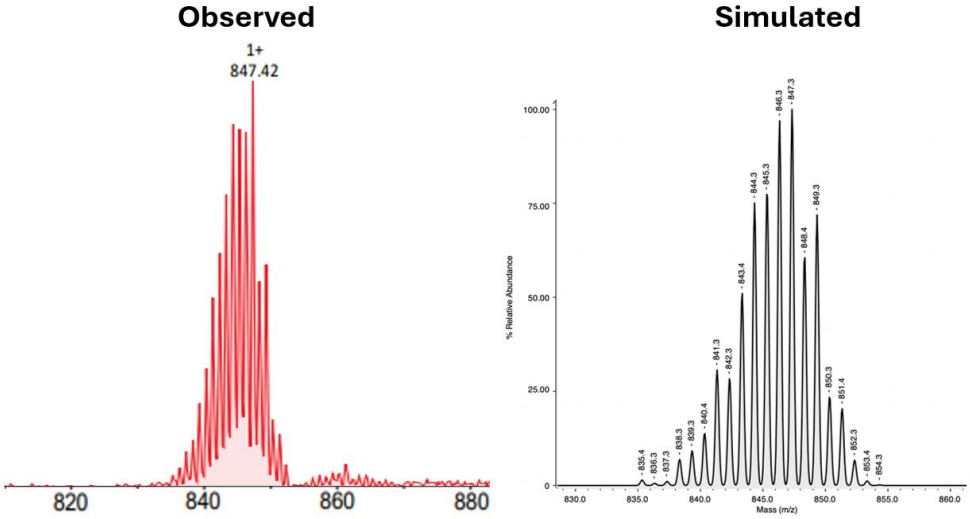

Figure 222. The observed (left) and simulated (right) mass spectrum peaks for [M+H]$^+$ $Ru_2N_4P_4C_{16}H_{78}$, showing a good agreement. This species likely forms from the dimerization of *P,P-cis*-Ru(^{i}Pr$_2$PCH$_2$CH$_2$NH$_2$)$_2$(OH)H (**11**), with the loss of 2 molecules of H_2O and 1 molecule of H_2.

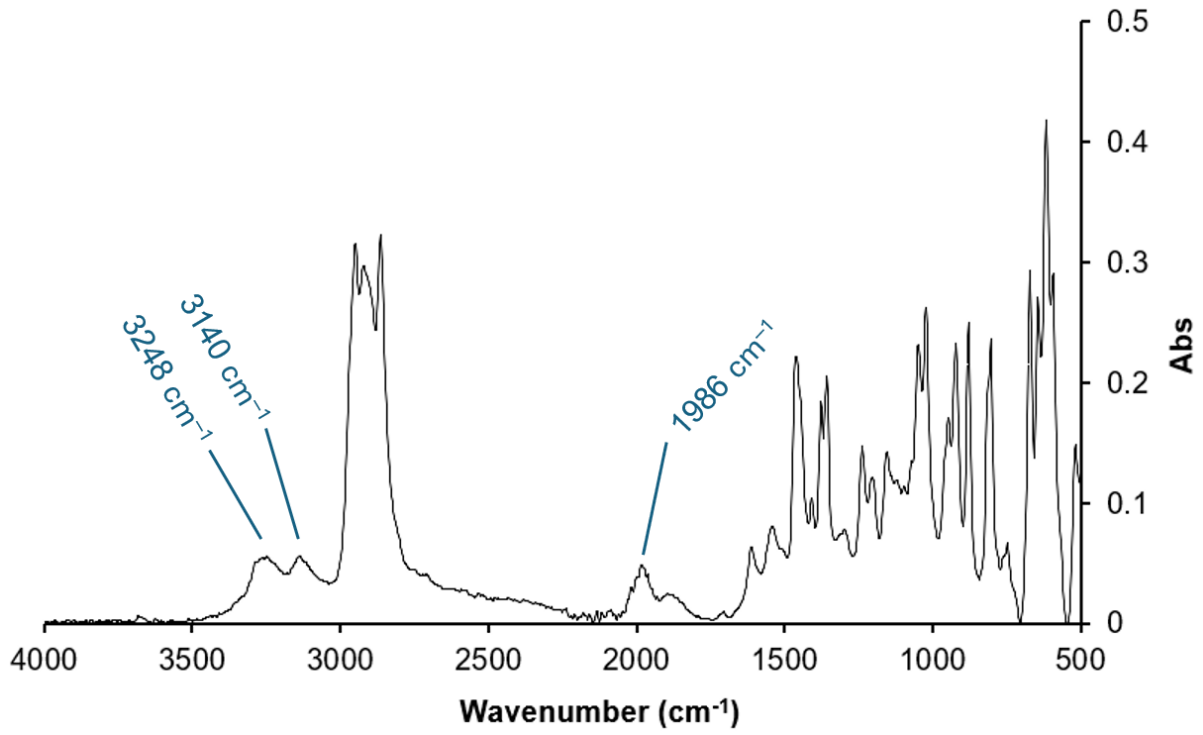

Figure 223. ATR IR spectrum recorded of *P,P-cis*-Ru(^{i}Pr$_2$PCH$_2$CH$_2$NH$_2$)$_2$(OH)H. ^{1}H NMR spectroscopy integrals of the ^{i}PrOH CH$_3$ signals present in this sample suggest an overall approximate mono-solvation (· 1 ^{i}PrOH) of this material. The stretch at 1986 cm^{-1} is predicted to correspond with the Ru-H, the O-H stretch is predicted to be low-intensity due to hydrogen bonding effects.

5.3.6 Synthesis and characterisation of *P,P-cis*-Ru(^{i}Pr$_2$PCH$_2$CH$_2$NH$_2$)$_2$(κ^1-BH$_4$)H (13)

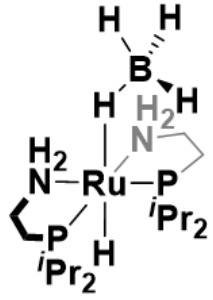

13

100 mg (0.2 mmol) of *P,P-cis*-Ru(^{i}Pr$_2$PCH$_2$CH$_2$NH$_2$)$_2$Cl$_2$ and 45 mg (1 mmol, excess) of NaBH$_4$ were dissolved in 5 cm^3 of ^{i}PrOH and stirred overnight after which a thick white precipitate had formed. The ^{i}PrOH was removed in-vacuo and 5 cm^3 of toluene was added. The mixture was stirred and then canula filtered, collecting the filtrate. The filtrate was then evaporated in-vacuo to leave an off-white solid of *P,P-cis*-Ru(^{i}Pr$_2$PCH$_2$CH$_2$NH$_2$)$_2$(κ^1-BH$_4$)H (**13**) (83 mg, 92 % yield). X-ray quality crystals were obtained by layering a toluene solution of *P,P-cis*-Ru(^{i}Pr$_2$PCH$_2$CH$_2$NH$_2$)$_2$(κ^1-BH$_4$)H (**13**) with pentane at room temperature.

^{1}H NMR (600 MHz, toluene-d$_8$) δ 3.50 [t, br, J_{HH} = 10 Hz, 2H, NH$_2$], 2.73 (m, 2H, CH$_2$), 2.37 [t, br, J_{HH} = 4 Hz, 2H, NH$_2$], 2.15 (m, 2H, CH$_2$), 1.91 [dsep, J_{HH} = 7.1 Hz, J_{HP} = 7.1 Hz, 2H, ^{i}Pr CH], 1.76 [dsep, J_{HH} = 7 Hz, J_{HP} = 7.1 Hz, 2H, ^{i}Pr CH], 1.28 (m, 2H, CH$_2$), 0.98 – 1.24 (overlapping m, 26 H, CH$_2$ and ^{i}Pr CH$_3$), –1.73 (s, br, 4H, BH$_4$), –17.30 [t, J_{HP} = 25 Hz, 1H, Ru–H].

^{31}P{^{1}H} NMR (600 MHz, toluene-d$_8$) δ 93.5 (s, 2P).

^{11}B NMR (600 MHz, toluene-d$_8$) δ –25.6 (pentet, J_{BH} = 80 Hz, 1B, BH$_4$).

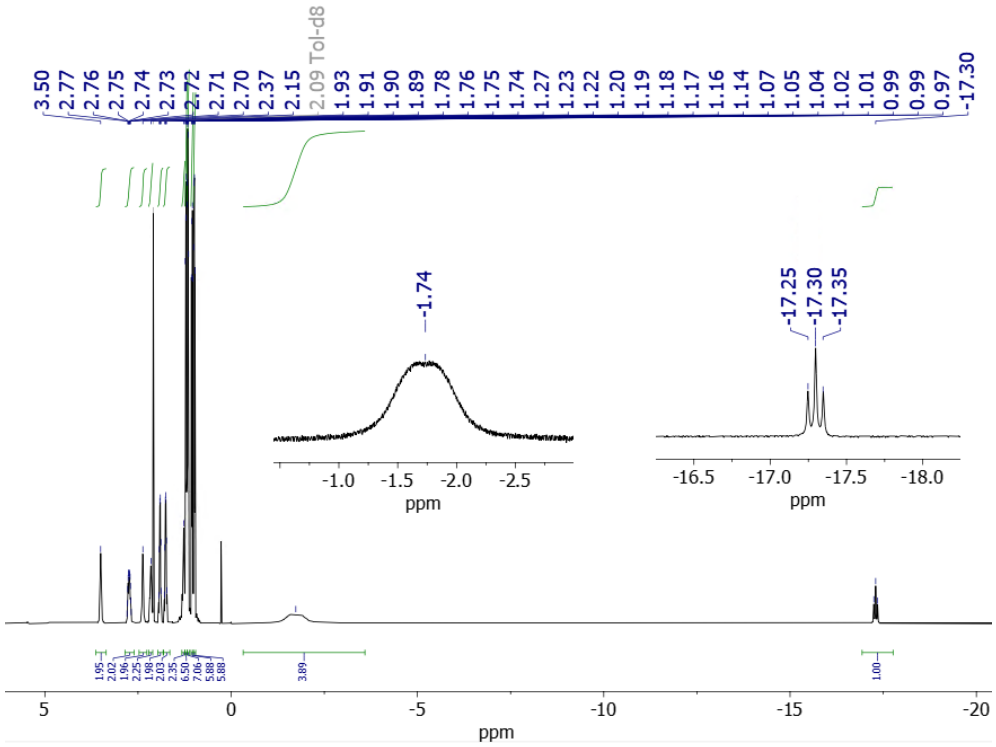

Figure 224. ^{1}H NMR of *P,P-cis*-Ru(^{i}Pr$_2$PCH$_2$CH$_2$NH$_2$)$_2$(κ^1-BH$_4$)H (**13**), highlighting the borohydride signal at –1.74 ppm and the hydride signal at –17.30 ppm. Recorded in toluene-d$_8$.

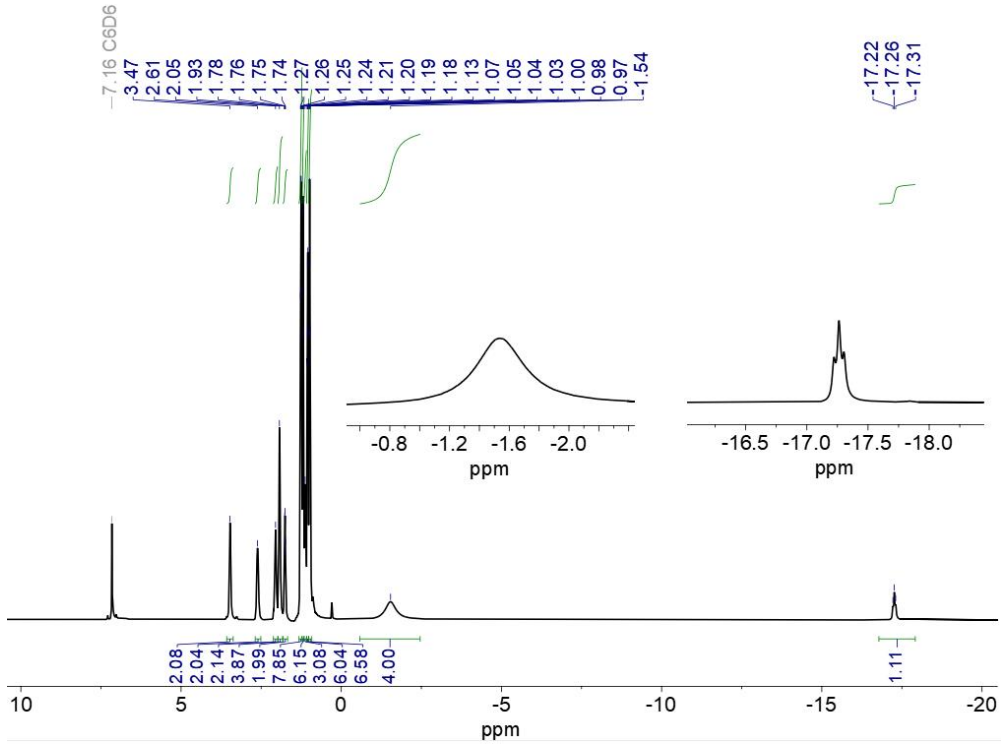

Figure 225. ^{1}H{^{11}B} NMR of *P,P-cis*-Ru(^{i}Pr$_2$PCH$_2$CH$_2$NH$_2$)$_2$(κ^1-BH$_4$)H (**13**), highlighting the borohydride signal at –1.54 ppm and the hydride signal at –17.26 ppm. Recorded in benzene-d$_6$.

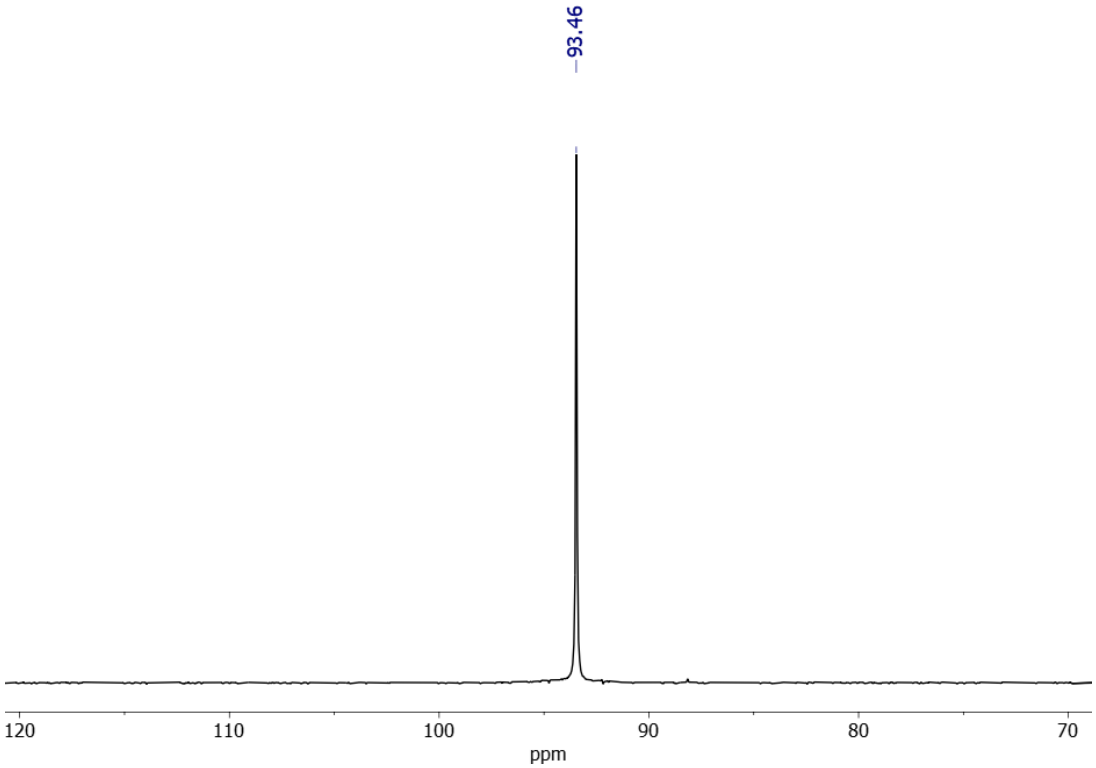

Figure 226. $^{31}P\{^{1}H\}$ NMR of *P,P-cis*-Ru($^{i}Pr_2PCH_2CH_2NH_2$)$_2$(κ^1-BH_4)H (**13**), recorded in toluene-d_8.

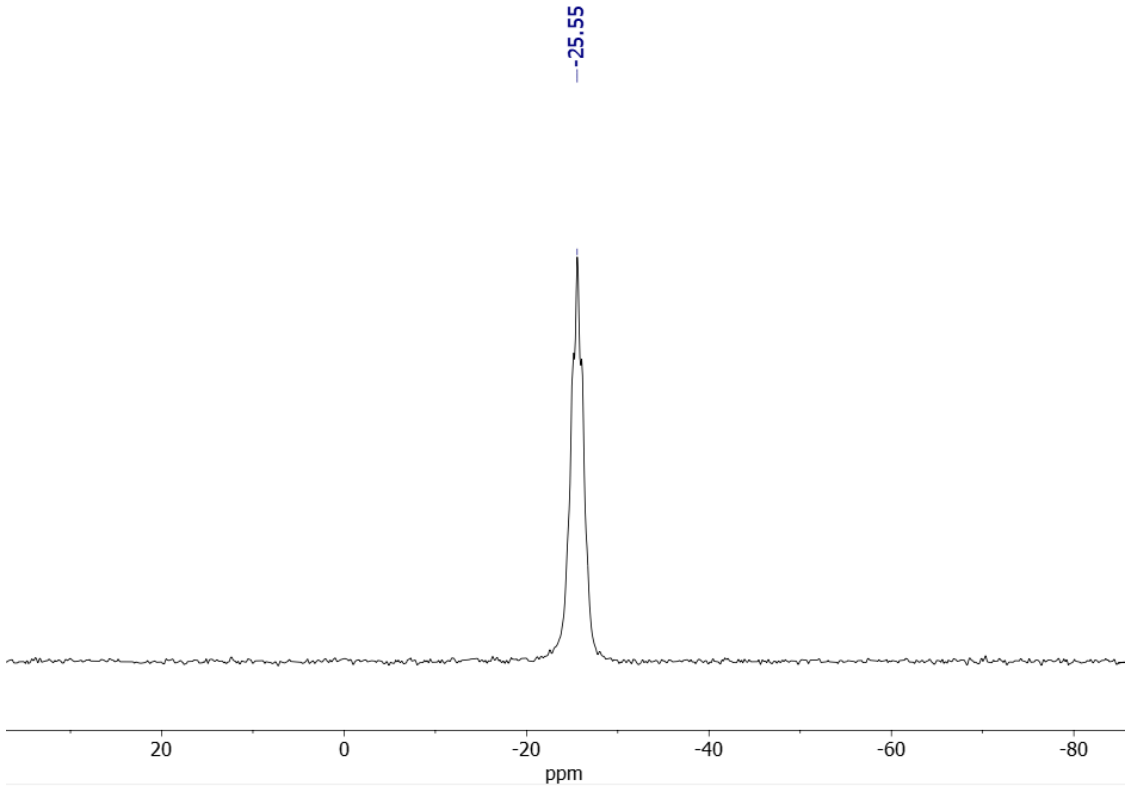

Figure 227. ^{11}B NMR of *P,P-cis*-Ru($^{i}Pr_2PCH_2CH_2NH_2$)$_2$(κ^1-BH_4)H (**13**), recorded in toluene-d_8.

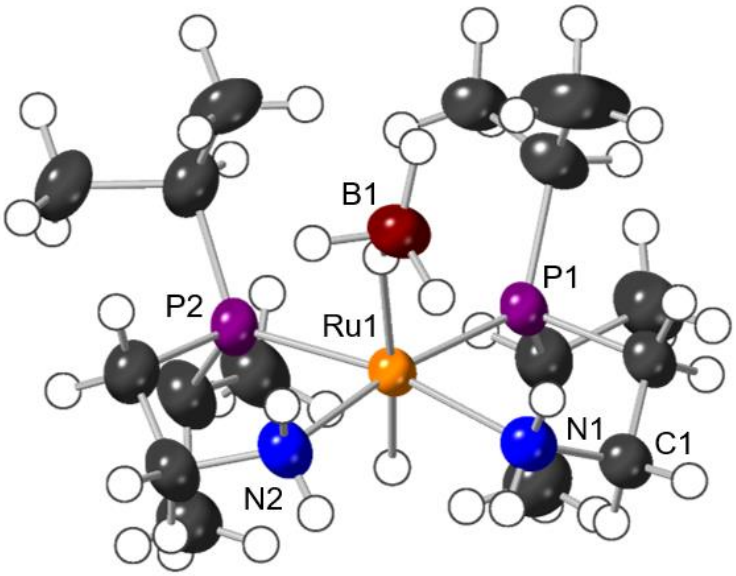

Figure 228. Molecular structure of Ru(^{i}Pr$_2$PCH$_2$CH$_2$NH$_2$)$_2$(κ^1-BH$_4$)H (**13**) as determined by single crystal X-ray diffraction. Displacement ellipsoids are shown at the 50% probability level. Hydrogen atoms are placed in calculated positions. Selected distances [Å], bond lengths [Å] and angles [°]: Ru(1)···B(1) 2.859(9), Ru(1) – N(1) 2.192(7), Ru(1) – N(2) 2.189(8), Ru(1) – P(1) 2.253(2), Ru(1) – P(2) 2.245(2), C(1) – N(1) 1.485(11), P(1) – Ru(1) – N(1) 83.8(2), C(1) – N(1) – Ru(1) 112.2(6).

5.3.7 Dehydropolymerisation of methyl amine-borane with *P,P-trans*-Ru(^{i}Pr$_2$PCH$_2$CH$_2$NH)$_2$ (9)

In a typical dehydropolymerisation experiment, 2 mg (0.004 mmol) of *P,P-cis*-Ru(^{i}Pr$_2$PCH$_2$CH$_2$NH$_2$)$_2$Cl$_2$ (**8**) (orange) and 2 equivalents of ^{t}BuOK (0.9 mg, 0.008 mmol) were weighed into an ampoule and dissolved in 0.5 cm^3 of THF and stirred for 30 minutes, selectively forming dark-red *P,P-trans*-Ru(^{i}Pr$_2$PCH$_2$CH$_2$NH)$_2$ (**9**) as measured by ^{31}P{^{1}H} NMR spectroscopy. This stock solution (0.008 mol dm^{-3}) was used immediately due to its time-sensitive decomposition. Separately 112 mg (2.5 mmol) of a recrystallised methyl amine-borane was weighed into a jacketed Schlenk which was then temperature equilibrated 20 ºC and connected to an upturned water-filled burette to collect the produced H_2 gas (**Figure 229**). To initiate catalysis, 2.5 – *n* cm^3 of THF was added to the amine-borane, stirred at 400 rpm, followed by *n* cm^3 (e.g. 0.093 cm^3 to give 0.03 mol% to methyl amine-borane) of the *P,P-trans*-Ru(^{i}Pr$_2$PCH$_2$CH$_2$NH)$_2$ (**9**) stock solution, resulting in the desired catalyst concentration (in this case 0.00030 mol dm^{-3}) in a total of 2.5 cm^3 of THF. The volume of evolved H_2 was recorded by the burette. Upon completion of H_2 evolution, an *in-situ* NMR sample was taken and analysed by ^{1}H, ^{31}P{^{1}H} and ^{11}B NMR spectroscopies. The catalysis mixture was then quenched in-air by the addition of ~ 50 cm^3 of pentane, resulting in the precipitation of white poly(*N*-methylaminoborane). The polymer was isolated by filtration and dried in-vacuo to give a white solid, 0.063 g (59% recovered yield), > 99% conversion and selectivity observed by in-situ ^{11}B NMR spectroscopy (**Figure 230**). This poly(*N*-methylaminoborane) was then analysed by GPC (M_n = 138,700 g mol^{-1}, dispersity = 1.46) (**Figure 231**).

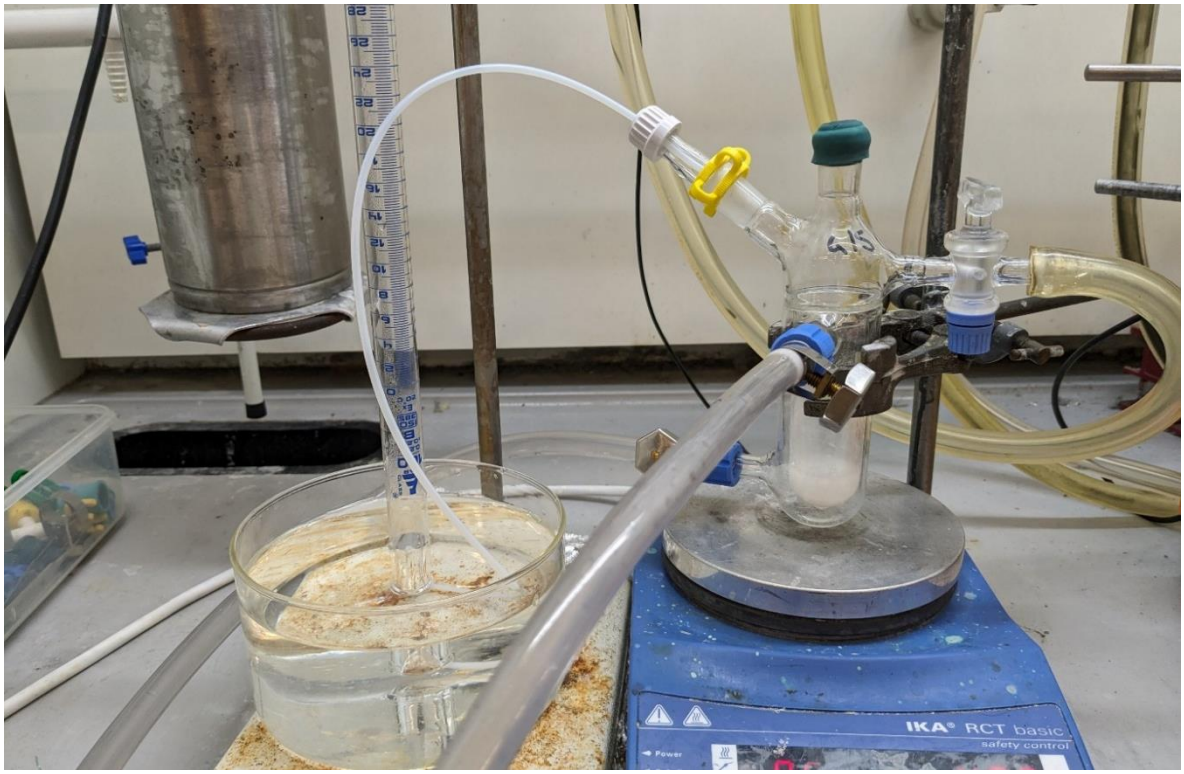

Figure 229. Eudiometric catalysis setup showing jacketed Schlenk flask and a connected upturned water-filled burette. 1:1 water:polyethylene glycol coolant at 20 ˚C is pumped by a recirculating cooler into the jacket around the Schlenk flask.

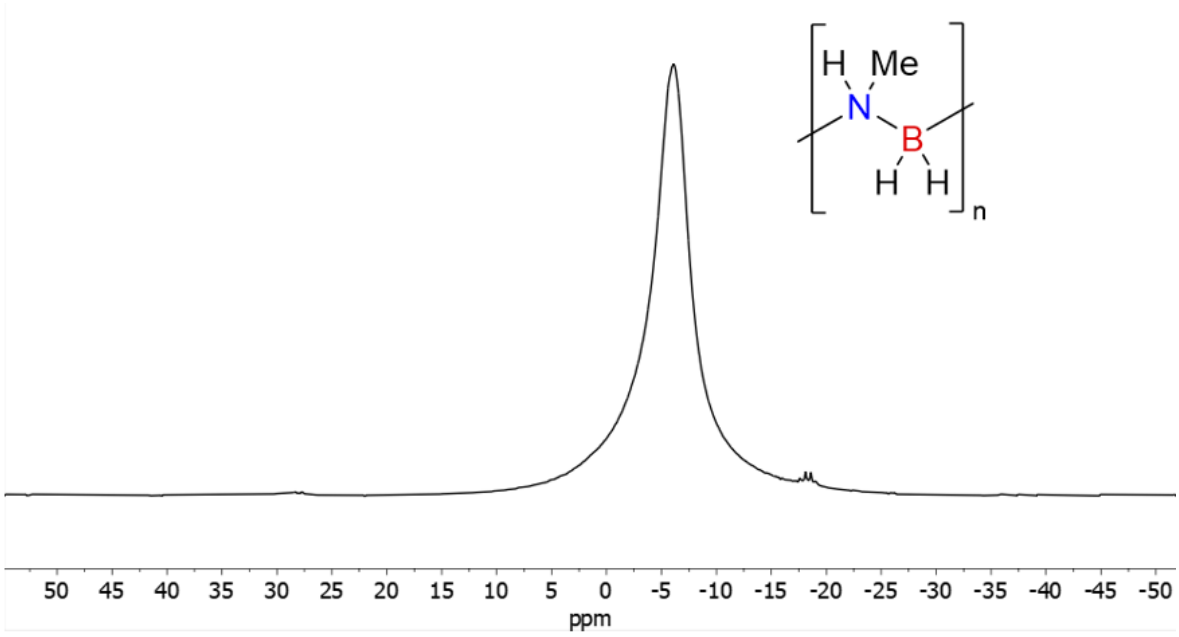

Figure 230. In-situ ^{11}B NMR of the catalysis mixture upon dehydrocoupling of methylamine-borane with *P,P-cis*-Ru(^{i}Pr$_2$PCH$_2$CH$_2$NH$_2$)$_2$Cl$_2$ (**8**) and 2 equivalents to catalyst of ^{t}BuOK, (forming *P,P-trans*-Ru(^{i}Pr$_2$PCH$_2$CH$_2$NH)$_2$ (**9**) in-situ). Selective dehydropolymerisation to form poly(*N*-methylaminoborane) shown. Catalyst loading at 0.03 mol% relative to methylamine-borane, 1 mol dm^{-3} methylamine borane in THF.

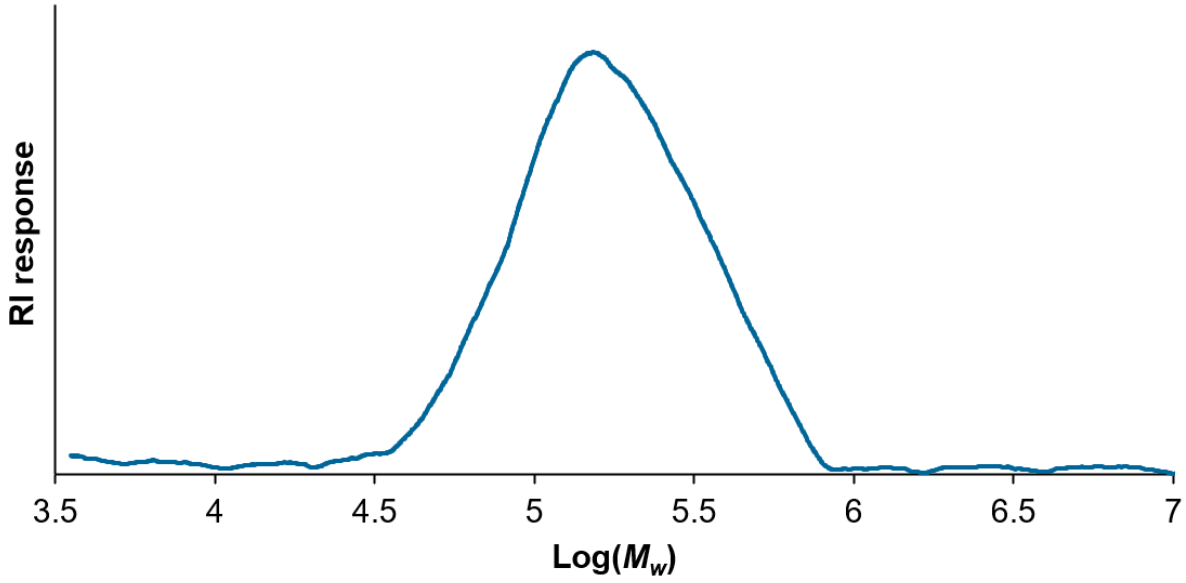

Figure 231. GPC trace highlighting the polymer peak $(H_2BNHMe)_n$, of the material precipitated from the dehydropolymerisation of methyl amine-borane (1 mol dm^{-3} in 2.5 cm^3 of THF) by *P,P-trans*-Ru(^{i}Pr$_2$PCH$_2$CH$_2$NH)$_2$ (**9**) at 0.03 mol%. M_n = 138,700 g mol^{-1}, M_w = 202,000 g mol^{-1}, dispersity = 1.46.

5.3.8 Dehydropolymerisation of methyl amine-borane with *P,P-cis*-Ru(^{i}Pr$_2$PCH$_2$CH$_2$NH$_2$)$_2$Cl$_2$ (8) and MeNH$_2$

In a typical dehydropolymerisation experiment, 3.1 mg (0.0063 mmol) of *P,P-cis*-Ru(^{i}Pr$_2$PCH$_2$CH$_2$NH$_2$)$_2$Cl$_2$ (**8**) was weighed into an ampoule and dissolved in 12.5 cm^3 of THF to make a stock solution. Separately 112 mg (2.5 mmol) of recrystallised methyl amine-borane was weighed into a jacketed Schlenk which was then temperature equilibrated to 20 ˚C and connected to an upturned water-filled burette to collect the produced H$_2$ gas (**Figure 229**). 0.85 cm^3 of THF was added to the amine-borane, stirred at 400 rpm, followed by a portion of stock pre-catalyst solution. For example, 1.65 cm^3 of the *P,P-cis*-Ru(^{i}Pr$_2$PCH$_2$CH$_2$NH$_2$)$_2$Cl$_2$ (**8**) stock solution (containing 0.00083 mmol of precatalyst), results in a catalyst concentration of 0.00033 mol dm^{-3} (0.033 mol%) in a total volume of 2.5 cm^3 of THF. MeNH$_2$ (12.5 µl of 2 mol dm^{-3} in THF) was then immediately added to the catalysis mixture (0.01 mol dm^{-3} in the reaction mixture), to initiate turnover. The volume of evolved H$_2$ was recorded by the burette. Upon completion of H$_2$ evolution, an *in-situ* NMR sample was taken and analysed by ^{1}H, ^{31}P{^{1}H} and ^{11}B NMR spectroscopies. The catalysis mixture was then quenched in-air by the addition of ~50 cm^3 of pentane, resulting in the precipitation of white poly(*N*-methylaminoborane), which was isolated by filtration and dried in-vacuo to give a white solid 0.063 g (59% recovered yield), > 99% conversion and selectivity observed by in-situ ^{11}B NMR spectroscopy (**Figure 232**). This poly(*N*-methylaminoborane) was then analysed by GPC (M_n = 108,200 g mol^{-1}, dispersity = 1.41) (**Figure 233**).

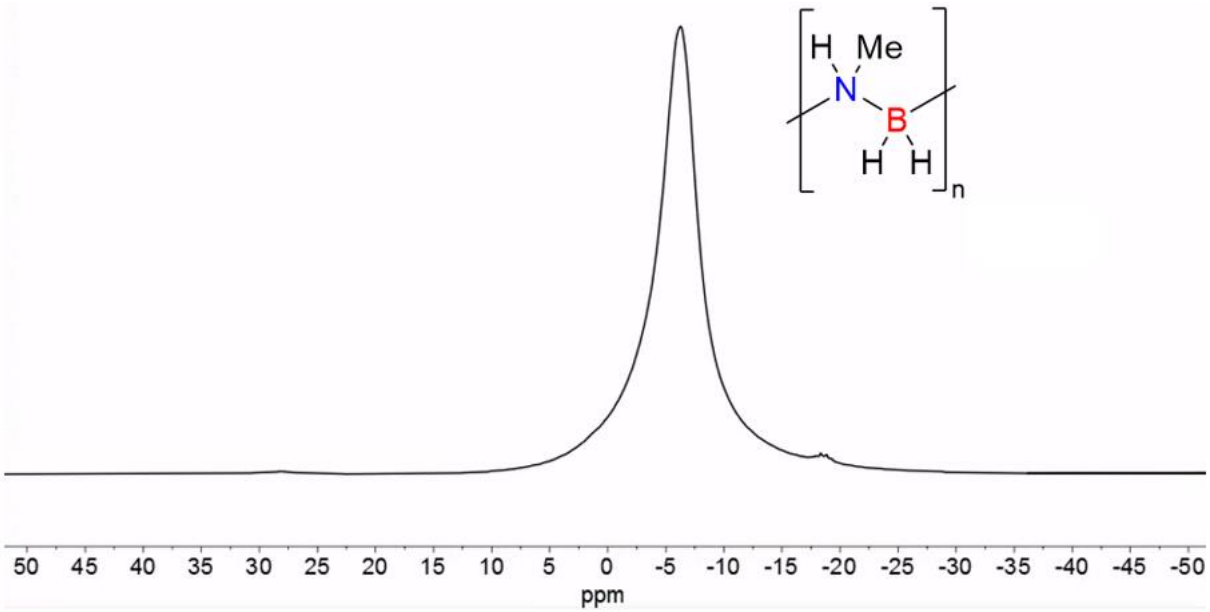

Figure 232. In-situ ^{11}B NMR of the catalysis mixture upon dehydrocoupling of methylamine-borane with *P,P-cis*-Ru(^{i}Pr$_2$PCH$_2$CH$_2$NH$_2$)$_2$Cl$_2$ (**8**) and 3 Eq. to catalyst of MeNH$_2$. Selective dehydropolymerisation to poly(*N*-methylaminoborane) shown. Catalyst loading at 0.033 mol% relative to methylamine-borane, 1 mol dm^{-3} methylamine borane in THF.

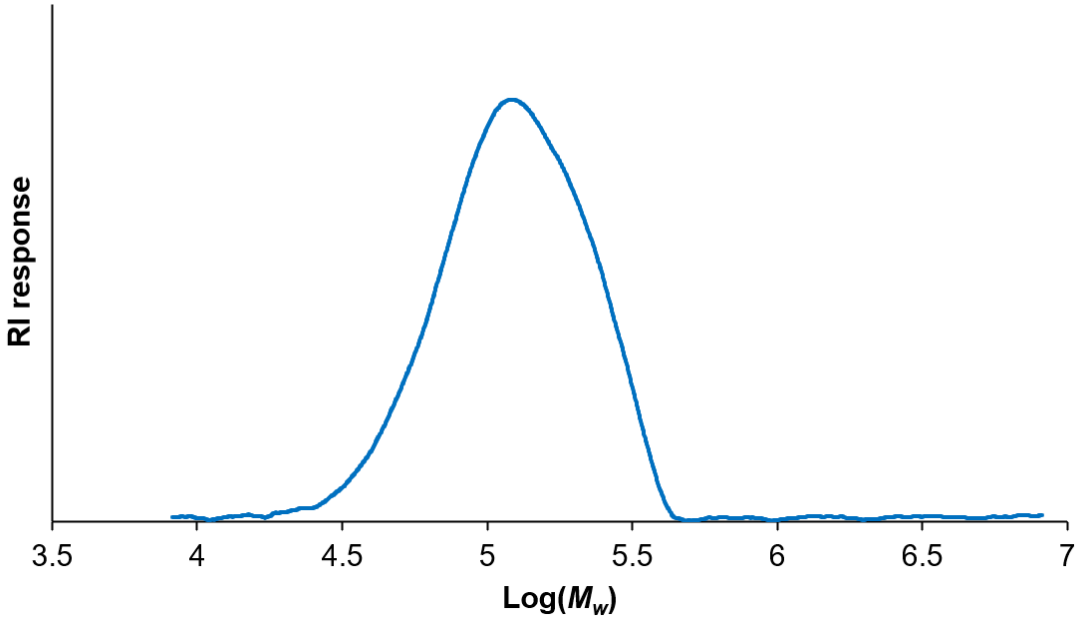

Figure 233. GPC trace highlighting the polymer peak (H$_2$BNHMe)$_n$, of the material precipitated from the dehydropolymerisation of methyl amine-borane (1 mol dm^{-3} in 2.5 cm^3 of THF) by *P,P-cis*-Ru(^{i}Pr$_2$PCH$_2$CH$_2$NH$_2$)$_2$Cl$_2$ (**1**) at 0.03 mol% with 3 equivalents of NH$_2$Me. M_n = 108,200 g mol^{-1}, M_w = 152,700 g mol^{-1}, dispersity = 1.41.

5.3.9 dehydroplymerisation of methyl amine-borane with *P,P-cis*-Ru(^{i}Pr$_2$PCH$_2$CH$_2$NH$_2$)$_2$(OH)H (11)

2.0 mg (0.004 mmol) of *P,P-cis*-Ru(^{i}Pr$_2$PCH$_2$CH$_2$NH$_2$)$_2$Cl$_2$ (**8**) (orange) and 2 equivalents of ^{t}BuOK (0.9 mg, 0.008 mmol) were weighed into an ampoule and dissolved in 0.5 cm^3 of THF and stirred for 30 minutes forming *P,P-trans*-Ru(^{i}Pr$_2$PCH$_2$CH$_2$NH)$_2$ (**9**) (pink/red solution), then 5 equivalents of ^{i}PrOH was added (2 µl) and the mixture stirred for a further 5 minutes forming *P,P-cis*-Ru(^{i}Pr$_2$PCH$_2$CH$_2$NH$_2$)$_2$(OH)H (**11**) (yellow solution), as measured by ^{31}P{^{1}H} NMR spectroscopy. This stock solution was used immediately. Separately 112 mg (2.5 mmol) of a recrystallised methyl amine-borane was weighed into a jacketed Schlenk which was then cooled to 20 ºC and connected to an upturned water-filled burette to collect the produced H$_2$ gas (**Figure 229**). To initiate catalysis, 2.4 cm^3 of THF was added to the amine-borane, stirred at 400 rpm, followed by 0.093 cm^3 (0.03 mol% relative to methyl amine-borane) of the *P,P-cis*-Ru(^{i}Pr$_2$PCH$_2$CH$_2$NH$_2$)$_2$(OH)H (**11**) stock solution, resulting in the desired catalyst concentration (0.0003 mol dm^{-3}) in a total of ~2.5 cm^3 of THF. The volume of evolved H$_2$ was recorded by the burette. Upon completion of H$_2$ evolution, an in-situ NMR sample was taken and analysed by ^{1}H, ^{31}P{^{1}H} and ^{11}B NMR spectroscopies. The catalysis mixture was then quenched in-air by the addition of ~ 50 cm^3 of pentane, resulting in the precipitation of white poly(*N*-methylaminoborane), which was isolated by filtration and dried in-vacuo to give a white solid, 0.064 g (60% recovered yield), > 99% conversion observed by ^{11}B NMR spectroscopy (**Figure 234**). This poly(*N*-methylaminoborane) was then analysed by GPC (M_n = 123,300 g mol^{-1}, dispersity = 1.70).

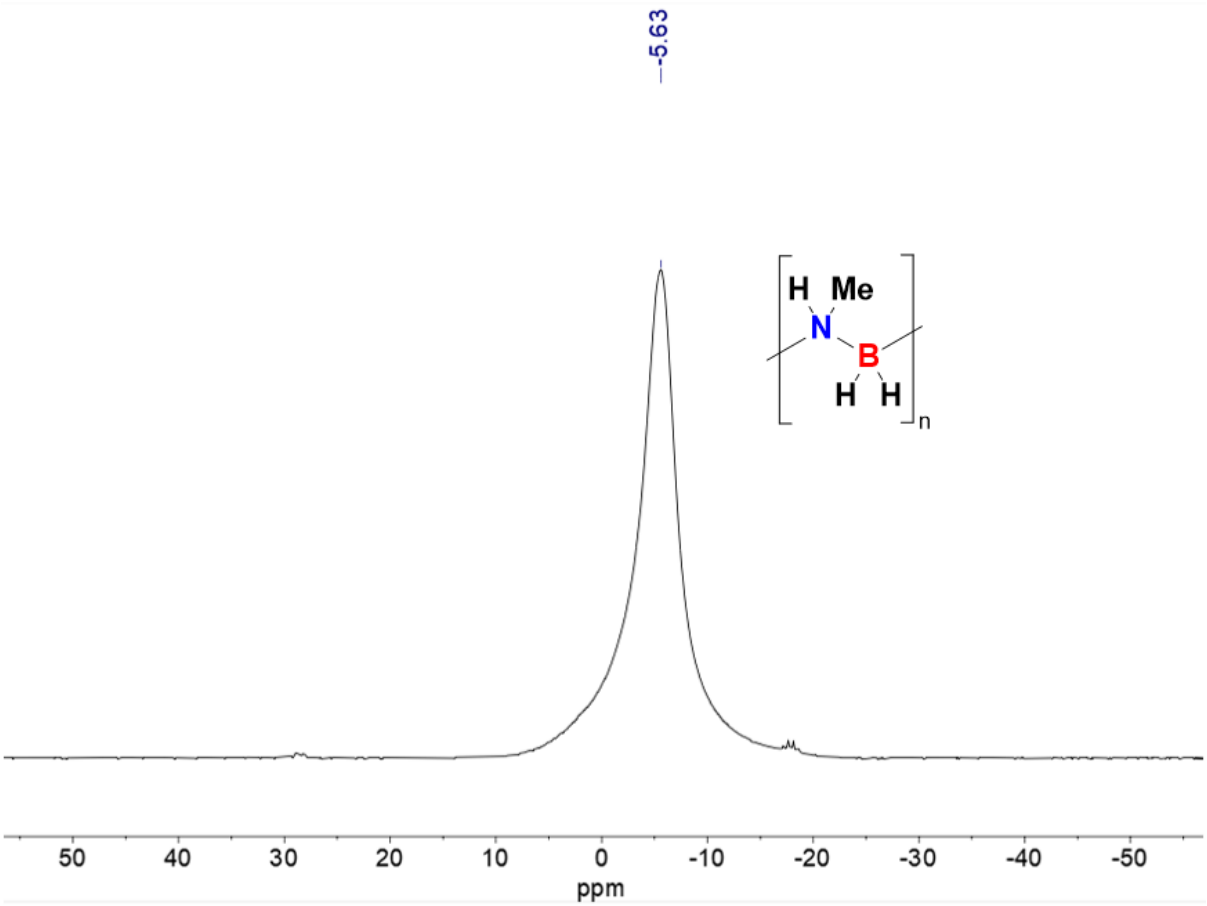

Figure 234. In-situ ^{11}B NMR of the catalysis mixture upon dehydrocoupling of methylamine-borane with *P,P-cis*-Ru(^{i}Pr$_2$PCH$_2$CH$_2$NH$_2$)$_2$Cl$_2$ (**8**), 2 equivalents to catalyst of ^{t}BuOK and 5 equivalents of ^{i}PrOH, (forming Ru(^{i}Pr$_2$PCH$_2$CH$_2$NH$_2$)$_2$(OH)H (**11**) in-situ). Selective dehydropolymerisation to form poly(*N*-methylaminoborane) shown. Catalyst loading at 0.03 mol% relative to methylamine-borane, 1 mol dm^{-3} methylamine borane in THF.

5.3.10 Dehydropolymerisation of methyl amine-borane with *P,P-cis*-Ru(^{i}Pr$_2$PCH$_2$CH$_2$NH$_2$)$_2$(κ^1-BH$_4$)H (13)

In a typical dehydropolymerisation experiment, 3.3 mg (0.0075 mmol) of *P,P-cis*-Ru(^{i}Pr$_2$PCH$_2$CH$_2$NH$_2$)$_2$(κ^1-BH$_4$)H (**13**) was weighed into an ampoule and dissolved in 15 cm^3 of THF to make a stock solution. Separately 112 mg (2.5 mmol) of recrystallised methyl amine-borane was weighed into a jacketed Schlenk which was then temperature equilibrated to 20 °C and connected to an upturned water-filled burette to collect the produced H_2 gas (**Figure 229**). 1 cm^3 of THF was added to the amine-borane followed by 1.5 cm^3 of the *P,P-cis*-Ru(^{i}Pr$_2$PCH$_2$CH$_2$NH$_2$)$_2$(κ^1-BH$_4$)H (**13**) stock solution (0.03 mol% relative to amine-borane), resulting in a catalyst concentration of 0.0003 mol dm^{-3} in a total of 2.5 cm^3 of THF. MeNH$_2$ (12.5 µl of 2 mol dm^{-3} in THF) was then immediately added to the catalysis mixture, resulting in a NH$_2$Me concentration of 0.01 mol dm^{-3}, to initiate turnover. The volume of evolved H_2 was recorded by the burette. Upon completion of H_2 evolution, an *in-situ* NMR sample was taken and analysed by ^{1}H, ^{31}P{^{1}H} and ^{11}B NMR spectroscopies. The catalysis mixture was then quenched in-air by the addition of ~50 cm^3 of pentane, resulting in the precipitation of white poly(*N*-methylaminoborane), which was isolated by filtration and dried in-vacuo to give a white solid (0.062 g, 56% yield), > 99% conversion observed by ^{11}B NMR spectroscopy (**Figure 235**). This poly(*N*-methylaminoborane) was then analysed by GPC (M_n = 132,600 g mol^{-1}, dispersity = 1.45).

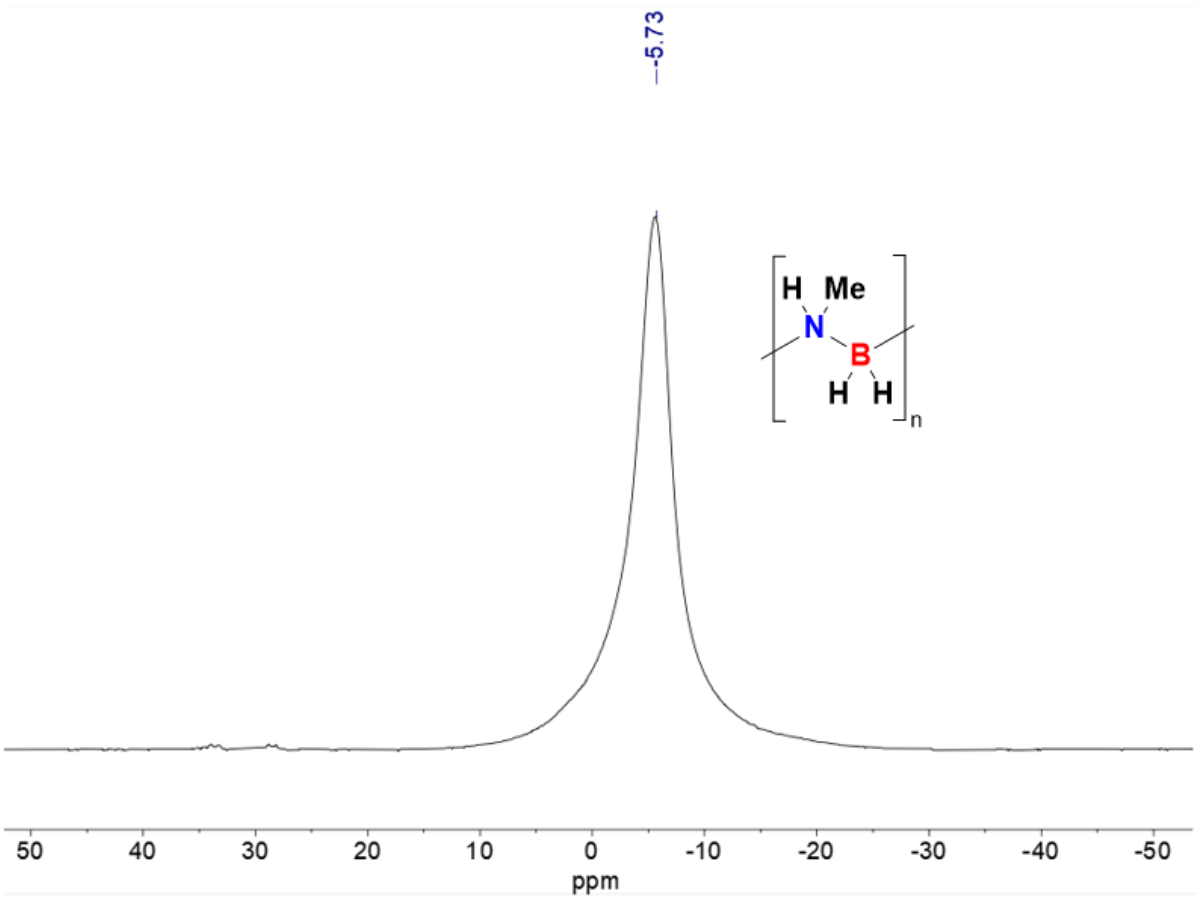

Figure 235. In-situ ^{11}B NMR of the catalysis mixture upon dehydrocoupling of methylamine-borane with Ru($^{i}Pr_2PCH_2CH_2NH_2)_2(\kappa^1$-$BH_4)H$ (**13**) with 0.01 mol dm^{-3} of $MeNH_2$. Selective dehydropolymerisation to poly(*N*-methylaminoborane) shown. Catalyst loading at 0.03 mol% relative to methylamine-borane, 1 mol dm^{-3} methylamine borane in THF.

5.3.11 Dehydropolymerisation of ethyl amine-borane with *P,P-cis*-Ru(^{i}Pr$_2$PCH$_2$CH$_2$NH$_2$)$_2$Cl$_2$ (8) and MeNH$_2$

6.2 mg (0.0125 mmol, 0.5 mol%) of *P,P-cis*-Ru(^{i}Pr$_2$PCH$_2$CH$_2$NH$_2$)$_2$Cl$_2$ (**8**) was weighed into an ampoule and dissolved in 2.5 cm^3 of toluene. Separately 147 mg (2.5 mmol) of recrystallised ethyl amine-borane was weighed into a jacketed Schlenk which was then temperature equilibrated to 20 °C and connected to an upturned water-filled burette to collect the produced H$_2$ gas (**Figure 229**). The *P,P-cis*-Ru(^{i}Pr$_2$PCH$_2$CH$_2$NH$_2$)$_2$Cl$_2$ (**8**) solution was added to the ethyl amine-borane and stirred at 400 rpm. This was immediately followed by the addition of MeNH$_2$ (62.5 µl of 2 mol dm^{-3} in THF) to the catalysis mixture (0.05 mol dm^{-3} of NH$_2$Me in the reaction mixture), to initiate turnover. The volume of evolved H$_2$ was recorded by the burette. Upon completion of H$_2$ evolution, an *in-situ* NMR sample was taken and analysed by ^{1}H, ^{31}P{^{1}H} and ^{11}B NMR spectroscopies. The catalysis mixture was then quenched in-air and then the THF solvent evaporated in-vacuo to leave yellow solid poly(*N*-ethylaminoborane), 0.081 g (57% recovered yield), 99% conversion and 94% selectivity observed by in situ ^{11}B NMR spectroscopy. This poly(*N*-ethylaminoborane) was then analysed by GPC (M_n = 118,600 g mol^{-1}, dispersity = 1.41).

^{11}B NMR (600 MHz, toluene-H$_8$) δ –7.16 (s, br, N–BH$_2$–N).

5.3.12 Dehydropolymerisation of *n*-propyl amine-borane with *P,P-cis*-Ru(^{i}Pr$_2$PCH$_2$CH$_2$NH$_2$)$_2$Cl$_2$ (8) and MeNH$_2$

6.2 mg (0.0125 mmol, 0.5 mol%) of *P,P-cis*-Ru(^{i}Pr$_2$PCH$_2$CH$_2$NH$_2$)$_2$Cl$_2$ (**8**) was weighed into an ampoule and dissolved in 2.5 cm^3 of toluene. Separately 182 mg (2.5 mmol) of recrystallised *n*-propyl amine-borane was weighed into a jacketed Schlenk which was then temperature equilibrated to 20 °C and connected to an upturned water-filled burette to collect the produced H$_2$ gas (**Figure 229**). The *P,P-cis*-Ru(^{i}Pr$_2$PCH$_2$CH$_2$NH$_2$)$_2$Cl$_2$ (**8**) solution was added to the *n*-propyl amine-borane and stirred at 400 rpm. This was immediately followed by the addition of MeNH$_2$ (62.5 µl of 2 mol dm^{-3} in THF) to the catalysis mixture (0.05 mol dm^{-3} of NH$_2$Me in the reaction mixture), to initiate turnover. The volume of evolved H$_2$ was recorded by the burette. Upon completion of H$_2$ evolution, an *in-situ* NMR sample was taken and analysed by ^{1}H, ^{31}P{^{1}H} and ^{11}B NMR spectroscopies. The catalysis mixture was then quenched in-air and then the toluene solvent was evaporated in-vacuo to leave yellow solid poly(*N*-n-propylaminoborane), 0.087 g (49% recovered yield), 99% conversion and selectivity observed by in-situ ^{11}B NMR spectroscopy. This poly(*N*-*n*-propylaminoborane) was then analysed by GPC (M_n = 115,800 g mol^{-1}, dispersity = 1.39).

^{11}B NMR (600 MHz, toluene-H$_8$) δ –6.79 (s, br, N–BH$_2$–N).

5.3.13 Dehydropolymerisation of methyl amine-borane with *P,P-cis*-Ru(^{i}Pr$_2$PCH$_2$CH$_2$NH$_2$)$_2$Cl$_2$ (8) and MeNH$_2$, recharge experiment

3.1 mg (0.0063 mmol) of *P,P-cis*-Ru(^{i}Pr$_2$CH$_2$CH$_2$NH$_2$)$_2$Cl$_2$ (**8**) was weighed into an ampoule and dissolved in 12.5 cm^3 of THF to make a stock solution. Separately 112 mg (2.5 mmol) of recrystallised methyl amine-borane was weighed into a jacketed Schlenk which was then temperature equilibrated to 20 °C and connected to an upturned water-filled burette to collect the produced H_2 gas. 0.85 cm^3 of THF was added to the amine-borane, stirred at 400 rpm, followed by 1.65 cm^3 of the *P,P-cis*-Ru(^{i}Pr$_2$CH$_2$CH$_2$NH$_2$)$_2$Cl$_2$ (**8**) stock solution (containing 0.00083 mmol of precatalyst), resulting in a catalyst concentration of 0.00033 mol dm^{-3} (0.033 mol%) in a total volume of 2.5 cm^3 of THF. MeNH$_2$ (12.5 µl of 2 mol dm^{-3} in THF) was then immediately added to the catalysis mixture, 30 equivalents relative to the catalyst (0.01 mol dm^{-3} in the reaction mixture), to initiate turnover. The volume of evolved H_2 was recorded by the burette (**Figure 236**). Upon completion of H_2 evolution, the reaction mixture was transferred onto a second equivalent of recrystallised methyl amine-borane in a jacketed Schlenk, also temperature equilibrated to 20 °C and connected to an upturned water-filled burette to collect the produced H_2 gas. This experiment was repeated twice so that both kinetics data and polymer molecular weight data could be recorded. To record polymer molecular weight data, after H_2 evolution was complete, the catalysis mixture was quenched in-air by the addition of ~50 cm^3 of pentane, resulting in the precipitation of white poly(*N*-methylaminoborane), which was isolated by filtration and dried in-vacuo to give a white solid (50 – 60 mg per charge, 50-60% recovered yield). This poly(*N*-methylaminoborane) was then analysed by GPC (**Table 8**).

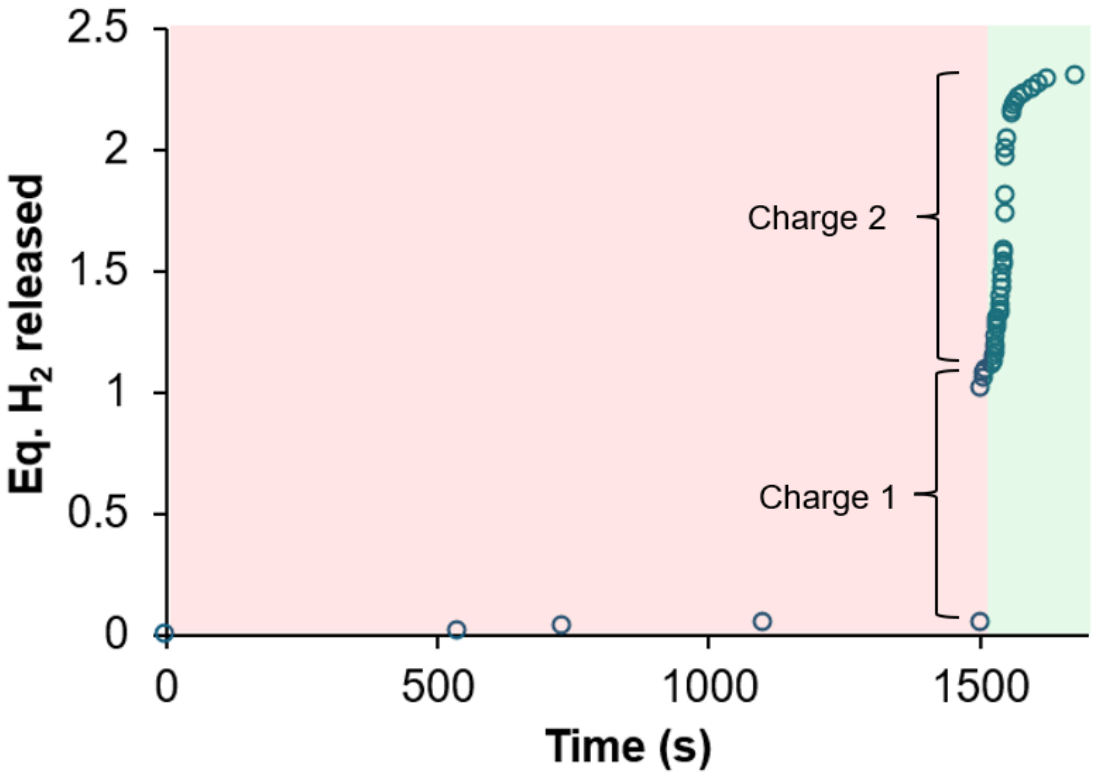

Figure 236. The H_2 evolution plot obtained from the dehydropolymerisation of methylamine-borane by *P,P-cis*-Ru(^{i}Pr$_2$CH$_2$CH$_2$NH$_2$)$_2$Cl$_2$ (**8**) with 0.01 mol dm^{-3} of $MeNH_2$, (first, red section), followed by a further charge of methylamine borane (second green section). The first charge shows the typical long induction period. The second charge shows almost no induction period. Catalyst loading at 0.033 mol% relative to methyl amine-borane (0.0003 mol dm^{-3} catalyst), 1 mol dm^{-3} methylamine borane in THF in each charge.

Catalyst	$H_3B{\cdot}NMeH_2$ concentration (mol dm^{-3})	Catalyst mol%	Catalyst concentration (mol dm^{-3})	$MeNH_2$ concentration (mol dm^{-3})	M_n (mol dm^{-3})	M_w (mol dm^{-3})	Đ
1 Charge 1	1	0.033	0.00033	0.01	168,500	286,600	1.70
1 Charge 2	1	0.033	0.00033	0.01	164,000	273,600	1.67

Table 8. Poly(*N*-methylaminoborane) M_n, M_w, and Đ (dispersity) data for the dehydopolymerisation of *N*-methylamine borane with *P,P-cis*-Ru(^{i}Pr$_2$CH$_2$CH$_2$NH$_2$)$_2$Cl$_2$ (**8**) recharge experiment: methylamine-borane charge 1 & 2, as measured by GPC.

5.4 Crystallography

Single-crystal X-Ray diffraction data was performed on a Rigaku SuperNova diffractometer (Cu-Kα radiation, λ = 1.54184 Å) at the University of York, equipped with a nitrogen gas Oxford Cryostream unit.[8] Diffraction images from raw frame data were reduced using the CryAlisPro suite of programmes. The structures were solved using SHELXT[9] and refined by full convergence on F^2 against all independent reflections by full-matrix least-squares using SHELXL[10] 2018/3 through the Olex2 GUI.[11] All non-hydrogen atoms were refined anisotropically and hydrogen atoms were geometrically placed and allowed to ride on their parent atoms, unless otherwise stated (see specific details for each molecular structure in the text and supplementary CIF information). Disordered groups and solvent molecules were restrained to maintain sensible chemical geometries.

5.4.1 Additional crystallographic details

$Rh(PN^HP^iPr)(\kappa^1\text{-}BH_4)H_2$ (**4**) crystallised without residual solvent in the lattice. One of the ligand isopropyl groups exhibited rotational disorder which was satisfactorily modelled. All 4 B–H hydride atoms were located in the Fourier difference map, freely refined and then restrained with a DFIX command to 1.1 Å relative to the boron.

$Rh\{\kappa^3\text{-}(Cy_2PCH_2CH_2)_2NH\}H_2Cl$ (**7**) crystallised with 1 equivalent of pentane per asymmetric unit which was highly disordered and modelled via SQUEEZE. A large (2.38 e $Å^{-3}$) residual electron density peak is present adjacent to hydride H1, likely due to a superimposed positional isomer component (~15 %) where the Cl occupies the position trans to the ligand N atom. The Rh-H1 distance was restrained to 1.7 Å by a DFIX command to prevent excessive lengthening caused by the adjacent residual electron density peak. The proton on the N–H, was located in the Fourier difference map, freely refined, and allowed to ride on the parent atom.

P,P-trans-$Ru(^iPr_2PCH_2CH_2NH_2)_2Cl_2$ (**8** trans-isomer) crystallised without residual solvent in the lattice. A large (2.52 e $Å^{-3}$) residual electron density peak is present adjacent to the phosphorous atoms due to disorder which could not be satisfactorily modelled. NH_2 protons were affixed instead of freely refined due to difficulty modelling equal N–H bond lengths.

P,P-trans-Ru(^{i}Pr$_2$PCH$_2$CH$_2$NH)$_2$ (**9**) crystallised without residual solvent in the lattice. The structure model is missing 8 high index reflections due to low intensity. Protons on the NH groups were located in the Fourier difference map, freely refined, and allowed to ride on the parent N atoms.

Ru$_2$H(μ$_2$-NHCH$_2$CH$_2$P^{i}Pr$_2$)$_2$(μ$_2$-NCH$_2$CH$_2$P^{i}Pr$_2$)(^{i}Pr$_2$PCH$_2$CH$_2$NH$_2$) (**10**) crystallised without residual solvent in the lattice. The structure model is missing 15 high index reflections due to low intensity. The Ru–H hydride was located in the Fourier difference map, allowed to ride the Ru atom and freely refined. The protons on the N=CH, NH and NH$_2$ groups were located in the Fourier difference map, freely refined, and allowed to ride on the parent atoms.

P,P-cis-Ru(^{i}Pr$_2$PCH$_2$CH$_2$NH$_2$)$_2$(OH)H·(^{i}PrOH)$_2$ (**11**·(^{i}PrOH)$_2$) crystallised with two equivalents of isopropanol hydrogen bonded to the Ru–OH, which were satisfactorily modelled. Protons on the NH$_2$ and OH groups were located in the Fourier difference map, freely refined, and allowed to ride on the parent N and O atoms. Disorder in the OH leads to the modelling of an abnormally short O–H bond (0.752 Å). The structure model is missing 9 high index reflections due to low intensity. The Ru–H hydride was located in the Fourier difference map, allowed to ride the Ru atom and freely refined.

P,P-cis-Ru(^{i}Pr$_2$PCH$_2$CH$_2$NH$_2$)$_2$(OH)H (**11**) crystallised without residual solvent in the lattice. The structure was modelled as a 1:1 inversion of the molecule upon itself. The disordered parts were restrained with SADI SIMU and ISOR restraints due to the close proximity of residual electron density peaks from each modelled part. NH$_2$ and OH protons were affixed instead of freely refined due to difficulty satisfactorily modelling these atoms within the disorder. The Ru–H hydrides were located in the Fourier difference map, allowed to ride the Ru atoms and freely refined.

P,P-cis-Ru(^{i}Pr$_2$PCH$_2$CH$_2$NH$_2$)$_2$(κ^1-BH$_4$)H (**13**) crystallised with two crystallographically independent units Ru(^{i}Pr$_2$PCH$_2$CH$_2$NH$_2$)$_2$(κ^1-BH$_4$)H per asymmetric unit and without residual solvent in the lattice. The structure model is missing 139 high index reflections due to low intensity and unusually thin crystals. Protons on the NH groups of N1, N2 & N3 were located in the difference Fourier difference map, N2 and N3 were freely refined, and allowed to ride on the parent N atoms. The protons on N1 were restrained with SADI to give similar N–H bond lengths. NH$_2$ protons on N4 were affixed instead of freely refined due to difficulty modelling these atoms. The Ru–H hydrides were

located in the Fourier difference map, allowed to ride the Ru atoms, restrained with SADI restraints to give similar Ru–H bond lengths and refined. The B–H hydrides were located in the Fourier difference map, allowed to ride the B atoms, restrained with SADI restraints to give similar B–H bond lengths and refined. 4 disordered isopropyl groups on the ligands of the unit containing Ru1 were modelled over two domains and freely refined.

5.4.2 Crystallographic tables

Table 2. Selected crystallographic and refinement data

	4	**7**
CCDC Number	N/A	N/A
Empirical formula	$C_{16}H_{43}BNP_2Rh$	$C_{28}H_{55}ClNP_2Rh \cdot 1[C5H_{12}]$
Formula weight	425.17	678.17
Temperature/K	110	110
Crystal system	triclinic	Monoclinic
Space group	P-1	*C2/c*
a/Å	8.1035 (2)	29.1684 (4)
b/Å	10.4919 (2)	19.4777 (3)
c/Å	14.0851 (3)	12.2302 (2)
α/°	71.558 (2)	90.0
β/°	84.020 (2)	96.930(1)
γ/°	81.442 (2)	90.0
Volume/Å³	1121.30 (4)	6897.62 (18)
Z	2	8
ρ_{calc}*g/cm³*	1.259	1.167
μ/mm⁻¹	7.45	5.686
F(000)	452.0	2576.0
Crystal size/mm³	0.06 × 0.05 × 0.02	× 0.10 × 0.08
Radiation	Cu Kα (λ = 1.54184)	Cu Kα (λ = 1.54184)
Reflections collected	4893	6714
Independent reflections	4557 [R_{int} = 0.040, R_{sigma} = 0.0787]	5884 [R_{int} = 0.032, R_{sigma} = 0.0967]
Data/restraints/parameters	4557/247/4	6642/314/1
Goodness-of-fit on F²	1.063	0.805
Final R indexes [I>=2σ (I)]	R_1 = 0.0309, wR_2 = 0.0787	R_1 = 0.032, wR_2 = 0.097
Final R indexes [all data]	R_1 = 0.0309, wR_2 = 0.0787	R_1 = 0.032, wR_2 = 0.097
Largest diff. peak/hole / e Å⁻³	0.68/-0.76	2.19/-0.61

Table 3. Selected crystallographic and refinement data

	***8** trans-isomer*	**9**	***10***
CCDC Number	2386380	2386379	2386381
Empirical formula	$C_{16}H_{40}Cl_2N_2P_2Ru$	$C_{16}H_{38}N_2P_2Ru$	$C_{32}H_{76}N_4P_4Ru_2$
Formula weight	494.41	421.49	842.98
Temperature/K	110.00(14)	109.95(10)	109.95(10)
Crystal system	monoclinic	triclinic	triclinic
Space group	$P2_1/c$	P-1	P-1
a/Å	11.3434(2)	6.8268(3)	11.0013(2)
b/Å	13.1508(2)	7.2199(4)	13.1780(3)
c/Å	7.72080(10)	10.6106(7)	15.0352(3)
α/°	90	105.035(5)	93.334(2)
β/°	106.264(2)	90.350(4)	91.030(2)
γ/°	90	98.223(4)	113.542(2)
Volume/Å³	1105.66(3)	499.38(5)	1992.90(8)
Z	2	1	2
ρ_{calc}*g/cm³*	1.485	1.402	1.405
μ/mm⁻¹	9.325	7.824	7.842
F(000)	516.0	222.0	888.0
Crystal size/mm³	0.11 × 0.07 × 0.06	0.13 × 0.11 × 0.03	0.09 × 0.07 × 0.03
Radiation	Cu Kα (λ = 1.54184)	Cu Kα (λ = 1.54184)	Cu Kα (λ = 1.54184)
2Θ range for data collection/°	8.12 to 153.834	8.638 to 153.436	7.336 to 154.008
Index ranges	-13 ≤ h ≤ 14, -16 ≤ k ≤ 16, -9 ≤ l ≤ 8	-7 ≤ h ≤ 8, -9 ≤ k ≤ 8, -13 ≤ l ≤ 12	-13 ≤ h ≤ 13, -16 ≤ k ≤ 16, -11 ≤ l ≤ 19
Reflections collected	11281	4722	23871
Independent reflections	2288 [R_{int} = 0.0343, R_{sigma} = 0.0266]	2005 [R_{int} = 0.0290, R_{sigma} = 0.0283]	8098 [R_{int} = 0.0435, R_{sigma} = 0.0462]
Data/restraints/parameters	2288/0/110	2005/0/101	8098/0/415
Goodness-of-fit on F²	1.063	1.103	1.056
Final R indexes [I>=2σ (I)]	R_1 = 0.0619, wR_2 = 0.1564	R_1 = 0.0339, wR_2 = 0.0911	R_1 = 0.0290, wR_2 = 0.0659
Final R indexes [all data]	R_1 = 0.0653, wR_2 = 0.1593	R_1 = 0.0339, wR_2 = 0.0911	R_1 = 0.0348, wR_2 = 0.0679
Largest diff. peak/hole / e Å⁻³	2.64/-1.70	1.51/-0.90	0.52/-0.73

Table 4. Selected crystallographic and refinement data

	11·*(ⁱPrOH)₂*	***11***	***13***
CCDC Number	2386387	2386384	N/A
Empirical formula	$C_{22}H_{58}N_2O_3P_2Ru$	$C_{16}H_{42}N_2OP_2Ru$	$C_{16}H_{45}BN_2P_2Ru$
Formula weight	561.71	441.52	878.71
Temperature/K	110.00(10)	110.00(10)	109.95(10)
Crystal system	triclinic	trigonal	monoclinic
Space group	P-1	$P3_2$	$P2_1/c$
a/Å	10.0257(2)	14.10010(10)	9.5408(3)
b/Å	11.7788(2)	14.10010(10)	18.1474(9)
c/Å	13.1244(2)	9.32090(10)	26.8151(12)
α/°	101.204(2)	90	90
β/°	103.290(2)	90	96.847(4)
γ/°	94.884(2)	120	90
Volume/Å³	1465.87(5)	1604.84(3)	4609.7(3)
Z	2	3	4
ρ_{calc}*g/cm³*	1.273	1.371	1.266
μ/mm⁻¹	5.530	7.361	6.788
F(000)	604.0	702.0	1872.0
Crystal size/mm³	0.09 × 0.08 × 0.04	0.24 × 0.16 × 0.12	0.3 × 0.04 × 0.03
Radiation	Cu Kα (λ = 1.54184)	Cu Kα (λ = 1.54184)	Cu Kα (λ = 1.54184)
2Θ range for data collection/°	7.096 to 154.084	7.24 to 154.276	8.238 to 136.49
Index ranges	-12 ≤ h ≤ 10, -14 ≤ k ≤ 14, -12 ≤ l ≤ 16	-17 ≤ h ≤ 16, -14 ≤ k ≤ 17, -11 ≤ l ≤ 11	-9 ≤ h ≤ 11, -21 ≤ k ≤ 17, -31 ≤ l ≤ 32
Reflections collected	15708	17416	23430
Independent reflections	5913 [R_{int} = 0.0446, R_{sigma} = 0.0476]	4369 [R_{int} = 0.0355, R_{sigma} = 0.0252]	8308 [R_{int} = 0.0966, R_{sigma} = 0.0904]
Data/restraints/ parameters	5913/0/293	4369/20/429	8308/9/497
Goodness-of-fit on F²	1.101	1.070	1.066
Final R indexes [I>=2σ (I)]	R_1 = 0.0321, wR_2 = 0.0832	R_1 = 0.0358, wR_2 = 0.0883	R_1 = 0.0630, wR_2 = 0.1549
Final R indexes [all data]	R_1 = 0.0354, wR_2 = 0.0848	R_1 = 0.0361, wR_2 = 0.0885	R_1 = 0.1056, wR_2 = 0.1747
Largest diff. peak/hole / e Å⁻³	0.76/-0.92	0.21/-0.38	0.86/-1.48

5.5 Computational details

The computational analysis of *P,P-trans*-Ru(^{i}Pr$_2$PCH$_2$CH$_2$NH)$_2$ (**9**) was performed by Dr M. Arif Sajjad under the supervision of Prof. Stuart Macgregor at the university of St. Andrews.

DFT calculations were run with Gaussian 16 (Revision C.01). [12] Ru and P centres were described with Stuttgart RECPs and associated basis sets with added d-orbital polarisation (z = 0.387) on the latter. [13, 14] 6-31G** basis sets used for all other atoms. [15, 16] Optimizations were run with both the BP86, and B3LYP functionals. [17-19] All stationary points were fully characterised via analytical frequency calculations as either minima (all positive eigenvalues) or transition states (one negative eigenvalue). Electronic energies were recomputed with the def2-TZVP, basis set, corrected for the effects of THF solvent using the PCM approach and for dispersion (D3 with Becke-Johnson damping). [20-24] TD-DFT calculations were performed on the BP86-optimised geometries using the BP86, B3LYP and CAM-B3LYP functionals. TD-DFT spectra and orbital plots were produced with Chemcraft. [25, 26]

5.5.1 Computed geometries and spin states of *P,P-trans*-Ru(^{i}Pr$_2$PCH$_2$CH$_2$NH)$_2$ (9)

Geometries were optimised in both the singlet and triplet states with both the BP86 and B3LYP functionals. For the singlet state both functionals provided square-planar geometries with C_i symmetry. For the triplet state a square-planar C_i minimum was also located with B3LYP, but this geometry corresponded to a transition state with BP86. A slightly lower C_1 form with a reduced N-Ru-N angle of 165° was located as a true minimum. With both functionals the singlet spin state was computed to be significantly more stable (BP86: $DG^{S\rightarrow T}$ = +16.6 kcal/mol; B3LYP: $DG^{S\rightarrow T}$ = +9.4 kcal/mol).

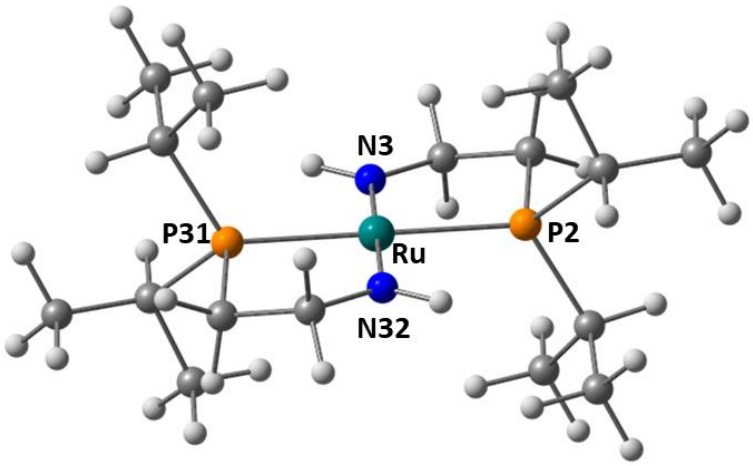

Ru−P2	2.316
Ru−P31	2.316
Ru−N3	1.940
Ru−N32	1.940
P2-Ru-P31	180.0
N3-Ru-N32	180.0
P2-Ru-N3	82.5
P2-Ru-N32	97.5
P31-Ru-N3	82.5
P31-Ru-N32	97.5

Figure 237. Optimised structure (BP86 functional) for Ru(^{i}Pr$_2$PCH$_2$CH$_2$NH)$_2$ (**9**) in the singlet spin state with tabulated data for selected distances (Å) and angles (°).

5.5.2 Time-Dependent Density Functional Theory (TDDFT) Calculations for *P,P-trans*-Ru(^{i}Pr$_2$PCH$_2$CH$_2$NH)$_2$ (9)

TD-DFT analyses were performed on the geometry computed with the BP86 functional in the singlet spin state. Spectra were simulated with the BP86, B3LYP and CAM=B3LYP functionals. Of these the BP86 gave the best agreement with experiment in terms of the excitation energies.

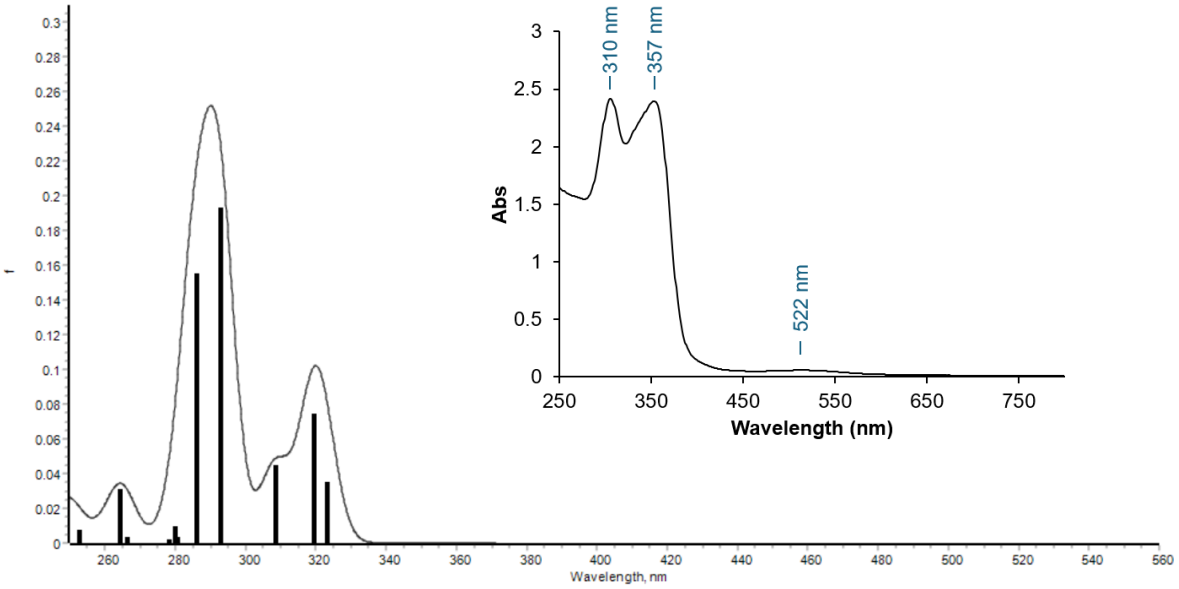

Figure 238. UV-vis spectrum for *P,P-trans*-Ru(^{i}Pr$_2$PCH$_2$CH$_2$NH)$_2$ (**9**) computed at B3LYP level. Inset shows the experimental spectrum.

Table 5. UV-vis spectral data for *P,P-trans*-Ru(^{i}Pr$_2$PCH$_2$CH$_2$NH)$_2$ (**9**) computed with TDDFT at B3LYP level.

Excited state	label	Energy (eV)	Wavelength (nm)	Oscillator strength (f)	Orbital transitions	Transition strength
1	^1A_g	1.4006	885.24	0.0000	87 -> 88	0.70725
2	^1A_g	2.1199	584.85	0.0000	86 -> 88	0.70473
3	^1A_g	2.3331	531.42	0.0000	85 -> 88	0.69886
4	^1A_g	3.7138	333.85	0.0000	87 -> 89	0.68913
					87 -> 94	-0.11917
5	^1A_u	3.8406	322.82	0.0351	87 -> 90	0.67773
					87 -> 91	0.16766
6	^1A_u	3.8862	319.04	0.0749	87 -> 90	-0.16386
					87 -> 91	0.67590
7	^1A_u	4.0214	308.31	0.0452	83 -> 88	0.60088
					84 -> 88	0.35567
8	^1A_u	4.2372	292.61	0.1935	83 -> 88	-0.35029
					84 -> 88	0.54641
					86 -> 90	-0.12123
					86 -> 91	-0.20703
9	^1A_g	4.2588	291.12	0.0000	86 -> 89	0.64149
					87 -> 94	-0.27055
10	^1A_g	4.2770	289.89	0.0000	86 -> 89	0.28365
					87 -> 89	0.11846
					87 -> 94	0.61498
11	^1A_u	4.3411	285.60	0.1556	83 -> 88	-0.10962
					84 -> 88	0.21320
					86 -> 90	0.35442
					86 -> 91	0.54336
12	^1A_u	4.4215	280.41	0.0036	86 -> 90	0.59249
					86 -> 91	-0.37744
13	^1A_u	4.4343	279.60	0.0098	87 -> 92	0.68035
					87 -> 93	-0.16342
14	^1A_u	4.4634	277.78	0.0019	85 -> 90	0.33486
					85 -> 91	0.58281
					85 -> 93	-0.18905
15	^1A_g	4.4737	277.14	0.0000	85 -> 89	0.64715
					85 -> 94	-0.26037
16	^1A_u	4.6614	265.98	0.0037	87 -> 92	0.16811
					87 -> 93	0.67559
17	^1A_u	4.6941	264.13	0.0308	85 -> 90	0.60778
					85 -> 91	-0.33922
18	^1A_g	4.7883	258.93	0.0000	85 -> 94	-0.16844
					86 -> 94	0.65105
19	^1A_g	4.8593	255.15	0.0000	82 -> 88	-0.18692
					84 -> 91	0.11578
					85 -> 89	0.24301
					85 -> 94	0.55776
					85 -> 96	0.12333
					86 -> 94	0.18975
20	^1A_u	4.9146	252.28	0.0079	84 -> 89	0.68749

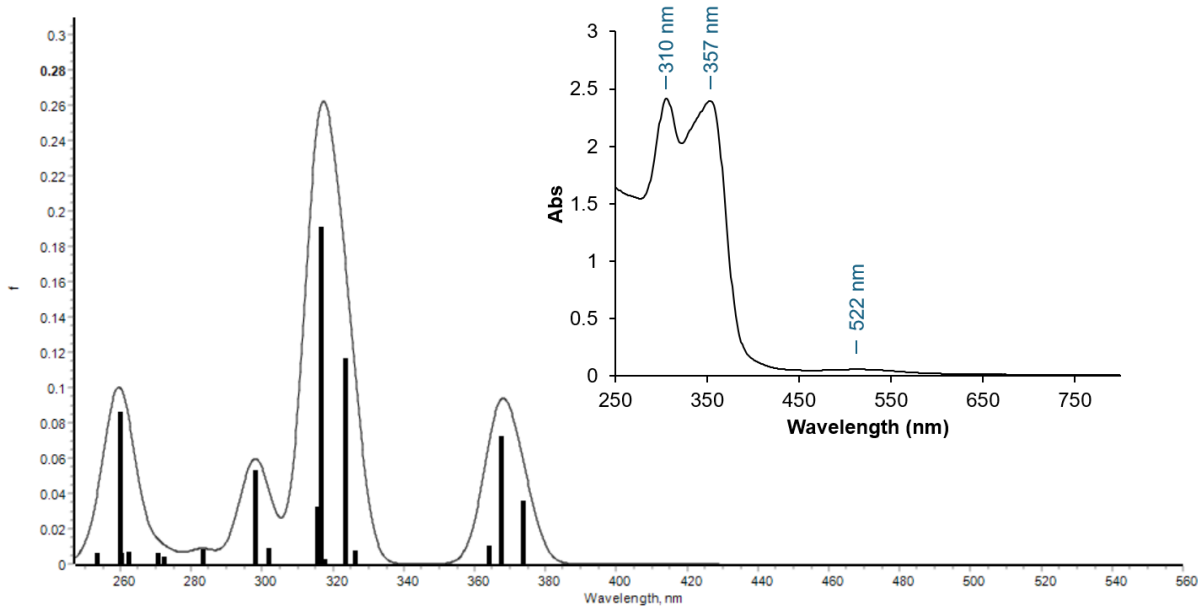

Figure 239. UV-vis spectrum for *P,P-trans*-Ru(^{i}Pr$_2$PCH$_2$CH$_2$NH)$_2$ (**9**) computed at BP86 level. Inset shows the experimental spectrum.

Table 6. UV-vis spectral data for *P,P-trans*-Ru(^{i}Pr$_2$PCH$_2$CH$_2$NH)$_2$ (**9**) computed with TDDFT at BP86 level.

Excited state	label	Energy (eV)	Wavelength (nm)	Oscillator strength (f)	Orbital transitions	Transition strength
1	^1A_g	1.5893	780.11	0.0000	87 -> 88	0.70820
2	^1A_g	2.2512	550.75	0.0000	86 -> 88	0.70640
3	^1A_g	2.4510	505.84	0.0000	85 -> 88	0.70292
4	^1A_g	3.2854	377.38	0.0000	87 -> 89	0.70117
5	^1A_u	3.3209	373.34	0.0358	87 -> 89	-0.48990
					87 -> 91	0.50339
6	^1A_u	3.3759	367.26	0.0725	83 -> 88	0.13864
					87 -> 89	0.49199
					87 -> 91	0.47296
7	^1A_u	3.4092	363.67	0.0105	83 -> 88	0.65833
					84 -> 88	0.19940
					87 -> 91	-0.13610
8	^1A_u	3.8018	326.12	0.0079	86 -> 89	-0.18025
					86 -> 93	0.67787
9	^1A_g	3.8344	323.34	0.0000	86 -> 90	0.69973
10	^1A_u	3.8362	323.19	0.1164	83 -> 88	0.10875
					84 -> 88	-0.32109
					86 -> 89	0.56382
					87 -> 93	0.19669
11	^1A_u	3.9043	317.56	0.0029	85 -> 89	0.65837
					86 -> 91	-0.24482
12	^1A_u	3.9207	316.23	0.1913	83 -> 88	-0.16943
					84 -> 88	0.52636
					85 -> 89	-0.15698
					85 -> 91	-0.10267
					86 -> 89	0.28288
					86 -> 91	-0.22211
13	^1A_u	3.9332	315.22	0.0327	84 -> 88	0.16665
					85 -> 89	0.19985
					86 -> 89	0.18341
					86 -> 91	0.61967
14	^1A_g	3.9345	315.12	0.0000	85 -> 90	0.10158
					87 -> 92	0.69093
15	^1A_g	4.0292	307.71	0.0000	85 -> 90	0.69938
					87 -> 92	-0.10091
16	^1A_u	4.1123	301.50	0.0091	87 -> 94	0.69940
17	^1A_u	4.1647	297.70	0.0532	85 -> 91	0.68475
					86 -> 89	0.11756
18	^1A_u	4.3786	283.16	0.0085	86 -> 93	0.70271
19	^1A_g	4.5114	274.82	0.0000	86 -> 92	0.67958
20	^1A_g	4.5445	272.82	0.0000	82 -> 88	-0.36625
					84 -> 89	0.41023
					85 -> 92	0.39958

Table 6. (cont)

Excited state	label	Energy (eV)	Wavelength (nm)	Oscillator strength (f)	Orbital transitions	Transition strength
21	^1A_u	4.5588	271.97	0.0038	87 -> 95	0.70599
22	^1A_u	4.5879	270.24	0.0064	85 -> 93	0.70511
23	^1A_g	4.6900	264.36	0.0000	82 -> 88	0.15817
					84 -> 89	-0.32049
					85 -> 92	0.56501
					87 -> 96	-0.14506
24	^1A_u	4.7296	262.14	0.0066	84 -> 90	0.69980
25	^1A_u	4.7701	259.92	0.0059	81 -> 88	0.69120
					86 -> 94	0.12464
26	^1A_u	4.7768	259.55	0.0866	81 -> 88	-0.12661
					85 -> 95	-0.10247
					86 -> 94	0.66893
27	^1A_g	4.8143	257.53	0.0000	80 -> 88	0.53403
					82 -> 88	0.14575
					84 -> 89	0.26105
					84 -> 91	-0.30205
					87 -> 96	-0.13435
28	^1A_g	4.8445	255.93	0.0000	80 -> 88	0.35448
					84 -> 91	0.60022
					87 -> 96	0.10390
29	^1A_g	4.8701	254.58	0.0000	80 -> 88	0.13431
					84 -> 89	-0.14387
					84 -> 91	-0.18405
					87 -> 96	0.60482
					87 -> 97	-0.21313
30	^1A_u	4.8941	253.33	0.0060	85 -> 94	0.70265
31	^1A_u	4.9198	252.01	0.0108	79 -> 88	0.68971

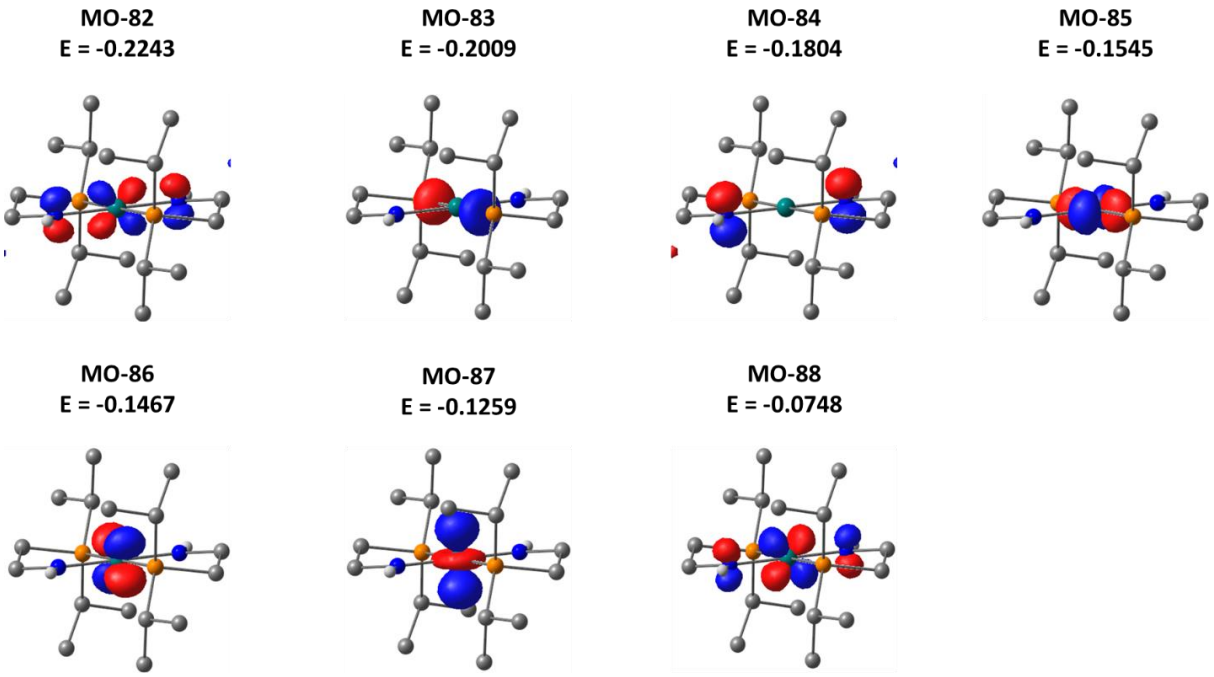

Figure 240. Selected molecular orbitals (MOs) along and energies (a.u) involved in electronic transitions in computed UV-vis spectrum at BP86 level for *P,P-trans*-Ru(^{i}Pr$_2$PCH$_2$CH$_2$NH)$_2$ (9). Surface contour value = 0.10 a.u. MO-89 to MO-97 inclusive are heavily delocalised onto the phosphine substituents and are not shown.

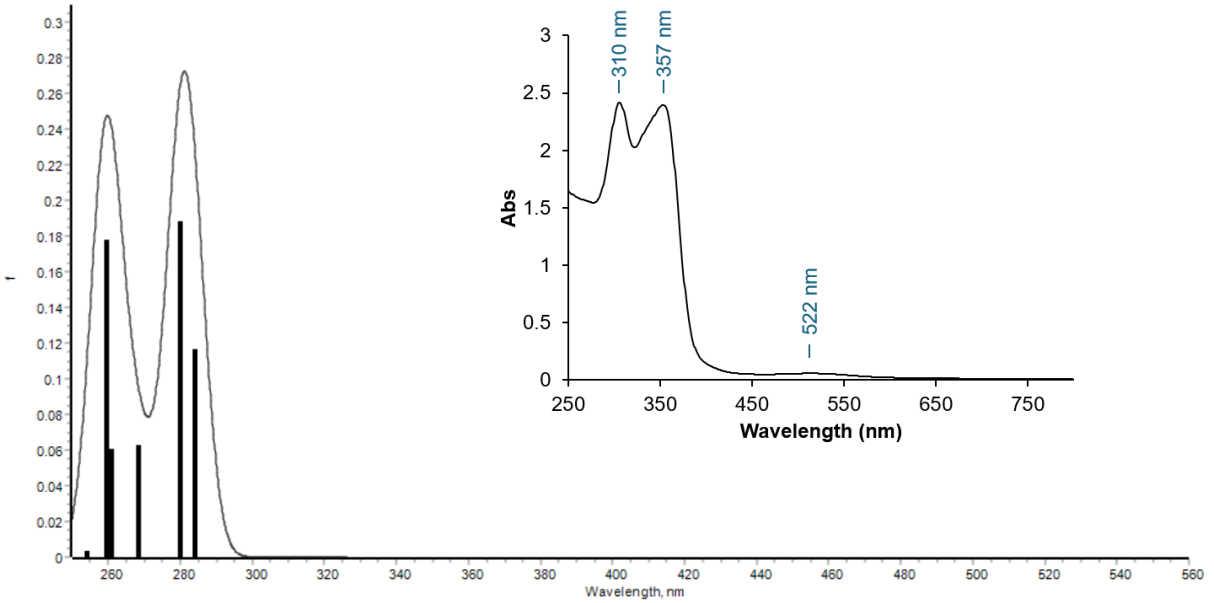

Figure 241. UV-vis spectrum for *P,P-trans*-Ru(^{i}Pr$_2$PCH$_2$CH$_2$NH)$_2$ (9) computed at CAM-B3LYP level. Inset shows the experimental spectrum.

Table 7. UV-vis spectral data for *P,P-trans*-Ru(^{i}Pr$_2$PCH$_2$CH$_2$NH)$_2$ (9) computed with TDDFT at CAM-B3LYP level.

Excited state	label	Energy (eV)	Wavelength (nm)	Oscillator strength (f)	Orbital transitions	Transition strength
1	^1A_g	1.2921	959.57	0.0000	87 -> 88	0.69675
					87 -> 89	0.11334
2	^1A_g	2.0272	611.61	0.0000	86 -> 88	0.69168
					86 -> 89	0.11282
3	^1A_g	2.2437	552.59	0.0000	85 -> 88	0.68511
					85 -> 89	0.11296
4	^1A_u	4.3673	283.89	0.1164	87 -> 91	0.58370
					87 -> 93	-0.37127
5	^1A_g	4.3885	282.52	0.0000	82 -> 88	-0.10534
					87 -> 89	-0.34134
					87 -> 94	0.54016
					87 -> 96	0.19149
6	^1A_u	4.4325	279.72	0.1882	83 -> 88	0.28764
					84 -> 88	0.62190
7	^1A_u	4.6275	267.93	0.0627	83 -> 88	0.61367
					84 -> 88	-0.26618
					87 -> 90	-0.10793
8	^1A_u	4.7609	260.42	0.0610	86 -> 91	0.28563
					86 -> 93	-0.18265
					87 -> 90	0.58747
					87 -> 95	-0.13579
9	^1A_g	4.7775	259.52	0.0000	87 -> 88	-0.10058
					87 -> 89	0.57977
					87 -> 94	0.32265
					87 -> 97	0.14628
10	^1A_u	4.7839	259.17	0.1784	83 -> 88	-0.10604
					84 -> 88	0.13477
					86 -> 91	0.49311
					86 -> 93	-0.31397
					87 -> 90	-0.31264
11	^1A_g	4.8765	254.25	0.0000	85 -> 89	-0.20808
					85 -> 94	0.53761
					85 -> 96	0.21164
					85 -> 97	0.11397
					86 -> 94	-0.20808
12	^1A_u	4.8881	253.64	0.0034	83 -> 88	0.10155
					85 -> 91	0.53629
					85 -> 93	-0.42051
13	^1A_u	4.9593	250.01	0.0000	85 -> 94	0.20232
					86 -> 89	-0.25470
					86 -> 94	0.53962
					86 -> 96	0.17522
					86 -> 97	0.10517

5.5.2 Computed Cartesian coordinates (Å) and energies (hartrees) for all species relating to *P,P-trans*-Ru(^{i}Pr$_2$PCH$_2$CH$_2$NH)$_2$ (9)

(i) BP86 Optimisation
2 (singlet)
E_{SCF} = -850.326462079
G = -849.875376
E_{corr} = -1520.41581793916
59
Ru 0.00000 0.00000 0.00000
P -0.80748 0.51524 2.10909
N -1.47815 1.12299 -0.56292
H -1.67224 1.33234 -1.54887
C 0.08446 1.81058 3.18890
H -0.56822 2.03283 4.05536
C -1.26020 -0.84157 3.37847
H -0.27182 -1.22163 3.70562
C -2.03288 -0.35016 4.61504
H -1.47549 0.40744 5.19059
H -2.24320 -1.19358 5.29849
H -3.00588 0.08855 4.33094
C -2.47420 1.32137 1.71225
H -3.22371 0.51357 1.77622
H -2.74723 2.09740 2.44794
C 1.42594 1.24483 3.68877
H 1.29593 0.36394 4.34115
H 1.97596 2.00725 4.27022
H 2.06023 0.95102 2.83294
C -2.42782 1.87818 0.27887
H -3.44405 1.85008 -0.16749
H -2.13279 2.94975 0.30392
C 0.30054 3.10123 2.37898
H 0.87169 2.88650 1.45849
H 0.86322 3.84167 2.97736
H -0.65359 3.56917 2.08213
C -1.99287 -1.99377 2.66652
H -3.00808 -1.69156 2.35175
H -2.10441 -2.85884 3.34590
H -1.44738 -2.31209 1.76227
P 0.80748 -0.51524 -2.10909
N 1.47815 -1.12299 0.56292
H 1.67224 -1.33234 1.54887
C -0.08446 -1.81058 -3.18890
H 0.56822 -2.03283 -4.05536
C 1.26020 0.84157 -3.37847
H 0.27182 1.22163 -3.70562
C 2.03288 0.35016 -4.61504
H 1.47549 -0.40744 -5.19059
H 2.24320 1.19358 -5.29849
H 3.00588 -0.08855 -4.33094
C 2.47420 -1.32137 -1.71225
H 3.22371 -0.51357 -1.77622
H 2.74723 -2.09740 -2.44794
C -1.42594 -1.24483 -3.68877
H -1.29593 -0.36394 -4.34115
H -1.97596 -2.00725 -4.27022
H -2.06023 -0.95102 -2.83294
C 2.42782 -1.87818 -0.27887
H 3.44405 -1.85008 0.16749
H 2.13279 -2.94975 -0.30392
C -0.30054 -3.10123 -2.37898
H -0.87169 -2.88650 -1.45849
H -0.86322 -3.84167 -2.97736
H 0.65359 -3.56917 -2.08213
C 1.99287 1.99377 -2.66652
H 3.00808 1.69156 -2.35175
H 2.10441 2.85884 -3.34590
H 1.44738 2.31209 -1.76227
2 (triplet C_i TS)
E_{SCF} = -850.298822434
G = -849.850193
E_{corr} = -1520.38654101725
59
Ru 0.00000 0.00000 0.00000
P -0.82657 0.53855 2.11274
N -1.62309 1.06686 -0.57494
H -1.81160 1.28638 -1.55671
C 0.09051 1.82519 3.17641
H -0.56281 2.07535 4.03472
C -1.25407 -0.83197 3.36947
H -0.26216 -1.18111 3.71714
C -2.07025 -0.36067 4.58553
H -1.55643 0.42963 5.15799
H -2.25299 -1.20322 5.27771
H -3.05654 0.03015 4.27931
C -2.49660 1.33522 1.72352
H -3.23890 0.51834 1.76553
H -2.77904 2.09486 2.47329
C 1.41790 1.23909 3.69113
H 1.26551 0.38637 4.37460
H 1.98976 2.00651 4.24409
H 2.04141 0.89605 2.84555
C -2.44147 1.91478 0.29643
H -3.47865 2.00549 -0.09380
H -2.05210 2.95990 0.35584
C 0.33739 3.09933 2.34850
H 0.93732 2.87028 1.44966
H 0.89229 3.84497 2.94709
H -0.60328 3.56857 2.01492
C -1.93427 -2.00478 2.63932
H -2.93220 -1.72198 2.25909
H -2.07346 -2.85915 3.32670
H -1.33092 -2.34225 1.77941
P 0.82657 -0.53855 -2.11274
N 1.62309 -1.06686 0.57494
H 1.81160 -1.28638 1.55671
C -0.09051 -1.82519 -3.17641
H 0.56281 -2.07535 -4.03472
C 1.25407 0.83197 -3.36947
H 0.26216 1.18111 -3.71714
C 2.07025 0.36067 -4.58553
H 1.55643 -0.42963 -5.15799
H 2.25299 1.20322 -5.27771
H 3.05654 -0.03015 -4.27931
C 2.49660 -1.33522 -1.72352
H 3.23890 -0.51834 -1.76553
H 2.77904 -2.09486 -2.47329

C	-1.41790	-1.23909	-3.69113
H	-1.26551	-0.38637	-4.37460
H	-1.98976	-2.00651	-4.24409
H	-2.04141	-0.89605	-2.84555
C	2.44147	-1.91478	-0.29643
H	3.47865	-2.00549	0.09380
H	2.05210	-2.95990	-0.35584
C	-0.33739	-3.09933	-2.34850
H	-0.93732	-2.87028	-1.44966
H	-0.89229	-3.84497	-2.94709
H	0.60328	-3.56857	-2.01492
C	1.93427	2.00478	-2.63932
H	2.93220	1.72198	-2.25909
H	2.07346	2.85915	-3.32670
H	1.33092	2.34225	-1.77941

2 (triplet C_1 minimum)

E_{SCF} = -850.299142662
G = -849.851134
E_{corr} = -1520.38626460985

59

Ru	-0.00230	0.02623	0.00375
P	2.32384	0.04836	0.15497
N	0.16472	-0.00209	2.01888
H	-0.65135	0.12735	2.62393
C	3.27561	1.64123	-0.28050
H	4.31662	1.51143	0.07370
C	3.37867	-1.31481	-0.66574
H	3.32061	-1.07176	-1.74501
C	4.85726	-1.32733	-0.24046
H	5.36840	-0.37470	-0.45850
H	5.40519	-2.12523	-0.77490
H	4.96130	-1.52780	0.84044
C	2.62930	-0.19548	2.00548
H	2.75261	-1.28284	2.15449
H	3.55382	0.30514	2.34240
C	3.27588	1.86722	-1.80323
H	3.81735	1.07450	-2.34698
H	3.76279	2.82832	-2.05025
H	2.24185	1.90213	-2.19115
C	1.38734	0.29775	2.77121
H	1.36503	-0.18498	3.77247
H	1.50388	1.39108	2.96706
C	2.64511	2.83824	0.45386
H	1.58286	2.95350	0.17252
H	3.17156	3.77353	0.18840
H	2.69110	2.72568	1.55004
C	2.70806	-2.68507	-0.45562
H	2.73519	-2.99061	0.60564
H	3.23525	-3.46446	-1.03581
H	1.65152	-2.66312	-0.77134
P	-2.32747	-0.01376	-0.16038
N	-0.15634	-0.47048	-1.94970
H	0.66095	-0.65616	-2.53714
C	-3.31662	-1.48071	0.54796
H	-4.36637	-1.36010	0.21616
C	-3.36845	1.49522	0.37301
H	-3.37392	1.42613	1.47839
C	-4.82136	1.49323	-0.13302
H	-5.37976	0.59822	0.18860
H	-5.36480	2.37608	0.25126
H	-4.86210	1.53936	-1.23546
C	-2.60584	-0.11273	-2.02814
H	-2.67141	0.93441	-2.37406
H	-3.55398	-0.61794	-2.28306
C	-3.25857	-1.47282	2.08639
H	-3.70488	-0.56297	2.52322
H	-3.80900	-2.33910	2.49680
H	-2.21111	-1.54578	2.42993
C	-1.38711	-0.79786	-2.67611
H	-1.32078	-0.47969	-3.73956
H	-1.57168	-1.89794	-2.70514
C	-2.76475	-2.80465	-0.01094
H	-1.69553	-2.91881	0.24047
H	-3.31110	-3.66128	0.42490
H	-2.86338	-2.86777	-1.10746
C	-2.62869	2.78950	-0.01290
H	-2.57298	2.91316	-1.10940
H	-3.15549	3.67283	0.39223
H	-1.59620	2.78944	0.37683

(ii) B3LYP Optimisation

2 (singlet)

E_{SCF} = -850.213690416
G = -849.746300
E_{corr} = -1520.31556296

59

Ru	0.00000	0.00000	0.00000
P	-0.81229	0.52175	2.13139
N	-1.48255	1.12922	-0.55287
H	-1.67919	1.33704	-1.52878
C	0.07583	1.81199	3.19979
H	-0.57715	2.04432	4.05090
C	-1.25696	-0.82919	3.39130
H	-0.27826	-1.20240	3.72248
C	-2.03441	-0.34503	4.62403
H	-1.48784	0.40996	5.19640
H	-2.23536	-1.18502	5.30018
H	-3.00317	0.08259	4.34239
C	-2.46583	1.31714	1.71930
H	-3.20700	0.51287	1.76521
H	-2.75471	2.07916	2.45070
C	1.40602	1.25146	3.72569
H	1.26539	0.38556	4.38093
H	1.93972	2.01512	4.30403
H	2.05242	0.94969	2.89378
C	-2.41407	1.88666	0.29349
H	-3.42640	1.87349	-0.13953
H	-2.11345	2.94652	0.33200
C	0.30917	3.10048	2.39718
H	0.90198	2.89624	1.49967
H	0.84925	3.83382	3.00867
H	-0.63029	3.56368	2.08027
C	-1.98012	-1.99128	2.69256
H	-2.98338	-1.69929	2.36151
H	-2.09849	-2.83406	3.38449
H	-1.42738	-2.33145	1.81277
P	0.81229	-0.52175	-2.13139
N	1.48255	-1.12922	0.55287

H	1.67919	-1.33704	1.52878
C	-0.07583	-1.81199	-3.19979
H	0.57715	-2.04432	-4.05090
C	1.25696	0.82919	-3.39130
H	0.27826	1.20240	-3.72248
C	2.03441	0.34503	-4.62403
H	1.48784	-0.40996	-5.19640
H	2.23536	1.18502	-5.30018
H	3.00317	-0.08259	-4.34239
C	2.46583	-1.31714	-1.71930
H	3.20700	-0.51287	-1.76521
H	2.75471	-2.07916	-2.45070
C	-1.40602	-1.25146	-3.72569
H	-1.26539	-0.38556	-4.38093
H	-1.93972	-2.01512	-4.30403
H	-2.05242	-0.94969	-2.89378
C	2.41407	-1.88666	-0.29349
H	3.42640	-1.87349	0.13953
H	2.11345	-2.94652	-0.33200
C	-0.30917	-3.10048	-2.39718
H	-0.90198	-2.89624	-1.49967
H	-0.84925	-3.83382	-3.00867
H	0.63029	-3.56368	-2.08027
C	1.98012	1.99128	-2.69256
H	2.98338	1.69929	-2.36151
H	2.09849	2.83406	-3.38449
H	1.42738	2.33145	-1.81277

2 (triplet)

E_{SCF} = -850.195744206

G = -849.732262

E_{corr} = -1520.29666515

59

Ru	0.00000	0.00000	0.00000
P	-0.83303	0.54324	2.13816
N	-1.62762	1.07412	-0.56225
H	-1.82572	1.29001	-1.53357
C	0.07730	1.82626	3.19184
H	-0.57844	2.08739	4.03247
C	-1.25452	-0.82113	3.38566
H	-0.27253	-1.17092	3.72987
C	-2.06367	-0.35481	4.60459
H	-1.55043	0.42575	5.17386
H	-2.24044	-1.19473	5.28732
H	-3.04372	0.03468	4.30823
C	-2.49002	1.33138	1.73516
H	-3.22574	0.52067	1.76744
H	-2.78232	2.08132	2.47823
C	1.39171	1.24688	3.73740
H	1.22690	0.40775	4.42052
H	1.94386	2.01528	4.29147
H	2.03136	0.89955	2.91809
C	-2.43694	1.91599	0.31318
H	-3.46870	2.00759	-0.06459
H	-2.05181	2.95166	0.37512
C	0.34432	3.09620	2.36960
H	0.96315	2.87259	1.49374
H	0.87897	3.83466	2.97912
H	-0.58000	3.56269	2.01700
C	-1.93767	-1.99763	2.67098
H	-2.92725	-1.72059	2.29053
H	-2.07746	-2.83370	3.36663
H	-1.34034	-2.35060	1.82520
P	0.83303	-0.54324	-2.13816
N	1.62762	-1.07412	0.56225
H	1.82572	-1.29001	1.53357
C	-0.07730	-1.82626	-3.19184
H	0.57844	-2.08739	-4.03247
C	1.25452	0.82113	-3.38566
H	0.27253	1.17092	-3.72987
C	2.06367	0.35481	-4.60459
H	1.55043	-0.42575	-5.17386
H	2.24044	1.19473	-5.28732
H	3.04372	-0.03468	-4.30823
C	2.49002	-1.33138	-1.73516
H	3.22574	-0.52067	-1.76744
H	2.78232	-2.08132	-2.47823
C	-1.39171	-1.24688	-3.73740
H	-1.22690	-0.40775	-4.42052
H	-1.94386	-2.01528	-4.29147
H	-2.03136	-0.89955	-2.91809
C	2.43694	-1.91599	-0.31318
H	3.46870	-2.00759	0.06459
H	2.05181	-2.95166	-0.37512
C	-0.34432	-3.09620	-2.36960
H	-0.96315	-2.87259	-1.49374
H	-0.87897	-3.83466	-2.97912
H	0.58000	-3.56269	-2.01700
C	1.93767	1.99763	-2.67098
H	2.92725	1.72059	-2.29053
H	2.07746	2.83370	-3.36663
H	1.34034	2.35060	-1.82520

References

1. A. B. Pangborn, M. A. Giardello, R. H. Grubbs, R. K. Rosen and F. J. Timmers, *Organometallics*, 1996, **15**, 1518-1520.
2. Y. Yamamoto, K. Miyamoto, J. Umeda, Y. Nakatani, T. Yamamoto and N. Miyaura, *J.Organomet. Chem.*, 2006, **691**, 4909-4917.
3. C. N. Brodie, T. M. Boyd, L. Sotorrios, D. E. Ryan, E. Magee, S. Huband, J. S. Town, G. C. Lloyd-Jones, D. M. Haddleton, S. A. Macgregor and A. S. Weller, *J. Am. Chem. Soc.*, 2021, **143**, 21010-21023.
4. T. M. Boyd, K. A. Andrea, K. Baston, A. Johnson, D. E. Ryan and A. S. Weller, *Chem Commun.*, 2020, **56**, 482-485.
5. W. Jia, X. Chen, R. Guo, C. Sui-Seng, D. Amoroso, A. J. Lough and K. Abdur-Rashid, *Dalton. Trans.*, 2009, 8301-8307.
6. M. O. Albers, T. V. Ashworth, H. E. Oosthuizen, E. Singleton, J. S. Merola and R. T. Kacmarcik, in *Inorg. Synth.*, 1989, 68-77.
7. D. E. Prokopchuk, A. Collado, A. J. Lough and R. H. Morris, *Dalton Trans*, 2013, **42**, 10214-10220.
8. J. Cosier and A. M. Glazer, *J. Appl. Crystallogr.*, 1986, **19**, 105-107.
9. G. M. Sheldrick, *Acta. Crystallogr. C Struct. Chem.*, 2015, **71**, 3-8.
10. G. M. Sheldrick, *Acta. Crystallogr. A*, 2008, **64**, 112-122.
11. O. V. Dolomanov, L. J. Bourhis, R. J. Gildea, J. A. K. Howard and H. Puschmann, *J. Appl. Crystallogr.*, 2009, **42**, 339-341.
12. G. W. T. M. J. Frisch, H. B. Schlegel, G. E. Scuseria, M. A. Robb, J. R. Cheeseman, G. Scalmani, V. Barone, G. A. Petersson, H. Nakatsuji, X. Li, M. Caricato, A. V. Marenich, J. Bloino, B. G. Janesko, R. Gomperts, B. Mennucci, H. P. Hratchian, J. V. Ortiz, A. F. Izmaylov, J. L. Sonnenberg, D. Williams-Young, F. Ding, F. Lipparini, F. Egidi, J. Goings, B. Peng, A. Petrone, T. Henderson, D. Ranasinghe, V. G. Zakrzewski, J. Gao, N. Rega, G. Zheng, W. Liang, M. Hada, M. Ehara, K. Toyota, R. Fukuda, J. Hasegawa, M. Ishida, T. Nakajima, Y. Honda, O. Kitao, H. Nakai, T. Vreven, K. Throssell, J. J. A. Montgomery, J. E. Peralta, F. Ogliaro, M. J. Bearpark, J. J. Heyd, E. N. Brothers, K. N. Kudin, V. N. Staroverov, T. A. Keith, R. Kobayashi, J. Normand, K. Raghavachari, A. P. Rendell, J. C. Burant, S. S. Iyengar, J. Tomasi, M. Cossi, J. M. Millam, M. Klene, C. Adamo, R. Cammi, J. W. Ochterski, R. L. Martin, K. Morokuma, O. Farkas, J. B. Foresman, D. J. Fox. Gaussian, Inc., Wallingford CT (2016) GaussView 5.0. Wallingford, E.U.A.
13. D. Andrae, U. Huermann, M. Dolg, H. Stoll and H. Preu, *Theoretica. Chimica. Acta.*, 1990, **77**, 123-141.
14. A. Höllwarth, M. Böhme, S. Dapprich, A. W. Ehlers, A. Gobbi, V. Jonas, K. F. Köhler, R. Stegmann, A. Veldkamp and G. Frenking, *Chem. Phys. Lett.*, 1993, **208**, 237-240.
15. P. C. Hariharan and J. A. Pople, *Theoretica. Chimica. Acta.*, 1973, **28**, 213-222.
16. W. J. Hehre, R. Ditchfield and J. A. Pople, *J. of Chem. Phys.*, 1972, **56**, 2257-2261.
17. A. D. Becke, *Phys. Rev. A Gen. Phys.*, 1988, **38**, 3098-3100.
18. J. P. Perdew, *Phys. Rev. B Condens. Matter.*, 1986, **33**, 8822-8824.
19. A. D. Becke, *J. Chem.l Phys.*, 1993, **98**, 5648-5652.
20. F. Weigend, *Phys. Chem. Chem. Phys.*, 2006, **8**, 1057-1065.
21. F. Weigend and R. Ahlrichs, *Phys. Chem. Chem. Phys.*, 2005, **7**, 3297-3305.

22. J. Tomasi, B. Mennucci and R. Cammi, *Chem. Rev.*, 2005, **105**, 2999-3093.
23. S. Grimme, J. Antony, S. Ehrlich and H. Krieg, *J. Chem. Phys.*, 2010, **132**, 154104.
24. S. Grimme, S. Ehrlich and L. Goerigk, *J. Comput. Chem.*, 2011, **32**, 1456-1465.
25. T. Yanai, D. P. Tew and N. C. Handy, *Chem. Phys. Lett.*, 2004, **393**, 51-57.
26. Chemcraft 1.8, https://www.chemcraftprog.com

Appendix

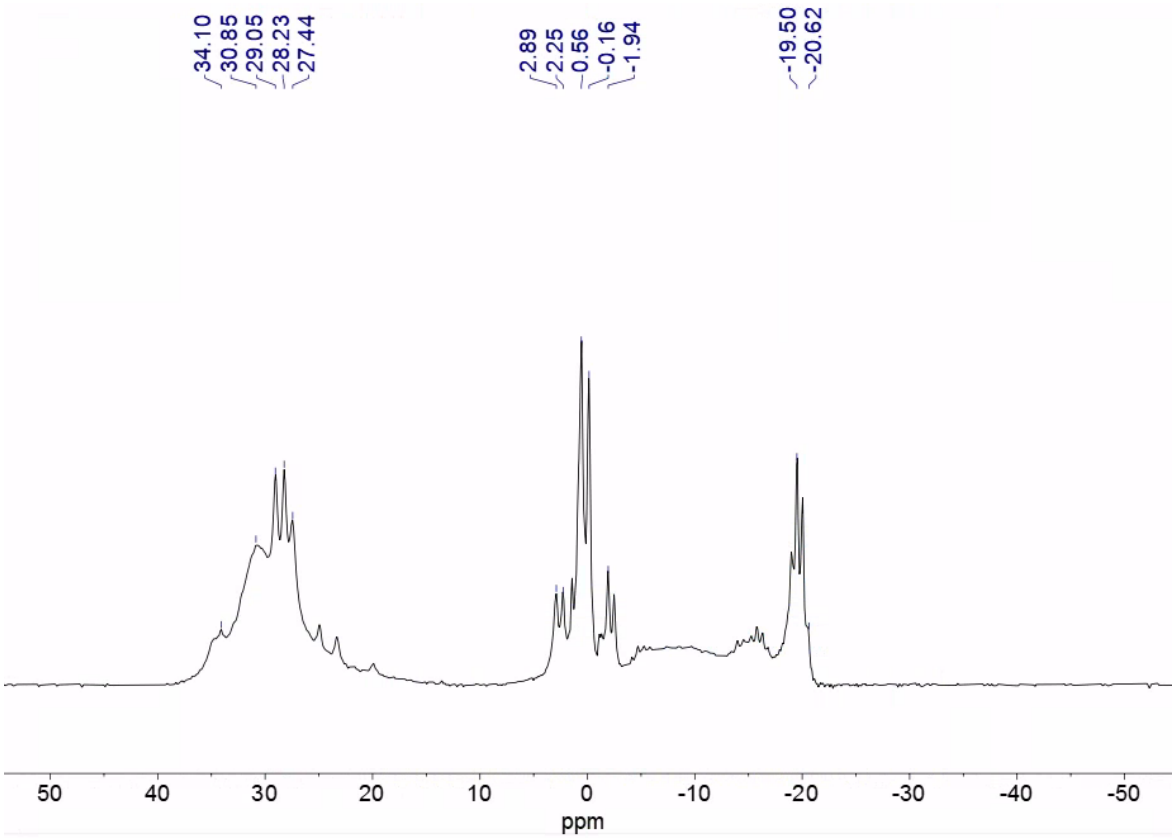

Figure S1 In-situ ^{11}B NMR spectrum from the unselective dehydrocoupling of $(H_2BNHMe)_n$ (1 mol dm^{-3} effective in THF) by **8** (0.33 mol%), with 30 equivalents of ^{t}BuOK added. A mixture of dehydrocoupled products is observed.

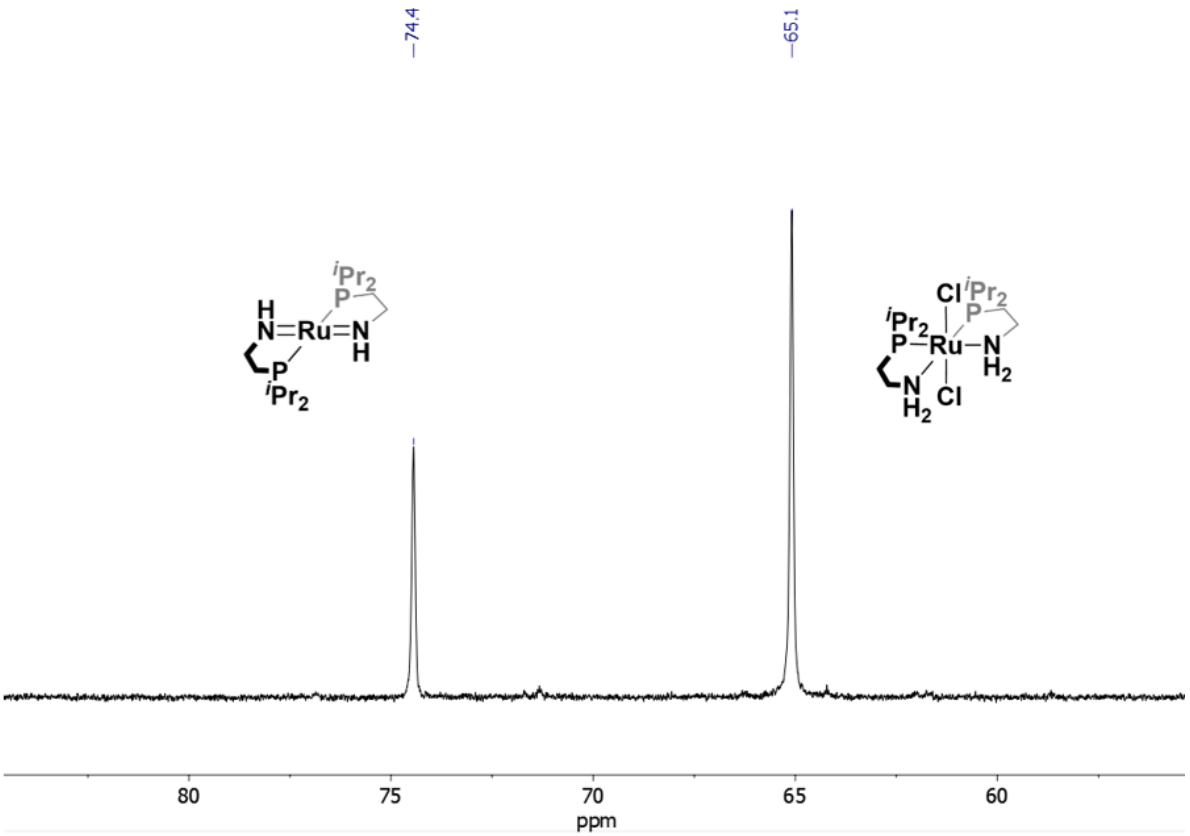

Figure S2 In-situ $^{31}P\{^{1}H\}$ NMR of the reaction between **8** and 1 eq. of *t*BuOK showing only **9** and unreacted **8**. Recorded in THF-H_8 at 298 K.

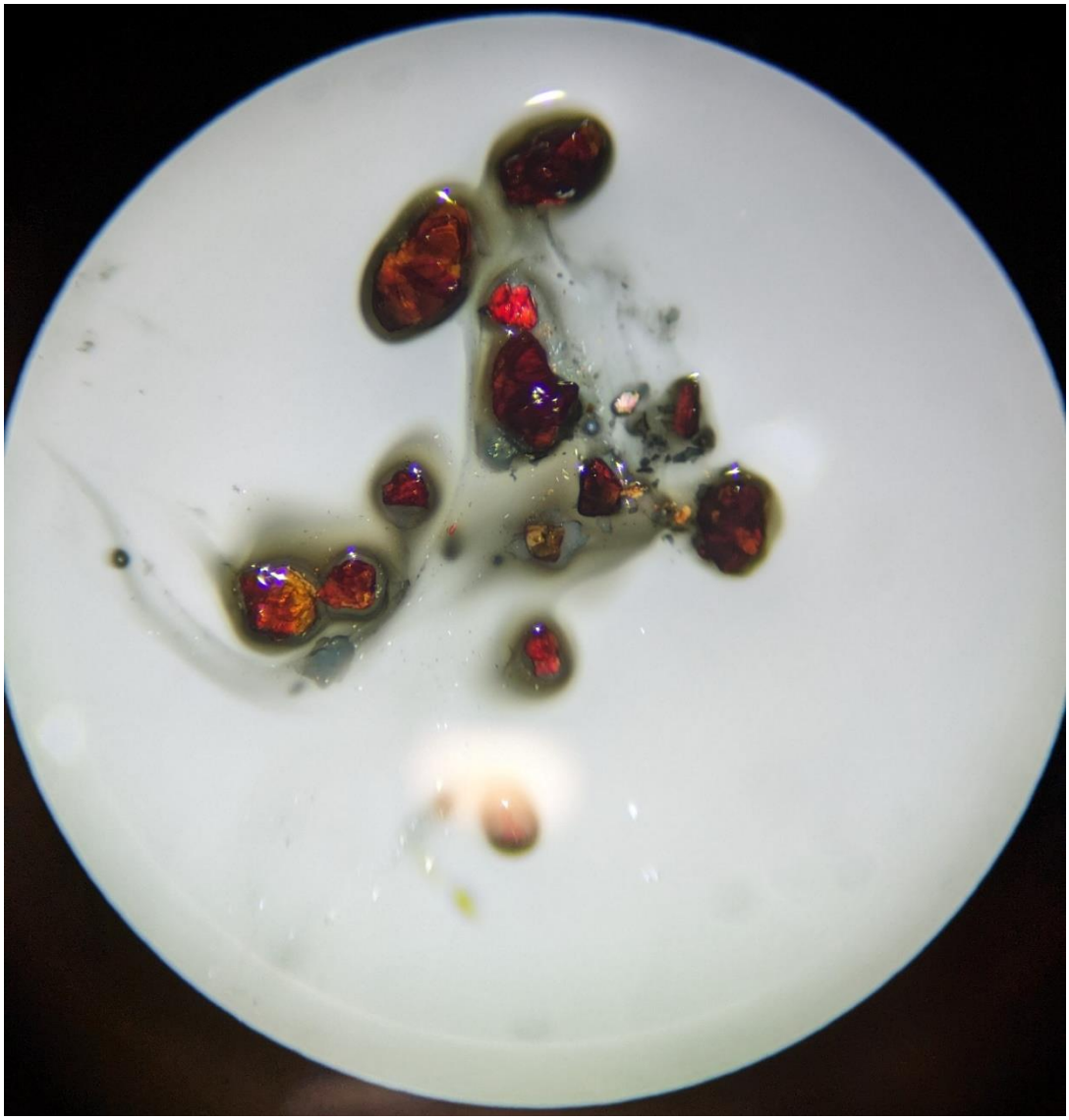

Figure S3. Crystals of pink *P,P-trans*-Ru(^{i}Pr$_2$PCH$_2$CH$_2$NH)$_2$ (**9**) decomposing under Fombulin oil and argon flow as seen under a microscope at 50x magnification

Figure S4. Fragments of $(H_2BNH^nPr)_n$ film obtained by evaporation of the toluene reaction solvent used in the dehydropolymerisation of $H_3B{\cdot}NH_2{}^nPr$ with **8** (0.5 mol%, activated with 0.05 mol dm^{-3} of NH_2Me).

Chapter 2 organometallic species index

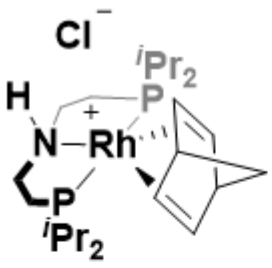

1

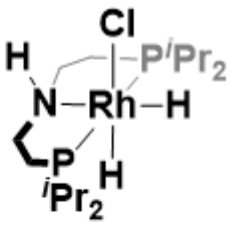

2

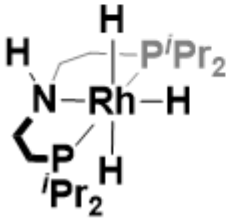

3

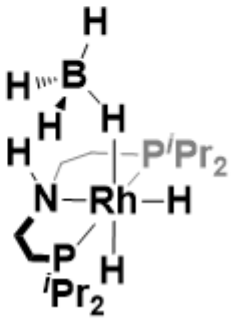

4

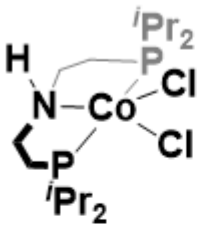

5

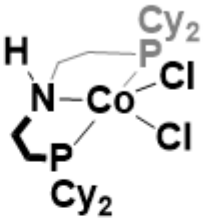

6

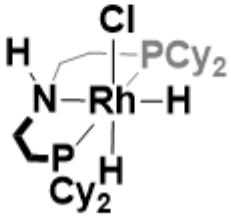

7

Chapter 3 and 4 organometallic species index

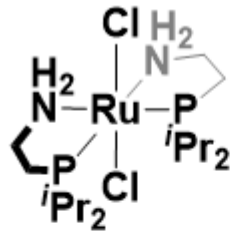

8

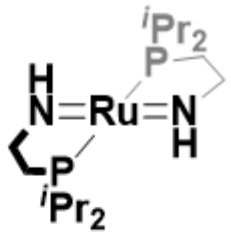

9

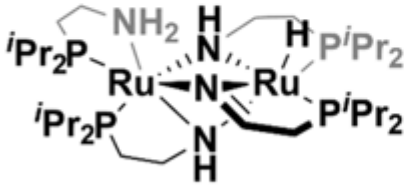

10

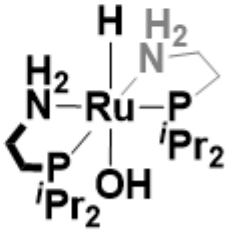

11

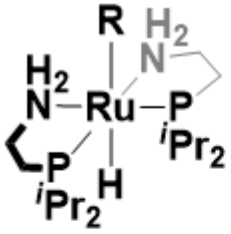

12

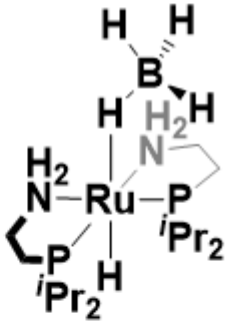

13

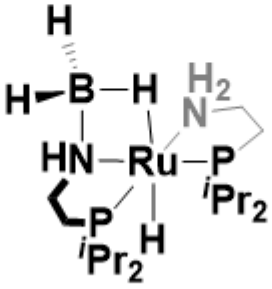

14